Vulnerability Assessment of Existing Buildings and Structures

Amirhosein Shabani

Dissertation for the degree of Philosophiae Doctor (PhD)

Department of Built Environment

Faculty of Technology, Art and Design

OsloMet – Oslo Metropolitan University

Autumn 2023

OsloMet Avhandling 2023 nr 34

ISSN 2535-471X (trykt)
ISSN ISSN 2535-5414 (PDF)

ISBN 978-82-8364-519-4 (trykt)
ISBN 978-82-8364-578-1 (PDF)

OsloMet – storbyuniversitetet
Universitetsbiblioteket
Skriftserien
St. Olavs plass 4,
0130 Oslo,
Telefon (47) 64 84 90 00

Postadresse:
Postboks 4, St. Olavs plass
0130 Oslo

Trykket hos Byråservice

Trykket på Scandia 2000 white, 80 gram på materiesider/200 gram på coveret

Preface

I am pleased to submit this PhD thesis in fulfillment of the requirements for the degree of Doctor of Philosophy at the Department of Built Environment of Oslo Metropolitan University. This thesis represents the culmination of my research at Oslo Metropolitan University, as a part of Hyperion project. Hyperion has received funding from the European Union's Framework Programme for Research and Innovation (Horizon 2020) under grant agreement No 821054. The contents of this thesis are the sole responsibility of Oslo Metropolitan University, which is responsible for work package 5, Task 2 of the project and do not necessarily reflect the opinion of the European Union.

The aim of the project is to deliver an integrated resilience assessment platform, addressing multi-hazard risk understanding, better preparedness, faster, adapted, and efficient response, and sustainable reconstruction of historic areas and the funding provided by the European Union has been instrumental in enabling this research and supporting my academic journey.

This study presents original insights into structural engineering, obtained through several years of research. Throughout the project, I received invaluable guidance and support from my supervisors, Dr. Mahdi Kioumarsi and Dr. Vagelis Plevris, who provided constructive feedback and expertise that helped me shape the research and improve the quality of the thesis. The study also benefited from the input and feedback of experts and colleagues from the academic community, including project partners from various universities and research institutions across Europe.

Amirhosein Shabani

April 2023

Oslo, Norway

Acknowledgement

This is an opportunity to express heartfelt appreciation and gratitude to all those who have supported and encouraged throughout my academic pursuit. Without their help, guidance, and support, I would not have been able to reach to this milestone.

I would like to express my deepest gratitude to my main supervisor Dr. Mahdi Kioumarsi for his patience, invaluable guidance, unwavering support, and insightful feedback throughout my PhD journey. I would also like to thank my second supervisor Dr. Vagelis Plevris for his valuable contributions and feedback to this research.

I would also like to thank my colleagues and friends for their support and encouragement. Their conversations, suggestions, and constructive criticism have helped me in refining my ideas and concepts. I am grateful for their friendship and the positive energy they brought to my academic life.

I am deeply indebted to my parents, Esfandiar and Molood and my little sister, Mahgol for their unconditional love and support throughout my academic journey. Their belief in me, encouragement, and sacrifices have been the driving force behind my success. I am grateful for their unwavering support, which has been a constant source of motivation and inspiration.

My beloved Jasmin has played an instrumental role in my success, providing me with love, support, and encouragement throughout my doctoral studies. Her belief in me, patience, and understanding have been instrumental in my success.

Last but not least, I want to thank me for believing in me. I want to thank me for doing all this hard work. I want to thank me for never quitting. I am proud of what I have accomplished, and I look forward to applying the knowledge and skills gained from this experience in my future endeavors.

Abstract

Vulnerability assessment of cultural heritage assets and unreinforced masonry buildings is important for providing a resilient framework and sustainable reconstruction proposals. Owing to the vulnerability of unreinforced masonry structures to earthquakes, different seismic vulnerability assessment methodologies have been developed and can be classified, based on the scale of application, into: 1) single structure scale 2) building stock scale, and 3) large scale. The thesis was mainly aimed at improving the current methodologies for seismic vulnerability assessment of historical constructions and proposing efficient methods using modern technologies.

First, topics related to simplified analytical methods for large-scale seismic vulnerability assessments were reviewed and investigated. Simplified analytical methods are presented for calculating the initial in-plane and maximum lateral strengths of unreinforced masonry walls with openings.

The seismic vulnerability of unreinforced masonry buildings at a single-structure scale was investigated using equivalent frame methods. A new macroelement and an open-source graphical user interface were developed. The efficiencies of the different equivalent frame methods were investigated by comparing the results of the nonlinear analysis of various case studies. Moreover, the effect of pulse-like near-field ground motions on the seismic behavior of low-rise unreinforced masonry buildings was evaluated using the proposed macroelement.

Finally, the seismic vulnerability assessment of cultural heritage assets, at a single structure scale, using the continuum homogeneous method, was evaluated by emphasizing model calibration based on operational modal analysis and the effect of soil-structure interaction. Two methodologies were proposed for deriving the simulation-based digital twins of historic structures and applied to two case studies. The application of different optimal sensor placement techniques for detecting the optimized location of accelerometer sensors for ambient vibration testing was explored. Furthermore, the effect of pulse-like near-field excitations on the seismic behavior of a masonry arch bridge was studied.

Sammendrag

Sårbarhetsvurdering av kulturminner og uarmerte murbygninger som er utbredt i historiske områder er viktig for å gi et robust rammeverk og forslag til bærekraftig gjenoppbygging. På grunn av sårbarheten til uarmerte mur konstruksjoner for jordskjelv, ble forskjellige metoder for vurdering av seismisk sårbarhet utviklet og kan klassifiseres basert på skalaen til applikasjonen i 1-enkeltstrukturskala 2- bygningsmasseskala og 3- storskala. Hovedmålet med denne doktorgradsavhandlingen er å forbedre dagens metodikk for seismisk sårbarhetsvurdering av historiske konstruksjoner og foreslå effektive metoder ved bruk av moderne teknologi.

For det første er temaene knyttet til de forenklede analysemetodene for seismisk sårbarhetsvurdering i stor skala gjennomgått og undersøkt. Det ble presentert forenklede analytiske metoder for å beregne den innledende i-planet og maksimal side styrke til uarmerte murvegger med åpninger.

Seismisk sårbarhet av uarmerte murbygninger i en enkelt strukturskala er undersøkt ved bruk av tilsvarende rammemetoder. Et nytt makroelement ble utviklet, og et grafisk brukergrensesnitt med åpen kildekode ble laget. Effektiviteten til ulike ekvivalente rammemetoder har blitt undersøkt ved å sammenligne resultatene fra den ikke-lineære analysen av ulike casestudier. Dessuten ble effekten av pulslignende nærfelt-bakkebevegelser på den seismiske oppførselen til lave, uarmerte murbygninger evaluert ved hjelp av det foreslåtte makroelementet.

Til slutt ble seismisk sårbarhetsvurdering av kulturminner i en enkelt strukturskala ved bruk av kontinuum homogen metode evaluert ved å vektlegge modellkalibrering basert på operasjonell modal analyse og effekten av jord-struktur interaksjon. To metoder for å utlede de simuleringsbaserte digitale tvillingene til historiske konstruksjoner ble foreslått og brukt på to casestudier. Anvendelsen av forskjellige optimale sensorplasseringsteknikker for å oppdage den optimaliserte plasseringen av akselerometersensorene for å utføre omgivelsesvibrasjonstesting ble utforsket. Videre ble effekten av pulslignende nærfelteksitasjoner på den seismiske oppførselen til en mur buebro studert.

Table of Contents

List of figures

List of acronyms

Acronym	Definition
2D	Two dimensional
3D	Three dimensional
AAL	Average annual loss
AVT	Ambient vibration test
CAD	Computer-aided design
CHM	Continuum homogeneous method
CSM	Composite spring method
DEM	Discrete element method
DM-MVELM	Double modified multiple-vertical-line-element-model
EFM	Equivalent frame method
EHM	Effective height method
FE	Finite element
FF	Far-field
FRCM	Fiber-reinforced cementitious matrices
GUI	Graphical user interface
IDA	Incremental dynamic analysis
IIPS	Initial in-plane stiffness
IM	Intensity measure
MAC	Modal assurance criterion
MBCSM	Modified boundary conditions stiffness method
MSA	Multi stripes analysis
MVLEM	multiple-vertical-line-element-model
NF	Near-field
NPL-NF	Non-pulse-like near-field
NTHA	Nonlinear time-history analysis
OMA	Operational modal analysis
OSP	Optimal sensor placement
PBO	Polyparaphenylene benzobisoxazole
PL-NF	Pulse-like near-field
POA	Pushover analysis

SAM	Simplified analytical method
SSI	Soil-structure interaction
STEP	Standard for the exchange of product
UM	Unified method
URM	Unreinforced masonry

List of articles

List of appended papers:

I. Shabani, A., Kioumarsi, M., Zucconi, M. State of the art of simplified analytical methods for seismic vulnerability assessment of unreinforced masonry buildings, (2021), Engineering Structures, https://doi.org/10.1016/j.engstruct.2021.112280.

II. Shabani, A., Plevris, V., Kioumarsi, M. A Comparative Study on the Initial In-plane Stiffness of Masonry Walls with Openings, (2021), In Proceedings of the World Conference on Earthquake Engineering, 17WCEE, Sendai, Japan.

III. Shabani, A., Kioumarsi, M. A novel macroelement for seismic analysis of unreinforced masonry buildings based on MVLEM in OpenSees, (2022), Journal of Building Engineering, https://doi.org/10.1016/j.jobe.2022.104019.

IV. Shabani, A., Kioumarsi, M. Pros and Cons of Various Equivalent Frame Models for Nonlinear Analysis of URM Buildings, (2022), 8th European Congress on Computational Methods in Applied Sciences and Engineering (ECCOMAS 2022), Oslo, Norway

V. Shabani, A., Kioumarsi, M. Hyperomet: An OpenSees interface for nonlinear analysis of unreinforced masonry buildings, (2022), Software X, https://doi.org/10.1016/j.softx.2022.101230.

VI. Shabani, A., Zucconi, M. Kazemian, D. Kioumarsi, M. Seismic fragility analysis of low-rise unreinforced masonry buildings subjected to near- and far-field ground motions, (2023), Results in Engineering.

VII. Shabani, A., Feyzabadi, M., Kioumarsi, M. Model updating of a masonry tower based on operational modal analysis: The role of soil-structure interaction, (2022), Case Studies in Construction Materials, https://doi.org/10.1016/j.cscm.2022.e00957.

VIII. Shabani, A., Kioumarsi, M., Plevris, V. Performance-based seismic assessment of a historical masonry arch bridge: Effect of pulse-like excitations, (2023), Frontiers of Structural and Civil Engineering.

IX. Shabani, A., Kioumarsi, M. Optimal sensor placement techniques for modal identification of historical masonry structures, (2022), 23rd European Conference on Fracture, Procedia Structural Integrity, https://doi.org/10.1016/j.prostr.2022.12.018.

X. Shabani, A., Kioumarsi, M. Seismic assessment and strengthening of a historical masonry bridge considering soil-structure interaction, (2023), Engineering Structures.

Other scientific papers:

I. Shabani, A., Kioumarsi, M., Plevris, V., Stamatopoulos, H. Structural vulnerability assessment of heritage timber buildings: A methodological proposal, (2020), Forests, https://doi.org/10.3390/f11080881.

II. Shabani, A., Hosamo, H., Plevris, V., Kioumarsi, M. A Preliminary Structural Survey of Heritage Timber Log Houses in Tønsberg, Norway, (2021), 12nd International Conference on Structural Analysis of Historical (SAHC).

III. Shabani, A., Skamantzari, M., Tapinaki, S., Georgopoulos, A., Plevris, V., Kioumarsi, M. 3D simulation models for developing digital twins of heritage structures: Challenges and strategies, (2021), The 4th International Conference on Structural Integrity, Procedia Structural Integrity, https://doi.org/10.1016/j.prostr.2022.01.090.

IV. Shabani, A., Alinejad, A., Teymouri, M., Costa, A.N., Shabani, M., Kioumarsi, M. Seismic vulnerability assessment and strengthening of heritage timber buildings: A review, (2021), Buildings, https://doi.org/10.3390/buildings11120661.

V. Shabani, A., Ademi, A., Kioumarsi, M. Structural Model Updating of a Historical Stone Masonry Tower in Tønsberg, Norway, (2022), Lecture Notes in Civil Engineering, https://doi.org/10.1007/978-3-030-90788-4_45.

VI. Kioumarsi, M, Plevris, V, Shabani, A. Vulnerability assessment of cultural heritage structures (2022) 8th European Congress on Computational Methods in Applied Sciences and Engineering (ECCOMAS 2022), Oslo, Norway

VII. Kheyroddin, A., Arabsarhangi, A., Shabani, A., Kioumarsi, M. Optimal placement of coupling elements of RC shear walls using endurance time method, (2022), 23rd European Conference on Fracture, Procedia Structural Integrity, https://doi.org/10.1016/j.prostr.2022.12.026.

1 Introduction

The conservation of heritage structures is essential because of their cultural or historical value and distinct features, such as architecture, ornaments, and valuable objects they contain. Historic structures have witnessed a rich tradition of craftsmanship and structural and material knowledge [1, 2]. Therefore, the loss of cultural heritage sites is irreplaceable. Technological knowledge of heritage construction techniques helps identify the best strategies for their conservation and can be used for improving the resilience of contemporary structures [3, 4]. Timber, brick, and stone are the most conventional construction materials used in historic areas [3].

Hyperion is a European Union-funded project dedicated to improving the resilience of historic areas, cultural heritage sites, and monuments. This thesis includes project tasks related to the structural vulnerability assessment of cultural heritage assets. Figure (1) depicts some of the structures studied within the context of the project.

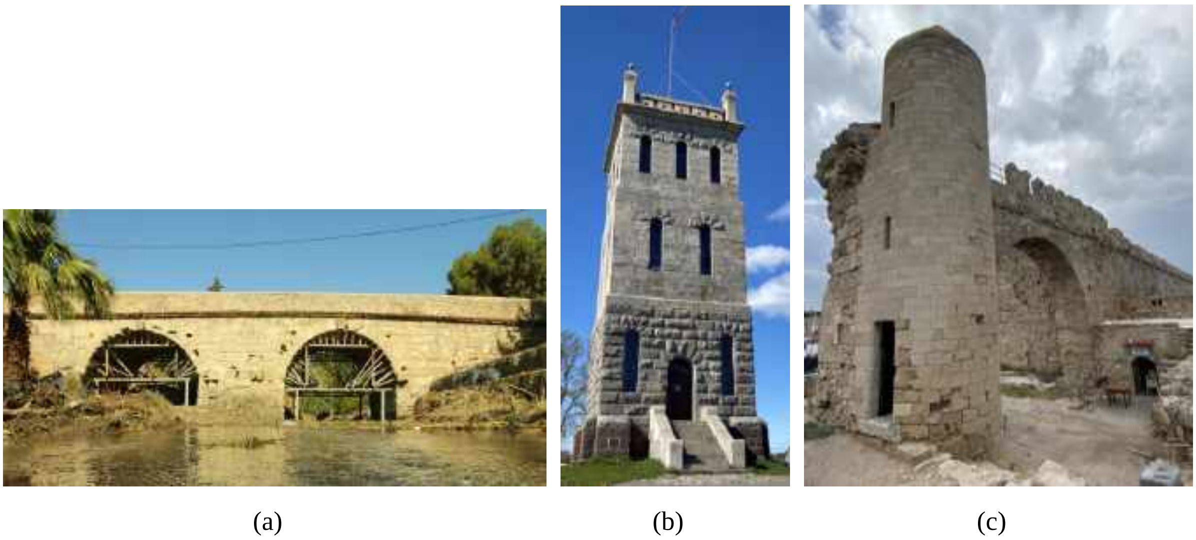
(a) (b) (c)

Figure 1: (a) Roman bridge in Rhodes, Greece, (b) Slottsfjel tower in Tønsberg, Norway, and (c) Nailac tower in Rhodes, Greece.

Historic masonry structures are vulnerable to earthquake loads because of the brittle construction material and because the structures were not designed based on current reliable design codes [5]. Moreover, their structural conditions change owing to material degradation, changes in boundary conditions, and changes in applied loads since the time they were built [6].

Unlike the number of timber buildings, the number of masonry buildings in southern European countries is higher than that in northern countries [7, 8]. Figure 2 shows the distribution of unreinforced masonry (URM) buildings [7] and cultural heritage assets in Europe. Thus, it can be concluded that URM is one of the most prevalent structural typologies.

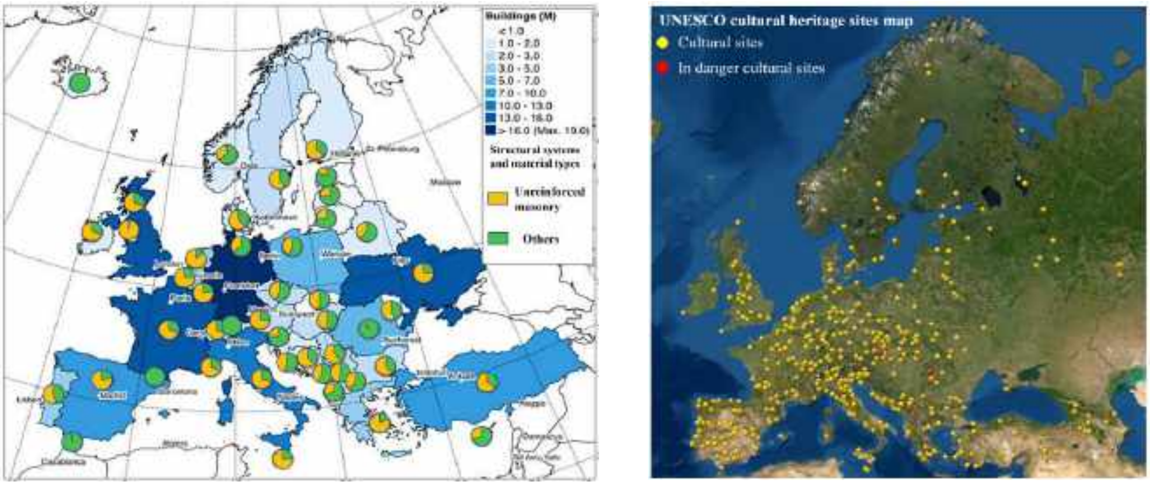

(a) (b)

Figure 2 Exposure of the distribution of (a) URM buildings [7] and (b) cultural heritage assets (adapted from https://whc.unesco.org/) in European countries.

URM is a prevalent structural system in high-seismicity zones, together with cultural heritage sites in European countries, based on the seismic hazard map illustrated in Figure 3 (a) [9] and the exposure data from Figure 2. As shown in Figure 3 (b), the average annual loss (AAL) in some parts of the high-seismicity zones is more than 5,000 USD per m^2, representing a severe economic loss for governments [10].

In addition to seismic hazards, the cultural heritage sites and URM structural typology are located in the landslides and volcanic eruption-prone areas based on the hazard maps presented in Figure 3 (c) and (d) [11, 12]. Consequently, reliable and fast vulnerability assessment methodologies at different scales must be developed for multi-hazard risk understanding, better preparedness, adapted and efficient responses, and sustainable reconstruction of historic areas.

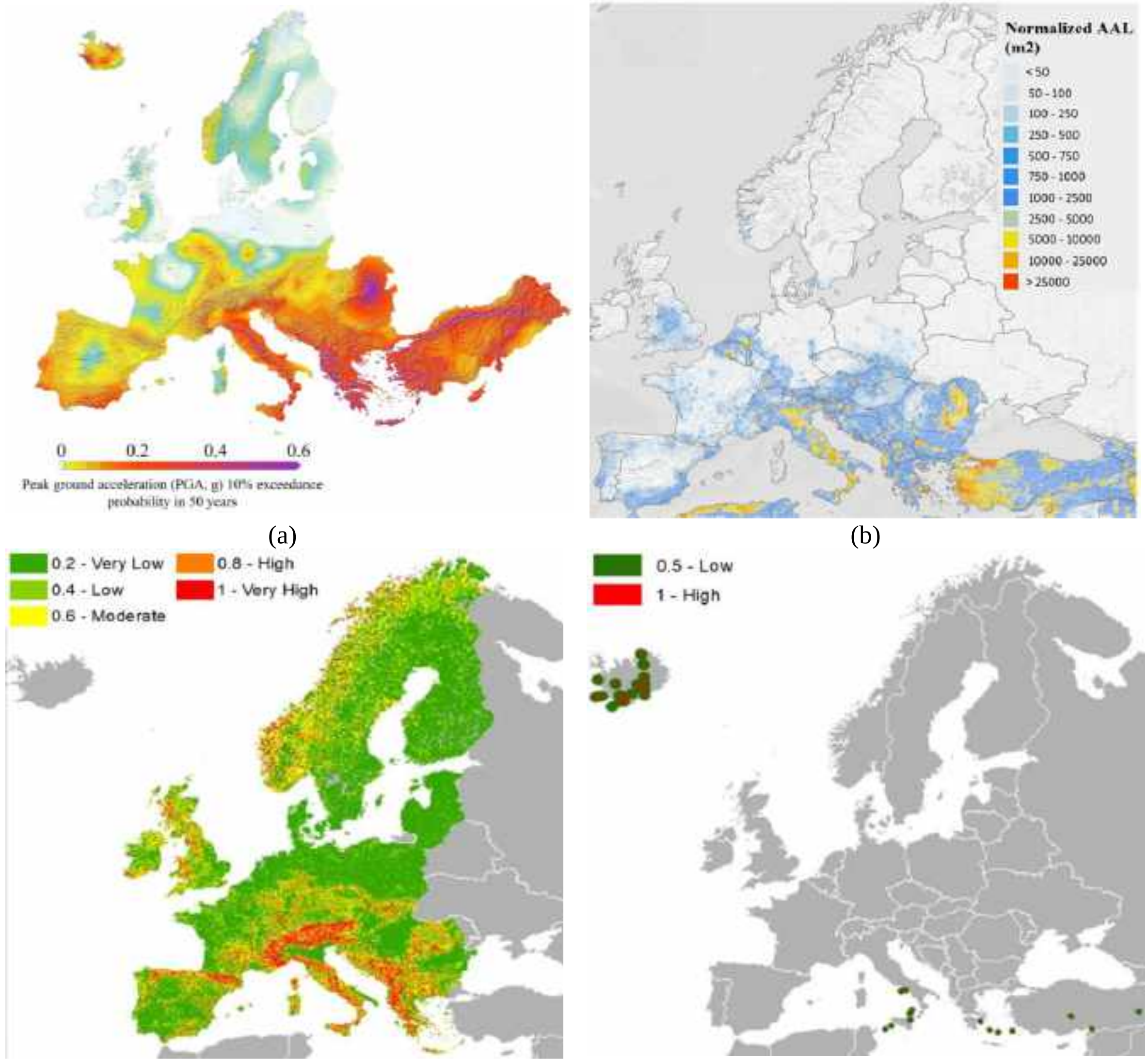

(a) (b)

(c) (d)

Figure 3: (a) seismic hazard map [9], (b) seismic risk map [13], (c) landslide susceptibility map [12], and (d) hazard map of volcanos [12] of the European countries.

Seismic vulnerability assessment methodologies can be categorized into two main groups: simplified and detailed methods. Simplified methods are associated with mechanics-based equations that evaluate the seismic vulnerability of masonry buildings. The simplified analytical methods (SAM) are subcategorized into three groups:1) collapse mechanism-based, 2) capacity spectrum-based, and 3) fully displacement-based [14]. The collapse multipliers for different probable collapse mechanisms of URM structures, subjected to lateral loadings, are obtained from the collapse-mechanism-based methods [15]. In capacity spectrum-based methods, the seismic behavior of a structure is derived from a capacity (pushover) curve [16]. The capacity curves are defined based on mechanics-based equations that depend on the material properties and geometries of the selected building typologies. Fully displacement-based methods mainly compare the displacement capacity of buildings for each damage threshold with the displacement demand to derive the possibility of crossing damage thresholds [17]. Except for some collapse mechanism-based methods [18, 19], numerical modeling of the structure in computer programs is not required, and the structures are assessed based on the collected data and equations.

However, detailed numerical modeling of structures and simulation of earthquake events are more accurate with lower uncertainty levels than SAMs. However, detailed assessment methods require significant computational effort and do not usually apply to the seismic assessment of structures on a large scale [14]. Different detailed modeling strategies can be categorized into three groups: 1) equivalent frame method (EFM), 2) continuum homogenous method (CHM), and 3) discrete element method (DEM) [20].

In EFMs, a perforated URM wall is represented by vertical (pier) and horizontal (spandrel) elements connected with rigid zones. Each element is modeled using a frame or spring element with a specific backbone curve and hysteresis rules. EFMs are rarely used for simulating cathedrals or masonry bridges but are widely used for the nonlinear dynamic analysis of masonry buildings. In EFMs, the out-of-plane mechanisms simulated using the CHM and DEM approaches are usually neglected.

In CHMs, no distinction between individual masonry units and mortar is considered, and the material properties of masonry prisms are assigned to models that can be membrane, shell, or three-dimensional (3D) solid elements [21]. However, in DEM, which is considered the most accurate methodology, the brick or stone units and mortar interfaces are modeled separately [22].

After developing an accurate model, an appropriate analysis method should be used for predicting the possible damage and structural demands when subjected to earthquake loads. Owing to the brittleness of masonry caused by its low tensile strength, existing URM buildings exhibit nonlinear behavior even in the early stages of seismic loading; therefore, nonlinear analysis is crucial for an accurate seismic vulnerability assessment methodology [23].

Nonlinear static or pushover analysis (POA) is widely used for the seismic vulnerability assessment of URM buildings [24], and different assessment methodologies based on POA results, such as the N2 method [25, 26], have been developed. POA results can highly depend on the load pattern applied to buildings, particularly the buildings with significant higher-mode effects, and may not reflect near-field velocity pulses, which can considerably influence the structural response [27]. To this end, nonlinear time history analysis (NTHA) is considered the most robust analysis method for seismic assessment [28]. It considers the earthquake record specifications, that are, the earthquake's duration, sequence of peaks, and frequency content, which may influence the structural response, which are neglected in the monotonic POA procedure [27]. However, NTHA has been scarcely utilized for the seismic vulnerability assessment of full-scale historic structures because of the need for considerable computational efforts, specialized practitioners for performing the analysis, high level of input data, and difficulty in interpreting the results [29].

Seismic fragility functions describe the conditional probability of a structure being damaged for a given intensity measure (IM). This is one of the main topics in performance-based earthquake engineering procedures that allow the prediction and evaluation of the probabilistic seismic performance of bridges and buildings in terms of loss of use, repair cost, and casualties [30, 31].

Incremental dynamic analysis (IDA) [32, 33] and multi-stripes analysis (MSA) [34] are the most well-known methods for deriving the fragility curves of structures. IDA is a parametric analysis method, in which the IM of a set of records is increased until it reaches a limit state [32]. However, in the MSA, different records are classified into groups with specific IMs [34]. Figure 4 summarizes the methodologies used for the seismic vulnerability assessment of URM structures.

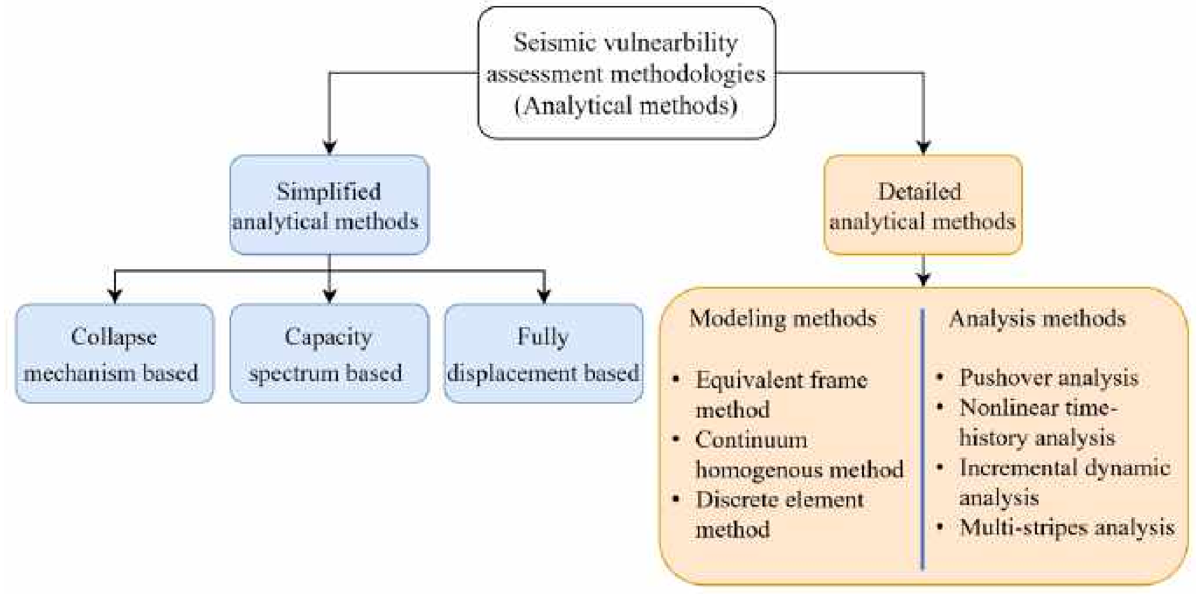

Figure 4: Schematic overview of different analytical methods for seismic vulnerability assessment of URM buildings.

Various historic URM structures with complex architectures must be preserved, similar to existing vernacular URM buildings. In recent decades, the resilience and sustainability of historic cities hosting cultural heritage sites and monuments have attracted considerable attention [1]. A robust vulnerability assessment methodology must be applied on a large scale for delivering an integrated resilience assessment platform. These methods should be user-friendly because of the presence of a large number of archetypes and the need for fast computations [14, 35].

The scale of vulnerability assessment procedures can be classified into three groups:1) single-structure scale, 2) small building stocks, and 3) large scale [35]. Figure 5 shows the classification of seismic vulnerability assessment methodologies based on the scale of the case studies.

Figure 5: Classification of different scales for seismic vulnerability assessment methodologies (adapted from Paper I).

Among the analytical methods, SAM is considered optimum for the seismic vulnerability assessment of URM buildings at a building stock or large scale [14]. Conversely, detailed analytical methods, especially EFMs, are typically used for the seismic vulnerability and damage assessments of URM buildings at a small scale [20, 36]. The CHM is considered the best for numerically modeling complex architecture or structures vulnerable to local failure mechanisms [20, 37]. Fewer input data and less computational effort are the two main advantages of CHM over DEM that encourage the use of CHM for the nonlinear analysis of full-scale masonry structures with complex architectures, such as masonry towers, bridges, cathedrals, and minarets [20, 35]. However, DEMs are typically used for the nonlinear analysis of URM structural elements for obtaining the most accurate crack patterns, crack widths, and in-plane and out-of-plane load-bearing behaviors [23].

1.1 Objectives

The main objectives of this thesis entail developing: 1) new SAMs to evaluate the seismic vulnerability of URM buildings at a large scale, 2) a novel EFM to assess the seismic vulnerability of URM buildings at a single building scale, and 3) efficient methodologies to build 3D simulation-based models and appraise the seismic vulnerability of URM structures at a single structure scale using CHM.

The sub-objectives of this thesis are as follows:

(A) Investigating the advantages and disadvantages of various SAMs and comparison of definitions of different limit states for seismic assessment of masonry buildings.

(B) Introducing accurate SAMs for estimating the initial in-plane stiffness (IIPS) and maximum lateral strength of masonry walls with openings.

(C) Developing a new macroelement that can simulate the seismic behavior of URM piers and spandrels and comparing it with existing models.

(D) Developing an open-source graphical user interface (GUI) for seismic analysis of URM buildings.

(E) Evaluating the effect of near-field excitations on the seismic demand of masonry structures.

(F) Developing a fast and accurate methodology for 3D simulation-based digital twins of historic structures.

(G) Investigating the effect of soil-structure interaction (SSI) on the optimal sensor placement (OSP) results and model updating process.

(H) Investigating the effect of SSI on the seismic behavior of masonry arch bridges.

(I) Comparing the efficiency of fiber-reinforced cementitious matrices (FRCM) systems and using improved masonry materials for strengthening a historical masonry bridge.

1.2 Thesis at a glance

The relationship between the papers published thus far and abovementioned main and sub-objectives is shown in Figure 6, which indicates objectives corresponding to each paper. Furthermore, papers that are mostly related to one of the main objectives are depicted in three colors as shown on the right side of the figure.

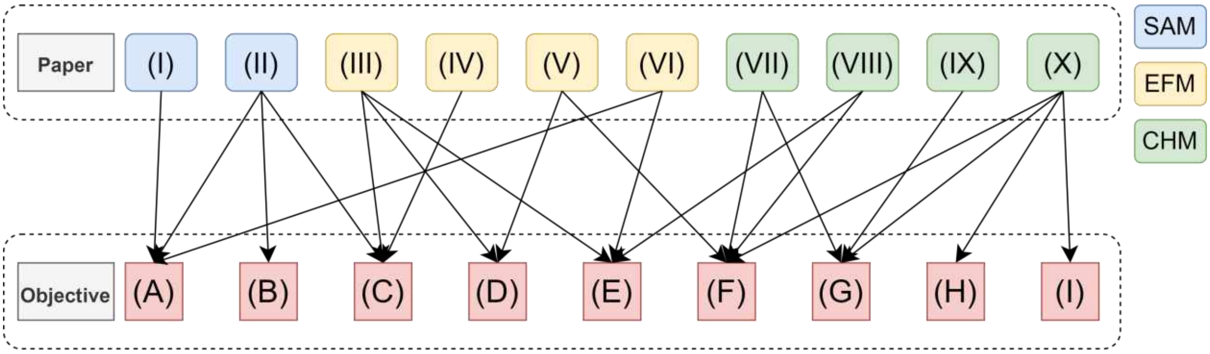

Figure 6: An overview of the relationships between the appended papers and the objectives.

This thesis presents a literature review corresponding to the three aforementioned main topics. Subsequently, the theories and methodologies used in the appended papers are briefly discussed. In the last section, the conclusions of each paper are appended and suggestions for future research are discussed.

2 Literature review

This section is dedicated to the background of the three main topics of this thesis: SAM, EFM, and CHM. First, SAMs developed for deriving the IIPS of perforated masonry walls are introduced. Subsequently, SAMs for calculating the maximum lateral strength of URM piers in a perforated wall were reviewed, emphasizing the zero-moment coefficient. In the following subsection, developed EFMs are reviewed. Finally, recent research studies related to 3D geometric documentation, finite element (FE) updating, soil-structure interaction effects, and strengthening strategies, which focus on CHM for the seismic assessment of cultural heritage assets, are reviewed. Moreover, previous studies concerning the effect of near-field ground motions on the seismic behavior of URM buildings and bridges are presented in the EFM and CHM sections, respectively.

2.1 Simplified analytical methods

Some of the SAMs are dedicated to calculating some characteristics of URM structural components without using numerical simulations [38, 39]. One of the most important parameters of the backbone curve of a URM structural component is IIPS. The IIPS of each pier of a perforated wall is calculated based on the deep beam theory by neglecting the flexibility of the two ends owing to the presence of spandrels and summing the IIPS of the piers [40]. However, this method overestimates the IIPS [40]. A similar approach was presented for calculating the IIPS of walls with regular and irregular openings; however, no validation studies have been presented [41]. The interior strip method is another SAM [42]; however, it inaccurately estimates the IIPS of perforated URM walls. In the modified boundary conditions stiffness method (MBCSM), modification factors are provided for the flexural stiffness of piers based on the mechanics-based equations for calculating the rotational deformations of the top and bottom spandrel of a pier [43]. The accuracy of the method was verified by comparing the results with FE analysis results [43, 44]. In the equivalent height method (EHM), a regression analysis based on the FE analysis of cantilever piers with different boundary conditions helps modify the pier stiffness and develop equations based on the geometry of the pier and spandrels at the two ends of the selected pier [40]. This method was validated by comparing the results with the FE analysis results of four perforated walls [40]. Paper II investigated the accuracy of the MBCSM and EHM by comparing the results of the FE analysis. In total, 15 perforated walls with regular and irregular opening configurations were modeled, and possible modifications to the SAMs were proposed.

The maximum lateral strength of URM elements is another effective parameter of the load-bearing behavior of URM buildings [45, 46]. Different equations have been presented and embedded in Eurocode 8 Part 3 [47], NTC [48], FEMA 356 [49], and FEMA 273 [50]. A zero-moment coefficient (α_0) was used for calculating the maximum lateral strength of the piers. In the aforementioned codes, values for the ideal and typical test layouts are suggested for α_0. One strategy is applying a mode proportional load pattern, based on the fundamental mode shape, to the elastic model of the wall and defining the moment distribution diagram of each pier and calculating the α_0 [51]. In Paper VI, different equations were proposed for calculating the α_0 parameters of piers of low-rise URM buildings, and the accuracy of the code-defined values was discussed.

2.2 Equivalent frame methods

The first developments in the EFM originated from the POR method, which considers a simple elastoplastic behavior for beam nonlinearity by assuming rigid spandrel and nodal zones [52]. Shear and rocking hinges were modeled separately for simulating the structural behavior of the pier and spandrel elements [53]. To investigate the axial-shear (N-V) interaction, a method implementing two rotational plastic hinges at the two ends of the beam elements was developed in SAP 2000 [51]. A two-node macroelement consisting of three parts, including the central part and two interfaces at the two ends of the element, was calibrated to account for the accurate cyclic behavior of both flexural and shear failure mechanisms and implemented in the 3Muri software package [54]. This macroelement was then modified to address the limitations, i.e., the inability to simultaneously capture both the axial and flexural stiffness of the element and neglecting the N-V interaction [55, 56]. Different methods have been proposed for considering the axial-flexural (N-M) interaction using fiber elements and shear spring elements in the middle of the macroelements [57, 58]. Double-modified multiple-vertical-line-element-model (DM-MVELM) is an EFM consisting of two modified multiple-vertical-line-element-models (MVLEMs) [59, 60] connected by a nonlinear shear spring in the middle, as presented in Paper III. This macroelement requires less computational effort than fiber-based macroelements and can be used to simulate the nonlinear behavior of spandrels. Different EFMs have been developed using nonlinear springs for simulating entire walls or structural components without utilizing frames or truss elements [41, 61, 62]. A comparative study of the efficiencies of the three EFMs is presented in Paper IV. Moreover, open-source software for the seismic analysis of URM buildings is not available. Therefore, in Paper V, a GUI was developed using the DM-MVLEM for modeling URM buildings.

Previous research on the effects of far-field (FF) and pulse-like near-field (PL-NF) ground motions on the seismic vulnerability assessment of URM buildings is limited, and one such study investigated a 3D one-story URM building [63]. The study found that the building was more susceptible to PL-NF seismic events than to FF ground motions [63]. Although some studies have examined the impact of NF ground motions on the seismic behavior of URM buildings, most have been limited to the POA of detailed numerical models and NTHA of the equivalent single-degree-of-freedom model of buildings [64, 65]. However, as is widely accepted, detailed numerical modeling approaches more accurately represent the seismic behavior of URM walls than equivalent single-degree-of-freedom models [66]. Paper VI examined the effect of PL-NF ground motion on the seismic fragility of low-rise URM buildings. In this study, nonlinear models of the walls were developed using the DM-MVLEM, and IDA was performed for deriving the fragility curves.

2.3 Continuum homogenous methods

The creation of 3D simulation-based digital twins of cultural heritage structures has recently garnered significant attention. [67]. 3D geometric documentation is important for developing simulation-based digital twins of historical constructions with complex architectures [68]. Various studies have attempted to find a fast and accurate methodology for building 3D models of historical constructions using new technologies and sensing devices, such as 3D laser scanners, digital cameras, and drones [69, 70]. Traditionally, 3D CHM-based FE models have been developed in FE analysis software packages based on the data measured and derived from geometric models. However, some semi- or fully automatic methodologies have been proposed for converting 3D point clouds of structures into CHM-based FE models [71-74]. In Paper VII, a semiautomatic methodology for developing 3D simulation-based digital twins of historic structures was proposed.

Conversely, defining accurate material properties is another step in developing a numerical model. Destructive tests cannot be used for determining the mechanical properties of historic structures [75]. Therefore, updating the model of cultural heritage structures based on the modal properties of a real structure, derived from an operational modal analysis (OMA), would be a solution. The initial stage of conducting the ambient vibration test (AVT) involves the installation of accelerometer sensors, after which a variety of OMA techniques can be applied to the data obtained from sensors for determining the natural frequencies and mode shapes of the structure under investigation [76-78]. The primary aim of the model-updating step is to minimize the differences in the dynamic characteristics of the numerical model and structure [79]. However, the cost of sensors is one of the main limitations of OMA, and various OSP methods have been proposed for detecting the best location for a limited number of sensors before performing AVTs [80-82]. The application of OSP methods for the modal identification of historic structures was investigated in Paper IX.

SSI effect is usually ignored in model updating and seismic analysis, but previous studies have shown an inevitable effect of SSI on the nonlinear dynamic analysis results of masonry structures [83-86]. Moreover, for heavy historic structures, such as masonry bridges or cathedrals, the inertial interaction effect that further deforms the soil and changes the base motion is more pronounced [84, 87]. A few studies have considered the effect of SSI on the results of the model-updating process accounting for historic masonry structures [88-91]. In Papers VII and X, the effect of considering the SSI on model updating and seismic analysis results was investigated.

Owing to the high computational effort, most numerical studies on the seismic behavior of URM bridges are limited to the POA or NTHA by applying a limited number of seismic ground motions to the structure [92-94]. Comparing the seismic responses of masonry bridges subjected to NF and FF seismic events is one of the main topics of these studies [95-97]. The findings of these studies indicated a higher vulnerability of masonry bridges to FF than to NF ground motions. In Paper VIII, masonry bridges were concluded to be more vulnerable to FF ground motions than PL-NF seismic events by applying relatively more seismic events to a masonry bridge than in previous studies. A few studies have focused on the seismic analysis of masonry bridges using IDA or MSA methods. The IDA of a masonry bridge was performed after calibrating the model based on OMA results [98]. In Paper X, MSA was performed on a calibrated bridge considering SSI effects for obtaining fragility curves.

Seismic strengthening is required for improving the resilience of cultural heritage assets after seismic damage analysis and defining the vulnerable parts [3]. The seismic strengthening of historic structures presents a complex challenge, given their significance as cultural heritage assets. Consequently, a set of guidelines must be adhered to, including principles such as authenticity, minimal intervention, compatibility, reversibility, and durability, which play a critical role in the preservation and protection of these structures [99, 100]. However, finding a strengthening strategy that satisfies all these rules is challenging. Studies have investigated the effects of different strengthening systems, including FRCM [101, 102], fiber-reinforced polymer (FRP) composites [103, 104], and steel anchorage [105], and enhancement of the existing masonry mechanical properties [106] on the seismic behavior of masonry structures. Paper X investigated the effects of different strengthening strategies on a masonry arch bridge.

3 Theoretical framework and methodology

Paper I examined the distribution of URM buildings across various high-seismic activity zones. In addition to outlining the various damage limit states for URM structures, multiple seismic vulnerability assessment methodologies and related software were explored.

In Paper II, the MBCSM and EHM were used for calculating the IIPS of a perforated URM wall, which were validated against FE analysis results. The FE modeling approach was validated against an experimental test result on a URM wall with an opening. In both methods, the piers and spandrels were converted into springs, a perforated URM wall was converted into a system of series or parallel springs, and the IIPS of the entire wall was calculated based on the series or parallel spring rules. To investigate the accuracy of the methods, the results of the EHM and MBCSM were compared with the FE analysis results of 15 URM walls with openings.

The EHM validated in Paper II was used for deriving the IIPS of URM walls for developing numerical models based on the unified method (UM) [41], which is the simplest macroelement discussed in Paper III. A perforated wall was modeled using a single UM macroelement composed of a nonlinear shear spring for simulating the lateral load-bearing behavior of the entire wall. The maximum lateral load-bearing strength was calculated from an equation with a conservative approach by assuming uncoupled piers, indicating consideration of null shear strength for the spandrels [41].

Understanding the probable failure modes of URM walls is crucial for understanding the load-bearing behavior of URM piers. The failure modes of URM walls, subjected to combined vertical and in-plane loadings, depend on different properties, such as the wall aspect ratio, mechanical properties of the masonry, and boundary conditions. The shear sliding failure mode, as depicted in Figure 7 (a), typically involves sliding along a single mortar bed joint line or stepwise sliding along the bed and head joints and is commonly observed in squat walls. The diagonal cracking failure mode involves both masonry units and mortar joints, with the formation of a diagonal crack starting from the middle of the wall and propagating toward the corners, as shown in Figure 7 (b). The rocking failure mode produces tensile or crushing cracks, or both, at the corner of the wall, as depicted in Figure 7 (c), which most frequently occurs in slender walls [45, 51].

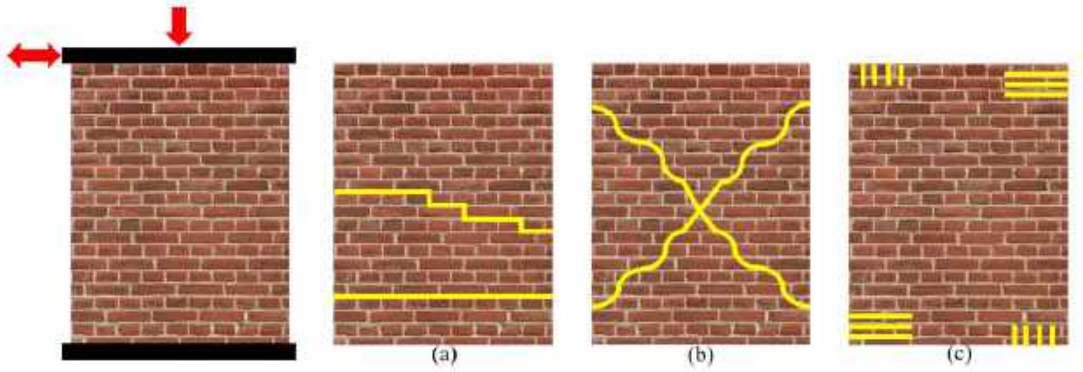

Figure 7: Crack patterns of a URM wall subjected to axial and cyclic lateral loadings for the (a) shear sliding (b) diagonal cracking, and (c) rocking failure modes (adapted from Paper III).

The composite spring method (CSM) [61] is the second method discussed and validated against the experimental test results in Paper III. In the CSM, a perforated URM wall is represented by piers and spandrels connected with rigid elements based on the Dolce method [107]. The lateral load-bearing behavior of the piers was simulated using nonlinear shear springs with a trilinear backbone curve. The spandrels were modeled using linear beam-column elements. The maximum lateral strength of the piers was defined as the minimum value of the lateral strength owing to the three aforementioned failure modes. The IIPSs of the piers were calculated based on the deep beam theory assumption by combining the shear and flexural stiffnesses of the pier with fixed-fixed boundary conditions. The IIPS and maximum lateral strength of the piers were calculated based on the height of a pier modified using the Dolce method.

A novel macroelement was proposed in Paper III based on an available element in the OpenSees library [108]. MVLEM is a macroelement model developed for modeling flexure-dominated reinforced concrete (RC) shear walls comprising a set of uniaxial nonlinear fiber elements connecting the upper and lower rigid beam elements and a nonlinear shear spring that is located at a specific height (ch) [59, 60]. Figure 8 shows the kinematics of the MVLEM element subjected to lateral and axial (compression) loadings.

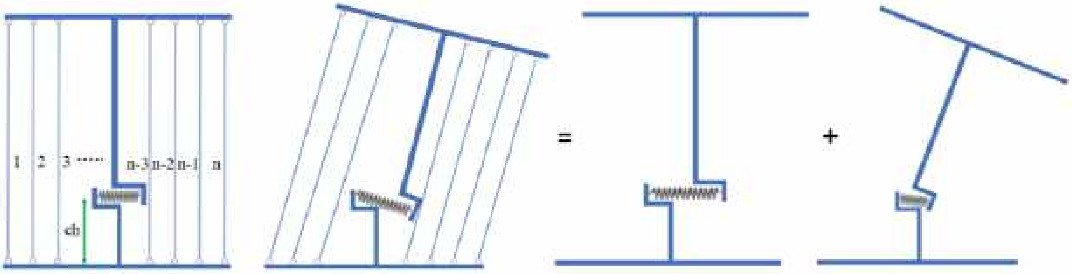

Figure 8: Kinematics of the conventional MVLEM element subjected to lateral and axial (compression) loadings (obtained from Paper III).

MVLEM elements were modified for accurately modeling the pure axial-flexural behavior of a wall and disregarding its shear behavior. The rotational center of the MVLEM element was repositioned at the end of the element, as shown in Figure 9 (a). Furthermore, the first (horizontal transition) degrees of freedom must be rigid, and all other degrees must be free. A DM-MVLEM macroelement is composed of two modified MVELM connected to a nonlinear shear spring, as illustrated in Figure 9 (b), for implementing an explicit shear behavior formulation for URM walls. A material exhibiting a masonry stress-strain curve was assigned to the fibers, and trilinear backbone curves were assigned to the material of the nonlinear shear springs. The maximum lateral strength of the pier elements can be determined as the minimum value of the maximum lateral strength owing to the shear sliding and diagonal cracking failure modes because the fibers control the rocking failure mode. The maximum lateral strength of the spandrels was determined as the minimum value of the maximum lateral strength, due to diagonal cracking, and interlocking strength at the bed joints at the intersection between the spandrel and piers. The shear stiffness of the wall, considering the deep beam theory for an element with fixed-fixed boundary conditions, was considered for deriving the trilinear backbone curve of the nonlinear shear springs.

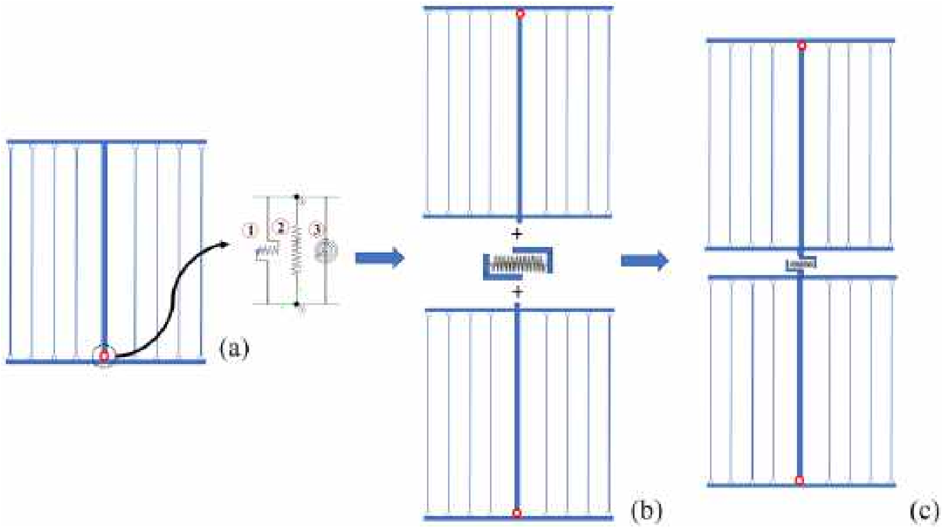

Figure 9: (a) modified MVLEM, (b) double modified MVLEM with nonlinear shear spring, (c) DM-MVLEM (adapted from Paper III)..

Paper IV focused on modeling three perforated URM walls using the UM, CSM, and DM-MVLEM approaches resulting in the development of nine distinct models. Subsequently, the POA and IDA were conducted for assessing the fragility and failure modes of the structural elements, and the resulting pushover and fragility curves were compared. Figure 10 shows the

Pavia door wall [109], a case study in Paper IV, tested by applying cyclic loadings, and the developed nonlinear models based on the UM, CSM, and DM-MVLEM methods.

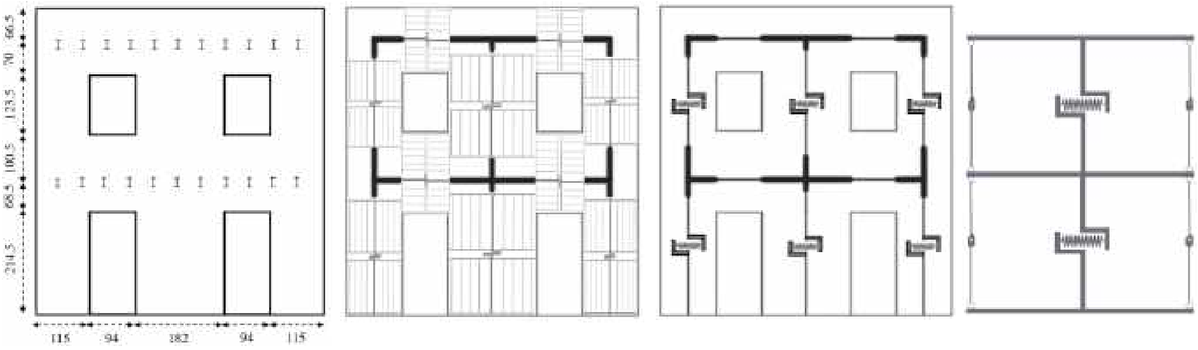

(a) (b) (c) (d)

Figure 10: (a) Pavia door wall [109] (b) DM-MVLEM (c) CSM and (d) UM models of the case study (obtained from Paper IV).

Open-source software for the nonlinear analysis of URM buildings is not available. Furthermore, the available MVLEM elements in the OpenSees library cannot be modeled horizontally for simulating URM spandrels based on DM-MVLEM [108]. Therefore, the spandrel elements should be modeled manually. Calculating the material properties of elements and assigning processes is demanding and can be affected by human error. Hyperomet, an open-source GUI for the OpenSees framework, was developed to bridge these gaps and is presented in Paper V.

Paper VI evaluated the seismic fragility of low-rise URM buildings subjected to FF and PL-NF ground motions. URM is considered the most conventional structural system for low-rise buildings. Four URM walls with a maximum of two stories were selected, and nonlinear models were used for the DM-MVLEM using the Hyperomet GUI. To obtain the maximum shear strength of the piers, the α_0 was calculated for each pier of a perforated URM wall while developing the nonlinear model. A linear static analysis was performed by applying a mass-proportional load pattern to nine case studies, and the coefficient was calculated for each pier. Subsequently, a regression analysis was performed to determine the equations for obtaining the α_0 values instead of creating linear equivalent frame models and performing a linear static analysis. Next, pushover curves were derived through nonlinear analysis, and the damage limit states were determined for each model. An IDA was then conducted by applying the FF and PL-NF ground motions to each case study. Based on the IDA results, fragility curves were developed for each damage limit state. This study examined the susceptibility of one- and two-story URM walls to FF and PL-NF seismic events by comparing the derived fragility curves.

The topic of this thesis is not limited to the numerical modeling and vulnerability assessment of URM buildings based on SAM and EFM but also includes simulations of URM structures, including bridges and towers, based on the CHM. Therefore, two methodologies were presented for creating simulation-based digital twins of masonry structures with complex architectures.

In Paper VII, a semiautomatic methodology for creating a 3D FE model of historic structures from point clouds was proposed and applied to a masonry tower called the Slottsfjel in Tønsberg, Norway. To build the 3D point clouds, the inside and outside of the tower were scanned 20 times using a 3D laser scanner. The point clouds were merged to provide 3D dense point clouds. Subsequently, a 3D model was developed based on the 3D dense point cloud file. To develop the 3D FE model of the tower, the industry foundation classes (IFC) format of the 3D model was exported and converted into the standard for the exchange of product model data (STEP) format, which is suitable for importing 3D models with solid elements in the DIANA (2020) software [110]. Imported computer-aided design (CAD) files must be repaired before generating the mesh. These files contain (unintended) small entities, small edges, duplicate curves, and surfaces, which can be removed using three tools available, and their shapes can be repaired in DIANA software [110].

Conversely, a vibration-based model updating procedure was followed using six 3-Axis MEMS accelerometers with a sampling rate of 250 Hz. The accelerometers were equipped with a global positioning system (GPS) antenna for recording time and synchronizing all data from the accelerometers based on the recorded time. After performing an AVT, operational modal analysis (OMA) was performed using three frequency-domain methods for deriving the modal properties of the tower. Finally, the model was updated using the FEMTools software package [111]. The objective of model updating is to adjust the selected material properties to reduce the weighted absolute relative difference between resonance frequencies and increase the diagonal elements of modal assurance criteria (MAC) matrix [111]. Figure 11 illustrates the methodology and software packages used at each step of developing the calibrated 3D FE model of the tower.

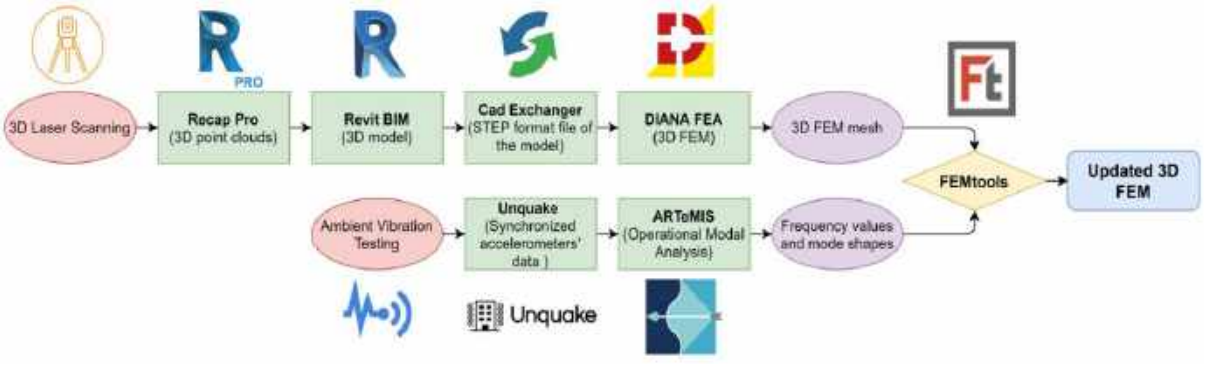

Figure 11: Methodology for constructing the 3D simulation-based digital twin of historic structures applied to the Slottsfjel tower together with utilized software packages (obtained from Paper VII).

Three FE models of the Slottsfjell tower were developed in Paper VII. The first model was the FB model with rigid boundary conditions at the base. The SM model was developed considering triaxial springs at the base of the tower for considering the SSI based on the substructure method, and in the DM model, the foundation and soil box were modeled using the direct method [84]. All three models were updated based on the first five natural frequencies derived from OMA. A linear time history was obtained by applying two seismic records to the models for comparing the structural demands.

Another approach for the 3D geometric documentation of cultural heritage assets was presented in Paper VIII and applied to developing a 3D model of the Roman Bridge on Rhodes Island, Greece. Aerial and ground images, respectively obtained using drones and cameras, were processed using image-based modeling software by filtering and reducing noise for developing a dense point cloud of the structure. In addition, 3D laser scanners were used for filling the gaps in the point clouds from digital images and providing the final dense point cloud [112, 113]. The target points were defined for the point clouds from the laser scanners and ground control points for the orientation of images using all stations. Georeferencing avoids possible errors when combining and processing datasets obtained from different instruments. Finally, the dense point cloud, 3D light model, and cross-sections were obtained from the process, and the 3D FE model of the bridge was developed based on the geometries derived from the 3D geometric documentation outcomes [68]. Figure 12 shows the 3D geometric documentation process.

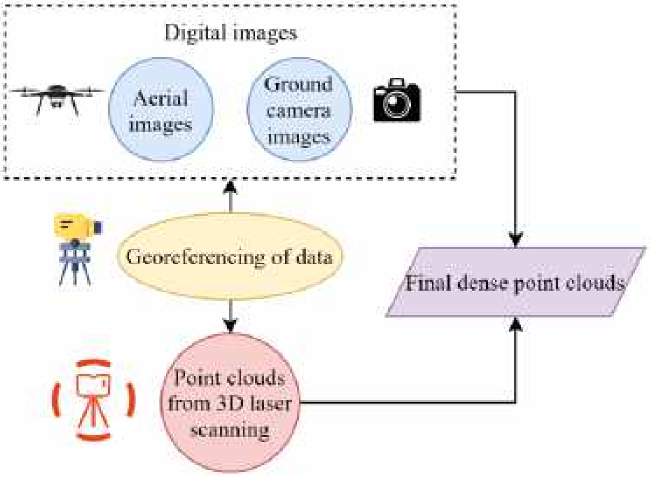

Figure 12: Methodology for obtaining the final dense point cloud of historic structures applied to the Roman bridge (obtained from Paper VIII)..

The material properties were defined using the empirical equations [114], and a 3D FE mesh was provided for further analysis. The seismic vulnerability of the Roman bridge was assessed in Paper VIII using POA for defining the limit states [115] and NTHA for deriving the structural demands. Notably, 15 seismic records were categorized into three different seismic records: 1) FF, 2) PL-NF, and 3) non-pulse-like near-field (NPL-NF) ground motions. These seismic excitations were scaled to the target spectrum with a 10 % probability of exceedance in 50 years with 475 years return period and applied to the bridge model in transverse direction [116, 117]. Furthermore, the correlation between the seismic excitation properties and seismic demand of the structure, in terms of the maximum displacement, cracked volume, and crack width, was investigated at the final time step of the analysis using linear regression analysis.

The application of OSP methods to non-updated FE models of the Slottsfjel tower and Roman bridge was investigated in Paper IX. OSP methods can be categorized into two main groups: sensor placement and sensor elimination [80]. The MAC matrix is the acceptance criterion for investigating the observability of the modes and their independence and is commonly used for mechanical and structural applications [111]. The OSP results of the Slottsfjel tower model with and without considering SSI effects were compared for investigating the effect of the SSI on the OSP analysis results. Furthermore, the most optimized locations were derived, and the best methods for checking the MAC values were determined for both case studies.

In Paper VII, a linear time history analysis was performed by neglecting the nonlinearity of the masonry, while in Paper VIII, the bridge was modeled without considering the SSI and was not calibrated based on the OMA results. To address these limitations, the Roman bridge model was modified by applying geometric details such as openings in the central pier, and the SSI effect was considered in Paper X. Furthermore, AVT was performed, and the OMA results revealed the first four natural frequency values and mode shapes of the bridge. The sensor locations were determined based on the OSP results presented in Paper IX. Subsequently, POA was performed to define the limit states of the updated model and MSA was performed to derive the fragility curves for each damage threshold based on the maximum likelihood method [118]. All the sensing devices used for creating the 3D simulation-based digital twin of the bridge are shown in Figure 13 (a), and the methodology for deriving the fragility curves is presented in Figure 13 (b).

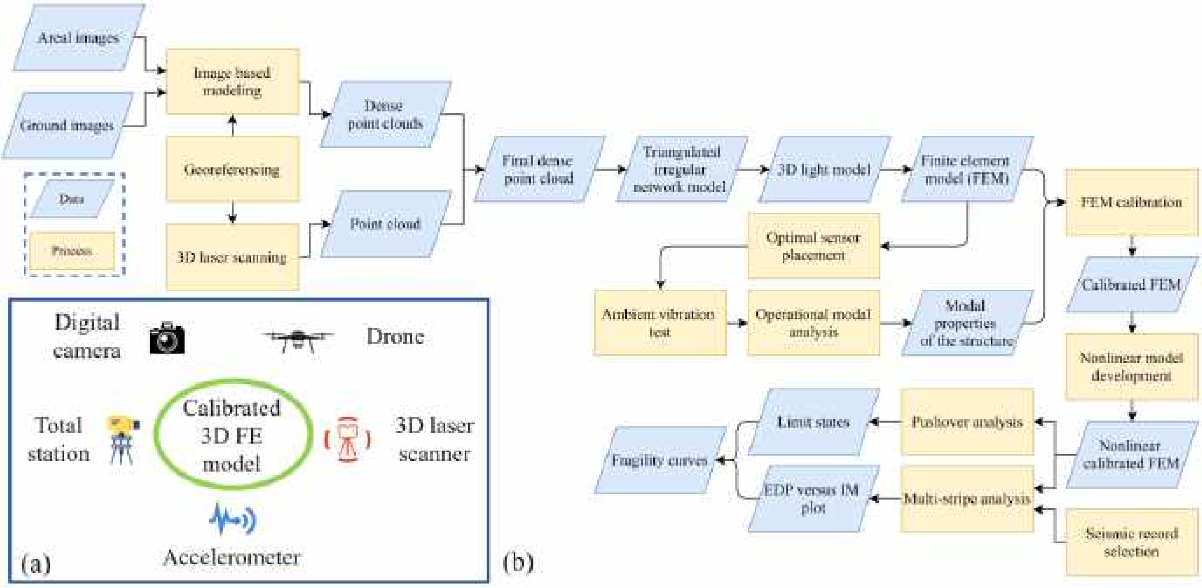

Figure 13: (a) Utilized sensing technologies for the 3D geometric documentation and (b) methodology of developing 3D simulation-based digital twins and seismic fragility of historic structures (adapted from Paper X).

To investigate the effect of SSI on model updating and seismic analysis results, two models were developed. In the fixed-based model, the SSI effects were neglected, and in the SSI model the foundations and soil media were modeled based on the direct method [84]. To perform model updating and POA, a rigid base with pinned supports was applied to the four sides of the soil. However, to perform NTHA and MSA, free-field boundary elements were utilized on the four sides of the finite soil domain [119, 120]. The soil finite domain size was decreased because of the presence of far-field elements, which led to less computational effort than in the SSI model without free-field elements. The free-field motions around the soil were converted into boundary tractions that were applied to the finite soil part. Free-field elements have dashpots to absorb the outgoing waves, which cause unrealistic effects on the main model using rigid boundary conditions [110, 119]. Figure 14 shows a schematic of a free-field boundary element.

Figure 14: Schematic representation of the free-field elements (obtained from Paper X).

After the seismic damage assessment, the most susceptible parts of the bridge were defined, and three strategies were proposed in Paper X. In all strategies, the material properties of the arches were improved using improved stone masonry with the same stone but a firmer lime mortar. Around the central pier, a depth of 50 cm was replaced with enhanced masonry in the newmat model [114]. Two other strengthening strategies covered the central pier with polyparaphenylene benzobisoxazole (PBO) and carbon FRCM systems [121]. Three FE models were developed based on the three strengthening strategies, and NTHAs were used for comparing the structural demands.

4 Discussion and conclusion

The importance of the seismic vulnerability assessment of URM buildings at different scales and understanding of different damage limit states proposed for URM buildings is highlighted in Paper I. Furthermore, the applications of each SAM are discussed.

The results of the comparative studies in Paper II, for investigating the efficiency of the SAM for deriving the IIPS of perforated masonry walls, indicated the efficiency of the EHM with R^2 of 97.16 %. Furthermore, conclusively, the MBCSM is not as accurate as the EHM, and two modifications have been proposed for improving the accuracy of this method. Initially, the stiffness of spandrels was incorporated into the formulations, which resulted in a significant improvement in the accuracy of the method, with the R^2 value increasing from 76.59% to 94.74%. Subsequently, the effect of the bending stiffness of the entire wall was considered, which further improved the R^2 value of 96.58%. Owing to these enhancements, this approach is the most accurate.

Therefore, the EHM was utilized in Paper III for calculating the IIPS of the perforated wall, modeled based on UM, which cannot predict the possible failure modes of the piers and spandrels. The cantilever idealization assumption and the use of an equation for all failure modes of masonry walls are two other weaknesses of the UM. CSM compensates for some of the weak points of UM. A comparison of the experimental test results and numerical modeling, based on the CSM, showed the accuracy of the method in predicting the structural response of the selectively tested two-story wall, called the Pavia door wall, subjected to quasi-static cyclic loadings. Although the failure modes of piers can be predicted, this method cannot predict combined shear-flexural failure modes. Furthermore, the analysis did not consider both– N-M and N-V interactions. To address the limitations of the UM and CSM and maintain simplicity in modeling, efficiency in computational efforts, and stability during nonlinear analyses, the DM-MVLEM was developed using the MVLEM element available in the OpenSees framework in Paper III. The DM-MVLEM was validated against experimental test results on two piers with different heights and failure modes: a spandrel and Pavia door wall. In Paper III, the validation of the model was not restricted solely to load-bearing behavior, but also included a comparison of the failure modes observed in the piers and spandrels between the model and test, thus demonstrating its efficacy.

The results of Paper IV show that, although the pushover and fragility curves of the Pavia door wall modeled based on the CSM and DM-MVLEM methods approximated each other, the differences were high for the model with weak spandrels. These differences were due to the assumption of linear behavior for the spandrel elements. The UM is considered to be the most conservative modeling strategy because of the null shear strength assumption of spandrels. However, the capacity curves of the UM and DM-MVLEM models of the wall with a weak spandrel were close to each other. The fragility curves derived from the UM and CSM were flatter than those derived from the DM-MVLEM because of the higher level of uncertainty. The DM-MVLEM is more accurate than the CSM in highlighting the combined flexural-shear failure modes and predicting the failure of spandrels. However, the shear failure modes can be predicted based on the CSM. Unlike the DM-MVLEM method, the UM is considered as the fastest method for performing IDA, with the highest level of uncertainty among the three modeling approaches.

The Hyperomet GUI accelerates the nonlinear modeling procedure of URM buildings based on the DM-MVLEM, as elaborated in Paper V. The GUI overcomes the limitations of DM-MVLEM modeling, including the positioning of MVLEM elements in the horizontal direction. Possible human errors were minimized by presenting calculators for deriving the IIPS based on the EHM and maximum lateral strength of the URM piers and spandrels. Furthermore, the computationally demanding IDA was automated using a hunt-and-fill algorithm, as discussed in Paper V. The functionalities of the Hyperomet are summarized in Figure 15.

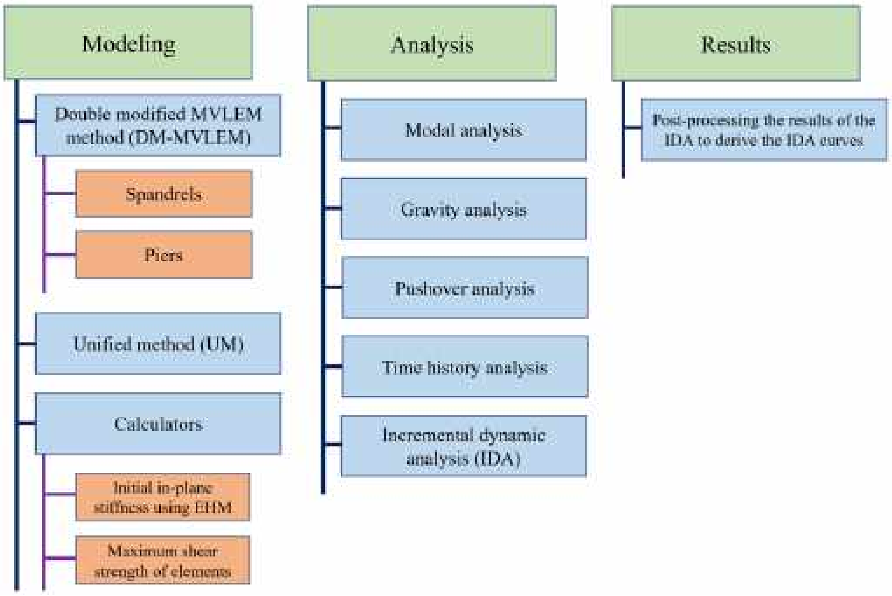

Figure 15: Functionalities of the Hyperomet GUI that are divided into three main sections: modeling, analysis, and the results (obtained from Paper V).

In Paper VI, a set of three equations is presented by performing a regression analysis on the results of the linear static analysis of nine walls. The accuracy of the proposed SAM was demonstrated by comparing the equality and linear fitted trend lines of the results of the maximum lateral strength values based on α_0, obtained from the static analysis and proposed equations. Additionally, the findings indicate that applying the values suggested for piers with fixed-fixed or fixed-free boundary conditions is insufficiently precise for piers of a perforated wall with flexible boundary conditions owing to spandrels. It is worth mentioning that the proposed equations can only determine the α_0 value of the piers in low-rise URM walls (up to two stories) with regular opening configurations. The calculated damage limit states show that using predefined fixed inter-story drift ratios for the limit states of URM walls is not sufficiently accurate because URM walls with different dominant failure modes have different displacement capacities. The fragility curves of the near-collapse and significant damage limit states are relatively close to each other, unlike the damage limitation limit state, which can be attributed to the brittleness of the URM material. The fragility curves illustrate the negligible difference in seismic demand between the FF and PL-NF ground motions for low-rise URM buildings, as highlighted in Paper VI. Therefore, as can be inferred, the seismic fragility analysis of low-rise URM buildings by applying the FF and ignoring the PL-NF ground motions is sufficiently accurate. However, for a more accurate approach, the inclusion of PL-NF ground motions in the case of seismic fragility analysis of two-story buildings is recommended.

The results of the model updating of the three FE models in Paper VII revealed that the FB model was paired with the test results for the first two modes. Considering the SSI effects in the SM model, the absolute differences in frequency values decreased, and the diagonal elements of MAC matrices increased for the higher modes; in the DM model, which is the most detailed model, the mentioned correlation between dynamic characteristics of the model and the real structure improved. The DM is considered the closest model to the real structure in terms of frequency values and mode shapes. Moreover, the updated elasticity and shear moduli of the FB model were lower and more conservative than those of the other two models. Negligible differences (less than 10%) can be detected between the maximum roof displacements. Although we attempted to calibrate the models based on the OMA results and the updated material properties of the FB model were conservative, larger values of maximum inter-story drift ratios were concluded from the linear time history analysis of the DM model. Furthermore, the inter-story drift of the SM was the lowest among the models. The SSI is effective for modal properties, model updating results, and seismic demand of structures that should be considered for vulnerability assessment purposes.

The results of the NLTHA of the Roman bridge in Paper VIII revealed that the structure was more susceptible to PL events than to NPL events. Furthermore, FF events were more destructive than NF events. The Arias intensity is the most accurate indicator of the characteristics of seismic records for predicting structural demands. Three performance levels were determined based on the pushover curve. The results of the NTHA indicated that the bridge passed the acceptability check of the life safety performance level and underwent extensive damage. Moreover, the arches were the most vulnerable structural components based on the crack patterns at the end of the NTHA of each record. This is consistent with the weakness of a real structure that can be visually inspected.

Paper IX reports on an OSP study demonstrating the superiority of sensor elimination methods over sensor metric methods when using MAC as a criterion. Based on these results, specific locations for sensor placement were recommended, including the middle of the spandrel walls, on top of the arches, and between the top of the arches and the two sides of the Roman bridge. Unlike the first floor, the roof of the Slottsfjell Tower was the most important location for installing the sensors. Furthermore, the MAC matrices did not change significantly when the SSI effect was considered; however, the candidate sensor locations shifted from the third floor to the second floor of the Slottsfjell tower. Thus, the sensors should cover the roof and the second and third floors. Unlike the Slottsfjell Tower, recording the vertical (Z) direction of the Roman Bridge was crucial. Sensor elimination using MAC is considered to be the most efficient OSP method.

In Paper X, a detailed model of the bridge considering SSI effects was developed and calibrated based on the OMA results. Calibration of the fixed-base and SSI models confirmed detection of the structural damage to the central pier and arches of the bridge based on visual inspection. The MSA of the SSI model with free-field boundary elements reveals the worsening of the damage to the susceptible parts by increasing seismic intensities. The seismic behavior of the SSI and fixed-base models in terms of displacement, crack pattern, and crack width indicate that neglecting the SSI effects underestimates the seismic behavior of masonry bridges in the transverse direction. A comparative study of the seismic response of the strengthened bridge models in Paper X revealed the newmat model to be the best strengthening strategy for improving the seismic behavior of the bridge and satisfying the criteria for the strengthening of historic structures. The strengthening strategy with improved masonry material maintains harmony between the different parts of the bridge without significantly increasing the stiffness or respecting the originality of this cultural heritage asset. However, FRCM systems can be more cost-effective, durable, and resilient than improved masonry strategies when a structure is subjected to strong ground motions. The PBO-FRCM system is more effective than the carbon-FRCM. The maximum crack width of the PBO-FRCM model is less than the carbon-FRCM model, the differences in terms of the maximum displacement responses of the crown node are negligible.

4.1 Limitations and recommendations

1. A SAM for calculating the IIPS of perforated URM walls was verified in Paper II and a SAM for calculating the maximum lateral strength of URM piers was presented in Paper VI. Therefore, after calculating the maximum lateral strength of a perforated wall, the capacity curve of a URM wall can be estimated based on the IIPS and maximum lateral strength of the wall without performing any numerical simulations.

2. Paper I proposes several different SAMs for the seismic fragility analysis of URM buildings. However, an accurate and novel methodology utilizing the SPO2FRAG software [122] can be proposed. Although this software has been primarily used for estimating the fragility curves of RC structures, it could be adapted in future work for incorporating the nonlinear behaviors, including hysteresis behaviors, of URM buildings. To achieve this, capacity curves can be derived from previous proposals, and the software can be modified for estimating the fragility curves of URM structures.

3. The novel macroelement proposed in Paper III does not consider the N-V interaction through an analysis. Therefore, the macroelements should be improved for considering this feature. Furthermore, the macroelement can be modified and validated against the test results of reinforced masonry walls and can be utilized for the seismic analysis of this structural system.

4. It is beneficial to discuss the sensitivity of the capacity and fragility curves to the spandrel width. A sensitivity analysis should be performed on multiple case studies that vary in the number of stories and opening configurations. Additionally, the impact of SSI on the seismic behavior of URM buildings can be investigated by using the DM-

MVLEM macroelement in the versatile OpenSees framework for modeling various case studies with different soil conditions.

5. The numerical modeling of URM buildings in Hyperomet, which is presented in Paper V, is limited to a two-dimensional (2D) environment. However, this software should be improved by facilitating the 3D numerical modeling of URM buildings using DM-MVLEM.

6. The study of the effects of FF and NF on the seismic fragility analysis of URM buildings in Paper VI was limited to low-rise buildings. This study can be performed by applying FF and NF ground motions to four to seven stories high-rise URM buildings, and the effects of the ground motion types can be discovered. Another topic is the effect of vertical ground motions on the seismic behavior of URM buildings, which is effective when NF ground motions are applied to buildings [123].

7. In Papers VII and X, the soil properties were assumed based on visual inspections of the site and reports from the soil type of the nearest location. Although the soil properties were calibrated based on the OMA results, a geotechnical test was required for deriving the elastic mechanical properties of the soil at the sites of the case studies. Furthermore, a linear time history analysis was performed in Paper VII, which should be performed considering the nonlinearity in masonry and soil material.

8. In Paper VIII, the considered limit states for a masonry bridge were derived based on the capacity curve of the bridge because of the absence of predefined fixed limit states. Therefore, the methodology for deriving the limit states of the masonry bridges described in Paper VIII should be applied to several masonry bridges with different geometries and material properties. Subsequently, a set of criteria to obtain the limit states applicable to all masonry bridges without performing a POA should be proposed.

9. In Paper IX, the application of OSP techniques to a two-span masonry bridge was studied. However, to establish general criteria for deriving optimum sensor locations, OSP methods should be applied to a broader range of masonry bridges with varying geometries and material properties. The findings of these studies can be useful for future OMA applications in masonry structures.

10. Although the limitation of considering the linear material properties in Paper VII was modified in Paper X, the soil was modeled using an elastic material model with a nonlinear shear stress-strain relationship. Furthermore, the effects of soil properties on the seismic behavior of masonry bridges should be investigated via sensitivity analysis.

References

[1] M. Kioumarsi, V. Plevris, and A. Shabani, "Vulnerability assessment of cultural heritage structures," in 8th European Congress on Computational Methods in Applied Sciences and Engineering (ECCOMAS Congress 2022), 2022: ECCOMAS.

[2] E. Hernández-Montes, M. A. Fernández-Ruiz, M. Aschheim, and L. M. Gil-Martín, "Structural Knowledge within the 6th Century AD Arch of Taq-iKisra," International Journal of Architectural Heritage, vol. 11, no. 6, pp. 891-900, 2017/08/18, (2017), doi: https://doi.org/10.1080/15583058.2017.1321699.

[3] A. Shabani, M. Kioumarsi, V. Plevris, and H. Stamatopoulos, "Structural Vulnerability Assessment of Heritage Timber Buildings: A Methodological Proposal," Forests, vol. 11, no. 8, p. 881, (2020), doi: https://doi.org/10.3390/f11080881.

[4] S. Miccoli, L. M. Gil-Martín, and E. Hernández-Montes, "New historical records about the construction of the Arch of Ctesiphon and their impact on the history of structural engineering," Notes and Records: the Royal Society Journal of the History of Science, vol. 77, no. 1, pp. 113-134, (2023), doi: doi:10.1098/rsnr.2021.0025.

[5] A. Aşıkoğlu, G. Vasconcelos, P. B. Lourenço, and B. Pantò, "Pushover analysis of unreinforced irregular masonry buildings: Lessons from different modeling approaches," Engineering Structures, vol. 218, p. 110830, 2020/09/01/, (2020), doi: https://doi.org/10.1016/j.engstruct.2020.110830.

[6] V. Sarhosis, S. De Santis, and G. de Felice, "A review of experimental investigations and assessment methods for masonry arch bridges," Structure and Infrastructure Engineering, vol. 12, no. 11, pp. 1439-1464, 2016/11/01, (2016), doi: https://doi.org/10.1080/15732479.2015.1136655.

[7] H. Crowley *et al.*, "The European Seismic Risk Model 2020 (ESRM 2020)," EFEHR Technical Report 002 V1.0.0, (2021). doi: https://doi.org/10.7414/EUC-EFEHR-TR002-ESRM20.

[8] A. Shabani, A. Alinejad, M. Teymouri, A. N. Costa, M. Shabani, and M. Kioumarsi, "Seismic Vulnerability Assessment and Strengthening of Heritage Timber Buildings: A Review," Buildings, vol. 11, no. 12, p. 661, (2021). [Online]. Available: https://www.mdpi.com/2075-5309/11/12/661.

[9] L. Danciu *et al.*, "The 2020 update of the European Seismic Hazard Model: Model Overview, EFEHR Technical Report 001, v1.0.0,," (2021). doi: https://doi.org/10.12686/a15.

[10] V. Silva *et al.*, "Development of a global seismic risk model," Earthquake Spectra, vol. 36, no. 1_suppl, pp. 372-394, (2020).

[11] A. Günther, M. Van Den Eeckhaut, J.-P. Malet, P. Reichenbach, and J. Hervás, "Climate-physiographically differentiated Pan-European landslide susceptibility assessment using spatial multi-criteria evaluation and transnational landslide

information," Geomorphology, vol. 224, pp. 69-85, 2014/11/01/, (2014), doi: https://doi.org/10.1016/j.geomorph.2014.07.011.

[12] A. Valagussa, P. Frattini, G. Crosta, D. Spizzichino, G. Leoni, and C. Margottini, "Multi-risk analysis on European cultural and natural UNESCO heritage sites," Natural Hazards, vol. 105, no. 3, pp. 2659-2676, 2021/02/01, (2021), doi: 10.1007/s11069-020-04417-7.

[13] D. A.-O. V Silva, A Calderon, J Dabbeek, V Despotaki, L Martins, A Rao, M Simionato, D Viganò, C Yepes, A Acevedo, N Horspool, H Crowley, K Jaiswal, M Journeay, M Pittore . , "Global Earthquake Model (GEM) Seismic Risk Map (version 2018.1)," (2018), doi: https://doi.org/10.13117/GEM-GLOBAL-SEISMIC-RISK-MAP-2018.

[14] G. M. Calvi, R. Pinho, G. Magenes, J. J. Bommer, L. F. Restrepo-Vélez, and H. Crowley, "Development of seismic vulnerability assessment methodologies over the past 30 years," ISET journal of Earthquake Technology, vol. 43, no. 3, pp. 75-104, (2006).

[15] G. Cocco, A. D'Aloisio, E. Spacone, and G. Brando, "Seismic Vulnerability of Buildings in Historic Centers: From the "Urban" to the "Aggregate" Scale," (in English), Frontiers in Built Environment, Original Research vol. 5, no. 78, 2019-June-11, (2019), doi: https://doi.org/10.3389/fbuil.2019.00078.

[16] D. D'Ayala and E. Speranza, "Definition of Collapse Mechanisms and Seismic Vulnerability of Historic Masonry Buildings," Earthquake Spectra, vol. 19, 08/01, (2003), doi: https://doi.org/10.1193%2F1.1599896.

[17] M. Faravelli, B. Borzi, D. Polli, and M. Pagano, "Calibration of a mechanics-based method for large-scale vulnerability assessment," Bulletin of Earthquake Engineering, vol. 17, no. 5, pp. 2485-2508, 2019/05/01, (2019), doi: https://doi.org/10.1007/s10518-019-00560-0.

[18] A. Chiozzi, N. Grillanda, G. Milani, and A. Tralli, "UB-ALMANAC: An adaptive limit analysis NURBS-based program for the automatic assessment of partial failure mechanisms in masonry churches," Engineering Failure Analysis, vol. 85, 12/01, (2017), doi: https://doi.org/10.1016/j.engfailanal.2017.11.013.

[19] L. Cascini, R. Gagliardo, and F. Portioli, "LiABlock_3D: a software tool for collapse mechanism analysis of historic masonry structures," International Journal of Architectural Heritage, vol. 14, no. 1, pp. 75-94, (2020), doi: https://doi.org/10.1080/15583058.2018.1509155.

[20] A. M. D'Altri *et al.*, "Modeling strategies for the computational analysis of unreinforced masonry structures: review and classification," Archives of computational methods in engineering, pp. 1-33, (2019), doi: https://doi.org/10.1007/s11831-019-09351-x.

[21] P. Roca, M. Cervera, G. Gariup, and L. Pela', "Structural Analysis of Masonry Historical Constructions. Classical and Advanced Approaches," Archives of

Computational Methods in Engineering, vol. 17, no. 3, pp. 299-325, 2010/09/01, (2010), doi: 10.1007/s11831-010-9046-1.

[22] J. V. Lemos, "Discrete Element Modeling of Masonry Structures," International Journal of Architectural Heritage, vol. 1, no. 2, pp. 190-213, 2007/05/31, (2007), doi: 10.1080/15583050601176868.

[23] P. G. Asteris *et al.*, "Seismic vulnerability assessment of historical masonry structural systems," Engineering Structures, vol. 62-63, pp. 118-134, 2014/03/15/, (2014), doi: https://doi.org/10.1016/j.engstruct.2014.01.031.

[24] A. Akhaveissy and G. Milani, "Pushover analysis of large scale unreinforced masonry structures by means of a fully 2D non-linear model," Construction and Building Materials, vol. 41, pp. 276-295, (2013).

[25] P. Fajfar, "A nonlinear analysis method for performance-based seismic design," Earthquake spectra, vol. 16, no. 3, pp. 573-592, (2000), doi: https://doi.org/10.1193%2F1.1586128.

[26] P. Fajfar, "Capacity spectrum method based on inelastic demand spectra," Earthquake Engineering & Structural Dynamics, vol. 28, no. 9, pp. 979-993, (1999), doi: https://doi.org/10.1002/(SICI)1096-9845(199909)28:9%3C979::AID-EQE850%3E3.0.CO;2-1.

[27] H. Krawinkler and G. D. P. K. Seneviratna, "Pros and cons of a pushover analysis of seismic performance evaluation," Engineering Structures, vol. 20, no. 4, pp. 452-464, 1998/04/01/, (1998), doi: https://doi.org/10.1016/S0141-0296(97)00092-8.

[28] Y. Endo, L. Pelà, and P. Roca, "Review of Different Pushover Analysis Methods Applied to Masonry Buildings and Comparison with Nonlinear Dynamic Analysis," Journal of Earthquake Engineering, vol. 21, no. 8, pp. 1234-1255, 2017/11/17, (2017), doi: 10.1080/13632469.2016.1210055.

[29] S. Lagomarsino and S. Cattari, "Seismic performance of historical masonry structures through pushover and nonlinear dynamic analyses," Perspectives on European Earthquake Engineering and Seismology: Volume 2, pp. 265-292, (2015).

[30] C. P. Contiguglia, A. Pelle, B. Briseghella, and C. Nuti, "IMPA versus Cloud Analysis and IDA: Different Methods to Evaluate Structural Seismic Fragility," Applied Sciences, vol. 12, no. 7, p. 3687, (2022), doi: https://doi.org/10.3390/app12073687.

[31] V. Silva *et al.*, "Current Challenges and Future Trends in Analytical Fragility and Vulnerability Modeling," Earthquake Spectra, vol. 35, no. 4, pp. 1927-1952, (2019), doi: 10.1193/042418eqs101o.

[32] D. Vamvatsikos and C. A. Cornell, "Incremental dynamic analysis," Earthquake Engineering & Structural Dynamics, vol. 31, no. 3, pp. 491-514, (2002), doi: https://doi.org/10.1002/eqe.141.

[33] D. Vamvatsikos and C. A. Cornell, "Applied Incremental Dynamic Analysis," Earthquake Spectra, vol. 20, no. 2, pp. 523-553, 2004/05/01, (2004), doi: https://doi.org/10.1193%2F1.1737737.

[34] F. Jalayer and C. A. Cornell, "Alternative non-linear demand estimation methods for probability-based seismic assessments," Earthquake Engineering & Structural Dynamics, vol. 38, no. 8, pp. 951-972, (2009), doi: https://doi.org/10.1002/eqe.876.

[35] T. M. Ferreira, N. Mendes, and R. Silva, "Multiscale Seismic Vulnerability Assessment and Retrofit of Existing Masonry Buildings," Buildings, vol. 9, no. 4, p. 91, (2019), doi: https://doi.org/10.3390/buildings9040091.

[36] I. Puncello and S. Caprili, "Seismic Assessment of Historical Masonry Buildings at Different Scale Levels: A Review," Applied Sciences, vol. 13, no. 3, p. 1941, (2023), doi: https://doi.org/10.3390/app13031941.

[37] E. Quagliarini, G. Maracchini, and F. Clementi, "Uses and limits of the Equivalent Frame Model on existing unreinforced masonry buildings for assessing their seismic risk: A review," Journal of Building Engineering, vol. 10, pp. 166-182, 2017/03/01/, (2017), doi: https://doi.org/10.1016/j.jobe.2017.03.004.

[38] L.-L. Yu, Z.-Q. Dong, and G. Li, "Simplified mechanical models for the seismic collapse performance prediction of unreinforced masonry structures," Engineering Structures, vol. 258, p. 114131, 2022/05/01/, (2022), doi: https://doi.org/10.1016/j.engstruct.2022.114131.

[39] S.-H. Hwang, S. Kim, and K.-H. Yang, "In-plane lateral load transfer capacity of unreinforced masonry walls considering presence of openings," Journal of Building Engineering, vol. 47, p. 103868, 2022/04/15/, (2022), doi: https://doi.org/10.1016/j.jobe.2021.103868.

[40] J. I. Craig, B. J. Goodno, Towashiraporn, and J. Park, "Response Modification Applications for Essential Facilities," Georgia Institute of Technology, School of Civil and Environmental Engineering, (2002).

[41] H. Xu, C. Gentilini, Z. Yu, H. Wu, and S. Zhao, "A unified model for the seismic analysis of brick masonry structures," Construction and Building Materials, vol. 184, pp. 733-751, (2018), doi: https://doi.org/10.1016/j.conbuildmat.2018.06.208.

[42] A. Neuenhofer, "Lateral stiffness of shear walls with openings," Journal of Structural Engineering, vol. 132, no. 11, pp. 1846-1851, (2006), doi: https://doi.org/10.1061/(ASCE)0733-9445(2006)132:11(1846).

[43] M. Qamaruddin, A. W. Hag, S. Al-Oraimi, and S. Hamoud, "Investigation on the Lateral Stiffness of Shear Walls with Openings," in 11th International Brick Block Masonry Conference, China, 1997.

[44] M. Qamaruddin, "In-plane stiffness of shear walls with openings," Building and Environment, vol. 34, no. 2, pp. 109-127, (1998), doi: https://doi.org/10.1016/S0360-1323(98)00006-7.

[45] G. Magenes and G. M. Calvi, "In-plane seismic response of brick masonry walls," Earthquake Engineering & Structural Dynamics, vol. 26, no. 11, pp. 1091-1112, (1997), doi: https://doi.org/10.1002/(SICI)1096-9845(199711)26:11<1091::AID-EQE693>3.0.CO;2-6.

[46] T. Celano, L. U. Argiento, F. Ceroni, and C. Casapulla, "Literature Review of the In-Plane Behavior of Masonry Walls: Theoretical vs. Experimental Results," Materials, vol. 14, no. 11, p. 3063, (2021), doi: https://doi.org/10.3390/ma14113063.

[47] *Eurocode 8: Design of structures for earthquake resistance—Part 3: Assessment and retrofitting of buildings*, CEN, Brussels, Belgium, (2010).

[48] *Aggiornamento delle "Norme tecniche per le costruzioni" (NTC)*, DM, Rome, Italy, (2018).

[49] *Prestandard and Commentry for the Seismic Rehabilitaion of Buildings, FEMA 356*, FEMA, Washington, D.C., (2000).

[50] *NEHRP Guidelines for the Seismic Rehabilitation of Buildings. Report FEMA 273*, FEMA, Washington, DC, USA., (1997).

[51] S. Petrovčič and V. Kilar, "Seismic failure mode interaction for the equivalent frame modeling of unreinforced masonry structures," Engineering structures, vol. 54, pp. 9-22, (2013), doi: https://doi.org/10.1016/j.engstruct.2013.03.050.

[52] M. Tomazevic, "The computer program POR: institute for testing and research in materials and structures-ZRMK.," Slovenia: Ljubljana, (1978).

[53] L. Pasticier, C. Amadio, and M. Fragiacomo, "Non-linear seismic analysis and vulnerability evaluation of a masonry building by means of the SAP2000 V. 10 code," Earthquake engineering & structural dynamics, vol. 37, no. 3, pp. 467-485, (2008), doi: https://doi.org/10.1002/eqe.770.

[54] A. Penna, S. Lagomarsino, and A. Galasco, "A nonlinear macroelement model for the seismic analysis of masonry buildings," Earthquake Engineering & Structural Dynamics, vol. 43, no. 2, pp. 159-179, (2014), doi: https://doi.org/10.1002/eqe.2335.

[55] S. Bracchi, A. Galasco, and A. Penna, "A novel macroelement model for the nonlinear analysis of masonry buildings. Part 1: Axial and flexural behavior," Earthquake Engineering & Structural Dynamics, (2021), doi: https://doi.org/10.1002/eqe.3445.

[56] S. Bracchi and A. Penna, "A novel macroelement model for the nonlinear analysis of masonry buildings. Part 2: Shear behavior," Earthquake Engineering & Structural Dynamics, (2021), doi: https://doi.org/10.1002/eqe.3444.

[57] R. Siano *et al.*, "Numerical investigation of non-linear equivalent-frame models for regular masonry walls," Engineering Structures, vol. 173, pp. 512-529, (2018), doi: https://doi.org/10.1016/j.engstruct.2018.07.006.

[58] M. Peruch, E. Spacone, and G. Camata, "Nonlinear analysis of masonry structures using fiber-section line elements," Earthquake Engineering & Structural Dynamics, vol. 48, no. 12, pp. 1345-1364, (2019), doi: https://doi.org/10.1002/eqe.3188.

[59] K. Orakcal, J. W. Wallace, and J. P. Conte, "Flexural modeling of reinforced concrete walls-model attributes," Structural Journal, vol. 101, no. 5, pp. 688-698, (2004).

[60] K. Orakcal and J. W. Wallace, "Flexural modeling of reinforced concrete walls-experimental verification," ACI Materials Journal, vol. 103, no. 2, p. 196, (2006).

[61] J. Park, P. Towashiraporn, J. I. Craig, and B. J. Goodno, "Seismic fragility analysis of low-rise unreinforced masonry structures," Engineering Structures, vol. 31, no. 1, pp. 125-137, (2009), doi: https://doi.org/10.1016/j.engstruct.2008.07.021.

[62] G. Rinaldin, C. Amadio, and L. Macorini, "A macro-model with nonlinear springs for seismic analysis of URM buildings," Earthquake Engineering & Structural Dynamics, vol. 45, no. 14, pp. 2261-2281, (2016), doi: https://doi.org/10.1002/eqe.2759.

[63] A. Afreen, A. Ahmed, and K. Moin, "Effect of near-field earthquake on masonry structure," Asian Journal of Civil Engineering, vol. 22, no. 5, pp. 895-910, 2021/07/01, (2021), doi: 10.1007/s42107-021-00353-4.

[64] H. Bilgin and M. Hysenlliu, "Comparison of near and far-fault ground motion effects on low and mid-rise masonry buildings," Journal of Building Engineering, vol. 30, p. 101248, 2020/07/01/, (2020), doi: https://doi.org/10.1016/j.jobe.2020.101248.

[65] M. Yekrangnia, A. Bakhshi, M. A. Ghannad, and M. Panahi, "Risk assessment of confined unreinforced masonry buildings based on FEMA P-58 methodology: a case study—school buildings in Tehran," Bulletin of Earthquake Engineering, vol. 19, no. 2, pp. 1079-1120, 2021/01/01, (2021), doi: 10.1007/s10518-020-00990-1.

[66] D. D'Ayala, A. Meslem, D. Vamvatsikos, K. Porter, and T. Rossetto, "Guidelines for analytical vulnerability assessment: Low/mid-rise, GEM vulnerability and loss modelling," Global Earthquake Model (GEM) Foundation, Pavia, (2015).

[67] A. Georgopoulos and E. K. Stathopoulou, "Data acquisition for 3D geometric recording: state of the art and recent innovations," Heritage and archaeology in the digital age, pp. 1-26, (2017).

[68] A. Shabani, M. Skamantzari, S. Tapinaki, A. Georgopoulos, V. Plevris, and M. Kioumarsi, "3D simulation models for developing digital twins of heritage structures: challenges and strategies," presented at the The 4th International Conference on Structural Integrity, Procedia Structural Integrity, 2022/01/01/, (2022). doi: https://doi.org/10.1016/j.prostr.2022.01.090.

[69] N. Kassotakis and V. Sarhosis, "Employing non-contact sensing techniques for improving efficiency and automation in numerical modelling of existing masonry structures: A critical literature review," Structures, vol. 32, pp. 1777-1797, 2021/08/01/, (2021), doi: https://doi.org/10.1016/j.istruc.2021.03.111.

[70] A. Shabani, H. Hosamo, V. Plevris, and M. Kioumarsi, "A Preliminary Structural Survey of Heritage Timber Log Houses in Tønsberg, Norway," presented at the 12th International Conference on Structural Analysis of Historical Constructions (SAHC 2021), Spain, (2021).

[71] G. Castellazzi, A. M. Altri, G. Bitelli, I. Selvaggi, and A. Lambertini, "From Laser Scanning to Finite Element Analysis of Complex Buildings by Using a Semi-Automatic Procedure," Sensors, vol. 15, no. 8, (2015), doi: https://doi.org/10.3390/s150818360.

[72] G. Castellazzi, A. M. D’Altri, S. de Miranda, and F. Ubertini, "An innovative numerical modeling strategy for the structural analysis of historical monumental buildings," Engineering Structures, vol. 132, pp. 229-248, 2017/02/01/, (2017), doi: https://doi.org/10.1016/j.engstruct.2016.11.032.

[73] G. Bartoli *et al.*, "From TLS data to FE model: a workflow for studying the dynamic behavior of the Pulpit by Giovanni Pisano in Pistoia (Italy)," Procedia Structural Integrity, vol. 29, pp. 55-62, 2020/01/01/, (2020), doi: https://doi.org/10.1016/j.prostr.2020.11.139.

[74] G. Castellazzi, N. Lo Presti, A. M. D’Altri, and S. de Miranda, "Cloud2FEM: A finite element mesh generator based on point clouds of existing/historical structures," SoftwareX, vol. 18, p. 101099, 2022/06/01/, (2022), doi: https://doi.org/10.1016/j.softx.2022.101099.

[75] A. Shabani, A. Ademi, and M. Kioumarsi, "Structural Model Updating of a Historical Stone Masonry Tower in Tønsberg, Norway," in Protection of Historical Constructions, Cham, I. Vayas and F. M. Mazzolani, Eds., 2022// 2022: Springer International Publishing, pp. 576-585.

[76] G. Standoli, E. Giordano, G. Milani, and F. Clementi, "Model Updating of Historical Belfries Based on Oma Identification Techniques," International Journal of Architectural Heritage, vol. 15, no. 1, pp. 132-156, 2021/01/02, (2021), doi: 10.1080/15583058.2020.1723735.

[77] F. J. Pallarés, M. Betti, G. Bartoli, and L. Pallarés, "Structural health monitoring (SHM) and Nondestructive testing (NDT) of slender masonry structures: A practical review," Construction and Building Materials, vol. 297, p. 123768, 2021/08/23/, (2021), doi: https://doi.org/10.1016/j.conbuildmat.2021.123768.

[78] V. Cardinali *et al.*, "Integrated techniques for the structural assessment of cultural heritage masonry buildings: application to Palazzo Cocchi-Serristori in Florence," Journal of Cultural Heritage Management and Sustainable Development, vol. 13, no. 1, pp. 123-145, (2023), doi: 10.1108/JCHMSD-02-2021-0024.

[79] M. Girardi, C. Padovani, D. Pellegrini, M. Porcelli, and L. Robol, "Finite element model updating for structural applications," Journal of Computational and Applied Mathematics, vol. 370, p. 112675, 2020/05/15/, (2020), doi: https://doi.org/10.1016/j.cam.2019.112675.

[80] Y. Tan and L. Zhang, "Computational methodologies for optimal sensor placement in structural health monitoring: A review," Structural Health Monitoring, vol. 19, no. 4, pp. 1287-1308, (2020), doi: 10.1177/1475921719877579.

[81] P. Pachón *et al.*, "Evaluation of optimal sensor placement algorithms for the Structural Health Monitoring of architectural heritage. Application to the Monastery of San Jerónimo de Buenavista (Seville, Spain)," Engineering Structures, vol. 202, p. 109843, 2020/01/01/, (2020), doi: https://doi.org/10.1016/j.engstruct.2019.109843.

[82] F. A. El-Qawasma, T. M. Elfouly, and M. H. Ahmed, "Minimising number of sensors in wireless sensor networks for structure health monitoring systems," IET Wireless

Sensor Systems, vol. 9, no. 2, pp. 94-101, (2019), doi: https://doi.org/10.1049/iet-wss.2018.5031.

[83] A. C. Altunişik, A. F. Genç, E. Ertürk, M. Günaydin, F. Y. Okur, and B. Sevİm, "Soil–Structure Interaction and Earthquake Input Models Effect on the Structural Response of the Santa Maria Church and Guesthouse Building," Journal of Earthquake Engineering, pp. 1-32, (2022), doi: 10.1080/13632469.2022.2158967.

[84] V. Anand and S. R. Satish Kumar, "Seismic Soil-structure Interaction: A State-of-the-Art Review," Structures, vol. 16, pp. 317-326, 2018/11/01/, (2018), doi: https://doi.org/10.1016/j.istruc.2018.10.009.

[85] A. Fathi, A. Sadeghi, M. R. Emami Azadi, and N. Hoveidaie, "Assessing Seismic Behavior of a Masonry Historic Building considering Soil-Foundation-Structure Interaction (Case Study of Arge-Tabriz)," International Journal of Architectural Heritage, vol. 14, no. 6, pp. 795-810, 2020/07/02, (2020), doi: 10.1080/15583058.2019.1568615.

[86] L. Pelà, A. Aprile, and A. Benedetti, "Seismic assessment of masonry arch bridges," Engineering Structures, vol. 31, no. 8, pp. 1777-1788, 2009/08/01/, (2009), doi: https://doi.org/10.1016/j.engstruct.2009.02.012.

[87] A. Bayraktar and E. Hökelekli, "Nonlinear soil deformability effects on the seismic damage mechanisms of brick and stone masonry arch bridges," International Journal of Damage Mechanics, vol. 30, no. 3, pp. 431-452, (2021).

[88] A. Karatzetzou, D. Pitilakis, and S. Karafagka, "System Identification of Mosques Resting on Soft Soil. The Case of the Suleiman Mosque in the Medieval City of Rhodes, Greece," Geosciences, vol. 11, no. 7, p. 275, (2021), doi: https://doi.org/10.3390/geosciences11070275.

[89] A. Brunelli *et al.*, "Numerical simulation of the seismic response and soil–structure interaction for a monitored masonry school building damaged by the 2016 Central Italy earthquake," Bulletin of Earthquake Engineering, vol. 19, no. 2, pp. 1181-1211, 2021/01/01, (2021), doi: 10.1007/s10518-020-00980-3.

[90] R. Lancellotta and D. Sabia, "Identification Technique for Soil-Structure Analysis of the Ghirlandina Tower," International Journal of Architectural Heritage, vol. 9, no. 4, pp. 391-407, 2015/05/19, (2015), doi: 10.1080/15583058.2013.793438.

[91] E. Aytulun, S. Soyoz, and E. Karcioglu, "System Identification and Seismic Performance Assessment of a Stone Arch Bridge," Journal of Earthquake Engineering, vol. 26, no. 2, pp. 723-743, 2022/01/25, (2022), doi: 10.1080/13632469.2019.1692740.

[92] Ö. Saygılı and J. V. Lemos, "Seismic vulnerability assessment of masonry arch bridges," Structures, vol. 33, pp. 3311-3323, 2021/10/01/, (2021), doi: https://doi.org/10.1016/j.istruc.2021.06.057.

[93] E. Bertolesi, G. Milani, F. D. Lopane, and M. Acito, "Augustus Bridge in Narni (Italy): Seismic Vulnerability Assessment of the Still Standing Part, Possible Causes of Collapse, and Importance of the Roman Concrete Infill in the Seismic-Resistant

Behavior," International Journal of Architectural Heritage, vol. 11, no. 5, pp. 717-746, 2017/07/04, (2017), doi: 10.1080/15583058.2017.1300712.

[94] L. Pelà, A. Aprile, and A. Benedetti, "Comparison of seismic assessment procedures for masonry arch bridges," Construction and Building Materials, vol. 38, pp. 381-394, 2013/01/01/, (2013), doi: https://doi.org/10.1016/j.conbuildmat.2012.08.046.

[95] N. Simos, G. C. Manos, and E. Kozikopoulos, "Near- and far-field earthquake damage study of the Konitsa stone arch bridge," Engineering Structures, vol. 177, pp. 256-267, 2018/12/15/, (2018), doi: https://doi.org/10.1016/j.engstruct.2018.09.072.

[96] H. Güllü and F. Özel, "Microtremor measurements and 3D dynamic soil–structure interaction analysis for a historical masonry arch bridge under the effects of near- and far-fault earthquakes," Environmental Earth Sciences, vol. 79, no. 13, p. 338, 2020/06/30, (2020), doi: 10.1007/s12665-020-09086-0.

[97] A. Özmen and E. Sayın, "Seismic Response of a Historical Masonry Bridge under Near and Far-fault Ground Motions," Periodica Polytechnica Civil Engineering, vol. 65, no. 3, pp. 946-958, 01/01, (2021), doi: 10.3311/PPci.17832.

[98] S. Gönen and S. Soyöz, "Seismic analysis of a masonry arch bridge using multiple methodologies," Engineering Structures, vol. 226, p. 111354, 2021/01/01/, (2021), doi: https://doi.org/10.1016/j.engstruct.2020.111354.

[99] F. Yavartanoo and T. H. K. Kang, "Retrofitting of unreinforced masonry structures and considerations for heritage-sensitive constructions," Journal of Building Engineering, vol. 49, p. 103993, 2022/05/15/, (2022), doi: https://doi.org/10.1016/j.jobe.2022.103993.

[100] M. R. Valluzzi, C. Modena, and G. de Felice, "Current practice and open issues in strengthening historical buildings with composites," Materials and Structures, vol. 47, no. 12, pp. 1971-1985, 2014/12/01, (2014), doi: 10.1617/s11527-014-0359-7.

[101] A. D'Ambrisi, F. Focacci, R. Luciano, V. Alecci, and M. De Stefano, "Carbon-FRCM materials for structural upgrade of masonry arch road bridges," Composites Part B: Engineering, vol. 75, pp. 355-366, (2015).

[102] P. Zampieri, N. Simoncello, J. Gonzalez-Libreros, and C. Pellegrino, "Evaluation of the vertical load capacity of masonry arch bridges strengthened with FRCM or SFRM by limit analysis," Engineering Structures, vol. 225, p. 111135, (2020).

[103] N. Simoncello, P. Zampieri, J. Gonzalez-Libreros, S. Perboni, and C. Pellegrino, "Numerical analysis of an FRP-strengthened masonry arch bridge," Frontiers in Built Environment, vol. 6, p. 7, (2020).

[104] Y. Tao, T. Stratford, and J.-F. Chen, "Behaviour of a masonry arch bridge repaired using fibre-reinforced polymer composites," Engineering Structures, vol. 33, no. 5, pp. 1594-1606, (2011).

[105] A. Bayraktar and E. Hökelekli, "Seismic performances of different spandrel wall strengthening techniques in masonry arch bridges," International Journal of Architectural Heritage, vol. 15, no. 11, pp. 1722-1740, (2021).

[106] F. Behnamfar and M. Afshari, "Collapse Analysis and Strengthening of Stone Arch Bridges Against Earthquake," International Journal of Architectural Heritage, vol. 7, no. 1, pp. 1-25, 2013/01/01, (2013), doi: 10.1080/15583058.2011.606594.

[107] M. Dolce, "Schematizzazionee modellazione degli edifici in muratura soggetti ad azioni sismiche. ," (in in Italian), L'industria delle Costruzioni vol. 25, pp. 44-57, in Italian, (1991).

[108] S. Mazzoni, F. McKenna, M. H. Scott, and G. L. Fenves, "OpenSees command language manual," vol. 264: Pacific Earthquake Engineering Research (PEER) Center, USA, (2006).

[109] G. Magenes, G. Kingsley, and G. Calvi, Seismic Testing of a Full-Scale, Two-Story Masonry Building: Test Procedure and Measured Experimental Response Report 3.0 - G.N.D.T. Department of Structural Mechanics, University of Pavia, 1995.

[110] DIANA, "DIANA FEA, Diana User's Manual, Release 10.4," in DIANA FEA BV, Delft University of Technology, Netherland, ed, (2020).

[111] FEMtools, "Dynamic Design Solutions, FEMtools 4 user guide," ed. Leuven, Belgium, (2021).

[112] S. Tapinaki, M. Skamantzari, A. Anastasiou, S. Koutros, E. Syrokou, and A. Georgopoulos, "3D Holistic Documentation of Heritage Monuments in Rhodes," ISPRS-International Archives of the Photogrammetry, Remote Sensing and Spatial Information Sciences, vol. XLVI-M-1-2021, pp. 739-744, (2021), doi: 10.5194/isprs-archives-XLVI-M-1-2021-739-2021.

[113] P. Kolokoussis, M. Skamantzari, S. Tapinaki, V. Karathanassi, and A. Georgopoulos, "3D and Hyperspectral Data Integration for Assessing Material Degradation in Medieval Masonry Heritage Buildings," ISPRS-International Archives of the Photogrammetry, Remote Sensing and Spatial Information Sciences, vol. 43, pp. 583-590, (2021).

[114] B. Ghiassi, A. T. Vermelfoort, and P. B. Lourenço, "Chapter 7 - Masonry mechanical properties," in *Numerical Modeling of Masonry and Historical Structures*, B. Ghiassi and G. Milani Eds.: Woodhead Publishing, (2019), pp. 239-261.

[115] S. Gönen and S. Soyöz, "Reliability-based seismic performance of masonry arch bridges," Structure and Infrastructure Engineering, pp. 1-16, (2021), doi: 10.1080/15732479.2021.1918726.

[116] PEER. "PEER Ground Motion Database." University of California. https://ngawest2.berkeley.edu/ (accessed.

[117] SeismoSoft, "SeismoMatch, Version 2021," ed: Earthquake Engineering Software Solutions Seismosoft Pavia, Italy, (2021).

[118] J. W. Baker, "Efficient Analytical Fragility Function Fitting Using Dynamic Structural Analysis," Earthquake Spectra, vol. 31, no. 1, pp. 579-599, (2015), doi: 10.1193/021113eqs025m.

[119] A. H. Nielsen, "Absorbing boundary conditions for seismic analysis in ABAQUS," in ABAQUS users' conference, 2006, pp. 359-376.

[120] M. Longo, M. Sousamli, P. A. Korswagen, P. van Staalduinen, and J. G. Rots, "Sub-structure-based 'three-tiered' finite element approach to soil-masonry-wall interaction for light seismic motion," Engineering Structures, vol. 245, p. 112847, 2021/10/15/, (2021), doi: https://doi.org/10.1016/j.engstruct.2021.112847.

[121] D. Arboleda, F. G. Carozzi, A. Nanni, and C. Poggi, "Testing Procedures for the Uniaxial Tensile Characterization of Fabric-Reinforced Cementitious Matrix Composites," Journal of Composites for Construction, vol. 20, no. 3, p. 04015063, (2016), doi: doi:10.1061/(ASCE)CC.1943-5614.0000626.

[122] G. Baltzopoulos, R. Baraschino, I. Iervolino, and D. Vamvatsikos, "SPO2FRAG: software for seismic fragility assessment based on static pushover," Bulletin of Earthquake Engineering, vol. 15, no. 10, pp. 4399-4425, 2017/10/01, (2017), doi: 10.1007/s10518-017-0145-3.

[123] N. Chieffo, M. Mosoarca, A. Formisano, P. B. Lourenço, and G. Milani, "The effect of ground motion vertical component on the seismic response of historical masonry buildings: The case study of the Banloc Castle in Romania," Engineering Structures, vol. 249, p. 113346, 2021/12/15/, (2021), doi: https://doi.org/10.1016/j.engstruct.2021.113346.

Appendix

Paper I

Shabani, A., Kioumarsi, M., Zucconi, M.

State of the art of simplified analytical methods for seismic vulnerability assessment of unreinforced masonry buildings

(2021), Engineering Structures, https://doi.org/10.1016/j.engstruct.2021.112280

Engineering Structures 239 (2021) 112280

Contents lists available at ScienceDirect

Engineering Structures

journal homepage: www.elsevier.com/locate/engstruct

Review article

State of the art of simplified analytical methods for seismic vulnerability assessment of unreinforced masonry buildings

Amirhosein Shabani [a,*], Mahdi Kioumarsi [a], Maria Zucconi [b]

[a] Department of Civil Engineering and Energy Technology, Oslo Metropolitan University, Pilestredet 35, 0166 Oslo, Norway
[b] Department of Engineering, University Niccolò Cusano, Via Don Carlo Gnocchi, 3, 00166 Rome, Italy

ARTICLE INFO

Keywords:
Seismic vulnerability
Analytical methods
Simplified methods
Urban scale
Unreinforced masonry buildings
Collapse mechanism-based methods
Capacity spectrum-based methods
Fully displacement-based methods

ABSTRACT

Cities in the developing world are facing outstanding economic and human losses caused by natural hazards such as earthquakes, and the amount of losses is affected by the quality of preventive measures and emergency management. For this reason, seismic vulnerability assessment is considered a crucial part of a strategy for seismic risk mitigation and for improving the resiliency of cities. Due to the high number of building archetypes for the seismic vulnerability assessment at a large scale, fast, simplified methods have been proposed that can facilitate the assessment procedure with low computational effort. Simplified methods can be categorized into three groups: analytical, empirical, and hybrid methods. In this study, simplified analytical methods for the seismic vulnerability assessment of unreinforced masonry (URM) buildings were reviewed, starting with their classification into three main groups: collapse mechanism-based, capacity spectrum-based, and fully displacement-based methods. Finally, attention was given to the corresponding software packages that were developed to facilitate the assessment procedure.

1. Introduction

In the past few decades, natural catastrophes, including earthquakes, have led to a dramatic increase in human and economic losses. A loss model for earthquake risk is required to predict the economic impact of future risks as well as to define risk mitigation plans by national authorities [1,2]. Seismic vulnerability assessment, which describes the susceptibility of a structure to damage due to ground shaking, is a pivotal part of a loss model [3,4]. Masonry buildings can be considered as the oldest construction type and represent a large part of the building portfolio in high seismicity zones. Fig. 1 presents a hazard map of the high seismicity zones in Europe and the Middle East based on the peak ground acceleration (PGA) of the area. Fig. 2 illustrates the ratio of the number of unreinforced masonry (URM) buildings compared to other types of structural systems in European countries, as well as the number of all buildings in each country [5]. URM is considered as a prevalent structural system in high seismicity zones, i.e., Italy, Greece, Bulgaria, Turkey, as depicted in Fig. 2, and Iran based on [6].

Fig. 3 (a) shows a hazard map of South America, and as illustrated in Fig. 3 (b), the prevalent construction type is URM. Fig. 3 (b) also shows the distribution of URM buildings, the number of all buildings (in millions), and the replacement cost for each country. The replacement cost is the value of replacing a constructed building based on the latest seismic code in a country [8].

URM buildings are characterized by a high seismic vulnerability; in fact, both the mortar and the masonry unit are known to be “quasi-brittle materials” whose mechanical performance could be deteriorated under seismic loadings. Due to the absence of a robust connection between structural components and insufficient stiffness of horizontal floors, URM buildings are highly susceptible to lateral cyclic loads that involve the out-of-plane bending behavior of walls and combined in-plane and out-of-plane collapse mechanisms [10–12].

Fig. 4 shows a seismic risk map of two susceptible zones where URMs are prevalent construction buildings. The reported average annual loss (AAL) in some parts of the high seismicity zones with high PGA is more than 5,000 USD per m^2, representing a severe economic loss for governments [13].

Based on the statistics from several earthquakes (1886–2003) in the United States, 20% of 4,457 URM buildings were either partially damaged or completely collapsed, and the reason for collapse for 83% of the damaged buildings was the brickwork fell [15]. As shown in Fig. 5, due to the vulnerability of this structural system, the construction of the

---

* Corresponding author.
E-mail addresses: amirhose@oslomet.no (A. Shabani), mahdik@oslomet.no (M. Kioumarsi), maria.zucconi@unicusano.it (M. Zucconi).

https://doi.org/10.1016/j.engstruct.2021.112280
Received 28 September 2020; Received in revised form 18 February 2021; Accepted 23 March 2021

new buildings made of URM is not permitted in some states of the United States [15].

In order to decrease human and economic losses, seismic vulnerability assessment of URM buildings is needed by national authorities at different scales. Different historical URM structures with complex architecture need to be preserved, as do existing vernacular URM buildings. In recent decades the resiliency of structures and infrastructures has attracted wide attention, and in order to facilitate a resiliency framework, a robust vulnerability assessment methodology is required to be applied at a large scale [16]. The methods should be user-friendly due to the high number of archetypes as well as be fast in computation [16,17]. Therefore, as illustrated in Fig. 6, the scale of vulnerability assessment procedures can be classified into three groups ranging from building scale to large scale [18].

Different seismic vulnerability assessment methods have been proposed in the literature and can be divided into three main groups: (1) empirical methods (EM), (2) analytical methods, and (3) hybrid methods (HM) (see Fig. 7). The most common methods for the seismic vulnerability assessment of building typologies at different scales aim to define a damage probability matrix [19] or fragility curves [20].

EMs are based on visual inspection of buildings in the post-emergency phase and damage data obtained from observed past earthquakes [21–25]. They refer to typological building classes or vulnerability indexes and can be correlated with construction techniques, types of materials, and different building features [26–31]. A limitation of these methods is their validity that can be limited to specific geographical and seismic regions [32].

Analytical methods require detailed vulnerability assessment algorithms to consider the physical and mechanical properties of buildings that can be calibrated to various characteristics of building stocks and hazards [33]. However, deriving analytical vulnerability curves is time-consuming and needs high computational effort. Consequently, basic users cannot easily develop curves for different areas or countries with diverse construction characteristics [3].

HMs are a combination of EMs and analytical methods whereby post-earthquake loss data is combined with results from analytical methods of a building typology [34,35]. Visual inspection data reduces computational efforts of analytical methods. Furthermore, HMs and EMs are utilized for calibrating the analytical methods [3].

Analytical methods can be divided into two sub-groups: detailed analytical methods (DAMs) and simplified analytical methods (SAMs). DAMs for the seismic vulnerability assessment of URM buildings comprise a sophisticated, detailed numerical simulation by conducting nonlinear analyses [36]. Different methods have been presented for nonlinear analysis of URM buildings in order to show their actual behavior when subjected to seismic loads. Nonlinear static (pushover) analysis (NSA) is the most popular method, where the lateral static load is applied to the model and is increased until a displacement target is reached [37]. Incremental dynamic analysis (IDA) is the most advanced type of detailed analysis, in which accelerograms are applied to the building model, and their intensity increased until the collapse occurs [10,38].

In order to reduce time consumption and computational effort, different simplified analytical methods (SAMs) for the seismic vulnerability assessment of URM buildings have been developed. Collapse mechanism-based (CMB) methods are based on the kinematic chain in order to derive the collapse multipliers for different probable collapse mechanisms of URM buildings subjected to a given intensity of a seismic record. Capacity curves are the result of the NSA. In capacity spectrum-based (CSB) methods, a predetermined capacity curve is computed for each building typology. The capacity curve is then intersected with the seismic demand to derive the performance points in different damage thresholds. In fully displacement-based (FDB) methods, an equivalent single-degree-of-freedom (ESDOF) model of a building is derived, and the displacement capacity for each damage threshold is compared to the displacement demand in each corresponding period of vibration in order to derive the possibility of crossing the damage thresholds [3,17,32].

When dealing with a single-building assessment, uncertainties are mainly due to the lack of expert knowledge of the structural features, which can be reduced by an on-site survey [39]. However, when dealing with vulnerability assessment at a large scale using the SAMs, a broad range of variables and a great deal of uncertainty are involved in both the modeling process and parameters [40,41]. Generally, uncertainty on capacity, demand, and damage thresholds are the sources that are

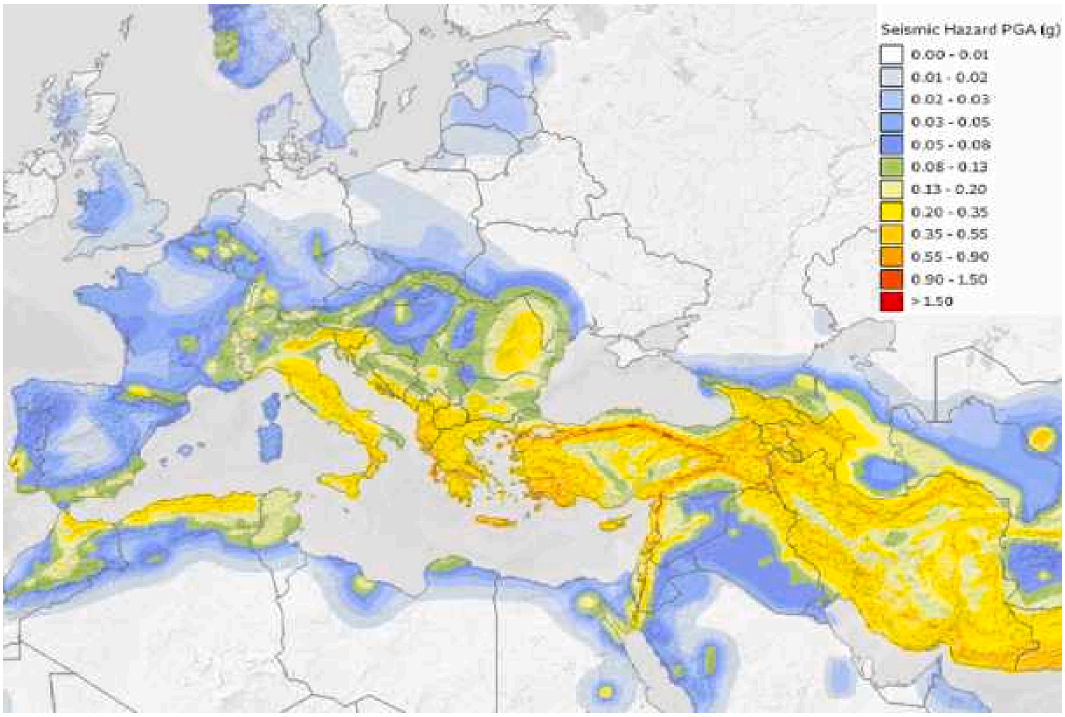

Fig. 1. Hazard map of the European and Middle-Eastern countries, based on PGA [7].

identified by most of the available seismic vulnerability assessment methods [42].

Fig. 8 presents a schematic overview of the scale of assessment and the complexity level of the analysis methodologies. As shown, the complexity and time consumption level increase from the green area to the red area, where the highest level is related to the IDA of detailed nonlinear models of all the buildings at a large scale, which is uncommon nowadays. Moreover, EMs requiring the lowest computational effort are not suitable for the seismic vulnerability assessment of single-building but only for the building stock scale and large scale. The yellow area shows the methods that nowadays are most commonly applied to a specific case study scale.

The aim of this paper is to provide a state-of-the-art review of the developments of the SAMs, which are categorized and illustrated in a black box in Fig. 8. The complexity and corresponding computational efforts of each method are investigated by emphasizing their mechanics basis, drawbacks, and advantages. Note that the main focus of this paper is on unreinforced brick masonry buildings; however, case studies about stone and adobe masonry have been addressed to present the operational scope of each method. Moreover, particular attention is given to different software packages that were developed to facilitate the application of the SAMs for the seismic vulnerability assessment of URM buildings by investigating their strengths and weaknesses.

2. Collapse mechanism-based methods

The main concept of CMB methods is to assess the vulnerability of URM buildings by defining predefined collapse mechanisms or decomposing them into rigid macroblocks. In CMB methods, first, collapse multipliers are computed, and the minimum value is defined. Then, the corresponding collapse mechanism is considered as the most critical mechanism.

VULNUS is one of the CMB methods proposed by Bernardini et al. [43] based on in-plane and out-of-plane collapse mechanisms of URM buildings. In this method, the collapse multipliers are derived from the ratio of shear strength and flexural of walls for in-plane and out-of-plane collapse mechanisms of URM walls by applying the virtual work principle according to the static theorem of limit analysis [44]. A comparative seismic assessment has been done for URM building aggregates within the historical center of Arsita damaged by the L'Aquila earthquake (2009, April 6th) in Italy [45]. A macroseismic EM was utilized to derive the vulnerability indexes and the corresponding fragility curves. Furthermore, the VULNUS method was used to derive the fragility curves. Within the VULNUS method, the terms I_1 and I_2 take into account the probable in-plane and out-of-plane mechanisms. Moreover, DAM was done by means of an equivalent frame method embedded in 3Muri software [46]. Detailed three-dimensional (3D) models were provided, NSA was done, which is described in detail in [47], and by means of the CSB method, the corresponding fragility curves have been derived. This study shows that the fragility curves derived from the VULNUS method are placed in the middle range between the upper limit (conservative) DAM and the lower limit ones derived from the EM of the fragility domain [45].

Performance-based assessment and the seismic risk mitigation of cultural heritage assets were incorporated into the Italian guidelines (PCM) [48] outlined by the Italian building code [49]. For this purpose, a CMB method was added to and recommended by the Italian guidelines [36]. Some of the predefined collapse mechanisms in the PCM are illustrated in Fig. 9 [50,51].

Using SAMs associated with an ESDOF modeling of buildings is not reliable enough for global evaluation of URM cultural heritage sites with complex architecture. Therefore, investigating the local mechanisms using the CMB methods is needed to be done. Not only the predefined collapse mechanisms but also the lack of connections with the orthogonal walls, infinite compression resistance (rigid blocks), and zero tensile resistance strength are the simplified hypotheses considered in this

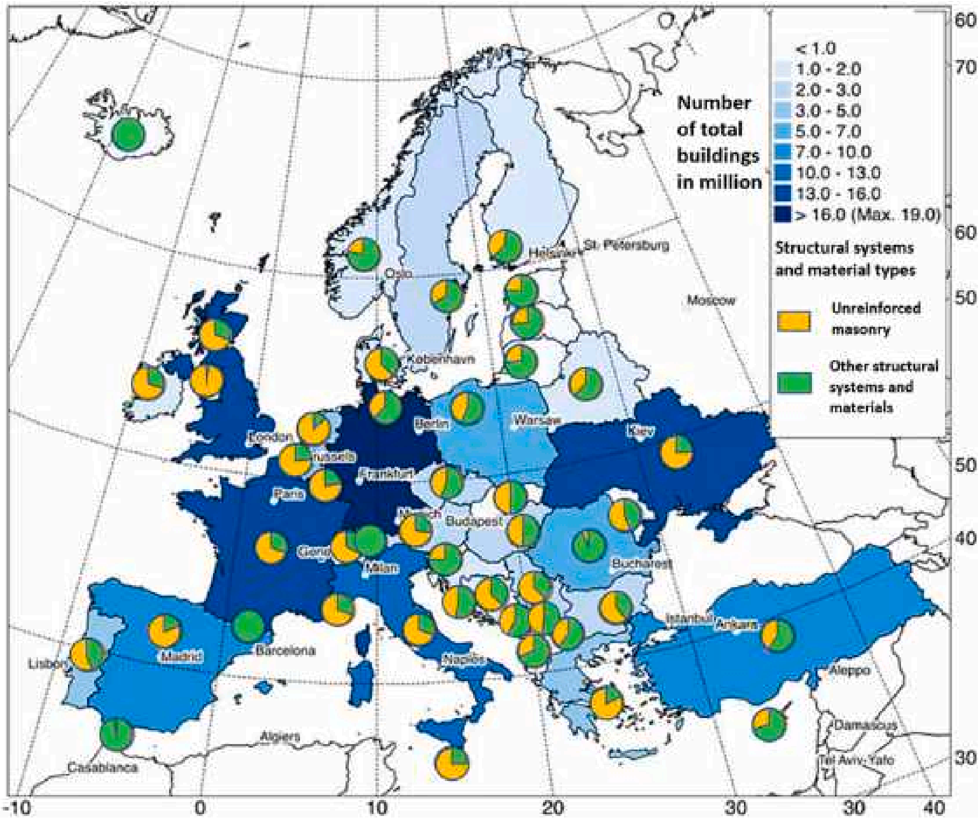

Fig. 2. Exposure of the distribution of URM buildings and the number of all buildings (in millions) in European countries, adapted from [5].

type of analysis [52].

A damage assessment was done for the churches after the L'Aquila earthquake (2009) using the PCM method, see [53]. Totally 28 predefined collapse mechanisms were considered to cover all the collapses that may occur for the macroelements of the churches such as façade, nave, transept, triumphal arch, dome, apse, roof covering, chapel, and bell tower. According to this study, seismic behavior evaluation of the URM churches using the PCM method has been proven as a rapid and reliable method. Moreover, it was concluded that the substitution of timber roofs with reinforced concrete (RC) slabs cause an increase in mass and stiffness, which produced negative effects on the behavior of the churches that should be avoided as a restoration method in the future [53].

The mentioned CMB methods were then developed by importing the actual 3D geometry by considering the irregularities of the masonry towers to assess the susceptibility of them subjected to different distributions of horizontal loads [54]. Five predefined collapse mechanisms, including rocking, Heyman's diagonal cracking, and base shear sliding, were hypothesized for the kinematic limit analysis (KLA) of the towers in [55], and an optimization algorithm was embedded to minimize the failure multiplier of each mechanism.

The 3D KLA-based method was applied to two URM towers, and the results were compared with the results of nonlinear static and dynamic analyses of the detailed finite element models (FEMs). The method is believed to be considered a reliable tool for most cases; however, increasing the number of failure mechanisms such as rocking on the upper corners or the collapse of the belfry can increase the method's accuracy [54].

The possibility of importing the actual 3D geometry of the case study and applying different distributions of horizontal loads are considered as the two main advantages of the 3D KLA-based method for the URM towers that can be expanded to be used for the assessment of URM building aggregates. Nevertheless, computing the collapse multipliers for the predefined collapse mechanisms is a limitation in the proposed KLA methods. To address this limitation and decrease the level of uncertainties related to modeling and capacity, mentioned CMB methods were developed by modeling the structures with rigid macroblocks considering indefinite collapse mechanisms [36].

The application of the CMB method for predicting the masonry domes' failure behavior subjected to static horizontal loads has been investigated in [56]. The dome was modeled by means of a few rigid non-uniform rational basis spline (NURBS) elements, with the hinges at the element edges forming the failure mechanism. KLA was performed on a NURBS model and compared with the results of the NSA of a detailed FEM, and the ultimate load factors were the same, which shows the reliability of this method [56].

The NURBS-based KLA method was then developed [57] to find the minimum collapse multiplier of historical URM building aggregates. In order to estimate the minimum collapse multiplier and investigate the exact position of the fracture lines, a genetic algorithm-based mesh adaptation was applied to a 3D model of the whole aggregate, modeled with NURBS surfaces.

Seismic vulnerability of one of the URM aggregates, named I1 Torrione in Arista, Italy, was assessed using different types of modeling approaches [58]. Four different structural units were chosen from the whole building and modeled using the NURBS-based KLA method to identify the local failure mechanism multipliers. Moreover, both local and global mechanisms were evaluated by performing the NSA on an equivalent frame model of the building in the 3Muri software package [46,59]. Furthermore, the FEM of the aggregate has been provided, and the results from the NSA were compared to other methods' results.

The evaluation of a safety factor, which is the ratio between the spectral acceleration and the maximum acceptable value has been performed for all the methods. Comparing the safety factors obtained from the analyses results of the four mentioned methods illustrates that the analyses using the equivalent frame method in 3Muri software have the

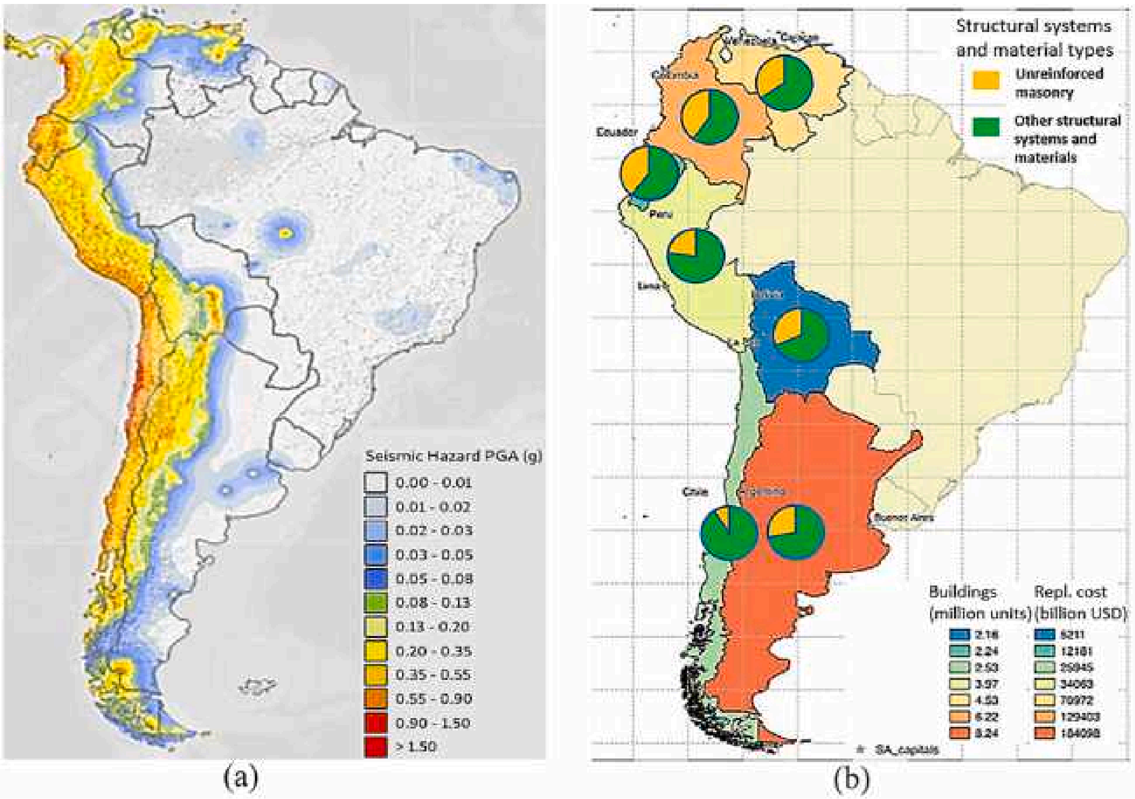

Fig. 3. Hazard map of South America based on PGA [7] (a), and distribution of structural systems, number of all buildings (in millions), and replacement costs (in billion USD), adapted from [9] (b).

largest safety factor value for the building since out-of-plane failure modes have been neglected. NSA was done on the FEM of the building with more computational effort compared to the analysis in the 3Muri software package. However, the safety factor derived from the finite element analysis is lower than the result from 3Muri since the out-of-plane collapse mechanism has been considered. Local mechanism analysis using the 3Muri software package is in the third rank with a fast and enough accurate methodology. Nevertheless, predefined collapse mechanisms have been considered. Finally, the lowest safety factor refers to the local analyses using the NURBS-based KLA method with low computational efforts and automatic mesh adaptation [58].

For the seismic vulnerability assessment of heritage URM buildings with complex architecture, that the global behavior of the structure is not guaranteed, CMB methods are recommended as a very fast and accurate enough method. Since in-situ destructive tests are rarely allowed for the heritage buildings and corresponding high level of uncertainties about structural details, several models need to be analyzed. Therefore, the FEM approach with high computational effort is not recommended.

Detail about each reviewed CMB method is summarized in Table 1, which can facilitate comparing the methods. Moreover, relevant references for some applications have been provided. Although it can be seen that for some of CMB methods (i.e., VULNUS, PCM) the in-plane collapse mechanisms have also been evaluated, the main focus of the CMB methods is to evaluate the local mechanisms occurring due to the presence of flexible diaphragms with a poor connection to the URM walls which can be observed in old buildings.

2.1. Software packages

c-Sisma is a KLA-based software designed to investigate the predetermined collapse mechanism multipliers in which the material properties, wall geometry, and seismic loads are considered as inputs for the software; where the multipliers for each collapse are the outputs [67]. c-Sisma is based on predetermined collapse mechanisms specially designed for typical residential URM buildings, but some software packages were developed to investigate all collapse mechanisms and different types of structures, including arches, domes, and vaults. Brickwork is one of the CMB method software packages that includes these developments in two-dimensional (2D) environments [68] to be developed and verified by comparing to finite element analysis results [69].

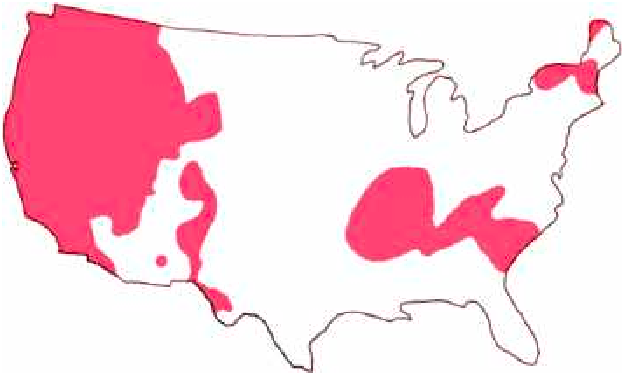

Fig. 5. Approximate mapping of the zones in which current seismic codes do not allow the construction of URM buildings in the United States [15].

A macro-block software [70] was developed for the assessment of out-of-plane behavior of URM walls based on the details elaborated by Lagomarsino [71] in the context of the PERPETUATE project [72] aimed for the performance-based assessment of cultural heritage assets. The interface software is developed and added to the 3Muri software as a module for local collapse mechanism assessment of URM walls based on the predefined collapse mechanisms that are prescribed by the user. A 3D model of a building can be defined, and the collapse mechanisms and the constraints for each component should be specified, and the corresponding collapse multipliers will be calculated based on the kinematic analysis rules [59].

UB-ALMANAC uses an adaptive NURBS-based KLA approach, which is another fast and user-friendly software for upper-bound limit analysis of URM buildings [56,73]. The UB-ALMANAC is used for the seismic vulnerability assessment of churches by 3D modeling of the structure with rigid macro blocks joined by elastoplastic interfaces to derive the collapse multiplier and the most probable collapse mechanism. It can consider the directions of seismic loads, different mesh sizes and types,

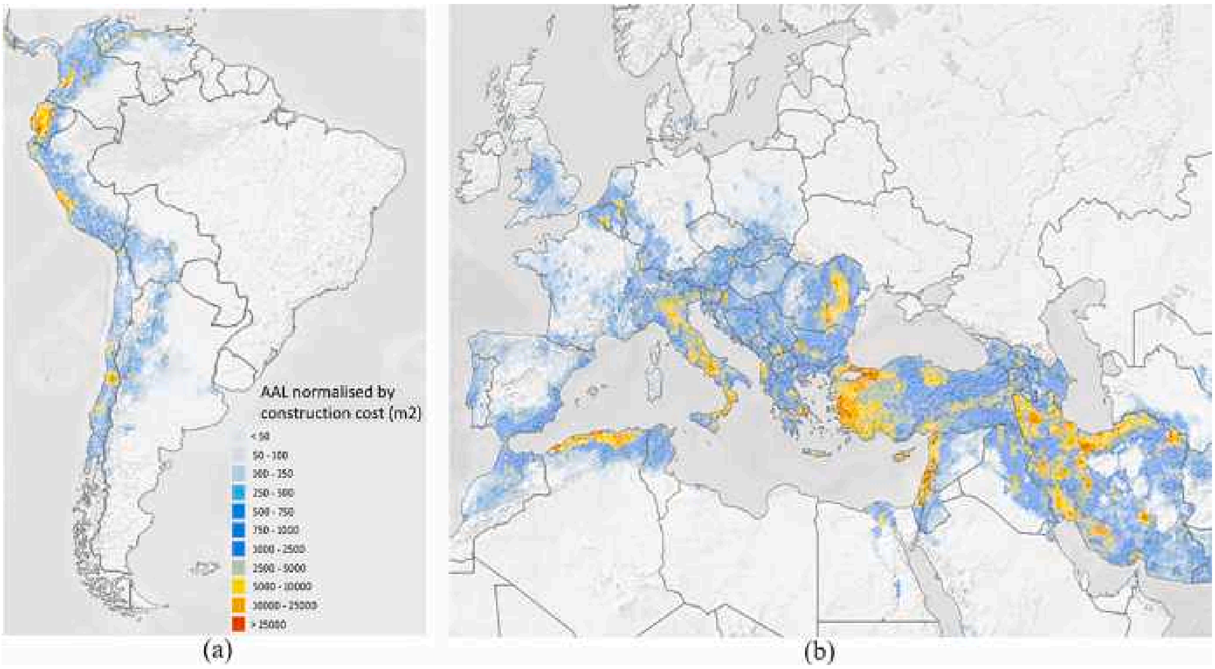

Fig. 4. Seismic risk map including exposure of AAL in South America (a), and European countries and Middle Eastern seismic susceptible zones (b) based on PGA as shown in Figs. 1 and 3(a) [14].

Large Scale

Small building stocks

Building Scale

Fig. 6. Different scales of the seismic vulnerability assessment procedures.

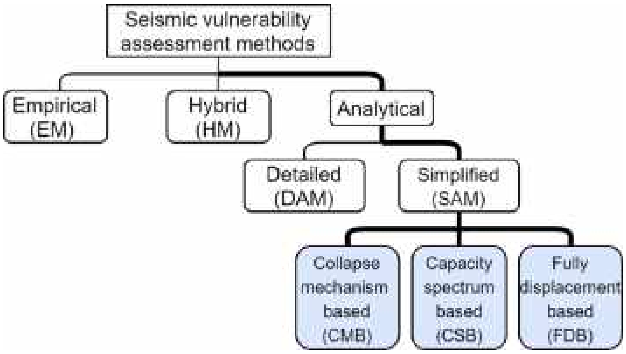

Fig. 7. Seismic vulnerability assessment methods classification. The methods in the blue boxes have been elaborated in this study. (For interpretation of the references to colour in this figure legend, the reader is referred to the web version of this article.)

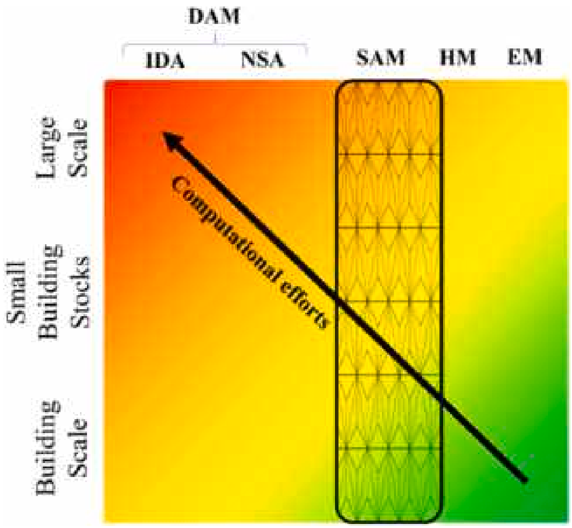

Fig. 8. Schematic overview of different methods as a function of the scales of assessment and corresponding computational efforts.

and interconnection of the walls [74]. LiABlock_3D is a MATLAB-based tool with a graphical user interface into which computer aided design (CAD) files can be easily imported, allowing high flexibility in structural configuration [75].

3. Capacity spectrum-based methods

The Capacity Spectrum-Based (CSB) Method has spread considerably in the last three decades because it can be considered a valid alternative to nonlinear time-history analysis. It was introduced in ATC-40 [76] and implemented in HAZUS methodology for earthquake loss estimation [77]. Other alternative versions of CSB methods are available in FEMA 273 [78] and the N2 method [79,80] that is introduced nowadays in Eurocode 8-part 3 [81]. The N2 method was formulated in the acceleration – displacement format by Fajfar [80], although the original idea of this method dates back to the mid-1980s [82].

The general procedure of the CSB methods is synthesized in Fig. 10. The capacity curve of a building is derived from NSA, and then it is transformed from a multi-degree-of-freedom (MDOF) system into an ESDOF system, as shown in Fig. 10 step 1. It is recommended that capacity curves for URM buildings be fitted via a bilinear elastoplastic capacity curve as illustrated in step 2 [38]. The idealized capacity curve will be intersected with seismic demand in order to compute the performance point of the structure. The seismic demand can be evaluated by selecting the ground motion record and deriving the inelastic response spectrum that allows identifying the performance point that defines the inelastic displacement demand for a specific ground motion, as shown in Fig. 10 step 3. A set of ground motion records can be selected, and the procedure above described can be repeated for increasing ground motion intensities (e.g., Fig. 10 step 3a) up to all limit states are reached so that the earthquake demand parameters can be evaluated for each damage state and the fragility curves that represent the probability of occurrence of a specific damage state for a given seismic demand can be derived [38,72,80]. Alternatively, the smoothed elastic code-based spectrum can be used as shown in Fig. 10 step 3-b. However, the last alternative cannot reflect record-to-record variability; consequently, it is not recommended to develop fragility curves because it does not account for uncertainties due to ground motions.

Different simplified CSB methods have been proposed in literature in a way that the pushover curves are derived for a simplified model [83]. Among them, the failure mechanism identification and vulnerability evaluation (FaMIVE) method is one of the most noteworthy. It was first introduced as a CMB method by D'Ayala [84] to assess the vulnerability of historic URM buildings in town centers.

The collapse multipliers were calculated for probable collapse mechanisms by considering both in-plane and out-of-plane failures through an equivalent static procedure. Twelve probable mechanisms are identified, as shown in Fig. 11, and the most probable mechanism is associated with the lowest base shear capacity [84].

The specific feature of FaMIVE is strictly related to how the data collection is organized by on-site inspection, concentrating on those parameters that can directly qualify the seismic performance of URM buildings and can mostly be surveyed from a rapid visual screening.

The buildings are classified with approximately the same typological layouts, masonry fabrics, and quality of materials. Data collection by performing the on-site inspection is the preliminary step of the FaMIVE method to collect specific information for each building, such as height, length, the thickness of each accessible façade, number of stories,

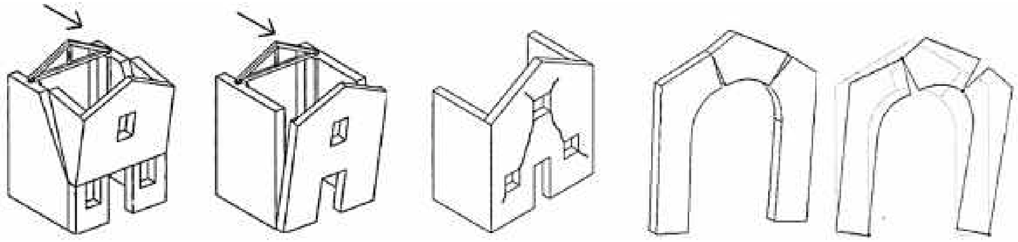

Fig. 9. Different predefined collapse mechanisms in PCM [48].

Table 1

Details about each CMB method and the relevant references for the applications.

Method	Collapse mechanism	Data collection	Output	Brief description	References
VULNUS	1 predefined in-plane and 1 predefined out-of-plane collapse mechanisms	On-site survey	Collapse mechanisms' acceleration and the most probable collapse mechanisms	Computation of collapse multipliers applicable for URM small building stocks.	[44,45,60–63]
PCM	28 predefined in-plane and out-of-plane collapse mechanisms	On-site survey	Collapse mechanisms' acceleration and the most probable collapse mechanisms	Computation of collapse multipliers applicable for URM churches or towers (at building scale).	[51–53,64–66]
3D KLA-based (Towers)	5 predefined collapse mechanisms	On-site and 3D geometrical survey	Collapse mechanisms' acceleration and the most probable collapse mechanisms	Deriving the most probable collapse mechanism of a 3D model applicable for URM towers (at building scale) using optimization algorithms.	[54]
NURBS-based KLA	Indefinite local mechanisms	On-site and 3D geometrical survey	Collapse acceleration and possible fracture lines	Deriving the most probable collapse mechanism of URM buildings' structural components modeled with rigid NURBS elements (at building scale).	[56–58]

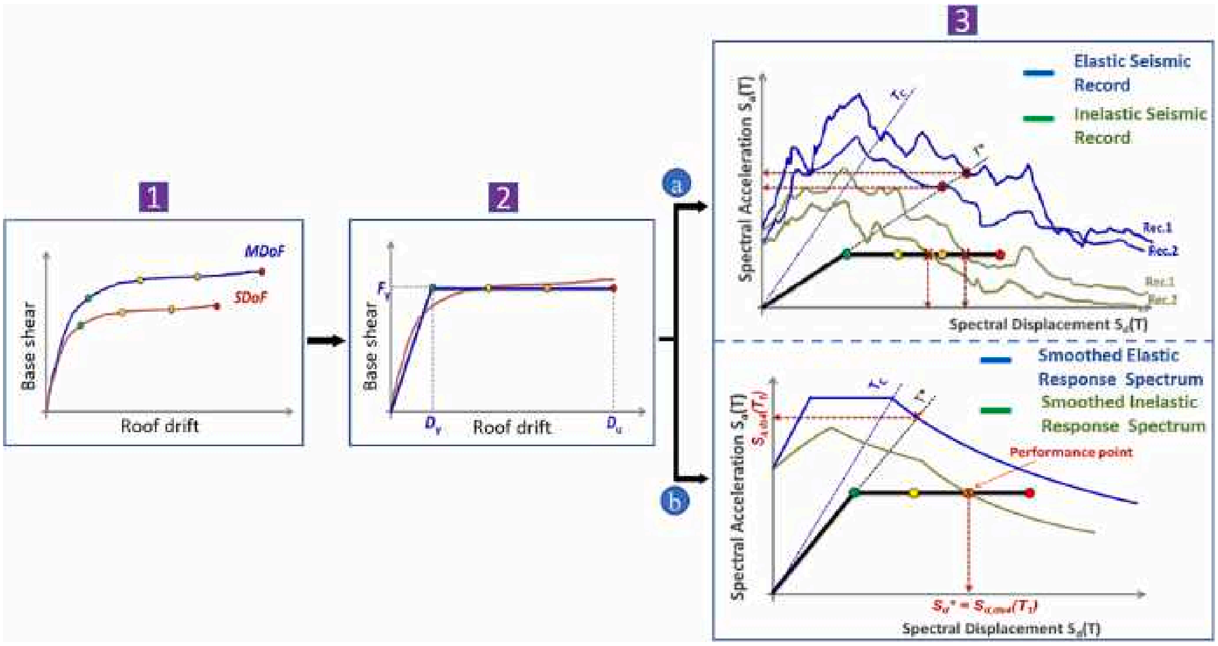

Fig. 10. General procedure of CSB methods, after [38].

strengthening devices, etc. It is possible to input on-site survey data electronically, which is automatically stored in the database sheet to calculate the failure load factors.

Based on the information collected, the ultimate load factor of each external wall for each collapse mechanism is calculated. The collapse mechanism for a given façade depends on the type of connections to the rest of the structure, mainly due to the type of horizontal structures, because if the floor is not rigid in its plane, like vaults or wood floors, it affects the redistribution due to a seismic action that depends from the connections with internal walls and position of the timber beams or vaults. The lower mechanism in terms of collapse acceleration is the most probable one, selected to calculate the fragility curves [85] that can directly be obtained from the collapse accelerations, as illustrated in Fig. 12 with the first alternative.

Then this method was extended from a purely CMB method into a CSB method [32,86]. For each failure mechanism, a specific capacity curve is defined with the aim to define fragility curves. The reliability of the procedure is strictly connected to the idealized capacity curves of the ESDOF model and to the selected limit states. In particular, the authors use the NSA by means of the N2 method, as proposed in Eurocode part 3 [81], where the performance point is evaluated using a degrading pushover curve. This procedure is illustrated in a simplified way in Fig. 12, alternative 2. The capacity curve can be computed and intersected to the acceleration-displacement seismic demand spectra to

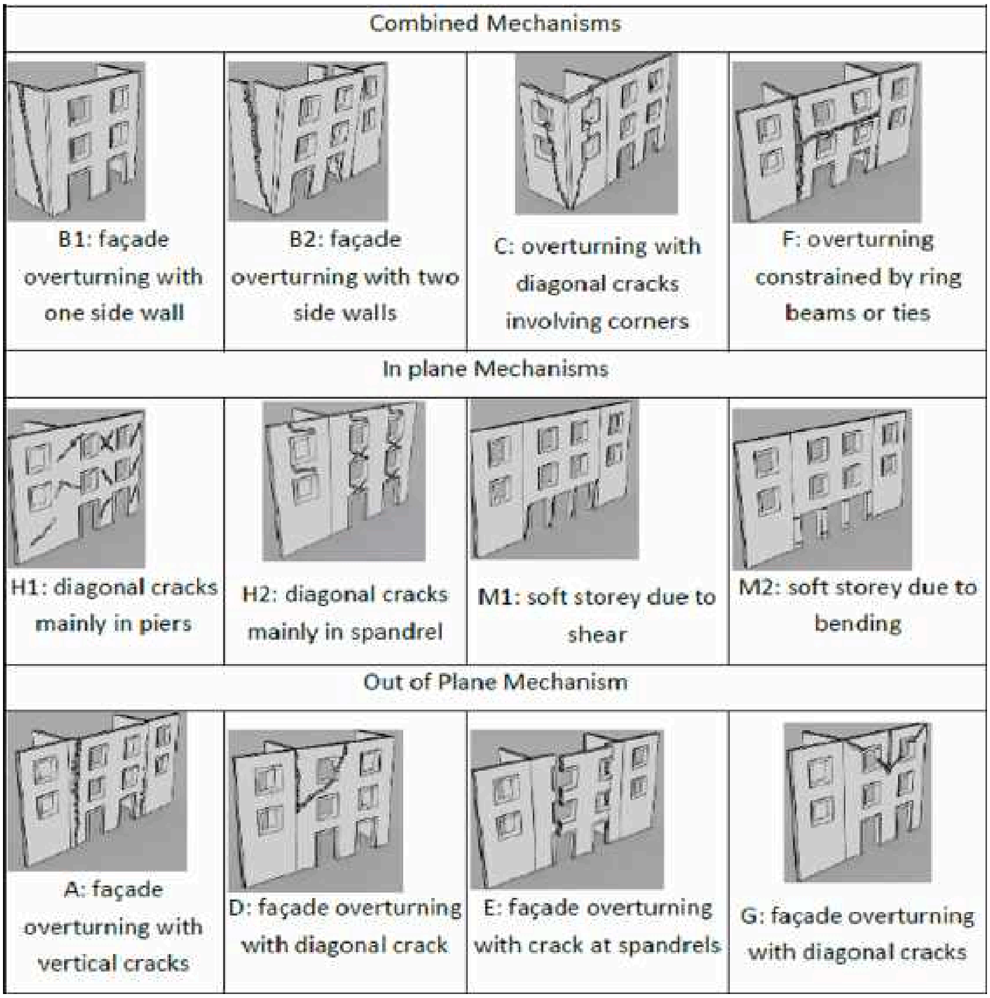

Fig. 11. Collapse mechanisms in FaMIVE methodology [84].

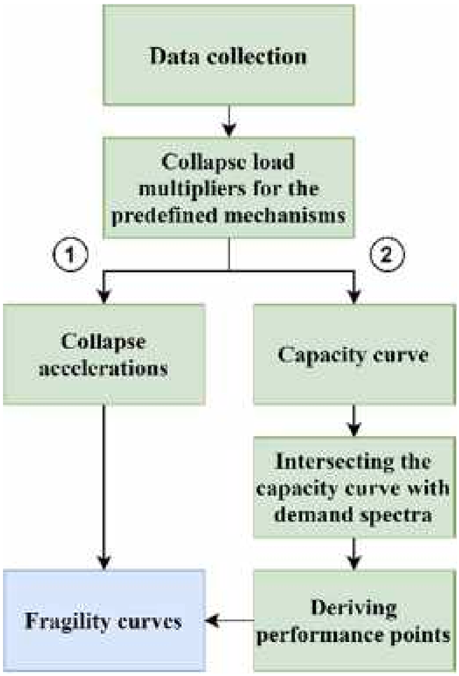

Fig. 12. Flowchart of FaMIVE methodology for deriving fragility curves [38].

define performance points. Fragility curves are then developed from performance points for each building typology [87–89].

Four limit states have been considered for the FaMIVE method based on the pushover curve. Damage limitation (DL) corresponds to the ultimate elastic capacity, significant damage (SD) corresponds to the first peak capacity point, near collapse (NC) limit state corresponds to the maximum displacement without shear resistance degradation, and the collapse (C) limit state corresponds to the ultimate capacity point. The corresponding computed inter-story drifts ratio (IDR) of the mentioned limit states have been summarized in Table 2.

The FaMIVE procedure allows the retention of a high level of detail of the geometry and kinematics of the problem. Simultaneously, since it computes only the ultimate condition, it does not require the computation or time demands of a typical NSA [38].

Uncertainties related to damage thresholds, capacity, and demand have been considered in the FaMIVE method, which are effective on fragility curves. Furthermore, epistemic uncertainties concerning the reliability of input data from the on-site survey form have been contemplated [32].

The FaMIVE method has been utilized for the seismic vulnerability assessment at a large scale for Casbah of Algiers in Algeria [90] in the context of Perpetuate project [72]. First of all, significant building typologies have been identified evaluating the seismic performance of these selected buildings in terms of lateral capacity and collapse mechanisms. Different intervention recommendations were proposed to enhance the Algerian construction quality [90].

The European Commission launched the RISK-UE project [91] in seismic risk analysis, concentrating on the distinctive features of European cities regarding modern and historical buildings [92]. For this purpose, Lagomarsino [93] presented a mechanical procedure for the seismic risk assessment of both URM and RC frames, which was proposed in the framework of the RISK-UE project.

This method uses simplified bilinear capacity spectra, derived depending on the building typology's geometrical and characteristics, including the number of floors, material properties, drift capacity, and timespan of construction. Moreover, for URM buildings designed without any seismic criteria, a prevailing collapse mode is defined based on the method presented in [94]. The uniform collapse mode or the soft-story collapse mode due to rocking or shear failures has been considered, while the out-of-plane mechanisms have been neglected.

By assuming a bilinear representation, the capacity curve is identified in terms of yield spectral displacement and acceleration (d_y and a_y respectively) and ultimate spectral displacement and acceleration (d_u and $a_{u,}$ respectively) points. In the further hypothesis to neglect hardening behavior, capacity curves can be defined by three parameters: the yield acceleration a_y, the fundamental period of the building T, and the structural ductility capacity μ.

The authors proposed a set of European building typology classifications for masonry and RC buildings. In particular, for URM buildings, they introduced six typologies for URM and one typology for reinforced masonry buildings. For each of them, different types of horizontal structures have been considered: wood slabs, masonry vaults, composite steel and masonry slabs, and reinforced concrete. Moreover, three possible intervals have been considered for the number of stories: low-rise with 1–2 stories, mid-rise with 3–5 stories, high- rise with more than six stories. For each building typology, the parameters that define the capacity curves are presented in a table, with the great advantage that the user can directly consider the capacity curve proposed by the authors, and it is not required to model the building. In this approach, once capacity spectra are derived for the building classes, the next step is to use the CSB method. The performance point of each building class is obtained by intersecting the capacity spectrum with the inelastic acceleration-displacement response spectrum, which is produced by using codified spectral shapes calibrated to the PGA obtained from the hazard analysis. Four damage states were considered in order to investigate the level of damage, which can be derived from predefined equations based on the yielding d_y and ultimate d_u displacements [93].

In the context of the RISK-UE project, the seismic risk evaluation of about 60,000 residential buildings in the city of Barcelona in Spain was done using the simplified mechanical method [93]. In particular, six-building classes were considered to develop two damage scenarios realized for deterministic and probabilistic seismic hazard. It was concluded that URM buildings show higher vulnerability compared to RC building typologies. Moreover, maximum damage values were expected for high-rise URM buildings located on soft soils [95].

Pagnini et al.[96] proposed an analytical method to assess the vulnerability of masonry buildings based on a few mechanical and geometrical characteristics of the buildings that are used to derive the bilinear capacity spectrum of the ESDOF model [96,97]. The capacity spectrum method has been applied considering the formulation of the N2 procedure. This method focuses on the effects of the uncertainties related to the mechanical properties and limit states, showing the role of each uncertainty on the results. In order to derive the capacity curve, a URM building of height H is schematized with a stick model based on [98] where each floor is represented with a lamped mass. The capacity curves have been extracted considering the effects of uncertainties related to the specific weight of masonry, shear modulus, shear strength, resistant wall areas, floor loading, inter-story height, and the non-uniform response of the masonry panels [97]. In particular, the authors use Taylor's series around the mean value to account for the uncertainties of the parameter. The propagation of uncertainties has been studied considering the influence of each parameter at a time on the capacity curve. The results show that the most relevant parameters are the resistant wall area in the considered direction and the shear strength. Four random limit states that lie on the mean point have been analyzed as a function of buildings parameters. Then, the fragility curves are derived, including all uncertainties' effects.

The damage thresholds' types and the corresponding values for each presented CSB method have been shown in Table 2 and compared with the limit states proposed in HAZUS [99], Eurocode 8-part 3 [81], and FEMA 356 [100]. The damage thresholds can significantly influence the fragility curve shape, but the values proposed by various authors and codes can be very different, as shown in Table 2, where the damage thresholds are defined as a function of the inter-story drift ratio IDR, the roof displacement, and the spectral displacement.

CSB methods cannot precisely reflect certain dynamic phenomena such as near-field velocity pulses that can considerably influence the structural responses [101]. Table 3 summarizes each aforementioned CSB methods' main feature comparing the type of data collection required to define the input data, the collapse mechanisms considered in the methods, and the relevant references for some case studies. Note that the input demand data is considered nonlinear response spectra with different return periods. The data collection type can be done by performing on-site surveys to record the structural and geometrical detail of the building samples or exposure database provided by the authorities to define the general data about the building typologies at a large scale. All methods are proposed for URM buildings with different horizontal structures, including the flexible, the semi-rigid, and the rigid floor. Among the analyzed methods, only the FaMIVE procedure [32] considers the out-of-plane collapse mechanism and the collapse multipliers that can be evaluated from the structural analysis. The simplified mechanical method (RISK-UE project) [93] considers only the global mechanism but propose a set of European typological masonry structures and, for each of them, the authors evaluated the capacity curves parameters that are presented in a table so that the user doesn't need to define a structural model for a large scale vulnerability assessment. The uncertainties have been considered both in FaMIVE and Pagini et al. [96] methods; in particular, the last method proposed a sensitivity analysis of the results as a function of each parameter. All the CSB methods are suitable to consider the record-to-record variability in terms of using seismic records as demands.

3.1. *Software packages*

The main concept of these methods is the intersection of the capacity curves and the seismic demands to derive the performance points in different damage thresholds [16,108]. Some software packages are related to a specific region, and the capacity curves are related to a typical structural system and configuration in that specific area. Moreover, their exposure can be at urban or multi-level scale, meaning country scale. Geographical Information Systems (GISs) and remote sensing technologies have helped create comprehensive databases and systems for data exposure, analysis, and damage evaluation [109]. All the information about the CSB software packages can be found in Table 4, including relevant references for more information.

A comprehensive study was carried out in a World Bank's Disaster Risk Management Section report, evaluating software packages developed for quantifying risk from natural hazards, including earthquakes [124]. Table 5 summarizes the advantages and disadvantages of some of the well-known CSB methods software packages.

4. Fully displacement-based methods

The main concept of the FDB methods is based on comparing displacement capacities of the ESDOF model of a URM building at different damage thresholds with seismic demands at the corresponding vibration period values of the model, which can be derived from secant stiffness of the capacity curve at each threshold. Although the FDB methods have some common aspects with the CSB methods, their

Table 2
Damage thresholds definition with corresponding values of the codes and the mentioned CSB methods.

Method name	Method type	Damage threshold type	Limit states and their values			
HAZUS (pre-code)	Code	IDR (%)	Slight damage	Moderate damage	Extensive damage	Complete damage
			0.2	0.5	1.2	2.8
HAZUS (low-code)			0.3	0.6	1.5	3.5
Eurocode 8-Part 3	Code	Roof (top) displacement	Limited damage	Significant damage	Near collapse	
			Yielding point of the idealized bilinear capacity curve	75% of the top displacement capacity corresponding the total base shear	Corresponding displacement of 80% of peak base shear	
FEMA 356	Code	IDR (%)	Immediate occupancy	Life safety	Collapse prevention	
			0.3	0.6	1	
FaMIVE (in-plane)	CSB	IDR (%)	Damage limitation	Significant damage	Near collapse	collapse
			0.18–0.23	0.65–0.9	1.23–1.92	1–2.8
FaMIVE (out-of-plane)			0.33	0.88	2.3	4.8
Mechanical method (RISK-UE project)	CSB	Spectral top displacement	Slight damage	Moderate damage	Extensive damage	Complete damage
			0.7 d_y	d_y	$d_y + 0.25(d_u - d_y)$	d_u
Pagini et al.	CSB	Spectral top displacement	0.7 d_y	1.5 d_y	0. 5 ($d_u + d_y$)	d_u

Table 3
Details about each CSB method and the relevant references for the applications.

Method	Data collection	Collapse type	Output	Brief description	References
FaMIVE	On-site survey	In-plane and out-of-plane	Collapse acceleration, the most probable collapse mechanism capacity curve, performance point, fragility curve	Collapse multipliers have been calculated for nine predefined collapse mechanisms, and the most probable mechanism has been derived. Fragility curves can be derived directly from the collapse multipliers or using the CSB procedure.	[32,90,102–104]
Mechanical method (RISK-UE Project)	Exposure Database and on-site survey	In-plane	Capacity curve, performance points, fragility curve	Derivation of bilinear capacity curves for building typologies based on structural description and using CSB procedure to derive the performance points.	[1,95,105,106]
Pagini et al.	Exposure Database and on-site survey	In-plane	Capacity curve, performance points, fragility curve	Derivation of bilinear capacity curves considering uncertainty effects based on the structural description and using CSB procedure to derive the performance point.	[96,107]

Table 4
CSB Loss estimation software packages.

Name	Modifiability[1]	GIS-based	Region	Exposure	Owner	Programming language	References
HAZUS-MH	CS	Yes	North America	Multi	FEMA, NIBS/USGS	VB6, C++, ArcGIS	[110,111]
CAPRA	OS	No	Central America	Multi	EIRD/World Bank	Visual Basic.NET	[112]
ELER	OS	No	Europe	Urban	NERIES/JRA-3, NORSAR, Imperial	Matlab	[113]
EQRM	OS/CS	No	Australia	Urban	Geoscience Australia	Matlab/Python	[114]
EQSIM	CS	No	Europe	Urban	CEDIM/KIT	C++, xmf	[115]
HAZ-Taiwan	CS	No	Asia	Multi	National Science Council/NCREE	Microsoft Visual C++ and MapInfo	[116]
LNECLOSS	CS	Yes	Europe	Urban	LNEC, Consortium	Fortran	[117]
Ergo (MAEviz/mHARP)	OS	Yes	World	Urban	University of Illinois at Urbana Champaign	EclipseRichClient, Geotools	[118]
OpenQuake	OS	No	World	Multi	GEM	Python, Java	[119]
SAFER	OS	No	World	Urban	23 Worldwide Institutions/Multiple EU	Matlab, C++	[120]
SELENA	OS	Yes	World	Urban	NORSAR	Matlab, C++	[121]
OOFIMS	OS	No	World	Multi	SYNER-G EC FP7/Univ. of Rome 'Sapienza'	Matlab	[122]
HAZTURK	CS	Yes	Turkey	Urban	Istanbul Technical University	Java, GIS plug-in	[123]

1 CS: Closed Source, OS: Open Source.

procedure appears to be quite different because the main aim of the CSB method is to evaluate the performance point of the structure from the intersection between the capacity curve of the structure and the demand response spectra. In contrast, in FDB methods for each building class, the displacement capacities are compared with the displacement demand considering the changing of the building stiffness, and the result is the probability of occurrence that specific limit state.

The first developments of the FDB method for URM buildings can be found in Calvi study [125]. The method evaluates the seismic building response for each limit state by the displacement capacity and introduces a correction factor as a function of the dissipated energy. The elastic displacement response is then defined as demand, derived based

Table 5
Advantages and disadvantages of software packages of CSB methods, adapted from [124].

Name	Advantages	Disadvantages
HAZUS-MH	✓ A well-known software package with a detailed user and technical manual. ✓ A full decision module with benefit-cost ratio calculators and mitigation aspects. ✓ Many US building typologies have been included in the software.	× The software is only calibrated to be used for the United States building stocks. × The package cannot operate without (ArcGIS) software. × The software does not explicitly include uncertainty, and the variability of the results can be examined by performing sensitivity analyses. × Epistemic uncertainty is not considered.
CAPRA	✓ Hazard can be input from other programs as long as the file is in the right format (.ame, .txt, or .atn). ✓ A very good rerun capability. ✓ A user-friendly software and easy for basic users to understand the errors. ✓ Well-handled uncertainty consideration. ✓ Inbuilt extendable GIS useful for loss estimations.	× The fatality and economic functions lack a lot of diversity. × The damage distribution is not calculated directly and only a mean damage ratio is available. × No formal manual is provided. × Mix of Spanish and English software language makes the entire interface quite challenging to maneuver.
EQRM	✓ The software offers a large number of exposure options for hazard and risk. ✓ Event-based probabilistic seismic hazard risk assessment with this level of detail and analysis has been provided. ✓ Easy level of modifiability for the MATLAB based type of the software.	× The software is not integrated with GIS. × There is no graphical user interface.
Ergo (MAEviz/ mHARP)	✓ Completely open source with an inbuilt GIS platform. ✓ Scenario risk assessment and decision support are provided. ✓ User-friendly with a large array of infrastructure types for analysis.	× Currently calibrated only for deterministic analysis.
OpenQuake	✓ A well-prepared user manual. ✓ A wide range of hazard and risk analysis tools has been included. ✓ It currently offers the most in-depth probabilistic analysis of any of the reviewed software packages for earthquakes. ✓ Uncertainties related to the seismic hazard is considered.	× Looks only at residential buildings. × No graphical user interface yet.
SELENA	✓ User-friendly with an easy-to-use graphical user interface. ✓ All types of logic trees are allowed in order to consider the uncertainties and calculate the loss.	× Outputs are quite difficult to manipulate compared to other packages. × The high number of input text files makes it complicated to run without errors.

on the return period, seismicity of the location, and local soil conditions. For each building class, two probabilistic limit values are evaluated for the period of vibration and the displacement capacity defining a series of rectangular in the displacement spectrum in which the probability density function is defined (see Fig. 13). Each rectangular can be intersected by the input motion defined by a spectral curve, so that the probability of occurrence of each limit state can be evaluated. This probability of occurrence indicates the percentage of buildings that reach a specific limit state. If the displacement response spectrum crosses the rectangular region, it is possible to evaluate whether the demand is greater or less than the capacity. Alternatively, this probability can be interpreted as the percentage of buildings that attain that limit state. In particular, four limit states have been considered for structural damage; but the out-of-plane collapse mechanisms are not included.[126]. The results of the study show hard soil spectra produce more damage than soft soil spectra due to the shorter periods of vibration [125].

MeBaSe (mechanical based procedure for the seismic risk estimation of unreinforced masonry buildings) was developed by Restrepo et al. [127] as one of the FDB methods presented for RC and masonry buildings. As illustrated in Fig. 14, an ESDOF model of the building is computed with the equivalent mass (m_{eff}) and stiffness (K_{eff}) based on the model proposed in [98]. K_{eff} is calculated as the ratio of the yielding force of the system (F_y) and the effective displacement (Δ_{eff}) for a given displacement demand or limit state (Δ_{LS}), and the simplified bilinear capacity curve will be computed as illustrated in Fig. 14.

Four damage thresholds are considered in the MeBaSe, as illustrated in Fig. 15. No damage (limit state 1) or minor structural damage (limit state 2) corresponds to profile (a) in which the structural components have not reached the yield displacement Δ_y and the triangular shape is considered for low-rise URM buildings dominated by a shear failure mode. Profile (b) is the most probable damage failure for URM buildings. Profile (c) occurs at the top or intermediate stories, depending on the relative stiffness of the story. Profile (d) is related to the strength of substructures such as piers and spandrels. Three aforementioned profiles correspond to limit state 3, and collapse is defined as limit state 4.

The maximum displacement for a given limit state (Δ_{LS}) can be computed as the sum of the yield displacement (Δ_y) and the plastic displacement (Δ_p) [127,128]. Δ_{LS} for each limit state is computed using equation (1).

$$\Delta_{LS} = \kappa_1 h_T \delta_y + \kappa_2 (\delta_{LS} - \delta_y) h_{sp} \quad (1)$$

where $\kappa_1$and κ_2 show the mass distribution in the height of the building that can be obtained from [127] based on the number of stories, δ_y and δ_{LS}correspond to the yielding and the specific limit state drift, h_T and h_{sp}correspond to the total height and effective height of the piers going to the inelastic range. Note that the values for the drift damage thresholds (δ_y,δ_{LS}) can be selected from the experimental test results.

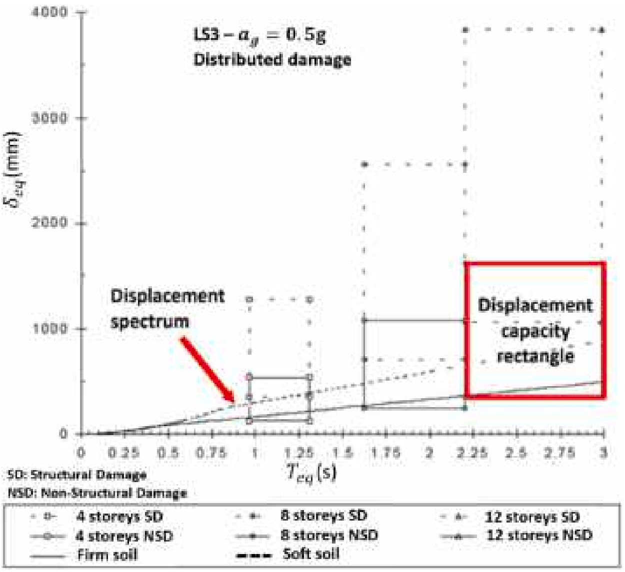

Fig. 13. Comparing displacement capacity rectangle and displacement spectrum-based on CALVI method, adapted from [125].

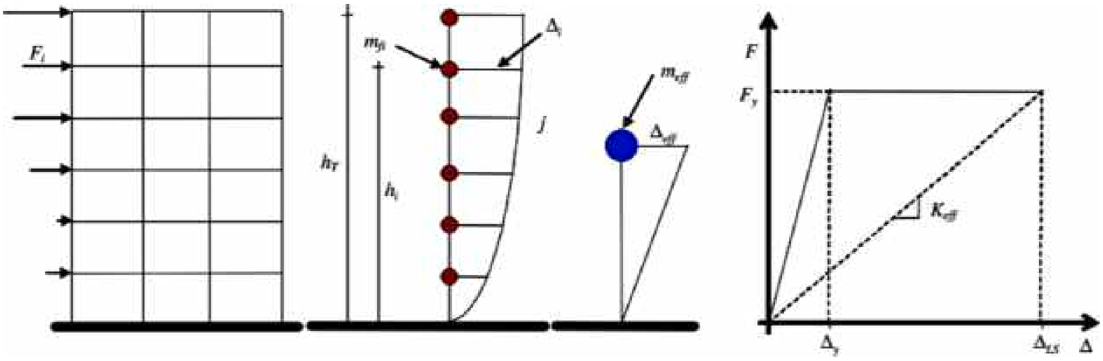

Fig. 14. Schematic view of the MDOF system versus ESDOF and the capacity curve.

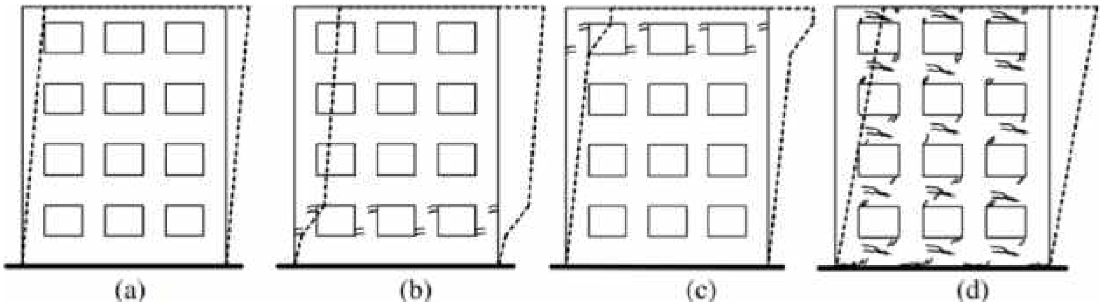

Fig. 15. Different damage thresholds based on the MeBaSe method [127].

The elastic displacement response spectrum, properly scaled for considering the effective damping of each damage threshold, will be considered as the seismic demand. The total probabilities of reaching or exceeding a damage threshold will be calculated for reporting the seismic vulnerability of the buildings.

One-way and two-way bending out-of-plane mechanisms and different levels of uncertainties have been considered in MeBaSe while they were not included in Calvi's method. Out-of-plane damage thresholds definitions of URM walls are based on [129], and one limit state has been considered for the out-of-plane collapse mechanism to define whether the structural component is collapsed or not. For this purpose, ultimate displacement considering the purely rocking behavior of the wall as a rigid body is defined and the collapse displacement is calculated as a fraction of the ultimate displacement based on the experimental tests' results [129]. However, in terms of demand for out-of-plane failure mode, seismic spectral demand for non-structural elements can be utilized.

The MeBaSe method was then developed for seismic fragility assessment of low-rise stone URM buildings in the old historic center of Quebec City, Canada [130]. Four drift thresholds for in-plane failure mechanism are considered and material properties are obtained from experimental tests of stone masonry walls to reduce the uncertainty level of the results. Note that out-of-plane failure mode is neglected in the case study by assuming a sufficient connection between the walls and the roof system [130].

The displacement-based earthquake loss assessment (DBELA) method is an FDB method that was originally developed for RC structures [131,132], but by considering the emerging concepts of performance-based engineering for URM buildings presented in [133], DBELA was then developed to be used for the assessment of URM buildings, as well [134].

The DBELA method [134] uses the basic concept of an ESDOF substitute model based on [98], with a bilinear capacity curve considering post-yield degradation behavior. A building will be converted into an ESDOF model with an equivalent mass and height. Furthermore, the ESDOF system tends to represent the actual behavior of a building in terms of its equivalent displacement and actual energy dissipation. A random population is derived using Monte Carlo simulation, and the displacement capacity of each building is then estimated at different damage thresholds considered for the global performance level of the buildings based on Equation (1). The displacement capacities are derived based on the simple mechanics of material principle for different inelastic deformation profiles [134]. The computed displacement capacity of the buildings will then be compared with the displacement demand of the expected ground motions on the site obtained in terms of 5% damped displacement response spectra, using site-specific empirical ground-motion prediction equation (GMPE) equation based on [135] at the corresponding fundamental vibration periods of different limit states.

The DBELA method was used to assess the seismic vulnerability of confined masonry buildings in Lima, Peru, as a reliable, fast, and computationally efficient FDB method [136]. Moreover, the DBELA method was used to derive the direct socio-economic losses of URM buildings in the city of Mansehra, Pakistan [134]. Three earthquake scenarios have been considered, and direct economic losses, homeless people in the city, and human injuries or death were estimated. These data can be very important for the government authorities to be aware of the expected seismic hazards to plan for the loss reduction. The formulation of DBELA is limited only to the URM building with rigid RC diaphragms that can be improved to consider other types of roof systems, i.e., wooden floors.

SP-BELA is another FDB method especially proposed for RC structures and then developed for the seismic vulnerability assessment of URM buildings [137]. A pushover curve is defined in SP-BELA so that the vibration period and the collapse mechanism are not predefined and can be derived from the NSA. However, since the NSA of the building aggregates is time-consuming, collapse multipliers and collapse mechanisms and the corresponding capacity curves can be computed based on simplified mechanical equations.

The probabilistic framework of the first-order reliability method has been used in MeBaSe to calculate the variability in the capacity and the time-invariant reliability formula to define the probability of collapse.

Nevertheless, the probabilistic structure in SP-BELA and DBELA for convolving variability in the displacement capacity and demand to calculate the probability of exceedance of limit states is based on the definition of the capacity curve for each building generated in a random dataset through Monte Carlo simulation with less computational efforts compared to the MeBaSe method. Simplified bilinear pushover curves are derived for the buildings of a dataset based on the mechanical-based equations with a reasonable level of computational effort.

The displacement demand is then calculated for each building and directly compared with the corresponding displacement capacity to determine whether a given limit state is exceeded or reached. The procedure to calculate the probability of exceedance of each limit state condition is graphically illustrated in Fig. 16. For each building in a sample, the equivalent period of vibration (T), the displacement capacity (Δ_{cap}), and the corresponding simplified capacity curve are computed. The demand in SP-BELA is modeled using spectral displacement ordinates (S_d). As shown in Fig. 16 (a), box 1, the displacement capacity of each limit state is converted into a spectral system and plotted for comparison with the spectral demand displacement. The dissipation of energy is taken into account through a coefficient η related to the damage and the ductility, based on [137]. The coefficient η, which is lower than 1, has been applied by multiplying the spectral demand ordinate or dividing the displacement capacity as illustrated in Fig. 16 (a), box 2.

As illustrated in Fig. 16 (a), if the point (spectral displacement capacity) is above the spectral curve, the capacity (Δ_{cap}) is higher than the demand (Δ_{dem}), and the corresponding building passes the damage threshold. When the point is below the spectrum, demand is higher than capacity, and the building does not attain the corresponding damage threshold and thus belongs to the higher limit state condition. As shown in Fig. 16 (b), the exceedance probability of the building aggregates has been carried out by repeating the comparison procedure and dividing the number of points below the spectral curve by the total population. Note that updating the building sample size during the methodology procedure is an advantage of SP-BELA compared to other mentioned FDB methods that reduces the computational efforts.

Capacity displacement damage thresholds are derived using Equation (1) for the in-plane failure mode. Three different drift limits have been identified for brick masonry with a low percentage of voids (LPV), a high percentage of voids (HPV), and for natural stones that just correspond to the third limit state as presented in Table 6. The methodology utilized for deriving the unique out-of-plane damage threshold and the corresponding capacity curve, which was embedded in the MeBaSe method, has been used in the SP-BELA method. Uncertainties related to damage thresholds, capacity, and demand have been inspected in SP-BELA by considering variability in drift limit states, buildings' characteristics, and spectral displacement demand, respectively [137].

SP-BELA is then calibrated for the large-scale vulnerability assessment by comparison with the results from the damage probability matrices elaborated in [93] and then by comparison with real damage data in terms of a damage scenario [138].

Recently SP-BELA is used to derive the fragility functions for adobe masonry buildings in Peruvian Andes, Peru, where 67% of rural buildings are adobe masonry. The simplified bilinear and trilinear capacity curves were derived by combining the in-plane and out-of-plane behavior of the buildings [139]. For this purpose, in-plane capacity was calculated based on the SP-BELA method, and out-of-plane behavior was represented by a lateral force-displacement curve based on [129]. First, displacement capacity for the out-of-plane actions was compared with the spectral displacement demands derived from a group of seismic records. If the building passed the acceptability check and did not satisfy the failure criteria, in-plane capacities for each damage threshold were compared with the demands. Finally, the combined fragility curves, considering both failure mechanisms, were derived [139].

The limit state values in CSB methods and the corresponding software packages are derived based on the mechanical equations related to the stiffness, mass, and height of the building after deriving the pushover curves; however, in well-known FDB methods (MeBaSe, DBELA, and SP-BELA) inter-story drift limit states should be defined performing experimental tests on the structural components to reduce the uncertainties. Afterward, the displacement capacities for each damage threshold can be defined using Equation (1). The inter-story drift limit states values utilized for the seismic vulnerability assessment of specific case studies with different construction material using mentioned FDB methods have been summarized in Table 6.

A simplified FDB loss assessment methodology for different building typologies, including URM buildings, was proposed by O'Reilly et al. [140] in the framework of the research consortium ReLUIS (Italian

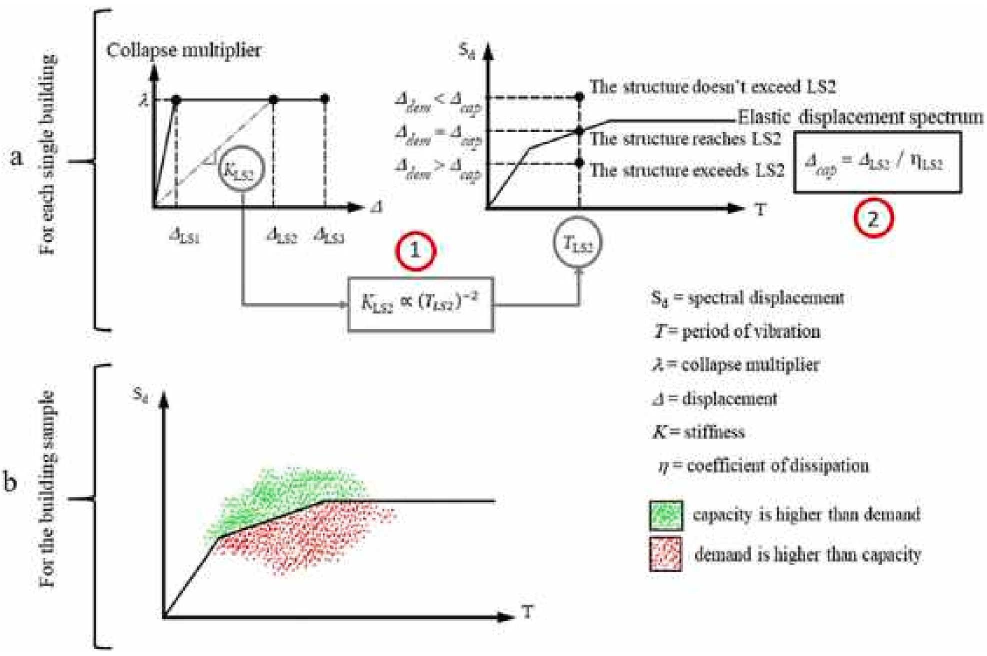

Fig. 16. Analytical methodology of SP-BELA, adapted from [138].

Table 6
Inter-storey drift limit states in percentage, utilized for the seismic vulnerability assessment of case studies using FDB methods.

Method name	Material type	Region	Limit states and their values in percentage (%)					References
Calvi	Brick masonry	Italy	Limit state 1	Limit state 2	Limit state 3			[125]
			0.1	0.3	0.5			
DBELA	Brick masonry	Northern Pakistan	0.08	0.15	0.35			[134]
SP-BELA	Adobe masonry	Peru (Peruvian Andes)	0.052	0.26	0.52			[139]
	Brick and stone masonry	Italy	Limit state 1	Limit state 2	Limit state 3 for LPV[1] (Brick)	Limit state 3 for HPV[2] (Brick)	Limit state 3 for Natural stone	[137]
			0.13	0.34	0.72	0.45	0.61	
MeBaSe	Stone masonry	Canada (Quebec)	Slight	Moderate	Extensive	Complete		[130]
			0.13	0.32	0.68	1.03		

1 low percentage of voids.
2 high percentage of voids.

acronym for University Laboratories Network of Seismic Engineering) in Italy, funded between 2014 and 2018. An FDB methodology for the seismic loss assessment of URM buildings, which needs nonlinear analysis of detailed numerical models of the buildings in the framework of the ReLUIS project was also developed, which lies outside the scope of this study [141]. Nevertheless, in another approach, a simplified loss assessment methodology was applied to a URM school in Italy using a simplified FDB method [140].

A bilinear capacity curve of the ESDOF model based on [142] was defined by a yielding base shear capacity depending mainly on input parameters such as geometric features, material properties, mode shapes, and expected failure mechanisms. The ultimate capacity was computed based on the main prevailing mode of failure. Subsequently, the displacement thresholds were determined for each limit state. The yield displacement is computed as a function of maximum base shear and the effective stiffness, and the second and the third damage thresholds are derived linearly with respect to the first limit state. The fourth failure mode corresponds to the combination between the critical failure mode and the adequate story drift proposed in [142]. The ultimate displacement is computed considering both mentioned failure modes. After characterizing the force-displacement relationship, fragility curves were computed using an analytical formulation [141].

The mean annual frequency of exceedance of each damage threshold was derived from the site hazard curve using the intensity computed from the FDB method, and expected annual loss can be estimated. Detail about the simplified loss assessment methodology lies outside the scope of this study described in [140,141].

The methodology proposed in [140] has been applied to a URM school to evaluate the annual expected loss value. The comparison between the results from this SAM with the results from NSA of the building modeled in the 3Muri software [46] shows a good correlation and, the methodology can be utilized for loss estimation of URM buildings with less computational efforts compared to time-demanding DAMs.

Although the CSB methods usually need less computational effort compared to the recent FDB methods and require fewer structural details, the FaMIVE method can be an exception as described in the text. Therefore, the CSB methods are usually considered efficient methods when details are not available, but in locations where a high level of details are available, the CSB methods can yield a higher level of uncertainties compared to the FDB methods [108,109]. Detail about each FDB method and relevant references for the case studies have been summarized in Table 7. One method for collecting data is the generation of a random population of buildings that should represent the whole building stock typology utilized in DBELA [134] and SP-BELA [137] methods. Note that FDB methods can be calibrated and utilized for the seismic vulnerability assessment of URM buildings with flexible, semi-rigid, and rigid floor systems; however, the connection of the walls to the floor plays a key role in investigating the out-of-plane collapse mechanisms. The out-of-plane collapse mechanisms, which can be critical for URM buildings, are considered in the MeBaSe [127] and SP-BELA methods and neglected in other FDB methods and can be neglected by assuming a robust connection between the floor and the URM walls.

Table 7
Details about each FDB method and the relevant references for the applications.

Method	Data collection	Collapse type	Input demand data	Applications	References
Calvi	Exposure database	In-plane	Design displacement spectra considering energy dissipation and damping effects	Computation of the probability of occurring a limit state by intersecting the capacity rectangles and the demand line.	[125,143]
MeBaSe	Exposure database	In-plane	Elastic Displacement spectrum considering damping effects	Computation of the limit states' capacity displacement and comparison of the values with the demand displacements at the limit state's corresponding vibration period of the structure.	[127,130]
		Out-of-plane	Acceleration demand for non-structural elements		
DBELA	Random population	In-plane	5% damped displacement spectra using site-specific GMPE	Derivation of the idealized bilinear capacity curve considering post-yield degradation, defining the limit states, and investigating the probability of reaching or exceeding each limit state to the demand displacements.	[134,136,144,145]
SP-BELA	Random population	In-plane	5% damped displacement spectra with definite PGA values	Computation of the displacement capacity, and the vibration period of the building at each limit state for in-plane and out-of-plane collapse mechanisms and investigating the probability of reaching or exceeding each limit state to the demand displacements.	[138,139,146,147]
		Out-of-plane	Acceleration demands for non-structural elements		
O'Reilly et al.	On-site survey	In-plane	Damped displacement spectra	Estimation of annual expected loss value by computing the mean annual frequency of exceedance of each damage threshold using FDB procedure.	[140]

4.1. Software packages

DBELA [134] and SP-BELA [137] are two software packages that used the FDB method. Each software program was developed by EUCENTRE in Pavia, Italy, with a different code-built structure that is applicable to the seismic vulnerability assessment of URM buildings at a large scale. SP-BELA can be connected to a user-friendly web-based GIS tool, thus allowing basic analysts to access the data on exposure, vulnerability, and hazard. The software highlights critical situations in terms of a seismic scenario by providing seismic risk maps. Moreover, near real-time damage scenario analysis is provided [138].

Although FDB software packages, compared to the well-known CSB software packages (i.e., HAZUS, ELER, SELENA), give less variability in results, they require a reasonable sample of building typology data. Therefore, in an area with low knowledge about the building samples, CSB software packages are recommended [108]. Furthermore, to evaluate the losses due to each earthquake scenario, two or more software packages should be used to reduce uncertainties and provide more robust data.

5. Conclusion

Different types of SAMs were reviewed for the seismic vulnerability assessment of URM buildings and were categorized into three groups: (1) CMB, (2) CSB, and (3) FDB by emphasizing their mechanics basis, pros, and cons. Different software packages for each method were presented and reviewed by explaining their limitations and advantages.

CMB methods were presented as fast and reliable tools to assess the final collapse loading. For the seismic vulnerability assessment of historical URM buildings with complex architecture, using only global mechanism analysis may not reflect the actual behavior of a building. Therefore, the CMB methods are recommended to derive the collapse loadings for different local mechanisms and define the critical collapse mechanism with the lowest collapse loading value. These methods are widely applied to the seismic vulnerability assessment at building scale as a fast tool, but due to the simplicity, they are also widespread in large scale use. Considering predefined collapse mechanisms may cause unrealistic results; therefore, modeling the buildings with rigid blocks has attracted wide attention to overcome this shortcoming. Recently in order to decrease the level of epistemic uncertainties and speed up the analysis procedure, importing 3D drawings is tried to be embedded into the CMB method software packages.

CSB methods using mechanical methods to derive the capacity curves and intersect the capacity curves with the demand spectra are widely used for the seismic vulnerability assessment of URM buildings. All the CSB methods and the software packages, except the FaMIVE method, neglect the out-of-plane behavior of URM walls, which can be critical collapse mechanisms in old URM buildings. Although the FaMIVE method needs a high level of detail and all sources of uncertainties are considered in the methodology, the main general feature of the CSB methods and software packages is their efficiency, which makes them suitable for the assessment at a large scale. A lower level of input data, simplicity of the procedure, less computational efforts, and a high number of software packages with user-friendly graphical user interfaces and well-prepared user manuals that can be linked to the GIS environment are the advantages of the CSB methods compared to other methods. These advantages make the CSB methods more efficient and suitable for the seismic vulnerability assessment at a large scale when detail input data is not provided for the location of a case study.

FDB methods investigate the probability of reaching or exceeding the limit state displacement values to the demand displacements at the corresponding secant stiffness of a building. The FDB methods and software packages usually need more detailed input data about the buildings and more computational efforts compared to the conventional CSB methods. Nevertheless, in locations that detail data about the building typologies is provided, the FDB methods can be more reliable with less level of uncertainty. Although the out-of-plane behavior of URM walls is usually neglected in the CSB methods, except for the FaMIVE method, this phenomenon is evaluated in the MeBaSe and SP-BELA methods.

All the methods for the seismic vulnerability assessment at a large scale should be verified based on the post-earthquake loss data from previous seismic events to find the most reliable method which can be applied in different areas, with different building typologies, as well as being fast and easy to use for the users. Although the mentioned software packages are used for the seismic vulnerability assessment of different cities and building stocks, it is necessary to use different well-known software packages in a specific area to reduce the uncertainty level and conclude robust results.

CRediT authorship contribution statement

Amirhosein Shabani: Conceptualization, Methodology, Investigation, Resources, Data curation, Writing - original draft, Visualization. **Mahdi Kioumarsi:** Conceptualization, Methodology, Writing - review & editing, Supervision, Project administration, Funding acquisition. **Maria Zucconi:** Conceptualization, Methodology, Resources, Writing - review & editing, Visualization, Supervision.

Declaration of Competing Interest

The authors declare that they have no known competing financial interests or personal relationships that could have appeared to influence the work reported in this paper.

Acknowledgements

This work is a part of the HYPERION project. HYPERION has received funding from the European Union's Framework Programme for Research and Innovation (Horizon 2020) under grant agreement No 821054. The contents of this publication are the sole responsibility of Oslo Metropolitan University (Work Package 5, Task 2) and do not necessarily reflect the opinion of the European Union.

References

[1] Vicente R, Parodi S, Lagomarsino S, Varum H, Silva JM. Seismic vulnerability and risk assessment: case study of the historic city centre of Coimbra, Portugal. Bull Earthq Eng 2011;9:1067–96. https://doi.org/10.1007/s10518-010-9233-3.

[2] Sorrentino L. Reconstruction plans after the 2009 L'Aquila earthquake. From building performance to historical centre performance. In: 9th International Conference on Structural Analysis of Historical Constructions; 2014. p. 11-006.

[3] Calvi GM, Pinho R, Magenes G, Bommer JJ, Restrepo-Vélez LF, Crowley H. Development of seismic vulnerability assessment methodologies over the past 30 years. ISET J Earthquake Technol 2006;43:75–104.

[4] Romano F, Faggella M, Gigliotti R, Zucconi M, Ferracuti B. Comparative seismic loss analysis of an existing non-ductile RC building based on element fragility functions proposals. Eng Struct 2018;177:707–23. https://doi.org/10.1016/j.engstruct.2018.08.005.

[5] Crowley H, Rodrigues D, Silva V, Despotaki V, Martins L, Romão X, et al. The European Seismic Risk Model 2020 (ESRM 2020); 2019.

[6] Motamed H, Calderon A, Silva V, Costa C. Development of a probabilistic earthquake loss model for Iran. Bull Earthq Eng 2018. https://doi.org/10.1007/s10518-018-0515-5.

[7] Pagani M, Garcia-Pelaez J, Gee R, Johnson K, Poggi V, Styron R, et al. Global Earthquake Model (GEM) Seismic Hazard Map (version 2018.1–December 2018), DOI: 10.13117. GEM-GLOBAL-SEISMIC-HAZARD-MAP-2018.1; 2018.

[8] Yepes-Estrada C, Silva V, Valcárcel J, Acevedo AB, Tarque N, Hube M, et al. Modeling the Residential Building Inventory in South America for Seismic Risk Assessment. Earthquake Spectra 2017;33. https://doi.org/10.1193/101915eqs155dp.

[9] Yepes-Estrada C, Silva V. Probabilistic Seismic Risk Assessment of the Residential Building Stock in South America. In: 16th World Conference on Earthquake, 16WCEE. Chile; 2016.

[10] Roca P, Cervera M, Gariup G, Pelà L. Structural Analysis of Masonry Historical Constructions. Classical and Advanced Approaches. Arch Comput Methods Eng 2010;17:299–325. https://doi.org/10.1007/s11831-010-9046-1.

[11] Valluzzi MR, Sbrogiò L. Vulnerability of Architectural Heritage in Seismic Areas: Constructive Aspects and Effect of Interventions. In: Amoruso G, Salerno R, editors. Cultural Landscape in Practice: Conservation vs Emergencies. Cham:

Springer International Publishing; 2019. p. 203–18. https://doi.org/10.1007/978-3-030-11422-0_14.

[12] Bruneau M. Seismic evaluation of unreinforced masonry buildings—A state-of-the-art report. Can J Civ Eng 1994;21:512–39. https://doi.org/10.1139/l94-054.

[13] Silva V, Amo-Oduro D, Calderon A, Costa C, Dabeek J, Despotaki V, et al. Development of a global seismic risk model. Earthquake Spectra 2020. https://doi.org/10.1177/8755293019899953.

[14] V Silva DA-O, Calderon A, Dabbeek J, Despotaki V, Martins L, Rao A, et al. Global Earthquake Model (GEM) Seismic Risk Map (version 2018.1); 2018. https://doi.org/10.13117/GEM-GLOBAL-SEISMIC-RISK-MAP-2018.

[15] Council AT, Reitherman R, Perry SC. Unreinforced Masonry Buildings and Earthquakes: Developing Successful Risk Reduction Programs: Prepared for Federal Emergency Management Agency. Federal Emergency Management Agency; 2009.

[16] Makhoul N, Argyroudis S. Loss Estimation Software: Dvelopments, Limitations and Future Needs. In: 16th European Conference on Earthquake Engineering (16ECEE); 2018.

[17] Silva V, Akkar S, Baker J, Bazzurro P, Castro J, Crowley H, et al. Current Challenges and Future Trends in Analytical Fragility and Vulnerability Modelling. Earthquake Spectra 2019. https://doi.org/10.1193/042418EQS101O.

[18] Ferreira TM, Mendes N, Silva R. Multiscale Seismic Vulnerability Assessment and Retrofit of Existing Masonry Buildings. Buildings 2019;9:91. https://doi.org/10.3390/buildings9040091.

[19] Rosti A, Rota M, Penna A. Damage classification and derivation of damage probability matrices from L'Aquila (2009) post-earthquake survey data. Bull Earthq Eng 2018;16:3687–720. https://doi.org/10.1007/s10518-018-0352-6.

[20] Biglari M, Formisano A. Damage Probability Matrices and Empirical Fragility Curves From Damage Data on Masonry Buildings After Sarpol-e-zahab and Bam Earthquakes of Iran. Front Built Environ 2020;6. https://doi.org/10.3389/fbuil.2020.00002.

[21] De Martino G, Di Ludovico M, Prota A, Moroni C, Manfredi G, Dolce M. Estimation of repair costs for RC and masonry residential buildings based on damage data collected by post-earthquake visual inspection. Bull Earthq Eng 2017;15:1681–706. https://doi.org/10.1007/s10518-016-0039-9.

[22] Del Gaudio C, De Martino G, Di Ludovico M, Manfredi G, Prota A, Ricci P, et al. Empirical fragility curves for masonry buildings after the 2009 L'Aquila, Italy, earthquake. Bull Earthq Eng 2019;17:6301–30. https://doi.org/10.1007/s10518-019-00683-4.

[23] Ferlito R, Guarascio M, Zucconi M. Assessment of a vulnerability model against post-earthquake damage data: the case study of the historic city centre of L'Aquila in Italy. In: 9th International Conference on Earthquake Resistant Engineering Structures,MuRiCo5, Bologna, Italy; 2013. p. 393–404.

[24] Romano F, Zucconi M, Ferracuti B. Seismic fragility curves for RC buildings at territorial scale. In: COMPDYN. ECCOMAS Thematic Conference on Computational Methods in Structural Dynamics and Earthquake Engineering. Crete, Greece: National Technical University of Athens; 2019. p. 24–6.

[25] Colonna S, Imperatore S, Zucconi M, Ferracuti B. Post-Seismic Damage Assessment of a Historical Masonry Building: The Case Study of a School in Teramo. Key Eng Mater 2017;747:620–7. https://doi.org/10.4028/www.scientific.net/KEM.747.620.

[26] Benedetti D, Benzoni G, Parisi MA. Seismic vulnerability and risk evaluation for old urban nuclei. Earthquake Eng Struct Dyn 1988;16:183–201. https://doi.org/10.1002/eqe.4290160203.

[27] Sisti R, Di Ludovico M, Borri A, Prota A. Damage assessment and the effectiveness of prevention: the response of ordinary unreinforced masonry buildings in Norcia during the Central Italy 2016–2017 seismic sequence. Bull Earthq Eng 2019;17:5609–29. https://doi.org/10.1007/s10518-018-0448-z.

[28] Zucconi M, Ferlito R, Sorrentino L. Simplified survey form of unreinforced masonry buildings calibrated on data from the 2009 L'Aquila earthquake. Bull Earthq Eng 2018;16:2877–911. https://doi.org/10.1007/s10518-017-0283-7.

[29] Zucconi M, Ferlito R, Sorrentino L. Validation and extension of a statistical usability model for unreinforced masonry buildings with different ground motion intensity measures. Bull Earthq Eng 2020;18:767–95. https://doi.org/10.1007/s10518-019-00669-2.

[30] Zucconi M, Sorrentino L, Ferlito R. Principal component analysis for a seismic usability model of unreinforced masonry buildings. Soil Dyn Earthquake Eng 2017;96:64–75. https://doi.org/10.1016/j.soildyn.2017.02.014.

[31] Aguado JL, Ferreira TM, Lourenço PB. The use of a large-scale seismic vulnerability assessment approach for masonry façade walls as an effective tool for evaluating, managing and mitigating seismic risk in historical centers. Int J Architectural Heritage 2018;12:1259–75. https://doi.org/10.1080/15583058.2018.1503366.

[32] D'Ayala D. Assessing the seismic vulnerability of masonry buildings. Handbook of Seismic Risk Analysis and Management of Civil Infrastructure Systems; 2013. p. 334–65. https://doi.org/10.1533/9780857098986.3.334.

[33] De Luca F, Verderame GM, Manfredi G. Analytical versus observational fragilities: the case of Pettino (L'Aquila) damage data database. Bull Earthq Eng 2015;13:1161–81. https://doi.org/10.1007/s10518-014-9658-1.

[34] Kappos AJ, Panagopoulos G, Panagiotopoulos C, Penelis G. A hybrid method for the vulnerability assessment of R/C and URM buildings. Bull Earthq Eng 2006;4:391–413. https://doi.org/10.1007/s10518-006-9023-0.

[35] Lang K, Bachmann H. On the seismic vulnerability of existing unreinforced masonry buildings. J Earthquake Eng 2003;7:407–26. https://doi.org/10.1080/13632460309350456.

[36] D'Altri AM, Sarhosis V, Milani G, Rots J, Cattari S, Lagomarsino S, et al. Modeling Strategies for the Computational Analysis of Unreinforced Masonry Structures: Review and Classification. Arch Comput Methods Eng 2019. https://doi.org/10.1007/s11831-019-09351-x.

[37] Rota M, Penna A, Magenes G. A methodology for deriving analytical fragility curves for masonry buildings based on stochastic nonlinear analyses. Eng Struct 2010;32:1312–23. https://doi.org/10.1016/j.engstruct.2010.01.009.

[38] Meslem A, D'Ayala D, Vamvatsikos D, Porter K, Rossetto T. Guidelines for Analytical Vulnerability Assessment - Low/Mid-Rise. Global Earthquake Model 2015.

[39] Bracchi S, Rota M, Magenes G, Penna A. Seismic assessment of masonry buildings accounting for limited knowledge on materials by Bayesian updating. Bull Earthq Eng 2016;14:2273–97. https://doi.org/10.1007/s10518-016-9905-8.

[40] Tondelli M, Rota M, Penna A, Magenes G. Evaluation of uncertainties in the seismic assessment of existing masonry buildings. J Earthquake Eng 2012;16:36–64. https://doi.org/10.1080/13632469.2012.670578.

[41] Rota M, Penna A, Magenes G. A framework for the seismic assessment of existing masonry buildings accounting for different sources of uncertainty. Earthquake Eng Struct Dyn 2014;43:1045–66. https://doi.org/10.1002/eqe.2386.

[42] Maio R, Tsionis G. Seismic fragility curves for the European building stock. JRC Technical Report. Brussels, Belgium: European Commission; 2015.

[43] Bernardini A, Gori R, Modena C. An application of coupled analytical models and experiential knowledge for seismic vulnerability analyses of masonry buildings. Eng Aspects Earthquake Phenomena 1990;3:161–80.

[44] Cocco G, D'Aloisio A, Spacone E, Brando G. Seismic Vulnerability of Buildings in Historic Centers: From the "Urban" to the "Aggregate" Scale. Frontiers. Built Environ 2019;5. https://doi.org/10.3389/fbuil.2019.00078.

[45] Chieffo N, Formisano A. Comparative seismic assessment methods for masonry building aggregates: a case study. Front Built Environ 2019;5:123. https://doi.org/10.3389/fbuil.2019.00123.

[46] Lagomarsino S, Penna A, Galasco A, Cattari S. TREMURI program: An equivalent frame model for the nonlinear seismic analysis of masonry buildings. Eng Struct 2013;56:1787–99. https://doi.org/10.1016/j.engstruct.2013.08.002.

[47] Chiumiento G, Formisano A. Simplified and Refined Analyses for Seismic Investigation of Historical Masonry Clusters: Comparison of Results and Influence of the Structural Units Position. Frontiers. Built Environ 2019;5. https://doi.org/10.3389/fbuil.2019.00084.

[48] PCM. Direttiva del Presidente del Consiglio dei Ministri per valutazione e riduzione del rischio sismico del patrimonio culturale con riferimento alle norme tecniche per le costruzioni. GU 2011 [in Italian].

[49] Ministero delle Infrastrutture. Norme tecniche per le costruzioni (NTC). Roma, Italy: Ministero delle Infrastrutture e dei Trasporti, Decreto Ministeriale del.; 2018 [in Italian].

[50] Bartoli G, Betti M, Vignoli A. A numerical study on seismic risk assessment of historic masonry towers: a case study in San Gimignano. Bull Earthq Eng 2016;14:1475–518. https://doi.org/10.1007/s10518-016-9892-9.

[51] Torelli G, D'Ayala D, Betti M, Bartoli G. Analytical and numerical seismic assessment of heritage masonry towers. Bull Earthq Eng 2019. https://doi.org/10.1007/s10518-019-00732-y.

[52] Criber E, Brando G, De Matteis G. The effects of L'Aquila earthquake on the St. Gemma church in Goriano Sicoli: part I—damage survey and kinematic analysis. Bull Earthq Eng 2015;13:3713–32. https://doi.org/10.1007/s10518-015-9792-4.

[53] Lagomarsino S. Damage assessment of churches after L'Aquila earthquake (2009). Bull Earthq Eng 2012;10:73–92. https://doi.org/10.1007/s10518-011-9307-x.

[54] Milani G. Fast Vulnerability Evaluation of Masonry Towers by Means of an Interactive and Adaptive 3D Kinematic Limit Analysis with Pre-assigned Failure Mechanisms. Int J Architec Heritage 2019;13:941–62. https://doi.org/10.1080/15583058.2019.1645241.

[55] Sarhosis V, Milani G, Formisano A, Fabbrocino F. Evaluation of different approaches for the estimation of the seismic vulnerability of masonry towers. Bull Earthq Eng 2018;16:1511–45. https://doi.org/10.1007/s10518-017-0258-8.

[56] Grillanda N, Chiozzi A, Milani G, Tralli A. Collapse behavior of masonry domes under seismic loads: An adaptive NURBS kinematic limit analysis approach. Eng Struct 2019;200:109517. https://doi.org/10.1016/j.engstruct.2019.109517.

[57] Grillanda N, Valente M, Milani G. ANUB-Aggregates: a fully automatic NURBS-based software for advanced local failure analyses of historical masonry aggregates. Bull Earthq Eng 2020. https://doi.org/10.1007/s10518-020-00848-6.

[58] Grillanda N, Valente M, Milani G, Chiozzi A, Tralli A. Advanced numerical strategies for seismic assessment of historical masonry aggregates. Eng Struct 2020;212:110441. https://doi.org/10.1016/j.engstruct.2020.110441.

[59] Lagomarsino S, Penna A, Galasco A, Cattari S. TREMURI program: seismic analyses of 3D masonry buildings, Verson 12.2.0. University of Genoa (mailto:tremuri@ gmail com); 2021.

[60] Bernardini A, D'Ayala D, Meroni F, Pessina V, Valluzzi M. Damage scenarios in the Vittorio Veneto town centre (NE Italy). Bollettino di Geofisica Teorica ed Applicata 2008;49:505–12.

[61] Cardani G, Modena C, Binda LA, Valluzzi MR. Seismic vulnerability methods for masonry buildings in historical centres: validation and application for prediction analyses and intervention proposals. In: 13th World Conference on Earthquake Engineering. Vancouver, B.C., Canada; 2004.

[62] Donà M, Carpanese P, Follador V, Sbrogiò L, da Porto F. Mechanics-based fragility curves for Italian residential URM buildings. Bull Earthq Eng 2020;1–29. https://doi.org/10.1007/s10518-020-00928-7.

[63] Bernardini A, Valluzzi M, Modena C, D'Ayala D, Speranza E. Vulnerability assessment of the historical masonry building typologies of Vittorio Veneto (NE Italy). Bollettino di Geofisica Teorica ed Applicata 2008;49:463–83.

[64] Lagomarsino S, Podesta S. Seismic vulnerability of ancient churches: I. Damage assessment and emergency planning. Earthquake Spectra 2004;20:377–94. https://doi.org/10.1193/1.1737735.

[65] Da Porto F, Silva B, Costa C, Modena C. Macro-scale analysis of damage to churches after earthquake in Abruzzo (Italy) on April 6, 2009. J Earthquake Eng 2012;16:739–58. https://doi.org/10.1080/13632469.2012.685207.

[66] Castori G, Borri A, De Maria A, Corradi M, Sisti R. Seismic vulnerability assessment of a monumental masonry building. Eng Struct 2017;136:454–65. https://doi.org/10.1016/j.engstruct.2017.01.035.

[67] Modena C, Valluzzi M, Zenere M. Manuale d'uso del Programma c-Sisma 3.0 PRO. Procedura automatica per il calcolo e la verifica di meccanismi di pareti in muratura. Università degli Studi di Padova 2009.

[68] Galassi S, Paradiso M. BrickWORK software-aided analysis of masonry structures. IERI Procedia 2014;7:62–70.

[69] Galassi S, Ruggieri N, Tempesta G. A novel numerical tool for seismic vulnerability analysis of ruins in archaeological sites. Int J Architec Heritage 2020;14:1–22. https://doi.org/10.1080/15583058.2018.1492647.

[70] Lagomarsino S, Ottonelli D. MB-Perpetuate - a Macro-Block program for the seismic assessment (Freeware software for the safety verification of seismic local mechanisms). PERPETUATE (EC-FP7 Project), Deliverable D29; 2012.

[71] Lagomarsino S. Seismic assessment of rocking masonry structures. Bull Earthq Eng 2015;13:97–128. https://doi.org/10.1007/s10518-014-9609-x.

[72] Lagomarsino S, Cattari S. PERPETUATE guidelines for seismic performance-based assessment of cultural heritage masonry structures. Bull Earthq Eng 2015;13:13–47. https://doi.org/10.1007/s10518-014-9674-1.

[73] Chiozzi A, Milani G, Tralli A. A Genetic Algorithm NURBS-based new approach for fast kinematic limit analysis of masonry vaults. Comput Struct 2017;182:187–204. https://doi.org/10.1016/j.compstruc.2016.11.003.

[74] Chiozzi A, Grillanda N, Milani G. UB-ALMANAC: An adaptive limit analysis NURBS-based program for the automatic assessment of partial failure mechanisms in masonry churches. Eng Fail Anal 2017;85. https://doi.org/10.1016/j.engfailanal.2017.11.013.

[75] Cascini L, Gagliardo R, Portioli F. LiABlock_3D: a software tool for collapse mechanism analysis of historic masonry structures. Int J Architec Heritage 2020;14:75–94. https://doi.org/10.1080/15583058.2018.1509155.

[76] Council AT. Seismic evaluation and retrofit of concrete buildings, Report ATC-40. Redwood City (CA); 1996.

[77] Committee E, Whitman R, Borcherdt R, Brookshire D, Eisner R, Holmes W, et al. HAZUS-MH 2.1 Earthquake Model Technical Manual. Washington, D.C.: Federal Emergency Management Agency; 2013.

[78] FEMA. NEHRP guidelines for the seismic rehabilitation of buildings, FEMA 273, and NEHRP Commentary on the guidelines for the seismic rehabilitation of buildings, FEMA 274. Washington, D.C.: Federal Emergency Management Agency; 1997.

[79] Fajfar P. A nonlinear analysis method for performance-based seismic design. Earthquake spectra 2000;16:573–92. https://doi.org/10.1193/1.1586128.

[80] Fajfar P. Capacity spectrum method based on inelastic demand spectra. Earthquake Eng Struct Dyn 1999;28:979–93. https://doi.org/10.1002/(SICI)1096-9845(199909)28:9%3C979::AID-EQE850%3E3.0.CO;2-1.

[81] Eurocode 8: Design of structures for earthquake resistance – Part 3: Assessment and retrofitting of buildings. EN 1998-3. Brussels: The European Union; 2005.

[82] Fajfar P, Fischinger M. Non-linear seismic analysis of RC buildings: implications of a case study. Eur Earthquake Eng 1987;1:31–43.

[83] Hannewald P, Michel C, Lestuzzi P, Crowley H, Pinguet J, Fäh D. Development and validation of simplified mechanics-based capacity curves for scenario-based risk assessment of school buildings in Basel. Eng Struct 2020;209:110290. https://doi.org/10.1016/j.engstruct.2020.110290.

[84] D'Ayala D, Speranza E. Definition of Collapse Mechanisms and Seismic Vulnerability of Historic Masonry Buildings. Earthquake Spectra 2003;19. https://doi.org/10.1193/1.1599896.

[85] D'Ayala D, Speranza E. An Integrated Procedure for the Assessment of Seismic Vulnerability of Historic Buildings. 12th European Conference Earthquake Engineering. 2002.

[86] D'Ayala D. Force and Displacement Based Vulnerability Assessment for Traditional Buildings. Bull Earthq Eng 2005;3:235–65. https://doi.org/10.1007/s10518-005-1239-x.

[87] Bosiljkov V, D'Ayala D, Novelli V. Evaluation of uncertainties in determining the seismic vulnerability of historic masonry buildings in Slovenia: use of macro-element and structural element modelling. Bull Earthq Eng 2014;1–19. https://doi.org/10.1007/s10518-014-9652-7.

[88] Lamego P, Lourenco P, Sousa M, Marques R. Seismic vulnerability and risk analysis of the old building stock at urban scale: application to a neighbourhood in Lisbon. Bull Earthq Eng 2017;15:2901–37. https://doi.org/10.1007/s10518-016-0072-8.

[89] Parameswaran S, Gajendran C, Praveen A. A fuzzy based approach for improving seismic safety of masonry building in Kerala context. Int J Civ Eng Technol 2018;9:1053–61.

[90] Novelli VI, D'Ayala D, Makhloufi N, Benouar D, Zekagh A. A procedure for the identification of the seismic vulnerability at territorial scale. Application to the Casbah of Algiers. Bull Earthq Eng 2015;13:177–202. https://doi.org/10.1007/s10518-014-9666-1.

[91] Mouroux P, Le Brun B. Presentation of RISK-UE project. Bull Earthq Eng 2006;4:323–39. https://doi.org/10.1007/s10518-006-9020-3.

[92] Mouroux P, Bertrand E, Bour M, Le Brun B, Depinois S, Masure P. The European RISK-UE project: an advanced approach to earthquake risk scenarios. In: Proc of the 13th World Conference on Earthquake Engineering; 2004.

[93] Lagomarsino S, Giovinazzi S. Macroseismic and mechanical models for the vulnerability and damage assessment of current buildings. Bull Earthq Eng 2006;4:415–43. https://doi.org/10.1007/s10518-006-9024-z.

[94] Cattari S, Curti E, Giovinazzi S, Lagomarsino S, Parodi S, Penna A. A mechanical model for the vulnerability assessment of masonry buildings in urban areas. In: Proceedings of the VI Congreso nazionale "L'ingegneria Sismica in Italia", Genova, Italy; 2004.

[95] Irizarry J, Lantada N, Pujades LG, Barbat AH, Goula X, Susagna T, et al. Ground-shaking scenarios and urban risk evaluation of Barcelona using the Risk-UE capacity spectrum based method. Bull Earthq Eng 2011;9:441–66. https://doi.org/10.1007/s10518-010-9222-6.

[96] Pagnini L, Vicente R, Lagomarsino S, Varum H. A mechanical model for the seismic vulnerability assessment of old masonry buildings. J Earthquakes Struct Technopress 2011;2:25–42. https://doi.org/10.12989/eas.2011.2.1.025.

[97] Pagnini L, Vicente R, Lagomarsino S, Varum H. A mechanical method for the vulnerability assessment of masonry buildings. Proceedings of 14th world conference on earthquake engineering structure. 2008.

[98] Shibata A, Sozen MA. Substitute-structure method for seismic design in R/C. J Struct Division 1976;102.

[99] Hazus. MH MR5, Earthquake Loss Estimation Methodology, Advanced Engineering Building Module (AEBM). Washington, D.C.: Department of Homeland Security, Federal Emergency Management Agency; 2001.

[100] FEMA. Prestandard and Commentary for the Seismic Rehabilitation of Buildings, FEMA 356. Washington, DC: Federal Emergency Management Agency; 2000.

[101] Krawinkler H, Seneviratna G. Pros and cons of a pushover analysis of seismic performance evaluation. Eng Struct 1998;20:452–64. https://doi.org/10.1016/S0141-0296(97)00092-8.

[102] D'Ayala D, Ansal A. Non linear push over assessment of heritage buildings in Istanbul to define seismic risk. Bull Earthq Eng 2012;10:285–306. https://doi.org/10.1007/s10518-011-9311-1.

[103] D'Ayala DF, Paganoni S. Assessment and analysis of damage in L'Aquila historic city centre after 6th April 2009. Bull Earthq Eng 2011;9:81–104. https://doi.org/10.1007/s10518-010-9224-4.

[104] Basset-Salom L, Guardiola-Víllora A. Seismic performance of masonry residential buildings in Lorca's city centre, after the 11th May 2011 earthquake. Bull Earthq Eng 2014;12:2027–48. https://doi.org/10.1007/s10518-013-9559-8.

[105] Maio R, Vicente R, Formisano A, Varum H. Seismic vulnerability of building aggregates through hybrid and indirect assessment techniques. Bull Earthq Eng 2015;13:2995–3014. https://doi.org/10.1007/s10518-015-9747-9.

[106] Erdik M, Sesetyan K, Demircioglu M, Hancilar U, Zulfikar C, Cakti E, et al. Rapid earthquake hazard and loss assessment for Euro-Mediterranean region. Acta Geophys 2010;58:855–92.

[107] Villani M, Demartinos K, Vanini M, Faccioli E. Application of ground shaking scenarios to PSHA and risk assessment in near field. In: 14th European conference on earthquake engineering. Ohrid, Republic of Macedonia; 2010.

[108] Daniell J, Contadakis M. Open Source Procedure for Assessment of Loss using Global Earthquake Modelling software (OPAL). Nat Hazards Earth Syst Sci 2011;11. https://doi.org/10.5194/nhess-11-1885-2011.

[109] Hosseinpour V, Saeidi A, Nollet M-J, Nastev M. Seismic loss estimation software: A comprehensive review of risk assessment steps, software development and limitations. Eng Struct 2021;232:111866. https://doi.org/10.1016/j.engstruct.2021.111866.

[110] HAZUS. MH2.1, Multi-hazard loss estimation methodology. Departament of Homeland Security Emergency Preparness and Response Directorate, FEMA; 2003.

[111] Methodology FM-hLE. Earthquake Model-Technical Manual, Hazus-MH 2.1. Washington DC: Department of Homeland Security, Federal Emergency Management Agency, Mitigation Division; 2013.

[112] Bernal G, Cardona O. Next generation CAPRA software. In: 16th European Conference on Earthquake Engineering, 16ECEE,. Thessaloniki, Greece; 2018.

[113] Corbane C, Hancilar U, Ehrlich D, De Groeve T. Pan-European seismic risk assessment: a proof of concept using the Earthquake Loss Estimation Routine (ELER). Bull Earthq Eng 2017;15:1057–83. https://doi.org/10.1007/s10518-016-9993-5.

[114] Robinson D, Fulford G, Dhu T. EQRM: Geoscience Australia's Earthquake Risk Model: Technical Manual: Version 3.0; 2005.

[115] McCallen D, Petersson N, Rodgers A, Miah M, Pitarka A, Petrone F, et al. The Earthquake Simulation (EQSIM) Framework for Physics-Based Fault-to-Structure Simulations. 17WCEE,. Sendai, Japan; 2020.

[116] Yeh C-H, Loh C-H, Tsai K-C. Overview of Taiwan Earthquake Loss Estimation System. Nat Hazards 2006;37:23–37. https://doi.org/10.1007/s11069-005-4654-z.

[117] Costa A, Sousa M, Carvalho A, Coelho E. Evaluation of seismic risk and mitigation strategies for the existing building stock: Application of LNECloss to the metropolitan area of Lisbon. Bull Earthq Eng 2009;8:119–34. https://doi.org/10.1007/s10518-009-9160-3.

[118] Illinois Uo. ERGO: Multi-hazard assessment, response and planning. University of Illinois; 2020.

[119] Silva V, Crowley H, Pagani M, Monelli D, Pinho R. Development of the OpenQuake engine, the Global Earthquake Model's open-source software for seismic risk assessment. Nat Hazards 2014;72:1409–27. https://doi.org/10.1007/s11069-013-0618-x.

[120] Esmaili O. Developing a rapid seismic performance based rating system in safety assessment of buildings. PhD thesis: Irvine: University of California; 2014.

[121] Molina S, Lang DH, Lindholm CD. SELENA – An open-source tool for seismic risk and loss assessment using a logic tree computation procedure. Comput Geosci 2010;36:257–69. https://doi.org/10.1016/j.cageo.2009.07.006.

[122] Cavalieri F, Franchin P, Giovinazzi S. Earthquake-altered flooding hazard induced by damage to storm water systems. Sustain Resilient Infrastruct 2016;1:14–31. https://doi.org/10.1080/23789689.2016.1178560.

[123] Elnashai AS, Hampton S, Karaman H, Lee JS, McLaren T, Myers J, et al. Overview and Applications of Maeviz-Hazturk 2007. J Earthquake Eng 2008;12:100–8. https://doi.org/10.1080/13632460802013750.

[124] Daniell J. Review of Open Source and Open Access Software Packages Available to Quantify Risk from Natural Hazards, Global Facility for Disaster Reduction and Recovery (GFDRR). Washington DC, United State of America: World Bank; 2014.

[125] Calvi GM. A displacement-based approach for vulnerability evaluation of classes of buildings. J Earthquake Eng 1999;3:411–38. https://doi.org/10.1080/13632469909350353.

[126] Magenes G, Calvi GM. In-plane seismic response of brick masonry walls. Earthquake Eng Struct Dyn 1997;26:1091–112. https://doi.org/10.1002/(SICI)1096-9845(199711)26:11%3C1091::AID-EQE693%3E3.0.CO;2-6.

[127] Restrepo-Velez L, Magenes G. Simplified procedure for the seismic risk assessment of unreinforced masonry buildings. In: 13th World Conference on Earthquake Engineering, Canada; 2004.

[128] Restrepo-Vélez L, Magenes G. Experimental testing in support of a mechanics-based procedure for the seismic risk evaluation of unreinforced masonry buildings. In: Proceeding of IV international Seminar SAHC, Padua, Italy; 2004. p. 1079–89.

[129] Doherty K, Griffith MC, Lam N, Wilson J. Displacement-based seismic analysis for out-of-plane bending of unreinforced masonry walls. Earthquake Eng Struct Dyn 2002;31:833–50. https://doi.org/10.1002/eqe.126.

[130] Abo-El-Ezz A, Nollet M-J, Nastev M. Seismic fragility assessment of low-rise stone masonry buildings. Earthquake Eng Eng Vib 2013;12:87–97. https://doi.org/10.1007/s11803-013-0154-4.

[131] Crowley H, Pinho R, Bommer JJ. A probabilistic displacement-based vulnerability assessment procedure for earthquake loss estimation. Bull Earthq Eng 2004;2:173–219. https://doi.org/10.1007/s10518-004-2290-8.

[132] Bal IE, Crowley H, Pinho R. Displacement-based earthquake loss assessment: Method development and application to Turkish building stock. IUSS Press; 2010.

[133] Abrams DP. Performance-based engineering concepts for unreinforced masonry building structures. Prog Struct Mat Eng 2001;3:48–56. https://doi.org/10.1002/pse.70.

[134] Ahmad N, Crowley H, Pinho R, Ali Q. Displacement-based earthquake loss assessment of masonry buildings in Mansehra City. Pakistan J Earthquake Eng 2010;14:1–37. https://doi.org/10.1080/13632461003651794.

[135] Boore DM, Atkinson GM. Ground-motion prediction equations for the average horizontal component of PGA, PGV, and 5%-damped PSA at spectral periods between 0.01 s and 10.0 s. Earthquake Spectra 2008;24:99–138. https://doi.org/10.1193/1.2830434.

[136] Lovon H, Tarque N, Silva V, Yepes-Estrada C. Development of Fragility Curves for Confined Masonry Buildings in Lima. Peru Earthquake Spectra 2018;34:1339–61. https://doi.org/10.1193/090517EQS174M.

[137] Borzi B, Crowley H, Pinho R. Simplified pushover-based earthquake loss assessment (SP-BELA) method for masonry buildings. Int J Architect Heritage 2008;2:353–76. https://doi.org/10.1080/15583050701828178.

[138] Faravelli M, Borzi B, Polli D, Pagano M. Calibration of a mechanics-based method for large-scale vulnerability assessment. Bull Earthq Eng 2019;17:2485–508. https://doi.org/10.1007/s10518-019-00560-0.

[139] Sumerente G, Lovon H, Tarque N, Chácara C. Assessment of Combined In-Plane and Out-of-Plane Fragility Functions for Adobe Masonry Buildings in the Peruvian Andes. Frontiers. Built Environ 2020;6. https://doi.org/10.3389/fbuil.2020.00052.

[140] O'Reilly GJ, Monteiro R, Nafeh AMB, Sullivan TJ, Calvi GM. Displacement-Based Framework for Simplified Seismic Loss Assessment. J Earthquake Eng 2020;24:1–22. https://doi.org/10.1080/13632469.2020.1730272.

[141] Ottonelli D, Cattari S, Lagomarsino S. Displacement-Based Simplified Seismic Loss Assessment of Masonry Buildings. J Earthquake Eng 2020;24:23–59. https://doi.org/10.1080/13632469.2020.1755747.

[142] Lagomarsino S, Cattari S. Performance-based earthquake engineering of URM buildings. Displacement-based loss assessment of masonry structures (First year Report of Reluis/DPC 2014–2018). Pavia, Italy: Reluis; 2015.

[143] Faccioli E, Pessina V, Calvi GM, Borzi B. A study on damage scenarios for residential buildings in Catania city. J Seismolog 1999;3:327–43. https://doi.org/10.1023/A:1009856129016.

[144] Ahmad N, Ali Q, Crowley H, Pinho R. Displacement-based seismic risk assessment of stone masonry buildings of Pakistan. In: 3rd Asia conference on earthquake engineering Bangkok, Thailand (electronic source); 2010.

[145] Ahmad N, Ali Q, Adil M, Khan AN. Developing Seismic Risk Prediction Functions for Structures. Shock Vib 2018;2018. https://doi.org/10.1155/2018/4186015.

[146] Colombi M, Borzi B, Crowley H, Onida M, Meroni F, Pinho R. Deriving vulnerability curves using Italian earthquake damage data. Bull Earthq Eng 2008;6:485–504. https://doi.org/10.1007/s10518-008-9073-6.

[147] Acevedo AB, Jaramillo JD, Yepes C, Silva V, Osorio FA, Villar M. Evaluation of the seismic risk of the unreinforced masonry building stock in Antioquia. Colombia Nat Hazards 2017;86:31–54. https://doi.org/10.1007/s11069-016-2647-8.

Paper II

Shabani, A., Plevris, V., Kioumarsi, M.

A Comparative Study on the Initial In-plane Stiffness of Masonry Walls with Openings.

(2021) In Proceedings of the World Conference on Earthquake Engineering, 17WCEE, Sendai, Japan.

A COMPARATIVE STUDY ON THE INITIAL IN-PLANE STIFFNESS OF MASONRY WALLS WITH OPENINGS

A. Shabani(1), V. Plevris(2), M. Kioumarsi(3)

(1) *PhD Candidate, Department of Civil Engineering and Energy Technology, Oslo Metropolitan University, Oslo, Norway, amirhose@oslomet.no*
(2) *Associate Professor, Department of Civil and Architectural Engineering, Qatar University, Doha, Qatar, vplevris@qu.edu.qa*
Professor, Dept. of Civil Engineering and Energy Technology, Oslo Metropolitan University, Oslo, Norway, vageli@oslomet.no
(3) *Associate Professor, Department of Civil Engineering and Energy Technology, Oslo Metropolitan University, Oslo, Norway, mahdik@oslomet.no*

Abstract

Masonry buildings have been used for centuries in various locations around the world, including areas with high seismicity. Studies about the behavior of masonry structural components subjected to lateral loadings and retrofitting techniques for improving their performance have gained much attraction lately. Various simplified methods have been presented in the literature for the seismic vulnerability assessment of masonry buildings. The initial in-plane stiffness of masonry walls is a key parameter which significantly affects the nonlinear backbone curve of the masonry walls as well as their ultimate in-plane strength.

Different simplified analytical methods have been proposed for deriving the initial in-plane stiffness of masonry buildings with regular or irregular openings by considering the flexible spandrels that can translate and rotate under lateral load and flexible piers' endings. In the analytical methods, the initial in-plane stiffness of each pier will be computed from the equations by considering the geometry of each component as input. Each structural component is considered as a spring and the stiffness of the whole system is computed based on equations of springs in series or in parallel.

The finite element method is considered as a reliable tool for verifying the analytical methods. For this purpose, a homogenization method has been employed for modeling the masonry walls and lateral loads have been applied on the walls with the assumption of linear material to derive the initial in-plane stiffness of the walls. For this purpose, three categories of masonry walls have been considered with one, two, and three openings where the openings' geometries also vary to investigate the effect of opening placements and irregularities on the initial in-plane stiffness of the walls. Afterwards, the stiffnesses computed from the analytical methods are compared with the stiffnesses that have been derived from the finite element analysis to investigate the accuracy of the analytical methods. It is shown that the analytical methods can be utilized for deriving the initial in-plane stiffness of masonry walls with openings, providing fast and accurate solutions in comparison to more detailed and time-consuming finite element implementations.

Keywords: Initial stiffness; masonry walls; in-plane stiffness; analytical methods; finite element analysis

1. Introduction

Unreinforced masonry (URM) buildings can be considered as the oldest construction technique in the world [1] that consists of URM shear walls as a load-bearing system [2, 3]. Moreover, nowadays, URM walls have been utilized in moment-resisting frames as an infill wall, effective on the building responses to the different types of loadings [4, 5]. The initial in-plane stiffness (IIPS) of each structural component is considered as a key parameter for design purposes and deriving the nonlinear analysis's backbone curve [6, 7], which is significantly effective on the nonlinear analysis results. Therefore, calculating an accurate enough value for the IIPS of URM walls could be critical for seismic performance evaluation of URM buildings [8-10] and designing the modern buildings with URM infill walls [11]. Instead of performing finite element (FE) analysis, different analytical hand methods have been developed for the estimation of IIPS of URM walls with less computational effort. For the URM walls without openings, the estimation of the IIPS by assuming the wall as a deep beam is easy and accurate enough since rigid boundary conditions are considered in both the theory and equations. Nevertheless, in terms of perforated URM walls, the estimation of this parameter is not accurate enough due to the possible flexibility of pier ends [9].

As the easiest method for the estimation of the IIPS of URM walls with openings, the wall is discretized to piers, and the IIPS of each pier can be derived based on the deep beam theory neglecting the flexible boundary conditions. It was investigated that the perforated wall's IIPS is overestimated using this method [9]. Another well-known analytical hand method is called the interior strip method [12]. By comparing the results with the results of FE analysis, it was investigated that the interior strip method is not accurate enough and overestimate the IIPS of the perforated URM wall in some cases [12]. Moreover, an analytical method was proposed in [13] considering flexible endings for piers by modifying the boundary conditions stiffnesses, and design tables were provided to facilitate the estimation process of the IIPS. The method's accuracy was then verified by comparing the results with the FE analysis results [13, 14]. Furthermore, the effective height method is an analytical method proposed in [9]. Modification of the pier stiffness due to the flexible boundary conditions has been performed using regression analysis based on the FE analysis of cantilever piers with different boundary conditions. The method has been validated by comparing the results with the FE analysis results of four perforated walls [9].

The last two mentioned analytical methods are chosen in the current study to investigate their performance against the FE analyses. Due to the low number of case studies investigating the performance of the methods in previous studies, a broader level of URM walls with different configurations of openings is needed to be developed. Firstly, a FE model has been developed and validated based on an experimental test performed by [15]. Afterward, URM wall case studies with openings in different configurations have been modeled and analyzed. Then, the IIPS of the walls is derived based on the modified boundary conditions stiffness method and the effective height method. Finally, the results from the two analytical methods have been compared with the FE analysis results to determine each analytical method's accuracy, and modifications have been proposed to improve the accuracy of the analytical methods.

2. Method

In this section, details about all the analysis types for estimating IIPS of URM walls are presented and investigated. Firstly, the experimental test is presented as the most robust method. Then the FE modeling procedure and the procedure of the two analytical methods utilized in this study are presented.

2.1 Experimental test

Quasi-static and monotonic tests on a single-leaf tuff masonry URM wall with an opening were performed by [15], where the geometrical data of the tested wall is shown in Figure 1. Vertical forces of 200 kN were applied to the piers by hydraulic jacks to simulate gravity loads [16]. A prescribed monotonic displacement was applied on one side of the wall through the test procedure, and the horizontal resistant force of the wall and the deformation were recorded.

2.2 FE modeling

Different methods have been presented for the numerical modeling of URM walls. Among them, the continuum-based method is utilized in this study. In this method, the masonry unit will be considered as a homogenous texture, and the masonry blocks and mortar joint have not been modeled in detail [2].

Based on a database from the test to derive the shear modulus (G) of masonry, see [17], it is concluded that G=0.15E, where E is the modulus of elasticity. This is a reasonable estimation equation for calculating the accurate enough G parameter. Using G=0.4E by assuming the masonry as an isotropic material overestimates the G parameter and the URM wall's stiffness [17]. The FE model of the test wall has been developed in DIANA FEA software [18] considering the mentioned assumptions with the material properties summarized in Table 1.

Table 1 – Material properties of masonry for the FE model validation.

	E(GPa)	**G(GPa)**	**ρ (kg/m^3)**
Tuff masonry (compression parallel to bed joints)	2.07	0.31	1600
Tuff masonry (compression perpendicular to bed joints)	2.22		

Furthermore, two blocks on top of each pier have been modeled to simulate the test set up with a specific density to simulate the constant vertical applied load of 200 kN as illustrated in Fig.1 [16]. However, it was investigated that the effect of vertical loads in FE analysis is negligible on the IIPS of URM walls, see [13].

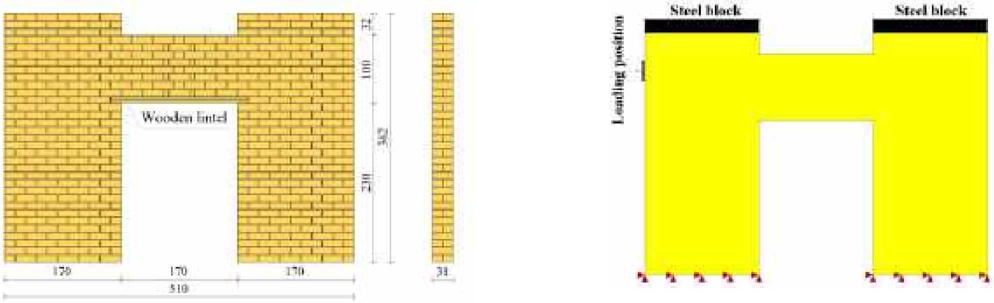

(a) (b)

Fig. 1 – (a) Geometry and (b) FE model of the test wall (Dimensions in cm).

2.3 Analytical methods

The deep beam is considered a suitable structural model for solid, prismatic, and unperforated shear walls. In deep beam theory, the cross-sections are assumed to remain plane, and unlike in Bernoulli beam theory, cross-sections do not remain perpendicular to the beam axis after deformation [12]. The elastic in-plane shear stiffness of the wall can be obtained from Eq. (1) that combines the flexibility of the wall due to shear and flexure:

$$K = \frac{1}{\frac{1}{K_{flex}} + \frac{1}{K_{shear}}} \tag{1}$$

where flexural stiffnesses for a cantilevered and two fixed end walls (K_{flex}) are calculated based on Eq. (2) and Eq. (3), respectively:

$$K_{flex} = \frac{3EI_g}{h^3} \tag{2}$$

$$K_{flex} = \frac{12EI_g}{h^3} \tag{3}$$

Moreover, the shear stiffness for a rectangular cross-section wall (K_{shear}) is calculated from Eq. (4):

$$K_{shear} = \frac{GA_v}{1.2h} \tag{4}$$

where E is elastic modulus, I_g is the moment of inertia for the gross section, h is the height of the pier, G is the shear modulus, and A_v is the cross-section area. Two ends of a pier are not stiff enough in perforated walls to satisfy the predefined stiffness boundary conditions of Eq. (2) and Eq. (3). For the estimation of the IIPS of perforated URM walls, in this paper, two analytical methods, (a) the effective height method (EHM) and (b) the modified boundary conditions stiffness method (MBCSM), have been studied in detail.

2.3.1 Effective Height Method (EHM)

In EHM, the pier is divided into equally two cantilever piers, and the stiffness of each segment can be calculated based on Eq. (2). The shear stiffness of the cantilever segment is calculated based on Eq. (4), but for the flexural stiffness, Eq. (5) is utilized.

$$K_{flex} = \frac{3EI_g}{(rh)^3} \tag{5}$$

Three parameters are defined based on the geometry of the pier segment to calculate the r factor: the aspect ratio of the pier $(\frac{W_p}{H_p})$, the ratio of the depth of the spandrel component to the pier $(\frac{H_s}{W_p})$, and the symmetry factor of the pier end (α). The first two parameters can be calculated based on the geometry of the pier and the spandrel. The third parameter defines the asymmetry of the end region, which is described in [9]. After calculating the three mentioned parameters from the geometry of the pier and the spandrel the stiffness of the pier segments, the r factor can be derived using Eq. (6):

$$r = \left[1.005 + 0.19\left(\frac{H_s}{W_p}\right)^{\frac{1}{5}}\right] \times \left[1 + 0.1\alpha^{\frac{1}{4}}\right] \times \left[0.803 + 0.281\left(\frac{W_p}{H_p}\right)^{\frac{7}{10}}\right] \tag{6}$$

After deriving the in-plane shear stiffness of two cantilever pier segments, the IIPS of the whole pier can be calculated based on the stiffness of the top (K_{top}) and bottom (K_{bot}) cantilever pier segments using Eq. (7):

$$K_{pier} = \frac{1}{\frac{1}{K_{top}} + \frac{1}{K_{bot}}} \tag{7}$$

For estimating the stiffness of a perforated wall, the wall can be discretized to horizontal (spandrels) and vertical (piers) elements, as illustrated in Fig.2b. Then the stiffness of the whole wall is defined by using the series or parallel spring rules for the elements, as is shown in Fig.2c.

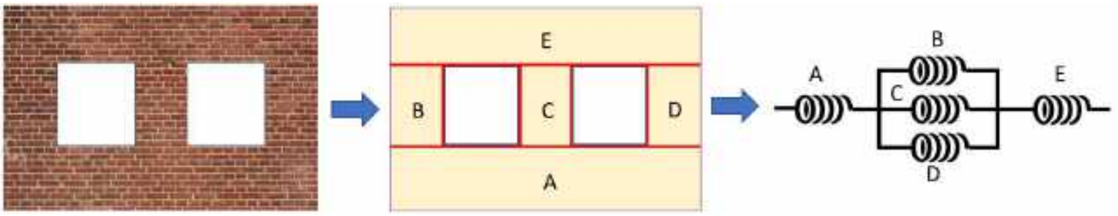

(a) (b) (c)

Fig. 2 – (a) A perforated URM wall, (b) dividing the wall to the spandrel and piers, and (c) composite spring model of the wall.

The IIPS of each spandrel can be roughly estimated based on Eq. (2), which K_{flex} is derived from Eq. (3), assuming a deep cantilever beam in a conservative way for all configurations of the spandrel. Then the effective stiffness of a perforated wall (K_{eff}) is calculated as described in [9].

K_{eff} is derived based on the shear stiffness of the components; however, the in-plane bending action of the wall needs to be taken into account. This effect will become larger when the wall aspect ratio increases [9]. For this purpose, K_{eff} should be modified based on Eq. (8):

$$K_{final} = \frac{1}{\frac{1}{K_{eff}} + \frac{1}{K_{bend}}} \tag{8}$$

where K_{bend} is the bending stiffness of a perforated wall and calculated based on Eq. (9):

$$K_{bend} = \frac{3EI_w}{\rho {h_t}^3} \tag{9}$$

In Eq. (9), the term I_w corresponds to the perforated wall's moment of inertia and h_t is the total height of the perforated wall. The term ρ is a correction factor to consider the opening effects calculated based on Eq. (10):

$$\rho = 1 + 0.0035\eta_p + 0.0004{\eta_p}^2 \tag{10}$$

where $\eta_p$is the ratio of the area of the openings to the area of the wall in percentage [9].

2.3.2 Modified Boundary Conditions Stiffness Method (MBCSM)

In MBCSM, the rotational deformations of the top and bottom spandrel of a pier are considered, but the shear stiffness term of Eq. (1) is not changed, and the flexural stiffness has been modified and calculated based on Eq. (11) [14]:

$$K_{flex} = \frac{6EI}{\left[\frac{k_t k_b + 2k_t + 2k_b + 3}{k_t + k_b + 2k_t k_b}\right] \times h^3} \tag{11}$$

where k_b and k_t are equal to $\frac{H_p}{H_{s(bottom)}}$ and $\frac{H_p}{H_{s(top)}}$ respectively. Making the calculation procedure easier, a simplified nondimensional relationship for estimating the IIPS of a pier is introduced [14]. Firstly, three nondimensional parameters should be defined as follows:

$$q = \frac{H_p}{L} \tag{12}$$

$$s = \frac{H_{s(bottom)}}{L} \tag{13}$$

$$r = \frac{H_{s(top)}}{L} \tag{14}$$

Furthermore, the stiffness nondimensional parameter will be calculated from Eq. (15):

$$\frac{K}{Et} = \frac{1}{2pq^3 + 3q} \tag{15}$$

where the term p is calculated based on $\frac{p_1}{p_2}$ where:

$$p_1 = 2qr + q^2 + 2qs + 3rs \tag{16}$$

and

$$p_2 = qr + 2q^2 + qs \tag{17}$$

After deriving the flexural stiffness part of the pier from Eq. (15), the pier's IIPS can be estimated based on Eq. (1) [14]. Note that the effect of asymmetry of pier ends, stiffness of spandrels and bending stiffness of the whole wall have been neglected in the MBCSM method.

2.4 Developed case studies

Totally 15 walls with an equal height, including the experimental test wall (model Ex) with one, two, and three openings in different configurations, have been developed for performing the comparative study. Geometry, opening configurations, and allocated name of each case study are presented in Fig.3.

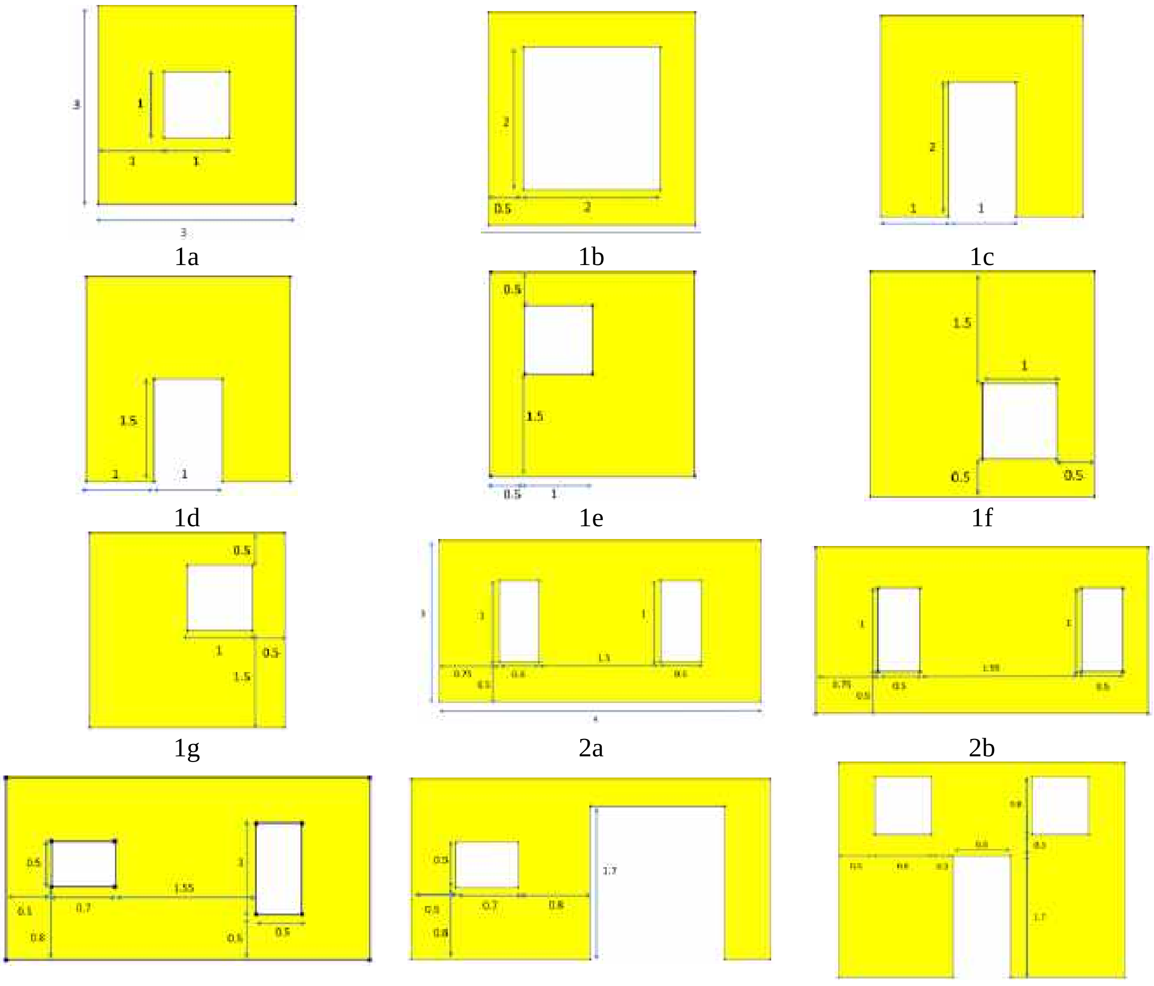

1a 1b 1c

1d 1e 1f

1g 2a 2b

2c 2d 3a

3b 3c

Fig. 3 – Geometry and opening configurations of the URM wall case studies (Dimensions in m).

2.5 Performance of the analytical methods

The IIPS of the case studies will be estimated using the two mentioned analytical methods. However, for the MBCSM, three scenarios have been considered. Firstly, the stiffness has been calculated just by summing the piers' stiffnesses. In the second scenario, the effect of spandrel stiffness has been considered (MBCSM+SE), and in the third scenario, the bending effect of the whole perforated wall is taken into account in the calculations (MBCSM+SE+BE).

2.5.1 Quantitative approach

The values of coefficient of determination (R^2), root mean square error (RMSE), and mean absolute error (MAE) are calculated based on Eqs. (18), (19), and (20), respectively, to evaluate the performance of the analytical methods.

$$R^2 = \left(\frac{\sum_{j=1}^{N}(p_{0,j}-\overline{p_0})(p_{t,j}-\overline{p_t})}{\sqrt{\sum_{j=1}^{N}\left(p_{0,j}-\overline{p_0}\right)^2 \sum_{j=1}^{N}\left(p_{t,j}-\overline{p_t}\right)^2}}\right)^2 \tag{18}$$

$$\text{RMSE}=\sqrt{\frac{1}{N}\sum_{\text{j}=1}^{N}(p_{0,\text{j}}\text{-}p_{\text{t,j}})^2} \tag{19}$$

$$\text{MAE}=\frac{1}{N}\sum_{\text{j}=1}^{N}\left|p_{0,\text{j}}\text{-}p_{\text{t,j}}\right| \tag{20}$$

where N is the number of the values in both datasets, $p_{0,\text{j}}$ and $p_{\text{t,j}}$ are the values from two datasets and $\overline{p_0}$ and $\overline{p_t}$ are the corresponding mean values. It is noted that a larger value of the R^2 and lower values of RMSE and MAE show a better correlation between the two datasets.

2.5.2 Qualitative approach

In the qualitative approach, the scatter plot of the results has been provided. The deviation of the equality line (Y=X) from the best fitted polynomial line (i.e., $Y=aX+b$) shows the correlation of the result of each method to the obtained results from the FE analysis; and therefore, the robustness of each analytical method.

3. Results and discussion

3.1 FE model validation and mesh sensitivity analysis

The effect of mesh element size has been investigated to achieve the most efficient and accurate enough meshing size. Table 3 shows the four maximum mesh element sizes assigned to the FE model of the test wall and the corresponding number of the elements.

Table 2: Mesh sizes and the number of elements for performing the mesh sensitivity analysis.

Mesh size (m)	0.02	0.05	0.1	0.2
Number of elements	36764	5859	1466	403

A displacement with the values of 1mm has been applied on the loading position, and the IIPS is calculated as the ratio of the base shear and the prescribed displacement. Figure 12 shows the ratio of the IIPS derived from the FE model to the experimental test and the mesh sensitivity analysis results. Based on Fig.4, the maximum mesh size of 0.1 m is considered the most efficient mesh size, and the FE model is validated with adequate accuracy.

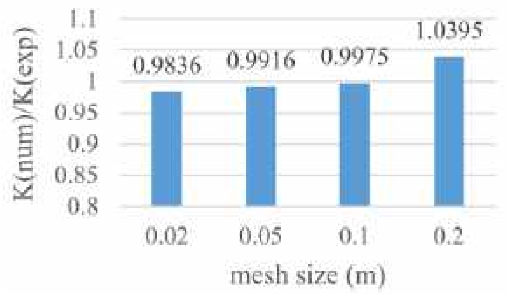

Fig. 4 – Results of the mesh sensitivity analysis.

3.2 FE analyses results

The material properties and the thickness of the developed case study walls are considered equal to the experimental tests. However, the elastic moduli in both X and Y directions are the same with a value of 2.07 GPa. After developing the FE models, the analysis has been done by applying a load on the top left of the wall and recording the displacement at the top right side of the wall. Based on the test procedure, a displacement-based analysis has been done for the validation of the FE model of the test wall. Nevertheless, for the analysis of the case studies, a load-based method has been utilized by applying a force and recording lateral displacement. Note that based on the previous studies on the perforated URM walls, the results from the displacement-based procedure are more conservative than the load-based procedure, see [19]. Moreover, the load-based method better reflects the loading that would be applied during a seismic event compared to the displacement-based procedure [19]. Fig.5 shows the displacement contour of the case study walls in the X direction from the FE analysis.

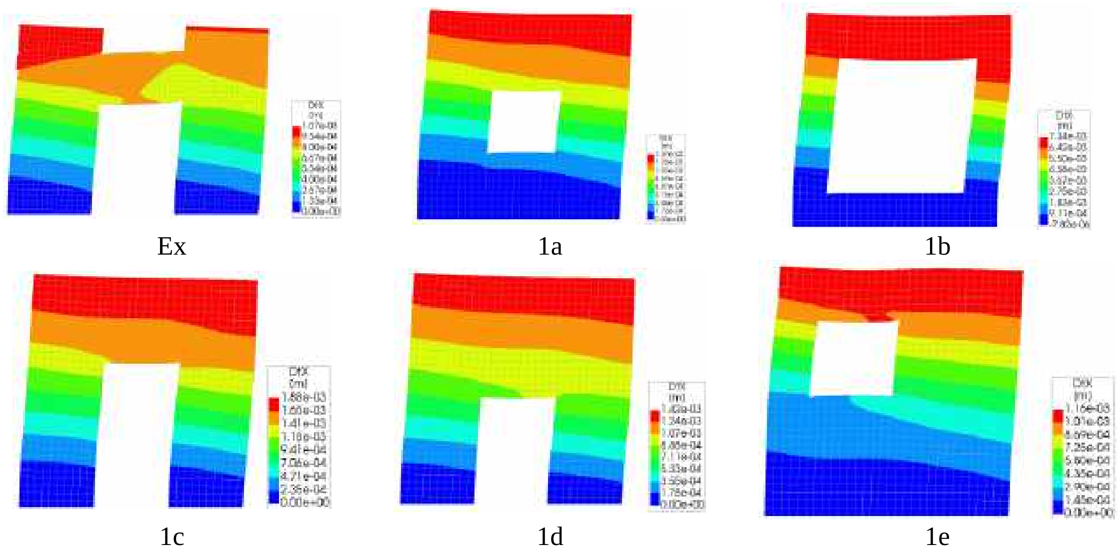
Ex
1a
1b
1c
1d
1e

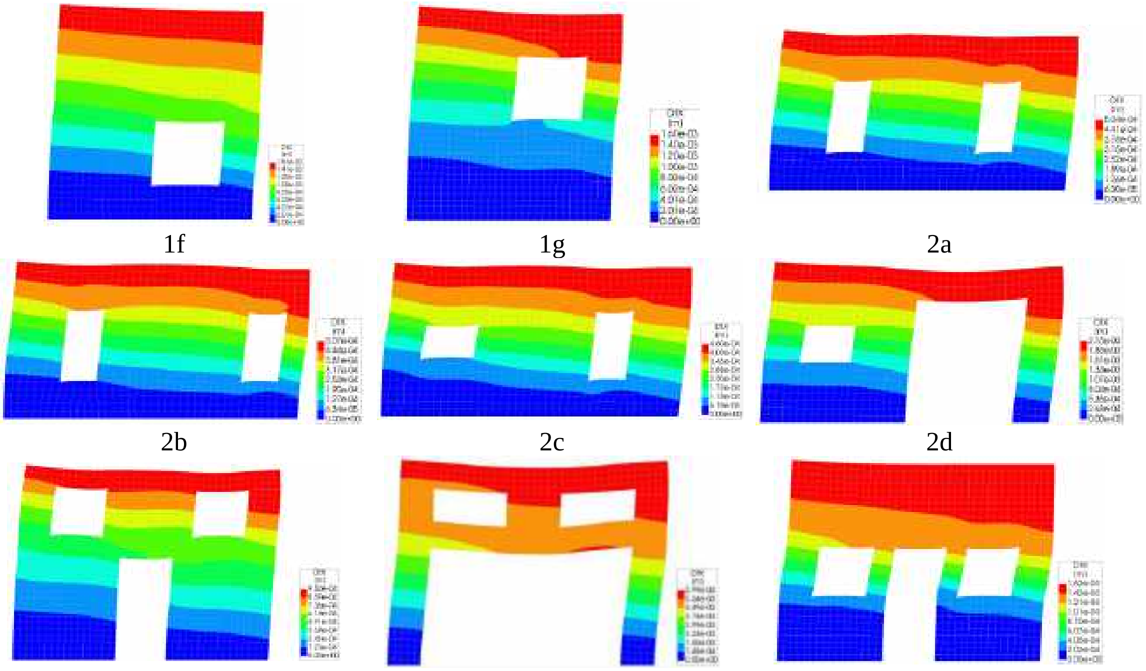
1f 1g 2a
2b 2c 2d
3a 3b 3c

Fig. 5 – Displacement contour of the URM wall case studies in X direction obtained from FE analyses.

3.3 Comparative study of the perforated URM wall case studies

All the results from the FE analyses and four analytical methods have been derived, and the IIPS of the perforated URM walls are shown in Table 5. For the results from the FE analyses, the IIPS values of the case studies are calculated by dividing the applied force by the recorded displacement. The results in Table 3 show that for models 1f, 1e, and 1g, the IIPS values calculated from the analytical methods are the same, but the FE analysis results are different. Therefore, the location of opening that affects the IIPS is not effective on the results derived from the analytical methods that can be the weakness of the analytical methods. For this purpose, analytical methods for walls with symmetric configurations of openings give more accurate results.

Table 3 –IIPS of the case studies from FE analysis and the analytical methods in (kN/mm)

Model name	**FE**	**EHM**	**MBCSM**	**MBCSM+SE**	**MBCSM+SE+BE**
Ex	57.1817	57.0973	87.7436	72.0029	64.3741
1a	37.7489	39.4851	106.95	55.178	40.1496
1b	6.9093	6.8225	8.9125	8.5899	8.1169
1c	27.5064	26.4202	44.5625	37.276	28.755
1d	36.3148	32.7925	68.448	46.2486	34.5878
1e	44.9309	39.1383	114.4097	56.0822	40.6262
1f	32.3233	39.1383	114.4097	56.0822	40.6262
1g	32.1328	39.1383	114.4097	56.0822	40.6262
2a	104.5415	99.0443	182.9935	116.2014	105.6221
2b	103.246	101.7857	188.5906	118.4334	107.463
2c	114.7652	111.0057	318.3407	126.3638	114.1944
2d	49.1843	64.1954	157.2289	71.5514	65.5155
3a	52.7841	48.4768	53.6991	49.5441	42.5073
3b	8.9398	10.2374	10.9736	10.7159	10.0469
3c	31.6113	36.7344	48.9335	34.4814	30.8833

The values of R^2, RSME, and MAE are illustrated in Fig.6 for investigating the accuracy of each analytical method. As illustrated in Fig. 6, the value of R^2 for the EHM is the largest, and the values of RSME and MAE are the lowest compared to other analytical methods. This method can be considered the most robust method compared to other analytical methods. Moreover, it is illustrated that the accuracy of the MBCSM is not enough to be employed for estimating the IIPS of URM walls. By considering the spandrel stiffness effects, the results improve, and by taking to account the bending effect stiffness, the results become more accurate. The values of R^2 for EHM and modified MBCSM are 0.97 and 0.96, respectively, which confirm them as the accurate methods for estimating the IIPS of URM walls.

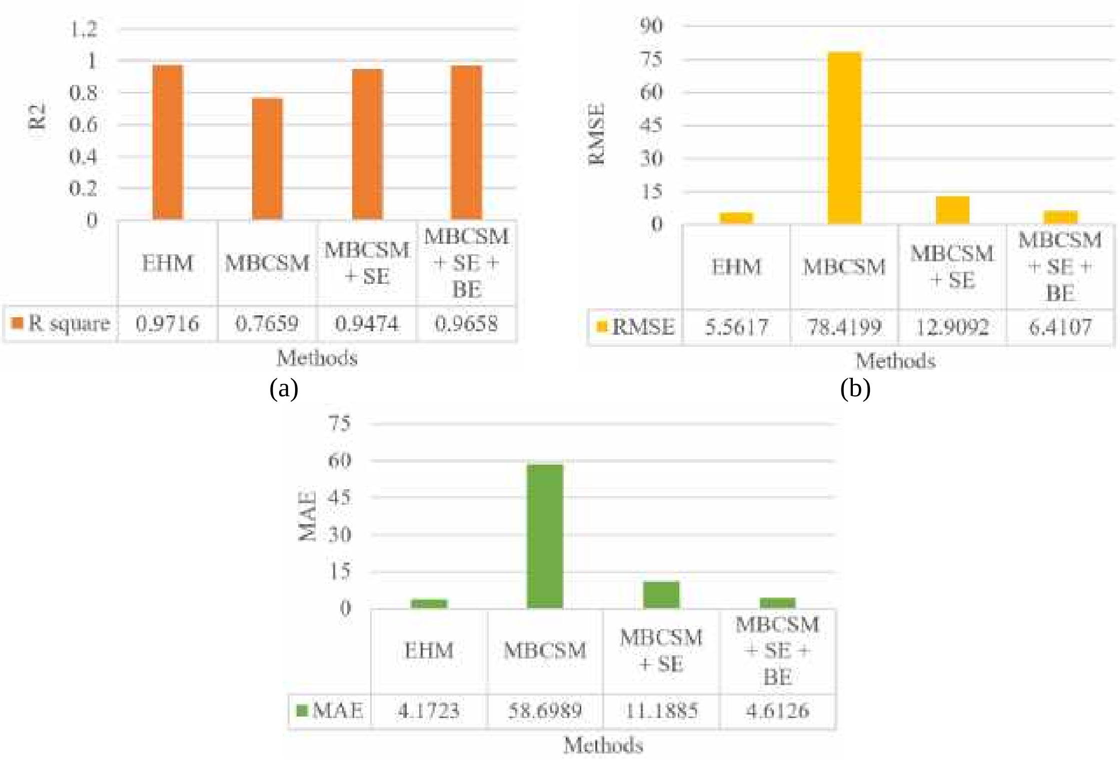

(a) (b)

(c)

Fig. 6 – (a) R^2, (b) RMSE, and (c) MAE values for the four mentioned analytical methods.

Based on the scatter plot of EHM in Fig.7 (a), the results of EHM are accurate enough, but the best-fitted polynomial line of the MBCSM is not close enough to the equality line as illustrated in Fig.7 (b). The modifications by considering the spandrel stiffness effects and bending stiffness effects are taken into account to increase the accuracy of MBCSM that can be seen in Fig.7 (c) and (d).

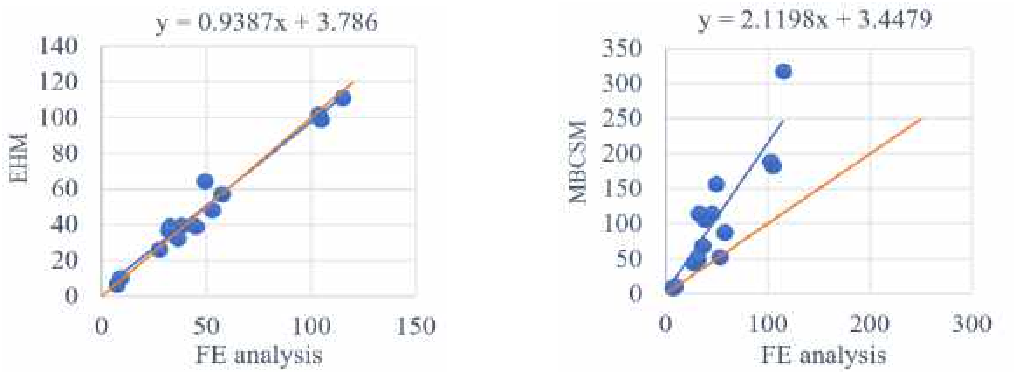

(a) (b)

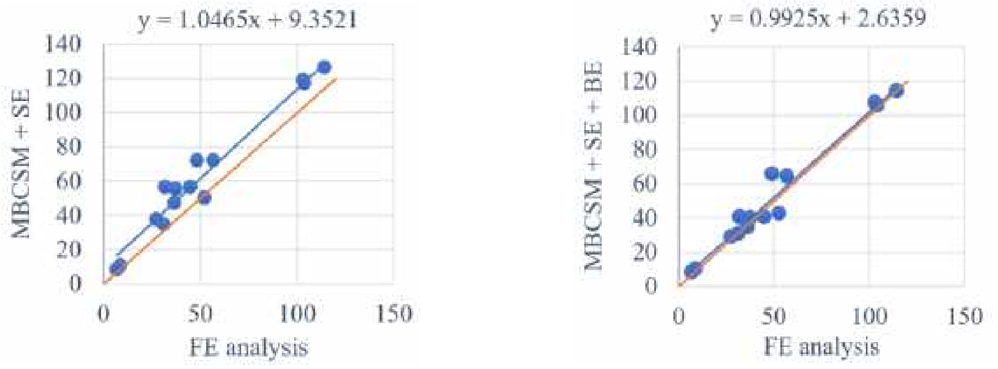

(c) (d)

Fig. 7 – Scatter plot and the equality line for the results of FE analysis and (a) EHM, (b) MBCSM, (c) MBCSM + SE, and (d) MBCSM + SE + BE (in kN/mm).

4. Conclusion

The IIPS of URM walls is considered an effective parameter on the structural vulnerability assessment of URM buildings and designing modern structural systems with URM infill walls. FE modeling is considered as a more robust method for deriving the IIPS of the URM walls with openings compared to the analytical methods. Nevertheless, expertise and high computational efforts are two main barriers that have limited the application of the FE method. Therefore, different analytical methods have been proposed for calculating the IIPS of URM walls with openings. The MBCSM and EHM are chosen as the analytical methods to investigate their performance against the FE analyses' results. For this purpose, URM wall case studies with different openings configurations have been developed, and the IIPS of the walls have been derived using the FE analyses and the mentioned analytical methods. The accuracy of each analytical method is evaluated quantitatively by calculating the RSME and MAE, and R^2 parameters and qualitatively by providing the scatter plots. Performance evaluations show that results using EHM have enough accuracy but results from MBCSM show a high deviation from the FE results. Two modifications have been applied to MBCSM. Firstly, the effect of spandrel stiffness has been considered, and through the second modification, the effect of bending stiffness of the wall is added to the previous one. The comparative studies show that the modified MBCSM is accurate enough to estimate the IIPS of URM walls with openings.

5. Acknowledgements

This work is a part of the HYPERION project. HYPERION has received funding from the European Union's Framework Programme for Research and Innovation (Horizon 2020) under grant agreement No 821054. The contents of this publication are the sole responsibility of Oslo Metropolitan University (Work Package 5, Task 2) and do not necessarily reflect the opinion of the European Union.

6. References

[1] Shabani, A., M. Kioumarsi, V. Plevris, and H. Stamatopoulos (2020): Structural Vulnerability Assessment of Heritage Timber Buildings: A Methodological Proposal. *Forests*. **11**(8): p. 881 https://doi.org/10.3390/f11080881.

[2] D'Altri, A.M., V. Sarhosis, G. Milani, J. Rots, S. Cattari, S. Lagomarsino, E. Sacco, A. Tralli, G. Castellazzi, and S. de Miranda (2020): Modeling strategies for the computational analysis of unreinforced masonry structures: review and classification. *Archives of Computational Methods in Engineering*. https://doi.org/10.1007/s11831-019-09351-x.

[3] Shabani, A., M. Kioumarsi, and M. Zucconi (2021): State of the art of simplified analytical methods for seismic vulnerability assessment of unreinforced masonry buildings. *Engineering Structures*. **239**: p. 112280 https://doi.org/10.1016/j.engstruct.2021.112280.

[4] Ozturkoglu, O., T. Ucar, and Y. Yesilce (2017): Effect of masonry infill walls with openings on nonlinear response of reinforced concrete frames. *Earthquakes and Structures*. **12**(3): p. 333-347 https://doi.org/10.12989/eas.2017.12.3.333.

[5] Shabani, A. and S. Erfani (2020): Seismic performance evaluation of SSMF with simple beam–column connections under the base level. *International Journal of Steel Structures*. **20**(1): p. 89-100 https://doi.org/10.1007/s13296-019-00273-9.

[6] Moradi, M.J., M.M. Roshani, A. Shabani, and M. Kioumarsi (2020): Prediction of the load-bearing behavior of spsw with rectangular opening by RBF network. *Applied Sciences*. **10**(3): p. 1185 https://doi.org/10.3390/app10031185.

[7] Bypour, M., M. Kioumarsi, and M. Yekrangnia (2021): Shear capacity prediction of stiffened steel plate shear walls (SSPSW) with openings using response surface method. *Engineering Structures*. **226**: p. 111340 https://doi.org/10.1016/j.engstruct.2020.111340.

[8] Xu, H., C. Gentilini, Z. Yu, H. Wu, and S. Zhao (2018): A unified model for the seismic analysis of brick masonry structures. *Construction and Building Materials*. **184**: p. 733-751 https://doi.org/10.1016/j.conbuildmat.2018.06.208.

[9] Craig, J.I., B.J. Goodno, Towashiraporn, and J. Park (2002): Response Modification Applications for Essential Facilities. *Georgia Institute of Technology, School of Civil and Environmental Engineering*.

[10] Park, J., P. Towashiraporn, J.I. Craig, and B.J. Goodno (2009): Seismic fragility analysis of low-rise unreinforced masonry structures. *Engineering Structures*. **31**(1): p. 125-137 https://doi.org/10.1016/j.engstruct.2008.07.021.

[11] Nicola, T., C. Leandro, C. Guido, and S. Enrico (2015): Masonry infilled frame structures: state-of-the-art review of numerical modelling. *Earthquakes and structures*. **8**(3): p. 733-759 https://doi.org/10.12989/eas.2015.8.1.225.

[12] Neuenhofer, A. (2006): Lateral stiffness of shear walls with openings. *Journal of Structural Engineering*. **132**(11): p. 1846-1851 https://doi.org/10.1061/(ASCE)0733-9445(2006)132:11(1846).

[13] Qamaruddin, M., A.W. Hag, S. Al-Oraimi, and S. Hamoud (1997): Investigation on the Lateral Stiffness of Shear Walls with Openings. in *11th International Brick Block Masonry Conference, China*.

[14] Qamaruddin, M. (1998): In-plane stiffness of shear walls with openings. *Building and Environment*. **34**(2): p. 109-127 https://doi.org/10.1016/S0360-1323(98)00006-7.

[15] Parisi, F., *Non-linear seismic analysis of masonry buildings*. 2010, PhD Thesis, Naples: University of Naples Federico II (URL: http://wpage ….

[16] Augenti, N., F. Parisi, A. Prota, and G. Manfredi (2011): In-plane lateral response of a full-scale masonry subassemblage with and without an inorganic matrix-grid strengthening system. *Journal of Composites for Construction*. **15**(4): p. 578-590 https://doi.org/10.1061/(ASCE)CC.1943-5614.0000193.

[17] Croce, P., M.L. Beconcini, P. Formichi, P. Cioni, F. Landi, C. Mochi, F. De Lellis, E. Mariotti, and I. Serra (2018): Shear modulus of masonry walls: a critical review. *Procedia Structural Integrity*. **11**: p. 339-346 https://doi.org/10.1016/j.prostr.2018.11.044.

[18] DIANA, *DIANA- Finite Element Analysis user manual version 10.4*. 2020: Delft, Netherlands.

[19] Liu, Z. and A. Crewe (2020): Effects of size and position of openings on in-plane capacity of unreinforced masonry walls. *Bulletin of Earthquake Engineering*. **18**(10): p. 4783-4812 https://doi.org/10.1007/s10518-020-00894-0.

Paper III

Shabani, A., Kioumarsi, M.

A novel macroelement for seismic analysis of unreinforced masonry buildings based on MVLEM in OpenSees

(2022) Journal of Building Engineering, https://doi.org/10.1016/j.jobe.2022.104019.

Journal of Building Engineering 49 (2022) 104019

Contents lists available at ScienceDirect

Journal of Building Engineering

journal homepage: www.elsevier.com/locate/jobe

A novel macroelement for seismic analysis of unreinforced masonry buildings based on MVLEM in OpenSees

Amirhosein Shabani [*], Mahdi Kioumarsi [**]

Department of Civil Engineering and Energy Technology, Oslo Metropolitan University, Pilestredet 35, 0166, Oslo, Norway

ARTICLE INFO

Keywords:
Seismic analysis
Unreinforced masonry buildings
Equivalent frame method
Macroelement model
MVLEM element

ABSTRACT

Unreinforced masonry (URM) buildings are susceptible to extraordinary actions such as earthquakes compared to steel or reinforced concrete buildings. Various methods have been developed for the computational analysis of URM buildings in the last few decades. The equivalent frame method (EFM) is one of the numerical modeling approaches widely used for the nonlinear analyses of URM buildings. Different macroelements in the context of the EFM have been proposed. However, there is still a need for an efficient modeling approach in the computational effort that can predict the real behavior of URM structural components with sufficient agreement and available in opensource structural analyses software packages. For this purpose, a new macroelement based on the multiple vertical line element method (MVLEM) element has been developed in this study. The MVLEM is available in the OpenSees software platform comprising vertical uniaxial macro-fibers and a shear spring as an efficient macroelement for nonlinear analysis of flexure-dominated reinforced concrete walls. The novel macroelement, double modified MVLEM (DM-MVELM) element has been proposed consisting of two modified MVLEM elements tied with a nonlinear shear spring at the middle with a trilinear backbone behavior. DM-MVLEM can capture the axial-flexural interaction with lower computational effort than finite element models and fiber beam-column elements. The DM-MVLEM has been validated against the test results at the structural components level and a full-scale perforated URM wall. Unified method (UM) and composite spring method (CSM) are two existing EFMs that are presented in this study. A study is performed by comparing the seismic behavior of the perforated URM walls modeled using the UM, CSM, and DM-MVLEM modeling strategies. Results show that the DM-MVLEM can predict the damage patterns, and nonlinear behavior of spandrels can be simulated that was usually modeled with linear behavior in EFMs.

---

[*] Corresponding author.
[**] Corresponding author.
E-mail addresses: amirhose@oslomet.no (A. Shabani), mahdik@oslomet.no (M. Kioumarsi).

https://doi.org/10.1016/j.jobe.2022.104019
Received 4 October 2021; Received in revised form 5 January 2022; Accepted 7 January 2022

Nomenclature

A	Cross-sectional area of URM components
b	Width of a Pier
b_{eff}	Effective interlocking length of URM units
b_h	Thickness of a brick plus a mortar joint
c	Location of center of rotation of the MVELM element
E	Elastic modulus of masonry
f_c	Compressive strength of masonry
f_{td}	Diagonal tensile strength of masonry
f_{teq}	Equivalent tensile resistance of a spandrel segment due to interlocking
f_{v0}	Shear strength of masonry at zero compressive stress (cohesion)
G	Shear modulus of masonry
h	Height of a pier
h_{sp}	Depth of a spandrel neglecting the lintel
h_t	Total height of a URM wall
H_{eff}	Height of piers considering cantilever idealization of spandrels
I_g	Inertia moment of a pier
I_w	Inertia moment of a whole URM wall
K_0	Initial in-plane stiffness of a URM wall
K_{Es}	Shear stiffness of a URM wall
K_{Eu}	Initial in-plane stiffness of a URM pier segment with definite boundary conditions
L	Length of a pier
t	Thickness of URM components
V_D	Maximum shear strength of a URM segment based on the diagonal cracking failure mode
V_I	Interlocking shear strength of bed joint of spandrels
V_m	Maximum shear strength of a URM segment
V_R	Maximum shear strength of a URM segment based on the rocking failure mode
V_S	Maximum shear strength of a URM segment based on the shear sliding failure mode
α_0	Zero-moment coefficient
α_y	Fraction of the yielding shear strength on the maximum shear strength
β	Stiffness degradation factor due to ductility
ζ	Shear stress distribution coefficient at the center of a pier
η	Ratio between the secant stiffness corresponding to V_m and K_0
η_{soft}	Softening stiffness coefficient
η_a	Coefficient for allocating the vertical compression
λ	Revision coefficient accounting for the compression ratio and aspect ratio for calculating V_m
σ_0	Vertical compression stress
σ_p	Vertical compressive stress in the adjacent piers of a spandrel
μ	Friction coefficient

1. Introduction

Unreinforced masonry (URM) construction system composed of brick units and mortar is a typology that is prevalent in high seismicity zones, i.e., southern European countries and the Middle East [1,2]. Experience from the past earthquakes has revealed that the URM construction system is vulnerable due to the brittle characteristic of the masonry, weak connections between the vertical and horizontal components, and susceptible connection between floor system and URM walls that leads to a considerable increase in losses for authorities [3–5]. Although studies on the seismic design and analyses of reinforced concrete and steel structures have gained more attention in recent years, studies on the seismic vulnerability assessment of URM structures have increased dramatically [3,6,7].

Masonry and timber are considered as the oldest construction material, abundantly found in historic areas [8,9]. Due to the brittle behavior of masonry as a low tensile strength material, existing URM buildings show nonlinear behavior even at the early stage of seismic loading; therefore, incremental iterative nonlinear analyses is a crucial part of an accurate seismic vulnerability assessment methodology [10,11]. Nonlinear static or pushover analysis (POA) is widely used for the seismic vulnerability assessment of URM buildings, and different assessment methodologies such as the N2 method [12] based on the POA results have been developed [13–15]. The POA results can be highly dependent on the load pattern applied on buildings [16]. Nonlinear time history analysis (NTHA) can be considered as the most robust analysis method for seismic vulnerability assessment [17,18]. Earthquake records specification, i.e., their duration, the sequence of peaks, and the frequency content are considered in NTHA, but are neglected in the monotonic POA procedure [13,19]. Nevertheless, the NTHA has been utilized sparingly for the seismic vulnerability assessment of buildings due to the considerable computational efforts required [20,21].

Limit analysis-based solutions have also been utilized to calculate the collapse multipliers and the collapse mechanisms [1]. Compared to the incremental iterative analyses approaches, load-bearing behavior, including maximum displacement or post-peak response, cannot be derived using the limit analysis-based solutions [22]. Limit analysis-based methods by modeling structures using rigid blocks were utilized for collapse analysis of masonry towers [23,24], arches [25,26], and buildings [27–30].

Understanding the probable failure modes of URM walls is a crucial part of nonlinear modeling. Failure modes of URM walls subjected to combined vertical and in-plane loadings are dependent on the different properties such as wall aspect ratio, mechanical properties of masonry, and boundary conditions [31–33]. Fig. 1 shows three types of failure modes of URM walls. In the shear sliding failure mode (see Fig. 1 (a)), sliding along a single mortar bed-joint line or in a stepwise fashion along bed-joints and head-joints occurs that usually can be detected in walls with a low aspect ratio (squat walls). The diagonal cracking failure mode involves both masonry units and mortar joints, with the formation of a diagonal crack starting from the middle of the wall and propagating toward the corners, as shown in Fig. 1 (b). The rocking failure mode produces tensile or crushing cracks or both at the corner of the wall, as depicted in Fig. 1 (c), which most frequently occurs in walls with high aspect ratios (slender walls) [19,21,31].

Due to the composite and non-homogenous nature of masonry, modeling URM buildings poses a challenge. Modeling procedures that are associated with the incremental-iterative analyses approaches can be divided into three main groups: 1) discrete element model (DEM) 2) continuum homogenous model (CHM), and 3) equivalent frame model (EFM) [1,14]. In DEMs, the actual texture of masonry is identified by modeling mortar joints and masonry units [34,35]. In CHMs, no distinction between individual masonry units and mortar is considered. Less computational effort and fewer input data, as well as an easy modeling procedure, are the main advantages of CHMs over DEMs [14]. CHMs are widely used for nonlinear analysis of full-scale cultural heritage assets with complex architecture where out-of-plane failure mechanics may be critical [4,36,37].

EFMs are widely used for the global seismic assessment of existing URM buildings in engineering practice [10]. In EFMs, a perforated wall is discretized to vertical (piers) and horizontal (spandrel) components that are connected with rigid zones [1]. Although both in-plane and out-of-plane collapse mechanisms are considered in other mentioned models, in the EFMs, the out-of-plane mechanisms have been usually neglected [10], and this approach is consistent with FEMA 356 guideline [38]. Moreover, well-known EFM software packages (e.g., 3Muri [39]) neglect the out-of-plane contribution of the walls, but investigate the local collapse mechanisms through a separate analysis by neglecting the interactions between the global and local seismic responses [29,40].

Fig. 2 shows a schematic overview of the two incremental iterative analysis methods versus related modeling approaches utilized for the seismic vulnerability assessment of URM buildings by emphasizing the computational efforts level. Fig. 2 indicates that the NTHA of DEMs is considered to be the least common methodology for the seismic vulnerability assessment of URM buildings, but the POA of EFMs is widely used nowadays by practitioners due to its simplicity and efficiency.

Keeping the simplicity of modeling and lowering the uncertainties, stochastic NTHA of the EFMs will be an alternative to the simplified analytical methods for seismic vulnerability assessment of URM buildings at a large scale or an efficient tool for analysts. This study focuses on the NTHA of EFMs as illustrated in the black box in Fig. 2.

The first developments of EFM originated from the POR method [41]. A simple elasto-plastic behavior was considered for beam nonlinearity with assuming rigid spandrel and nodal zones. This approach was then developed by implementing shear and rocking hinges for piers and spandrels in SAP 2000 software package [19]. However, due to the high level of computational efforts for the NTHA, the rocking hinges at the two ends of the piers and shear springs in the middle of the spandrels were omitted [19]. In order to investigate the axial-shear (N-V) interaction, a method implementing two rotational plastic hinges at two ends of beam elements was developed in SAP 2000 [21]. This method was then simplified by neglecting the N-V interaction in the pier hinges and considering linear spandrels [42]. A two-node macroelement consists of three parts: a central body, where only shear deformations are possible, and two interfaces, where the external degrees of freedom has been developed [43]. This macroelement is calibrated to account for the accurate enough cyclic behavior of both flexural and shear failure mechanisms and implemented in the 3Muri software package [39]. This macroelement is then modified to tackle the limitations i.e., the inability to capture at the same time both axial and flexural stiffnesses of the element and neglect of the N-V interaction during the analysis procedure [44,45]. By developing fiber beam elements considering a spread plasticity model, different methods were proposed to consider the axial-flexural (N-M) interaction in structural

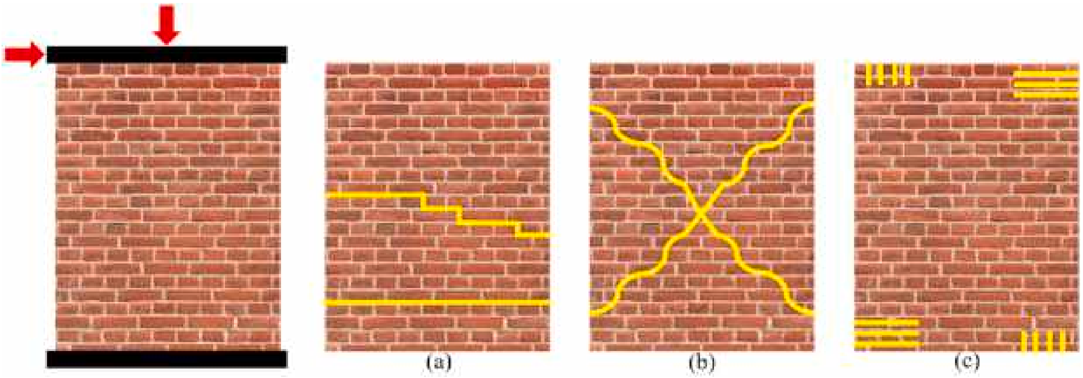

Fig. 1. Crack patterns of a URM wall subjected to axial and lateral loadings for the shear sliding (a) diagonal cracking (b), and rocking (c) failure modes [21].

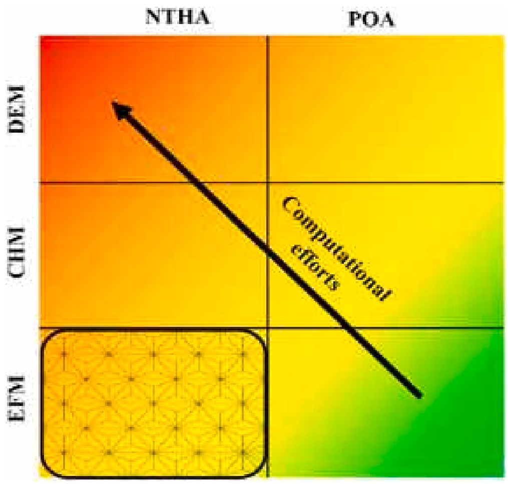

Fig. 2. Schematic overview of different incremental iterative analysis methods as a function of the relevant numerical modeling methods and corresponding computational efforts.

components [46,47]. The nonlinear response of the fibers is simulated by the mono-axial constitutive law of masonry, and a nonlinear shear spring has been implemented in the middle of the element to represent shear failure behavior [47].

Using spring elements for modeling both perforated and unperforated URM walls is a simplified approach that has been employed in the unified method (UM) [48]. In the UM, a URM wall is characterized by a nonlinear shear spring per story [48]. However, by using the composite spring method (CSM) as a more detailed method than the UM, nonlinear shear springs are assigned to each structural component [49]. A nonlinear shear spring is characterized by a definite backbone curve and hysterics rules dependent on the possible failure mode of the structural components [49]. In order to capture all the failure modes, including the combined flexural and shear failure modes, in piers and spandrels and incorporate an exact enough hysterics model for performing the NTHA, a spring-based macroelement was developed and validated against the experimental tests [50]. The macroelement comprises two rotational

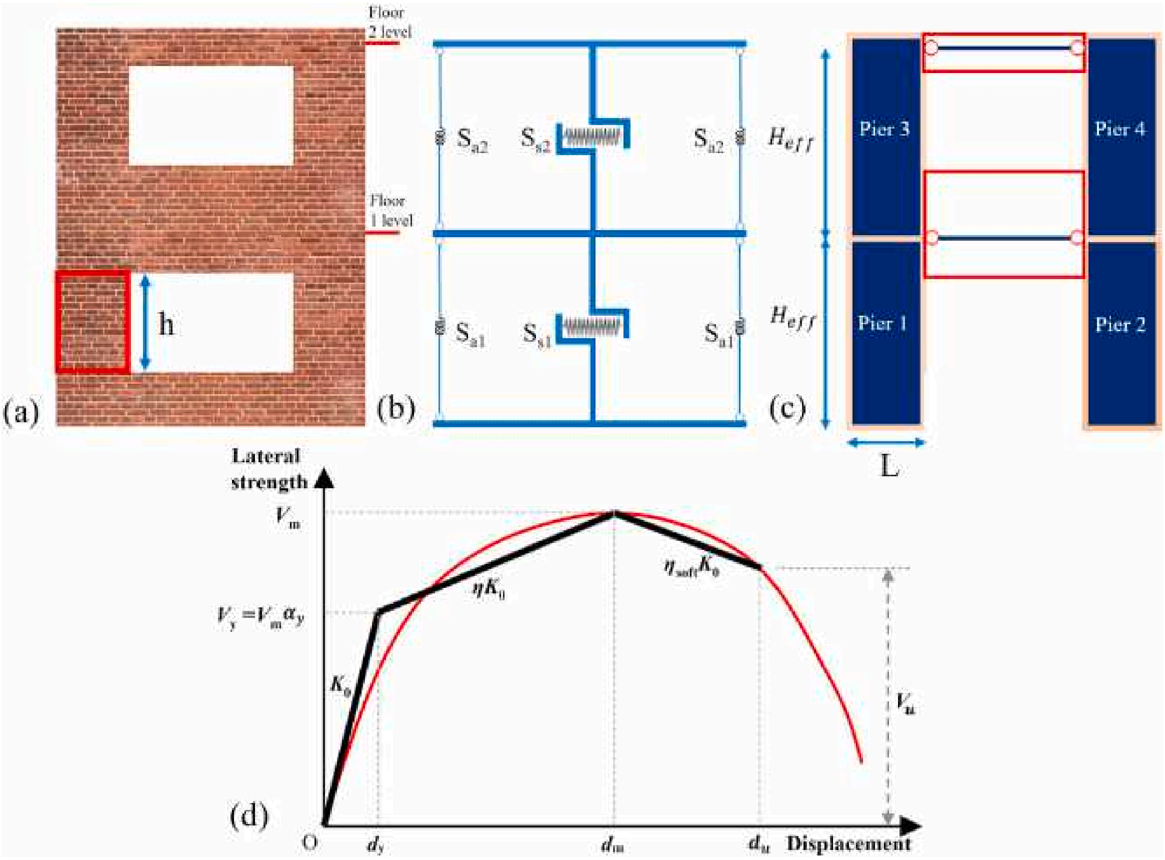

Fig. 3. (a) A perforated URM wall, (b) a schematic view of the wall modeled using the UM and configuration of axial and shear springs, (c) the discretization of the wall to piers to derive the maximum shear strength of each story, and (d) the backbone curve of the nonlinear shear spring.

springs at the two ends of the structural components to capture the flexural behavior and a shear spring to reflect the shear failure [50].

In this study, multiple-vertical-line-element-model (MVLEM), a macroelement model developed for modeling the flexure dominated reinforced concrete (RC) shear walls, is utilized to innovate a macroelement for the seismic analysis of URM buildings. An MVLEM element comprises a set of uniaxial nonlinear fiber elements connecting upper and lower rigid beam elements and a nonlinear shear spring which is located at a specific height [51,52]. Simple formulation, numerical stability, the efficiency of computational effort, the ability to capture important features such as shifting of the neutral axis, and the effect of a fluctuating axial force on strength and stiffness are the main characteristics of the MVLEM element that is available in OpenSees framework [51,53]. The MVLEM element cannot reflect the N-V interaction. To tackle this limitation, this element was improved by incorporating macro-fiber elements that allow coupling of N-M and shear responses at the model element level [54–56].

The new macroelement called DM-MVLEM consists of two modified MVLEMs that are tied together with a nonlinear shear spring. DM-MVLEM validated against the experimental tests on two piers, one spandrel, and a full-scale perforated URM wall. Furthermore, UM and CSM are selected and among the existing EFMs and modified to perform a comparative study. The methods' performance for capturing the nonlinear behavior and damage pattern prediction of URM buildings has been investigated by performing pushover and incremental dynamic analyses.

2. Overview of existing macroelements

In this section, the procedure of two existing macroelements for nonlinear dynamic analysis of URM buildings is presented. Firstly, the UM procedure is reviewed as the simplest method in this study, and some modifications have been suggested. Moreover, as the second method, the CSM is developed based on the shear constitutive law of URM piers presented in the UM with manipulation of the hysteresis rules validated against the test results.

2.1. Unified method (UM)

The UM was proposed as a simplified method for the seismic analysis of confined and unconfined masonry structures with and without openings [48]. In this approach, a URM wall of a story is modeled with a unique macroelement that consists of two vertical linear springs at two corners of a wall to transfer the axial loads and a nonlinear shear spring modeled at the middle of the wall to represent the nonlinear shear behavior of the wall as it is illustrated in Fig. 3 (b). The two axial springs (S_a) are located at two sides of a wall with the stiffness of $\frac{EA}{2h}$, where E is the elasticity modulus, A is the cross-section area, and h is the height of the wall. As illustrated in Fig. 3 (d), the shear spring (S_s) consists of a nonlinear material with the backbone curve to capture the shear failure behavior of the wall in such a way that two other degrees of freedom are free [48].

For the perforated URM walls, a conservative approach by assuming uncoupled piers is considered for deriving the maximum shear strength. This corresponds to the cantilever idealization that null shear strength is considered for the spandrels [39], and the term H_{eff} is the height of the vertical component as illustrated in Fig. 3 (c). Therefore, as shown in Fig. 3 (c), the total height of each floor is utilized for all the piers of each floor, and the total shear strength is calculated as the sum of the shear strength of the piers. As investigated in Ref. [48], the maximum shear strength can be computed for the piers based on:

$$V_m = 2.15\lambda^{0.256}\left[\frac{1}{1.2}\sqrt{1+\eta_a\frac{\sigma_0}{f_{v0}}}+\mu(1-\eta_a)\frac{\sigma_0}{f_{v0}}\right]f_{v0}A \tag{1}$$

where σ_0 is the compression stress, f_{v0} is the shear strength of the masonry at zero compressive stress, a value of 0.6 is suggested for the term η_a which is the coefficient for allocating the vertical compression, μ which is the friction coefficient is suggested to be 0.4 [48], A is the cross section of each pier segment, and λ factor is calculated as:

$$\lambda = \begin{cases} \frac{\sigma_0}{f_c}e^{-\frac{H_{eff}}{L}} \; when \; 0 < \frac{H_{eff}}{L} \leq 0.675 \\ \frac{\sigma_0}{f_c}e^{-1.55\frac{H_{eff}}{L}} \; when \; \frac{H_{eff}}{L} > 0.675 \end{cases} \tag{2}$$

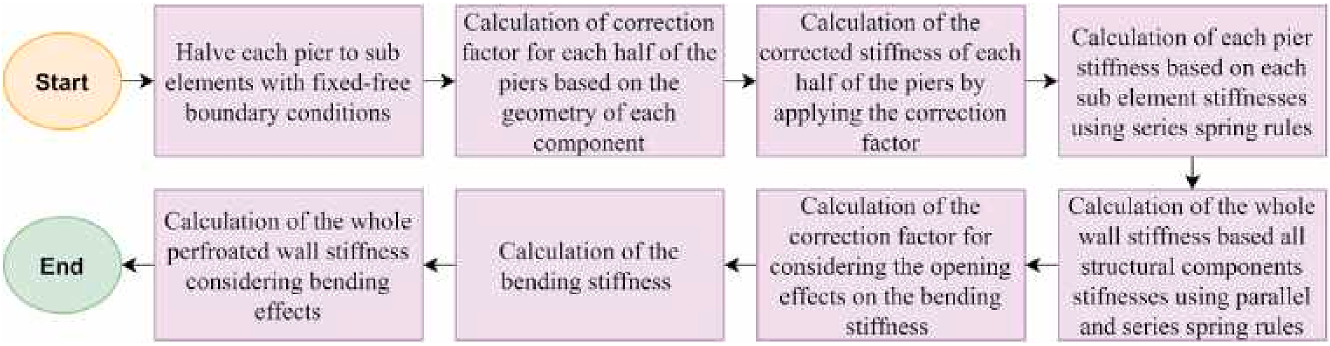

Fig. 4. Workflow of EHM for calculating the initial in-plane stiffness of perforated URM walls.

where f_c is the compressive strength of masonry, and L is the length of the piers as illustrated in Fig. 3 (c).

Initial in-plane stiffness is a crucial parameter for defining the backbone curve that can be calculated as follows for unperforated URM walls with fixed-fixed and fixed-free boundary conditions, respectively:

$$K_{Eu} = \frac{1}{\frac{h^3}{12EI_g} + \frac{1.2h}{GA}} \tag{3}$$

$$K_{Eu} = \frac{1}{\frac{h^3}{3EI_g} + \frac{1.2h}{GA}} \tag{4}$$

where h is the height of a pier as illustrated in Fig. 3 (a), G is shear modulus, and I_g is the moment of inertia of the wall cross section. However, due to flexible boundary conditions of piers in perforated URM walls, utilizing Equation (3) will overestimate the initial in-plane stiffness. In order to calculate the initial stiffness of perforated walls, effective height method (EHM) is considered a simplified analytical method clarified in Refs. [57,58]. A comparative study was done in Ref. [59], and it is investigated that the EHM can be an exact enough method validated against the FEM results compared to the analytical method presented in the UM literature [48]. The workflow of the EHM to derive the initial in-plane stiffness (K_0) of a perforated URM wall is depicted in Fig. 4, and more details are in Refs. [58,59].

After deriving V_m, and K_0, as illustrated in Fig. 3 (d) trilinear backbone curve can be derived based on α_y for calculating the yielding strength, η which is the ratio between the secant stiffness corresponding to V_m and K_0, and η_{soft} is the softening stiffness coefficient [48]. For simulating the hysteresis rules, the Hysteretic material in the OpenSees framework can be utilized, and details about the effects of each parameter are presented in Ref. [53]. The pinching factors for strain and stress during reloading and the stiffness degradation factor are presented in Table 1 in accordance with [48], and a value of 0.05 is considered for the damage due to the energy factor.

2.2. Composite spring method (CSM)

The well-known EFM characterized by assigning nonlinear shear springs to the middle of linear beam-column elements for simulating the nonlinear behavior of piers is presented in Refs. [19,49,60]. In the CSM, a perforated URM wall is discretized to piers and spandrels, and a nonlinear spring is assigned to each pier. For discretizing the structural components, the method proposed by Dolce [61] was utilized. Based on this method, the spandrels and piers were divided and connected with rigid elements such that the length of the spandrels equals the length of the openings, and the effective height of the piers has been derived by the intersection between the vertical centroidal axis of each pier with the lines forming a 30° angle from the corners of the adjacent openings as illustrated in Fig. 5 (a) [61].

In different studies, it was assumed that spandrel elements remained elastic throughout the analysis due to the high dependency of this element on different parameters (i.e., the type of lintel, effective interlocking length etc.), and failure is assumed to occur in piers [19,42,60].

Nonlinear shear springs are assigned to the piers with an elastic axial stiffness (see Fig. 5 (b)). The spring element acts as a pure shear spring with a length equal to the height of a pier by tying the rotational degree of freedom and an elastic stiffness to represent the axial stiffness with the value of $\frac{EA}{h}$ for each pier. The initial in-plane stiffness of the nonlinear shear spring can be calculated based on Equation (3). Moreover, the maximum shear strength of each pier can be considered as the minimum value of the shear strength for the three failure modes for URM piers [21,50]. The maximum shear strength for the three failure modes can be obtained using the equations proposed in Table 2 [21,47,50].where f_{td} is the diagonal tensile strength of masonry, b is the width, t is the thickness of a pier, and ζ is the shear stress distribution coefficient at the center of a pier considering the aspect ratio calculated based on the equations in Table 3:

Moreover, the parameter α_0 is the zero-moment coefficient relevant to the moment distribution along with the height of a pier that should be defined by applying a static lateral load with a load pattern similar to the first mode of the building [21]. Then this parameter is calculated as the maximum value of the fraction of the height of a pier (H_0) with a positive or negative moment value as depicted in Fig. 5 (c) to the total height of a pier.

Table 1

Parameters and the corresponding equations for deriving the backbone curve of nonlinear shear spring of the UM and defining the hysteresis rules.

Parameter section	Parameter		Unperforated URM wall	Perforated URM wall
Backbone	α_y		$\frac{\sigma_0 + 0.0049f_c}{0.86\sigma_0 + 0.15f_c} \geq 0.4$	$\frac{0.81\sigma_0 + 0.043f_c}{\sigma_0 - 0.067f_c} \geq 0.4$
	η		0.14	0.19
	η_{soft}		$-0.168\frac{\sigma_0}{f_c} - 0.0168$	$-0.365\frac{\sigma_0}{f_c} - 0.01$
Hysteresis	pinching factor for strain during reloading		0.5	0.3
	pinching factor for stress during reloading	If $\frac{\sigma_0}{f_c} < 0.15$	0.8	0.3
		If $\frac{\sigma_0}{f_c} \geq 0.15$	0.6	0.25
	Damage due to energy		0.05	0.05
	Stiffness degradation factor due to ductility (β)		0.5	0.6

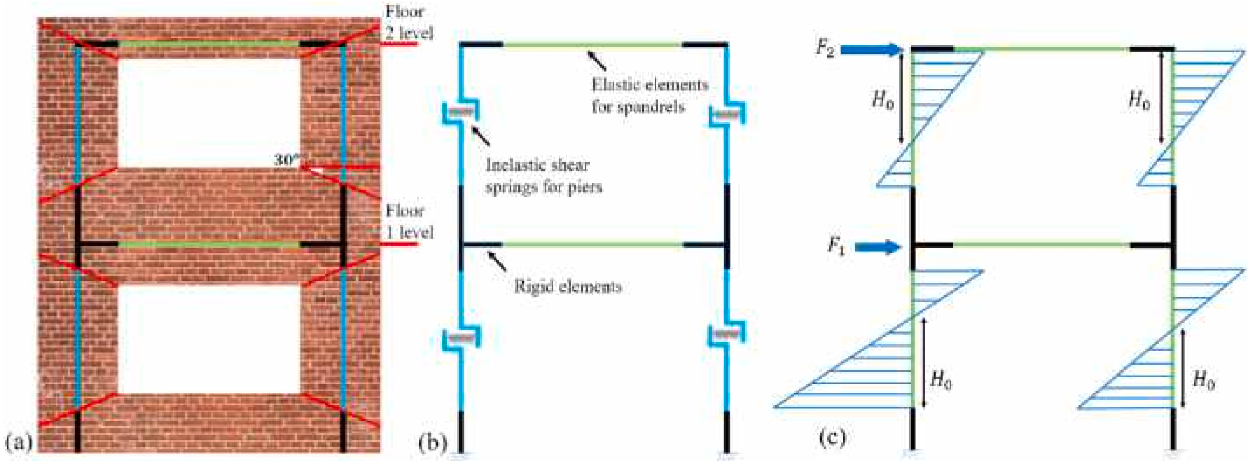

Fig. 5. (a) Discretization of a perforated URM wall to piers and spandrels based on Dolce's method, (b) schematic view of the wall modeled based on the CSM, and (c) moment distribution of the modeled wall subjected to lateral loadings as a sample.

Table 2
Equations for calculating the maximum shear strength of a URM wall based on shear sliding, diagonal cracking, and rocking failure modes.

Parameter (failure mode)	Equation
V_S (shear sliding)	$\left(\dfrac{f_{td}+0.4\sigma_0}{1+\dfrac{3\alpha_0 h f_{v0}}{\sigma_0 b}}\right)bt$
V_D (diagonal cracking)	$\dfrac{f_{td}bt}{\zeta}\sqrt{1+\dfrac{\sigma_0}{f_{td}}}$
V_R (rocking)	$\dfrac{\sigma_0}{2\alpha_0 h}\left(1-\dfrac{\sigma_0}{0.85f_c}\right)b^2t$

Table 3
Equations for deriving ζ (the shear stress distribution coefficient at the center of a pier considering the aspect ratio).

Aspect ratio	Shear stress distribution coefficient
$\frac{h}{b}\leq 1\rightarrow$	$\zeta=1$
$1<\frac{h}{b}<1.5\rightarrow$	$\zeta=\frac{h}{b}$
$\frac{h}{b}\geq 1\rightarrow$	$\zeta=1.5$

2.2.1. Validation of the CSM

A full-scale two-story perforated URM wall as illustrated in Fig. 6 (a) was tested at the University of Pavia, and cyclic prescribed displacements as shown in Fig. 6 (b) were applied to the first and second floors with a ratio of 0.65 [62]. Fig. 6 (c) shows the stress-strain curve of the masonry material used in the experimental test with $f_{td}=0.21$ MPa and $f_{v0}=0.345$ MPa based on the material properties presented in Ref. [62]. The wall was modeled using CSM and the phenomenological laws of the unperforated URM walls presented in Table 1 (as utilized in the UM [48]) could be applied to each pier's nonlinear shear spring. However, the β factor was considered to be 0.6, and the accuracy of this assumption was investigated by comparing the test and numerical results.

A displacement control analysis using a Modified-newton solution algorithm was performed, and the convergence was controlled by means of an energy convergence test with a tolerance of 10^{-4}. The results were plotted as the base shear versus the roof displacement and compared with the test result in Fig. 6 (d) [62]. The comparison of the CSM results with the experimental data shows a good match in terms of roof displacement and base shear that confirms the use of the phenomenological laws of the unperforated URM walls utilized in the UM with manipulation of β factor.

3. Development and validation of the novel macroelement

Defining critical components is not possible in the UM, and a conservative procedure is considered for deriving the maximum shear strength of the perforated wall. In the CSM, detecting the critical components is possible, but the failure of a perforated wall is assumed to occur due to the piers assuming a linear element for the spandrels. Moreover, N-M interaction has not been considered in the CSM since all nonlinear behavior has been concentrated in a nonlinear shear spring. Considering similar hysteresis rules for both shear and flexural failure modes is another limitation of the CSM. To tackle all the limitations by keeping the simplicity of modeling, stability in

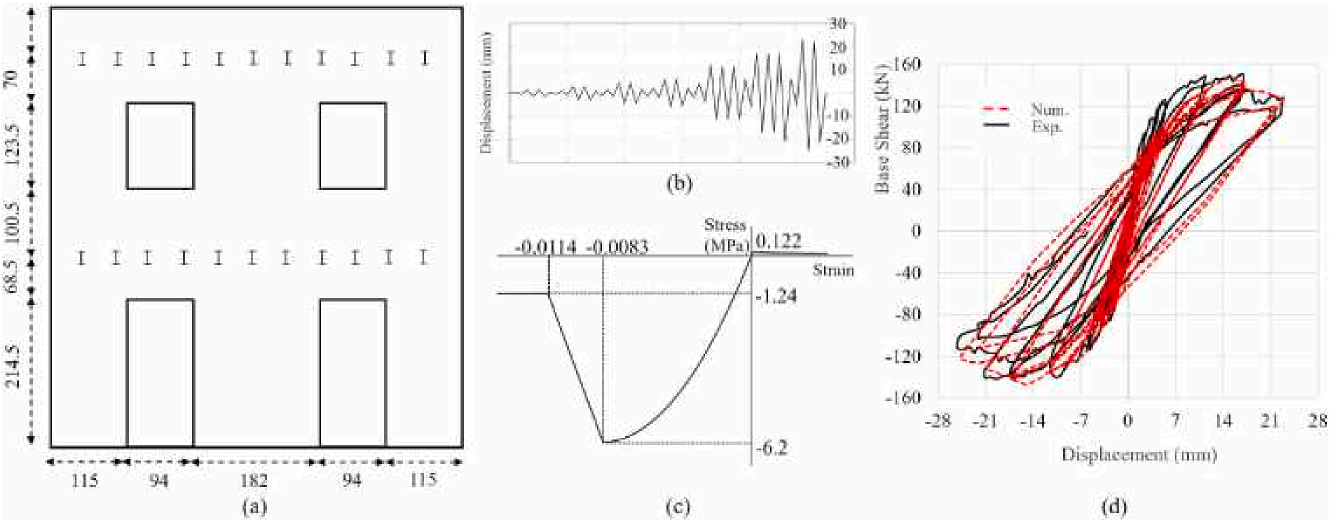

Fig. 6. (a) Geometry of the Pavia door wall, (b) cyclic displacement protocol of the test, (c) stress-strain curve of masonry [62], and (d) experimental-numerical comparison curves of the walls.

analysis, and efficiency in terms of the computational effort, a novel macroelement has been proposed and validated against the test results in this section.

3.1. Multiple vertical line element method (MVLEM)

The MVLEM element is available in the OpenSees framework [53] utilized to define the exact axial-flexural and shear behavior of a URM structural component with a high level of convergence during the nonlinear analyses and less computational effort [51,63]. The MVLEM element comprises multiple vertical nonlinear uniaxial fibers (nonlinear truss elements) that connect the upper and lower rigid elements, whereas the shear response is simulated by a shear spring located at height *ch* from the bottom of the wall element as depicted in Fig. 7 (a) [56]. The rotation of the wall due to axial-flexural loadings and transverse displacement due to the shear spring occurs independently and is summed up as the lateral displacement of a wall with fixed-free boundary conditions as highlighted in Fig. 7 (a) [56]. The MVLEM element has been utilized for the nonlinear analysis of flexural behavior dominated reinforced concrete walls and verified against the test walls with fixed-free boundary conditions [51,52,63]. Although, for employing the MVLEM elements in fixed-free boundary conditions, a sensitivity analysis should be done to investigate the most efficient number of elements that can predict the plastic hinge length. But, in order to implement an exact enough shear behavior formulation that is common for URM with the minimum number of elements for the fixed-fixed boundary conditions, modifications and new formulations are needed.

In order to simulate the pure axial-flexural behavior of a wall by neglecting shear behavior, the MVLEM undergoes modification. For this purpose, the rotational center of the MVLEM element is considered at the end of the element as illustrated in Fig. 7 (b). Furthermore, the first degree of freedom of the spring, the horizontal transition, must be rigid, with all other degrees (two and three) free.

3.2. Double modified multiple vertical line element method (DM-MVLEM)

In order to implement an explicit shear behavior formulation for URM walls, double modified MVLEMs (DM-MVLEM) are connected via a nonlinear shear spring, and two modified MVLEM elements are tied with a rigid connection in other degrees of freedom, as illustrated in Fig. 8 (a). Fig. 8 (b) shows fixed-fixed, and fixed-free boundary conditions and Fig. 8 (c) illustrates the kinematics of the novel macroelement subjected to lateral and compressive loadings in fixed-fixed and fixed-free boundary conditions. Therefore, the novel element can predict the actual flexural and shear behavior of URM components in both fixed-fixed and fixed-free boundary conditions by means of two MVLEM elements.

The stress-strain constitutive law of masonry is assigned to each uniaxial fiber, and for the shear constitutive law, shear sliding and

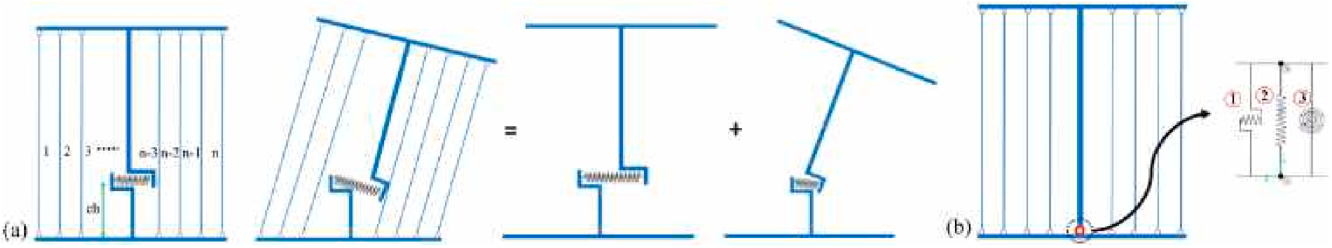

Fig. 7. (a) Kinematics of the conventional MVLEM element subjected to lateral and axial (compression) loadings, and (b). the modified MVLEM element for developing the macroelement to nonlinear modeling of URM buildings.

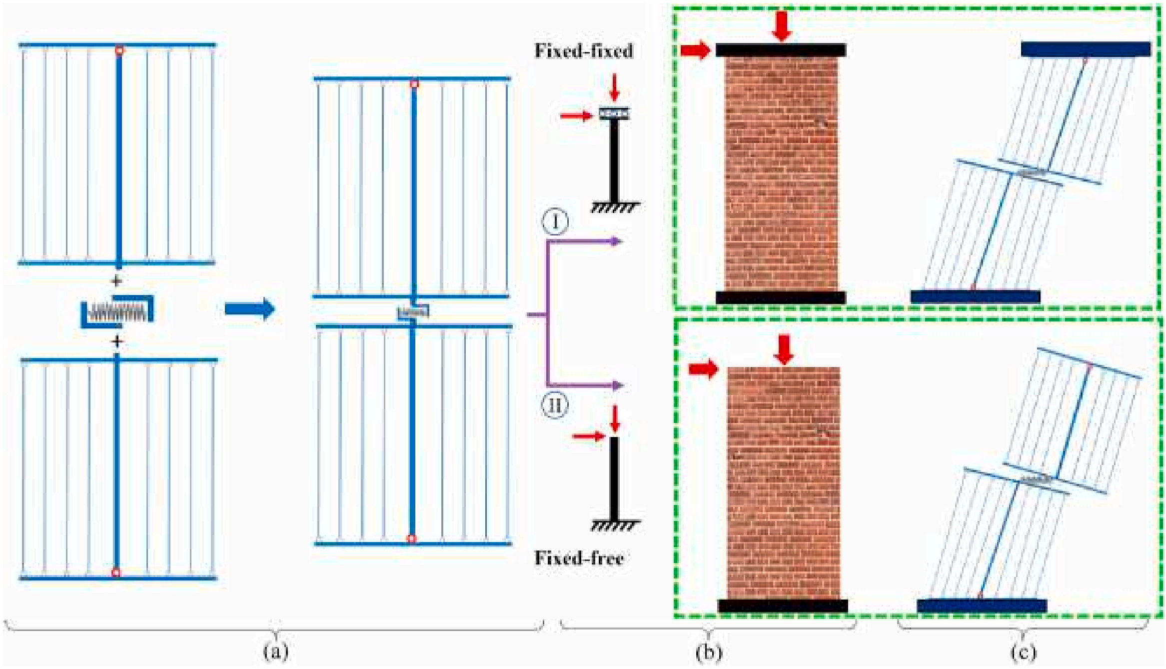

Fig. 8. (a) The DM-MVLEM macroelement composing two modified MVLEM element and a nonlinear shear spring at the middle, (b) fixed-fixed and fixed-free boundary conditions of URM walls, and (c) the kinematics of the novel macroelement with the two mentioned boundary conditions subjected to lateral and axial loadings.

diagonal cracking failure modes are considered since the fiber elements represent the flexural failure mode. For the mechanical properties of the nonlinear shear spring, the maximum shear strength can be determined as the minimum value of V_S and V_D based on the equations in Table 2, and the initial stiffness is derived based on Equation (5) since this spring only contributes to the shear behavior of the element [21,50].

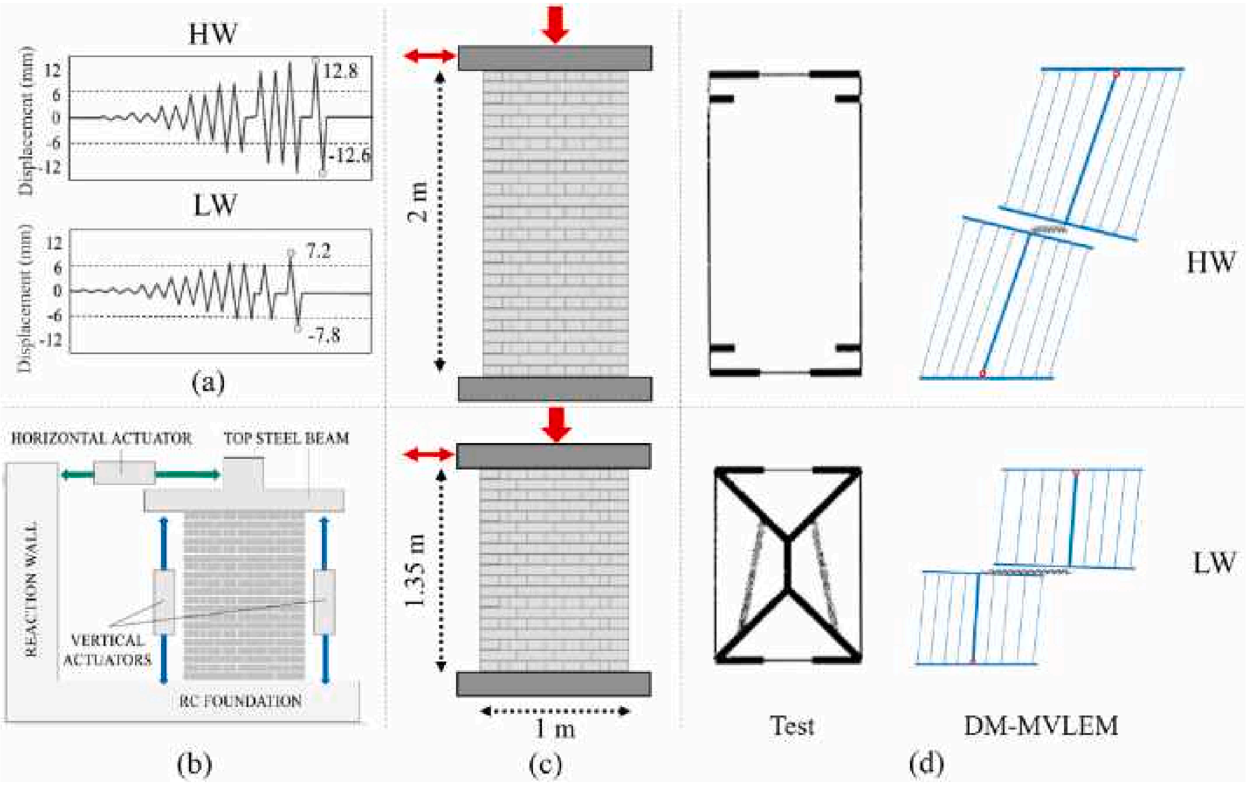

Fig. 9. (a) Displacement protocols applied to the HW and LW specimen, (b) experimental test setup [11], (c) geometry of the HW and LW, (d) the crack patterns (failure mode) based on the test results and kinematics of the DM-MVLEM models of the walls [32].

$$K_{Es} = \frac{GA}{1.2h} \tag{5}$$

The DM-MVLEM can be utilized for modeling spandrels by presenting new constitutive laws based on the experimental tests for the nonlinear shear spring. A macro-model was developed by employing the Euler-Bernoulli beam since Timoshenko's shear contribution is simulated in the shear spring at the middle of the macroelement [64]. For this purpose, the modified MVLEM elements are employed as an alternative to the Euler-Bernoulli beam (similar to modeling pier elements), and a nonlinear shear spring is implemented at the middle of the spandrel.

The maximum shear strength of the shear spring is derived as the minimum value of the V_D (diagonal cracking) derived from the equation in Table 2 and the interlocking strength at bed joints at the intersection between spandrel and piers (V_I) [65] which is:

$$V_I = \frac{f_{teq} t h_{sp}{}^2}{3L} \tag{6}$$

where h_{sp} is the spandrel's depth without lintel, and f_{teq} represents the equivalent tensile resistance due to interlocking, which is calculated based on:

$$f_{teq} = \frac{b_{eff}}{b_h}\left(f_{v0} + 0.65\sigma_p\right) \tag{7}$$

where b_{eff} is the effective interlocking length and b_h is the thickness of a brick plus a mortar joint, and σ_p corresponds to the vertical compressive stress in the adjacent piers [64,65].

3.2.1. Validation of piers modeled with the DM-MVLEM

To validate the DM-MVLEM, two URM walls with two different (shear and rocking) failure mechanisms were modeled based on the experimental tests presented in Refs. [32,66]. A constant vertical load of 150 kN was applied on top, and a quasi-static static test was done by applying a lateral cyclic displacement, as illustrated in Fig. 9 (a). Fig. 9 (b) shows the test setup for performing the quasi-static on the double clamped URM wall. The two-wythe clay-brick walls with the same thickness of 25 cm but different heights (see Fig. 9 (c)) were modeled with the DM-MVLEM. The material properties of the wall are similar to the Pavia door wall as presented in Ref. [32]. In the OpenSees framework, Concrete02 material has been utilized to model the fibers with the stress-strain curve based on the material properties presented in Ref. [32], and the Hysteretic material was utilized to model the trilinear shear spring as illustrated in Fig. 3 (d). Values utilized to derive the trilinear curve of the shear spring are presented in Table 4 based on [46,47,50], and the validity was investigated.

As illustrated in Fig. 9 (d), rocking failure mode with large horizontal cracks at the two ends of the wall occurs in the high wall (HW) test specimen [32]. The DM-MVLEM model of the HW indicates that the fiber elements are involved, and the deformation of the fibers is dominant compared to the deformation of the shear spring. Moreover, the test result shows the diagonal shear failure mode in the low wall (LW) specimen [32]. The contribution of the shear spring deformation of the DM-MVLEM model of the wall is more than the fiber elements that shows the shear failure mode. Therefore, the DM-MVLEM can predict both flexural and shear failure modes when compared with the test results.

The results of the displacement control analyses for the walls are depicted in Fig. 10 and compared with the experimental tests' results. Fig. 10 shows that the LW is characterized by wide cycles; the HW represents smaller cycles with lower dissipative capacity compared to the LW. The numerical-experimental comparison for both walls indicates that the DM-MVLEM provides an accurate enough estimation of shear capacity and cyclic behavior for the walls with specific failure mechanisms.

3.2.1.1. Comparative study of the accuracy of the DM-MVLEM. In order to compare the accuracy and efficiency of the novel DM-MVLEM element, results of the pushover analysis of the LW and HW specimens were carried out based on different modeling approaches and the results were compared with the test backbone curve result. Pushover analysis results of models developed using five, ten, and twenty MVLEM elements connected vertically with the nodes at the endings, as well as the CSM macroelement are depicted in Fig. 11 for both walls. Furthermore, FE analysis results were derived for the walls with Total strain crack material (TSCM) and Engineering masonry material (EMM) models in DIANA FEA software [51,67] plotted in Fig. 11. Compared with the TSCM, a shear failure mechanism based on the standard Coulomb friction failure criterion is included in the EMM model.

Initial stiffness, loading capacity, and post-peak stiffness are three main parameters for predicting the bilinear pushover curve of

Table 4
The values of the parameters utilized for defining the backbone curve of nonlinear shear spring for piers in the DM-MVLEM and the corresponding hysteresis rules.

parameters	Values
d_m	$0.0015h$
d_u	$0.01h$
V_u	$0.2V_m$
Pinching factor for strain during reloading	0.4
Pinching factor for stress during reloading	0.2
Damage due to energy	0.05
β	0.75

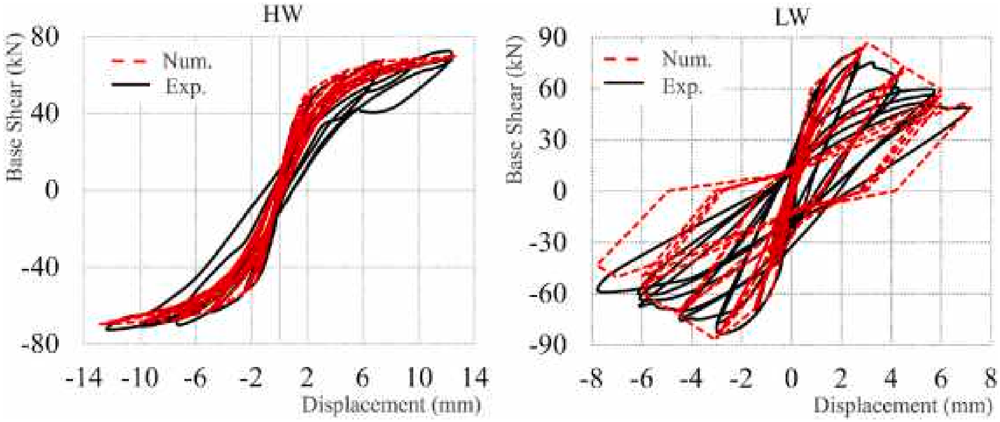

Fig. 10. Experimental-numerical comparison curves of the HW and LW walls.

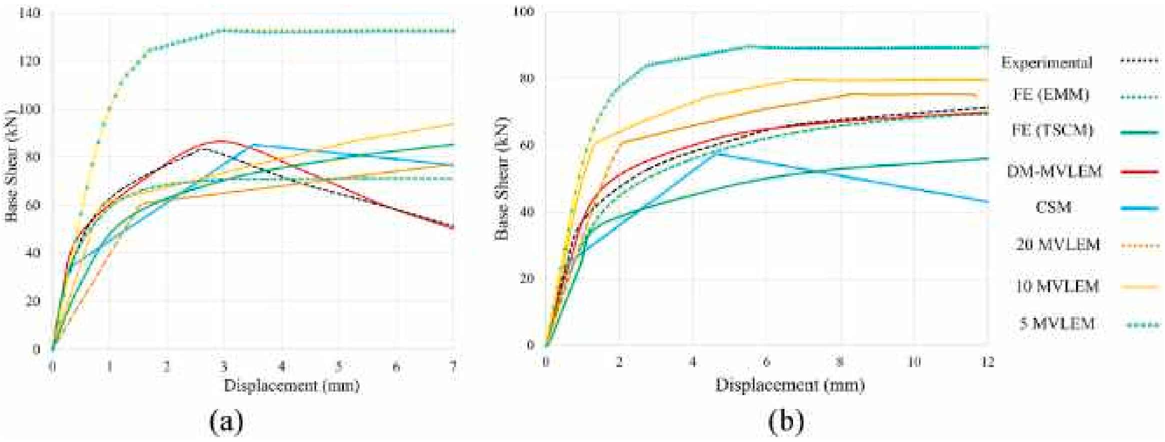

Fig. 11. POA results of the (a) LW and (b) HW modeled based on various modeling strategies and the backbone curve of the tests' results.

URM buildings. Backbone curves of the test result are considered as references and based on Fig. 11, the percent error values of the initial stiffness, loading capacity, and post-peak stiffness of various numerical simulations are presented in Fig. 12 (a) and (b) for the LW and HW specimens respectively. Note that the percent error value equals to the absolute error value divided by the test results' values. The average of percent error values that might not be a robust enough parameter for evaluating each numerical method are calculated and presented in Fig. 12 (c) for each wall to summarize the detailed results of Fig. 12 (a) and (b) and facilitate the comparative study. It can be pointed out that among the FE models, EMM is more accurate compared to the TSCM for the prediction of the load-bearing behavior and the damage pattern [67]. The CSM can predict the lateral load-bearing behavior of the LW with shear failure behavior with a good agreement but with a poor agreement for the HW with flexural failure mode. The poor agreement is shown for the backbone properties of the specimens modeled with the MVLEM elements; however, the loading capacity of the HW is in a good agreement with the test results and the error value is decreased by increasing the number of MVLEM elements [68]. The results of the models with MVLEM elements are sensitive to the number of the elements in fixed-fixed boundary conditions, and failure mode prediction cannot be investigated for the models developed using MVLEM elements. Therefore, using MVLEM elements for the nonlinear analysis of URM walls is not recommended. The DM-MVLEM models show a good agreement with the test results for both walls so that the average of percent error values are less than 13% for both specimens. Although more computational effort is needed to analyze the FE models compared to the EFM approaches as reported in Refs. [2,29,69], a better correlation between the DM-MVLEM models and test results is concluded compared to the FE model with EMM.

3.2.2. Validation of a spandrel modeled with the DM-MVLEM

Validation of a spandrel using the DM-MVLEM was carried out based on a quasi-static cyclic test presented in Ref. [70]. A three-wythe clay-brick URM spandrel with a thickness of 38 cm was tested as shown in Fig. 13 (a) so that the pier (a) was fixed, but the pier (b) could move vertically. Moreover, the rotation of the two ends of the pier (a) was fixed during the analysis, and a constant uniform compressive stress of 0.5 MPa was applied on the piers [70]. Note that in the OpenSees framework, modeling the MVLEM macroelements in a horizontal direction is not possible; therefore, to simulate the spandrel elements, the modified MVLEM elements had to be modeled manually by employing nonlinear truss elements for modeling the fibers, rigid beam elements for the top and bottom of the element, and the twoNodeLink element available in OpenSees to connect the rigid top and bottom parts [53]. Moreover, two modified MVLEMs were connected using a zero-length element to represent the nonlinear shear behavior of the DM-MVLEM

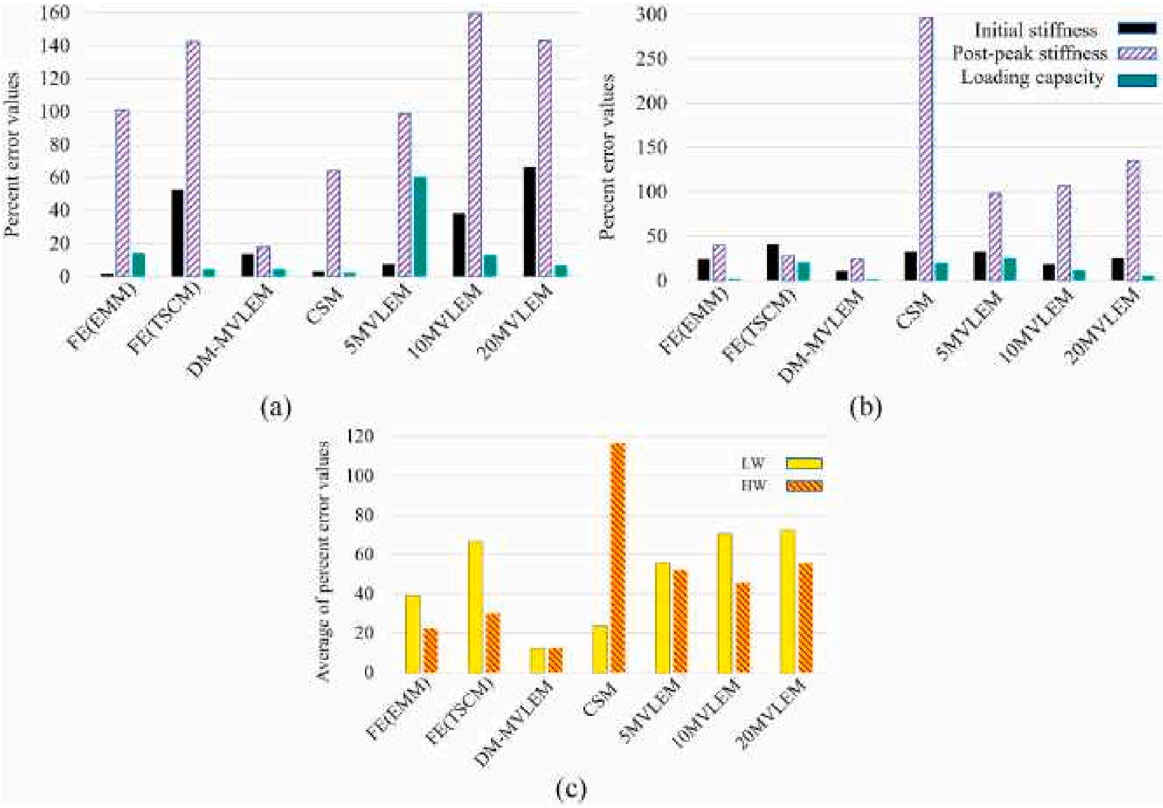

Fig. 12. Percent error values for the initial stiffness, post-peak stiffness, and loading capacity values for the (a) LW, (b) HW specimens, and (c) the average of the percent error values.

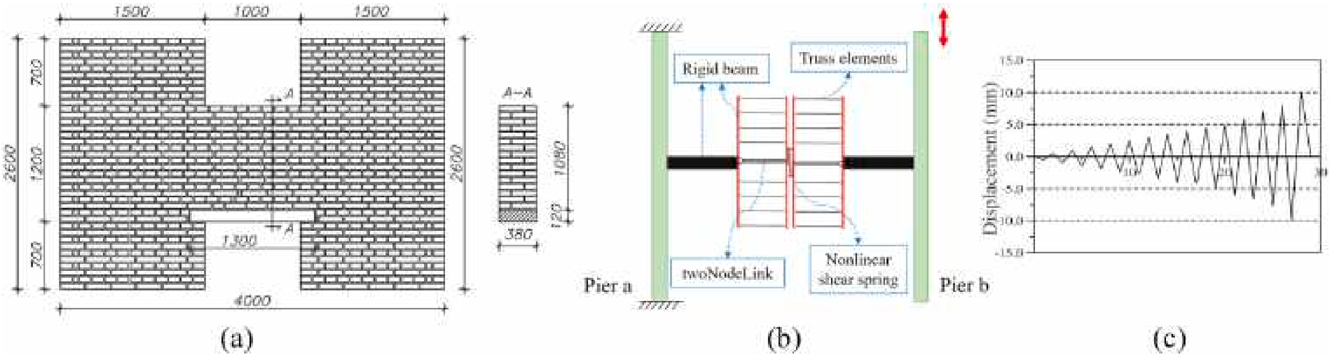

Fig. 13. (a) Geometry of the H shape model, (b) numerical model of the test specimen based on DM-MVLEM, and (c) displacement protocol applied to the specimen [70].

element. The numerical model developed using the DM-MVLEM and the displacement protocol applied vertically to the pier (b) has been illustrated in Fig. 13 (b) and (c).

The stress-strain constitutive law for masonry is depicted in Fig. 14 (a), and the values for f_{td} and f_{v0} are considered 0.19 MPa and 0.28 MPa, respectively based on [70]. Values for the pinching factors and damage due to energy are taken from Table 4, similar to the values for the masonry piers. Other parameters are summarized in Table 5 for defining the spandrels' nonlinear shear springs validated after the calibration process by plotting the experimental and numerical curves as depicted in Fig. 14 (b). Differences between the maximum shear strength and the initial stiffness of the test specimen and the numerical model are 1.3% and 9.7%, respectively.

3.2.3. Validation of a full-scale perforated wall modeled with the DM-MVLEM

In order to investigate the accuracy of the proposed method, the Pavia door wall (see Fig. 6) was modeled using the DM-MVLEM as illustrated in Fig. 15 (a), and the cyclic prescribed displacements were applied based on the experimental test [62]. Differences between the maximum shear strength and the initial stiffness of the test specimen and the numerical model are 5.2% and 11.7%, respectively. The comparison of test results and the numerical simulation, as illustrated in Fig. 15 (b), shows a good agreement between roof displacement and base shear.

Fig. 16 (a) shows the crack patterns and failure mechanisms of the Pavia door wall after performing the test. Combined diagonal

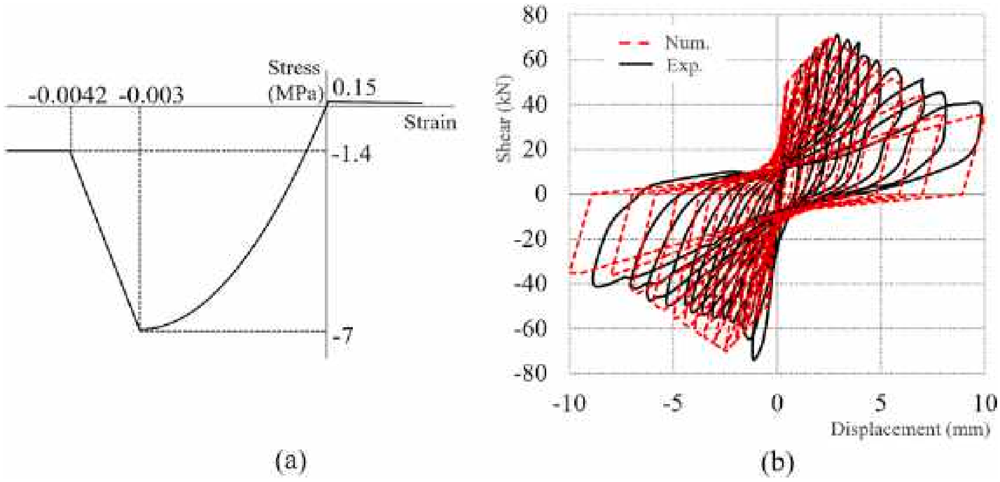

Fig. 14. (a) stress-strain curve of masonry based on the Concrete02 material, and (b) experimental-numerical comparison curves of the spandrel element.

Table 5
The values of the parameters utilized for defining the backbone curve of nonlinear shear spring for spandrels in the DM-MVLEM and the corresponding hysteresis rules.

Parameters	values
d_m	$0.002h$
d_u	$0.008h$
V_u	$0.5V_m$
B	0.5

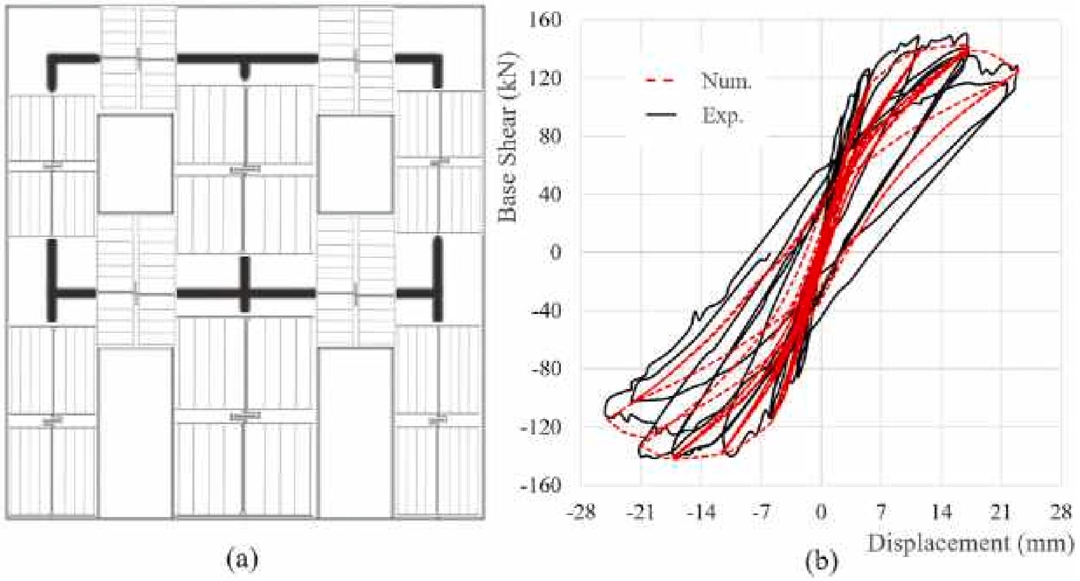

Fig. 15. (a) The developed model of the wall based on the DM-MVLEM and (b) experimental-numerical comparison curves of the perforated URM wall.

shear and flexural failure mechanisms cause the soft story in the first floor, with cracks visible in the spandrels of the first story. As illustrated in Fig. 16 (b), the DM-MVLEM is able to predict the failure mechanisms of the URM structural components in agreement with the results from the test. Failure of the fiber elements of the DM-MVLEM elements in the first story and the shear springs shows the mixed shear-flexural failure. Moreover, cracks in spandrel elements are predicted in the numerical model, as seen in the test.

In order to investigate the accuracy of the model developed using the DM-MVLEM when subjected to more realistic seismic events, incremental dynamic analysis (IDA) [71,72] of a single record was performed. The IDA results were compared to the pushover analyses results. Mass proportional and mode proportional load patterns were chosen for performing the POA to investigate their accuracy compared to the IDA results.

The results associated with Rayleigh damping based on mass and tangent (current) stiffness matrix and last committed stiffness show an approximate consistency based on [73]. Therefore, considering convergence issues and prolongation of analysis caused by

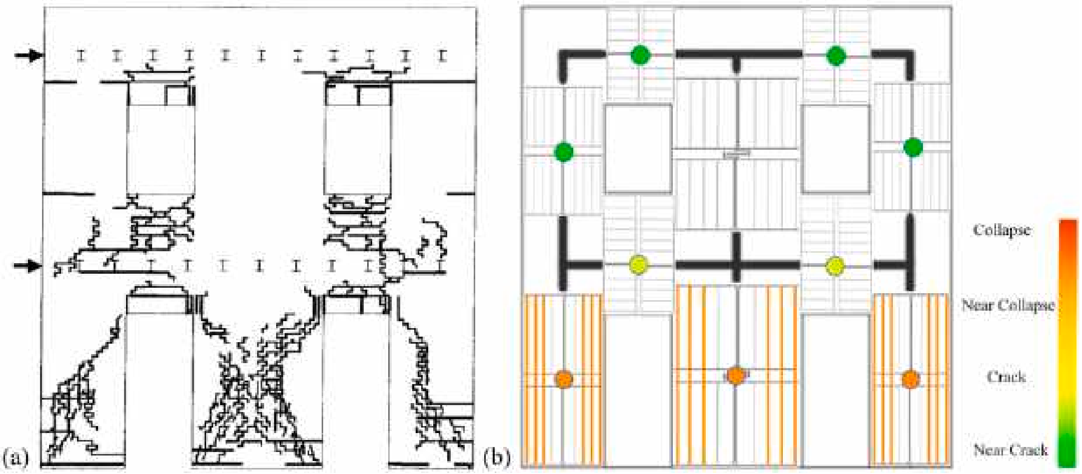

Fig. 16. (a) Crack patterns of the Pavia door wall at the end of the test, and (b) damage representation of the wall modeled with the DM-MVLEM.

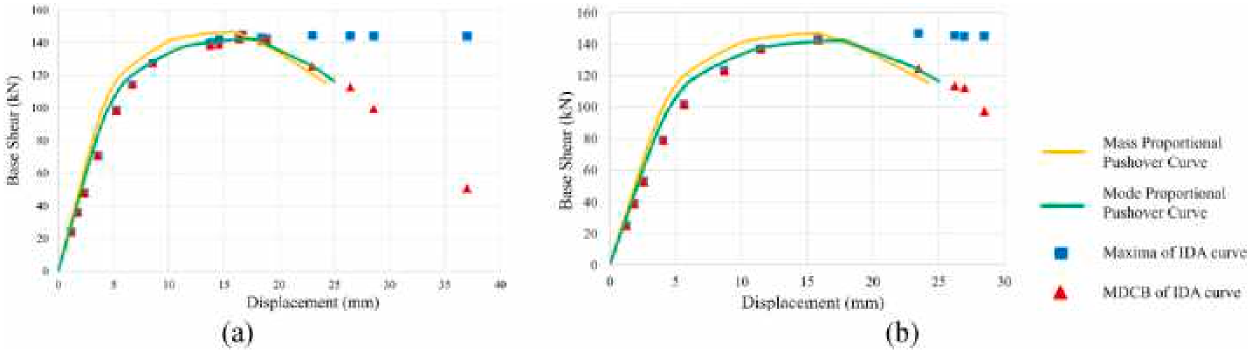

Fig. 17. Pushover curves of Pavia door wall based on mass-proportional and mode-proportional loading patterns and results from the IDA based on the Maxima and MDCB scenarios for the (a) Kobe and (b) Landers seismic records.

using the current stiffness matrix, it may be judicious to apply the committed stiffness matrix in lieu of the current stiffness matrix which results in saving computational time. An equivalent damping ratio of 2% at the first and second modal frequencies is considered [47] proportional to the mass and the last committed stiffness matrix for performing the IDA.

For performing the IDA, a seismic record was applied to the model, and the intensity of the record was increased. Two seismic records were chosen from the FEMA P-695 seismic records [74]. Fig. 17 (a) shows the diagram of base shear versus roof displacement resulting from the NTHA of the modeling subjected to the Kobe seismic record, which occurred in Japan with a magnitude of 6.9, and Fig. 17 (b) shows the results of the Landers record in the United States which had a magnitude of 7.3.

To investigate the most accurate process for the comparison, two scenarios were considered to illustrate the IDA results in the versatile OpenSees framework. For each record's result, maximum displacement and the corresponding base shear (MDCB) and the maxima of base shear and displacement curve (Maxima) were extracted, with the curves provided for the records, as illustrated in Fig. 17. The results of the Maxima and MDCB scenarios are not distinguishable before the peak base shear as shown in Fig. 17, but the

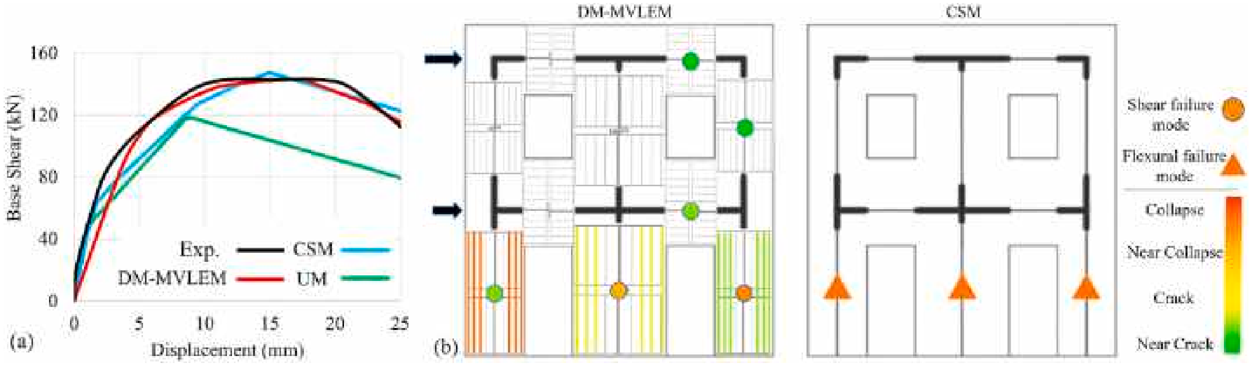

Fig. 18. (a) Pushover curve of the Pavia door wall developed based on the UM, CSM, and the DM-MVLEM and (b) damage representation of the Pavia door wall modeled using the DM-MVELM and CSM.

envelope curve of the results from the NTHA based on the Maxima scenario cannot reflect the post-peak degradation that the MDCB results can exhibit.

The mode proportional pushover curves are closer to the IDA envelope curves before the peak base shear due to the stiffness degradation and the damage due to energy. However, the mass proportional pushover curves can exhibit maximum base shear and the corresponding roof displacement in better agreement with the IDA results. As illustrated in Fig. 17, the post-peak degradation visible in both mode and mass proportional pushover curves is in good agreement with the results from the IDA based on the MDCB scenario, which shows the accuracy of this scenario for the evaluation of the accuracy of the pushover load patterns compared to the conventional Maxima scenario utilized in Refs. [18,21,50,60].

4. *Seismic behavior of the full-scale wall modeled with the UM, CSM, and DM-MVLEM*

The Pavia door wall as shown in Fig. 6 (a) was modeled using the UM, CSM, and DM-MVLEM as case study 1 for performing a comparative study. A comparative study is carried out to evaluate the performance of each method. Discussions of the results of the seismic analyses in this section are elaborated in the next section by emphasizing the characteristic of each modeling approach.

4.1. *Pushover analysis*

The POA was performed considering the load pattern of the test for the Pavia door wall to enable comparison of the results with the test results. The POA results of the CSM, and DM-MVLEM models are illustrated in Fig. 18 (a). As illustrated in Fig. 16, failure modes can be predicted in good agreement with the test results for the DM-MVLEM model during the cyclic displacement control analysis. In order to compare the failure modes occurring in the case study, the damage patterns for the model developed using the DM-MVLEM and CSM by performing a monotonic POA are illustrated in Fig. 18 (b) at the final prescribed displacement of the pushover curves.

4.2. *Multiple records IDA*

Twenty-two pairs of far-field seismic records from the FEMA-P 695 guideline [74] were chosen, and the IDA was done by increasing the intensity of the records until a limit state was reached. The inter-story drift of 1% was considered for the collapse limit state based on [38]. An IDA curve is a diagram of the ground motion intensity measure (IM) against an engineering demand parameter (EDP). The IM and EDP are the spectral acceleration corresponding to the first mode elastic vibration period of the structure considering 5% of damping ($Sa(T_1, 5\%)$), and the maximum inter-story drift respectively in this study [75]. Fig. 19 shows the result of the IDA of the case study modeled using the three methods.

To facilitate the comparison of the IDA results, the mean value of the IMs that cause an inter-story drift limit state to occur was derived and is summarized in Fig. 20. The first limit state is considered as the immediate occupancy (IO) with an inter-story drift of 0.3%, the second is life safety (LS) with an inter-story drift of 0.6%, and the third is collapse prevention with an inter-story drift of 1% based on [38].

5. Discussion

The main advantages of UM are that it obviates the need for the discretization of structural components (piers and spandrels), uses simple formulations for deriving the nonlinear spring parameters, requires less computational effort and results in a good convergence during the nonlinear analyses are the main advantages of the UM. However, using the EHM for deriving the initial in-plane stiffness of URM walls is approximate that cannot reflect the effects of the unsymmetrical openings. Furthermore, the equation for deriving the maximum shear strength considers the rocking and shear sliding failure modes for a perforated wall with a simplified conservative assumption and does not consider the failure mode of each pier separately. Since a perforated wall is not discretized into piers and spandrels, the most critical structural components cannot be detected using the UM approach.

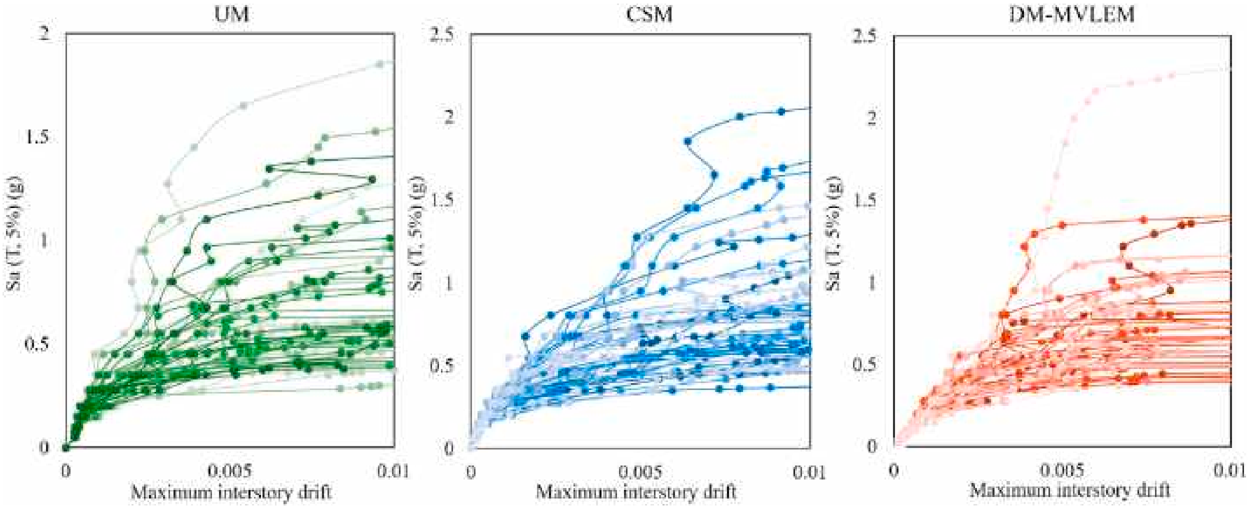

Fig. 19. IDA curves of the Pavia door wall modeled based on the UM, CSM and DM-MVLEM.

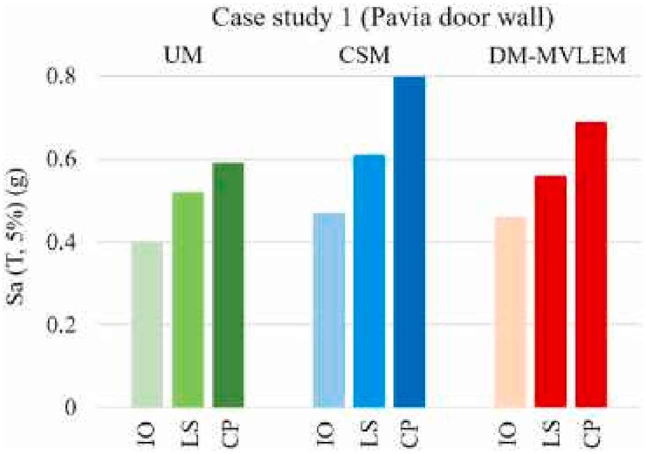

Fig. 20. The mean values of IMs that cause the IO, LS and CP limit states to occur in the case study modeled based on the UM, CSM and DM-MVLEM.

By discretizing the piers and spandrels through the modeling and calculating the maximum shear strength based on three failure modes of piers, the most probable failure mode of each pier, as well as cracked or damaged components that cannot be predicted using the UM can be detected using the CSM. However, concentrating all the failure behavior of the wall (flexural and shear modes) in a single shear spring is not realistic enough. Considering the same deformation limits and the same hysteresis rule for the piers with rocking and shear failure modes is another limitation of this method. Moreover, N-M interaction and the effect of a fluctuating axial force on the strength and stiffness of the components are not investigated in the CSM. Furthermore, a reliable method for modeling spandrels is needed to investigate the effect of this structural component on the results. The DM-MVLEM is an alternative to tackle the limitations and maintain simplicity, efficiency in computations, and stability during the nonlinear analyses. The main features of the methods and FE method using EMM [67,76] are synthesized in Table 6 to facilitate comparison.

A comparative study was carried out on the nonlinear analyses' results of the Pavia door wall developed using the UM, CSM and DM-MVLEM. The POA results show good agreement of the CSM and DM-MVLEM with the test results for deriving the pushover curve (see Fig. 18 (a)). However, due to the conservative approach of the UM for calculating the maximum shear strength by assuming weak connections of spandrels to piers, the pushover curve is derived conservatively compared to the test. The damage patterns for the Pavia door wall show that the CSM model cannot reflect the combined shear-flexural failure mode, as seen in the test. Therefore, the diagonal shear failure mode that can be seen in the test cannot be seen in the CSM model. Nevertheless, the damage pattern is predicted with a good agreement to the test results using the DM-MVLEM model, as illustrated in Fig. 18 (b). The results of the IDA show that the DM-MVLEM reflects a more conservative approach in terms of hysteresis rules compared to the CSM since the pushover curves are close to each other, but the mean acceleration values for the IO and CP limit states as shown in Fig. 20 are less than in the CSM. Moreover, as expected from the pushover curves the UM yields the most conservative results in the IDA.

6. Conclusion

Various simplified methods have been developed for the nonlinear modeling of URM buildings to perform seismic analysis with sufficient speed and accuracy. The UM is a simplified method that is considered the most efficient method reviewed and modified by

Table 6
Comparison of the main features of the UM, CSM, and DM-MVLEM.

Feature section	Feature	UM	CSM	DM-MVLEM	FEM (EMM)
Modeling and calculation	Discretization of the structural components	×	✓	✓	×
	Consideration of N-M interaction	×	×	✓	✓
	Consideration of N-V interaction	×	×	×	✓
	Stress-strain curve input data	×	×	✓	✓
	Explicit hysteresis behavior for different in-plane failure modes	×	×	✓	✓
	Combined in-plane and out-of-plane response	×	×	×	✓
In-plane failure mechanisms	Soft story	✓	✓	✓	✓
	Flexural failure mode of piers	×	✓	✓	✓
	Shear failure mode of piers	×	✓	✓	✓
	Flexural failure mode of spandrels	×	×	✓	✓
	Shear failure mode of spandrels	×	×	✓	✓
	Combined flexural and shear failure modes	×	×	✓	✓
Type of analyses	Modal analysis	✓	✓	✓	✓
	Static linear	✓	✓	✓	✓
	Nonlinear pushover	✓	✓	✓	✓
	Nonlinear dynamic	✓	✓	✓	✓
	Local collapse analysis	×	×	×	×
Availability	Availability in openaccess or opensource software	✓	✓	✓	×

employing accurate enough EHM to derive the initial in-plane stiffness of perforated URM walls. But in a more detailed approach, the CSM is entailing a model of a perforated wall with nonlinear shear springs for the piers, with the linear spandrels. Definite equations for deriving the maximum shear strength of the piers were utilized for different failure modes, and the accuracy of using phenomenological laws of the unperforated URM walls presented in the UM with manipulation was investigated through the validation process.

To tackle the limitations of the UM and CSM and maintain simplicity in modeling, efficiency in computational efforts, and stability during nonlinear analyses, a novel macroelement is developed using the MVLEM element available in the OpenSees framework. The new macroelement consists of two modified MVLEMs to reflect the axial-flexural behavior of the wall connected via a nonlinear shear spring at the middle. The DM-MVLEM is validated against the experimental tests results on piers, a spandrel, and a full-scale perforated URM wall. Results of the POA of two piers with different modeling strategies show that MVLEM cannot reflect the actual behavior of URM piers, but the DM-MVLEM can predict the real behavior of the piers with good agreements with the tests' results. Even more correlation between the DM-MVELM and tests' results is concluded compared to the FE model using EMM with more computational effort. In order to investigate the accuracy of the DM-MVLEM subjected to dynamic loading and detect the most accurate load pattern for performing the POA, the results of the IDA for the Maxima and MDCB scenarios of two seismic records have been plotted against the mode proportional and mass proportional POA results. The results show that the IDA results of the Maxima and MDCB are indistinguishable before and including the point with the maximum base shear strength, but after that point, the envelope curve of the MDCB can reflect the post-peak degradation that cannot be seen for the Maxima curve. Hence, compared to the conventional Maxima scenario, the MDCB scenario can be a more realistic way to plot the IDA curves and compare the POA and IDA results.

A study was conducted to compare the seismic behavior of the Pavia door wall case study developed using the three aforementioned modeling approaches. The results from the POA show a good agreement of the CSM and DM-MVLEM with the experimental test results. The damage pattern is predicted by the DM-MVLEM in good agreement with the test. Nevertheless, the combined flexural and shear failure modes detected in the test are not predicted by the CSM. The IM values derived from the IDA of CSM and DM-MVLEM are close to each other for IO and LS limit states, but the DM-MVLEM is on the safe side in predicting the occurrence of the CP limit state.

The UM can be utilized as a fast tool for seismic analysis of ordinary URM buildings with conservative results. Given that not only the global analysis results but also detection of the most critical component are crucial, the CSM can be an accurate enough alternative for modeling the URM buildings without weak spandrels compared to the pier elements. The novel DM-MVLEM is an accurate enough method to predict the combined shear and flexural failure modes, nonlinear behavior of spandrel elements, and capture the N-M interaction effects. Future studies are required to improve the load-bearing behavior of the DM-MVLEM by implementing a new formulation to consider the N-V interaction during the analysis. Moreover, the element can be utilized for the nonlinear modeling of reinforced masonry walls.

Credit author statement

Amirhosein Shabani Conceptualization; Methodology; Investigation; Resources; Data Curation; Writing - Original Draft; Visualization;

Mahdi Kioumarsi Conceptualization; Writing - Review & Editing; Supervision; Project administration; Funding acquisition.

Declaration of competing interest

The authors declare that they have no known competing financial interests or personal relationships that could have appeared to influence the work reported in this paper.

Acknowledgements

This work is a part of the HYPERION project. HYPERION has received funding from the European Union's Framework Programme for Research and Innovation (Horizon 2020) under grant agreement No 821054. The contents of this publication are the sole responsibility of Oslo Metropolitan University (Work Package 5, Task 2) and do not necessarily reflect the opinion of the European Union.

References

[1] A.M. D'Altri, V. Sarhosis, G. Milani, J. Rots, S. Cattari, S. Lagomarsino, et al., Modeling strategies for the computational analysis of unreinforced masonry structures: review and classification, Arch. Comput. Methods Eng. (2019) 1–33, https://doi.org/10.1007/s11831-019-09351-x.

[2] A. Shabani, M. Kioumarsi, M. Zucconi, State of the art of simplified analytical methods for seismic vulnerability assessment of unreinforced masonry buildings, Eng. Struct. 239 (2021), 112280, https://doi.org/10.1016/j.engstruct.2021.112280.

[3] A. Aşıkoğlu, G. Vasconcelos, P.B. Lourenço, B. Pantò, Pushover analysis of unreinforced irregular masonry buildings: lessons from different modeling approaches, Eng. Struct. 218 (2020), 110830, https://doi.org/10.1016/j.engstruct.2020.110830.

[4] P. Roca, M. Cervera, G. Gariup, Structural analysis of masonry historical constructions. Classical and advanced approaches, Arch. Comput. Methods Eng. 17 (2010) 299–325, https://doi.org/10.1007/s11831-010-9046-1.

[5] F. Romano, M.S. Alam, M. Zucconi, M. Faggella, A.R. Barbosa, B. Ferracuti, Seismic demand model class uncertainty in seismic loss analysis for a code-designed URM infilled RC frame building, Bull. Earthq. Eng. 19 (2021) 429–462, https://doi.org/10.1007/s10518-020-00994-x.

[6] M. Aschheim, E. Hernández-Montes, D. Vamvatsikos, Design of Reinforced Concrete Buildings for Seismic Performance: Practical Deterministic and Probabilistic Approaches, Taylor and Francis Group, 2019.

[7] M. Yekrangnia, P.G. Asteris, Multi-strut macro-model for masonry infilled frames with openings, J. Build. Eng. 32 (2020), 101683, https://doi.org/10.1016/j.jobe.2020.101683.

[8] A. Shabani, M. Kioumarsi, V. Plevris, H. Stamatopoulos, Structural vulnerability assessment of heritage timber buildings: a methodological proposal, Forests 11 (2020) 881, https://doi.org/10.3390/f11080881.

[9] E. Hernández-Montes, M.A. Fernández-Ruiz, M. Aschheim, L.M. Gil-Martín, Structural knowledge within the 6th century AD Arch of Taq-iKisra, Int. J. Architect. Herit. 11 (2017) 891–900, https://doi.org/10.1080/15583058.2017.1321699.

[10] E. Quagliarini, G. Maracchini, F. Clementi, Uses and limits of the Equivalent Frame Model on existing unreinforced masonry buildings for assessing their seismic risk: a review, J. Build. Eng. 10 (2017) 166–182, https://doi.org/10.1016/j.jobe.2017.03.004.

[11] D. Malomo, M.J. DeJong, A Macro-Distinct Element Model (M-DEM) for simulating the in-plane cyclic behavior of URM structures, Eng. Struct. 227 (2021), 111428, https://doi.org/10.1016/j.engstruct.2020.111428.

[12] P. Fajfar, A nonlinear analysis method for performance-based seismic design, Earthq. Spectra 16 (2000) 573–592, https://doi.org/10.1193/1.1586128.

[13] D. D'Ayala, A. Meslem, D. Vamvatsikos, K. Porter, T. Rossetto, Guidelines for analytical vulnerability assessment: low/mid-rise, GEM vulnerability and loss modelling, in: Global Earthquake Model, GEM) Foundation, Pavia, 2015.

[14] T.M. Ferreira, N. Mendes, R. Silva, Multiscale seismic vulnerability assessment and retrofit of existing masonry buildings, Buildings 9 (2019) 91, https://doi.org/10.3390/buildings9040091.

[15] A. Maria D'Altri, N. Lo Presti, N. Grillanda, G. Castellazzi, S. de Miranda, G. Milani, A two-step automated procedure based on adaptive limit and pushover analyses for the seismic assessment of masonry structures, Comput. Struct. 252 (2021), 106561, https://doi.org/10.1016/j.compstruc.2021.106561.

[16] H. Krawinkler, G.D.P.K. Seneviratna, Pros and cons of a pushover analysis of seismic performance evaluation, Eng. Struct. 20 (1998) 452–464, https://doi.org/10.1016/S0141-0296(97)00092-8.

[17] A. Shabani, A. Alinejad, M. Teymouri, A. Nascimento Costa, M. Shabani, M. Kioumarsi, Seismic vulnerability assessment and strengthening of heritage timber buildings: a review, Buildings 11 (2021) 661, https://doi.org/10.3390/buildings11120661.

[18] Y. Endo, L. Pelà, P. Roca, Review of different pushover analysis methods applied to masonry buildings and comparison with nonlinear dynamic analysis, J. Earthq. Eng. 21 (2016) 1234–1255, https://doi.org/10.1080/13632469.2016.1210055.

[19] L. Pasticier, C. Amadio, M. Fragiacomo, Non-linear seismic analysis and vulnerability evaluation of a masonry building by means of the SAP2000 V. 10 code, Earthq. Eng. Struct. Dynam. 37 (2008) 467–485, https://doi.org/10.1002/eqe.770.

[20] C. Chácara, F. Cannizzaro, B. Pantò, I. Caliò, P.B. Lourenço, Assessment of the dynamic response of unreinforced masonry structures using a macroelement modeling approach, Earthq. Eng. Struct. Dynam. 47 (2018) 2426–2446, https://doi.org/10.1002/eqe.3091.

[21] S. Petrovčič, V. Kilar, Seismic failure mode interaction for the equivalent frame modeling of unreinforced masonry structures, Eng. Struct. 54 (2013) 9–22, https://doi.org/10.1016/j.engstruct.2013.03.050.

[22] D. Baraldi, A. Cecchi, A full 3D rigid block model for the collapse behaviour of masonry walls, Eur. J. Mech. Solid. 64 (2017) 11–28, https://doi.org/10.1016/j.euromechsol.2017.01.012.

[23] G. Milani, S. Casolo, A. Naliato, A. Tralli, Seismic assessment of a medieval masonry tower in Northern Italy by limit, nonlinear static, and full dynamic analyses, Int. J. Architect. Herit. 6 (2012) 489–524, https://doi.org/10.1080/15583058.2011.588987.

[24] G. Milani, Fast vulnerability evaluation of masonry towers by means of an interactive and adaptive 3D kinematic limit analysis with pre-assigned failure mechanisms, Int. J. Architect. Herit. 13 (2019) 941–962, https://doi.org/10.1080/15583058.2019.1645241.

[25] F.P.A. Portioli, Rigid block modelling of historic masonry structures using mathematical programming: a unified formulation for non-linear time history, static pushover and limit equilibrium analysis, Bull. Earthq. Eng. 18 (2020) 211–239, https://doi.org/10.1007/s10518-019-00722-0.

[26] F. Cannizzaro, B. Pantò, S. Caddemi, I. Caliò, A Discrete Macro-Element Method (DMEM) for the nonlinear structural assessment of masonry arches, Eng. Struct. 168 (2018) 243–256, https://doi.org/10.1016/j.engstruct.2018.04.006.

[27] M. Malena, F. Portioli, R. Gagliardo, G. Tomaselli, L. Cascini, G. de Felice, Collapse mechanism analysis of historic masonry structures subjected to lateral loads: a comparison between continuous and discrete models, Comput. Struct. 220 (2019) 14–31, https://doi.org/10.1016/j.compstruc.2019.04.005.

[28] A. Fortunato, F. Fabbrocino, M. Angelillo, F. Fraternali, Limit analysis of masonry structures with free discontinuities, Meccanica 53 (2018) 1793–1802, https://doi.org/10.1007/s11012-017-0663-8.

[29] N. Grillanda, M. Valente, G. Milani, A. Chiozzi, A. Tralli, Advanced numerical strategies for seismic assessment of historical masonry aggregates, Eng. Struct. 212 (2020), 110441, https://doi.org/10.1016/j.engstruct.2020.110441.

[30] F. Portioli, C. Casapulla, L. Cascini, An efficient solution procedure for crushing failure in 3D limit analysis of masonry block structures with non-associative frictional joints, Int. J. Solid Struct. 69–70 (2015) 252–266, https://doi.org/10.1016/j.ijsolstr.2015.05.025.

[31] H. Pirsaheb, M.J. Moradi, G. Milani, A Multi-Pier MP procedure for the non-linear analysis of in-plane loaded masonry walls, Eng. Struct. 212 (2020), 110534, https://doi.org/10.1016/j.engstruct.2020.110534.

[32] G. Magenes, G.M. Calvi, In-plane seismic response of brick masonry walls, Earthq. Eng. Struct. Dynam. 26 (1997) 1091–1112, https://doi.org/10.1002/(sici)1096-9845(199711)26:11<1091::aid-eqe693>3.0.co;2-6.

[33] M. Yekrangnia, A. Bakhshi, M.A. Ghannad, Force-displacement model for solid confined masonry walls with shear-dominated failure mode, Earthq. Eng. Struct. Dynam. 46 (2017) 2209–2234, https://doi.org/10.1002/eqe.2902.

[34] J.V. Lemos, Discrete element modeling of masonry structures, Int. J. Architect. Herit. 1 (2007) 190–213, https://doi.org/10.1080/15583050601176868.

[35] B. Pulatsu, E. Erdogmus, P.B. Lourenço, J.V. Lemos, K. Tuncay, Simulation of the in-plane structural behavior of unreinforced masonry walls and buildings using DEM, Structures 27 (2020) 2274–2287, https://doi.org/10.1016/j.istruc.2020.08.026.

[36] M. Mistler, A. Anthoine, C. Butenweg, In-plane and out-of-plane homogenisation of masonry, Comput. Struct. 85 (2007) 1321–1330, https://doi.org/10.1016/j.compstruc.2006.08.087.

[37] F. Greco, P.B. Lourenço, Seismic assessment of large historic vernacular adobe buildings in the Andean Region of Peru. Learning from Casa Arones in cusco, J. Build. Eng. 40 (2021), 102341, https://doi.org/10.1016/j.jobe.2021.102341.

[38] FEMA, Prestandard and Commentry for the Seismic Rehabilitaion of Buildings, FEMA 356, Federal Emergency Management Agency, Washington, D.C., 2000.

[39] S. Lagomarsino, A. Penna, A. Galasco, S. Cattari, TREMURI program: an equivalent frame model for the nonlinear seismic analysis of masonry buildings, Eng. Struct. 56 (2013) 1787–1799, https://doi.org/10.1016/j.engstruct.2013.08.002.

[40] R. Maio, T.M. Ferreira, J.M.C. Estêvão, B. Pantò, I. Caliò, R. Vicente, Seismic performance-based assessment of urban cultural heritage assets through different macroelement approaches, J. Build. Eng. 29 (2020), 101083, https://doi.org/10.1016/j.jobe.2019.101083.

[41] M. Tomazevic, The Computer Program POR: Institute for Testing and Research in Materials and Structures-ZRMK, 1978. Slovenia: Ljubljana.

[42] J.K. Shrestha, S. Bhandari, S. Pradhan, D. Gautam, Simplified frame model for capacity assessment of masonry buildings, Soil Dynam. Earthq. Eng. 131 (2020), https://doi.org/10.1016/j.soildyn.2020.106056, 106056.

[43] A. Penna, S. Lagomarsino, A. Galasco, A nonlinear macroelement model for the seismic analysis of masonry buildings, Earthq. Eng. Struct. Dynam. 43 (2014) 159–179, https://doi.org/10.1002/eqe.2335.

[44] S. Bracchi, A. Galasco, A. Penna, A Novel Macroelement Model for the Nonlinear Analysis of Masonry Buildings. Part 1: Axial and Flexural Behavior, Earthquake Engineering & Structural Dynamics, 2021, https://doi.org/10.1002/eqe.3445.

[45] S. Bracchi, A. Penna, A Novel Macroelement Model for the Nonlinear Analysis of Masonry Buildings. Part 2: Shear Behavior, Earthquake Engineering & Structural Dynamics, 2021, https://doi.org/10.1002/eqe.3444.

[46] R. Siano, P. Roca, G. Camata, L. Pelà, V. Sepe, E. Spacone, et al., Numerical investigation of non-linear equivalent-frame models for regular masonry walls, Eng. Struct. 173 (2018) 512–529, https://doi.org/10.1016/j.engstruct.2018.07.006.

[47] M. Peruch, E. Spacone, G. Camata, Nonlinear analysis of masonry structures using fiber-section line elements, Earthq. Eng. Struct. Dynam. 48 (2019) 1345–1364, https://doi.org/10.1002/eqe.3188.

[48] H. Xu, C. Gentilini, Z. Yu, H. Wu, S. Zhao, A unified model for the seismic analysis of brick masonry structures, Construct. Build. Mater. 184 (2018) 733–751, https://doi.org/10.1016/j.conbuildmat.2018.06.208.

[49] J. Park, P. Towashiraporn, J.I. Craig, B.J. Goodno, Seismic fragility analysis of low-rise unreinforced masonry structures, Eng. Struct. 31 (2009) 125–137, https://doi.org/10.1016/j.engstruct.2008.07.021.

[50] G. Rinaldin, C. Amadio, L. Macorini, A macro-model with nonlinear springs for seismic analysis of URM buildings, Earthq. Eng. Struct. Dynam. 45 (2016) 2261–2281, https://doi.org/10.1002/eqe.2759.
[51] K. Orakcal, J.W. Wallace, J.P. Conte, Flexural modeling of reinforced concrete walls-model attributes, Struct. J. 101 (2004) 688–698.
[52] K. Orakcal, J.W. Wallace, Flexural modeling of reinforced concrete walls-experimental verification, ACI Mater. J. 103 (2006) 196.
[53] S. Mazzoni, F. McKenna, M.H. Scott, G.L. Fenves, OpenSees Command Language Manual. Pacific Earthquake Engineering Research (PEER) Center, 2006, p. 264.
[54] K. Kolozvari, K. Orakcal, J.W. Wallace, Modeling of cyclic shear-flexure interaction in reinforced concrete structural walls. I: Theory, J. Struct. Eng. 141 (2015), 04014135, https://doi.org/10.1061/(ASCE)ST.1943-541X.0001059.
[55] K. Kolozvari, T.A. Tran, K. Orakcal, J.W. Wallace, Modeling of cyclic shear-flexure interaction in reinforced concrete structural walls. II: experimental validation, J. Struct. Eng. 141 (2015), 04014136, https://doi.org/10.1061/(ASCE)ST.1943-541X.0001083.
[56] K. Kolozvari, K. Orakcal, J.W. Wallace, New opensees models for simulating nonlinear flexural and coupled shear-flexural behavior of RC walls and columns, Comput. Struct. 196 (2018) 246–262, https://doi.org/10.1016/j.compstruc.2017.10.010.
[57] J. Park, Investigation of the geometric variation effect on seismic performance of low-rise unreinforced masonry structures through fragility analysis, Int. J. Civ. Eng. 16 (2018) 93–106, https://doi.org/10.1007/s40999-016-0070-x.
[58] J. Craig, B. Goodno, P. Towashiraporn, J. Park, Response Modification Applications for Essential Facilities, Project ST-4 Final Report, Georgia Institute of Technology, The United States, 2007.
[59] A. Shabani, V. Plevris, M. Kioumarsi, A Comparative Study on the Initial In-Plane Stiffness of Masonry Walls with Openings. 17th World Conference on Earthquake Engineering, 17WCEE. Sendai, Japan, 2021.
[60] K. Demirlioglu, S. Gonen, S. Soyoz, M.P. Limongelli, In-plane seismic response analyses of a historical brick masonry building using equivalent frame and 3D FEM modeling approaches, Int. J. Architect. Herit. (2018), https://doi.org/10.1080/15583058.2018.1529208.
[61] M. Dolce, Schematizzazione e modellazione degli edifici in muratura soggetti ad azioni sismiche, L'industr. Costr. 25 (1991) 44–57 (in Italian).
[62] G. Magenes, G. Kingsley, G. Calvi, Seismic Testing of a Full-Scale, Two-Story Masonry Building: Test Procedure and Measured Experimental Response Report 3.0, G.N.D.T. Department of Structural Mechanics, University of Pavia, 1995.
[63] P. Esmaeiltabar, J. Vaseghi, H. Khosravi, Nonlinear macro modeling of slender reinforced concrete shear walls, Struct. Concr. 20 (2019) 899–910, https://doi.org/10.1002/suco.201800206.
[64] G. Rinaldin, C. Amadio, N. Gattesco, Review of experimental cyclic tests on unreinforced and strengthened masonry spandrels and numerical modelling of their cyclic behaviour, Eng. Struct. 132 (2017) 609–623, https://doi.org/10.1016/j.engstruct.2016.11.063.
[65] S. Cattari, S. Lagomarsino, A strength criterion for the flexural behaviour of spandrels in un-reinforced masonry walls, in: The 14th World Conference on Earthquake Engineering. Beijing, China, 2008.
[66] A. Anthoine, G. Magonette, G. Magenes, Shear-compression testing and analysis of brick masonry walls, Tenth Eur. Conf. Earthq. Eng. 3 (1995) 1657–1662.
[67] G.M.A. Schreppers, A. Garofano, F. Messali, J.G. Rots, DIANA Validation Report for Masonry Modelling, DIANA FEA Report 2016-DIANA-R1601, Delft University of Technology, Netherland, 2016, p. 143.
[68] K. Kolozvari, J.W. Wallace, Practical nonlinear modeling of reinforced concrete structural walls, J. Struct. Eng. 142 (2016), G4016001, https://doi.org/10.1061/(ASCE)ST.1943-541X.0001492.
[69] S. Cattari, D. Camilletti, A.M. D'Altri, S. Lagomarsino, On the use of continuum Finite Element and Equivalent Frame models for the seismic assessment of masonry walls, J. Build. Eng. 43 (2021), 102519, https://doi.org/10.1016/j.jobe.2021.102519.
[70] N. Gattesco, L. Macorini, A. Dudine, Experimental response of brick-masonry spandrels under in-plane cyclic loading, J. Struct. Eng. 142 (2016), 04015146, https://doi.org/10.1061/(ASCE)ST.1943-541X.0001418.
[71] D. Vamvatsikos, C.A. Cornell, Incremental dynamic analysis, Earthq. Eng. Struct. Dynam. 31 (2002) 491–514, https://doi.org/10.1002/eqe.141.
[72] D. Vamvatsikos, C.A. Cornell, Applied incremental dynamic analysis, Earthq. Spectra 20 (2004) 523–553, https://doi.org/10.1193/1.1737737.
[73] N. Mohammadgholibeyki, M. Banazadeh, The effects of viscous damping modeling methods on seismic performance of RC moment frames using different nonlinear formulations, Structures 15 (2018) 232–243, https://doi.org/10.1016/j.istruc.2018.07.009.
[74] FEMA, Quantification of Building Seismic Performance Factors, FEMA P695, Federal Emergency Management Agency, United States, Washington, D.C., 2009.
[75] A. Zaherdannak, A. Shabani, S. Erfani, Seismic performance evaluation of special RC frames with gravity steel columns under the base level, Shock Vib. (2020), https://doi.org/10.1155/2020/8825258, 2020:8825258.
[76] V.G. Haach, G. Vasconcelos, P.B. Lourenço, Parametrical study of masonry walls subjected to in-plane loading through numerical modeling, Eng. Struct. 33 (2011) 1377–1389, https://doi.org/10.1016/j.engstruct.2011.01.015.

Paper IV

Shabani, A., Kioumarsi, M.

Pros and Cons of Various Equivalent Frame Models for Nonlinear Analysis of URM Buildings

(2022) 8th European Congress on Computational Methods in Applied Sciences and Engineering (ECCOMAS 2022), Oslo, Norway

The 8th European Congress on Computational Methods in Applied Sciences and Engineering
ECCOMAS Congress 2022
5 – 9 June 2022, Oslo, Norway

PROS AND CONS OF VARIOUS EQUIVALENT FRAME MODELS FOR NONLINEAR ANALYSIS OF URM BUILDINGS

AMIRHOSEIN SHABANI[*] AND MAHDI KIOUMARSI[†]

[*] Department of Civil Engineering and Energy Technology
Oslo Metropolitan University
Pilestredet 35, 0166, Oslo, Norway
e-mail: amirhose@oslomet.no, https://www.oslomet.no/om/ansatt/amirhose/

[†] Department of Civil Engineering and Energy Technology
Oslo Metropolitan University
Pilestredet 35, 0166, Oslo, Norway
e-mail: mahdik@oslomet.no, https://www.oslomet.no/om/ansatt/mahdik/

Key words: Equivalent Frame model, Macroelement, Nonlinear Analysis, Unreinforced Masonry, DM-MVLEM, Seismic Fragility.

Abstract. Brick masonry is considered as one of the old construction materials, and several cultural heritage assets are made of unreinforced masonry (URM), which is susceptible to earthquakes due to its brittle behavior. The equivalent frame method (EFM) is a nonlinear modeling method widely utilized for the seismic analysis of URM buildings with lower computational efforts than finite and discrete element methods. In this study, three macroelements, including the unified method (UM), composite spring method (CSM), and double modified multiple vertical line element model (DM-MVLEM), were utilized to model three case studies. The first case study is a full-scale two-story URM wall that was tested by applying the cyclic prescribed displacements, and two other case studies were developed by changing the configuration of openings. The second case study is with short piers, and weak spandrels exist in the third model. The efficiency of the methods in terms of the accuracy of the pushover results, prediction of damage patterns, and duration of the incremental dynamic analysis (IDA) are discussed. Finally, seismic fragility curves are provided to compare the IDA results.

1 INTRODUCTION

Recently, developing an integrated resilience assessment platform by utilizing a fast, adapted, and efficient multi-hazard risk assessment tool has gained acceptance for the sustainable reconstruction of historic areas [1]. Although different simplified analytical methods have been proposed to assess the vulnerability of unreinforced masonry (URM) buildings at a large scale, by developing computer technology and emerging supercomputers, accurate and fast nonlinear modeling approaches should be utilized for the near-real-time assessment or prediction of seismic risk purposes with a lower level of uncertainty [2]. Moreover, simplified methods could be necessary tools for the seismic analysis of buildings for designers who lack specialized skills. The equivalent frame method (EFM) is considered as the most efficient method for nonlinear analysis of URM buildings [3]. Figure 1 shows the number of published journal articles regarding the EFM based on the related keywords searched in the Scopus database. The evolution of different macroelement models and their applications for seismic analysis of buildings with unreinforced masonry walls depicts the significance and the efficiency of the EFM.

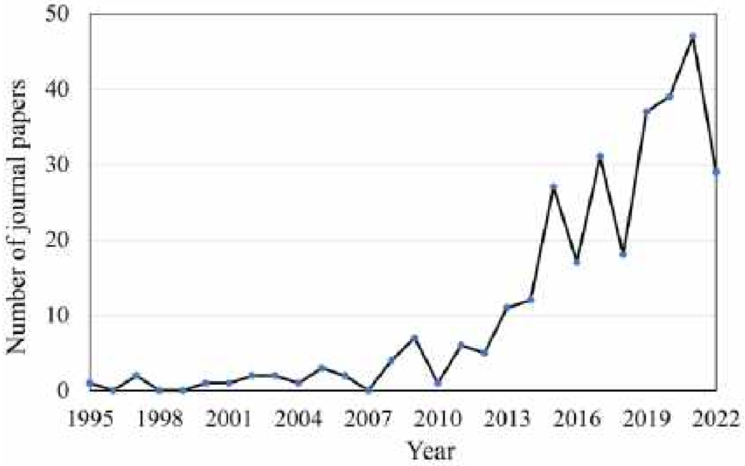

Figure 1: Number of relevant published journal papers since 1995 adapted from Scopus.

Various macroelements were developed to represent the nonlinear behavior of URM pier and spandrels, in which the unified method (UM) is considered one of the most simplified macroelements [4]. The main concept of UM is to model each URM wall in each story with a macroelement. The macroelement was then modified using the equivalent height method (EHM) for calculating the initial in-plane stiffness of the perforated URM walls [5, 6]. Shear and rocking hinges were employed at the middle and two sides of the elastic beam-column elements, respectively representing the failure modes and nonlinear behavior of masonry piers and spandrels in [7, 8]. As a simplified version, the composite spring method (CSM) was developed [3, 5]. Each pier can be modeled using a nonlinear shear spring with a specific backbone curve and ignoring the nonlinear behavior of spandrel elements. Fiber elements were also utilized to represent the nonlinear behavior of URM structural components considering the effect of axial-flexural interaction (N-M) [9, 10]. DM-MVLEM was developed considering the N-M effects with a lower computational effort than the fiber elements [3]. DM-MVLEM consists of two modified MVLEM elements available in OpenSees [11]. Two modified MVLEM elements are tied with a zero-length element to simulate the nonlinear shear behavior of the URM segments [3].

Seismic risk analysis should be performed to define the most vulnerable structures and determine the most efficient strategy for retrofitting the existing structures. The seismic fragility curves can be utilized to evaluate the expected social and economic losses [12]. Fragility is structure-specific and depends on the structure's design properties and condition. More specifically, fragility is defined as the probability of a structure reaching or exceeding a definite limit state subjected to an earthquake with an intensity level [13]. The fragility curves can be derived based on empirical, analytical, or hybrid methods. Around 64% of the literature studies from 2005-2021 related to seismic fragility analysis utilized analytical methods, and only 10% of the studies are related to the URM buildings [14]. Derivation of fragility curves based on the

IDA is one of the most accurate analytical methods [15]. Although this method is computationally demanding compared to other analytical methods, no prior assumptions are required regarding the probabilistic distribution of seismic demand for the derivation of fragility functions [16].

In this study, the UM, CSM, and DM-MVLEM were utilized to develop the nonlinear models of three case studies with different configurations of openings. The UM and DM-MVLEM are considered as the simplest and the most detailed methods, respectively. To investigate the accuracy of the methods, pushover analysis and IDA were carried out. The efficiency of the methods in terms of the accuracy of the pushover curves, prediction of damage patterns, and duration of the incremental dynamic analysis (IDA) are discussed. Furthermore, fragility curves were provided based on the IDA results by determining the record-to-record variability and modeling uncertainties, and the curves were compared to each other.

2 DEVELOPMENT OF NONLINEAR MODELS

Three case studies with different configurations of openings were modeled based on the UM, CSM, and DM-MVLEM. Therefore, nine nonlinear models were developed, and more details about the modeling based on each method in the OpenSees framework are presented in the following sections.

2.1 Unified method (UM)

The unified method (UM) was developed for the nonlinear analysis of confined and unconfined masonry walls. The UM macroelement consists of two truss elements at the two ends of the wall with linear behavior and a nonlinear shear spring in the middle of a wall. A nonlinear material with a trilinear backbone curve can be assigned to the lateral degree of freedom of the UM macroelement, and the other two degrees are free [4]. For this aim, two node link element and the hysteretic material model, available in the OpenSees library, were utilized. The maximum lateral strength of an unconfined URM wall can be calculated based on an equation that is not validated to calculate the value in the presence of the openings [4]. Another strategy was proposed to derive the maximum lateral strength by considering a weak connection between the piers and spandrels [3]. This conservative approach corresponds to the cantilever idealization in which null shear strength is considered for the spandrels. The maximum lateral strength is the sum of the maximum lateral strength of the vertical URM segments. The initial in-plane stiffness of URM walls with openings can be calculated based on the EHM. The EHM is a simplified analytical method that considers the flexibility of the two ends of piers due to the presence of spandrels for calculating the initial in-plane stiffness of URM walls with openings [6]. Details about the backbone curve and hysteresis parameters are presented in [3].

2.2 Composite spring method (CSM)

CSM is more accurate than the UM by discretizing perforated URM walls into piers and spandrels that are connected with the rigid elements based on the Dolce method [17]. The two node link element with a linear axial stiffness, fixed rotational degree of freedom, and a nonlinear shear spring were utilized to model a pier. The maximum lateral strength of piers is defined as the minimum value of the lateral strength due to shear sliding (V_s), diagonal cracking

(V_D), and rocking (V_R) failure modes [3]. The failure modes of piers can be roughly estimated by calculating the maximum lateral strength of each pier and defining the corresponding failure mode, which cannot be predicted using the UM. The initial in-plane stiffness of piers can be calculated based on the deep beam theory assumption by combining the shear and flexural stiffness of a wall with fixed-fixed boundary conditions [6]. Other specifications of the nonlinear shear spring are similar to unperforated walls presented for the UM macroelement elaborated in [3]. Note that, in this model, the nonlinear behavior of spandrel elements is not taken into account by modeling them using elastic beam-column elements.

2.3 Double modified MVLEM (DM-MVLEM)

Considering the nonlinearity in the spandrel element, N-M interaction effects, and prediction of the combined shear and flexural failure modes, DM-MVLEM is the most accurate macroelement used in this study. The DM-MVELM consists of two modified MVLEM connected with a zero-length element as a nonlinear shear spring [3]. The number of fiber elements is equal on two sides of the connection nodes of the MVLEM [18]. Therefore, the MVLEM elements cannot be used to simulate the asymmetrical segments that are common for URM spandrels. Furthermore, MVLEM elements cannot be utilized for modeling in the horizontal direction, and for modeling spandrel elements, the MVLEM elements should be modeled manually. For this aim, truss elements simulate the fiber elements of the MVLEM elements and connect two rigid parts to simulate the original MVLEM element for simulating the spandrels. Concrete 02 or Concrete 03 material with the stress-strain curve of masonry and the hysteretic material with a trilinear backbone curve can be assigned to the elements. Note that the former is assigned to the MVLEM fibers of piers and truss elements of spandrels, and the latter is assigned to the transitional degree of freedom of zero-length elements in the transverse direction to simulate the nonlinear shear behavior of the segments. The maximum lateral strength of the pier elements can be determined as the minimum value of the V_S and V_D based on [3]. Note that the maximum lateral strength of spandrels is determined as the minimum value of the V_D and the interlocking strength at bed joints at the intersection between spandrel and piers (V_I) based on [19]. The shear stiffness of the wall considering the deep beam theory for a pier with fixed-fixed boundary conditions can be considered as the initial in-plane stiffness of the zero-length elements [6].

2.4 Nonlinear models of full-scale URM walls

A full-scale two-story URM wall with openings tested at the University of Pavia (case study A) was considered the benchmark model in this study, see [20]. Case studies B and C were developed by changing the opening size of the benchmark model. Case study B is with an asymmetric configuration of openings and short piers, and case study C is with weak spandrels as illustrated in Figure 2 (a). All the case studies were modeled based on the DM-MVLEM, CSM, and UM as shown in Figure 2 (b), (c), and (d), respectively. Note that the UM models are the same based on the same length and height of the floor walls. Stress-strain curve of the URM material is depicted in Figure 2 (e) with the diagonal tensile strength (f_{td}) of 0.21 MPa and the shear strength of the masonry at zero compressive stress (f_{v0}) of 0.345 MPa based on [20].

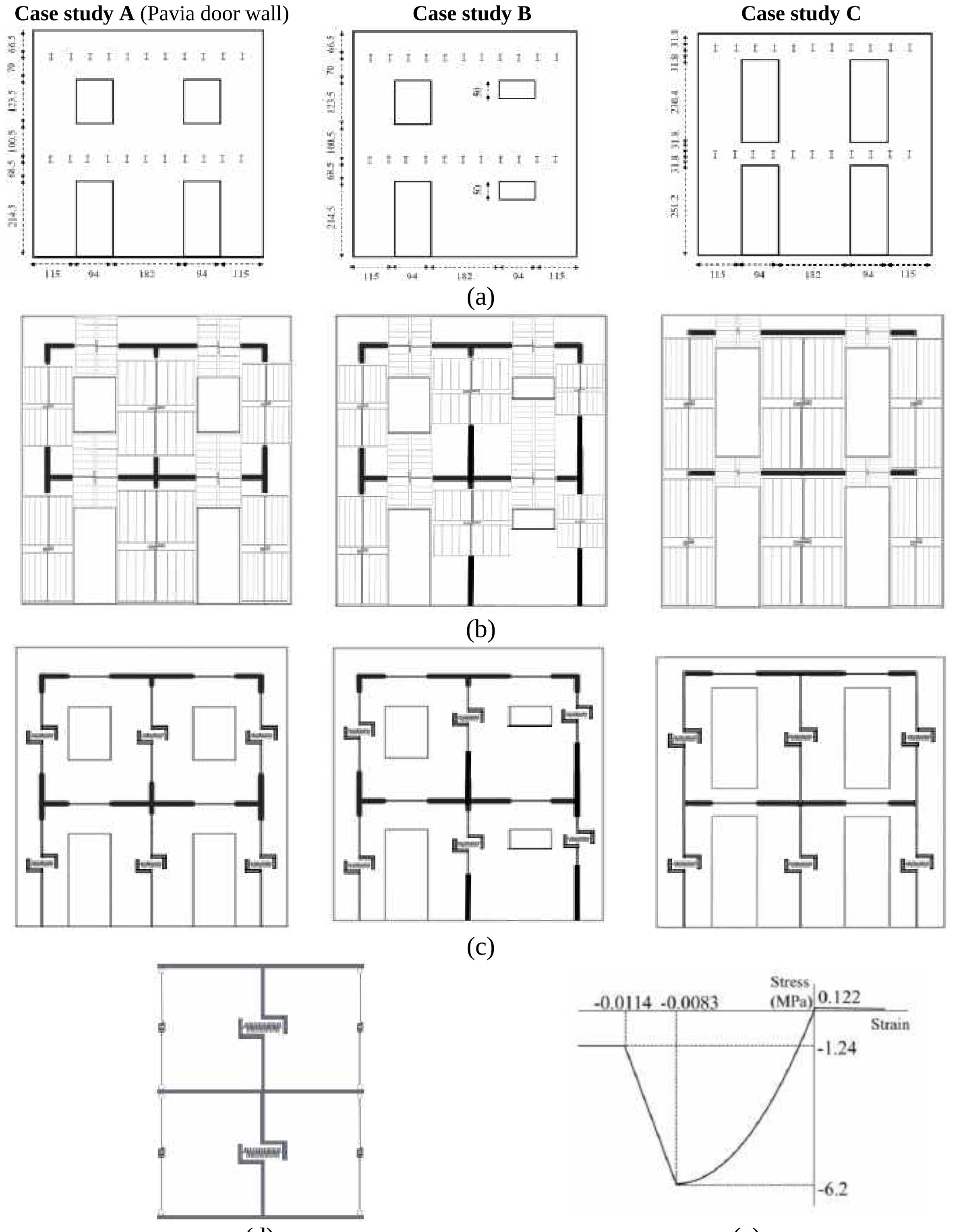

Figure 2: (a) Geometry of the case studies and the configuration of openings, (b) DM-MVLEM, (c) CSM, (d) UM models of the case studies, and (e) stress-strain curve of masonry.

3 PUSHOVER ANALYSIS

The pushover analysis was performed by applying the load pattern of the test for the Pavia door wall to compare the results with the test results and mass distribution load pattern for the other two case studies. The POA results are illustrated in Figure 17 for three case studies modeled according to the three aforementioned modeling approaches.

The Pavia door wall is the first case study, and the POA results show good agreement of the CSM and DM-MVLEM with the test results for deriving the pushover curve, as highlighted in Figure 3 (a) [20]. However, due to the conservative approach of the UM for calculating maximum shear strength by assuming weak connections of spandrels to piers, the pushover curve is conservative compared to the test result. For the case study B, with short piers and asymmetric opening configurations, pushover curves are close in the elastic phase. However, the post-peak behavior of the DM-MVLEM is more conservative than the CSM, see Figure 3 (b). Since the nonlinear behavior of spandrels was considered in the DM-MVELM, for the case study C, the pushover curves of the UM and DM-MVLEM models are close to each other, see Figure 3 (c). Nevertheless, the ultimate lateral strength is overestimated for the CSM model.

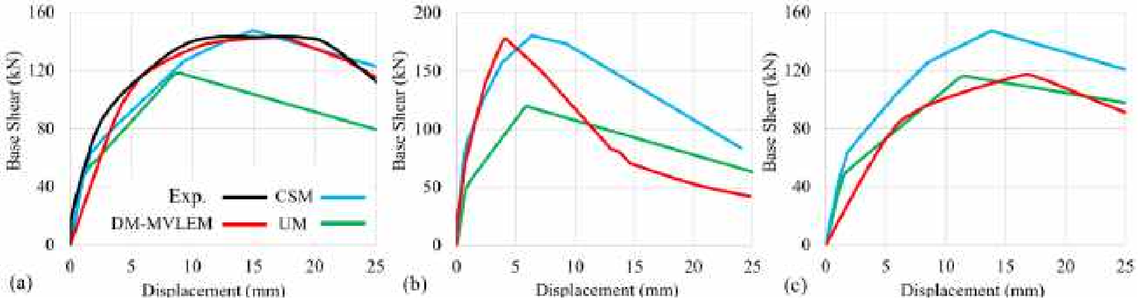

Figure 3: Pushover curves of (a) case study A (with the backbone curve from the test results [20]), (b) case study B, and (c) case study C.

3.1 Damage pattern prediction

In order to compare the failure modes occurring in the case studies, the damage patterns for the DM-MVLEM and CSM models by performing a monotonic POA are illustrated in Figure 4. Figure 4 (a) illustrates the damage pattern of the tested wall subjected to the cyclic displacements. The damage patterns for the Pavia door wall show that the CSM model cannot reflect the combined shear-flexural failure mode, as seen in the test, but this is reflected in the DM-MVLEM model, as illustrated in Figure 4 (b). Thus, the diagonal shear failure mode that can be seen in the test is not observed in the CSM model. Results from the failure modes representation of case study B show that the CSM can reflect the shear failure modes (which usually occurs in short piers) in good agreement with the DM-MVLEM as shown in Figure 4 (b). The failure of the spandrels was critical for case study C due to the presence of weak spandrels. Damage to spandrels has been predicted in the DM-MVLEM model but does not occur in the CSM due to the assumption of considering linear spandrel elements. Furthermore, combined shear-flexural failure modes cannot be defined using the CSM.

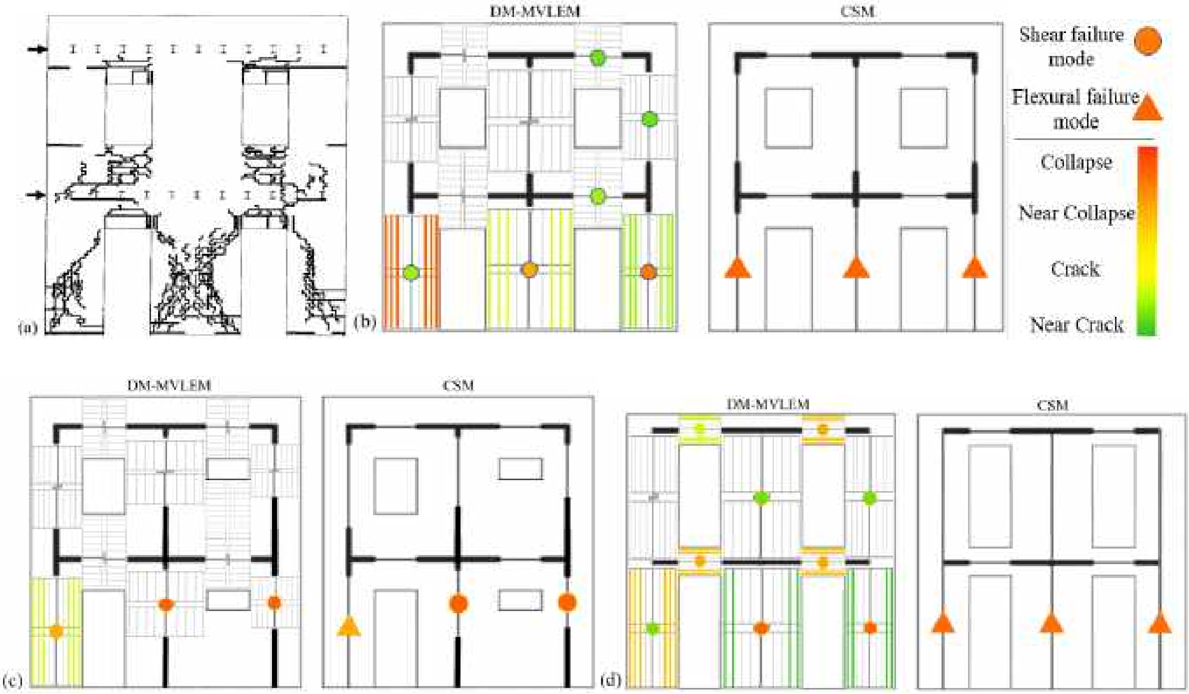

Figure 4: Damage patterns of the (a) tested wall [20], CSM, and DM-MVLEM models of the (b) case study A, (c) case study B, and (d) case study C.

4 INCREMENTAL DYNAMIC ANALYSIS (IDA)

For performing the IDA, an equivalent damping ratio of 2% at the first and second modal frequencies was considered proportional to the mass and the last committed stiffness matrix [3, 21]. Twenty-two pairs of far-field seismic records from the FEMA-P 695 guideline [22] were chosen, and the IDA was done by increasing the intensity of the records until the target limit state. The inter-story drift of 1% was considered for the collapse limit state [23].

The analysis duration and the average values for the models developed based on the methods are illustrated in Figure 5. The UM is the fastest method with the lowest computational effort. The analysis time of the UM and CSM models is 21% and 7% faster than DM-MVLEM models.

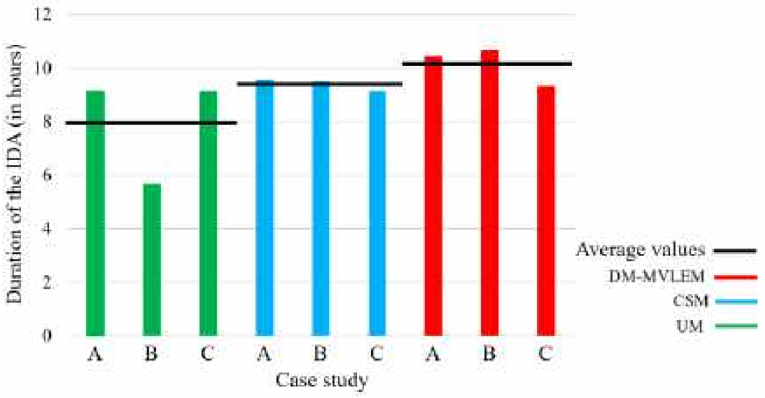

Figure 5: Duration of the IDA analysis of case study developed based on the UM, CSM, and DM-MVLEM.

An IDA curve is a diagram of the ground motion intensity measure (IM) against an engineering demand parameter (EDP). The IM and EDP are the spectral acceleration corresponding to the first mode elastic vibration period of the structure considering 5% of damping (Sa (T_1, 5%)) and the maximum inter-story drift, respectively [21]. Figure 6 shows the result of the IDA of the case studies modeled using the three methods.

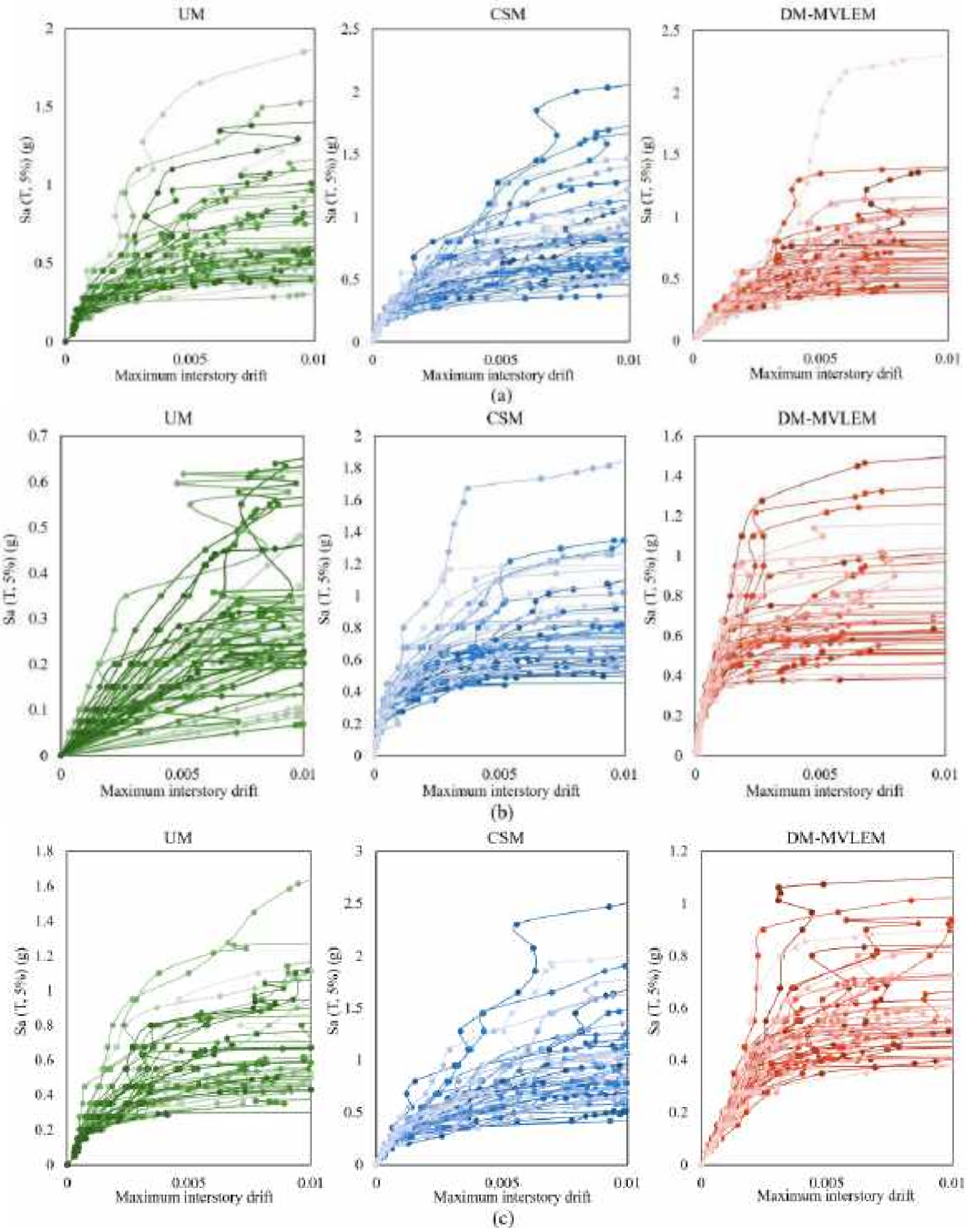

(a)

(b)

(c)

Figure 6: IDA curves of (a) Pavia door wall, (b) case study 2, and (c) case study 3 modeled based on the UM, CSM and DM-MVLEM.

5 SEISMIC FRAGILITY ANALYSIS

This study uses a lognormal cumulative distribution function to define a fragility function based on Equation (1).

$$P[C|IM = im] = \Phi\left[\frac{ln(im) - \eta}{\beta}\right] \tag{1}$$

where $P[C|IM = im]$ is the probability that a ground motion with $IM = im$ will cause the structure to collapse. $\Phi()$ is the standard normal cumulative distribution function, $ln()$ is the natural logarithm function, η and β are the mean and standard deviation, respectively, of the *ln(im)* values . In order to incorporate the modeling uncertainty in the seismic fragility analysis, the β value is calculated based on Equation (2), considering both the record-to-record variability and the modeling uncertainty [24].

$$\beta = \sqrt{\beta_M^2 + \beta_D^2} \tag{2}$$

where β_D is the dispersion associated with uncertainty in demand (record-to-record variability) which is calculated as the mean of the *ln(im)* values and β_M is the modeling uncertainty. The predefined β_M values represent collapse characteristics, and the accuracy and robustness of the models can be derived from [22].

Considering a medium level for the representation collapse characteristics of the case studies, the β_M values are assigned to each modeling approach based on Table 1. The low level of the accuracy was assigned to the UM, due to the cantilever idealization and the simplified formulation of the modeling approach. But piers and spandrels were modeled separately based on CSM, and different equations were proposed to define the maximum lateral strength. Nevertheless, the inelastic behavior of the spandrel elements is ignored, the N-M interaction is not taken into account, explicit hysteresis behaviors for different in-plane failure modes are not considered and the combined shear-flexural failure modes cannot be predicted using the CSM. Hence the medium level of accuracy of the model can be assigned to the CSM. All the aforementioned shortcomings of the CSM were modified in the DM-MVLEM, but the N-V interaction is not considered during the nonlinear analysis, and the high accuracy level is assigned to the DM-MVLEM.

Table 1: The quality rating of archetype models

The level of accuracy and robustness	High	Medium	Low
Description	Nonlinear models simulate all predominant inelastic effects with robust computational solution algorithms.	Nonlinear models capture most nonlinear deterioration and response mechanisms leading to collapse.	Nonlinear models capture the onset of yielding and subsequent strain hardening but do not simulate the degrading response and capture the effects of deterioration and redistribution.
β_M	0.2	0.35	0.5

All the uncertainty values for the models are presented in Table 2 and fragility curves are illustrated in Figure 7. The fragility curves derived from the analysis of UM and CSM with the higher uncertainty values, as presented in Table 2, are flatter than the curves of the DM-MVLEM models. The fragility curves of case study A are close to each other without a considerable change. For case study B, the results of the fragility analysis of the UM are more conservative than the other two approaches. The curves of case study B for the CSM and DM-MVLEM are close to each other. Moreover, for case study C, the median values of the IM for the UM and DM-MVLEM models are close to each other; however, the differences are due to the higher level of uncertainty of UM and the IM that causes damage is overestimated for the CSM model. Considering the collapse margin ratio of 10% based on [22], UM and CSM are considered the most and the least conservative approaches, respectively. The IM values for the CSM and DM-MVLEM models are close to each other for the 10% of collapse margin ratio.

Table 2: Calculated parameters of the fragility curves, including the uncertainty values

Modeling type	Name of the case study	η	β_D	β_M	β
UM	Case study A	-0.432	0.412	0.5	0.648
	Case study B	-1.336	0.51	0.5	0.715
	Case study C	-0.423	0.379	0.5	0.627
CSM	Case study A	-0.229	0.387	0.35	0.522
	Case study B	-0.255	0.318	0.35	0.473
	Case study C	-0.067	0.406	0.35	0.536
DM-MVLEM	Case study A	-0.354	0.383	0.2	0.432
	Case study B	-0.355	0.32	0.2	0.377
	Case study C	-0.515	0.284	0.2	0.347

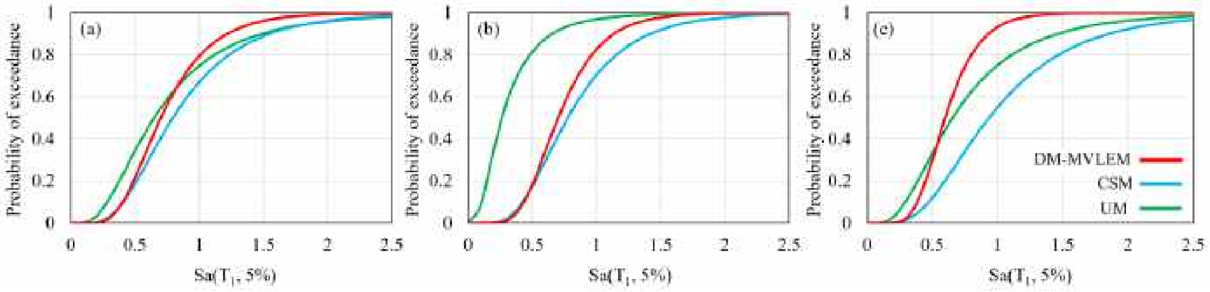

Figure 7: Seismic fragility curves of the (a) case study A, (b) case study B, and (c) case study C.

6 CONCLUSIONS

- Except for case study C with weak spandrels, the pushover curve of UM models is conservative in terms of the ultimate base shear. However, due to neglecting the nonlinear behavior in the CSM, the results overestimate the maximum base shear for case study C, and the UM results are in good agreement with the DM-MVLEM.
- Damage patterns cannot be predicted using the UM. Moreover, DM-MVLEM is more accurate than the CSM by highlighting the combined flexural-shear failure modes and prediction of the failure of spandrels. However, the shear failure modes can be

predicted based on the CSM, which usually can be observed in short piers.

- UM is considered the fastest method for performing IDA with the highest level of uncertainty, and DM-MVLEM is the opposite. Results of the IDA were summarized in the fragility curves by incorporating the effect of record-to-record variability and modeling uncertainty. The fragility curves derived from the UM and CSM are flatter than DM-MVLEM due to the higher level of uncertainty. CSM cannot be a robust method in case of existing weak spandrels.

ACKNOWLEDGMENT

This work is a part of the HYPERION project. HYPERION has received funding from the European Union's Framework Programme for Research and Innovation (Horizon 2020) under grant agreement No 821054. The contents of this publication are the sole responsibility of Oslo Metropolitan University (Work Package 5, Task 2) and do not necessarily reflect the opinion of the European Union.

REFERENCES

[1] Shabani, A., Skamantzari, M., Tapinaki, S., Georgopoulos, A., Plevris, V., and Kioumarsi, M. 3D simulation models for developing digital twins of heritage structures: challenges and strategies. *Procedia Struct. Integr.*, (2022), **37**: p. 314-320, https://doi.org/10.1016/j.prostr.2022.01.090.

[2] Shabani, A., Kioumarsi, M., and Zucconi, M. State of the art of simplified analytical methods for seismic vulnerability assessment of unreinforced masonry buildings. *Eng. Struct.*, (2021), **239**: p. 112280, https://doi.org/10.1016/j.engstruct.2021.112280.

[3] Shabani, A. and Kioumarsi, M. A novel macroelement for seismic analysis of unreinforced masonry buildings based on MVLEM in OpenSees. *J. Build. Eng.*, (2022), **49**: p. 104019, https://doi.org/10.1016/j.jobe.2022.104019.

[4] Xu, H., Gentilini, C., Yu, Z., Wu, H., and Zhao, S. A unified model for the seismic analysis of brick masonry structures. *Constr Build Mater.*, (2018), **184**: p. 733-751, https://doi.org/10.1016/j.conbuildmat.2018.06.208.

[5] Park, J. Investigation of the Geometric Variation Effect on Seismic Performance of Low-Rise Unreinforced Masonry Structures Through Fragility Analysis. *Int. J. Civ. Eng.*, (2018), **16**(1): p. 93-106, https://doi.org/10.1007/s40999-016-0070-x.

[6] Shabani, A., Plevris, V., and Kioumarsi, M. *A Comparative Study on the Initial In-plane Stiffness of Masonry Walls with Openings*. Proceedings of the World Conference on Earthquake Engineering, 17WCEE, Sendai, Japan. (2021).

[7] Pasticier, L., Amadio, C., and Fragiacomo, M. Non-linear seismic analysis and vulnerability evaluation of a masonry building by means of the SAP2000 V. 10 code. *Earthq Eng Struct Dyn*, (2008), **37**(3): p. 467-485.

[8] Petrovčič, S. and Kilar, V. Seismic failure mode interaction for the equivalent frame modeling of unreinforced masonry structures. *Eng. Struct.*, (2013), **54**: p. 9-22, https://doi.org/10.1016/j.engstruct.2013.03.050.

[9] Siano, R., Roca, P., Camata, G., Pelà, L., Sepe, V., Spacone, E., and Petracca, M. Numerical investigation of non-linear equivalent-frame models for regular masonry walls. *Eng. Struct.*, (2018), **173**: p. 512-529, https://doi.org/10.1016/j.engstruct.2018.07.006.

[10] Peruch, M., Spacone, E., and Camata, G. Nonlinear analysis of masonry structures using fiber-section line elements. *Earthq Eng Struct Dyn*, (2019), **48**(12): p. 1345-1364, https://doi.org/10.1002/eqe.3188.

[11] Mazzoni, S., McKenna, F., Scott, M.H., and Fenves, G.L. *OpenSees command language manual*. Pacific Earthquake Engineering Research (PEER) Center, USA. (2006).

[12] Shabani, A., Alinejad, A., Teymouri, M., Costa, A.N., Shabani, M., and Kioumarsi, M. Seismic Vulnerability Assessment and Strengthening of Heritage Timber Buildings: A Review. *Buildings*, (2021), **11**(12): p. 661.

[13] Silva, V., Akkar, S., Baker, J., Bazzurro, P., Castro, J.M., Crowley, H., Dolsek, M., Galasso, C., Lagomarsino, S., Monteiro, R., Perrone, D., Pitilakis, K., and Vamvatsikos, D. Current Challenges and Future Trends in Analytical Fragility and Vulnerability Modeling. *Earthq. Spectra*, (2019), **35**(4): p. 1927-1952, https://doi.org/10.1193%2F042418EQS101O.

[14] Rajkumari, S., Thakkar, K., and Goyal, H. Fragility analysis of structures subjected to seismic excitation: A state-of-the-art review. *Structures*, (2022), **40**: p. 303-316, https://doi.org/10.1016/j.istruc.2022.04.023.

[15] Muntasir Billah, A.H.M. and Shahria Alam, M. Seismic fragility assessment of highway bridges: a state-of-the-art review. *Struct. Infrastruct. Eng.*, (2015), **11**(6): p. 804-832, https://doi.org/10.1080/15732479.2014.912243.

[16] Zhang, J. and Huo, Y. Evaluating effectiveness and optimum design of isolation devices for highway bridges using the fragility function method. *Eng. Struct.*, (2009), **31**(8): p. 1648-1660.

[17] Cattari, S., D'Altri, A.M., Camilletti, D., and Lagomarsino, S. Equivalent frame idealization of walls with irregular openings in masonry buildings. *Eng. Struct.*, (2022), **256**: p. 114055, https://doi.org/10.1016/j.engstruct.2022.114055.

[18] Orakcal, K., Wallace, J.W., and Conte, J.P. Flexural modeling of reinforced concrete walls-model attributes. *Structural Journal*, (2004), **101**(5): p. 688-698.

[19] Rinaldin, G., Amadio, C., and Gattesco, N. Review of experimental cyclic tests on unreinforced and strengthened masonry spandrels and numerical modelling of their cyclic behaviour. *Eng. Struct.*, (2017), **132**: p. 609-623, https://doi.org/10.1016/j.engstruct.2016.11.063.

[20] Magenes, G., Kingsley, G.R., and Calvi, G.M. *Seismic testing of a full-scale, two-story masonry building: test procedure and measured experimental response*. Consiglio nazionale delle ricerche, Gruppo nazionale per la Difesa dai terremoti. (1995).

[21] Vamvatsikos, D. and Cornell, C.A. Incremental dynamic analysis. *Earthq Eng Struct Dyn*, (2002), **31**(3): p. 491-514, https://doi.org/10.1002/eqe.141.

[22] FEMA. *Quantification of Building Seismic Performance Factors, FEMA P695*. Federal Emergency Management Agency: United States, Washington, D.C. (2009).

[23] FEMA. *Prestandard and Commentry for the Seismic Rehabilitaion of Buildings, FEMA 356*. Federal Emergency Management Agency: Washington, D.C. (2000).

[24] D'Ayala, D., Meslem, A., Vamvatsikos, D., Porter, K., and Rossetto, T. *Guidelines for analytical vulnerability assessment: Low/mid-rise, GEM vulnerability and loss modelling*. Global Earthquake Model (GEM) Foundation, Pavia. (2015).

Paper V

Shabani, A., Kioumarsi, M.

Hyperomet: An OpenSees interface for nonlinear analysis of unreinforced masonry buildings

(2022) Software X, https://doi.org/10.1016/j.softx.2022.101230.

SoftwareX 20 (2022) 101230

Contents lists available at ScienceDirect

SoftwareX

journal homepage: www.elsevier.com/locate/softx

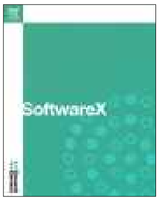

Original software publication

Hyperomet: An OpenSees interface for nonlinear analysis of unreinforced masonry buildings

Amirhosein Shabani [*], Mahdi Kioumarsi

Department of Civil Engineering and Energy Technology, Oslo Metropolitan University, Pilestredet 35, 0166, Oslo, Norway

ARTICLE INFO

Article history:
Received 5 May 2022
Received in revised form 22 September 2022
Accepted 7 October 2022

Keywords:
Unreinforced masonry
Numerical modeling
Double modified MVLEM
Unified method
Nonlinear analysis
OpenSees

ABSTRACT

Seismic vulnerability assessment of historical unreinforced masonry (URM) buildings is crucial for the authorities due to the high susceptibility of historical URM buildings to earthquakes. Open system for earthquake engineering simulation (OpenSees) is a well-known, powerful, and versatile seismic analysis platform. In a lack of a free graphical user interface (GUI) for seismic analysis of URM buildings, Hyperomet was designed to bridge the gap between nonlinear analysis of URM buildings and OpenSees platform. The Hyperomet GUI includes an accurate enough macroelement representing the nonlinear behavior of URM components. The structures can be modeled based on the double-modified multiple vertical line element model (DM-MVLEM) and the Unified method (UM) using the GUI. Calculators for deriving the mechanical properties are provided to minimize the modeling time. Furthermore, the ability to perform various analysis types including incremental dynamic analysis (IDA) is facilitated.

Code metadata

Current code version	V1.0
Permanent link to code/repository used for this code version	https://github.com/ElsevierSoftwareX/SOFTX-D-22-00103
Permanent link to reproducible capsule	None
Legal code license	EUPL-1.2
Code versioning system used	git
Software code languages, tools and services used	JavaScript, TypeScript, Node.js, React, Electron, and third-party libraries
Compilation requirements, operating environments and dependencies	Microsoft Windows
If available, link to developer documentation/manual	None
Support email for questions	Hyperomet@oslomet.no

1. Motivation and significance

Unreinforced masonry (URM) buildings compose a high portion of building typologies in high seismicity zones and historic areas [1]. Therefore seismic vulnerability assessment of URM structures is a crucial task for responsible authorities [2]. Developing an integrated resilience assessment platform utilizing a fast, adapted, and efficient multi-hazard risk assessment tool has recently gained acceptance for the sustainable reconstruction of historic areas [3]. Moreover, simplified modeling approaches could be necessary tools for the seismic analysis of buildings for analysts or designers who lack specialized skills [4]. For this purpose, different simplified analytical methods have been proposed to assess the vulnerability of URM buildings at a large scale, see [1]. Nevertheless, by developing computer technology and emerging supercomputers, accurate and fast nonlinear modeling approaches should be utilized for the near real-time (n-RT) assessment or prediction of seismic risk with a lower level of uncertainty [4].

Open system for earthquake engineering simulation (OpenSees) is an open-source finite element framework used broadly for seismic analyses purposes [5]. Various graphical

---

[*] Corresponding author.
E-mail addresses: amirhose@oslomet.no (Amirhosein Shabani), mahdik@oslomet.no (Mahdi Kioumarsi).

https://doi.org/10.1016/j.softx.2022.101230

user interfaces (GUI) have been developed to facilitate using the OpenSees platform and automate the numerical modeling and analysis procedures [6–14]. Nevertheless, most of the mentioned GUIs are not free to use for researchers and industry, and there is still a need to develop an open-source GUI to automate the numerical modeling and analysis of URM buildings.

As one of the most common modeling approaches, the equivalent frame method (EFM) is used for seismic analysis of URM buildings with lower computational efforts and input data than the well-known continuum homogeneous method [15,16]. In the EFM, URM structural components are modeled via macroelements representing their nonlinear behavior [4].

The unified method (UM) is considered as one of the simplified EFMs for seismic analysis of URM buildings. In the UM approach, each perforated or unperforated URM wall is modeled with a single macroelement [17]. The macroelement consists of a nonlinear shear spring at the middle part that can be modeled using the twoNodeLink element in OpenSees and two twoNodeLink elements at two sides of the wall with an elastic behavior representing the axial stiffness.

However, the double-modified multiple vertical line element model (DM-MVLEM) was calibrated based on the experimental tests and is more accurate method than the UM. MVLEM is an available macroelement for the simulation of flexure-dominated reinforced concrete (RC) wall behavior [18,19]. MVLEM elements underwent modifications to simulate the pure axial–flexural behavior of a wall by neglecting the shear behavior [4]. Each DM-MVLEM comprises two modified MVLEM elements that are connected with a nonlinear shear spring using the zero-length element in OpenSees that represents the nonlinear shear behavior of the segment and more detail of the modeling procedure are presented in [4]. Each pier or spandrel can be modeled with a DM-MVLEM and connected with rigid elements to model a perforated URM wall [20]. MVLEM element comprises conventional FEM elements such as truss, beam–column, and spring element. The MVLEM macroelement that can be used for nonlinear analysis of RC walls was assembled using the basic elements and the macroelement is available in the OpenSees library. However, a unique macroelement for nonlinear analysis of URM building is not available in OpenSees library. The available MVLEM elements in OpenSees library can be utilized for modeling the URM pier elements; however the MVLEM elements cannot be modeled horizontally to simulate the URM spandrels based on DM-MVLEM.

Hyperomet is designed, through an EU-sponsored Horizon 2020 project at Oslo Metropolitan University in Norway, to bridge the gap between the OpenSees users and analysts of URM buildings by addressing an efficient modeling approach in a more effectual process in terms of cost and time. In Hyperomet, modeling URM buildings using the UM and DM-MVLEM macroelements have been automated and eased. Furthermore, various analysis procedures, including incremental dynamic analysis (IDA) [21,22], are available to be used efficiently and in an automated way. Hyperomet can be utilized as a tool for probabilistic seismic analyses in which a high number of models are required to be developed, and iterative analyses are needed to be performed. The tool can be utilized for seismic vulnerability assessment of existing URM buildings by predicting their behavior subjected to different seismic records and hazard scenarios. Moreover, the GUI can be utilized as a simplified and fast tool for n-RT analysis of cultural heritage assets at a small scale and historic areas at a large scale.

2. Software description

Hyperomet is a GUI to produce the .tcl format file of the model and build .tcl format subroutine files for performing various types of analysis including pushover analysis and IDA. Therefore, Hyperomet provides fuel for the OpenSees as the engine for performing the nonlinear analyses.

2.1. Software architecture

The Hyperomet architecture for the modeling and analysis is illustrated in Fig. 1. The main steps for the modeling (4 steps) and analysis (2 steps) parts are highlighted and elaborated below. Due to high number of variables and complicated equations for defining the mechanical properties of the elements, various calculators are provided to reduce the human error. Note that Hyperomet is only available for 2D modeling in the current version. For the modeling phase and in step m1, the nodes will be defined by determining the coordinates in a 2D environment. It should be mentioned that for the UM approach, three coordinate geometry values in *x*-direction are required for modeling a wall. The middle nodes connect the twoNodeLink element for carrying the shear force, and two twoNodeLinks elements tolerate the axial loads at two sides of each wall. The rigid beams will also be modeled automatically to connect the twoNodeLink elements. Moreover, after defining the geometries of the nodes, the rigid length should be defined for the DM-MVLEM modeling approach. The numbering of the nodes and modeling of rigid elements are automatically created in the software.

In step m2, material properties are defined; the user defines an alias for each material and fills the corresponding properties' blanks. In order to facilitate the calculation of the material properties of the elements, the provided calculators can be utilized. These calculators can be utilized for defining the maximum shear strength and initial in-plane stiffness of the URM components and other features of the trilinear backbone can be derived based on these two main values as elaborated in [4]. For the UM, calculators are provided to derive the maximum shear (lateral) strength of the URM wall based on [17]. Moreover, the complicated process of calculating the initial in-plane stiffness of perforated URM walls using the equivalent height method (EHM) is eased [23,24]. The geometry of each pier and the elastic material properties are the input for calculating the initial in-plane stiffness of each URM pier section based on the deep beam theory. Afterward the initial in-plane stiffness of the whole perforated wall will be calculated based on the stiffnesses of all structural components using the parallel and series spring rules. More detail about the procedure of the EHM can be found in [23]. For the DM-MVLEM, the calculators can derive the elastic stiffness of the nonlinear shear spring and the maximum shear strength of piers and spandrels based on the deep beam theory. Note that for calculating the maximum shear strength of the piers and spandrels, different values for different damage patterns will be calculated, but the minimum value should be selected and assigned to the corresponding material [4]. The lateral nonlinear shear spring at the middle of the DM-MVLEM would simulate the shear behavior of the URM components. The maximum lateral strength of piers due to the rocking failure mode can be calculated but should be neglected for the definition of the hysteretic material for the zero-length elements of the pier elements.

For Step m3, the mass of each node should be assigned. For this purpose, the user can see the model, choose a specific node, and assign a mass. Note that for DM-MVLEM, a very small value should be assigned to the mass of the middle point of the element due to possible numerical instability for the MVLEM.

Now the elements should be assigned in step m4. For the UM modeling approach, the user chooses the elements in the GUI

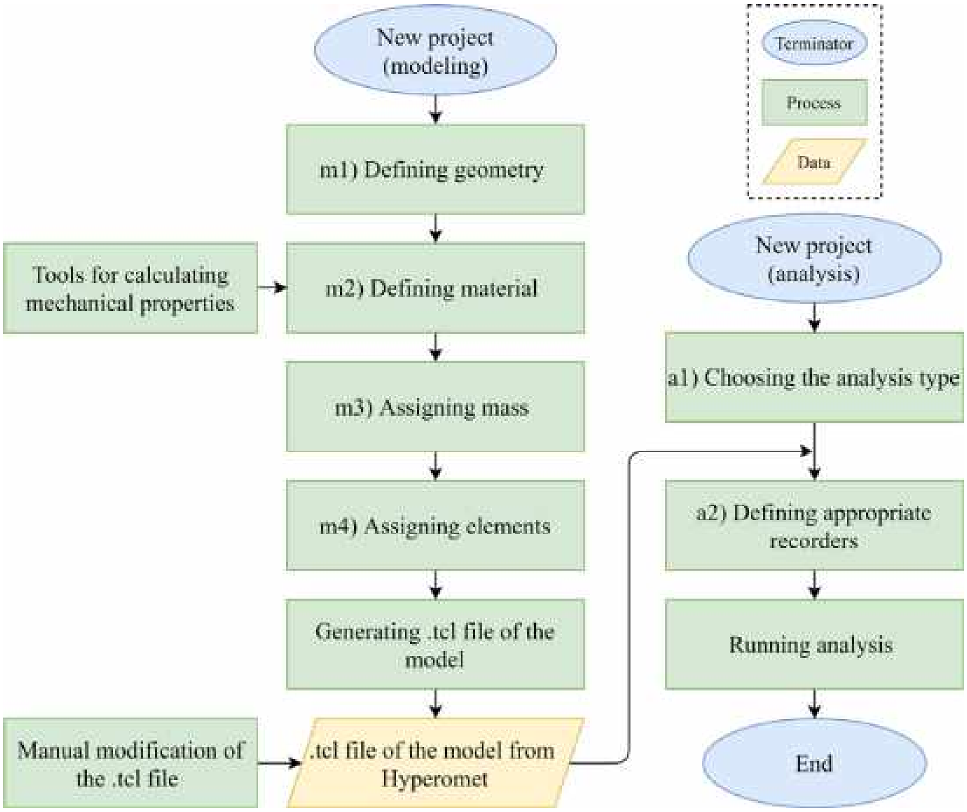

Fig. 1. Software architecture and the main six steps of the Hyperomet.

and then chooses the predefined material in step m2 and the corresponding direction. Afterward, the twoNodeLink elements will automatically be defined and assigned. However, for the DM-MVLEM approach, this procedure is different, and three sub-steps are presented. The zero-length elements in the middle of DM-MVLEM elements are assigned, and DM-MVLEM elements will be assigned to simulate the piers and spandrel elements. For assigning the zero-length elements to connect the two modified MVLEM elements, the nodes will be selected, and the suitable material will be assigned in three directions. Afterward, the DM-MVLEM elements are assigned by selecting the pier element, defining the fiber numbers, and assigning the corresponding material properties that were defined in step m2. For modeling piers, the user can define a specific location and assign the DM-MVLEM elements in the Hyperomet GUI which facilitate the modeling procedure and decrease human errors. As mentioned, the MVLEM elements cannot be used to model spandrel elements and cannot be placed in a horizontal direction. Therefore, the MVLEM elements should be modeled manually and modified to produce the DM_MVLEM element. In the case of modeling spandrel elements based on the DM-MVLEM and using the OpenSees framework by writing the scripts, the nodes should be defined manually for modeling the MVLEM elements, and rigid link elements should be encoded to connect the nodes. Furthermore, the twoNodeLink elements should be modeled to produce the modified MVLEM. However, the whole procedure for modeling the modified MVELM elements and connecting them with zero-length at the middle has been automated. The asymmetry of spandrel elements is taken into account. This procedure works by defining the number of truss elements for the upper and lower parts of the elements. Furthermore, the related material will be assigned to the truss and twoNodeLink elements. Then the model is ready to be generated. The produced .tcl format file should be checked and modified if needed.

The .tcl format models should be selected as input for the analysis sections, and relevant .tcl format subroutine files will be produced based on the user's input. The generated subroutine files will be automatically called inside each model file. Therefore, the selected analysis will be carried out by opening the .tcl file of the model. No input is needed for performing the modal analysis, and the first six natural periods of the structure will be concluded. For gravity analysis, the nodes and the gravity load should be defined. The load pattern is defined by determining the displacement values for pushover analysis, and suitable recorders can be selected to derive the pushover curve. Time history analysis can be done by mentioning the name of the seismic record file which must be available in the model folder and other details related to the seismic record characteristics, such as the number of data points in each record, time steps, and response spectrum time history. Note that the record will be multiplied by the gravity of earth (g) automatically in the subroutine file, and the scale factor defined by the user is another influential factor. Several features are provided to ease the IDA as the most demanding analysis type. The inputs for performing the IDA are divided into 1- limit state values 2- start and increment acceleration 3- number of analyses and records 4- damping properties 5- recorders 6- node-height pairs. In the case of URM, a very little value can be considered for the collapse slope ratio; it is considered 20% for steel frame structures based on [25]. For the damping section, the nodes with mass should be listed to be assigned with the mass-proportional term of the Rayleigh damping [26]. The stiffness-proportional term will be automatically applied to the model. The recorders are helping to evaluate the roof displacement and the base shear of the structure in every step, and in the last part, one node for each floor should be selected, and the corresponding height should be mentioned to let the GUI calculate the inter-story drift in each step and compare with the limit state.

The hunt & fill algorithm [22] is employed for performing the IDA to decrease the analysis duration. Three phases should be

```
if {($tetaMax > $tetaLimit) || ($slpRato < $slpRato_limit)}
#checking the collapse criteria
{
                set clpseFlag YES
                puts $clpseFlag
                set saClpse $sa
                set clpseRsln [expr ($saClpse-$saStble)/$saStble]
                if {$clpseRsln < 0.025} {set goFill YES}
                set sa [expr $saStble + ($saClpse-$saStble)/3.]
#Phase 2: increase step for Sa for bracketing collapse
            } else {
                if {$clpseFlag == NO } {set nLastStble $nn}
                set nPrevStep $nn
                set saStble $sa
                if {$clpseFlag == YES} {
                    set clpseRsln [expr ($saClpse-$saStble)/$saStble]
                    if {$clpseRsln < 0.025 } {set goFill YES}
                    set sa [expr $saStble + ($saClpse-$saStble)/3.] ;
# Phase 2: increase step for Sa for bracketing collapse
                } else { set sa [expr $sa +  $nn*0.05] } ;
#Phase 1: start increasing Sa to reach the collapse
            }
            if {$goFill == YES} {
                set sa [ expr ( $saArray($nLastStble) + $saArray([expr
$nLastStble-1]) )/2. ] ;
#Phase 3: filling gaps before collapse
                set nLastStble [expr $nLastStble-1]
                if {$nLastStble < 1} {set continue N0}
            }
            set nn [expr $nn +1]
```

Listing 1: Three main steps of the hunt & fill algorithm and the collapse criteria in the IDA subroutine file.

considered: 1- increasing the intensity to reach the collapse, 2- finding the accurate intensity that the structure reaches collapse (improving the capacity resolution) 3- going back and filling the gaps of the first step. The steps in the subroutine file are presented in the Listing 1 to clarify the code.

Note that the values assigned for each phase can be changed based on the model type. For instance, the bracket criterion (BC) for the sufficient resolution of the collapse point in step 2 is calculated based on:

$$BC = \frac{S_{a,i} - S_{a,j}}{S_{a,j}} \tag{1}$$

where $S_{a,i}$ and $S_{a,j}$ are the values $S_{(T,5\%)}$ of the current and previous step of the analysis, respectively. The default limit state value is 0.025, which can be changed manually.

Although adaptive time-step, adaptive convergence criteria and adaptive solution algorithms are the routine of every finite element software, these features are not available in the OpenSees framework. In this light various convergence tolerances are considered for different levels of the analysis. If the analysis is not converged, the algorithms are tried to decrease the tolerance step by step to reach the convergence. Furthermore, different types of solution algorithms available in OpenSees that efficiently analyze the model are provided in the subroutine files that are changed automatically until convergence is reached.

2.2. Software functionalities

The main sections of the software are modeling, analysis, and results and all the functionalities of the GUI are highlighted in Fig. 2. Note that the modeling section comprises assigning mass to the nodes, defining material, and assigning elements for the UM and DM-MVLEM.

In the final section, which is the result tab, the user can post-process the IDA results to derive the IDA curves. The $S_{(T,5\%)}$ values and the maximum inter-story drifts and other results for each step of IDA of a record will be recorded in the text format files. However, for developing the IDA curves the $S_{(T,5\%)}$ and the corresponding maximum inter-story should be selected and the $S_{(T,5\%)}$ values are required to be sorted from the smallest to the largest. These processes can be automatically performed on the IDA results to develop the IDA curves.

3. Illustrative examples

A full-scale URM wall was tested at the University of Pavia by applying prescribed displacement to the first and second floors with a ratio of 0.65. The details of the case study are presented in [27]. The assigned material properties are based on [27], while the modeling steps of the wall using DM-MVLEM are illustrated in Fig. 3. Pushover analysis was performed when the gravity loads were applied to the system. Fig. 4(a) depicts the pushover curve derived from the numerical modeling versus the backbone curve of the experimental test result. The results show a good match between numerical and experimental test results regarding roof displacement and base shear. Furthermore, IDA was carried out by applying 44 seismic records of FEMA using the Hyperomet GUI, and the IDA curves are plotted in Fig. 4(b) after post-processing the results. More illustrative examples and details are presented in: https://www.youtube.com/playlist?list=PLmph2U5TqH1x0zeqYDtsJb9f-QXzuxBg2

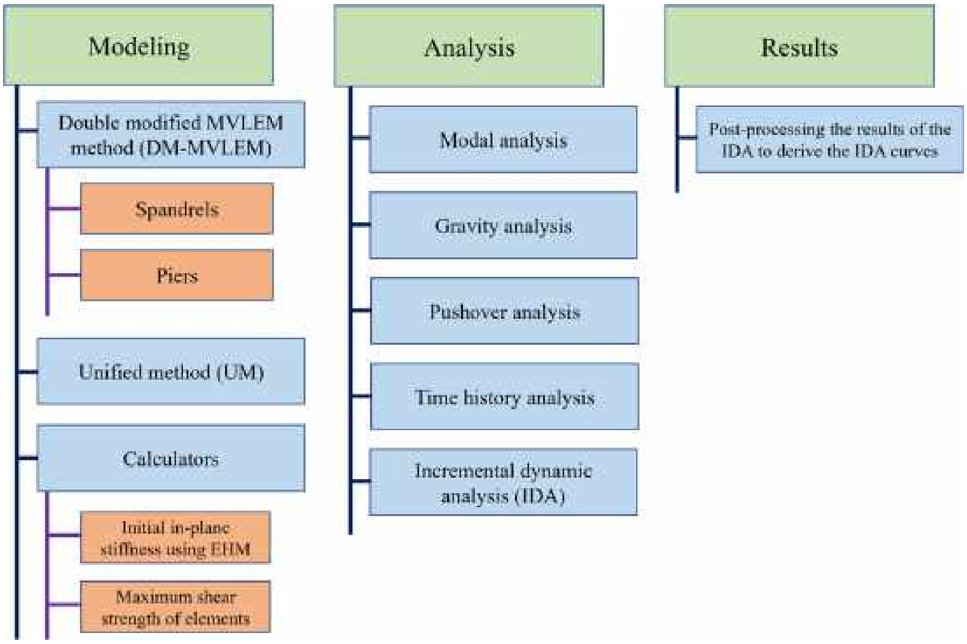

Fig. 2. Hyperomet functionalities that are divided into three main sections: modeling, analysis, and the results.

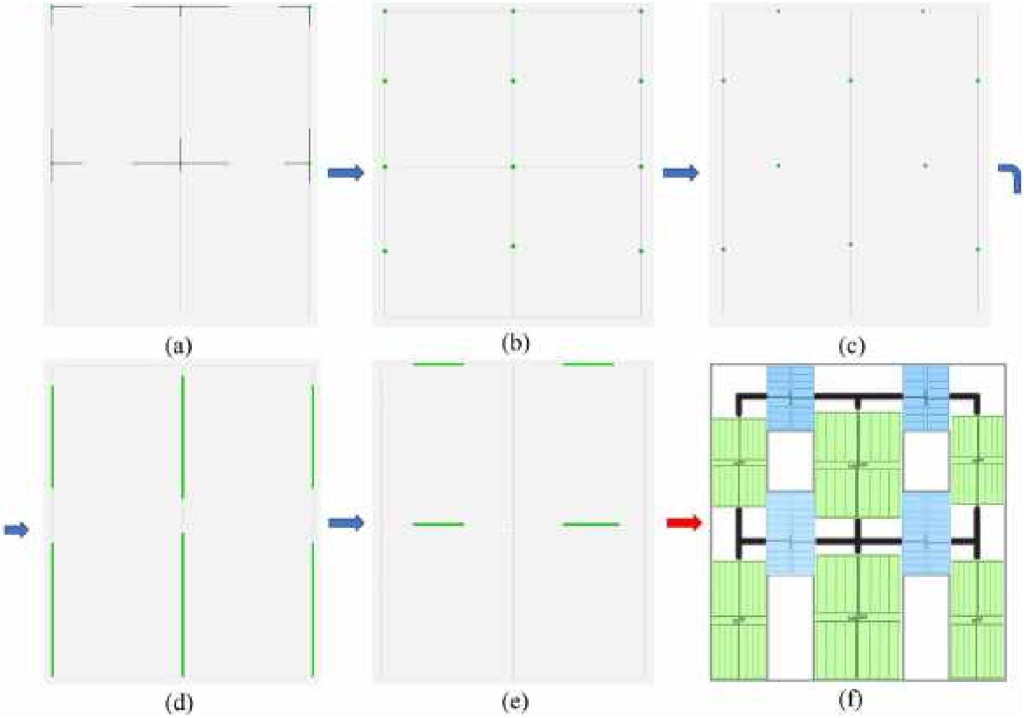

Fig. 3. The modeling procedure includes (a) defining the rigid elements (b) assigning mass (c) assigning zero-length elements, assigning DM-MVLEM elements to (d) pier and (e) spandrel elements, and (f) the final model of Pavia door wall using the DM-MVLEM.

4. Impact

Since no predefined macroelement is available in OpenSees library, developing DM-MVLEM and facilitating the modeling procedure is essential for researchers and analysts who use this powerful and versatile platform for nonlinear analysis purposes. On that account, the GUI can be utilized as a fast and efficient tool for performing time-consuming probabilistic analysis with a high number of variables, performing IDA, n-RT analysis, and seismic analysis at a large scale.

The MVLEM is a predefined macroelement available in the OpenSees library. The DM-MVLEM consists of two modified MVLEMs. DM-MVLEM cannot be modeled in OpenSees by connecting two modified MVLEMs horizontally, and modified MVLEMs should be modeled in detail using rigid beam–columns and truss elements. To tackle this limitation, the modeling procedure is eased for the spandrels by just defining the geometries and the properties of truss elements in the Hyperomet GUI.

Furthermore, various calculators for deriving the initial in-plane stiffness of masonry walls with openings using the EHM, maximum shear strength of masonry piers and spandrels etc.,

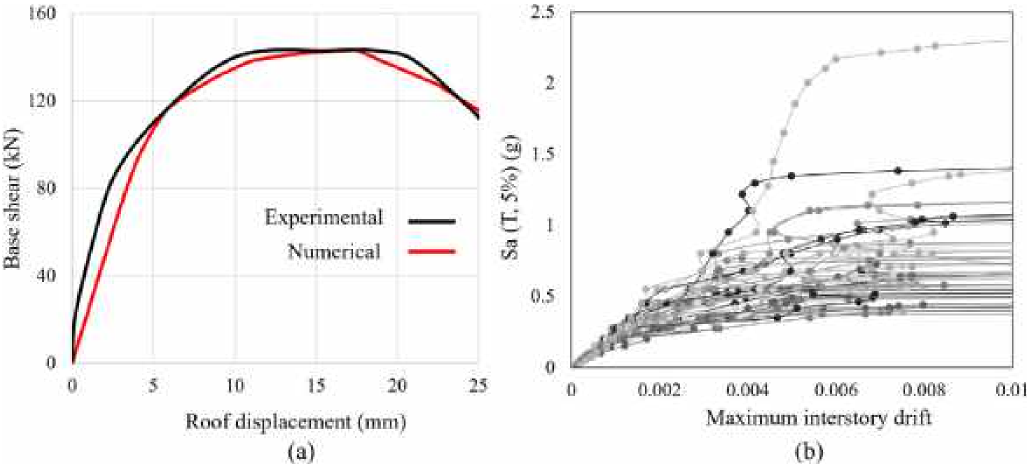

Fig. 4. (a) Pushover curve versus backbone curve of the test result, and (b) IDA curves of the Pavia door wall.

were provided to decrease uncertainty related to the modeling of the URM structures.

In Hyperomet, performing IDA is eased by defining the seismic records and appropriate recorders, and a post-processor is embedded to derive the IDA curves. Furthermore, IDA is automized since the seismic records are changed and applied, intensities are increased, solution algorithms are changed, and convergence tolerances are changed automatically.

Hyperomet can be used by the authorities to improve the resiliency of the historic areas hosting a large number of URM buildings to predict the economic impact of future earthquakes and to define risk mitigation plans. It will also facilitate future research studies on the vulnerability of URM buildings in OpenSees, including reliability analysis, stochastic analysis, soil–structure interaction analysis etc., that are demanding and time-consuming by employing existing commercial finite element software packages.

5. Conclusions

The main aim of Hyperomet was to allow OpenSees users to perform various types of nonlinear analysis for vulnerability assessment of URM buildings. The UM and DM-MVLEM approaches, and many types of analysis were provided in the GUI to facilitate and automize the assessment procedure. The main features include but are not limited to 1- providing calculators for defining the maximum shear strength of elements, 2- providing calculators to derive the initial in-plane stiffness of perforated URM walls using the EHM, 3- modeling spandrel elements using DM-MVLEM, and 4- automatization of IDA and using the hunt & fill algorithm. The users and authorities can benefit from the open-source Hyperomet GUI to perform computational demanding nonlinear analyses to improve the resiliency of historic areas comprising a large number of URM buildings.

Declaration of competing interest

The authors declare that they have no known competing financial interests or personal relationships that could have appeared to influence the work reported in this paper.

Data availability

The code can be downloaded via the share link in the article

Acknowledgments

This work is a part of the HYPERION project. HYPERION has received funding from the European Union's Framework Programme for Research and Innovation (Horizon 2020) under grant agreement No 821054. The contents of this publication are the sole responsibility of Oslo Metropolitan University (Work Package 5, Task 2) and do not necessarily reflect the opinion of the European Union.

References

[1] Shabani A, Kioumarsi M, Zucconi M. State of the art of simplified analytical methods for seismic vulnerability assessment of unreinforced masonry buildings. Eng Struct 2021;239:112280. http://dx.doi.org/10.1016/j.engstruct.2021.112280.
[2] Shabani A, Skamantzari M, Tapinaki S, Georgopoulos A, Plevris V, Kioumarsi M. 3D simulation models for developing digital twins of heritage structures: challenges and strategies. Procedia Struct Integr 2022;37:314–20. http://dx.doi.org/10.1016/j.prostr.2022.01.090.
[3] Kohrangi M, Bazzurro P, Vamvatsikos D. Seismic risk and loss estimation for the building stock in Isfahan: part II—hazard analysis and risk assessment. Bull Earthq Eng 2021;19:1739–63. http://dx.doi.org/10.1007/s10518-020-01037-1.
[4] Shabani A, Kioumarsi M. A novel macroelement for seismic analysis of unreinforced masonry buildings based on MVLEM in OpenSees. J Build Eng 2022;49:104019. http://dx.doi.org/10.1016/j.jobe.2022.104019.
[5] Mazzoni S, McKenna F, Scott MH, Fenves GL. OpenSees command language manual. Pac Earthq Eng Res (PEER) Center 2006;264:137–58.
[6] ASDEA Software Technology. Scientific ToolKit for OpenSees, STKO. Pescara, Italy. 2022.
[7] Psyrras NK, Sextos AG. Build-X: Expert system for seismic analysis and assessment of 3D buildings using OpenSees. Adv Eng Softw 2018;116:23–35. http://dx.doi.org/10.1016/j.advengsoft.2017.11.007.
[8] Yang T, Schellenberg A, Kohama E. OpenSees navigator. Berkeley, California, USA: Pacific Earthquake Engineering Research Center; 2017.
[9] Papanikolaou VK, Kartalis-Kaounis T, Protopapadakis E, Papadopoulos T. A new graphical user interface for OpenSees. In: 1st European conference on OpenSees. 2017, p. 73–6.
[10] Baltzopoulos G, Baraschino R, Iervolino I, Vamvatsikos D. Dynamic analysis of single-degree-of-freedom systems (DYANAS): A graphical user interface for OpenSees. Eng Struct 2018;177:395–408. http://dx.doi.org/10.1016/j.engstruct.2018.09.078.
[11] NextFEM. NextFEM designer, User manual version 1.9. Oderzo, Italy. 2022.
[12] Rahman MM, Nahar TT, Kim D. FeView: Finite element model (FEM) visualization and post-processing tool for OpenSees. SoftwareX 2021;15:100751. http://dx.doi.org/10.1016/j.softx.2021.100751.
[13] Chen J. OSLite-0.5.5. 2022, http://www.oslite.tech/.
[14] Elkady A. FM-2D - open-source platform for the 2-dimensional numerical modeling and seismic analysis of buildings. SoftwareX 2022;17:100927. http://dx.doi.org/10.1016/j.softx.2021.100927.
[15] D'Altri AM, Sarhosis V, Milani G, Rots J, Cattari S, Lagomarsino S, et al. Modeling strategies for the computational analysis of unreinforced masonry structures: review and classification. Arch Comput Methods Eng 2019;1–33. http://dx.doi.org/10.1007/s11831-019-09351-x.

[16] Shabani A, Feyzabadi M, Kioumarsi M. Model updating of a masonry tower based on operational modal analysis: The role of soil–structure interaction. Case Stud Constr Mater 2022;16:e00957. http://dx.doi.org/10.1016/j.cscm.2022.e00957.

[17] Xu H, Gentilini C, Yu Z, Wu H, Zhao S. A unified model for the seismic analysis of brick masonry structures. Constr Build Mater 2018;184:733–51. http://dx.doi.org/10.1016/j.conbuildmat.2018.06.208.

[18] Orakcal K, Wallace JW, Conte JP. Flexural modeling of reinforced concrete walls-model attributes. Struct J 2004;101:688–98.

[19] Orakcal K, Wallace JW. Flexural modeling of reinforced concrete walls-experimental verification. ACI Mater J 2006;103:196.

[20] Shabani A, Kioumarsi M. Pros and cons of various equivalent frame models for nonlinear analysis of URM buildings. In: 8th European congress on computational methods in applied sciences and engineering. ECCOMAS 2022, Oslo, Norway; 2022, p. 12.

[21] Vamvatsikos D, Cornell CA. Incremental dynamic analysis. Earthq Eng Struct Dyn 2002;31:491–514.

[22] Vamvatsikos D, Cornell CA. Applied incremental dynamic analysis. Earthq Spectra 2004;20:523–53.

[23] Shabani A, Plevris V, Kioumarsi M. A comparative study on the initial in-plane stiffness of masonry walls with openings. In: 17th world conference on earthquake engineering. 17WCEE, Sendai, Japan; 2021.

[24] Park J, Towashiraporn P, Craig JI, Goodno BJ. Seismic fragility analysis of low-rise unreinforced masonry structures. Eng Struct 2009;31:125–37. http://dx.doi.org/10.1016/j.engstruct.2008.07.021.

[25] Hamburger R, Hooper J, Sabol T, Shaw R, Reaveley L, Tide R. Recommended seismic design criteria for new steel moment-frame buildings (FEMA 350). Federal Emergency Management Agency; 2000.

[26] Charney FA. Unintended consequences of modeling damping in structures. J Struct Eng 2008;134:581–92.

[27] Magenes G, Kingsley GR, Calvi GM. Seismic testing of a full-scale, two-story masonry building: test procedure and measured experimental response. Consiglio nazionale delle ricerche, Gruppo nazionale per la Difesa dai terremoti; 1995.

Paper VI

Shabani, A., Zucconi, M. Kazemian, D. Kioumarsi, M.

Seismic fragility analysis of low-rise unreinforced masonry buildings subjected to near- and far-field ground motions

(2023) Results in Engineering, https://doi.org/10.1016/j.rineng.2023.101221.

Results in Engineering 18 (2023) 101221

Contents lists available at ScienceDirect

Results in Engineering

journal homepage: www.sciencedirect.com/journal/results-in-engineering

Seismic fragility analysis of low-rise unreinforced masonry buildings subjected to near- and far-field ground motions

Amirhosein Shabani [a,*], Maria Zucconi [b], Delaram Kazemian [c], Mahdi Kioumarsi [a]

[a] Department of Built Environment, Oslo Metropolitan University, Pilestredet 35, 0166, Oslo, Norway
[b] Department of Engineering, University Niccolò Cusano, Via Don Carlo Gnocchi, 3, 00166, Rome, Italy
[c] Department of Civil Engineering, Norwegian University of Science and Technology, Høgskoleringen 1, 7034, Trondheim, Norway

ARTICLE INFO

Keywords:
Low-rise buildings
Seismic fragility
Unreinforced masonry
Near-field ground motions
Pulse-like ground motions

ABSTRACT

Unreinforced masonry (URM) is considered one of the most cost-effective structural typologies for low-rise buildings in seismic regions. Near-field (NF) ground motions are sometimes characterized by high-velocity pulses that are typically more destructive than far-field (FF) seismic events. Therefore, a seismic fragility analysis of low-rise URM building typologies subjected to NF and FF seismic events was performed. Four URM walls were chosen, and nonlinear models of the walls were developed based on the double-modified, multiple vertical line element model (DM-MVLEM). The zero-moment coefficient was used to determine the effective uncracked section length of a pier. This parameter must be calculated for each pier of a perforated URM wall to derive the maximum shear strength of the piers used in a nonlinear model development process. A simplified analytical method was proposed to obtain the zero-moment coefficient factor of piers by performing linear static analysis on nine perforated walls and regression analyses of the results. Subsequently, nonlinear pushover analysis was performed to derive the capacity curves, and the damage limit states were defined for each model according to the Eurocode 8 standard. Subsequently, incremental dynamic analysis (IDA) was performed for each case study by applying FF and NF ground motions. Finally, fragility curves were developed based on the IDA results for each damage limit state. The susceptibilities of one- and two-story URM walls subjected to FF and NF seismic events were investigated by examining the derived fragility curves.

1. Introduction

Recent earthquakes revealed the high vulnerability of unreinforced masonry (URM) buildings to seismic loads [1–3]. URM buildings constitute one of the oldest structural systems built without considering modern seismic design criteria [4]. Furthermore, the brittle material type with low-tensile strength and large mass, and the lack of connection between the walls and ceilings are other reasons for the high susceptibility of this structural typology to earthquake events [5,6]. URM is considered a prevalent structural system in high-seismicity zones and historic areas [7]. Furthermore, URM is considered to be one of the most popular and cost-effective structural systems for constructing low-rise buildings [8–10]. Therefore, seismic vulnerability assessment and the proposal of a strengthening strategy are required to improve the resiliency of this structural typology and sustainable reconstruction of historic areas.

Various methodologies have been proposed for the nonlinear modeling of URM structures, which can be categorized into 1) the discrete element method, 2) the continuum homogenous method, and 3) the equivalent frame method (EFM) [11,12]. The discrete element method is usually utilized for the nonlinear modeling of URM structural elements owing to its high-computational effort [13]. The continuum homogeneous method is typically utilized to model URM structures with complex architectures, such as churches, towers, or bridges [14,15]. However, various EFMs have been developed and are usually used for the nonlinear modeling of URM residential buildings with the lowest computational effort compared with the other two methods [16–18].

EFMs facilitate the performance of highly computationally demanding nonlinear dynamic analysis of URM buildings to obtain fragility curves [19–21]. Simulation-based analytical fragility curves more accurately represent damage probabilities than curves derived using simplified analytical, empirical, or hybrid methodologies [4]. The

---

* Corresponding author.
E-mail addresses: Amirhose@oslomet.no (A. Shabani), maria.zucconi@unicusano.it (M. Zucconi), delaramk@ntnu.no (D. Kazemian), Mahdik@oslomet.no (M. Kioumarsi).

https://doi.org/10.1016/j.rineng.2023.101221
Received 12 March 2023; Received in revised form 31 May 2023; Accepted 4 June 2023

analytical fragility curves of URM buildings, which show the probability of exceeding a damage limit state for a structure subjected to an earthquake with a specific intensity measure (IM), can be obtained based on cloud analysis, multi stripe analysis, and incremental dynamic analysis (IDA) [8,22–25]. In these approaches, various seismic records with different intensities are applied to the model to evaluate the structural response [26]. IDA has the highest computational demand among the aforementioned methods; however, simplicity of implementation and no prior assumptions for the probabilistic distribution of seismic demand for the derivation of fragility functions are the two main advantages of this method [27,28].

The seismic events that were recorded and applied to a model for dynamic analysis were categorized into 1) far-field (FF), 2) pulse-like near-field, and 3) non-pulse-like near-field based on the site-to-source distance and presence of strong velocity pulses [29]. High-amplitude long-duration acceleration or velocity pulses occurring primarily in the fault-normal direction are the main characteristics of pulse-like near-field (NF) ground motions [30]. The main cause of pulses is the forward directivity effect, which typically occurs at sites in the direction of rupture propagation when the rupture velocity is close to the shear-wave velocity [29]. Different methodologies have been developed to distinguish pulse-like ground motions [31–33], and various studies have emphasized the higher level of damage that can be imposed on structures compared with other ground motion types [34–37]. In one of the few studies concerning the seismic vulnerability assessment of URM buildings subjected to FF and NF excitations, a three-dimensional (3D) one-story URM building was modeled, and it was concluded that the model was more susceptible to NF seismic events than FF ground motions [38]. Most studies concerning the effect of NF ground motions on the seismic behavior of URM buildings are limited to the pushover analysis of detailed numerical models and nonlinear time history analysis of the equivalent single-degree-of-freedom model of buildings [39, 40]. However, equivalent single-degree-of-freedom models do not accurately reflect the seismic behavior of URM walls compared with the aforementioned numerical modeling approaches [4]. Therefore, a comparative study of the effects of NF and FF ground motions on the seismic fragility of URM buildings is required to develop sufficiently accurate numerical models and perform nonlinear dynamic analyses.

In this study, the macroelement utilized for the nonlinear modeling of URM case studies is first introduced. Subsequently, a simplified analytical method is proposed to calculate the maximum lateral strength (V_m) of the URM piers of a perforated URM wall. The proposed simplified analytical method enhances the efficiency of the nonlinear modeling process. This study was dedicated to the seismic fragility analysis of low-rise URM buildings. Unlike previous studies, this study employs detailed nonlinear modeling with the double-modified, multiple vertical line element model (DM-MVLEM) to capture accurately the complex behavior of URM walls. Four low-rise URM-perforated walls were chosen as case studies, and nonlinear models were constructed. Pushover analyses were performed, and the damage limit states were calculated for each case study. Subsequently, IDA was performed by applying FF and NF excitations to the case studies. The selected NF ground motions were pulse-like excitations used to investigate the pulse effects on the seismic behavior of the buildings. Finally, the fragility curves of each case study subjected to three seismic events were produced to facilitate a comparison of the seismic responses of the case studies. By conducting IDA and developing fragility curves, this study aims to enhance the understanding of the seismic response and vulnerability of low-rise URM buildings, thus contributing to effective strengthening strategies.

2. Case studies and nonlinear modeling

2.1. Case studies

The selected case studies were limited to low-rise URM walls with a maximum of two stories. Four perforated URM walls were selected as representatives of different structural typologies. Case study A was a wall tested at the University of Pavia subjected to prescribed cyclic displacements on the first and second floors [41]. The wall was made of solid fired-clay brick, and the mortar was a mixture of hydraulic lime and sand [41]. Case study B involved a two-story URM wall with five openings. Case studies C and D involved one-story URM walls with three and four openings, respectively. The four case studies and their geometries are shown in Fig. 1. All walls have a thickness of 25 cm and are made of the same material as the Pavia door wall [41].

2.2. Development of nonlinear models

3D modeling is necessary to predict the actual seismic behavior of buildings owing to the unpredictability of the seismic loading direction. Moreover, the asymmetry of the rigidity and mass distributions of each component with respect to the loading direction could be accurately predicted by performing 3D analyses. However, for simplicity, two-dimensional (2D) models were developed in this study that focused on horizontal motion in a single plane. These models suit buildings with simple plan forms that lack mass or stiffness cross-coupling between orthogonal horizontal directions [8]. Despite this simplification, it is believed that essential in-plane structural behaviors can be adequately represented. The main objective of this study was to compare intensively the analytical fragility curves obtained computationally from IDA. Hence, a 2D modeling strategy that disregards the out-of-plane behavior of walls but accurately depicts the in-plane behavior of structural elements has been adopted [18].

The geometry of the piers and spandrels was determined based on the Dolce method [42], which is defined as the most reliable method for the equivalent frame idealization of perforated URM walls [43]. Based on this method, spandrels and piers are connected with rigid elements such that the length of the spandrels equals the length of the openings. The effective height of the piers is derived from the intersection between the vertical centroidal axis of each pier and the lines forming a 30° angle from the corners of the adjacent openings [42]. The DM-MVLEM was used to develop the nonlinear models of the case studies [18]. The DM-MVLEM is a macroelement for the nonlinear analysis of URM buildings composed of two modified MVLEM elements to simulate the flexural behavior and a nonlinear shear spring that connects the modified MVLEM elements to simulate the shear behavior of URM structural components [18,20,44]. The DM-MVLEM was verified by comparing the results of the tests to the numerical analysis of two piers, a spandrel, and a full-scale two-story URM wall subjected to cyclic loading [18]. To accelerate the modeling procedure and reduce human errors, Hyperomet was utilized for the nonlinear modeling of walls based on the DM-MVLEM [45]. Hyperomet is a graphical user interface for the OpenSees software framework [46] designed for the nonlinear modeling of URM walls [45]. Fig. 2 depicts all the models developed using the DM-MVLEM macroelement.

The stress–strain curve of the URM material is depicted in Fig. 3(a), with a diagonal tensile strength (f_{td}) of 0.21 MPa and shear strength of the masonry at zero compressive stress (f_{v0}) of 0.345 MPa based on [41]. The strain–stress curve was assigned to the fibers of the DM-MVLEM, and a nonlinear material with a trilinear backbone curve was assigned to the nonlinear shear springs in the middle of the DM-MVLEMs [18]. Fig. 3(b) shows the typical backbone curve of a nonlinear shear spring. The lateral strength parameters of the curve are proportional to V_m and the corresponding displacements are proportional to the initial in-plane shear stiffness and height of the elements, as described in Ref. [18].

V_m is considered as the minimum value of the maximum lateral strength owing to the shear sliding (V_S) and diagonal cracking (V_D) failure modes calculated using Equations (1) and (2) [18].

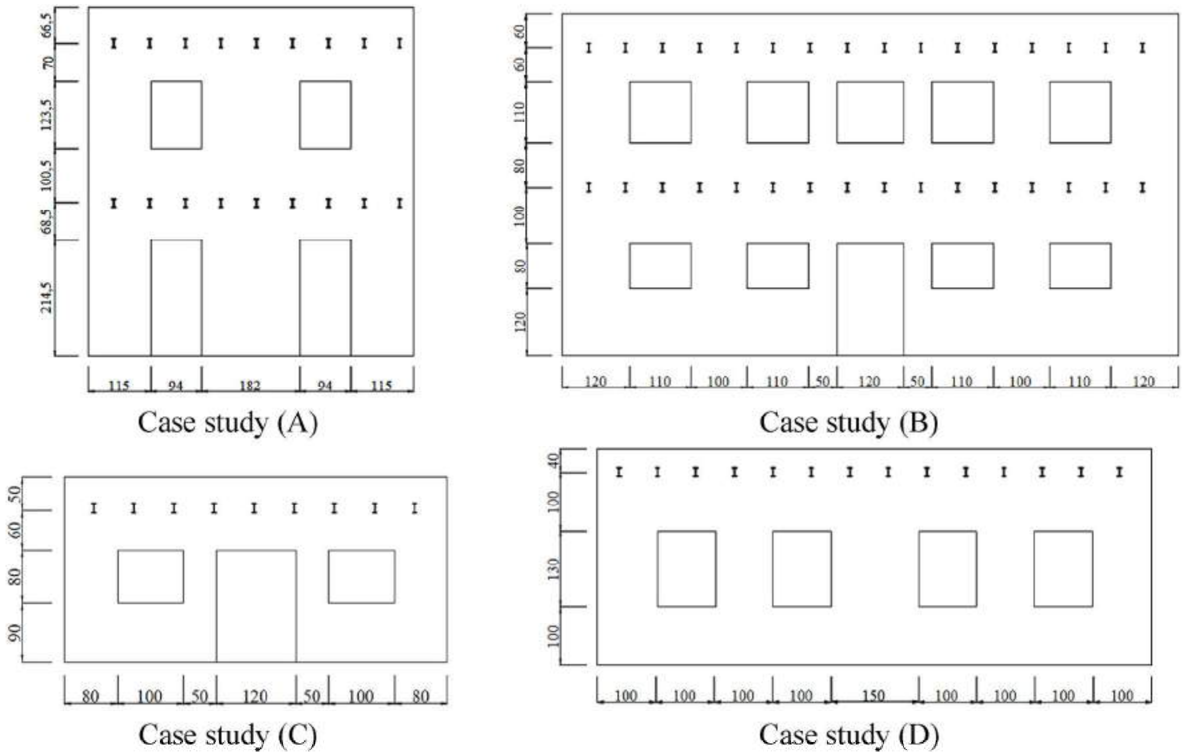

Case study (A)
Case study (B)
Case study (C)
Case study (D)

Fig. 1. Four low-rise URM walls as case studies.

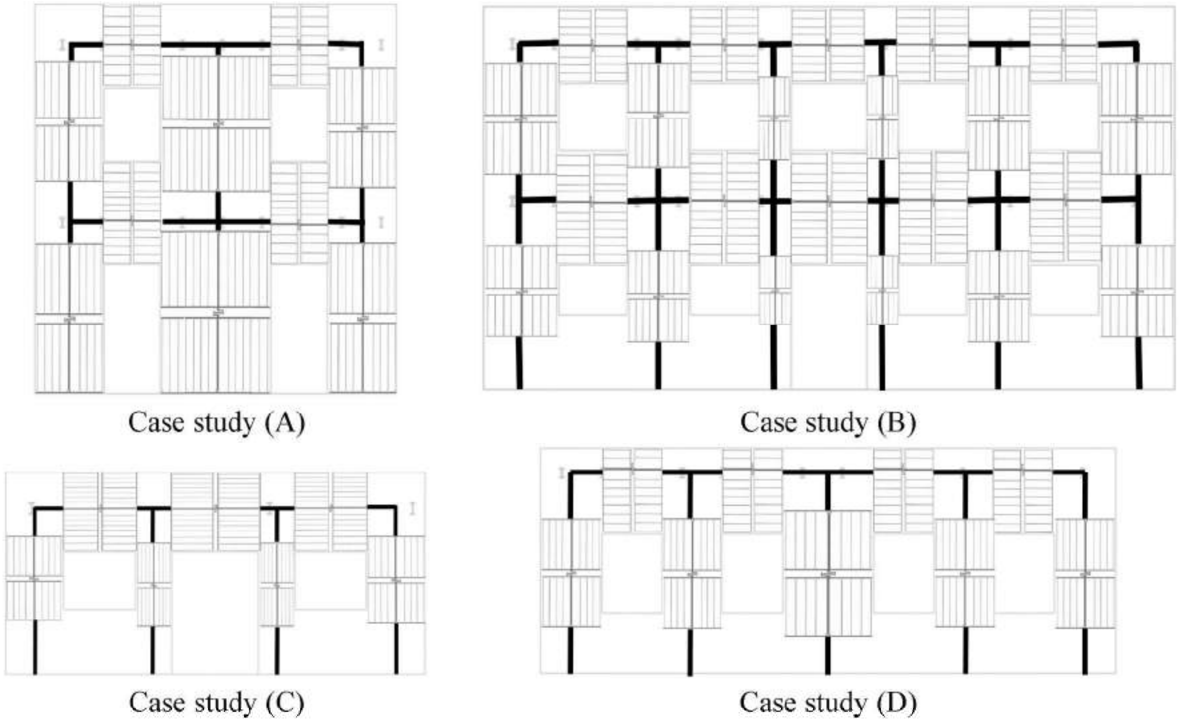

Case study (A)
Case study (B)
Case study (C)
Case study (D)

Fig. 2. Developed nonlinear models of the four case studies using DM-MVLEM macroelement.

$$V_S = \left(\frac{f_{td} + 0.4\sigma_0}{1 + \frac{3\alpha_0 h f_{t0}}{\sigma_0 b}} \right) bt \quad (1)$$

$$V_D = \frac{f_{td} bt}{\zeta} \sqrt{1 + \frac{\sigma_0}{f_{td}}} \quad (2)$$

where b is the width, h is the height, and t is the thickness of a pier, is the axial compression stress, and ζ is the shear stress distribution coefficient at the center of a pier considering the aspect ratio calculated based on

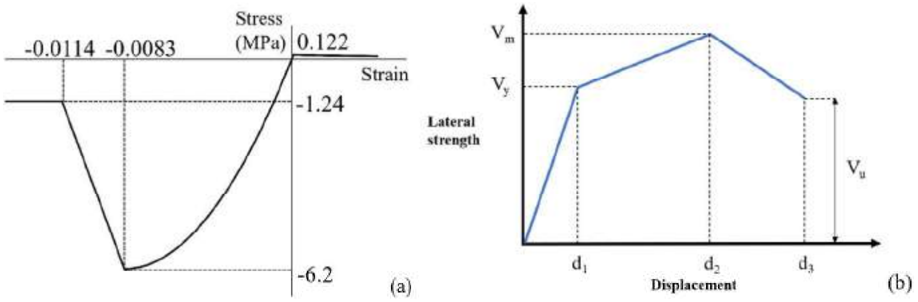

Fig. 3. (a) Stress–strain curve of URM and (b) trilinear backbone curve of the nonlinear shear spring.

the equations in Table 1:

Moreover, parameter α_0 is the zero-moment coefficient relevant to the moment distribution along the height of the pier, which is elaborated on in the next section.

2.3. Zero-moment coefficient

The zero-moment coefficient was calculated to determine the effective uncracked section length of a pier, neglecting the tensile strength of the bed joints and assuming a simplified distribution of compression stresses [47]. The parameter was utilized to calculate the V_S of the piers, as shown in Equation (1). The parameter α_0 is calculated as the maximum value of the fraction of the height of a pier (H_0) with a positive or negative moment value as depicted in Fig. 4 to the total height of a pier (h) [19]. For ideal typical test layouts, the α_0 is assumed to be equal to one in a cantilever scheme and 0.5 in a fixed-fixed boundary condition. No further description of this value is provided in Eurocode 8 Part 3 [48], NTC [49], FEMA 356 [50], or FEMA 273 [51]. This parameter depends on the geometry and boundary conditions of piers. Therefore, predefined ideal values cannot be assigned to α_0 of piers of a perforated URM wall due to the flexibility of spandrels on two ends of the pier.

One strategy is to apply a mode proportional load pattern based on the fundamental mode shape to the elastic model of the wall and define the moment distribution diagram of each pier and calculate α_0 [19]. However, different studies have indicated the accuracy of a pushover analysis of URM buildings with the mass-proportional load pattern compared with the mode-proportional load pattern by comparing the results with the IDA curves [18,52,53]. Therefore, in this study, the parameter α_0 was calculated by applying a mass-proportional lateral loading to the elastic model of the walls.

To investigate the variation in this parameter and define the equations that facilitate the process of attaining this parameter for the analysis of low-rise URM buildings, nine perforated URM walls were modeled in SAP 2000, considering the elastic behavior of piers and spandrels. The five added URM walls are illustrated in Fig. 5.

Mass-proportional lateral loads were applied to the case studies and the α_0 values were determined based on the moment diagram. The results show that the α_0 values of the piers of the two sides of the walls of the first story are higher than the values of the internal piers. Furthermore, if a load was applied in the right direction, the α_0 value of the leftmost pier was higher than that of the external pier. However, because the seismic events applied cyclic loads to the structures, the highest α_0 value was considered for both external piers using a more conservative approach.

Table 1
Equations used to derive ζ (the shear stress distribution coefficient at the center of a pier considering the aspect ratio).

Aspect ratio	Shear stress distribution coefficient
$\frac{h}{b} \leq 1 \rightarrow$	$\zeta = 1$
$1 < \frac{h}{b} < 1.5 \rightarrow$	$\zeta = \frac{h}{b}$
$\frac{h}{b} \geq 1.5 \rightarrow$	$\zeta = 1.5$

To determine an equation to derive the α_0 values, the piers are subcategorized into three groups: 1) internal piers of the first story, 2) external piers of the first story, and 3) piers of the second story. The differences between the α_0 values of the interior and exterior piers of the second story were not as high as those of the first story; therefore, no distinction was considered. The piers of the one-story walls were assigned to groups 1 and 2. Moreover, $\frac{b^3}{h}$ was considered a parameter proportional to the flexural stiffness of each pier, depending on the geometry of each pier utilized for the prediction of the parameter α_0. Fig. 6 shows the diagrams of the α_0 versus $\frac{b^3}{h}$ for all three subcategories of all piers in the nine case studies. The log-normal trendlines were utilized to determine the prediction equations. The range of the calculated α_0 values, equations that can be used for the prediction of the parameter α_0 and the corresponding coefficient of determination (R^2) values are listed in Table 2. The range of the parameter shows that assuming fixed-fixed boundary conditions for the piers of the first story of a two-story perforated wall which corresponds to 0.5 for the parameter α_0 will overestimate the V_m of the piers since the calculated α_0 are more than 0.5, as presented in Table 2. Furthermore, assuming cantilever piers on the second floor of a two-story wall or piers of a one-story wall and assigning the value of one to the parameter α_0 will underestimate the V_m values of the piers.

Finally, to investigate the accuracy of the proposed equations, the V_m values of all piers of the nine walls were calculated using the α_0 values derived from the equations in Table 2 and the linear static analysis of the walls. A scatter plot of the results of the two approaches is shown in Fig. 7. The maximum R^2 value in Table 2, which shows the correlation of the calculated α_0 values based on the equations and numerical analysis is 75.78%. However, the R^2 value, which shows the correlation of the calculated V_m values is 99.95%, and the negligible deviation of the equality line from the best-fitted linear trendline indicates the robustness of the proposed simplified analytical method. Despite the relatively high dispersion between the predicted and exact α_0 values, the predicted and exact V_m values were similar. It is worth mentioning that the equations can only be used to define the α_0 parameter of the piers of the low-rise URM wall (maximum two-story) with a regular opening configuration; in other cases, static analysis is recommended (by applying the mass-proportional lateral load) instead of using fixed values from the codes.

3. Pushover analysis

Pushover analysis was performed by applying the mass-proportional load pattern, and the pushover curves are illustrated in Fig. 8. Furthermore, for the Pavia door wall, a pushover curve derived by applying a load pattern similar to that in the test and the backbone of the test result were presented to demonstrate the accuracy of the DM-MVLEM method, as shown in Fig. 8(a). Although a difference can be detected between the

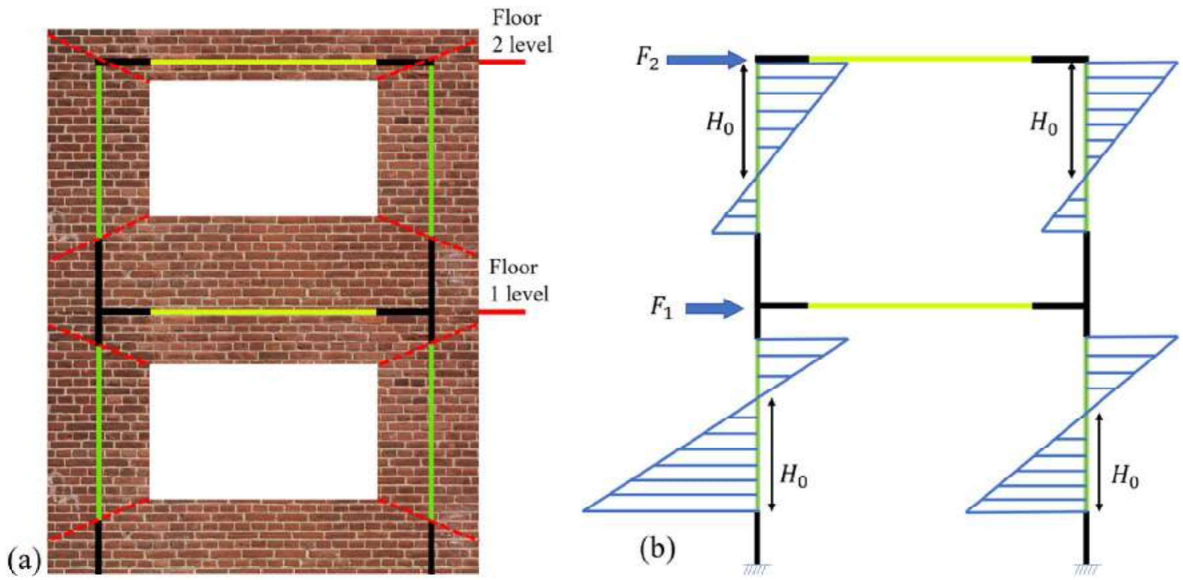

Fig. 4. (a) A perforated two-story URM wall and (b) the moment diagram of the wall subjected to lateral loadings and definition of H_0.

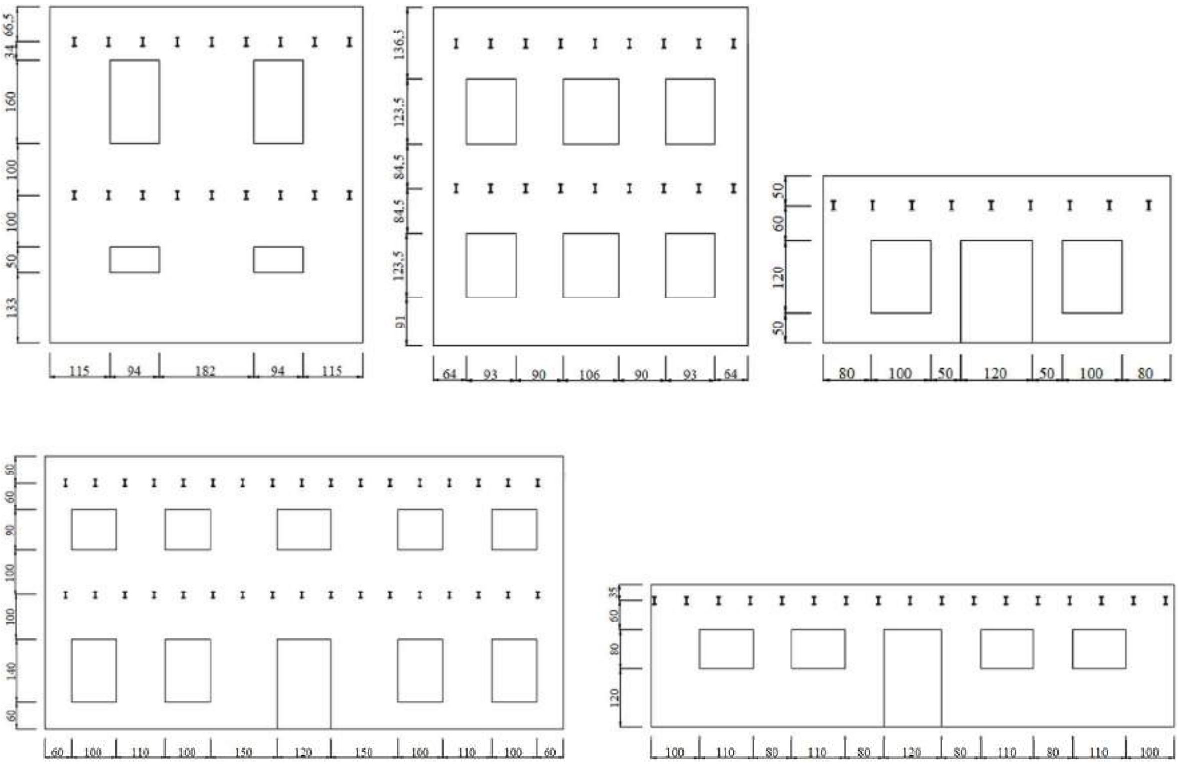

Fig. 5. Added five case studies chosen for the evaluation of the zero-moment coefficient factor.

initial stiffness of the test and the numerical model curves, the maximum base shear is predicted with good accuracy, and the nonlinear behavior, evaluated in terms of ductility, was estimated accurately. Note that the vertical applied load of the Pavia door wall was based on the test, but for other case studies, a uniform load (set at 20 $\frac{kN}{m}$) was applied to each floor, which is relatively lower than the vertical load applied to the Pavia door wall [41]. It can be inferred from Fig. 8 that the inclusion of piers or extension of the wall length, as seen in the two-story walls, leads to an increase in the maximum base shear for the one-story walls. The combined flexural and shear failure mode is the dominant failure mode of the piers in the case study (A), which can be concluded from the pushover curve analysis and is consistent with the test results. However, the shear failure mode is more dominant in other case studies. Therefore, the ductility of the case study (A) is greater than that of the other case studies.

3.1. *Definition of limit states*

Instead of considering predefined damage limit state values, a more accurate structure-specific approach based on the pushover curve was used to derive the inter-story drifts corresponding to the limit states [54]. Qualitative and quantitative descriptions of the three limit states

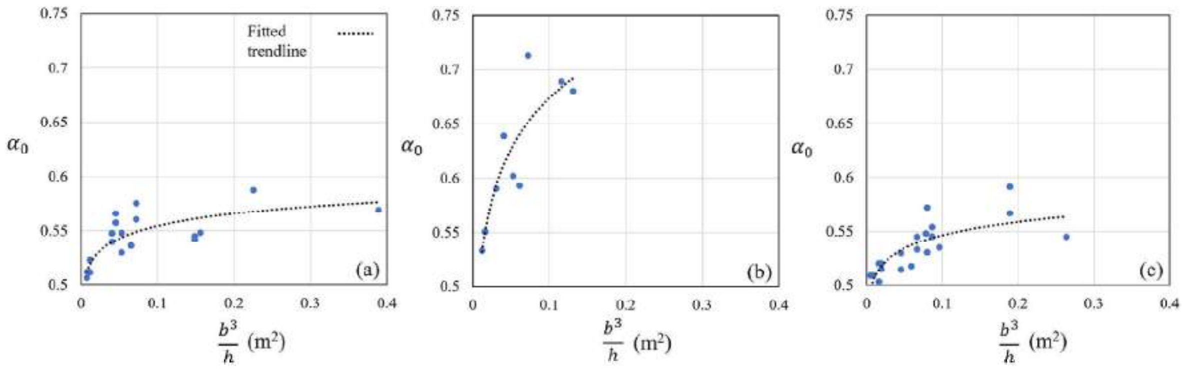

Fig. 6. Regression analysis results and trendlines of the data derived from analysis of (a) internal piers of the first story, (b) external piers of the first story, and (c) piers of the second story.

Table 2
Range of the calculated α_0 values, derived equations, and R^2 values for the piers in different positions.

Pier position	Range of α_0	Equation	R^2 (%)
Internal piers of the first story	$0.51 \le \alpha_0 \le 0.58$	$\alpha_0 = 0.0163 \ln\left(\frac{b^3}{h}\right) + 0.5919$	65.45
External piers of the first story	$0.53 \le \alpha_0 \le 0.71$	$\alpha_0 = 0.0677 \ln\left(\frac{b^3}{h}\right) + 0.8299$	75.78
Piers of the second story	$0.5 \le \alpha_0 \le 0.59$	$\alpha_0 = 0.0169 \ln\left(\frac{b^3}{h}\right) + 0.5834$	62.62

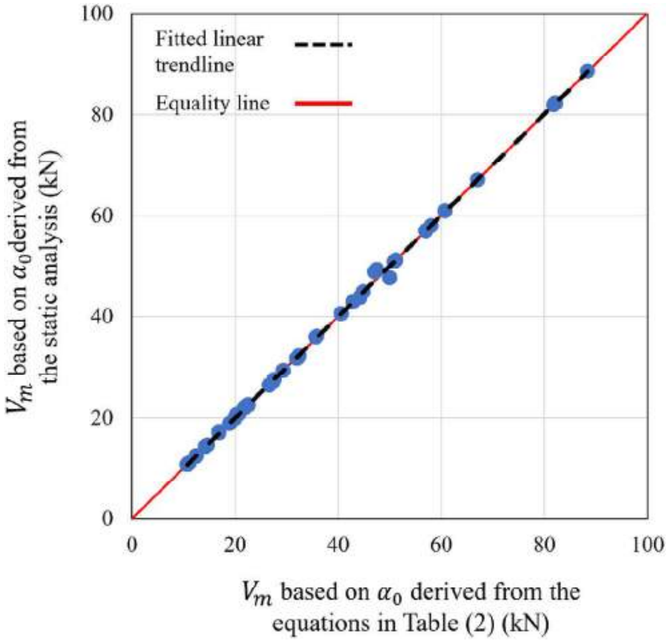

Fig. 7. Scatter plot and equality line for the results of the V_m based on α_0 derived from the static analysis and proposed equations.

selected based on Eurocode 8 Part 3 [48] are presented in Table 3.

The yielding points of the pushover curves were calculated after bilinear-elastic–perfectly plastic idealization of the pushover curves performed following the procedure recommended by Eurocode 8 part 1 [55] and using the SPO2FRAG user interface [56]. The yielding displacement was calculated by defining the area-balancing criterion between the area under the capacity curve and the idealized curve, and the corresponding maximum inter-story drift was considered as the damage limitation (DL) limit-state definition.

The ultimate displacement that corresponds to the near collapse (NC) limit state was calculated when the pushover analysis stopped converging, or the corresponding displacement was 80% of the peak base shear [56]. Furthermore, the significant damage (SD) limit state was estimated as the maximum inter-story drift corresponding to 75% of the ultimate displacement value, which approximately corresponds to the displacement of the maximum base shear [57].

The limit state values are influenced by the dominant failure modes of the piers, which are dependent on the opening configurations that affect the geometry of the piers and spandrels and the applied vertical loads, as highlighted in Refs. [57,58]. The differences between the calculated inter-story drifts corresponding to each limit state of the walls are shown in Fig. 9. Therefore, structure-specific methods for deriving the limit states of URM buildings are recommended instead of using predefined values from the literature, although for cases B, C, and D, the obtained values are similar. These results highlight the need to investigate this issue further to identify fixed values of the damage states according to specific structural features.

4. Incremental dynamic analysis

The Rayleigh damping model was implemented with an equivalent damping ratio of 2% at the first and second modal frequencies of each model [18,59,60]. Considering the convergence issues and prolonged analysis associated with using the current stiffness matrix, it may be advisable to replace it with a committed stiffness matrix [61]. This alternative results in significant computational time savings. Therefore, Rayleigh damping was incorporated based on the mass and last committed stiffness matrix to perform IDA.

IDA was performed by applying 22 FF and 14 NF pairs of seismic records from FEMA P695 [62]. A boundary of 10 km was considered to categorize the records into FF and NF [62]. The average of the Campbell and Joyner–Boore fault distances was used as the source-to-site distance. NF records were selected based on the three criteria mentioned in Ref. [31]. Wavelet analysis was used to extract the largest velocity pulse from a given ground motion. The presence of a pulse that occurs early in the time history is satisfied by calculating an indicator and checking the

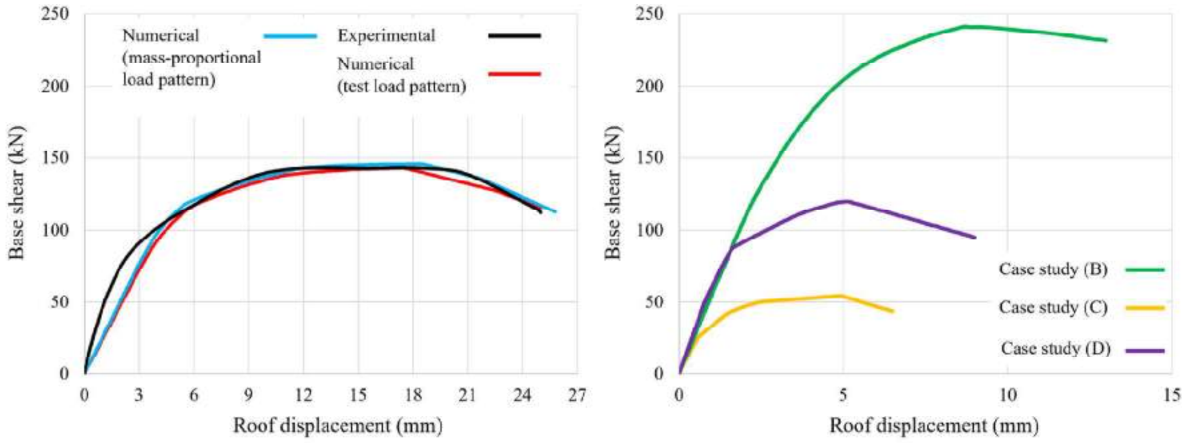

(a)

(b)

Fig. 8. Pushover curves of (a) case study (A) (Pavia door wall) with the test results, and (b) other case studies.

Table 3
Quantitative and qualitative descriptions of defined three performance levels [48].

Description type	Performance levels		
	Damage limitation	Significant damage	Near collapse
Qualitative description	Building is considered as slightly damaged. Sustain minimal or no damage to their structural elements and only minor damage to their nonstructural components	Building is considered as significantly damaged—extensive damage to structural and non-structural components	Building is considered as heavily damaged. Experience a significant hazard to life safety resulting from the failure of non-structural components
Quantitative description	Yielding point of the idealized bilinear capacity curve	75% of the ultimate top displacement capacity	Maximum displacement corresponds to 80% of the peak base shear

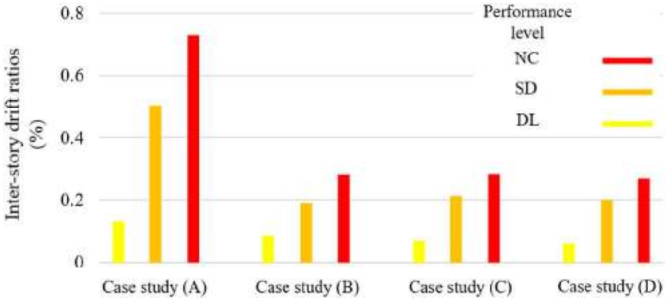

Fig. 9. Determined limit states for the case studies from the pushover analysis.

pulse occurrence time [31]. Another criterion is that the ground motion should have a PGV greater than 30 $cm/_{s}$. The occurrence of an early pulse in the ground motion was independent of the scaling process of the IDA. However, a PGV greater than 30 $cm/_{s}$ may not be satisfied for ground motions scaled to intensities lower than the original ground motion. Therefore, the PGV criterion was neglected in this study because of the downscaling process of the IDA. A summary of the ground motions selected from FEMA P695 [62] and their characteristics, including the record sequence numbers (RSN) in the PEER database [63] and the maximum peak ground acceleration (PGA) of the two components of each earthquake, are presented in Table 4. The FF and NF ground motions' spectra are shown in Fig. 10.

An IDA curve is a diagram of the ground motion IM against an engineering demand parameter (EDP) [28,65]. In this study, the IM is the spectral acceleration corresponding to the first mode of the structure considering 5% of damping (Sa (T_1, 5%)), and EDP is the maximum inter-story drift. Note that the fundamental period of the two-story walls (case studies (A) and (B)) was 0.21 s. The fundamental periods of one-story walls were 0.12 s and 0.13 s for case studies (C) and (D), respectively. The IDA curves for the case studies are shown in Fig. 11.

5. Seismic fragility analysis

A log-normal cumulative distribution function was used to define the fragility function based on Equation (3).

$$P[C|IM = im] = \Phi\left[\frac{ln(im) - \eta}{\beta}\right] \tag{3}$$

where $P[C|IM = im]$ is the probability that a ground motion with $IM = im$ causes the structure to collapse. $\Phi()$ is the standard normal cumulative distribution function, ln (Z) is the natural logarithm function, η and β are the mean and standard deviation of the ln*(im)* values, respectively [66,67].

The fragility curves were produced based on the results from the IDA, considering together all 72 time-history analyses. The analyses outcomes related to the FF and those related to the NF seismic events for all three mentioned limit states are presented, as shown in Fig. 12. Unlike the fragility curves for the DL limit state, the fragility curves for the NC and SD limit states are close to each other. This is in part due to the brittle behavior of URM material that causes a lower difference between the seismic demand when it is significantly or heavily damaged, especially for earthquakes characterized by a medium–high magnitude (Magnitude = 6.5–7.5 M), as in the cases if the selected ones (see Table 4). It can be concluded that case study (B) is the most vulnerable case study, with the lowest IM corresponding to a 50% probability of reaching a limit state (median IM), whereas case study (D) yielded the opposite results.

The maximum difference between the median IMs of FF and NF ground motions is 6.2%. This corresponds to the case study (A), considering the Sa (T_1, 5%) as the IM. Therefore, it can be inferred that the seismic fragility analysis of low-rise URM buildings by applying FF

Table 4
Summary of earthquake events and recording station data for the FF and NF record sets [64].

Earthquake	Magnitude (M)	Year	FF ground motions			NF ground motions		
			Station	RSN	PGA$_{max}$	Station	RSN	PGA$_{max}$
Northridge	6.7	1994	Beverly Hills-Mulhol	953	0.52	Rinaldi Receiving Sta	1063	0.87
Northridge	6.7	1994	Canyon Country	960	0.48	Sylmar - Olive View	1086	0.73
Duzce, Turkey	7.1	1999	Bolu	1602	0.82	Duzce	1605	0.52
Hector Mine	7.1	1999	Hector	1787	0.34	–	–	
Imperial Valley	6.5	1979	Delta	169	0.35	El Centro Array #6	181	0.44
Imperial Valley	6.5	1979	El Centro Array #11	174	0.38	El Centro Array #7	182	0.46
Kobe, Japan	6.9	1995	Nishi-Akashi	1111	0.51	–	–	
Kobe, Japan	6.9	1995	Shin-Osaka	1116	0.24	–	–	
Kocaeli, Turkey	7.5	1999	Duzce	1158	0.36	Izmit	1165	0.22
Kocaeli, Turkey	7.5	1999	Arcelik	1148	0.22	–	–	
Landers	7.3	1992	Yermo Fire Station	900	0.24	Lucerne	879	0.79
Landers	7.3	1992	Coolwater	848	0.42	–	–	
Loma Prieta	6.9	1989	Capitola	752	0.53	Saratoga–Aloha	802	0.38
Loma Prieta	6.9	1989	Gilroy Array #3	767	0.56	–	–	
Manjil, Iran	7.4	1990	Abbar	1633	0.51	–	–	
Superstition Hills	6.5	1987	El Centro Imp. Co.	721	0.36	–	–	
Superstition Hills	6.5	1987	Poe Road (temp)	725	0.45	–	–	
Cape Mendocino	7	1992	Rio Dell Overpass	829	0.55	Petrolia	828	0.63
Chi-Chi, Taiwan	7.6	1999	CHY101	1244	0.44	TCU065	1503	0.82
Chi-Chi, Taiwan	7.6	1999	TCU045	1485	0.51	TCU102	1529	0.29
San Fernando	6.6	1971	LA - Hollywood Stor	68	0.21	–	–	
Friuli, Italy	6.5	1976	Tolmezzo	125	0.35	–	–	
Irpinia, Italy-01	6.9	1980	–	–		Sturno	292	0.31
Superstition Hills-02	6.5	1987	–	–		Parachute Test Site	723	0.42
Erzican, Turkey	6.7	1992	–	–		Erzincan	821	0.49

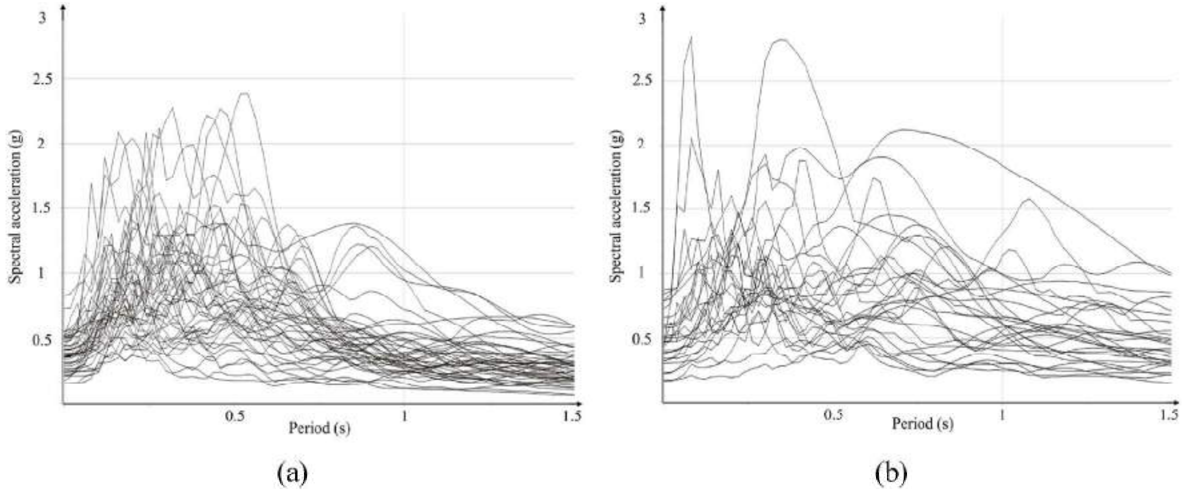

Fig. 10. (a) FF and (b) and NF ground motions' spectra.

and ignoring NF ground motions was sufficiently accurate for the selected case studies subject to strong ground motions. However, further investigations are required for seismic events characterized by medium intensities (Magnitude = 5.5–6.5 M).

Furthermore, the results showed that the median IMs of the NF ground motions applied to the two-story walls are lower than those of the FF seismic events. This difference is negligible in the case study (B). Nevertheless, for one-story buildings, the obtained results are the opposite. In one-story walls, the differences between the fragility curves of the FF are indistinguishable from those of the NF ground motions. It can be concluded that for two-story walls, the NF ground motions are more damaging than those for the FF motions; however, for one-story walls, the FF ground motions are more destructive. This difference shows that for the two-story walls with a fundamental period of 0.21 s, the NF records can impose more damages in terms of inter-story drifts. However, for one-story walls with a fundamental period of around 0.12 s, the FF seismic events are more damaging, which is consistent with the results of nonlinear analysis of stiff and low-period structures, such as masonry mosques [68], masonry bridges [69,70], and nuclear structures [71]. The NF ground motions caused more damage to the models with higher fundamental period values, which can be observed in the two-story walls.

A general rule that can exhibit the vulnerability of low-rise URM buildings cannot be determined because the seismic demand depends on the dynamic characteristics and failure modes of the structural elements. The same results were derived from a similar study on the seismic damage assessment of low-rise moderate reinforced concrete frames subjected to NF and FF ground motions [72]. Furthermore, it is mentioned that the derived fragility curves from both groups of ground motions are close to each other [72]. Applying NF ground motions is not required for the seismic fragility analysis of one-story URM buildings subjected to medium–high seismic events. Nonetheless, applying NF ground motions for the seismic fragility analysis of the two-story URM building mode is suggested for accurate analysis.

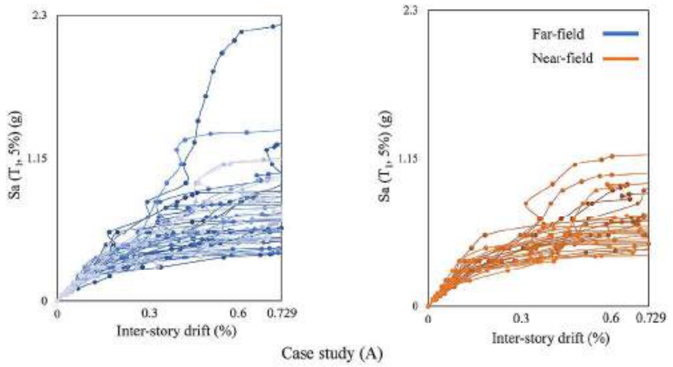

Case study (A)

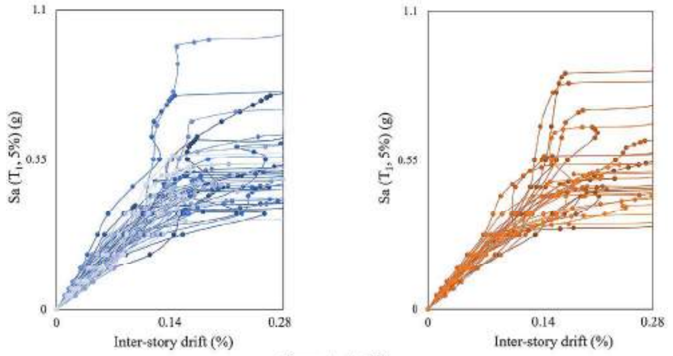

Case study (B)

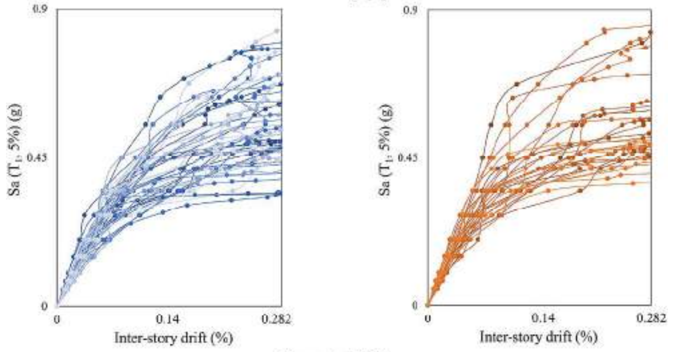

Case study (C)

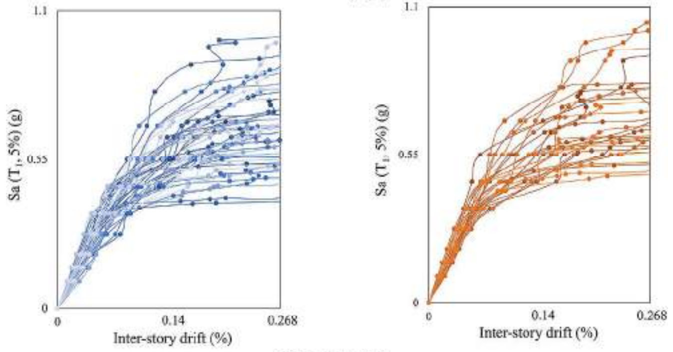

Case study (D)

Fig. 11. IDA curves of the case studies subjected to FF and NF ground motions.

6. Conclusion

Because of the widespread use of low-rise (URM) buildings in high-seismic zones, this study aimed to evaluate the vulnerability in terms of the fragility curves of this structural system subjected to far-field (FF) and near-field (NF) ground motions. Four low-rise perforated URM walls were chosen, and nonlinear models were developed based on the double-modified multiple vertical line element model (DM-MVLEM). The maximum lateral strength (V_m) is an effective parameter on the trilinear backbone curve of the nonlinear shear spring of the DM-MVLEM macroelement, which is calculated based on the minimum value of the maximum lateral strength due to the shear sliding (V_S) and diagonal cracking (V_D) failure modes. Moreover, for the calculation of the V_S, the zero-moment coefficient (α_0) was required to be determined. The value of α_0 can be defined based on the moment diagram of each pier by applying lateral loads to a wall and performing linear static analysis. The main findings of this study can be synthesized as follows:

- A set of three equations was presented by performing regression analysis on the results of the linear static analysis of the nine walls. Comparison of the equality line and linear fitted trendline of the results of the V_m based on α_0 derived from the static analysis and proposed equations show the accuracy of the proposed simplified analytical method. Therefore, parameter α_0 can be derived based on the proposed equations instead of developing the linear equivalent frame model of the wall and performing static analysis. Furthermore, the results showed that using the α_0 values proposed for piers with ideal fixed or fixed-free boundary conditions was not sufficiently accurate for piers of a perforated wall with flexible boundary conditions owing to the presence of spandrels. Note that the proposed equations can only be used to define the parameter α_0 of the piers of a low-rise URM wall (maximum two-story) with regular opening configurations.
- A nonlinear pushover analysis was performed, and structure-specific damage limit states were calculated based on the pushover curves. The results showed that using predefined fixed inter-story drift ratios for the limit states of URM walls was not sufficiently robust. These differences were due to the different displacement capacities of the piers with shear or flexural failure modes.
- IDA was performed by applying 44 FF and 28 NF ground motions to the models, and the fragility curves for the three performance levels were obtained for each case study. The fragility curves for the NC and SD limit states were relatively close to each other, unlike the fragility curve for the DL limit state. The fragility curves revealed that the difference between the seismic demands of the buildings subjected to FF and NF ground motions was not significant for the low-rise URM buildings analyzed in this study. The maximum difference between the median IMs of FF and NF ground motions required to reach a limit state was 6.2%. This was achieved in case study (A), considering the Sa (T_1, 5%) as the IM. This behavior can be attributed to the brittle nature of the URM material, which results in a reduced disparity in seismic demand when the material is significantly or heavily damaged, especially for buildings subject to strong ground motions, such as those considered in this study, characterized by a magnitude in the range of 6.5–7.5 M.
- Thus, the seismic fragility analysis of low-rise URM buildings following the application of FF ground motions and the ignorance of NF ground motions is sufficiently accurate for medium-high-intensity seismic events. The study found that for two-story walls with a fundamental period of 0.21 s, the NF ground motions were more damaging than FF motions, while for one-story walls with a fundamental period of around 0.12 s, the FF ground motions were more destructive. Additionally, the fragility curves of the FF for one-story buildings were indistinguishable from those of the NF ground motions. Therefore, the use of NF ground motions was not necessary for the seismic fragility analysis of one-story URM buildings; however, for an accurate analysis of two-story URM buildings, NF ground motions should be included.

While efforts were made to encompass various opening configurations and geometries, additional case studies can be conducted to reduce further the uncertainty associated with the prediction of α_0. The comparative study procedure outlined in this study can also be extended to 3D models, considering the impact of irregular mass and stiffness in the plan and local collapse mechanisms. Additionally, investigating the

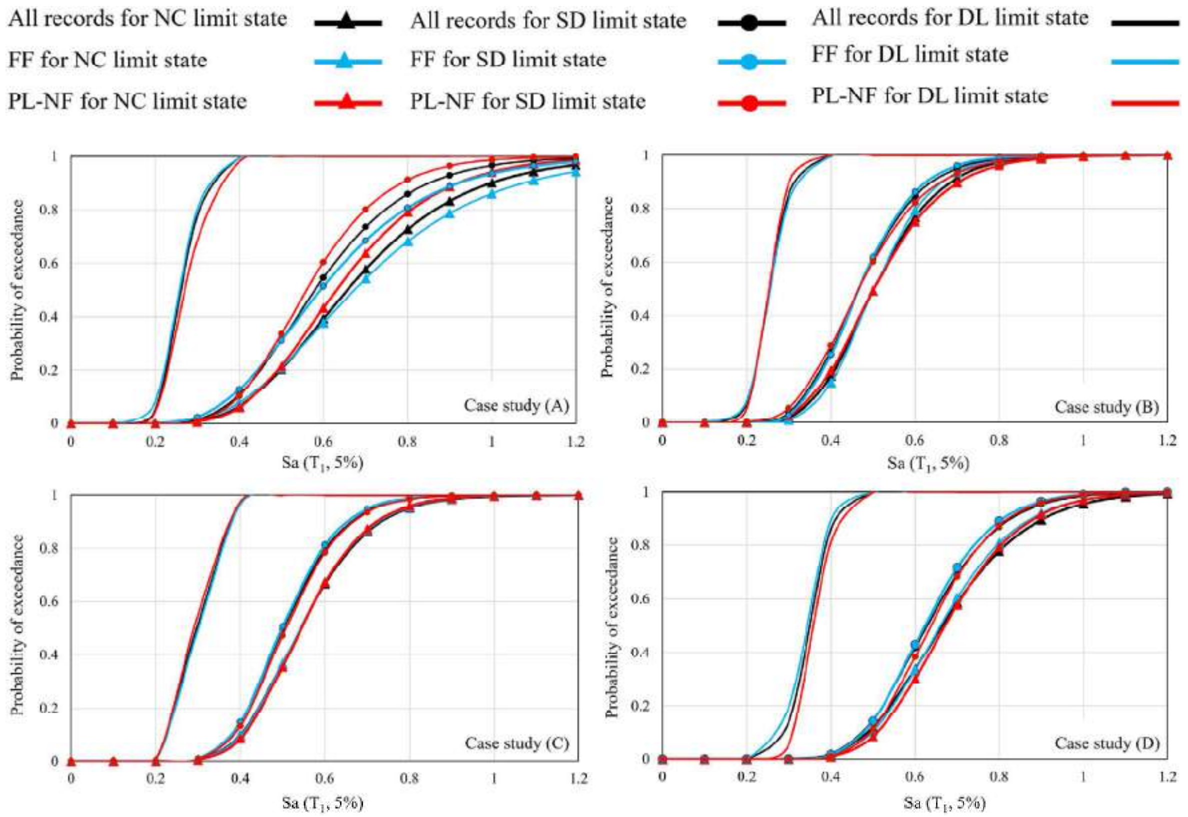

Fig. 12. Fragility curves of the case studies subjected to FF and NF ground motions for all three damage limit states for case studies A-D.

influence of different types of ground motion IM on seismic fragility curves could serve as a potential subject for future research.

Declaration of competing interest

The authors declare that they have no known competing financial interests or personal relationships that could have appeared to influence the work reported in this paper.

Data availability

No data was used for the research described in the article.

Acknowledgments

This work is a part of the HYPERION project. HYPERION has received funding from the European Union's Framework Programme for Research and Innovation (Horizon 2020) under grant agreement No 821054. The contents of this publication are the sole responsibility of Oslo Metropolitan University (Work Package 5, Task 2) and do not necessarily reflect the opinion of the European Union.

References

[1] M. Biglari, A. Formisano, Damage probability matrices and empirical fragility curves from damage data on masonry buildings after sarpol-e-zahab and bam earthquakes of Iran, Frontiers in Built Environment 6 (2020), https://doi.org/10.3389/fbuil.2020.00002.

[2] Z. Celep, A. Erken, B. Taskin, A. Ilki, Failures of masonry and concrete buildings during the march 8, 2010 kovancılar and palu (elazığ) earthquakes in Turkey, Eng. Fail. Anal. 18 (2011) 868–889, https://doi.org/10.1016/j.engfailanal.2010.11.001.

[3] M. Zucconi, M. Di Ludovico, L. Sorrentino, Census-based typological usability fragility curves for Italian unreinforced masonry buildings, Bull. Earthq. Eng. 20 (2022) 4097–4116, https://doi.org/10.1007/s10518-022-01361-8.

[4] A. Shabani, M. Kioumarsi, M. Zucconi, State of the art of simplified analytical methods for seismic vulnerability assessment of unreinforced masonry buildings, Eng. Struct. 239 (2021), 112280, https://doi.org/10.1016/j.engstruct.2021.112280.

[5] A. Aşıkoğlu, G. Vasconcelos, P.B. Lourenço, B. Pantò, Pushover analysis of unreinforced irregular masonry buildings: lessons from different modeling approaches, Eng. Struct. 218 (2020), 110830, https://doi.org/10.1016/j.engstruct.2020.110830.

[6] S. Colonna, S. Imperatore, M. Zucconi, B. Ferracuti, Post-seismic damage assessment of a historical masonry building: the case study of a school in teramo, Key Eng. Mater. 747 (2017) 620–627, https://doi.org/10.4028/www.scientific.net/KEM.747.620.

[7] M. Zucconi, R. Ferlito, L. Sorrentino, Typological damage fragility curves for unreinforced masonry buildings affected by the 2009 L'aquila, Italy earthquake, Open Civ. Eng. J. 15 (2021) 117–134, https://doi.org/10.2174/1874149502115010117.

[8] J. Park, P. Towashiraporn, J.I. Craig, B.J. Goodno, Seismic fragility analysis of low-rise unreinforced masonry structures, Eng. Struct. 31 (2009) 125–137, https://doi.org/10.1016/j.engstruct.2008.07.021.

[9] R. Marques, P.B. Lourenço, Unreinforced and confined masonry buildings in seismic regions: validation of macro-element models and cost analysis, Eng. Struct. 64 (2014) 52–67, https://doi.org/10.1016/j.engstruct.2014.01.014.

[10] P. Joyklad, Q. Hussain, Development of strength models for brick walls: experimental and theoretical study, Results in Engineering 18 (2023), 101103, https://doi.org/10.1016/j.rineng.2023.101103.

[11] A.M. D'Altri, V. Sarhosis, G. Milani, J. Rots, S. Cattari, S. Lagomarsino, et al., Modeling strategies for the computational analysis of unreinforced masonry structures: review and classification, Arch. Comput. Methods Eng. 27 (2020) 1153–1185, https://doi.org/10.1007/s11831-019-09351-x.

[12] T.M. Ferreira, N. Mendes, R. Silva, Multiscale seismic vulnerability assessment and retrofit of existing masonry buildings, Buildings 9 (2019) 91, https://doi.org/10.3390/buildings9040091.

[13] B. Pulatsu, S. Gonen, F. Parisi, E. Erdogmus, K. Tuncay, M.F. Funari, et al., Probabilistic approach to assess URM walls with openings using discrete rigid block analysis (D-RBA), J. Build. Eng. 61 (2022), 105269, https://doi.org/10.1016/j.jobe.2022.105269.

[14] A. Shabani, M. Skamantzari, S. Tapinaki, A. Georgopoulos, V. Plevris, M. Kioumarsi, 3D simulation models for developing digital twins of heritage structures: challenges and strategies, Procedia Struct. Integr. 37 (2022) 314–320, https://doi.org/10.1016/j.prostr.2022.01.090.

[15] A. Shabani, M. Feyzabadi, M. Kioumarsi, Model updating of a masonry tower based on operational modal analysis: the role of soil-structure interaction, Case Stud. Constr. Mater. 16 (2022), e00957, https://doi.org/10.1016/j.cscm.2022.e00957.

[16] M. Peruch, E. Spacone, G. Camata, Nonlinear analysis of masonry structures using fiber-section line elements, Earthq. Eng. Struct. Dynam. 48 (2019) 1345–1364, https://doi.org/10.1002/eqe.3188.

[17] S. Lagomarsino, A. Penna, A. Galasco, S. Cattari, TREMURI program: an equivalent frame model for the nonlinear seismic analysis of masonry buildings, Eng. Struct. 56 (2013) 1787–1799, https://doi.org/10.1016/j.engstruct.2013.08.002.

[18] A. Shabani, M. Kioumarsi, A novel macroelement for seismic analysis of unreinforced masonry buildings based on MVLEM in OpenSees, J. Build. Eng. 49 (2022), 104019, https://doi.org/10.1016/j.jobe.2022.104019.

[19] S. Petrovčič, V. Kilar, Seismic failure mode interaction for the equivalent frame modeling of unreinforced masonry structures, Eng. Struct. 54 (2013) 9–22, https://doi.org/10.1016/j.engstruct.2013.03.050.

[20] A. Shabani, M. Kioumarsi, Pros and cons of various equivalent frame models for nonlinear analysis of URM buildings, in: 8th European Congress on Computational Methods in Applied Sciences and Engineering ECCOMAS, 2022, p. 12.

[21] K. Demirlioglu, S. Gonen, S. Soyoz, M.P. Limongelli, In-plane seismic response analyses of a historical brick masonry building using equivalent frame and 3D FEM modeling approaches, Int. J. Architect. Herit. 14 (2020) 238–256, https://doi.org/10.1080/15583058.2018.1529208.

[22] K.R. Mackie, B. Stojadinović, Comparison of incremental dynamic, cloud, and stripe methods for computing probabilistic seismic demand models, Structures Congress (2005) 1–11, 2005.

[23] L. Su, X-l Li, Y-p Jiang, Comparison of methodologies for seismic fragility analysis of unreinforced masonry buildings considering epistemic uncertainty, Eng. Struct. 205 (2020), 110059, https://doi.org/10.1016/j.engstruct.2019.110059.

[24] L. Pasticier, C. Amadio, M. Fragiacomo, Non-linear seismic analysis and vulnerability evaluation of a masonry building by means of the SAP2000 V.10 code, Earthq. Eng. Struct. Dynam. 37 (2008) 467–485, https://doi.org/10.1002/eqe.770.

[25] P. Debnath, L. Halder, S. Chandra Dutta, Damage survey and seismic vulnerability assessment of unreinforced masonry structures in low-intensity Ambasa earthquake of northeast India, Structures 44 (2022) 372–388, https://doi.org/10.1016/j.istruc.2022.08.005.

[26] O. Souri, M. Mofid, Seismic evaluation of concentrically braced steel frames equipped with yielding elements and BRBs, Results in Engineering 17 (2023), 100853, https://doi.org/10.1016/j.rineng.2022.100853.

[27] L. Di Sarno, G. Karagiannakis, On the seismic fragility of pipe rack—piping systems considering soil–structure interaction, Bull. Earthq. Eng. 18 (2020) 2723–2757, https://doi.org/10.1007/s10518-020-00797-0.

[28] D. Vamvatsikos, C.A. Cornell, Incremental dynamic analysis, Earthq. Eng. Struct. Dynam. 31 (2002) 491–514.

[29] M. Kohrangi, D. Vamvatsikos, P. Bazzurro, Pulse-like versus non-pulse-like ground motion records: spectral shape comparisons and record selection strategies, Earthq. Eng. Struct. Dynam. 48 (2019) 46–64, https://doi.org/10.1002/eqe.3122.

[30] J.W. Baker, C.A. Cornell, Vector-valued intensity measures for pulse-like near-fault ground motions, Eng. Struct. 30 (2008) 1048–1057, https://doi.org/10.1016/j.engstruct.2007.07.009.

[31] J.W. Baker, Quantitative classification of near-fault ground motions using wavelet analysis, Bull. Seismol. Soc. Am. 97 (2007) 1486–1501.

[32] S.K. Shahi, J.W. Baker, An efficient algorithm to identify strong-velocity pulses in multicomponent ground motions, Bull. Seismol. Soc. Am. 104 (2014) 2456–2466.

[33] V. Dimakopoulou, M. Fragiadakis, I. Taflampas, A wavelet-based approach for truncating pulse-like records, Bull. Earthq. Eng. (2022) 1–24.

[34] F. Pugliese, L. Di Sarno, Probabilistic structural performance of RC frames with corroded smooth bars subjected to near- and far-field ground motions, J. Build. Eng. 49 (2022), 104008, https://doi.org/10.1016/j.jobe.2022.104008.

[35] H. Sha, X. Chong, L. Xie, P. Huo, T. Yue, J. Wei, Seismic performance of precast concrete frame with energy dissipative cladding panel system: half-scale test and numerical analysis, Soil Dynam. Earthq. Eng. 165 (2023), 107712, https://doi.org/10.1016/j.soildyn.2022.107712.

[36] F. Ahmad, A. Phillips, Buckling restrained braced frame seismic response for far-field, near-field, and long-duration earthquakes, J. Constructional Steel Res. 199 (2022), 107625, https://doi.org/10.1016/j.jcsr.2022.107625.

[37] A. Daei, M. Poursha, M. Zarrin, Seismic performance evaluation of code-compliant RC moment-resisting frame buildings subjected to near-fault pulse-like and non-pulse-like ground motions, J. Earthq. Eng. 26 (2022) 5058–5085, https://doi.org/10.1080/13632469.2020.1859003.

[38] A. Afreen, A. Ahmed, K. Moin, Effect of near-field earthquake on masonry structure, Asian Journal of Civil Engineering 22 (2021) 895–910, https://doi.org/10.1007/s42107-021-00353-4.

[39] H. Bilgin, M. Hysenlliu, Comparison of near and far-fault ground motion effects on low and mid-rise masonry buildings, J. Build. Eng. 30 (2020), 101248, https://doi.org/10.1016/j.jobe.2020.101248.

[40] M. Yekrangnia, A. Bakhshi, M.A. Ghannad, M. Panahi, Risk assessment of confined unreinforced masonry buildings based on FEMA P-58 methodology: a case study—school buildings in Tehran, Bull. Earthq. Eng. 19 (2021) 1079–1120, https://doi.org/10.1007/s10518-020-00990-1.

[41] G. Magenes, G. Kingsley, G. Calvi, Seismic Testing of a Full-Scale, Two-Story Masonry Building: Test Procedure and Measured Experimental Response Report 3.0, G.N.D.T. Department of Structural Mechanics, University of Pavia, 1995.

[42] M. Dolce, Schematizzazione e modellazione degli edifici in muratura soggetti ad azioni sismiche, in: L'industria Delle Costruzioni, vol. 25, 1991, pp. 44–57 (Italian).

[43] S. Cattari, A.M. D'Altri, D. Camilletti, S. Lagomarsino, Equivalent frame idealization of walls with irregular openings in masonry buildings, Eng. Struct. 256 (2022), 114055, https://doi.org/10.1016/j.engstruct.2022.114055.

[44] M. Kioumarsi, V. Plevris, A. Shabani, Vulnerability assessment of cultural heritage structures, in: 8th European Congress on Computational Methods in Applied Sciences and Engineering (ECCOMAS Congress 2022), ECCOMAS, 2022.

[45] A. Shabani, M. Kioumarsi, Hyperomet: an OpenSees interface for nonlinear analysis of unreinforced masonry buildings, SoftwareX 20 (2022), 101230, https://doi.org/10.1016/j.softx.2022.101230.

[46] S. Mazzoni, F. McKenna, M.H. Scott, G.L. Fenves, OpenSees command language manual, Pacific Earthquake Engineering Research (PEER) Center 264 (2006) 137–158.

[47] G. Magenes, G.M. Calvi, In-plane seismic response of brick masonry walls, Earthq. Eng. Struct. Dynam. 26 (1997) 1091–1112, https://doi.org/10.1002/(SICI)1096-9845(199711)26:11%3C1091::AID-EQE693%3E3.0.CO;2-6.

[48] C.E.N. Eurocode 8, in: Belgium Brussels (Ed.), Design of Structures for Earthquake Resistance—Part 3: Assessment and Retrofitting of Buildings, 2010.

[49] D.M. Aggiornamento delle, "Norme tecniche per le costruzioni" (NTC), in: Italian Ministry of Infrastructures and Transportation, 2018. Rome, Italy.

[50] Fema, Prestandard and Commentry for the Seismic Rehabilitaion of Buildings, FEMA 356, Federal Emergency Management Agency, Washington, D.C., 2000.

[51] FEMA, NEHRP guidelines for the seismic rehabilitation of buildings. Report FEMA 273, in: Federal Emergency Management Agency, 1997. Washington, DC, USA.

[52] G. Rinaldin, C. Amadio, L. Macorini, A macro-model with nonlinear springs for seismic analysis of URM buildings, Earthq. Eng. Struct. Dynam. 45 (2016) 2261–2281, https://doi.org/10.1002/eqe.2759.

[53] Y. Endo, L. Pelà, P. Roca, Review of different pushover analysis methods applied to masonry buildings and comparison with nonlinear dynamic analysis, J. Earthq. Eng. 21 (2017) 1234–1255, https://doi.org/10.1080/13632469.2016.1210055.

[54] A. Mouyiannou, M. Rota, A. Penna, G. Magenes, Identification of suitable limit states from nonlinear dynamic analyses of masonry structures, J. Earthq. Eng. 18 (2014) 231–263, https://doi.org/10.1080/13632469.2013.842190.

[55] Eurocode 8, Design of structures for earthquake resistance-part 1: general rules, seismic actions and rules for buildings, in: EN 1998-1, European Committee for Standardization, Brussels, 2005.

[56] G. Baltzopoulos, R. Baraschino, I. Iervolino, D. Vamvatsikos, SPO2FRAG: software for seismic fragility assessment based on static pushover, Bull. Earthq. Eng. 15 (2017) 4399–4425, https://doi.org/10.1007/s10518-017-0145-3.

[57] K. Beyer, E.A.I. Araya, S. Saloustros, Drift capacity models for the new masonry chapter of Eurocode 8 Part 1-2, in: R. Vacareanu, C. Ionescu (Eds.), Progresses in European Earthquake Engineering and Seismology, Springer International Publishing, Cham, 2022, pp. 398–416.

[58] M.K. Howlader, M.J. Masia, M.C. Griffith, Numerical analysis and parametric study of unreinforced masonry walls with arch openings under lateral in-plane loading, Eng. Struct. 208 (2020), 110337, https://doi.org/10.1016/j.engstruct.2020.110337.

[59] M. Peruch, E. Spacone, G. Camata, Nonlinear analysis of masonry structures using fiber-section line elements, Earthq. Eng. Struct. Dynam. 48 (2019) 1345–1364, https://doi.org/10.1002/eqe.3188.

[60] A. Aldemir, M. Altuğ Erberik, I.O. Demirel, H. Sucuoğlu, Seismic performance assessment of unreinforced masonry buildings with a hybrid modeling approach, Earthq. Spectra 29 (2013) 33–57, https://doi.org/10.1193/1.4000102.

[61] N. Mohammadgholibeyki, M. Banazadeh, The effects of viscous damping modeling methods on seismic performance of RC moment frames using different nonlinear formulations, Structures 15 (2018) 232–243, https://doi.org/10.1016/j.istruc.2018.07.009.

[62] Fema, in: United States, D.C. Washington (Eds.), Quantification of Building Seismic Performance Factors, FEMA P695, Federal Emergency Management Agency, 2009.

[63] PEER., in: PEER Ground Motion Database, University of California, Berkeley, USA, 2021. https://ngawest2.berkeley.edu/.

[64] ATC, Quantification of Building Seismic Performance Factors, FEMA P695: US Department of Homeland Security, FEMA, 2009.

[65] D. Vamvatsikos, C.A. Cornell, Applied incremental dynamic analysis, Earthq. Spectra 20 (2004) 523–553.

[66] C.A. Cornell, F. Jalayer, R.O. Hamburger, D.A. Foutch, Probabilistic basis for 2000 SAC federal emergency management agency steel moment frame guidelines, J. Struct. Eng. 128 (2002) 526–533, https://doi.org/10.1061/(ASCE)0733-9445(2002)128:4(526).

[67] J.W. Baker, Efficient analytical fragility function fitting using dynamic structural analysis, Earthq. Spectra 31 (2015) 579–599, https://doi.org/10.1193/021113eqs025m.

[68] H. Güllü, M. Karabekmez, Effect of near-fault and far-fault earthquakes on a historical masonry mosque through 3D dynamic soil-structure interaction, Eng. Struct. 152 (2017) 465–492, https://doi.org/10.1016/j.engstruct.2017.09.031.

[69] N. Simos, G.C. Manos, E. Kozikopoulos, Near- and far-field earthquake damage study of the Konitsa stone arch bridge, Eng. Struct. 177 (2018) 256–267, https://doi.org/10.1016/j.engstruct.2018.09.072.

[70] H. Güllü, F. Özel, Microtremor measurements and 3D dynamic soil–structure interaction analysis for a historical masonry arch bridge under the effects of near- and far-fault earthquakes, Environ. Earth Sci. 79 (2020) 338, https://doi.org/10.1007/s12665-020-09086-0.

[71] P. Labbé, A. Altinyollar, Conclusions of an IAEA–JRC research project on the safety significance of near-field seismic motions, Nucl. Eng. Des. 241 (2011) 1842–1856, https://doi.org/10.1016/j.nucengdes.2011.02.006.

[72] R. Dadashi, K. Nasserasadi, Seismic damages comparison of low-rise moderate reinforced concrete moment frames in the near- and far-field earthquakes by a probabilistic approach, International Journal of Advanced Structural Engineering (IJASE) 7 (2015) 171–180, https://doi.org/10.1007/s40091-015-0090-9.

Paper VII

Shabani, A., Feyzabadi, M., Kioumarsi, M.

Model updating of a masonry tower based on operational modal analysis: The role of soil-structure interaction

(2022) Case Studies in Construction Materials, https://doi.org/10.1016/j.cscm.2022.e00957.

Case Studies in Construction Materials 16 (2022) e00957

Contents lists available at ScienceDirect

Case Studies in Construction Materials

journal homepage: www.elsevier.com/locate/cscm

Model updating of a masonry tower based on operational modal analysis: The role of soil-structure interaction

Amirhosein Shabani *, Mohyeddin Feyzabadi, Mahdi Kioumarsi

Department of Civil Engineering and Energy Technology, Oslo Metropolitan University, Oslo 0166, Norway

ARTICLE INFO

Keywords:
Digital twins
Model updating
Soil-structure interaction
Masonry tower
Operational modal analysis
Resonance effect

ABSTRACT

Vibration-based finite element model (FEM) updating of cultural heritage assets is gaining so much attraction these days since destructive tests are usually not allowed to be performed. In this study, a framework for developing three-dimensional (3D) FEMs is proposed using 3D laser scanners and applied on Slottsfjell tower, a stone masonry tower in Tønsberg, Norway. Operational modal analysis (OMA) was done based on the ambient vibration testing (AVT) data to define the frequency values and corresponding mode shapes of the tower. Mechanical properties of the tønsbergite stone were utilized to derive the base values of the material properties of the homogenized masonry for performing sensitivity analysis and FEM updating. To investigate the effect of the soil-structure interaction (SSI) on the FEM updating results, three FEMs are developed. The fixed-base model is the FEM without considering the SSI effects, and two other FEMs are developed using the substructure and direct methods for simulating the SSI effects. Sensitivity analysis was performed to investigate the effective parameters on the dynamic characteristics of the models. FEM updating was conducted on the three FEMs, and results are compared to each other to show the role of the SSI on the FEM updating results. The resonance effect can cause damages to buildings located even in low seismicity zones. For this aim, the risk of resonance effect has been evaluated for the tower. Finally, linear dynamic analysis was performed on the three calibrated models, and the results were compared to each other.

1. Introduction

Heritage structures are the symbolic representation of ancient engineering, and preservation of the so-called architectural heritage is pivotal for every societies [1]. Masonry and timber are considered as the oldest construction materials [2]. The structural behavior of masonry structures is strictly tied to the geometrical parameters, material properties, and environmental situation of the location site [3,4]. Moreover, providing a robust model called digital twins with a structural behavior similar to the real structure is crucial for a structural vulnerability assessment methodology [5]. Various equipment and strategies have been proposed to decrease the uncertainties related to the aforementioned effective parameters on masonry structures and facilitate the assessment and damage detection process [1].

A geometrical survey is a crucial part of the methodology to develop digital twins of historic structures. Nowadays, 3D laser scanners have gained attention in the structural engineering community, and engineers are trying to find optimum solutions for obtaining 3D models based on point clouds [6,7]. Various methods have been developed to automatically and semi-automatically convert the point clouds to 3D finite element models (FEMs) [8–12]. Obtaining 3D models in computer-aided (CAD) software

---

* Corresponding author.

https://doi.org/10.1016/j.cscm.2022.e00957
Received 25 August 2021; Received in revised form 11 February 2022; Accepted 15 February 2022
Available online 16 February 2022

packages based on the point clouds and converting the 3D model to the 3D FEMs with meshing is a conventional method that is widely used nowadays [6,13,14].

Soil-structure interaction (SSI) influences the dynamic characteristics of structures that should be considered to provide more robust simulation models [15,16]. Considering fixed-based boundary conditions is widely used for analysis and design purposes when geotechnical data is not provided [17]. But solutions for considering the SSI effects can be classified into direct and substructure approaches [15,18]. In the direct method that is considered as the most accurate modeling approach, soil, foundation, and structure are modeled by applying proper boundary conditions [18]. Studies on historical masonry structures using the direct method show the significant effects of SSI on their dynamic characteristics and seismic behavior [17,19–22]. In the substructure approach, the SSI is simulated using springs and dashpots [18]. Although the substructure approach is efficient in terms of computational efforts and is widely used in analyzing compared to the direct method [23], its accuracy has been questioned recently in [24].

Material properties are other effective parameters on the dynamic characteristics of the structures. Destructive tests on historical structures are usually forbidden due to their values, and non-destructive tests should be utilized [2,14]. Operational modal analysis (OMA) of historical masonry towers or minarets based on ambient vibrating testing (AVT) method using accelerometers has gained so much attraction recently [25–32]. Calibration of structures based on the OMA results is one of the non-destructive methods to define the material properties of historical structures and minimize the differences of the dynamic characteristics of numerical model and structure [3,33–39]. Although SSI is significantly effective on the dynamic characteristics of structures, a few studies have been done to calibrate the numerical models considering the SSI effects using the substructure method [40–44]. However, there is still a gap in the numerical model updating of historical structures so that soil parameters are also updated. Moreover, different types of SSI modeling approaches are needed to be considered, including the direct method.

Calibrated digital twins can be utilized for predicting the vulnerability of structures subjected to various types of risks, including earthquake [33,41,45–48]. Masonry structures are susceptible to seismic actions, and seismic risk assessment of historic masonry structures is a pivotal task for the authorities [49,50]. Furthermore, experiences of past earthquake events show considerable damage due to the resonance effect [51,52]. A building will approach a state of partial resonance when the fundamental period of soil and structure have matched each other, and seismic waves will be amplified that result in the increasing of inertial faces acting on the structures [53,54]. Therefore, investigating the risk of this phenomenon on existing structures and considering it for designing buildings should be taken into account even in low seismicity zones.

In this paper, a framework for developing simulation-based digital twins of historical structures using 3D laser scanners and accelerometers considering the SSI effects is explained. A digital twin of the Slottsfjell tower in the city of Tønsberg in Norway has been developed. 3D laser scanners are utilized to facilitate the geometrical survey and the procedure of the conversion of the point clouds to the FEM has been discussed. Afterward, AVT was done, and three frequency domain OMA methods were utilized to derive the tower's natural frequencies and mode shapes. SSI effects are considered using both the direct (DM) and substructure (SM) methods, and a model with fixed-based (FB) boundary conditions has been developed without considering the SSI effects. The tower was constructed by the tønsbergite stone, and mechanical properties of the stone were utilized to derive the base values of the material properties of the homogenized masonry for performing sensitivity analysis and the FEM updating. A sensitivity analysis is performed to investigate the most effective parameters on the dynamic characteristics of the tower for the three mentioned FEMs and the results are compared to each other. FEM updating of the three models was done by updating the SSI parameters, and the results of the updated materials have

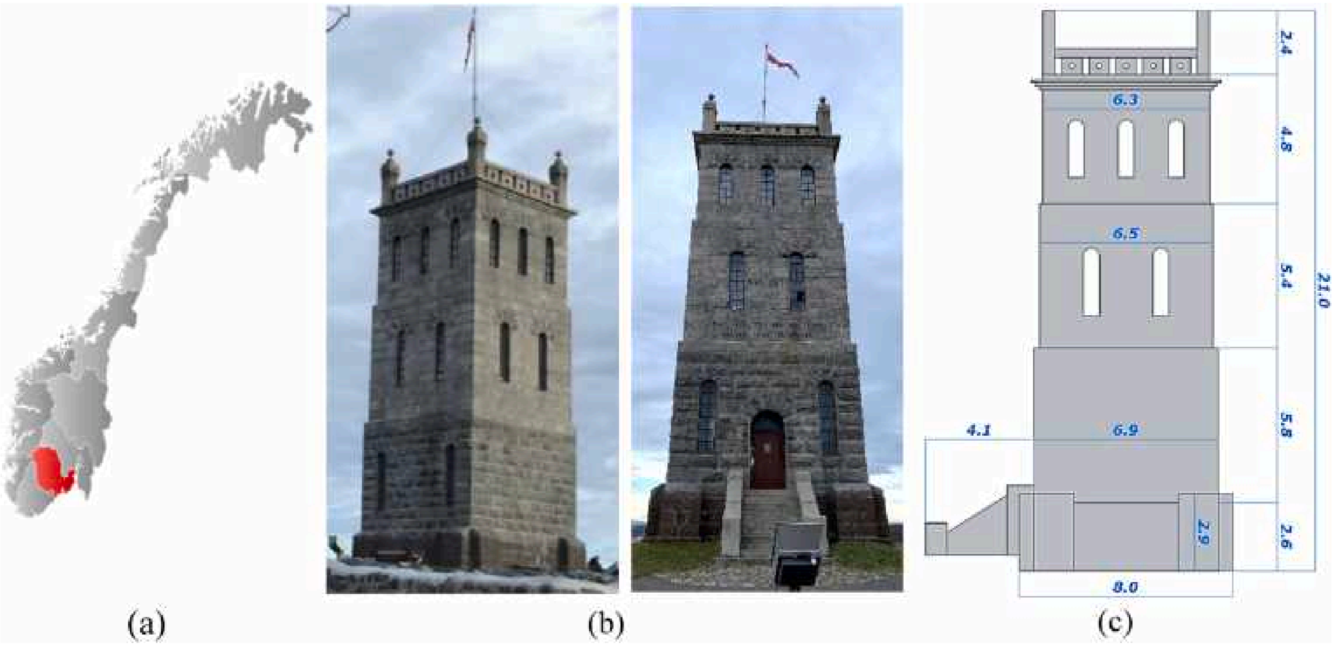

Fig. 1. (a) Location of Tønsberg in Norway, (b) Different views of the Slottsfjell tower, and (c) Geometry of the tower.

been compared to each other. After providing the calibrated DM model, the risk of resonance effect has been evaluated. Finally, linear time history has been carried out on all three calibrated models and the results are compared to each other.

2. Overview of the case study

The Slottsfjell tower is in the city of Tønsberg in the southeastern part of Norway (see Fig. 1(a)). It is centrally located in the ruined park from one of the Nordic region's largest medieval castles. The tower is not older than 150 years and was built to celebrate 1000 years since the city of Tønsberg was founded in 871. On top of the entrance, it is written the years 871–1871 with the corresponding text "May the city that stands on the hill, flourish a thousand new year" in Norwegian. Fig. 1(b) shows the Slottsfjell tower in different views. The tower is made of stone masonry with a square shape which can typically be seen in medieval constructions. The tower has a historical value for the county of Vestfold and Telemark because of the region's identification with the Viking age due to the most magnificent burial site from the Viking era in Norway located in that area. The tower's total height is 21 m, with one basement and three stories on top of the soil level. Each story is like a box, and the width of each box is decreased from the basement level to the top floor. The geometry of the tower is depicted in Fig. 1(c).

3. Numerical modeling

3.1. 3D Geometric documentation

Totally twenty scans were performed using a Topcon 2000 3D laser scanner inside and outside the tower to provide dense point clouds. The raw point clouds of the scans were imported to Autodesk Recap Pro software [55] to be combined, and a unique dense point cloud model is provided as depicted in Fig. 2(a), and each circle shows the location of the scans. The 3D point cloud file is imported to Autodesk Revit software [56], as illustrated in Fig. 2(b). The 3D model of the tower was provided in the Revit software based on the point clouds as presented in Fig. 2(c).

3.2. Finite element modeling

A semi-automatic procedure to provide the 3D FEM based on the point clouds data was utilized in this study. After providing the 3D model of the tower, the industry foundation classes (IFC) format of the model was exported from the Revit Autodesk software. The CAD exchanger software was utilized to convert the IFC format file to the standard for the exchange of product model data (STEP) format, which is suitable for importing the 3D solid models in DIANA FEA [57] software to develop the 3D FEM. After importing the STEP file to DIANA FEA, several cleaning tools have been chosen to modify the 3D model, including healing the edge inaccuracies, removing duplicate surfaces and small entities, etc.

For 3D finite element modeling of the tower, the homogenized method has been considered by neglecting the discretization of masonry units and mortar, which is widely used for modeling full-scale structures [58,59]. This approach needs fewer input data and less computational effort than the discrete element method which masonry units and mortar are modeled separately by defining the interface elements [4].

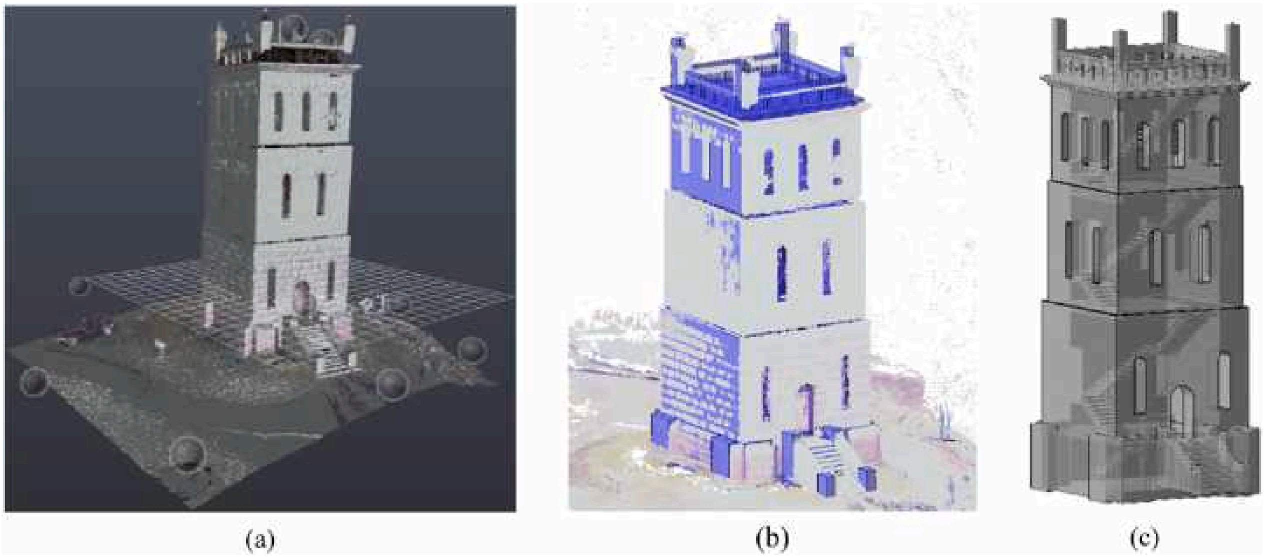

Fig. 2. (a) Point clouds derived from the 3D laser scanner and position of the scanners during the data acquisition, (b) imported dense 3D point to the Revit Autodesk software, and (c) 3D drawing of the tower in the Revit Autodesk software.

3.3. Soil-structure interaction modeling

Three models with three various boundary conditions were developed. For the FB model, the SSI was neglected by employing rigid supports in three degrees of freedom beneath the tower, as illustrated in Fig. 3(a). Note that neither soil spring nor rigid supports are not modeled around the basement walls, based on [60].

The second model (SM) is provided based on the substructure method to consider the SSI by modeling springs beneath the tower, as depicted in Fig. 3(b). Based on the Winkler method, springs have stiffness in three directions to support the normal and shear stiffnesses [61].

The third model (DM) is characterized by modeling the foundation and soil box as the most detailed model in terms of considering the SSI effects (see Fig. 3(c)). In this model, the foundation is modeled beneath the tower as a box with a height of 2.5 m based on the data provided by the slottsfjell museum. Regarding the dimension of the soil box, the depth and the length should be considered larger than 1,5 and 3 times the dimension of the foundation based on [62]. Therefore, the soil box is modeled with the depth and length of 11 m and 22 m, respectively. Rigid boundary conditions are considered for the bottom of the soil box, but for four side faces of the box, roller supports are employed to constrain the displacement in the normal direction of the faces [15,63].

The FEMs are developed in the DIANA FEA software and then imported to the FEMtools software [64] for performing future analyses. Hexahedron mesh type was chosen for meshing the model, so that hexahedron elements are the dominant choice, and tetrahedron and pentahedron mesh elements were used to fill parts of the geometry. The total number of elements of the FB, SM, and DM models are 66,676, 66,286, and 93,832, respectively, with a maximum mesh size of 65 cm.

3.4. Material properties of soil and masonry

The Slottsfjell tower was constructed using the tønsbergite stone, which is a variant of the Norwegian igneous rock larvikite and the

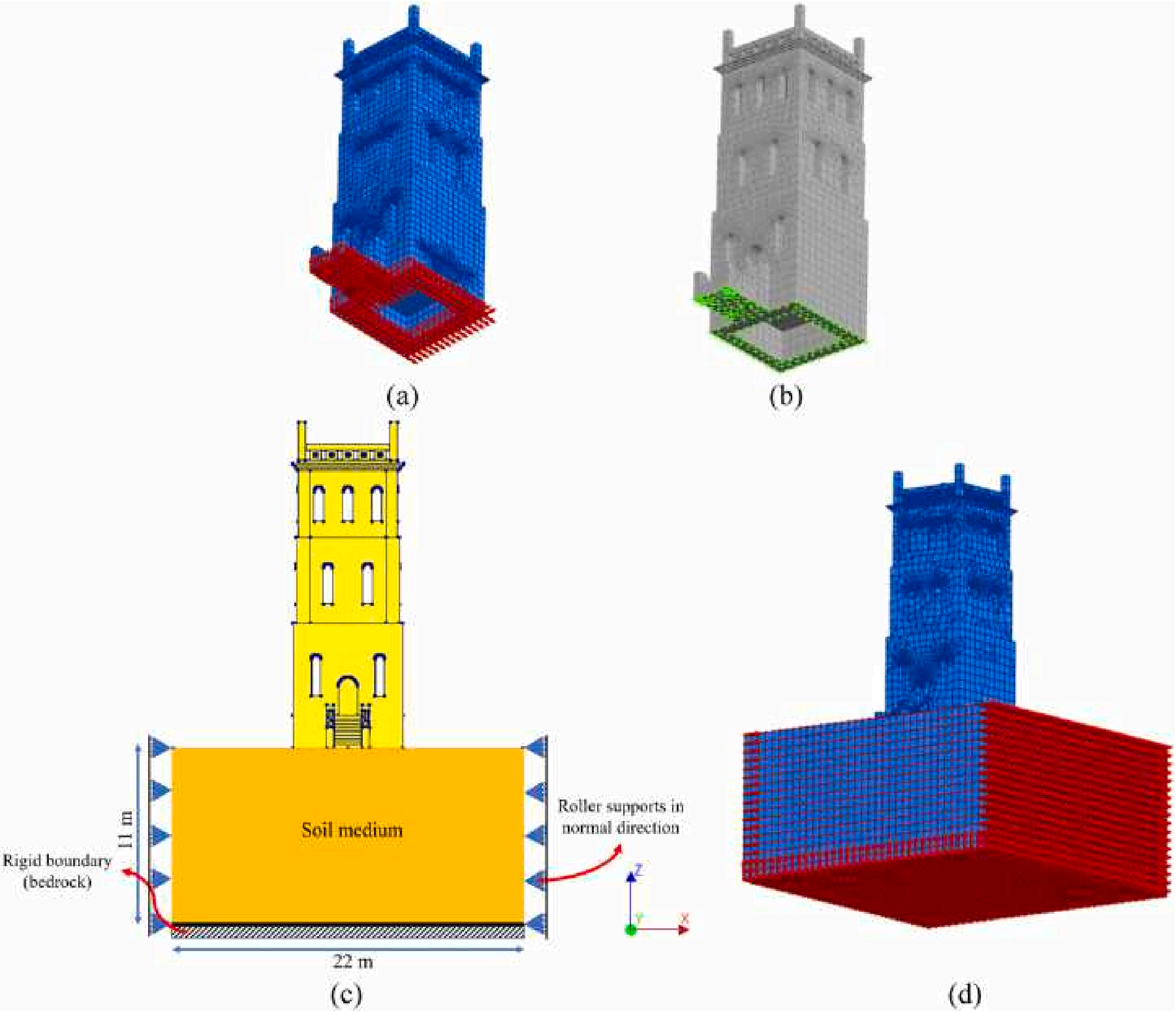

Fig. 3. The 3D mesh of (a) FB, (b) SM models, (c) detail of modeling DM model, and (d) 3D mesh of DM model of the tower.

larvikite rock is classified as a variant of the monzonite rock [65,66]. Compared to granite, which is more broadly known, monzonite has a lower percentage of quartz [67]. The elasticity modulus of the stone unit is considered 61 GPa based on [68], and stiff mortar type is considered with an elasticity modulus value of 12 GPa based on [69]. Orthotropic material is considered for masonry, and homogenized masonry properties are derived based on an empirical equation presented in [70]. Although the elasticity modules of the homogenized masonry derived from the empirical equations are more than the real values since the deformations of the bed joint mortar are not considered [70], the value can be utilized for the base value and will be updated through the calibration process. Furthermore, the shear modulus of masonry is considered 0.15 times the elasticity modulus based on [36,71].

Since no laboratory test has been conducted on the soil properties, hard soil properties based on the field investigation and the properties are selected based on [15]. Normal subgrade reaction factor of the boundary condition of the SM is calculated based on the simplified Vesic model [72] and Eq. (1).

$$K_z = \frac{E_s}{B.(1-\nu_s{}^2)} \tag{1}$$

Where E_s and ν_s are the elasticity modulus, and the Poisson's ratio of soil, respectively, and B is the foundation length. Furthermore, the shear stiffnesses (K_x and K_y) are considered 0.01 times of the normal stiffness [73,74]. All material properties and spring reaction factors are summarized in Table 1, which are utilized for the sensitivity analysis and the base values for the model updating in the next sections. It should be noted that as a limitation of this model, the effect of foundation interaction is neglected. Moreover, the springs have the same stiffness in different locations beneath the tower, which is not realistic considering the non-homogeneous behavior of soil and foundation. Orthotropic material was considered for the soil media of the DM model with mechanical properties of the hard soil [15] as presented in Table 1.

4. Sensitivity analysis on the effects of material properties

To have a better understanding of the effective parameters on the dynamic characteristics of the tower, a sensitivity analysis was done. The tower is discretized into different sets, as illustrated in Fig. 4. The same set names based on the order of the sections that appeared in Fig. 4 for the first floor (sets 2–6) were considered for the sets of the second and the third floor. For the DM model, the soil and foundation are discretized into eight and four sections, respectively. The soil box is halved in all dimensions to be discretized to eight sets, and the foundation is divided into four equal sets in plan view. Elasticity modulus and shear modulus of different sets of masonry in three directions are considered the parameters. Their influence is investigated on the first five natural frequency values of the three developed models of the tower.

Fig. 5 depicts the sensitivity graphs of the elasticity modulus for the three developed models. It can be concluded that Ez is the most effective parameter that mostly influences the first two natural frequencies. Moreover, higher sensitivities are related to the first-floor elements compared to other floors. The graphs also show that the changes in elasticity modulus of the foundation and soil sets have less effect on the frequencies than the masonry material properties.

Based on the sensitivity graph of the shear modulus presented in Fig. 6, G_{xy} is the least effective parameter, and responses are more sensitive to G_{yz} and G_{xz}. Sensitivity values are highest for the first-floor sets and lowest for the third-floor sets. Unlike the elasticity modulus, it should be noted that the shear modulus is effective on higher modes. The graphs also show that the changes in shear modulus of the foundation and soil sets have negligible effects on the frequencies compared to the masonry material properties.

A sensitivity analysis is performed to investigate the effect of spring stiffnesses of the SM model's boundary conditions, and the graph is illustrated in Fig. 7. K_z is the most effective parameter that affects more on the first two modes' frequencies, and the torsional mode is highly sensitive to K_x. By comparing the normalized sensitivity values of the sensitivity graph illustrated in Fig. 7, with other parameters' sensitivity values presented in previous graphs, it can be pointed out that the SM model is more sensitive to springs' stiffnesses values than the masonry properties.

Table 1
Material properties of the homogenized stone masonry of the tower, soil, normal and shear reaction factors of boundary conditions of the SM model.

Material	Properties	Value
Masonry	Density (kg/m^3)	2800
	Elasticity modulus in X, Y and Z directions (E_x,E_y,E_z) (GPa)	40
	Shear modulus in XY, YZ and ZY directions (G_{xy},G_{yz},G_{zy}) (GPa)	6
	Poisson ratio in XY, YZ and ZY directions (u_{xy}, u_{yz}, u_{zy})	0.25
Soil	Density (kg/m^3)	2000
	E_x,E_y,E_z (GPa)	6
	G_{xy},G_{yz},G_{zy} (GPa)	0.9
	u_{xy}, u_{yz}, u_{zy}	0.3
Spring	Normal reaction factor (K_z) (GPa/m)	51.2
	Shear reaction factor (K_x,K_y) (GPa/m)	0.512

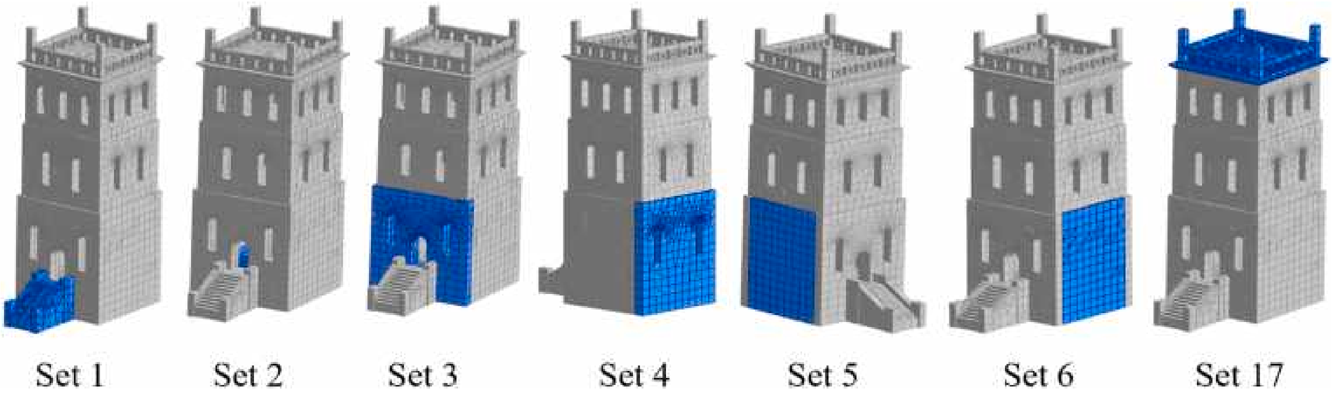

Fig. 4. The different sets of the tower and their corresponding names.

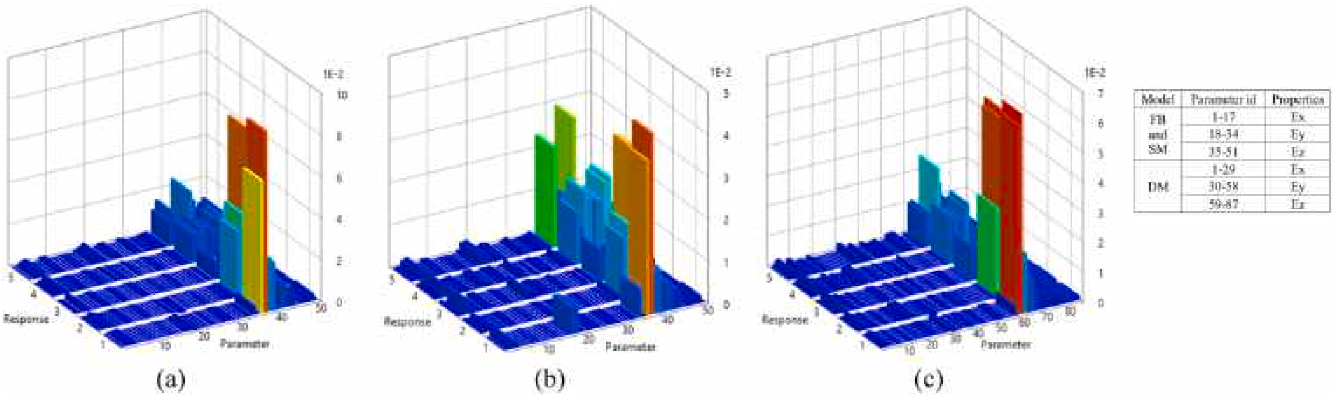

Model	Parameter id	Properties
FB and SM	1-17	Ex
	18-34	Ey
	35-51	Ez
DM	1-29	Ex
	30-58	Ey
	59-87	Ez

Fig. 5. Sensitivity graphs to a change in elasticity modulus for the (a) FB, (b) SM, and (c) DM models.

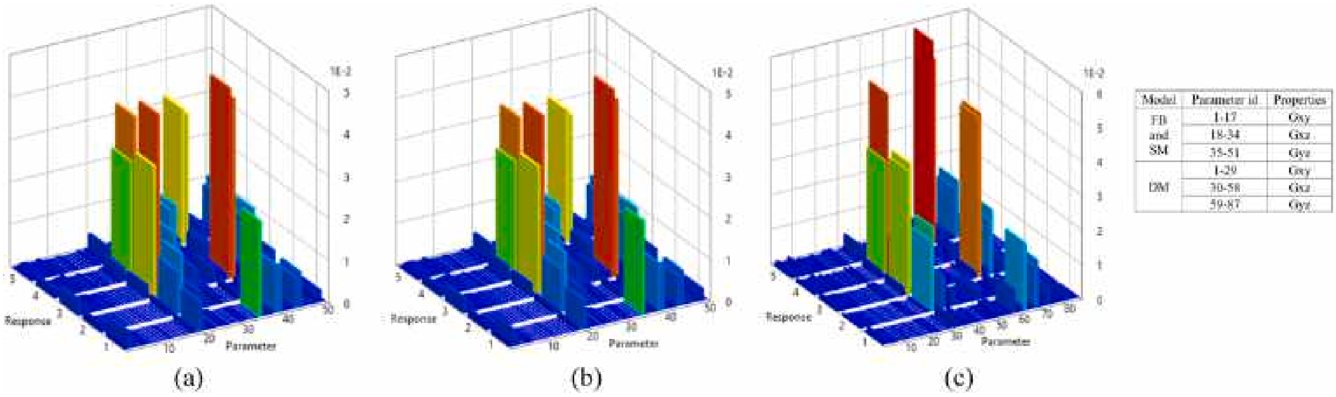

Model	Parameter id	Properties
FB and SM	1-17	Gxy
	18-34	Gxz
	35-51	Gyz
DM	1-29	Gxy
	30-58	Gxz
	59-87	Gyz

Fig. 6. Sensitivity graphs to a change in shear modulus for the (a) FB, (b) SM, and c) DM models.

5. System identification

5.1. Ambient vibration testing

Ambient vibration testing was performed using 3-Axis MEMS digital Unquake accelerometers with a sampling rate of 250 Hz. Compared to the more sensitive piezoelectric accelerometers, lower cost and power consumption are two main characteristics of MEMS accelerometers [1,47]. However, the reliability of the OMA results of various low-cost MEMS accelerometers was confirmed with low error values compared to the low-noise piezoelectric accelerometers [75].

The accelerometers' locations have been decided based on engineering judgment and previous studies [3,36], as depicted in Fig. 8 (a). The accelerometers are equipped with the global positioning system (GPS) antenna and a global navigation satellite system (GNSS) receiver. GPS data were used to record the time and synchronize all the data from the accelerometers based on the recorded time. Fig. 8 (b) shows the test setup, and Fig. 8(c) shows a sample of an acceleration graph derived from an accelerometer.

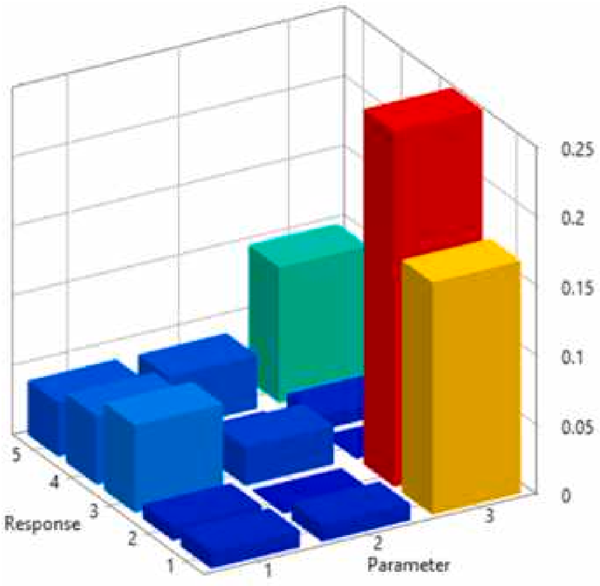

Model	Parameter id	Properties
SM	1	Kx
	2	Ky
	3	Kz

Fig. 7. Sensitivity graph to a change in spring stiffnesses of the SM model.

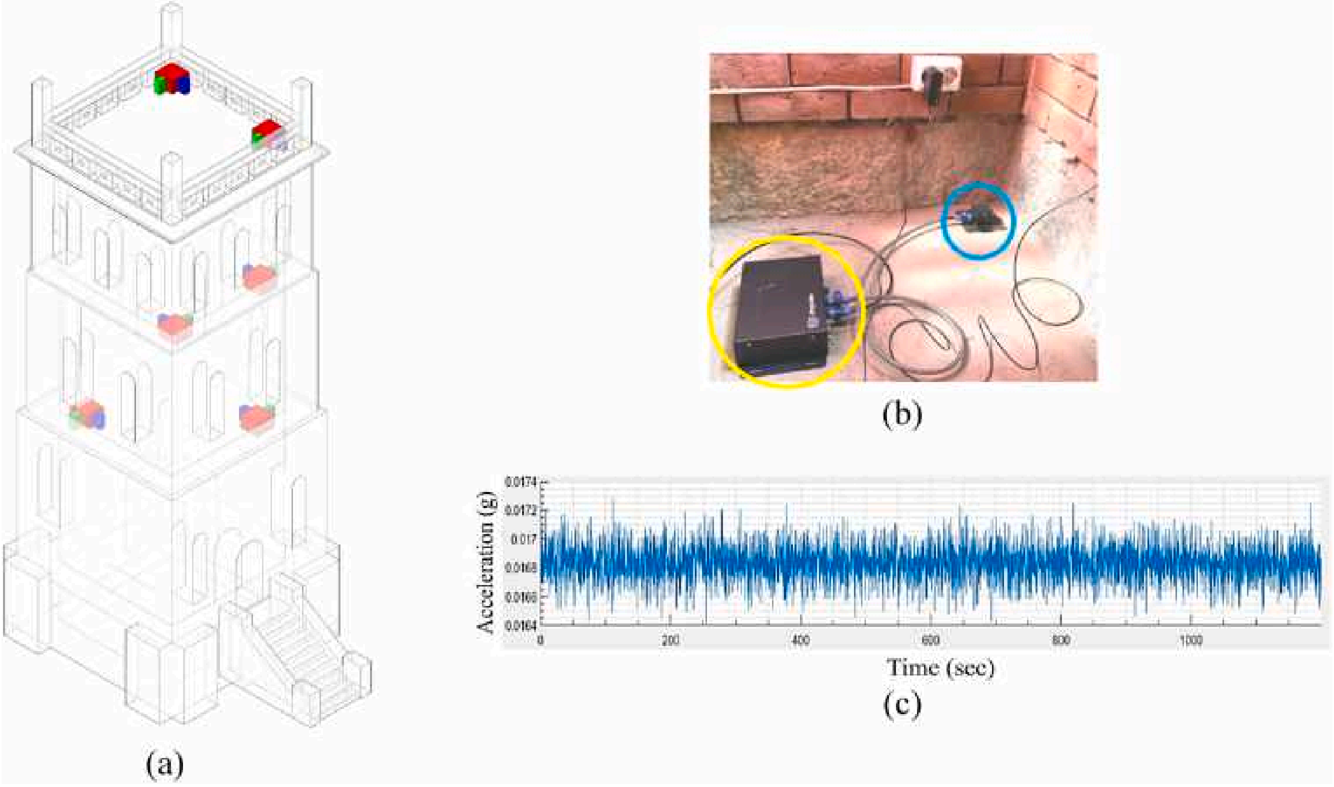

Fig. 8. (a) Locations of the accelerometers [66], (b) test setup including the accelerometer (in blue circle) and datalogger (in yellow circle), and (c) sample of an acceleration graph derived from an accelerometer.

5.2. *Operational modal analysis*

A preliminary analysis has been done by performing Fast Fourier Transform (FFT) on single sensor measurements in [76]. For confirming the results, frequency domain methods are utilized to investigate the dynamic characteristics of the tower based on the distributed sensor network measurements. Frequency Domain Decomposition (FDD), Enhanced Frequency Domain Decomposition (EFDD), and Curve-Fitted Enhanced Frequency Domain Decomposition (CFDD) methods are three frequency-domain methods that were utilized to derive the natural frequencies and corresponding mode shapes of the tower. The idea of FDD method is to carry out an approximate decomposition of a system response into a set of independent single-degree-of-freedom systems for each mode. First, the spectral density matrices are estimated. Singular value decomposition of the spectral density matrices is done, and finally, the peak pick on the average singular values will be performed to derive the modal parameters [77,78]. EFDD and CFDD are the improved versions of the FDD method that damping ratio estimation is available, and the accuracy of the dynamic characteristics is enhanced. In EFDD, the FDD peak picking is extended with a simple time domain least squares estimation technique, and in CFDD, the extension relies on a frequency domain least squares estimation technique [79,80]. Artemis Modal software was utilized to perform the operational modal analysis [81]. The differences between the values of the natural frequencies are negligible (less than 0.3%); moreover, the mode shapes are equal. Therefore, the singular value decomposition (SVD) graph of the FDD method is reported in Fig. 9(a), and the five first peaks of the graph were selected to represent the first five modes of the tower. Mode shapes and corresponding frequency values of the first five modes of the tower are illustrated in Fig. 9(b). All modes are flexural except the third mode, which is a torsional mode.

6. Finite element model updating

After performing sensitivity analysis to understand the effect of material properties on the dynamic characteristics of the tower and performing system identification to derive the first five natural frequencies and mode shapes of the real structure, the FEM updating is the last step to develop the digital twins.

The objective of model updating is to adjust the selected parameters' values so that a reference correlation coefficient is minimized. The weighted absolute relative difference between resonance frequencies and the weighted difference between target and average actual modal assurance criteria (MAC) are two correlation coefficients that are considered through the FEM updating procedure. MAC value is a measure of the squared cosine of the angle between two modes shapes that is derived based on Eq. (2).

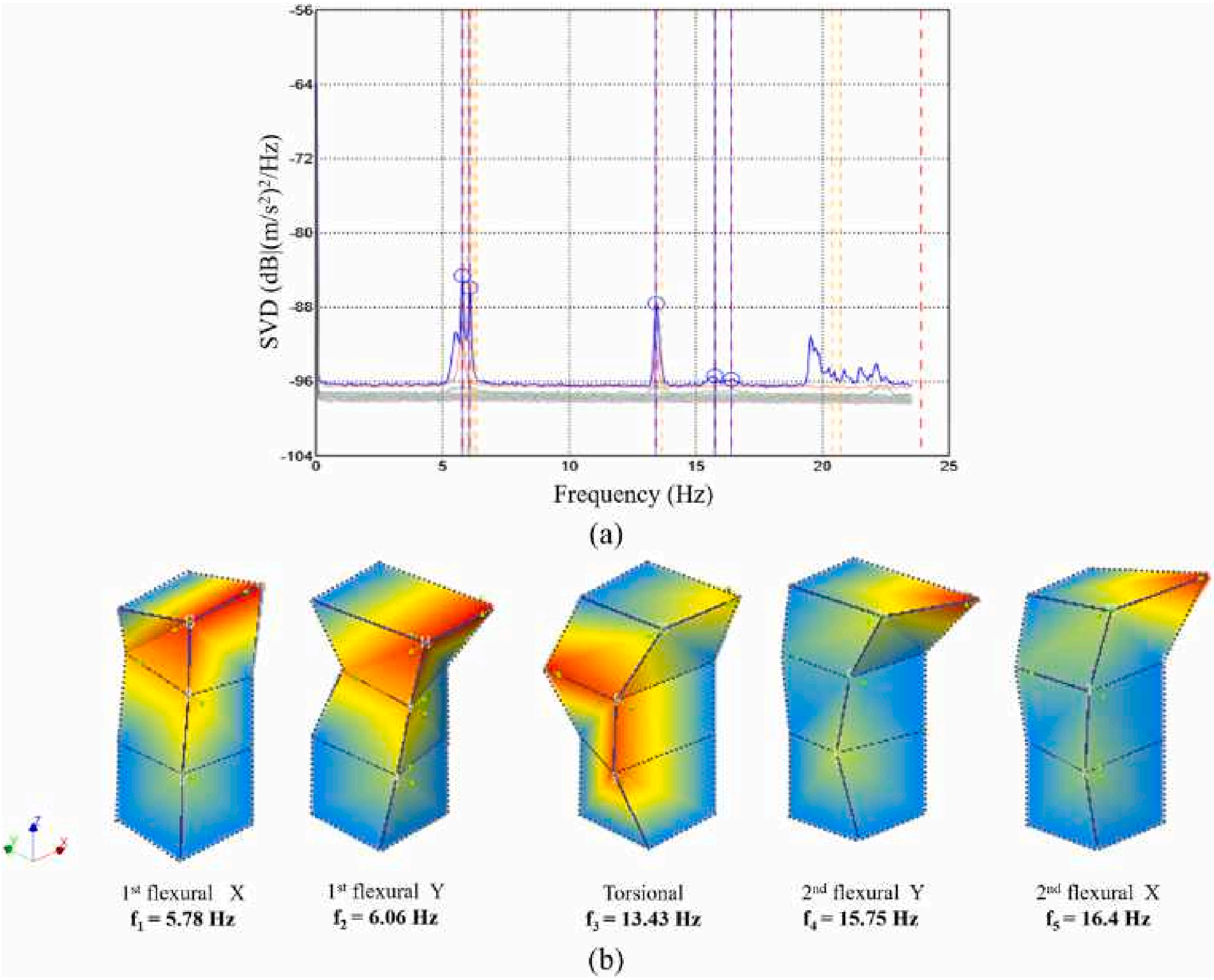

Fig. 9. (a) SVD graph of the FDD method, and (b) mode shapes and corresponding frequencies of the tower based on the OMA results.

$$MAC(\psi_a, \psi_e) = \frac{\left|\left(\{\psi_a\}^t\{\psi_e\}\right)\right|^2}{(\{\psi_a\}^t\{\psi_a\})(\{\psi_e\}^t\{\psi_e\})} \tag{2}$$

Where ψ_e and ψ_a are respectively the experimental and analytical eigenvectors. Bayesian parameter estimation by minimizing a weighted error as presented in Eq. (3) is utilized for FEM updating in the FEMtools software package.

$$E = \{\Delta R\}^t[C_R]\{\Delta R\} + \{\Delta P\}^t[C_P]\{\Delta P\} \tag{3}$$

Where ΔR is a difference between a vector containing the reference and predicted system responses, ΔP is a difference between a vector containing the given state and predicted system parameters, C_R and C_P represent weighting matrices expressing the confidence in the model responses and parameters respectively.

FEM updating was done on the FB model, and absolute differences of frequency values (ADFV) derived from the OMA and FEA are presented for the first five modes of the model in Table 2. A good correlation between the frequency values of the first two modes is reached after the updating process, but the differences for the other modes are high. Moreover, MAC values and a 3D plot are presented in Fig. 10 (a) and (b), respectively. MAC values show the same correlations for the first two modes, but the differences of the higher modes are significant. Based on the MAC value matrix in Fig. 10 (a), modes 4 and 5 of FEA are paired to modes 5 and 4, respectively. However, since the modes are not in sequence based on the frequency values, this correlation is not accepted, and diagonal MAC values should be considered for the pairing modes. Fig. 10 (c) shows the paired mode shapes of the first three modes to show the correlation between the mode shapes derived from the FEA and the OMA after model updating.

FEM updating of the SM model was performed by calibrating the masonry and the boundary condition spring stiffnesses. Based on Table 3, frequency values of the first three modes are close enough, but ADFVs more than 5% can be seen for the other modes. Moreover, all mode shapes are paired with MAC values of more than 65% based on Fig. 11.

FEM updating of the DM model was done by calibrating the masonry, foundation, and soil material properties. Based on Table 4, differences between the frequencies' values are negligible, with values less than 3%. Moreover, based on Fig. 12 (a) and (b), MAC values of more than 65% depicts that mode shapes from FEA follow the OMA mode shapes, and lower values for the off-diagonal MAC matrix show a good correlation of the modes shapes and Fig. 12 (c) also approves the good correlation of the mode shapes.

6.1. Comparison of updating results

To compare the calibration results for the three FEMs, the average values of ADFVs are presented in Fig. 13 (a). Moreover, MAC values of the first five modes (corners of the diagram) are depicted in Fig. 13 (b) for the three developed and updated FEMs. Based on Fig. 13 (a), The average ADFVs are decreased by considering the SSI effect in the numerical models, and the DM model is considered as the most robust model with an average ADFV of 1.6%.

This claim is also approved based on Fig. 13 (b) since higher MAC values are derived from the models that SSI effects are considered. Furthermore, the DM model is considered as the closest updated model to the test in terms of the mode shapes. The MAC values of the first two modes do not change considerably for the FB and SM models, but the MAC values of the higher modes are increased in the SM model. Moreover, in the DM model compared to the SM model, MAC values of the first modes are improved, but no significant improvement is reached for other modes.

6.2. Comparison of updated material properties

In order to compare the material properties of the updated models, E_z is the most effective parameter on the first two natural frequencies, G_{xz} and G_{yz} are effective parameters on higher modes that are chosen based on the performed sensitivity analysis. Fig. 14 shows the average values of the parameters for each floor that is presented for the three models. The changes in material properties in different floors for the FB model are not as significant as the other two models. Furthermore, based on Fig. 14 (a), in both models with SSI effects, E_z of the second floor has a lower value compared to the other two floors. Based on Fig. 14 (b) and (c), the shear modulus of the second floor is more than two other floors in the DM model, but it is not reported in two other models. Except for the E_z of the second floor and the SM model, other updated material properties for the models with SSI effects are more than the FB model. Therefore, in terms of linear material properties effective on the structural stiffness, calibrated results of the FB model are conservative with lower values.

Updated values for the spring stiffnesses of the boundary condition of the SM model and average values of the selected material

Table 2
OMA and FEA natural frequencies and ADFVs for the first five modes of the FB model.

Modes	OMA frequencies (f_e)	FEA frequencies (f_a)	ADFV (%)
1	5.778	5.757	0.365
2	6.063	6.009	0.899
3	13.428	10.964	22.473
4	15.747	17.513	10.084
5	16.398	18.165	9.727

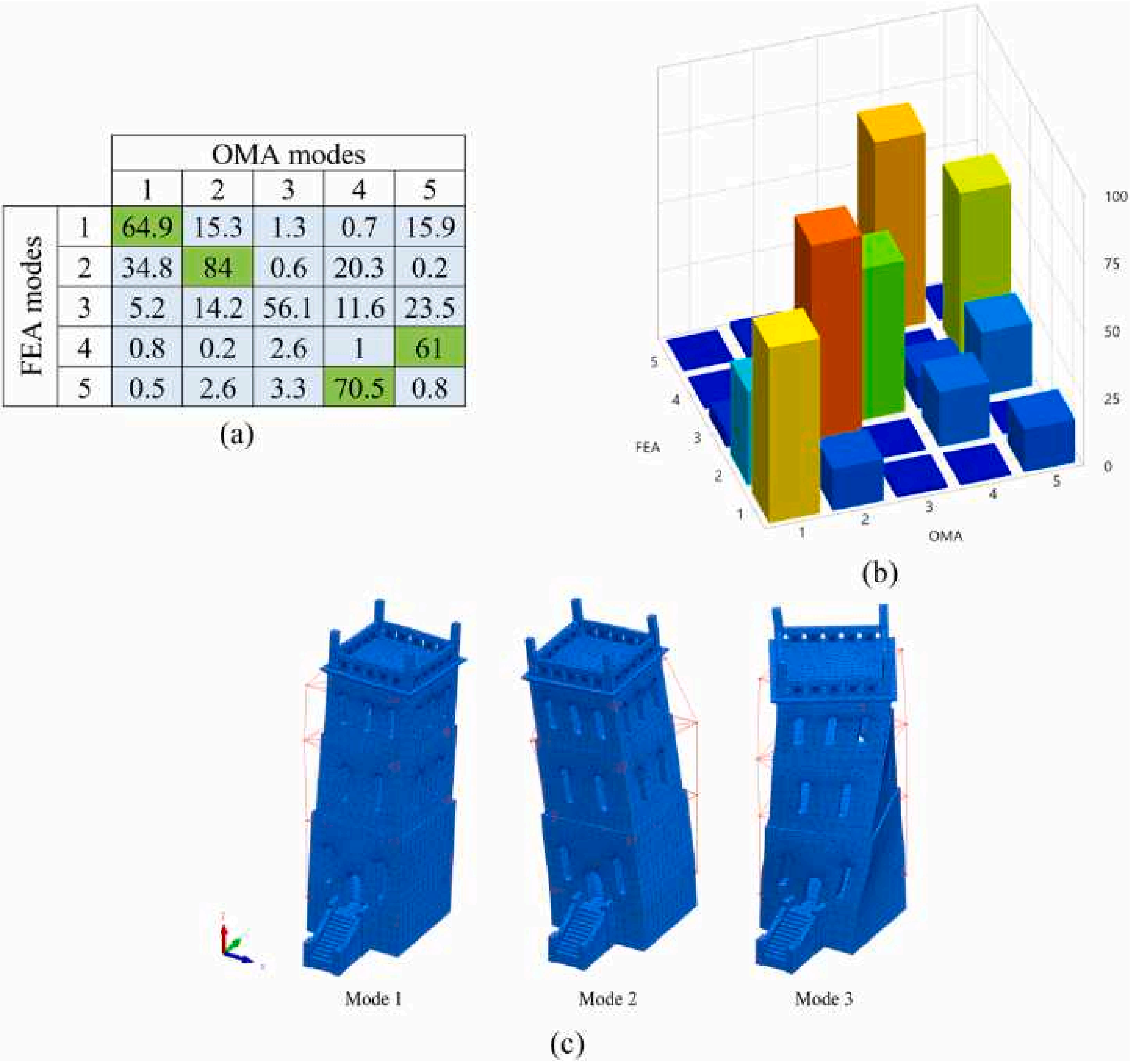

		OMA modes				
		1	2	3	4	5
FEA modes	1	64.9	15.3	1.3	0.7	15.9
	2	34.8	84	0.6	20.3	0.2
	3	5.2	14.2	56.1	11.6	23.5
	4	0.8	0.2	2.6	1	61
	5	0.5	2.6	3.3	70.5	0.8

Fig. 10. (a) MAC matrix, (b) 3D MAC plot, and (c) mode shape pairing of the first three modes of the FB model after model updating.

Table 3
OMA and FEA natural frequencies and ADFVs for the first five modes of the SM model.

Modes	OMA frequencies (f_e)	FEA frequencies (f_a)	ADFV (%)
1	5.778	6.065	4.963
2	6.063	6.11	0.774
3	13.428	13.661	1.738
4	15.747	16.816	6.789
5	16.398	17.61	7.398

properties of the soil and foundation are presented in Table 5. The normal reaction factor of the soil-foundation is increased, but the shear values for all to directions are decreased after the calibration process in the SM model. For the DM model, no significant change can be seen for the foundation and soil compared to the changes of the spring stiffnesses in the SM model.

7. Resonance effect and dynamic analysis

In this section, firstly, the resonance effect has been evaluated for the tower based on the calibrated DM model. Moreover, a code equation has confirmed the results from the modal analysis of the soil media in the DM model. Afterward, time history analysis was performed on the three calibrated models by applying two seismic records, and the results were compared.

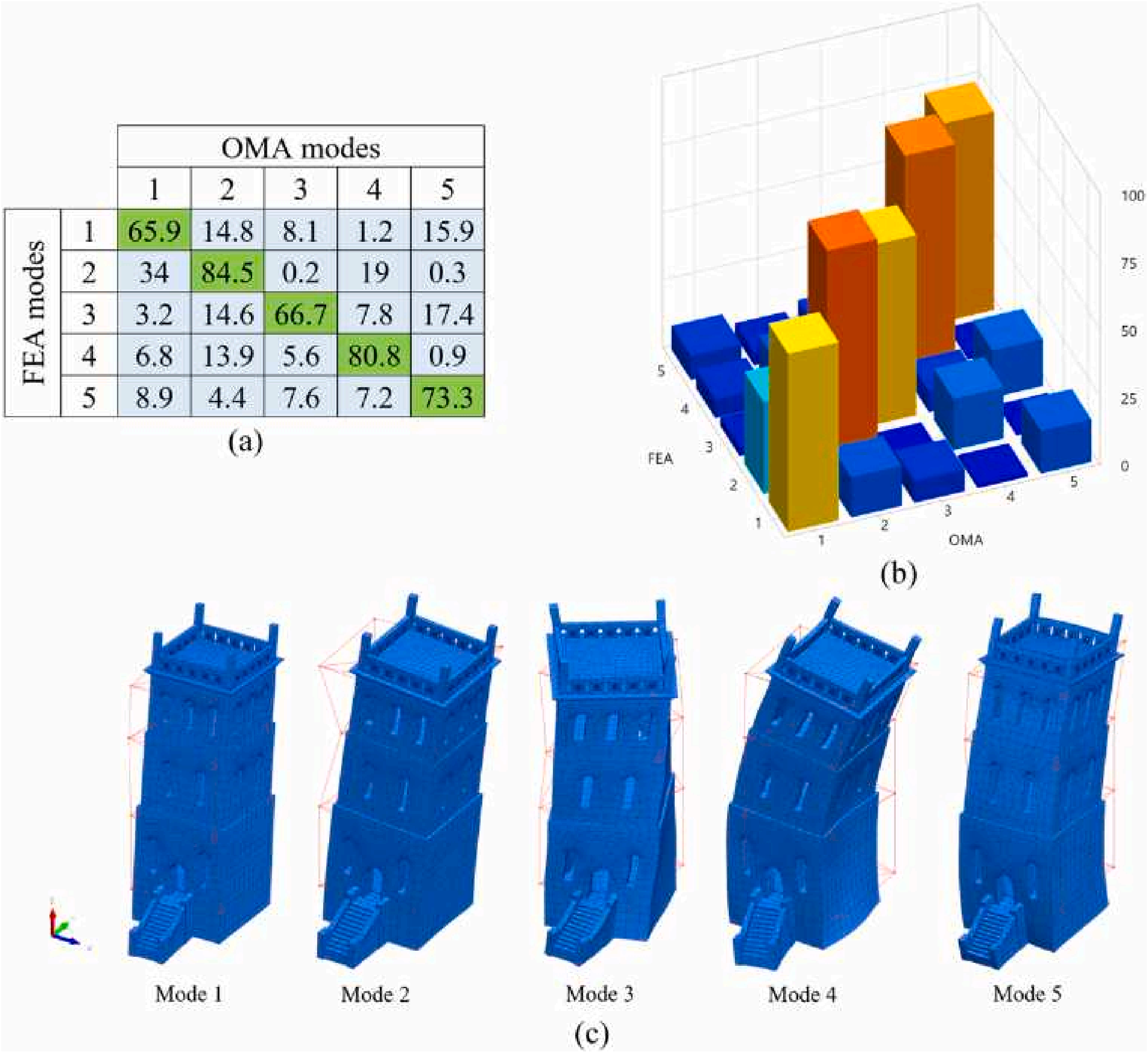

		OMA modes				
		1	2	3	4	5
FEA modes	1	65.9	14.8	8.1	1.2	15.9
	2	34	84.5	0.2	19	0.3
	3	3.2	14.6	66.7	7.8	17.4
	4	6.8	13.9	5.6	80.8	0.9
	5	8.9	4.4	7.6	7.2	73.3

(a)

(b)

(c)

Fig. 11. (a) MAC matrix, (b) 3D MAC plot, and (c) mode shape pairing of the first five modes of the SM model after model updating.

Table 4
OMA and FEA natural frequencies and ADFVs for the first five modes of the DM model.

Modes	OMA frequencies (f_e)	FEA frequencies (f_a)	ADFV (%)
1	5.778	5.838	1.05
2	6.063	6.123	0.99
3	13.428	13.53	0.76
4	15.747	16.22	3
5	16.398	16.773	2.29

7.1. Resonance effect

The fundamental period of the soil box of the calibrated DM model is 0.044 s based on the modal analysis. In order to confirm the result of the modal analysis of the FEM, the fundamental period of the soil box was calculated using Eq. (4) presented by SHAKE code [82].

$$T = \frac{4SLT}{(2n-1)V_s} \tag{4}$$

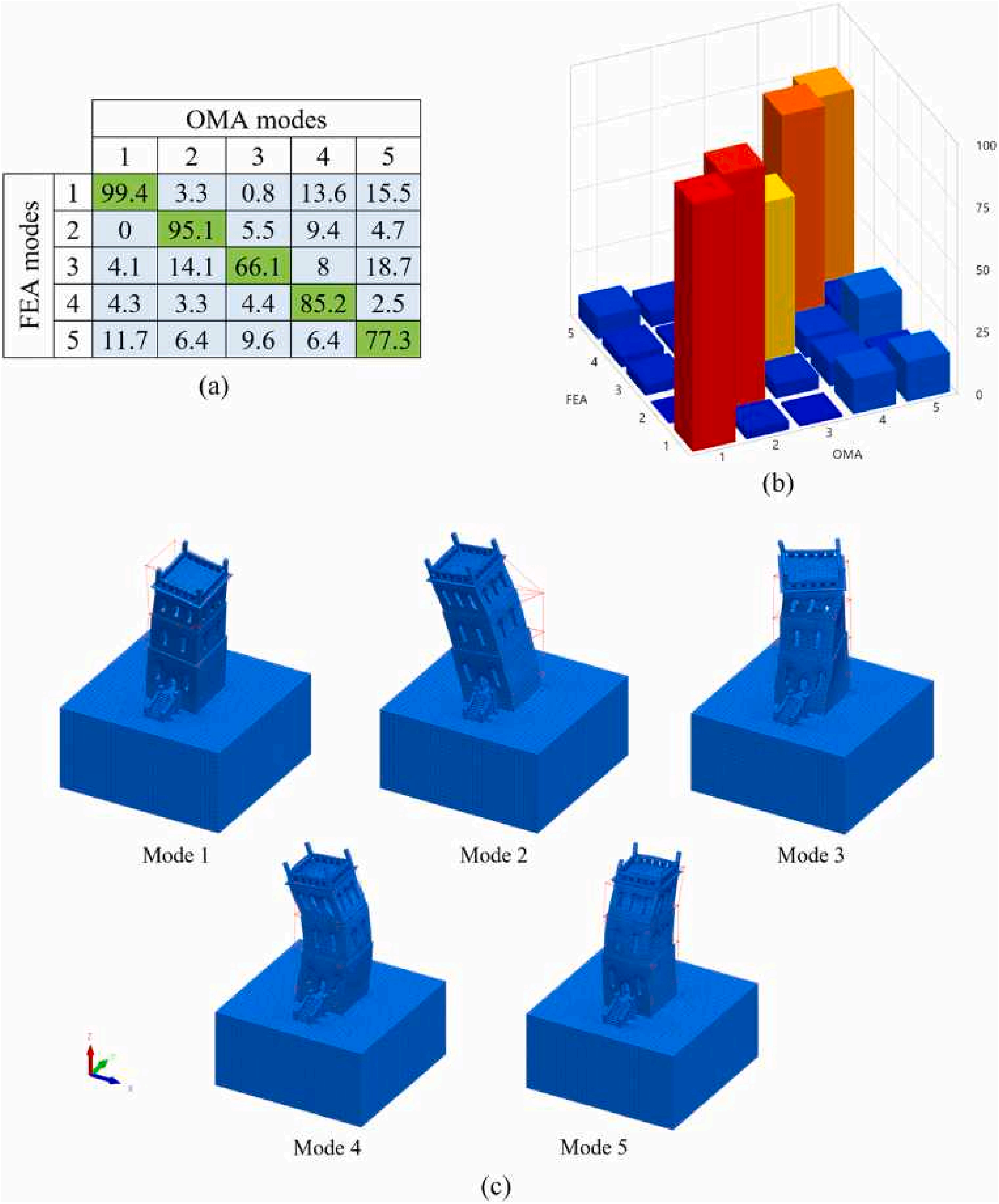

FEA modes	OMA modes 1	2	3	4	5
1	99.4	3.3	0.8	13.6	15.5
2	0	95.1	5.5	9.4	4.7
3	4.1	14.1	66.1	8	18.7
4	4.3	3.3	4.4	85.2	2.5
5	11.7	6.4	9.6	6.4	77.3

(a)

(b)

(c)

Fig. 12. (a) MAC matrix, (b) 3D MAC plot, and (c) mode shape pairing of the first five modes of the DM model after model updating.

Where T is the fundamental period of soil, SLT is the soil layer thickness above the bedrock, n is the mode number and V_s is the soil shear wave velocity.

Considering 11 m for SLT based on the model assumption, and 1000 $\frac{m}{s}$ for the V_s as suggested in [21], for hard soil, 0.044 s is calculated as the fundamental period ($n = 1$) and confirms the results from the finite element analysis. However, natural period of the tower is more than three times the fundamental period of soil. Therefore, the resonance effect cannot influence the tower structural

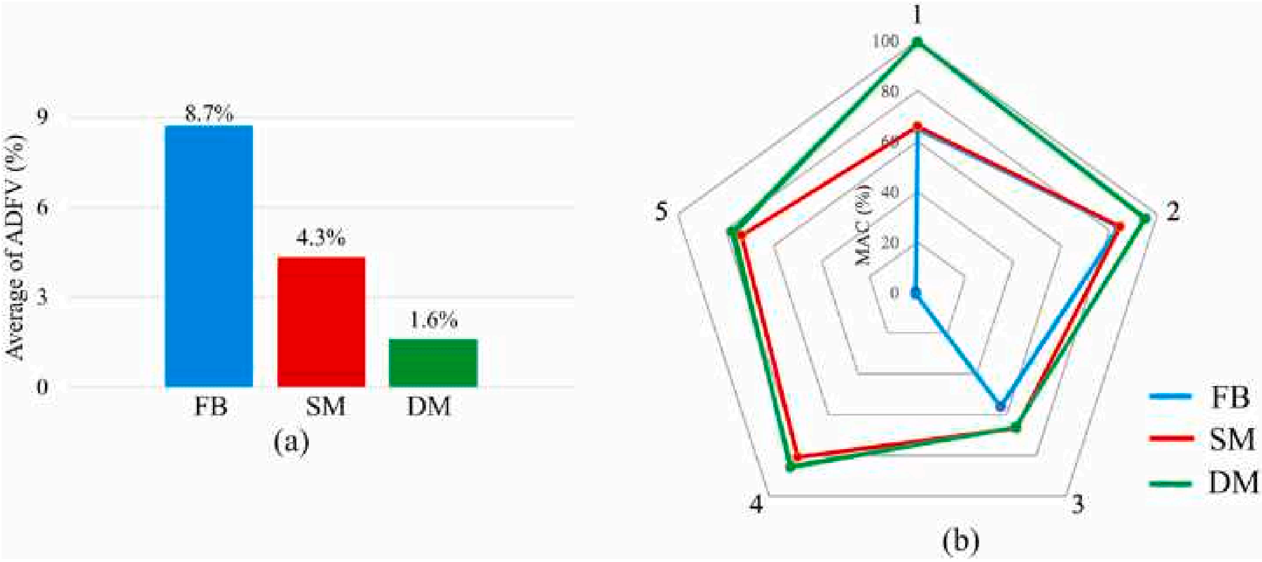

Fig. 13. (a) Average values of the ADFVs, and (b) MAC values for the first five modes of the three developed models.

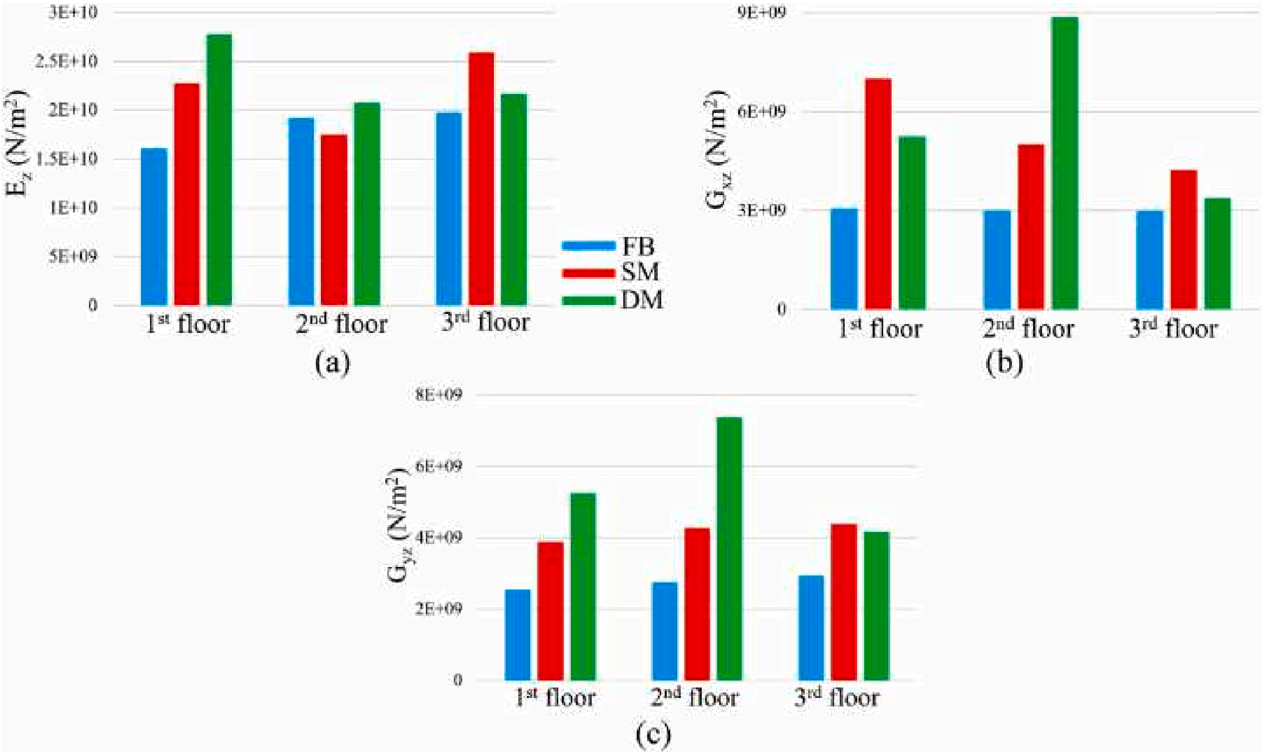

Fig. 14. Updated values of the three developed FEMs presented for three floors: (a) E_z, (b) G_{xz}, and (c) G_{yz}.

behavior subjected to vibrations.

7.2. Time history analysis

Tønsberg is located in a low seismicity zone with peak ground acceleration (PGA) of 0.02–0.03 g, as illustrated in the seismic hazard map [83], in Fig. 15 (a). However, in order to perform a comparative study on the structural response of the calibrated models subjected to seismic excitations, linear time history analysis was carried out by applying two far-field seismic records in the X direction. Fig. 15 (b) and (c) shows the acceleration versus time plots of Manjil and Northridge seismic records that have been chosen from the PEER strong ground motions database [84], and detail about them are provided in Table 6.

Rayleigh damping coefficients were computed considering 5% damping ratio for the first and third modes of vibration [85]. For the DM model, mass and stiffness damping coefficients of hard soil are $3.92\,\frac{1}{s}$ and $0.00047\,s$ based on [21]. The results of top

Table 5
Base and updated values of soil parameters in SM and DM models.

Model name	Parameter	Base value	Updated value
SM (GPa/m)	K_x	0.512	0.15
	K_y	0.512	0.15
	K_z	51. 2	114
DM (foundation in GPa)	E_z	40	41.1
	G_{xz}	6	5.97
	G_{yz}	6	5.61
DM (soil in GPa)	E_z	6	5.4
	G_{xz}	0.9	1.05
	G_{yz}	0.9	0.63

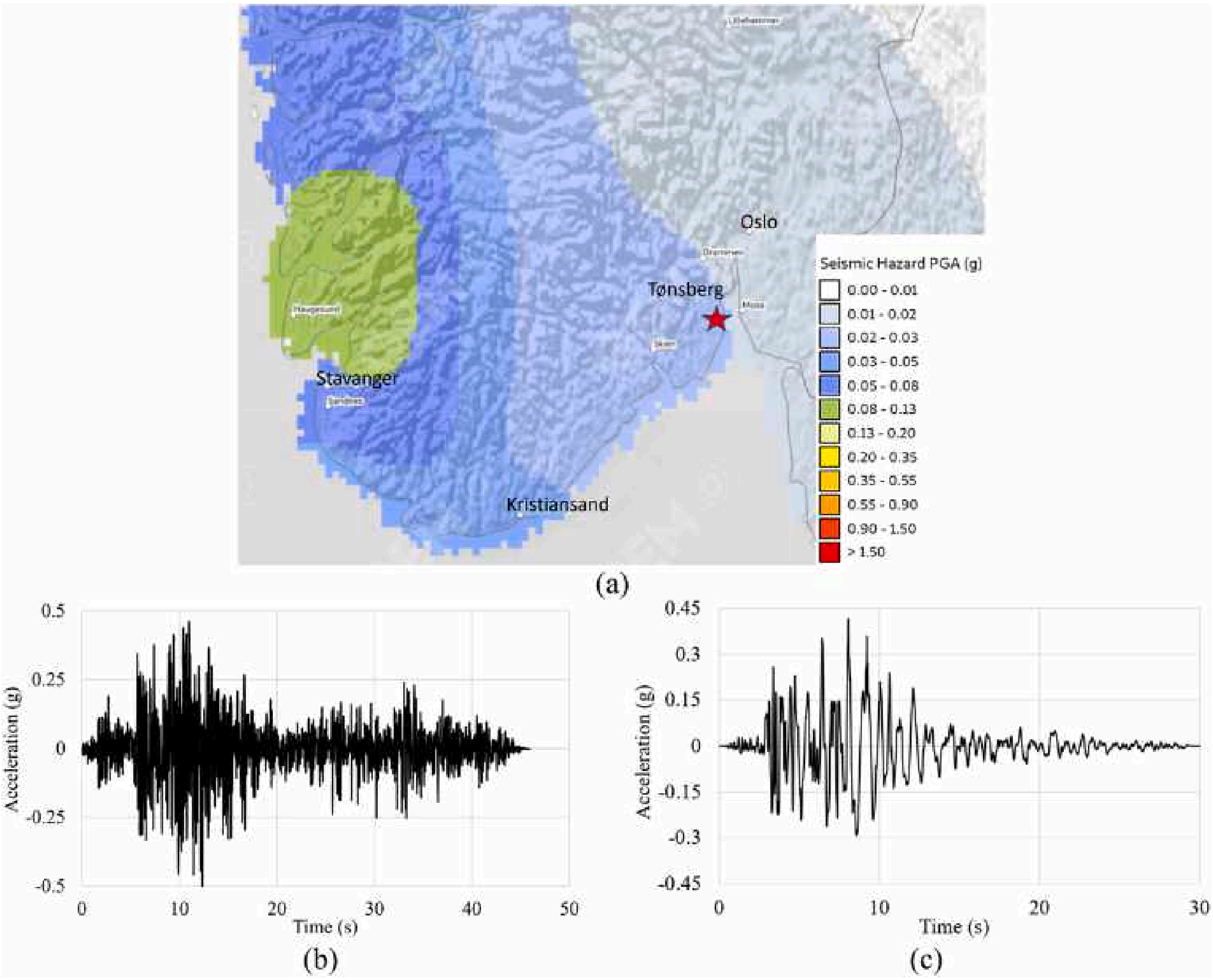

Fig. 15. (a) Seismic hazard map of southern Norway cities including Tønsberg [83], and acceleration versus time plots of (b) Manjil and (c) Northridge seismic records [84].

Table 6
Detail of the Manjil and Northridge seismic records [84].

Event	Station	Year	Magnitude	Duration (s)	Time step (s)	PGA (g)	Arias intensity $(\frac{m}{s})$
Manjil	Abbar	1990	7.37	45.96	0.02	0.49687	7.5
Northridge	Beverly Hills	1994	6.69	29.99	0.01	0.416	4.5

displacement versus time of the three models are presented in Fig. 16 (a) and (b) for Manjil and Northridge records, respectively. Furthermore, to facilitate the comparison, maximum top displacement values of all models are presented in Fig. 16 (c) for both records. Negligible differences can be detected and differences between the maximum top displacement (less than 10%). As it is shown in Fig. 16 (c), maximum inter-story drift ratios (IDR) of the DM model subjected to both records are more than other models. Therefore, FB and SM models show more conservative results in terms of IDR, which is a parameter for defining structural safety. IDR of 0.13% is considered for light damage, which is the first limit state for stone and brick masonry buildings based on [86]. The maximum IDR values of the tower for both analyzes are less than 0.13% which can confirm the tower passed the acceptability check and did not satisfy the failure criteria.

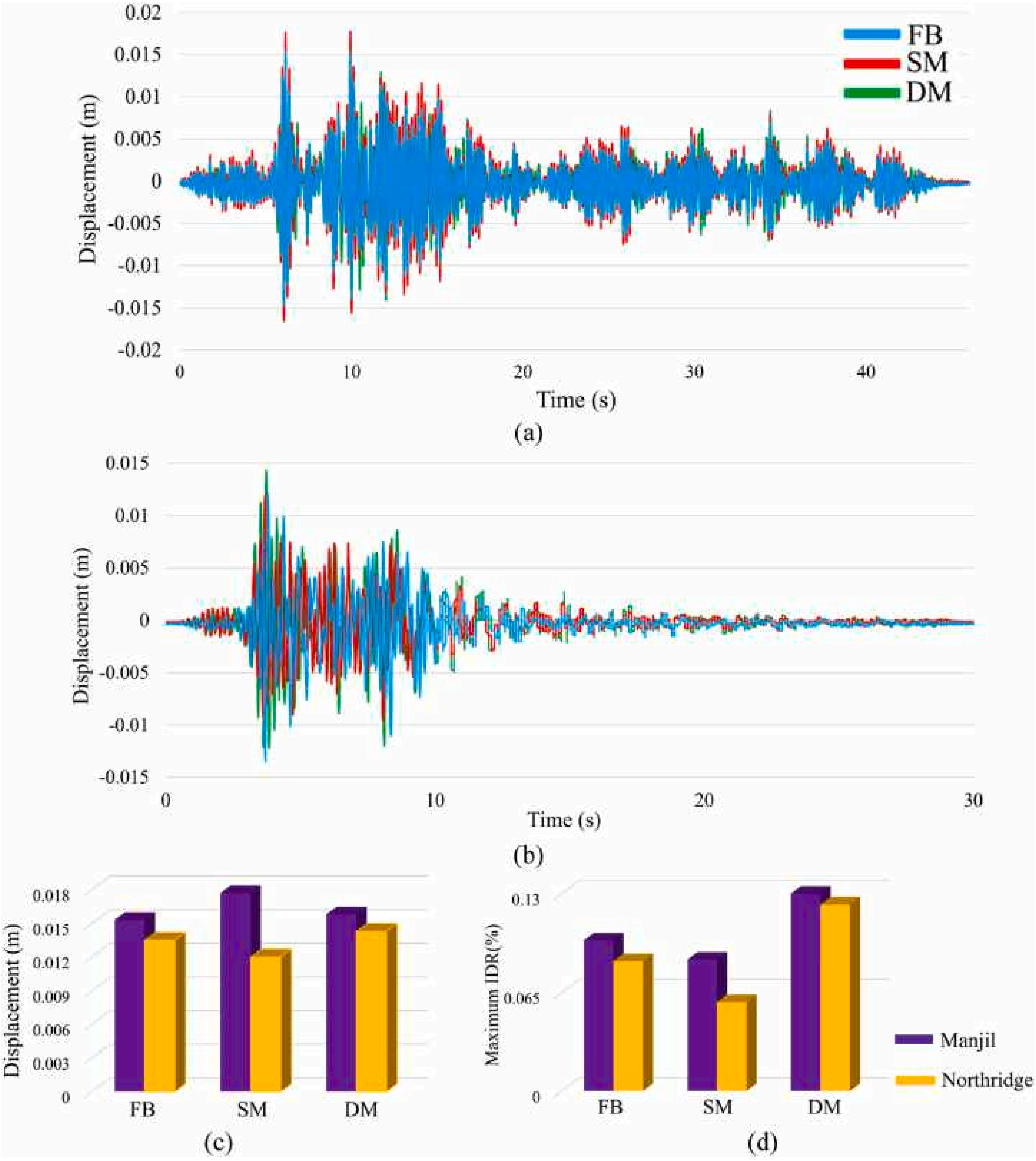

Fig. 16. Top displacement versus time plot for (a) Manjil, and (b) Northridge seismic records' analyses, (c) top displacement and (c) maximum IDR values of the models for two seismic records' analyses.

8. Conclusion

A framework for developing digital twins of the cultural heritage assets is proposed using 3D laser scanners and accelerometer sensors, and its application is investigated on a case study called Slottsfjell tower in Tønsberg, Norway. Geometrical survey of the tower was conducted using 3D laser scanners and a semi-automatic procedure for converting the point clouds to the FEM is presented in this study. Afterward, system identification of the tower was carried out by performing AVT and OMA. Three different frequency domain OMA techniques were utilized to define the natural frequencies and corresponding mode shapes of the tower. Since destructive tests are not allowed on cultural heritage assets, vibration-based FEM updating is done to investigate the material properties of different parts of the tower. Mechanical properties of the tønsbergite stone were utilized to derive the base values of the material properties of the homogenized masonry for performing the FEM updating. To investigate the influence of the SSI on the FEM updating results, three FEMs were developed. In the FB model, the SSI was neglected by considering rigid boundary conditions, the SM model was developed by modeling triaxial springs beneath the structure and the DM model was generated by modeling the foundation and soil box using the direct method. Firstly, a sensitivity analysis was performed on the three developed FEMs so that E_z, G_{xz}, G_{yz} are the most effective parameters effective on the frequency values. Unlike E_z, which is effective on the first two modes, G_{xz} and G_{yz} are effective on higher modes. Properties of soil are not as effective as the masonry properties in the DM model, but in the SM model, soil spring stiffnesses are considered as the most effective parameters. After performing FEM updating of the models, ADFVs and MAC values show that the FB model is paired with the test results on the first two modes. By considering the SSI effects in the SM model, the ADFVs and MAC values enhanced for the higher modes, and in the DM model as the most detailed model, the correlation is improved. The DM model is considered as the closest model to the real structure in terms of the frequency values and mode shapes. Moreover, it is investigated that updated material properties of the FB model are conservative compared to the other two models that SSI effects are considered. Fundamental periods of soil and structure are computed for the DM model separately that are not close to each other. It confirms that the tower is not at the risk of resonance effect. Furthermore, linear time history analyses were carried out by applying two strong ground motions. The results show negligible differences in term of the top displacement, but the maximum IDR values of DM model are more than the other two models. Although, it is tried to calibrate the models based on the OMA results, and the updated material properties of the FB model are conservative, the larger values of maximum IDR are concluded from dynamic analyses of DM model. SSI is effective on the dynamic response of structures that can facilitate the FEM updating procedure to obtain reliable enough FEMs for performing vulnerability assessments. Nonlinear time history analyses using various seismic records with different characteristics as well as performing in-situ tests on soil layers' material properties are still needed to be done to evaluate the reliability of various SSI modeling approaches.

Declaration of Competing Interest

The authors declare that they have no known competing financial interests or personal relationships that could have appeared to influence the work reported in this paper.

Acknowledgements

This work is a part of the HYPERION project. HYPERION has received funding from the European Union's Framework Programme for Research and Innovation (Horizon 2020) under Grant agreement no. 821054. The contents of this publication are the sole responsibility of Oslo Metropolitan University (Work Package 5, Task 2) and do not necessarily reflect the opinion of the European Union.

References

[1] F.J. Pallarés, M. Betti, G. Bartoli, L. Pallarés, Structural health monitoring (SHM) and Nondestructive testing (NDT) of slender masonry structures: a practical review, Constr. Build. Mater. 297 (2021), 123768, https://doi.org/10.1016/j.conbuildmat.2021.123768.

[2] A. Shabani, M. Kioumarsi, V. Plevris, H. Stamatopoulos, Structural vulnerability assessment of heritage timber buildings: a methodological proposal, Forests 11 (8) (2020) 881, https://doi.org/10.3390/f11080881.

[3] G. Standoli, E. Giordano, G. Milani, F. Clementi, Model updating of historical belfries based on oma identification techniques, Int. J. Archit. Herit. 15 (1) (2021) 132–156, https://doi.org/10.1080/15583058.2020.1723735.

[4] A. Shabani, M. Kioumarsi, M. Zucconi, State of the art of simplified analytical methods for seismic vulnerability assessment of unreinforced masonry buildings, Eng. Struct. 239 (2021), 112280, https://doi.org/10.1016/j.engstruct.2021.112280.

[5] G. Angjeliu, D. Coronelli, G. Cardani, Development of the simulation model for Digital Twin applications in historical masonry buildings: the integration between numerical and experimental reality, Comput. Struct. 238 (2020), 106282, https://doi.org/10.1016/j.compstruc.2020.106282.

[6] M. Korumaz, M. Betti, A. Conti, G. Tucci, G. Bartoli, V. Bonora, A.G. Korumaz, L. Fiorini, An integrated Terrestrial Laser Scanner (TLS), Deviation Analysis (DA) and Finite Element (FE) approach for health assessment of historical structures. A minaret case study, Eng. Struct. 153 (2017) 224–238, https://doi.org/10.1016/j.engstruct.2017.10.026.

[7] R.S. Panah, M. Kioumarsi, Application of building information modelling (BIM) in the health monitoring and maintenance process: a systematic review, Sensors 21 (3) (2021) 837, https://doi.org/10.3390/s21030837.

[8] G. Castellazzi, A.M. D'Altri, S. de Miranda, F. Ubertini, An innovative numerical modeling strategy for the structural analysis of historical monumental buildings, Eng. Struct. 132 (2017) 229–248, https://doi.org/10.1016/j.engstruct.2016.11.032.

[9] D.F. Laefer, L. Truong-Hong, Toward automatic generation of 3D steel structures for building information modelling, Autom. Constr. 74 (2017) 66–77, https://doi.org/10.1016/j.autcon.2016.11.011.

[10] L. Barazzetti, F. Banfi, R. Brumana, G. Gusmeroli, D. Oreni, M. Previtali, F. Roncoroni, G. Schiantarelli, BIM from laser clouds and finite element analysis: combining structural analysis and geometric complexity, ISPRS – International Archives of the Photogrammetry, Remote Sensing and Spatial Information Sciences XL-5/W4, 2015, pp. 345–50. ⟨http://dx.doi.org/10.5194/isprsarchives-XL-5-W4-345-2015⟩.

[11] G. Castellazzi, A.M. Altri, G. Bitelli, I. Selvaggi, A. Lambertini, From laser scanning to finite element analysis of complex buildings by using a semi-automatic procedure, Sensors 15 (8) (2015) 18360–18380, https://doi.org/10.3390/s150818360.

[12] G. Bartoli, M. Betti, V. Bonora, A. Conti, L. Fiorini, V.C. Kovacevic, V. Tesi, G. Tucci, From TLS data to FE model: a workflow for studying the dynamic behavior of the Pulpit by Giovanni Pisano in Pistoia (Italy), Procedia Struct. Integr. 29 (2020) 55–62, https://doi.org/10.1016/j.prostr.2020.11.139.

[13] C. Pepi, N. Cavalagli, V. Gusella, M. Gioffrè, An integrated approach for the numerical modeling of severely damaged historic structures: application to a masonry bridge, Adv. Eng. Softw. 151 (2021), 102935, https://doi.org/10.1016/j.advengsoft.2020.102935.

[14] N. Kassotakis, V. Sarhosis, Employing non-contact sensing techniques for improving efficiency and automation in numerical modelling of existing masonry structures: a critical literature review, Structures 32 (2021) 1777–1797, https://doi.org/10.1016/j.istruc.2021.03.111.

[15] S.L. Kramer, Geotechnical Earthquake Engineering, Pearson Education India, 1996.

[16] A. Shabani, A. Alinejad, M. Teymouri, A.N. Costa, M. Shabani, M. Kioumarsi, Seismic vulnerability assessment and strengthening of heritage timber buildings: a review, Buildings 11 (12) (2021) 661, https://doi.org/10.3390/buildings11120661.

[17] A. Fathi, A. Sadeghi, M.R. Emami Azadi, N. Hoveidaie, Assessing seismic behavior of a masonry historic building considering soil-foundation-structure interaction (case study of Arge-Tabriz), Int. J. Archit. Herit. 14 (6) (2020) 795–810, https://doi.org/10.1080/15583058.2019.1568615.

[18] V. Anand, S.R. Satish Kumar, Seismic soil-structure interaction: a state-of-the-art review, Structures 16 (2018) 317–326, https://doi.org/10.1016/j.istruc.2018.10.009.

[19] F. de Silva, F. Ceroni, S. Sica, F. Silvestri, Non-linear analysis of the Carmine bell tower under seismic actions accounting for soil–foundation–structure interaction, Bull. Earthq. Eng. 16 (7) (2018) 2775–2808, https://doi.org/10.1007/s10518-017-0298-0.

[20] A. Mortezaei, A. Motaghi, Seismic assessment of the world's tallest pure-brick tower including soil-structure interaction, J. Perform. Constr. Facil. 30 (5) (2016), 04016020, https://doi.org/10.1061/(ASCE)CF.1943-5509.0000861.

[21] E. Hökelekli, A. Al-Helwani, Effect of soil properties on the seismic damage assessment of historical masonry minaret–soil interaction systems, Struct. Des. Tall Spec. Build. 29 (2) (2020), e1694, https://doi.org/10.1002/tal.1694.

[22] Y.S. Erdogan, Discrete and continuous finite element models and their calibration via vibration and material tests for the seismic assessment of masonry structures, Int. J. Archit. Herit. 11 (7) (2017) 1026–1045, https://doi.org/10.1080/15583058.2017.1332255.

[23] A. Drougkas, E. Verstrynge, P. Szekér, G. Heirman, L.-E. Bejarano-Urrego, G. Giardina, K. Van Balen, Numerical modeling of a church nave wall subjected to differential settlements: soil-structure interaction, time-dependence and sensitivity analysis, Int. J. Archit. Herit. 14 (8) (2020) 1221–1238, https://doi.org/10.1080/15583058.2019.1602682.

[24] A. Rahmani, M. Taiebat, W.D. Liam Finn, C.E. Ventura, Evaluation of substructuring method for seismic soil-structure interaction analysis of bridges, Soil Dyn. Earthq. Eng. 90 (2016) 112–127, https://doi.org/10.1016/j.soildyn.2016.08.013.

[25] R. Mario Azzara, G. De Roeck, M. Girardi, C. Padovani, D. Pellegrini, E. Reynders, The influence of environmental parameters on the dynamic behaviour of the San Frediano bell tower in Lucca, Eng. Struct. 156 (2018) 175–187, https://doi.org/10.1016/j.engstruct.2017.10.045.

[26] P. Barsocchi, G. Bartoli, M. Betti, M. Girardi, S. Mammolito, D. Pellegrini, G. Zini, Wireless sensor networks for continuous structural health monitoring of historic masonry towers, Int. J. Archit. Herit. 15 (1) (2021) 22–44, https://doi.org/10.1080/15583058.2020.1719229.

[27] A. Bayraktar, İ. Çalik, T. Türker, A. Ashour, Restoration effects on experimental dynamic characteristics of masonry stone minarets, Mater. Struct. 51 (6) (2018) 141, https://doi.org/10.1617/s11527-018-1272-2.

[28] D. Bru, S. Ivorra, M. Betti, J.M. Adam, G. Bartoli, Parametric dynamic interaction assessment between bells and supporting slender masonry tower, Mech. Syst. Signal Process. 129 (2019) 235–249, https://doi.org/10.1016/j.ymssp.2019.04.038.

[29] C. Castagnetti, E. Bassoli, L. Vincenzi, F. Mancini, Dynamic assessment of masonry towers based on terrestrial radar interferometer and accelerometers, Sensors 19 (6) (2019) 1319, https://doi.org/10.3390/s19061319.

[30] B. Erdil, M. Tapan, İ. Akkaya, F. Korkut, Effects of structural parameters on seismic behaviour of historical masonry minaret, Period. Polytech. Civ. Eng. 62 (1) (2018) 148–161, https://doi.org/10.3311/PPci.10687.

[31] R.M. Azzara, M. Girardi, V. Iafolla, C. Padovani, D. Pellegrini, Long-term dynamic monitoring of medieval masonry towers, Front. Built Environ. 6 (9) (2020), https://doi.org/10.3389/fbuil.2020.00009.

[32] F. Ubertini, G. Comanducci, N. Cavalagli, Vibration-based structural health monitoring of a historic bell-tower using output-only measurements and multivariate statistical analysis, Struct. Health Monit. 15 (4) (2016) 438–457, https://doi.org/10.1177%2F1475921716643948.

[33] A. D'Ambrisi, V. Mariani, M. Mezzi, Seismic assessment of a historical masonry tower with nonlinear static and dynamic analyses tuned on ambient vibration tests, Eng. Struct. 36 (2012) 210–219, https://doi.org/10.1016/j.engstruct.2011.12.009.

[34] I. Capanna, R. Cirella, A. Aloisio, R. Alaggio, F. Di Fabio, M. Fragiacomo, Operational modal analysis, model update and fragility curves estimation, through truncated incremental dynamic analysis, of a masonry belfry, Buildings 11 (3) (2021) 120, https://doi.org/10.3390/buildings11030120.

[35] E. García-Macías, L. Ierimonti, I. Venanzi, F. Ubertini, An innovative methodology for online surrogate-based model updating of historic buildings using monitoring data, Int. J. Archit. Herit. 15 (1) (2021) 92–112, https://doi.org/10.1080/15583058.2019.1668495.

[36] C. Gentile, A. Saisi, A. Cabboi, Structural identification of a masonry tower based on operational modal analysis, Int. J. Archit. Herit. 9 (2) (2015) 98–110, https://doi.org/10.1080/15583058.2014.951792.

[37] G. Lacanna, M. Betti, M. Ripepe, G. Bartoli, Dynamic identification as a tool to constrain numerical models for structural analysis of historical buildings, Front. Built Environ. 6 (40) (2020), https://doi.org/10.3389/fbuil.2020.00040.

[38] A.C. Altunişik, A.F. Genç, M. Günaydin, F.Y. Okur, O.Ş. Karahasan, Dynamic response of a historical armory building using the finite element model validated by the ambient vibration test, J. Vib. Control 24 (22) (2018) 5472–5484, https://doi.org/10.1177%2F1077546318755559.

[39] E. Bassoli, L. Vincenzi, A.M. D'Altri, S. de Miranda, M. Forghieri, G. Castellazzi, Ambient vibration-based finite element model updating of an earthquake-damaged masonry tower, Struct. Control Health Monit. 25 (5) (2018), e2150, https://doi.org/10.1002/stc.2150.

[40] R. Lancellotta, D. Sabia, Identification technique for soil-structure analysis of the Ghirlandina Tower, Int. J. Archit. Herit. 9 (4) (2015) 391–407, https://doi.org/10.1080/15583058.2013.793438.

[41] M. Ferraioli, L. Miccoli, D. Abruzzese, A. Mandara, Dynamic characterisation and seismic assessment of medieval masonry towers, Nat. Hazards 86 (2) (2017) 489–515, https://doi.org/10.1007/s11069-016-2519-2.

[42] L.F. Ramos, L. Marques, P.B. Lourenço, G. De Roeck, A. Campos-Costa, J. Roque, Monitoring historical masonry structures with operational modal analysis: two case studies, Mech. Syst. Signal Process. 24 (5) (2010) 1291–1305, https://doi.org/10.1016/j.ymssp.2010.01.011.

[43] F. Ceroni, S. Sica, M. Rosaria Pecce, A. Garofano, Evaluation of the natural vibration frequencies of a historical masonry building accounting for SSI, Soil Dyn. Earthq. Eng. 64 (2014) 95–101, https://doi.org/10.1016/j.soildyn.2014.05.003.

[44] A. Karatzetzou, D. Pitilakis, S. Karafagka, System identification of mosques resting on soft soil. the case of the Suleiman mosque in the Medieval City of Rhodes, Greece, Geosciences 11 (7) (2021) 275, https://doi.org/10.3390/geosciences11070275.

[45] S. Gönen, S. Soyöz, Seismic analysis of a masonry arch bridge using multiple methodologies, Eng. Struct. 226 (2021), 111354, https://doi.org/10.1016/j.engstruct.2020.111354.

[46] K. Demirlioglu, S. Gonen, S. Soyoz, M.P. Limongelli, In-plane seismic response analyses of a historical brick masonry building using equivalent frame and 3D FEM modeling approaches, Int. J. Archit. Herit. 14 (2) (2020) 238–256, https://doi.org/10.1080/15583058.2018.1529208.

[47] H. Güllü, F. Özel, Microtremor measurements and 3D dynamic soil–structure interaction analysis for a historical masonry arch bridge under the effects of near- and far-fault earthquakes, Environ. Earth Sci. 79 (13) (2020) 338, https://doi.org/10.1007/s12665-020-09086-0.

[48] F. Ubertini, N. Cavalagli, A. Kita, G. Comanducci, Assessment of a monumental masonry bell-tower after 2016 Central Italy seismic sequence by long-term SHM, Bull. Earthq. Eng. 16 (2) (2018) 775–801, https://doi.org/10.1007/s10518-017-0222-7.

[49] H. Güllü, H.S. Jaf, Full 3D nonlinear time history analysis of dynamic soil–structure interaction for a historical masonry arch bridge, Environ. Earth Sci. 75 (21) (2016) 1421, https://doi.org/10.1007/s12665-016-6230-0.

[50] A. Shabani, M. Kioumarsi, A novel macroelement for seismic analysis of unreinforced masonry buildings based on MVLEM in OpenSees, J. Build. Eng. 49 (2022), 104019, https://doi.org/10.1016/j.jobe.2022.104019.

[51] A.M. Chandler, N.T.K. Lam, M.N. Sheikh, Response spectrum predictions for potential near-field and far-field earthquakes affecting Hong Kong: soil sites, Soil Dyn. Earthq. Eng. 22 (6) (2002) 419–440, https://doi.org/10.1016/S0267-7261(02)00041-6.

[52] N.T.K. Lam, J.L. Wilson, A.M. Chandler, Seismic displacement response spectrum estimated from the frame analogy soil amplification model, Eng. Struct. 23 (11) (2001) 1437–1452, https://doi.org/10.1016/S0141-0296(01)00049-9.

[53] H. Güllü, M. Pala, On the resonance effect by dynamic soil–structure interaction: a revelation study, Nat. Hazards 72 (2) (2014) 827–847, https://doi.org/10.1007/s11069-014-1039-1.

[54] M. Tolun, B. Emirler, A. Yildiz, H. Güllü, Dynamic response of a single pile embedded in sand including the effect of resonance, Period. Polytech. Civ. Eng. 64 (4) (2020) 1038–1050, https://doi.org/10.3311/PPci.15027.

[55] ReCap, Autodesk ReCap Pro, California, U.S, 2021.

[56] Revit, Autodesk Revit BIM (Building Information Modeling), California, U.S, 2021.

[57] DIANA, Diana User's Manual, Release 10.4, DIANA FEA BV, Delft University of Technology, Netherland, 2020.

[58] M.A. Adam, T.S. El-Salakawy, M.A. Salama, A.A. Mohamed, Assessment of structural condition of a historic masonry minaret in Egypt, Case Stud. Constr. Mater. 13 (2020), e00409, https://doi.org/10.1016/j.cscm.2020.e00409.

[59] K.V. Katakalos, I.A. Arnaoutis, G.C. Manos, Identification of failure mechanism of the ottoman bath (hamam) at apollonia (pazarouda) exploiatation of historical data, Case Stud. Constr. Mater. 14 (2021), e00475, https://doi.org/10.1016/j.cscm.2020.e00475.

[60] A. Shabani, S. Erfani, Seismic performance evaluation of SSMF with simple beam–column connections under the base level, Int. J. Steel Struct. 20 (1) (2020) 89–100, https://doi.org/10.1007/s13296-019-00273-9.

[61] E. Winkler, Die Lehre von der Elasticitaet und Festigkeit: mit besonderer Rücksicht auf ihre Anwendung in der Technik, für polytechnische Schulen, Bauakademien, Ingenieure, Maschinenbauer, Architecten, etc, H. Dominicus, 1867.

[62] M. Choinière, P. Paultre, P. Léger, Influence of soil-structure interaction on seismic demands in shear wall building gravity load frames, Eng. Struct. 198 (2019), 109259, https://doi.org/10.1016/j.engstruct.2019.05.100.

[63] C. Yoo, Interaction between tunneling and bridge foundation – a 3D numerical investigation, Comput. Geotech. 49 (2013) 70–78, https://doi.org/10.1016/j.compgeo.2012.11.005.

[64] Dynamic Design Solutions, FEMtools 4, Leuven, Belgium, 2021.

[65] I.T. Rosenqvist, Electron-microscope investigations of larvikite and tönsbergite feldspars, Nor. Geol. Tidsskr. 45 (1) (1965) 69–71.

[66] A. Ademi, Finite Element Model Updating of A Stone Masonry Tower Using 3D Laser Scanner and Accelerometers, Department of Civil Engineering and Energy Technology, Oslo Metropolitan University, Oslo, Norway, 2020.

[67] J.S. Petersen, Structure of the larvikite-lardalite complex, Oslo-region, Norway, and its evolution, Geol. Rundsch. 67 (1) (1978) 330–342.

[68] A. Palmström, R. Singh, The deformation modulus of rock masses—comparisons between in situ tests and indirect estimates, Tunn. Undergr. Space Technol. 16 (2) (2001) 115–131, https://doi.org/10.1016/S0886-7798(01)00038-4.

[69] B. Ghiassi, A.T. Vermelfoort, P.B. Lourenço, Chapter 7 – masonry mechanical properties, in: B. Ghiassi, G. Milani (Eds.), Numerical Modeling of Masonry and Historical Structures, Woodhead Publishing, 2019, pp. 239–261, https://doi.org/10.1016/B978-0-08-102439-3.00007-5.

[70] R. Zavalis, B. Jonaitis, P.B. Lourenço, Analysis of bed joint influence on masonry modulus of elasticity, in: Proceedings of the 9th International Masonry Conference 2014, Guimarães, Portugal, 2014.

[71] P. Croce, M.L. Beconcini, P. Formichi, P. Cioni, F. Landi, C. Mochi, F. De Lellis, E. Mariotti, I. Serra, Shear modulus of masonry walls: a critical review, Procedia Struct. Integr. 11 (2018) 339–346, https://doi.org/10.1016/j.prostr.2018.11.044.

[72] A.B. Vesić, Bending of beams resting on isotropic elastic solid, J. Eng. Mech. Div. 87 (2) (1961) 35–53.

[73] L.R. Herrmann, Finite element analysis of contact problems, J. Eng. Mech. Div. 104 (5) (1978) 1043–1057.

[74] S. Shamloo, M. Imani, Subgrade reaction modulus of rock masses under the load of single and multiple footings, Geomech. Geoengin. (2021) 1–19, https://doi.org/10.1080/17486025.2021.1889687.

[75] R. Ribeiro, R. Lameiras, Evaluation of low-cost MEMS accelerometers for SHM: frequency and damping identification of civil structures, Lat. Am. J. Solids Struct. 16 (2019) 203, https://doi.org/10.1590/1679-78255308.

[76] A. Shabani, A. Ademi, M. Kioumarsi, Structural Model Updating of a Historical Stone Masonry Tower in Tønsberg, Norway, Springer International Publishing, Cham, 2022, pp. 576–585, https://doi.org/10.1007/978-3-030-90788-4_45.

[77] F.B. Zahid, Z.C. Ong, S.Y. Khoo, A review of operational modal analysis techniques for in-service modal identification, J. Braz. Soc. Mech. Sci. Eng. 42 (8) (2020) 398, https://doi.org/10.1007/s40430-020-02470-8.

[78] R. Brincker, C. Ventura, Introduction to Operational Modal Analysis, John Wiley & Sons, 2015.

[79] N.-J. Jacobsen, P. Andersen, R. Brincker, Applications of frequency domain curve-fitting in the EFDD technique, in: Conference Proceedings: IMAC-XXVI: A Conference & Exposition on Structural Dynamics, Society for Experimental Mechanics, 2008.

[80] M. Masjedian, M. Keshmiri, A review on operational modal analysis researches: classification of methods and applications, in: Proceedings of the 3rd IOMAC, 2009, pp. 707–18.

[81] SVIBS, ARTeMIS Modal, Structural Vibration Solution, Aalborg, Denmark, 2021.

[82] P.B. Schnabel, SHAKE: A Computer Program for Earthquake Response Analysis of Horizontally Layered Sites (EERC Report 72-12), University of California, Berkeley, 1972.

[83] V. Silva, D. Amo-Oduro, A. Calderon, J. Dabbeek, V. Despotaki, L. Martins, A. Rao, M. Simionato, D. Viganò, C. Yepes, Global earthquake model (GEM) seismic risk map (version 2018.1), 2018.

[84] PEER, PEER ground motion database, NGA West2, 2014. (Accessed 18 January 2022).

[85] H. Güllü, M. Karabekmez, Effect of near-fault and far-fault earthquakes on a historical masonry mosque through 3D dynamic soil-structure interaction, Eng. Struct. 152 (2017) 465–492, https://doi.org/10.1016/j.engstruct.2017.09.031.

[86] B. Borzi, H. Crowley, R. Pinho, Simplified pushover-based earthquake loss assessment (SP-BELA) method for masonry buildings, Int. J. Archit. Herit. 2 (4) (2008) 353–376, https://doi.org/10.1080/15583050701828178.

Paper VIII

Shabani, A., Kioumarsi, M., Plevris, V.

Performance-based seismic assessment of a historical masonry arch bridge: Effect of pulse-like excitations

(2023) Frontiers of Structural and Civil Engineering,
https://doi.org/10.1007/s11709-023-0972-z.

Front. Struct. Civ. Eng.
https://doi.org/10.1007/s11709-023-0972-z

RESEARCH ARTICLE

Performance-based seismic assessment of a historical masonry arch bridge: Effect of pulse-like excitations

Amirhosein SHABANI[a], **Mahdi KIOUMARSI**[a*], **Vagelis PLEVRIS**[b]

[a] *Department of Built Environment, Oslo Metropolitan University, Oslo 0166, Norway*
[b] *Department of Civil and Architectural Engineering, Qatar University, Doha 2713, Qatar*
[*] *Corresponding author. E-mail: mahdi.kioumarsi@oslomet.no*

ABSTRACT Seismic analysis of historical masonry bridges is important for authorities in all countries hosting such cultural heritage assets. The masonry arch bridge investigated in this study was built during the Roman period and is on the island of Rhodes, in Greece. Fifteen seismic records were considered and categorized as far-field, pulse-like near-field, and non-pulse-like near-field. The earthquake excitations were scaled to a target spectrum, and nonlinear time-history analyses were performed in the transverse direction. The performance levels were introduced based on the pushover curve, and the post-earthquake damage state of the bridge was examined. According to the results, pulse-like near-field events are more damaging than non-pulse-like near-field ground motions. Additionally the bridge is more vulnerable to far-field excitations than near-field events. Furthermore, the structure will suffer extensive post-earthquake damage and must be retrofitted.

KEYWORDS masonry arch bridges, seismic behavior, modal properties, pulse-like records, nonlinear time history analysis

1 Introduction

Masonry arches are one of the earliest structural forms that have been used for thousands of years as parts of structures such as bridges and cathedrals [1]. It is widely accepted that the use of the arch as a structural form was developed independently in China and the Middle East more than 5000 years ago [2]. Masonry arch bridges still play a crucial role in transportation infrastructure in European countries because they form a significant part of the road and railway bridge inventory [3]. Historical masonry arch bridges must be preserved because of their importance as cultural heritage assets that carry lessons from past generations, in addition to their functional value as important infrastructure. Historical masonry arch bridges have been exposed to material degradation, scouring effects on boundary conditions, and changes in applied loads during their lifetime. In addition, they have been exposed to exceptional natural hazards such as earthquakes and floods. Furthermore, they were not originally built for the heavy loads they are often exposed to currently, and there are serious concerns about their safety for our society today [4].

Numerical modeling is an important part of seismic vulnerability assessment methodology [5,6]. The seismic vulnerability of masonry arch bridges must be assessed, because of the vulnerability of masonry subjected to earthquakes. Several different modeling strategies have been proposed for the simulation of the behavior of masonry arch bridges exposed to seismic events. Finite element (FE) modeling has been widely used to model masonry arch structures [3]. Using one-dimensional frame elements is the simplest approach for modeling masonry arch structures [7,8]. However, the effect of spandrel side walls and backfill soil material cannot be considered, and to tackle this limitation, nonlinear springs or nonlinear truss elements need to be used to simulate the interaction between the backfill, spandrel walls, and adjacent arches [9]. Two-dimensional (2D) FE models have also been used to explicitly model the fill soil and spandrel walls with higher computational effort compared with the one-dimensional modeling approach [10,11].

Article history: Received Sep 19, 2022; Accepted Dec 26, 2022

Finally, as the most detailed and complex method, three-dimensional (3D) FE modeling has been proposed, with detailed 3D modeling of all different parts of a bridge and the assignment of nonlinear constitutive relationships to both masonry and fill soil [12,13].

However, the considerable uncertainties related to the fill-structure interactions are possible limitations of the 3D FE modeling approach for masonry arch bridges. Contact interface elements (CIEs) were used comprising zero-thickness plane interface elements with normal and tangential stiffnesses derived based on the equations proposed for discrete element modeling of masonry structures [14,15]. A comprehensive study to investigate the effect of CIEs was performed, which emphasized the significant effect of CIEs on the modal properties as well as on the seismic behavior of a bridge [14]. A strategy was proposed to model a plane CIE with high normal stiffness to avoid the interpenetration of masonry and soil media such that no tension stiffness is considered [4,16,17]. Therefore, the CIE transfers only the compression and shear forces. Normal stiffness can be derived based on the soil−structure interaction equations, and the tangential stiffness is considered as 0.01–0.1 times the calculated normal stiffness [18,19]. However, the Coulomb friction model can also be used for a CIE with zero cohesion and friction coefficients [4,16,17].

Several studies have shown that structures subjected to near-field (NF) seismic events typically exhibit higher levels of damage owing to the strong velocity pulses of the excitations [20–22]. The results of linear time-history analysis of a two-span masonry bridge by applying one far-field (FF) and one NF event revealed that, in general, NF events cause more destructive damage than FF events [23]. However, by comparing the seismic response of a single-span masonry bridge subjected to FF and NF seismic events, it was concluded that the bridge is more susceptible to FF events [24]. This conclusion was further confirmed by performing linear seismic analyses on a single-span masonry bridge considering the soil−structure interaction [25]. Furthermore, similar results were obtained by performing a comparative study on a three-span masonry bridge by applying a set of eight FF and NF seismic events [26]. This finding is consistent with the conclusions drawn for nuclear structures [27].

Pulse-like near-field (PL-NF) ground motions are often caused by forward-directivity effects, and several different quantitative methods have been proposed for identifying pulse-like ground motions [28–31]. Studies have revealed that pulse-like events impose more significant demands on structures than non-pulse-like near-field (NPL-NF) seismic excitations [32–34]. However, these records cannot be labeled as aggressive without reference to structural characteristics [35]. Therefore, there is still a gap regarding the need to investigate the influence of PL-NF earthquake excitations on the seismic behavior of masonry arch bridges and compare the effect of FF and NF seismic excitations by applying a large number of events with several different characteristics.

2 Methodology and case study overview

In this study, the modeling procedure of a case study, the Roman Bridge located on the island of Rhodes, in Greece, was developed. The 3D geometric documentation was conducted using digital images, laser scanners, and total stations. The dimensions were obtained from the 3D product of geometric documentation. Using these data, an FE model was developed.

In the first part of the study, a dynamic modal analysis was performed, and the model was calibrated using an analytical equation to derive the first natural frequency value of masonry bridges.

As the examined bridge structure is located in a high seismicity zone, the second part of the study focused on investigating the seismic behavior of the bridge. To this end, 15 seismic events were selected that were categorized as FF, PL-NF, and NPL-NF. The records of these seismic events were scaled to a target response spectrum, and nonlinear time-history analyses (NLTHAs) were performed by applying the scaled seismic records in the transverse direction to assess the seismic vulnerability of the bridge. Three performance levels were calculated based on the pushover curve of the bridge, and the values of displacement capacity and demand were compared to assess the bridge performance levels.

The Roman Bridge, illustrated in Fig. 1 is located on the island of Rhodes, in Greece. It was built across the Rhodini stream before its outfall into the Mediterranean Sea at the main exit of the city on the east coast of the island. The bridge is 38.85 m long, 8.4 m wide, with a thickness of 0.6 m for the arch and spandrel components. The arch span is 6.4 m, and the height of the bridge is 5.2 m. Bridge building was a key part of the underlying Roman infrastructure [36,37], and the studied stone masonry bridge dates back to the Roman period. It is one of the few existing ancient bridges that still survive in Greece and remains in continuous use today. Later, repairs to the spandrel walls were reported, and temporary wooden scaffolds were built beneath the arches owing to falling stones. The island of Rhodes is in a high seismicity zone with peak ground acceleration (PGA) from $0.35g$ to $0.55g$ with 10% probability of

Fig. 1 Roman Bridge located on the island of Rhodes, in Greece.

exceedance in 50 years, equivalent to a return period of 475 years [38]. Documentation also reveals that several earthquakes have occurred in the island region, some of which are also associated with tsunamis [39,40]. For this purpose, the seismic vulnerability of the Roman Bridge as a cultural heritage asset and infrastructure must be assessed.

3 Numerical modeling

3.1 Three-dimensional geometric documentation

Geometric documentation is crucial for developing detailed and accurate 3D simulation models [41]. Geodetic, photogrammetric, and laser scanning data acquisition methods were used to provide an accurate 3D model of the bridge. In total, 2576 aerial images from drones and 271 ground digital images were processed using image-based modeling software to develop the 3D dense point cloud of the case study. The aerial images (using drones) were processed separately from the ground images because they had a lower resolution. Furthermore, 24 scans were performed using 3D laser scanners to provide point clouds to fill the gaps in 3D dense point clouds derived from the digital images. A local reference coordinate system was established using two total stations, and the coordinates of the required points, such as targets for the point cloud registration and ground control points for the orientation of the images, were determined. The workflow for obtaining the final 3D point cloud is illustrated in Fig. 2. Further details regarding this methodology can be found in the literature [42,43].

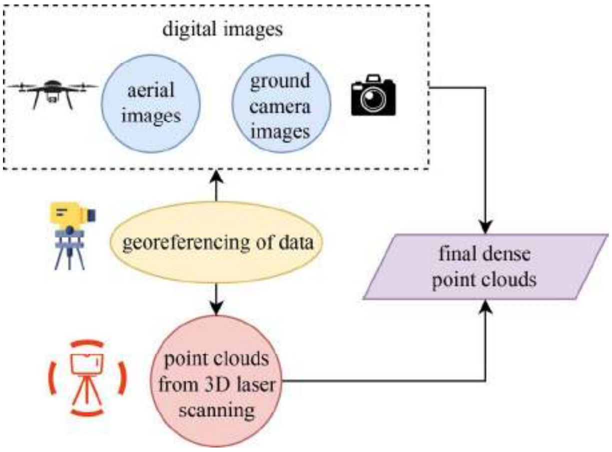

Fig. 2 Workflow of holistic methodology for generating final 3D point clouds.

After providing the final 3D point clouds, the triangular irregular network method was used to represent continuous surfaces. The light 3D model of the bridge shown in Fig. 3(a) was developed by reducing the number of triangular meshes without compromising the surface detail or color. Furthermore, cross sections were produced with different interval distances, as illustrated in Fig. 3(b). A 3D light model was used for visualization, and the dimensions of the bridge were determined from both products [44].

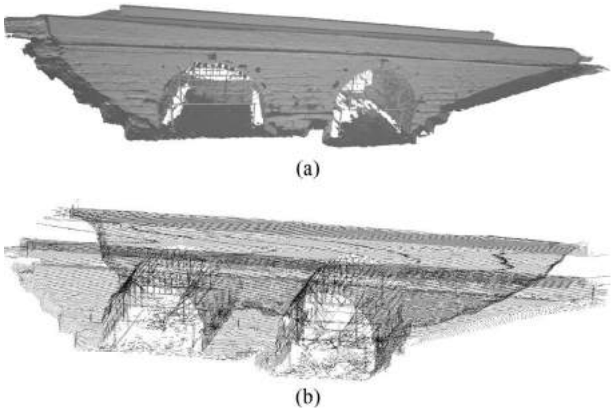
(a)

(b)

Fig. 3 (a) 3D light model; (b) cross sections of the bridge.

3.2 Three-dimensional finite element modeling

The geometry of the bridge was obtained from the 3D models used to develop the 3D FE model with DIANA FEA software [45]. Masonry is a construction material with complex mechanical behavior [46], and in the discrete element modeling approach, masonry units and mortar are modeled separately by means of interface elements to decrease the corresponding uncertainties [47]. For 3D FE modeling of the masonry part of the bridge, the homogenized method was used in which the discretization of the masonry units and mortar was ignored, which is widely used as a simplistic approach for modeling full-scale unreinforced masonry structures [48]. This approach requires less input data and computational effort than the discrete element method [49]. Figure 4(a) illustrates the different parts of the masonry arch bridge comprising spandrel walls, arches, and parapets made of stone masonry and backfill soil. To model the backfill-spandrel and backfill-arch interaction, CIEs were used, as shown in Fig. 4(b), as described previously [50]. The effect of soil−structure interaction was not considered, and rigid boundary conditions were set for the models.

The CIE can transfer normal compression and tangential friction with zero tensile strength; thus, the tensile forces are not transferred. Modeling the CIE is recommended not only to represent the actual behavior of the bridge but also to avoid early convergence problems owing to the low stiffness of the backfill material compared with the stiffness of the masonry material [4]. Nevertheless, the higher computational effort and level of input data and the additional need for a skilled analyst to model the CIE can be considered as limitations of

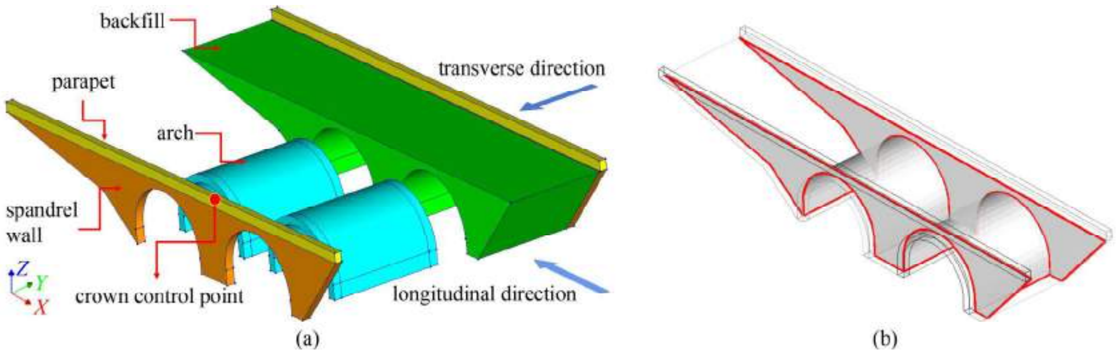

Fig. 4 (a) Different components of the numerical model of the Roman Bridge and loading directions in addition to the location of control (crown) point; (b) CIE used to model the bridge.

modeling masonry arch bridges using the CIE.

A high value was considered for the normal and lateral stiffnesses of the CIE to prevent the interpenetration of the two bodies. The CIEs follow the Coulomb friction model in such a way that the two media can carry shear stresses up to a certain magnitude, $\tau_{\max}$ calculated using Eq. (1), before sliding across one another

$$\tau_{\max} = c + \sigma \tan \varphi, \tag{1}$$

where c is the cohesion value (considered to be zero), σ is the normal stress, and φ is the friction angle of the soil. The friction coefficient (tangent of the friction angle) is recommended to be in the range of 0.4–0.5 [51–53].

3.3 Material properties

The total strain fixed crack model was applied for the nonlinear modeling of the masonry parts to define the tensile and compressive behaviors of the homogenized stone masonry with a single stress−strain relationship [54]. The area under the exponential softening curve is calculated based on the tension fracture energy (G_f^t) divided by the definition of the crack bandwidth (h) of an element. For the compression part, the area under the parabolic curve is calculated based on the compression fracture energy (G_f^c) divided by h to define the stress−strain curve of the masonry, as shown in Fig. 5. Note that the crack bandwidth model was used in this study, and parameter h is related to the volume of the element [55].

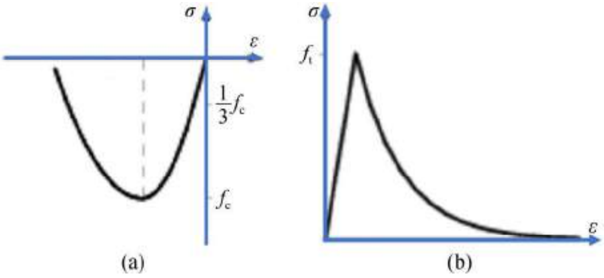

Fig. 5 Uniaxial stress−strain diagrams of homogenized stone masonry: (a) compression behavior; (b) tension behavior.

The damage-based shear retention model was selected for the masonry shear behavior. The shear retention was simulated based on the material damage caused by cracking, and the shear capacity was reduced to zero when the masonry was sufficiently damaged. The bridge is made of “sfouggaria stone”, which was a common construction material on the island of Rhodes in the past, with a compressive strength (f_b) estimated at 9 MPa [56]. Moreover, the compressive strength of mortar (f_m) is considered to be 1 MPa by choosing a soft mortar type [57], owing to the presence of mildly leached mortar that can be raked out. The recommended equations and corresponding values for the material properties of the bridge masonry used in this study are listed in Table 1.

Moreover, the Mohr−Coulomb material model was selected for the simulation of the backfill soil. The corresponding material properties are presented in Table 2

Table 1 Equations recommended for calculating the mechanical properties of the homogenized unreinforced masonry [57] with the corresponding values calculated for the Roman Bridge case study

parameter	description	equation	value for the bridge
f_c	compressive strength (MPa)	$0.6 f_\mathrm{b}^{0.65} f_\mathrm{m}^{0.35}$	2.503
f_t	tensile strength (MPa)	$(10\%–20\%) f_\mathrm{c}$	0.375
E	modulus of elasticity (GPa)	$(300–700) f_\mathrm{c}$	1.001
G_f^c	fracture energy in compression (for the f_c lower than 12 MPa) ($\mathrm{N{\cdot}mm^{-1}}$)	$1.6 f_\mathrm{c}$	4.004
G_f^t	fracture energy in tension ($\mathrm{N{\cdot}mm^{-1}}$)	$0.029 f_\mathrm{c}$	0.011
ρ	density ($\mathrm{kg{\cdot}m^{-3}}$)	–	2200
ν	Poisson’s ratio	–	0.29

Table 2   Mechanical properties of the backfill soil

parameter	description	value
E_{bs}	modulus of elasticity (GPa)	0.3
ρ_{bs}	density (kg·m^{-3})	2000
ν_{bs}	Poisson's ratio	0.3
c_{bs}	cohesion (kPa)	10
φ_{bs}	friction angle of the backfill soil (°)	37
$f_{t(max)}$	tensile strength (kPa)	10

[58]. The friction coefficient value of the CIE was considered to be 0.4.

3.4 Finite element mesh

A preliminary analysis to assess the optimal mesh dimensions was performed on the FE model, and an adaptive mesh size of 0.5 m was used. Moreover, to simulate deformation across the arches accurately enough, a mesh size of 0.3 m was used for the arches. The 8-node quadratic element was selected for the FE modeling, which is the dominant type of element for such simulations. Tetrahedral volume elements were also used in the model to fill parts of the geometry. The FE mesh of the bridge is shown in Fig. 6. The model with the CIE is composed of 12699 mesh elements, of which 1936 are CIE elements.

4 Modal analysis and validation

Modal analysis was performed to derive the first five natural frequencies and corresponding mode shapes of the structure. The direction-dependent participation factors and modal mass percentages were also calculated for each natural mode and are presented in Table 3.

The first five modes with relatively high participation factor values were selected to perform the sensitivity analyses. Figure 7 shows the natural frequency values and corresponding mode shapes with a contour map of the normalized displacement values of the mode vectors of the first five modes of the model. Based on the results in

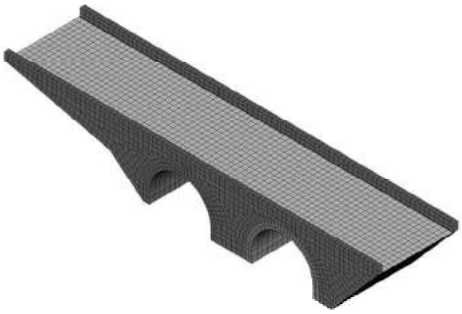

Fig. 6   3D FE mesh of Roman Bridge.

Table 3   Frequency values and direction dependent participation factors for the first five modes of the bridge

mode	frequency values (Hz)	direction dependent participation factors			modal mass (%)
		x direction	*y* direction	*z* direction	
1	9.38	−0.055	938.110	−0.009	15.39
2	11.34	969.080	0.073	−9.381	21.33
3	11.47	−0.237	22.829	−0.014	12.04
4	15.18	0.065	358.830	−0.109	10.53
5	15.44	−23.327	−0.009	105.340	8.28

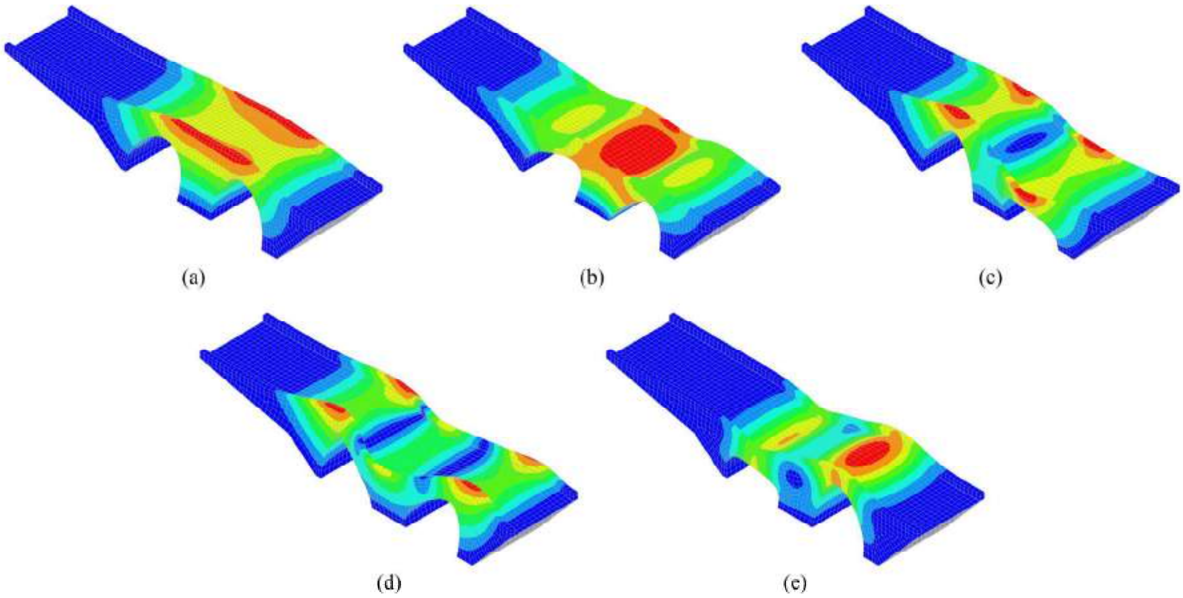

Fig. 7   Natural frequency values (f) and mode shapes of first five modes of developed models: (a) f_1 = 9.38 Hz; (b) f_2 = 11.34 Hz; (c) f_3 = 11.47 Hz; (d) f_4 = 15.18 Hz; (e) f_5 = 15.44 Hz.

Table 3 and Fig. 7 it can be reported that the first, third and fourth modes are in the transverse (y) direction, the second mode is in the longitudinal (x) direction, and the fifth mode is in the vertical (z) direction of the bridge.

A comprehensive experimental study was conducted to investigate the dynamic characteristics of historical masonry arch bridges by performing an operational modal analysis of eight bridges [59]. Equation (2) was proposed to calculate the first frequency value of masonry arch bridges (y) (Hz) based on the maximum arch span (x) (m).

$$y = -3.935\ln x + 16.824. \tag{2}$$

The calculated first natural frequency of the Roman Bridge based on Eq. (2) is 9.46, which is very close to the first natural frequency derived from the modal analysis of the FE models ($< 2\%$). Although Eq. (2) is only based on the span of the bridge by neglecting the effect of material properties and other geometrical characteristics, it shows a good estimation of the first natural frequency value of masonry bridges, as reported in Ref. [60]. However, operational modal analysis based on in situ tests is required to calibrate the model based on the natural frequency values and corresponding mode shapes of the real structure.

5 Performance-based seismic assessment methodology

In this section, earthquake records are selected and scaled to a target response spectrum. NLTHAs are then performed, and the performance level of the bridge is assessed based on a damage index. Finally, a comparative study is performed to investigate the influence of the type of seismic event on the seismic behavior of the structure.

5.1 Earthquake record selection and scaling

In total, 15 seismic events were selected from the PEER NGA-West2 ground-motion database [61]. The flowchart used for selecting seismic events according to different criteria for the three main groups is shown in Fig. 8. Note that the ground type is considered as type B with a shear wave velocity of 360–800 m·s^{-1} [62,63], and the average of the Campbell and Joyner–Boore fault distances was used as the source-to-site distance (SSD) [64]. PL-NF event records were chosen based on the method presented in the literature [28] with pulse indicator values > 0.85, early pulses in the time history, and a peak ground velocity (PGV) > 30 cm·s^{-1}. The characteristics of the selected seismic records, including the record sequence numbers (RSNs) in the PEER database, are presented in Table 4.

All of the selected 15 seismic records were scaled to the target response spectrum [62]. For deriving the target response spectrum, the PGA of the island of Rhodes is considered to be 0.47g for soil class B based on the latest seismic hazard map of Europe in the context of the SHARE project [65,66].

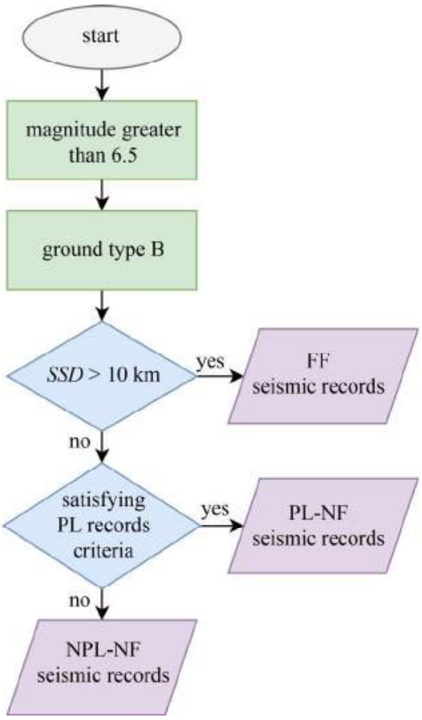

Fig. 8 Flowchart of seismic record selection and categorization.

The bridge is more susceptible in the transverse direction than in the longitudinal direction because the mode shape of the fundamental frequency is in the transverse direction. Moreover, the Northridge seismic record with an intensity of 6.7 M was scaled to a PGA of 0.8g and applied to the structure in two directions for preliminary seismic analysis. The results showed that the displacement in the transverse direction of the crown point was ten times greater than that in the longitudinal direction, and the crack width (CW) of the model with longitudinal loading was less than that of the model subjected to transverse loading. Therefore, the seismic vulnerability of the bridge was assessed in the transverse direction.

The earthquake records were scaled and matched to the target response spectrum using the SeismoMatch software package [67] in periods from $0.2T_1$–$2T_1$, where T_1 is the fundamental period of the bridge in the transverse direction [62]. An improved scaling method was used to adjust the recorded ground motions without baseline correction [68]. Figure 9(a) shows the single-record spectrum after scaling, and Fig. 9(b) illustrates the mean-matched spectrum.

Five indicators were selected for the scaled seismic

Table 4 Characteristics of selected seismic records [61]

record type	*RSN*	event	station	year	magnitude	*SSD*	*PGA*	*PGV*
FF	313	Corinth, Greece	Corinth	1981	6.6	10.27	0.236	22.955
	3750	Cape Mendocino	Loleta Fire Station	1992	7.01	24.685	0.265	35.525
	1083	Northridge-01	Sunland–Mt Gleason Ave	1994	6.69	12.865	0.132	15.73
	1613	Duzce, Turkey	Lamont 1060	1999	7.14	25.83	0.053	5.755
	1633	Manjil, Iran	Abbar	1990	7.37	12.55	0.514	42.457
PL-NF	828	Cape Mendocino	Petrolia	1992	7.01	4.09	0.590	49.327
	1086	Northridge-01	Sylmar–Olive View Med FF	1994	6.69	3.52	0.604	77.549
	802	Loma Prieta	Saratoga–Aloha Ave	1989	6.93	8.04	0.514	41.579
	879	Landers	Lucerne	1992	7.28	2.19	0.725	133.40
	1013	Northridge-01	LA Dam	1994	6.69	2.96	0.426	74.841
NPL-NF	495	Nahanni, Canada	Site 1	1985	6.76	6.04	1.107	43.926
	825	Cape Mendocino	Cape Mendocino	1992	7.01	3.48	1.493	122.32
	126	Gazli, USSR	Karakyr	1976	6.8	4.69	0.701	66.218
	1004	Northridge-01	LA–Sepulveda VA Hospital	1994	6.69	4.22	0.752	77.673
	741	Loma Prieta	BRAN	1989	6.93	7.285	0.456	51.390

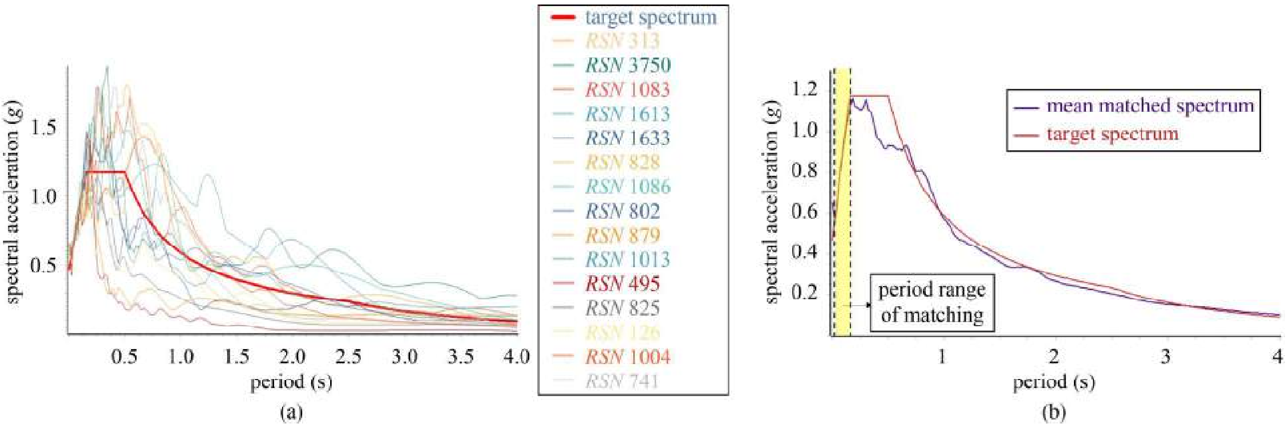

Fig. 9 (a) Seismic records' spectra scaled to the target response spectrum; (b) period range of matching.

records, including *PGA*, *PGV*, Arias intensity (*Ai*), significant duration (*SD*), and specific energy density (*SED*), which are illustrated in Fig. 10, with average values for each group of records. Note that the *Ai* and *SED* are calculated based on:

$$Ai = \frac{\pi}{2g}\int_0^{t_{\max}} [a_{(t)}]^2 \mathrm{d}t, \tag{3}$$

$$SED = \int_0^{t_{\max}} [v_{(t)}]^2 \mathrm{d}t, \tag{4}$$

where $a_{(t)}$ and $v_{(t)}$ are the acceleration and velocity values, respectively, for each time interval, and $t_{\max}$ is the length of the accelerogram. The significant duration is considered as the interval of time in which 5%–95% of the total *Ai* is accumulated [67]. The average values of the *PGA* are close to each other, and the average values of the *PGV* for PL-NF events are closer to the values for FF events and greater than those for the other two types of records. However, the *Ai*, *SED*, and *SD* values of the NF seismic records are less than those of the FF records after scaling.

Scaled seismic event records were applied to the transverse direction of the structure to assess the seismic vulnerability of the bridge, and NLTHAs were performed. Rayleigh damping is used for the models with factors of 3.641 and 0.0006 applied to the mass and stiffness matrices, respectively. Note that the damping factors were calculated by considering a 5% damping ratio for the first and third modes of the bridge models [14,69].

5.2 Seismic performance criteria

Because there are no performance limit states for

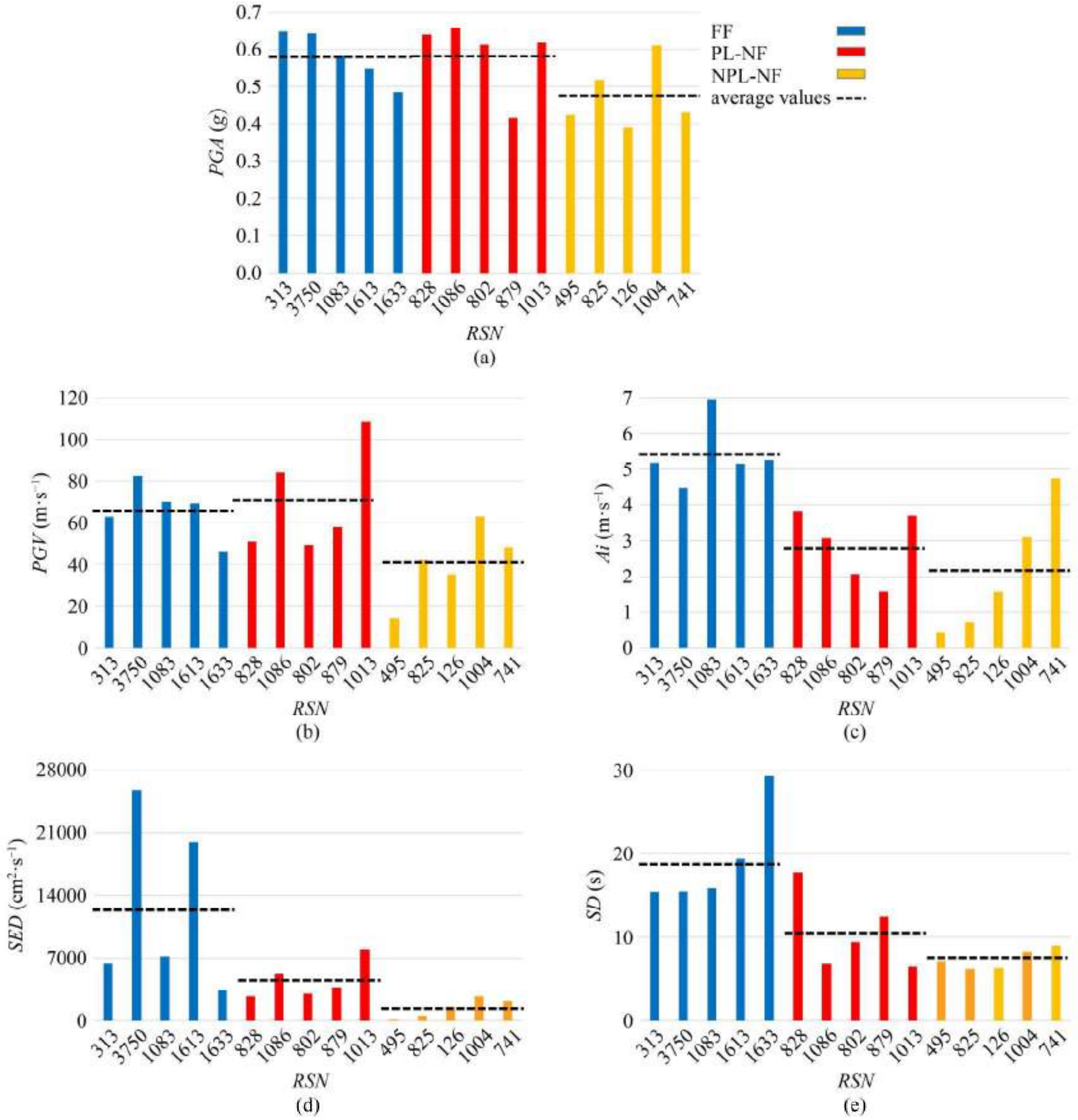

Fig. 10 Scaled seismic event records: (a) *PGA*; (b) *PGV*; (c) *Ai*; (d) *SED*; (e) *SD*.

masonry arch bridges, comprehensive studies are required to define performance criteria. A methodology for determining the quantitative damage criteria for masonry arch bridges was presented in Ref. [70] based on the pushover curve. Three performance levels were considered, and the displacement limit states were determined based on the criteria listed in Table 5. The relationship between the performance levels and the damage states is shown in Fig. 11.

Modal pushover analysis was performed based on the load pattern proportional to the first mode shape [71]. The pushover curves are presented in Fig. 12, by defining the displacement limit states based on the criteria listed in Table 5. The displacement values for the F, LS, and NC limit states are 2.76, 5.78, and 18.5 mm, respectively, as highlighted in Fig. 12. The limit states are derived for the bridge in this study, and a comprehensive study, by developing masonry arch bridges with different geometries, morphologies, and material properties is required to generalize the limit states.

6 Results and discussion

The results for the maximum displacement of the crown point (*Disp*) of the bridge and the three aforementioned limit states are shown in Fig. 13(a). The percentage of the cracked volume of the structure relative to the total volume of the masonry is calculated as a cracked volume damage index (*CVDI*) for each record at the final step of the analysis and illustrated in Fig. 13(b). The *CW*s in the final step of each seismic analysis are shown in Fig. 13(c). Furthermore, the average (Ave) values of the three aforementioned indices are calculated for FF, PL-

Table 5 Performance levels and criteria for determining displacement limit states based on the pushover curve

performance level	functional (F)	life safety (LS)	near collapse (NC)
quantitative description	displacement corresponds to 75% of the maximum base shear (or acceleration)	displacement corresponds to the point on the pushover curve with 7% of the initial (elastic) stiffness	displacement corresponds to 90% of the maximum displacement attained on the pushover curve
qualitative description	structure is mostly elastic with little or no damage; traffic is not interrupted, and damage can be repaired in a couple of days	plasticity starts increasing before and after this performance level; bridge is expected to suffer medium to significant damage; it should still be feasible to repair but cannot be used for a short duration	damage is heavy and distributed to the extent that the bridge is near to collapse state; bridge may even be out-of-service or replaced completely

NF, NPL-NF, and NF events and all event records, as presented in Fig. 13.

By focusing on the response of the bridge to single records, it can be concluded that different damage indices reflect different structural behaviors. The volume of the cracked parts is relatively high for *RSN* 828, but the other two indices are not significantly large. By comparing the seismic behavior of the bridge subjected to *RSN* 3750 and *RSN* 1083, it can be concluded that a higher value of the

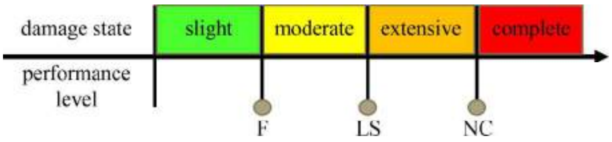

Fig. 11 Relationships between performance levels and damage states.

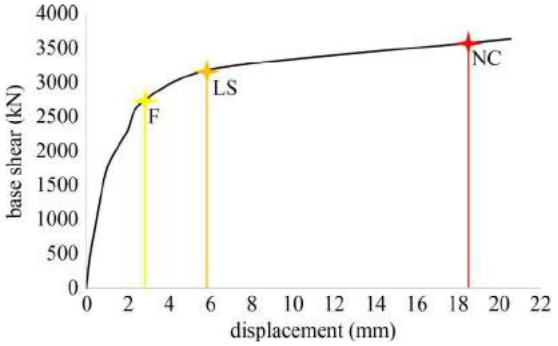

Fig. 12 Pushover curve of the bridge with performance limits.

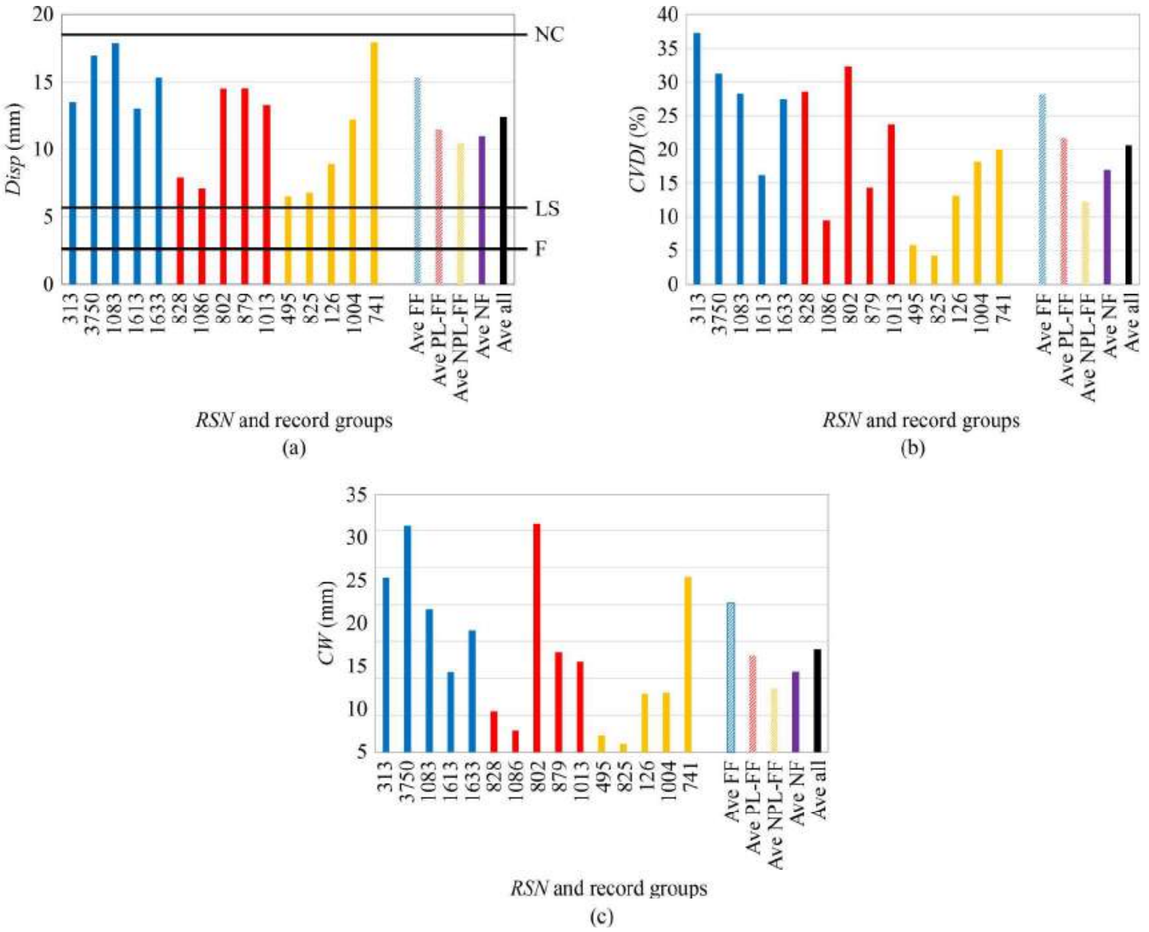

Fig. 13 Results of NLTHA in terms of: (a) *Disp*; (b) *CVDI*; (c) *CW*.

displacement does not necessarily result in a higher value of the cracked volume damage index and *CW*. Furthermore, the displacement damage index cannot necessarily reflect the seismic damage state of the bridge, and performance level criteria should be defined for the cracked volume damage index and verified based on the experimental tests for stone masonry bridges. As can be seen, some events, such as *RSN* 802 or *RSN* 879 as PL-NF events and *RSN* 741 as an NPL-NF event, have destructive effects on the bridge, similar to FF events. Therefore, it should be noted that it is not sufficiently reliable to perform a comparative study on the effect of earthquake excitation characteristics on the seismic behavior of structures by applying one or two pairs of event records.

The results show that the PL-NF events are more destructive than the NPL-NF excitations. Moreover, more extensive damage occurs to the structure subjected to FF events than NF events. The cracked volume damage index and displacement values of the bridge subjected to PL-NF events were 9.6% and 76.6% higher than those of the bridge subjected to NPL-NF events. Therefore, PL-NF events are more destructive in terms of the cracked volume damage index.

6.1 Regression and correlation analysis

To investigate the correlation between the excitation properties and seismic behavior of the structure in terms of the three damage indices, a linear regression analysis was performed, and the results, including the linear trendline and R^2 values, are presented in Fig. 14. The positive slope of the trend lines reveals that, generally, all parameters have a positive correlation with the damage indices, however, exceptions can also be seen by comparing the characteristics of some seismic records and the corresponding structural demands.

The R^2 values are presented in Fig. 15 on a scale of 0–0.5 to facilitate the comparison. Higher values of R^2 indicate that the change in parameter can explain the change in structural demand in a better way. *Ai* can be a good seismic intensity indicator for predicting the seismic behavior of a bridge in terms of all damage indices.

6.2 Seismic performance evaluation of the bridge

The bridge subjected to seismic events scaled to the target response spectrum with a 10% probability of exceeding it in 50 years with a 475-year return period passed the acceptance criteria for the LS performance level and reported extensive post-earthquake damage. Therefore, the bridge should be repaired after an earthquake; however, this may not be practical for economic reasons. Furthermore, the bridge should be strengthened to prevent future seismic losses.

The applied accelerograms of the *RSN* 1083, *RSN* 1013, and *RSN* 126 events are illustrated in Fig. 16(a) as samples of the FF, PL-NF, and NPL-NF excitations. Figure 16(b) shows the displacement time-history response of the crown point of the bridge subjected to the

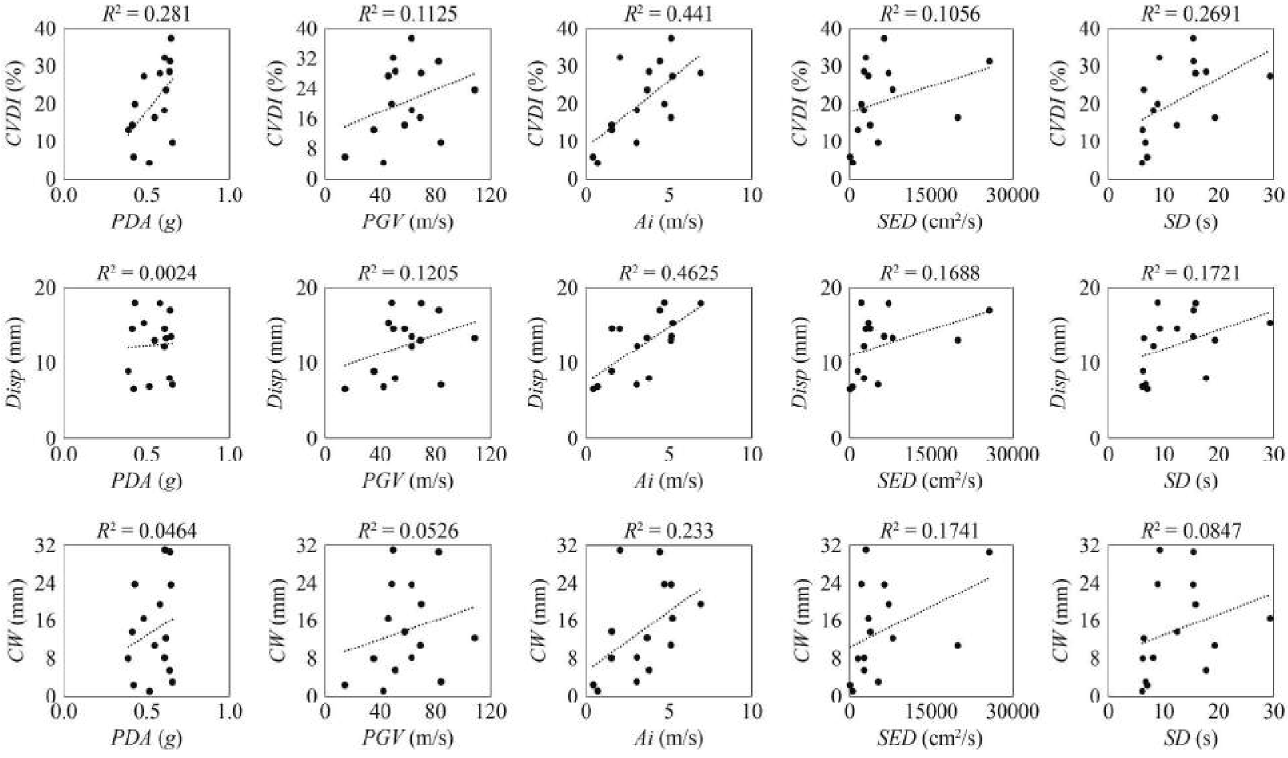

Fig. 14 Trendlines and R^2 values for seismic record properties and structural demands.

selected events. The residual displacements that are presented in Fig. 16(b) are due to the fact that most of the bridge elements were in their plastic phase after applying the selected records. Figure 16(c) shows the magnified deformed shape of the bridge at the end of the analysis time of the *RSN* 1083 event, which is a common shape in almost all simulations. The results revealed that the relative displacement of the crown points of the two spandrel walls increased in the transverse direction by applying the seismic records.

Figure 17 shows the crack pattern and principal crack strain values (E_{knn}) of the model at the final step of analyzing the bridge subjected to the *RSN* 1083, *RSN* 1013, and *RSN* 126 events. The results show that arches are the most susceptible areas, with higher crack strain values than spandrel walls. Cracks can be found in all the models in the arches and close to the spandrel walls, as shown in Fig. 17 for three-sample earthquake records. The area between the arches is the most vulnerable section of the spandrel wall. Therefore, a strategy to strengthen the arches (especially the area close to the spandrel walls) is needed so that the spandrel wall between the two arches can be sufficiently efficient to reduce the seismic vulnerability of the structure.

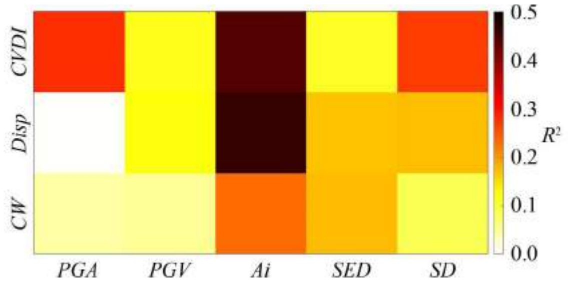

Fig. 15 R^2 values for different seismic record parameters and structural demand.

7 Conclusions

In this study, geometric documentation of the Roman Bridge on the island of Rhodes, in Greece, was performed using advanced digital imaging, 3D laser scanning, and total stations, and the methodology for providing an accurate 3D model was described. Because the bridge is located in a high-seismicity zone, the seismic vulnerability of the bridge also needs to be assessed. Fifteen seismic records were therefore selected based on site specifications and categorized as FF, Pl-NF, or NPL-NF.

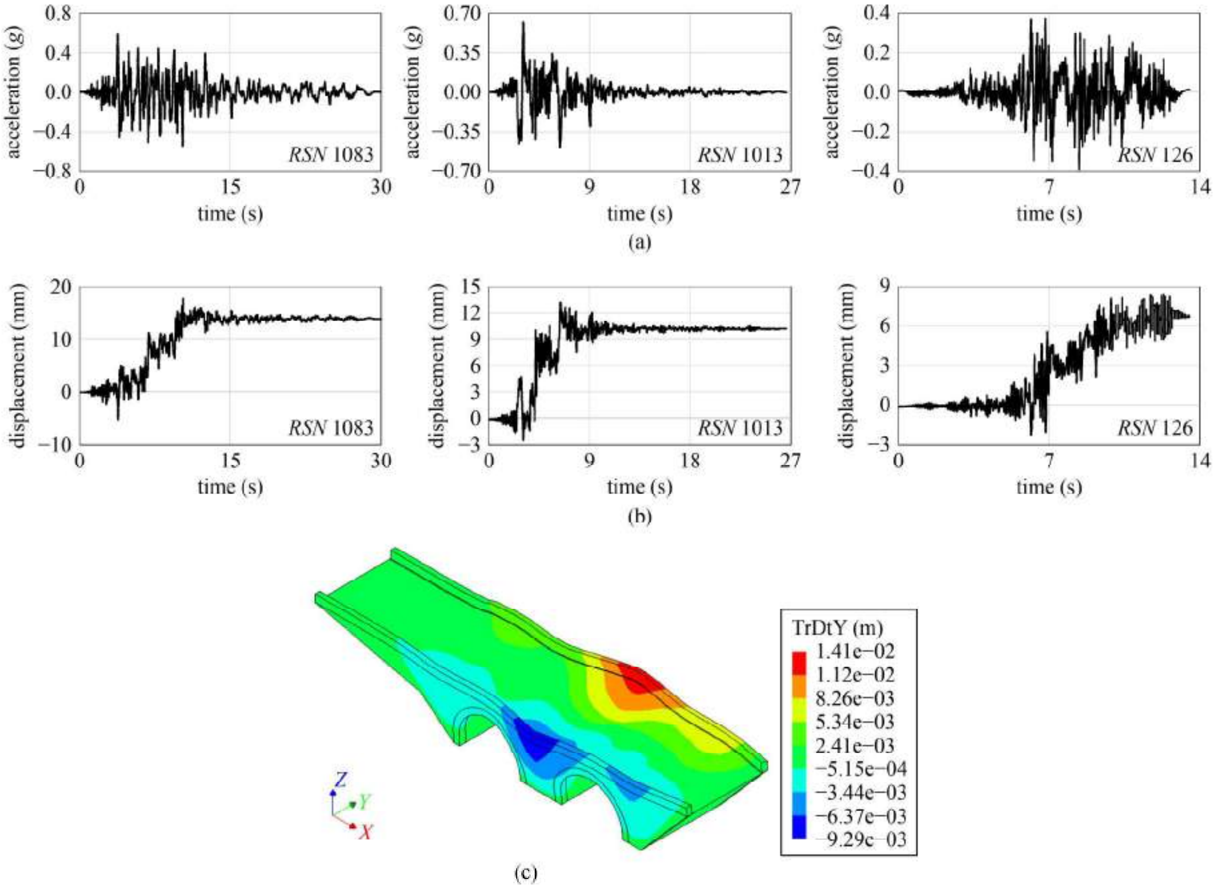

Fig. 16 (a) Accelerograms of *RSN* 1083, *RSN* 1013, and *RSN* 126 events; (b) displacement response time history of the crown points; (c) magnified deformed shape of the bridge subjected to *RSN* 1083 record at the end of the analysis.

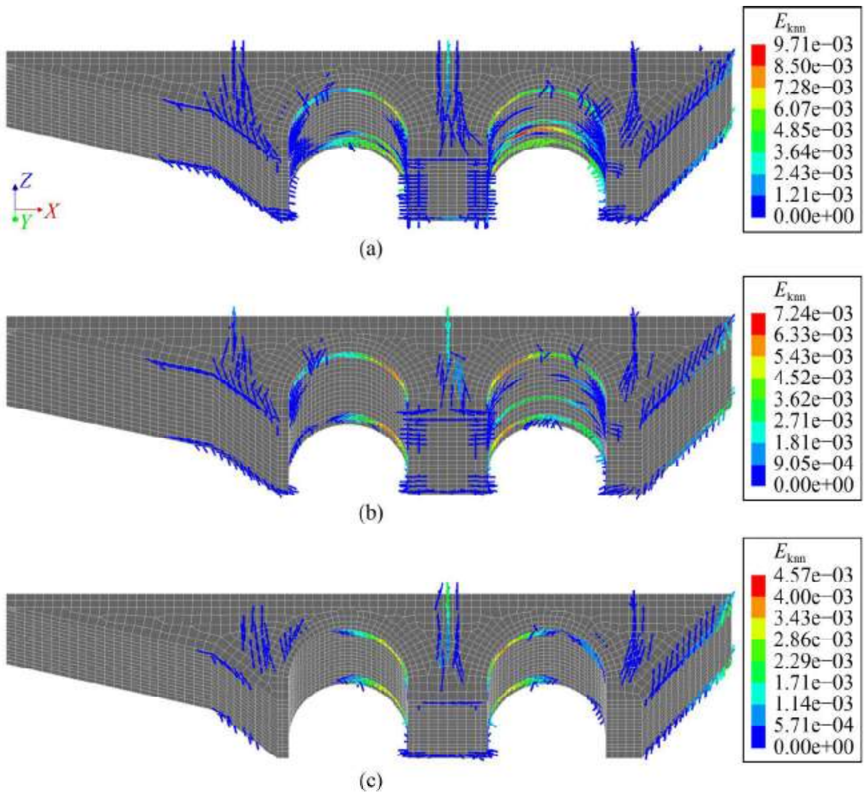

Fig. 17 Crack pattern and principal crack strain values for: (a) *RSN* 1083; (b) *RSN* 1013; (c) *RSN* 126.

The event records were scaled to the target spectrum and applied to the FE model in the transverse direction. The results of the NLTHA revealed that the structure is more susceptible to PL events than to NPL events by comparing the three damage indices. Furthermore, FF events are more destructive than NF events. Linear regression analysis revealed that the *Ai* is the most accurate indicator as one of the seismic records' properties for prediction of the structural demands to different types of excitations. The seismic performance of the bridge was evaluated by defining three performance levels based on the pushover curve. The time-history analysis indicates that the structure passes the acceptability check of the LS performance level and undergoes extensive damage. Temporary wooden scaffolds were built beneath the arches owing to the falling of the stones. Moreover, based on the damage patterns concluded from the numerical analyses, the arches are the most vulnerable structural components, which is consistent with the weakness of the real structure. The observed crack patterns indicate that the structure must be retrofitted by strengthening the arches, focusing on the area close to the spandrel walls and the spandrel wall between the arches. The model should be calibrated based on the operational modal analysis results of the on-site ambient vibration tests, and advanced seismic analyses should be conducted considering soil−structure interaction effects for future studies.

Acknowledgements This work was part of the HYPERION project. HYPERION has received funding from the European Union's Framework Programme for Research and Innovation (Horizon 2020) under grant agreement No. 821054. The contents of this publication are the sole responsibility of the Oslo Metropolitan University (Work Package 5, Task 2) and do not necessarily reflect the opinion of the European Union.

Funding note Open Access funding provided by OsloMet-Oslo Metropolitan University.

References

1. Khosrowjerdi S, Sarkardeh H, Kioumarsi M. Effect of wind load on different heritage dome buildings. European Physical Journal

Plus, 2021, 136(11): 1180

2. van Beek G W. Arches and vaults in the ancient Near East. Scientific American, 1987, 257(1): 96–103
3. Sarhosis V, de Santis S, de Felice G. A review of experimental investigations and assessment methods for masonry arch bridges. Structure and Infrastructure Engineering, 2016, 12: 1439–1464
4. Gönen S, Soyöz S. Seismic analysis of a masonry arch bridge using multiple methodologies. Engineering Structures, 2021, 226: 111354
5. Shabani A, Kioumarsi M, Zucconi M. State of the art of simplified analytical methods for seismic vulnerability assessment of unreinforced masonry buildings. Engineering Structures, 2021, 239: 112280
6. Yekrangnia M, Mobarake A A. Restoration of historical Al-Askari shrine. II: Vulnerability assessment by numerical simulation. Journal of Performance of Constructed Facilities, 2016, 30(3): 04015031
7. Brencich A, de Francesco U. Assessment of multispan masonry arch bridges. I: Simplified approach. Journal of Bridge Engineering, 2004, 9(6): 582–590
8. de Felice G. Assessment of the load-carrying capacity of multi-span masonry arch bridges using fibre beam elements. Engineering Structures, 2009, 31(8): 1634–1647
9. de Santis S, de Felice G. A fibre beam-based approach for the evaluation of the seismic capacity of masonry arches. Earthquake Engineering & Structural Dynamics, 2014, 43(11): 1661–1681
10. Audenaert A, Fanning P, Sobczak L, Peremans H. 2-D analysis of arch bridges using an elasto-plastic material model. Engineering Structures, 2008, 30(3): 845–855
11. Zampieri P, Zanini M A, Faleschini F, Hofer L, Pellegrino C. Failure analysis of masonry arch bridges subject to local pier scour. Engineering Failure Analysis, 2017, 79: 371–384
12. Fanning P, Sobczak L, Boothby T E, Salomoni V. Load testing and model simulations for a stone arch bridge. Bridge Structures, Assessment, Design and Construction, 2005, 1: 367–378
13. Milani G, Lourenco P B. 3D non-linear behavior of masonry arch bridges. Computers & Structures, 2012, 110: 133–150
14. Hokelekli E, Yilmaz B N. Effect of cohesive contact of backfill with arch and spandrel walls of a historical masonry arch bridge on seismic response. Periodica Polytechnica. Civil Engineering, 2019, 63: 926–937
15. Bayraktar A, Hökelekli E. Seismic performances of different spandrel wall strengthening techniques in masonry arch bridges. International Journal of Architectural Heritage, 2021, 15(11): 1722–1740
16. Banerji P, Chikermane S. Condition assessment of a heritage arch bridge using a novel model updation technique. Journal of Civil Structural Health Monitoring, 2012, 2(1): 1–16
17. Zampieri P, Tetougueni C D, Pellegrino C. Nonlinear seismic analysis of masonry bridges under multiple geometric and material considerations: Application to an existing seven-span arch bridge. Structures, 2021, 34: 78–94
18. van Langen H, Vermeer P. Interface elements for singular plasticity points. International Journal for Numerical and Analytical Methods in Geomechanics, 1991, 15(5): 301–315
19. Herrmann L R. Finite element analysis of contact problems. Journal of the Engineering Mechanics Division, 1978, 104(5): 1043–1057
20. Zhang S, Wang G. Effects of near-fault and far-fault ground motions on nonlinear dynamic response and seismic damage of concrete gravity dams. Soil Dynamics and Earthquake Engineering, 2013, 53: 217–229
21. Pang Y T, Cai L, Zhong J. Seismic performance evaluation of fiber-reinforced concrete bridges under near-fault and far-field ground motions. Structures, 2020, 28: 1366–1383
22. Yekrangnia M, Bakhshi A, Ghannad M A, Panahi M. Risk assessment of confined unreinforced masonry buildings based on FEMA P-58 methodology: A case study—School buildings in Tehran. Bulletin of Earthquake Engineering, 2021, 19(2): 1079–1120
23. Sevim B, Atamturktur S, Altunişik A C, Bayraktar A. Ambient vibration testing and seismic behavior of historical arch bridges under near and far fault ground motions. Bulletin of Earthquake Engineering, 2016, 14(1): 241–259
24. Simos N, Manos G C, Kozikopoulos E. Near- and far-field earthquake damage study of the Konitsa stone arch bridge. Engineering Structures, 2018, 177: 256–267
25. Güllü H, Özel F. Microtremor measurements and 3D dynamic soil–structure interaction analysis for a historical masonry arch bridge under the effects of near- and far-fault earthquakes. Environmental Earth Sciences, 2020, 79(13): 338
26. Özmen A, Sayın E. Seismic response of a historical masonry bridge under near and far-fault ground motions. Periodica Polytechnica Civil Engineering, 2021, 65: 946–958
27. Labbé P, Altinyollar A. Conclusions of an IAEA–JRC research project on the safety significance of near-field seismic motions. Nuclear Engineering and Design, 2011, 241(5): 1842–1856
28. Baker J W. Quantitative classification of near-fault ground motions using wavelet analysis. Bulletin of the Seismological Society of America, 2007, 97(5): 1486–1501
29. Shahi S K, Baker J W. An efficient algorithm to identify strong-velocity pulses in multicomponent ground motions. Bulletin of the Seismological Society of America, 2014, 104(5): 2456–2466
30. Chang Z, Sun X, Zhai C, Zhao J X, Xie L. An improved energy-based approach for selecting pulse-like ground motions. Earthquake Engineering & Structural Dynamics, 2016, 45(14): 2405–2411
31. Dimakopoulou V, Fragiadakis M, Taflampas I. A wavelet-based approach for truncating pulse-like records. Bulletin of Earthquake Engineering, 2022, 20(1): 1–24
32. Daei A, Poursha M, Zarrin M. Seismic performance evaluation of code-compliant RC moment-resisting frame buildings subjected to near-fault pulse-like and non-pulse-like ground motions. Journal of Earthquake Engineering, 2021, 26(10): 5058–5085
33. Zuo Z, Gong M, Sun J, Zhang H. Seismic performance of RC frames with different column-to-beam flexural strength ratios under the excitation of pulse-like and non-pulse-like ground motion. Bulletin of Earthquake Engineering, 2021, 19(12): 5139–5159
34. Wibowo H, Sritharan S. Effects of vertical ground acceleration on the seismic moment demand of bridge superstructure connections. Engineering Structures, 2022, 253: 113820

35. Kohrangi M, Vamvatsikos D, Bazzurro P. Pulse-like versus non-pulse-like ground motion records: Spectral shape comparisons and record selection strategies. Earthquake Engineering & Structural Dynamics, 2019, 48(1): 46−64
36. Orfeo B, Todisco L, León J. Construction process of vaults in masonry bridges: The importance of centrings. International Journal of Architectural Heritage, 2022, 16(7): 1032−1046
37. Gençer F U, Turan M H. The masonry techniques of a historical bridge in Hypokremnos (İçmeler). Metu Journal of the Faculty of Architecture, 2017, 34(1): 187−207
38. Pagani M, Garcia-Pelaez J, Gee R, Johnson K, Poggi V, Silva V, Simionato M, Styron R, Viganò D, Danciu L, Monelli D, Weatherill G. The 2018 version of the global earthquake model: Hazard component. Earthquake Spectra, 2020, 36(1_suppl): 226−251
39. Stiros S, Papageorgiou S, Kontogianni V, Psimoulis P. Church repair swarms and earthquakes in Rhodes Island, Greece. Journal of Seismology, 2006, 10(4): 527−537
40. Howell A, Jackson J, England P, Higham T, Synolakis C. Late Holocene uplift of Rhodes, Greece: Evidence for a large tsunamigenic earthquake and the implications for the tectonics of the eastern Hellenic Trench System. Geophysical Journal International, 2015, 203(1): 459−474
41. Shabani A, Alinejad A, Teymouri M, Costa A N, Shabani M, Kioumarsi M. Seismic vulnerability assessment and strengthening of heritage timber buildings: A review. Buildings, 2021, 11(12): 661
42. Tapinaki S, Skamantzari M, Anastasiou A, Koutros S, Syrokou E, Georgopoulos A. 3D holistic documentation of heritage monuments in Rhodes. The International Archives of the Photogrammetry, Remote Sensing and Spatial Information Sciences, 2021, XLVI-M-1-2021: 739−744
43. Kolokoussis P, Skamantzari M, Tapinaki S, Karathanassi V, Georgopoulos A. 3D and hyperspectral data integration for assessing material degradation in medieval masonry heritage buildings. The International Archives of the Photogrammetry, Remote Sensing and Spatial Information Sciences, 2021, XLIII-B2-2021: 583−590
44. Shabani A, Skamantzari M, Tapinaki S, Georgopoulos A, Plevris V, Kioumarsi M. 3D simulation models for developing digital twins of heritage structures: Challenges and strategies. Procedia Structural Integrity, 2022, 37: 314−320
45. DIANA. Version 10.4. Delft: DIANA FEA BV. 2020
46. Plevris V, Asteris P G. Modeling of masonry failure surface under biaxial compressive stress using Neural Networks. Construction & Building Materials, 2014, 55: 447−461
47. D’Altri A M, Sarhosis V, Milani G, Rots J, Cattari S, Lagomarsino S, Sacco E, Tralli A, Castellazzi G, de Miranda S. Modeling strategies for the computational analysis of unreinforced masonry structures: Review and classification. Archives of Computational Methods in Engineering, 2020, 27(4): 1153−1185
48. Asteris P G, Chronopoulos M P, Chrysostomou C Z, Varum H, Plevris V, Kyriakides N, Silva V. Seismic vulnerability assessment of historical masonry structural systems. Engineering Structures, 2014, 62–63: 118–134
49. Asteris P G, Sarhosis V, Mohebkhah A, Plevris V, Papaloizou L, Komodromos P, Lemos J V. Numerical modeling of historic masonry structures. In: Asteris P G, Plevris V, eds. Handbook of Research on Seismic Assessment and Rehabilitation of Historic Structures. Hershey, PA: IGI Global, 2015, 213–256
50. Kioumarsi M, Plevris V, Shabani A. Vulnerability assessment of cultural heritage structures. In: The 8th European Congress on Computational Methods in Applied Sciences and Engineering (ECCOMAS 2022). Oslo: Scipedia, 2022, C52
51. Fanning P J, Boothby T E. Three-dimensional modelling and full-scale testing of stone arch bridges. Computers & Structures, 2001, 79(29–30): 2645−2662
52. Aytulun E, Soyoz S, Karcioglu E. System identification and seismic performance assessment of a stone arch bridge. Journal of Earthquake Engineering, 2022, 26(2): 723−743
53. Wang J. Numerical modelling of masonry arch bridges: Investigation of spandrel wall failure. Dissertation for the Doctoral Degree. Bath: University of Bath, 2014
54. Selby R G. Three-dimensional constitutive relations for reinforced concrete. Dissertation for the Doctoral Degree. Toronto: University of Toronto, 1993
55. Rots J G. Computational modeling of concrete fracture. Dissertation for the Doctoral Degree. Delft: Delft University of Technology, 1988
56. Psycharis I N, Avgenakis E, Taflampas I M, Kroustallaki M, Farmakidou E, Pikoula M, Michailidou M, Moropoulou A. Seismic response of the Temple of Pythian Apollo in Rhodes Island and recommendations for its restoration. In: Osman A, Moropoulou A, eds. Nondestructive Evaluation and Monitoring Technologies, Documentation, Diagnosis and Preservation of Cultural Heritage. Berlin: Springer, 2019, 160–177
57. Ghiassi B, Vermelfoort A T, Lourenço P B. Chapter 7—Masonry mechanical properties. In: Ghiassi B, Milani G, eds. Numerical Modeling of Masonry and Historical Structures. Sawston: Woodhead Publishing, 2019, 239–261
58. Forgács T, Rendes S, Ádány S, Sarhosis V. Mechanical role of spandrel walls on the capacity of masonry arch bridges. In: Proceedings of ARCH 2019. Berlin: Springer, 2020, 221–229
59. Bayraktar A, Türker T, Altunişik A C. Experimental frequencies and damping ratios for historical masonry arch bridges. Construction & Building Materials, 2015, 75: 234−241
60. Onat O. Impact of mechanical properties of historical masonry bridges on fundamental vibration frequency. Structures, 2020, 27: 1011−1028
61. PEER. PEER Ground Motion Database. Berkeley, CA: University of California, 2021
62. EN 1998-1. Eurocode 8: Design of Structures for Earthquake Resistance-Part 1: General Rules, Seismic Actions and Rules for Buildings. Brussels: European Committee for Standardization, 2004
63. Karatzetzou A, Pitilakis D, Karafagka S. System identification of mosques resting on soft soil. The case of the Suleiman Mosque in the Medieval City of Rhodes, Greece. Geosciences, 2021, 11(7): 275
64. FEMA P695. Quantification of Building Seismic Performance Factors. Washington, D.C.: Federal Emergency Management Agency, 2009

65. Giardini D, Wössner J, Danciu L. Mapping Europe's seismic hazard. Eos, Transactions American Geophysical Union, 2014, 95(29): 261−262
66. Pitilakis K, Riga E, Roumelioti Z. The urgent need for an improvement of the Greek seismic code based on a new seismic hazard map for Europe and a new site classification system. In: Kavvadas M, ed. Jubilee Volume, Andreas Anagnostopoulos, 50 Years of Service at The National Technical University of Athens. Athens: Tsotras, 2016, 437–461
67. SeismoMatch: Earthquake software for response spectrum matching. Version 2021. Pavia: SeismoSoft–Earthquake Engineering Software Solutions. 2021
68. Al Atik L, Abrahamson N. An improved method for nonstationary spectral matching. Earthquake Spectra, 2010, 26(3): 601−617
69. Bertolesi E, Milani G, Lopane F D, Acito M. Augustus Bridge in Narni (Italy): Seismic vulnerability assessment of the still standing part, possible causes of collapse, and importance of the Roman concrete infill in the seismic-resistant behavior. International Journal of Architectural Heritage, 2017, 11(5): 717−746
70. Gönen S, Soyöz S. Reliability-based seismic performance of masonry arch bridges. Structure and Infrastructure Engineering, 2022, 18(12): 1658−1673
71. Chopra A K, Goel R K. A modal pushover analysis procedure for estimating seismic demands for buildings. Earthquake Engineering & Structural Dynamics, 2002, 31(3): 561−582

Paper IX

Shabani, A., Kioumarsi, M.

Optimal sensor placement techniques for modal identification of historical masonry structures,

(2022), 23rd European Conference on Fracture, Procedia Structural Integrity, https://doi.org/10.1016/j.prostr.2022.12.018.

Available online at www.sciencedirect.com

ScienceDirect

Procedia Structural Integrity 42 (2022) 147–154

Structural Integrity
Procedia

www.elsevier.com/locate/procedia

23 European Conference on Fracture - ECF23

Optimal sensor placement techniques for modal identification of historical masonry structures

Amirhosein Shabani*, Mahdi Kioumarsi

Department of Civil Engineering and Energy Technology, Oslo Metropolitan University, 0166 Oslo, Norway

Abstract

Since destructive tests are not allowed for historical structures, numerical model updating using accelerometers has gained a lot of attraction in the last decade. Furthermore, another application of structural health monitoring is damage detection for near-real-time monitoring of cultural heritage assets of infrastructures such as masonry bridges. However, high cost is the main problem that discourages the use of large-scale structural health monitoring systems, and a modal pretest analysis is required to plan and optimize the modal tests procedure. For this purpose, various optimal sensor placement (OSP) techniques have been developed to derive the operational modal analysis results with a minimum number of sensors, leading to a lower cost. In this study, various OSP techniques have been applied to optimize sensor placement in two selected case studies. The first case study is a two-span masonry arch bridge in Rhodes, Greece and the second is a stone masonry tower located in Tønsberg, Norway. Baseline finite element models were developed before performing the ambient vibration tests and model updating process. The optimum sensor locations were detected using various techniques, and a comparative study was conducted on the results. Furthermore, the effect of considering soil-structure interaction on the OSP results was investigated.

Keywords: Optimal sensor placement; Structural health monitoring; Historical masonry structures.

1. Introduction

Conservation of cultural heritage assets is crucial for every nation not only due to their spiritual point of view but also for their importance as tourist attractions that influence the economic growth of countries, as highlighted by

---

* Corresponding author. Tel.: +4767237972.
E-mail address: amirhose@oslomet.no

10.1016/j.prostr.2022.12.018

Shabani et al. (2020). However, irreparable loss of cultural heritage assets because of man-made and natural hazards has been warned by the international organizations involved in the preservation of cultural heritage assets, based on Valagussa et al. (2021). Fig. 1 illustrates the UNESCO cultural heritage sites map of the European countries and the seismic, landslide and active volcanoes hazard maps. The concentration of cultural heritage assets in high seismicity zones with high susceptibility to landslide and active volcanoes risks can be concluded, especially in southern European countries.

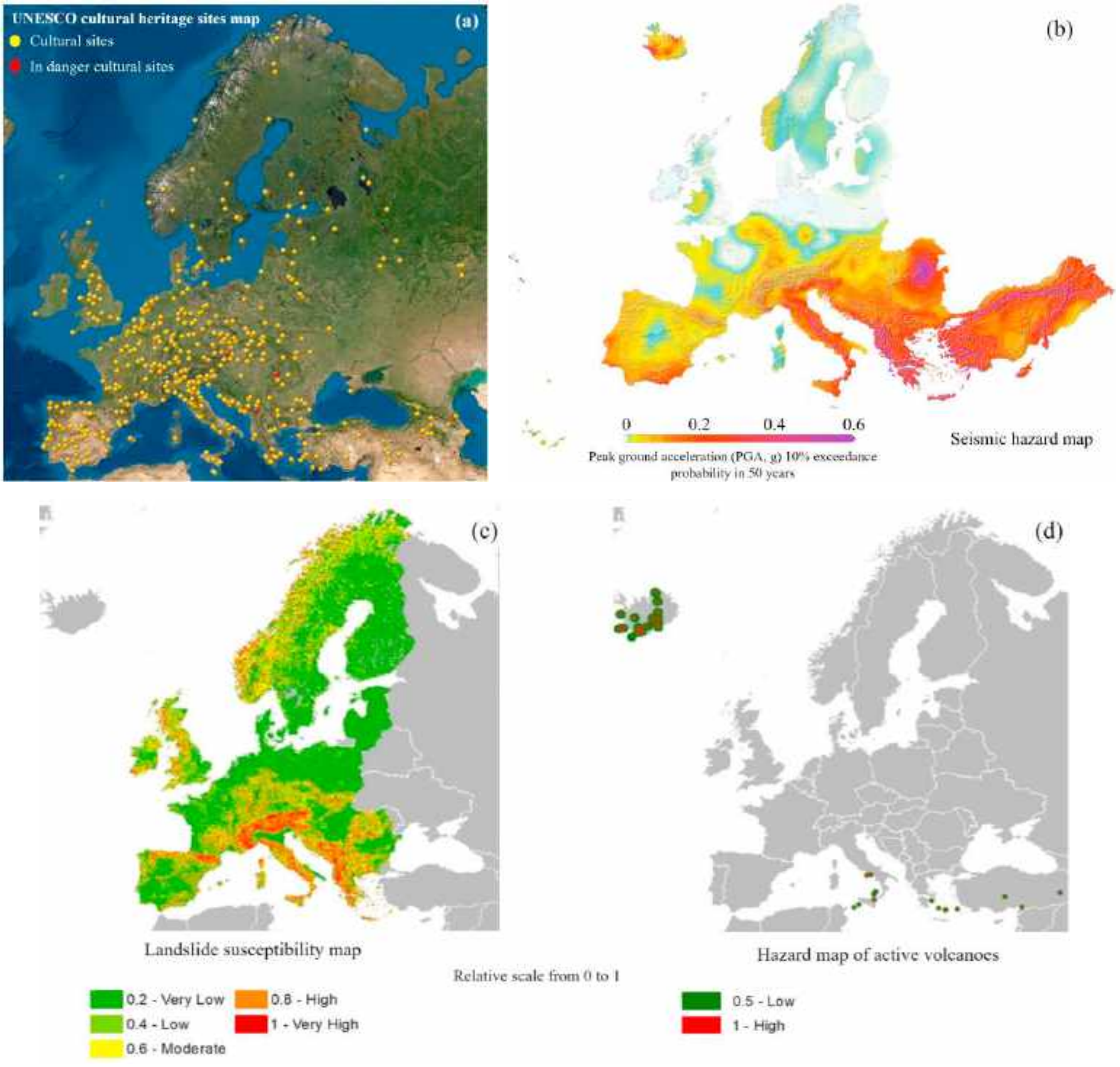

Fig. 1. (a) The UNESCO cultural heritage sites map (adapted from https://whc.unesco.org/), (b) seismic hazard map developed by Danciu et al. (2021), (c) landslide susceptibility map presented by Günther, Van Den Eeckhaut, et al. (2014) and (d) hazard map of volcanoes presented by Günther, Hervás, et al. (2014).

Various methodologies have been developed and applied for the vulnerability assessment and conservation of architectural heritages, as highlighted by Shabani, Kioumarsi, et al. (2021), and Shabani, Alinejad, et al. (2021). Destructive tests are not allowed to be employed for investigating the mechanical properties of historic structures.

Therefore, structural health monitoring and damage detection using accelerometer sensors can be one of the most reliable methods for either predicting the vulnerability or near-real-time assessment of historical structures as presented by Angjeliu et al. (2020). Furthermore, material properties can be defined by calibrating the FEMs based on the operational modal analysis (OMA) results which are based on ambient vibration testing (AVT) using accelerometers as elaborated by Pallarés et al. (2021). However, the cost of sensors is one of the main limitations of these methods. To tackle this limitation, various optimal sensor placement (OSP) methods have been proposed for detecting the best location of the limited number of sensors before performing the tests to derive the dynamic characteristics of structures such as mode shapes as presented in Tan & Zhang (2020). In recent decades, there have been many contributions in this area. Fig. 2 shows the evolution of the number of journal papers related to the OSP topic, structural health monitoring, and damage detection topics using the Scopus database. However, the application of the OSP methods to historical structures with complex architecture should be investigated.

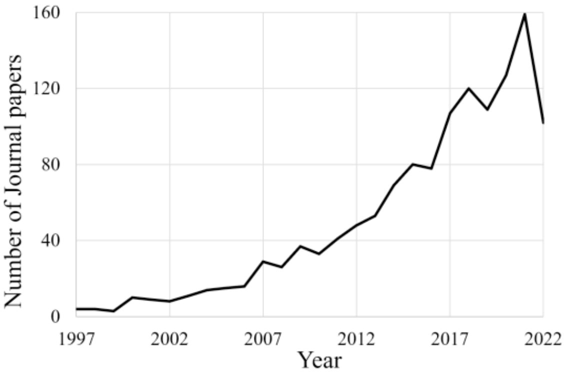

Fig. 2. The number of journal papers related to the OSP and structural health monitoring using the Scopus database.

In this paper, a stone masonry tower and a stone masonry arch bridge were chosen to be studied as two representations of historical structures. The application of five OSP methods to the selected case studies has been investigated. In the first step, finite element models of the case studies were developed, and the initial material properties were assigned. Afterward, the OSP analyses were carried out, and the results of different methods were compared. In addition, the effect of soil-structure interaction was taken into account for the tower, and the results of the OSP methods were compared to the results of the models with rigid boundary conditions.

2. OSP methods and acceptance criterion

OSP methods can be categorized into two main groups as presented in Fig. 3, which are sensor placement metrices and sensor elimination methods. Each method in Fig. 3 was chosen to be applied to the case studies and presented in this section.

Sensor placement methods are based on sensor placement metrices to detect the candidate sensors. Normalized modal displacement (NMD) is based on the observability of target modes using the information on weighted modal displacement. Although various types of modal displacements can be utilized, the weighted modal displacement was chosen as prescribed by FEMtools (2021). In the Normalized kinetic (NKE) method, the distribution of the kinetic energy for a particular mode is considered the metric for detecting the locations with large modal participation.

The main aim of the sensor elimination methods is to reduce the sensors from the first candidates and investigate the effect of elimination criteria. The Effective independence method (EIM) uses linear independence of mode shapes as an elimination criterion by avoiding the singularity of the Fisher information matrix based on Demirlioglu et al. (2023). The modal assurance criterion (MAC) is commonly utilized to compare the mode shape by calculating the squared cosine of the angle between two mode shapes. The main goal of the sensor elimination using MAC (SEMAC) method sensor elimination process is to minimize the off-diagonal terms of the MAC matrix. The idea of the iterative Guyan reduction (IGR) method is to eliminate the degree of freedom with small mass-to-stiffness ratios from the model by computing the reduced mass and stiffness matrices based on Ostachowicz et al. (2019).

Although sensor placement metrices methods are computationally efficient, the linear independence is not investigated and can be checked based on the MAC matrix. Unlike sensor placement metrices methods, linear independence, which is important for distinguishing each mode from others, is taken into account in the sensor elimination methods. Various acceptance criteria have been suggested to investigate the quality of the OSP methods as described by Tan & Zhang (2020). MAC matrix is one of the acceptance criteria to investigate the observability of the modes and their independence. MAC matrix criterion is commonly used for mechanical and structural applications, which is utilized as the criterion in this study. There is no standard for this criterion, but the off-diagonal terms of the MAC matrix should be less than 40% suggested by FEMtools (2021).

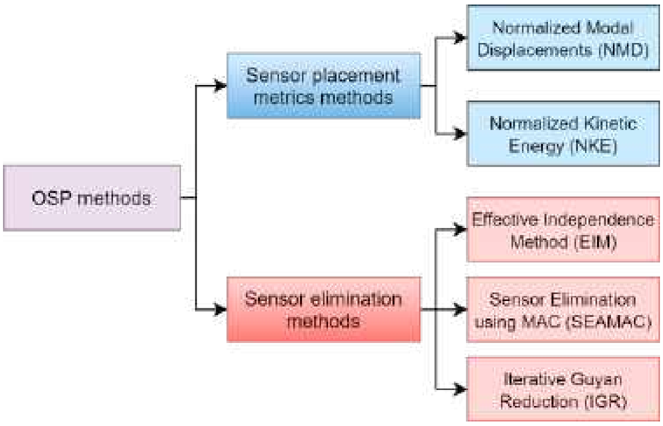

Fig. 3. Different OSP methods and their classification.

3. Case studies

Historical structures are known to be complex in terms of architecture, as mentioned by Miccoli et al. (2021). Masonry arch bridges and masonry towers are two conventional types of historical structures together with mosques, churches, monasteries, and aqueducts. In this section, the OSP methods were applied to a masonry arch bridge and a masonry tower. For the OSP analysis, seven uniaxial accelerometers were taken into account for both case studies.

3.1. Stone Masonry Bridge (Roman Bridge)

The Roman bridge (see Fig. 4.) is on Rhodes Island in Greece and is dated back to the Roman period. The structure is under service load, but extensive damages can be seen under the arches. Although temporary timber scaffolds were installed, a strengthening strategy should be decided to avoid future damages due to the car and truck loads and the possible seismic loads. The Roman bridge is a stone masonry bridge with two arches. The radius of the arches and the widths are 3.2 m and 8.4 m, respectively. 3D models of the structure were provided using the areal images (drones) and ground images (cameras) together with 3D laser scanners. In addition, 3D finite element models were developed as elaborated by Shabani, Skamantzari, et al. (2022). The bridge was made of Sfoggaria stone; the mechanical properties of the homogenized masonry were derived based on the mechanical properties of the stone presented by Psycharis et al. (2019) and the equations by Ghiassi et al. (2019). Furthermore, the material properties of the backfill soil were considered, as stated by Forgács et al. (2020).

Modal analyses of the initial finite element model reveal that the first, third and fourth modes are in the transverse (Y) direction, the second mode is in the longitudinal (X) direction, and the fifth mode is in the vertical (Z) direction of the bridge. Since the bridge was under the service load, installing sensors on the way is not permitted. Therefore, two sides of the bridge were selected, and OSP analyses were performed. The MAC matrices as well as the sensor locations and their directions, are illustrated in Fig. 4. The results revealed that sensor placement metrices methods are not robust enough to detect the best locations by considering the MAC as a criterion. However, the off-diagonal members of the MAC matrices of the sensor elimination methods are less than 40%. The typical location in the sensor configurations is in the middle of the spandrel wall between the arches. Furthermore, the second most essential locations are the top of the arches. Based on the results from the EIM and considering the effect of kinetic energy and normal modal displacements concluded from the NKE and NMD, the locations on top of the arches which are closer to the sides of the bridge should be taken into account. Therefore, installing sensors in two configurations with a reference sensor for covering these locations is recommended.

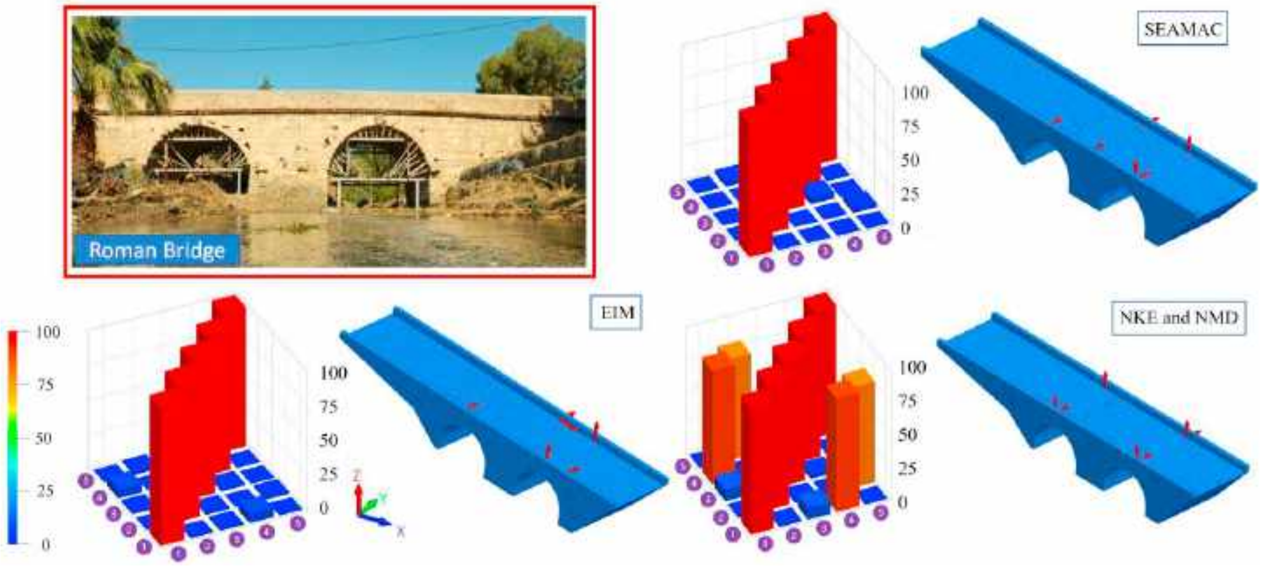

Fig. 4. The results of the OSP of the masonry arch bridge (the Roman bridge), including the MAC matrices and the prescribed locations.

3.2. Stone Masonry Tower (Slottsfjell Tower)

Slottsfjell is a three-story tower with a basement floor in Tønsberg, Norway. The tower (see Fig. 5 (a)) was dated back to 1888 on top of a rocky hill and in the area of a ruined historical castle called Tunsbergis. Fig. 5 (b) illustrates the model of the Tunsbergus castle, which was the largest castle in Norway in the 14th century and was destroyed in 1503 based on Norli (2021). The 3D finite element mesh of the tower was developed using 3D laser scanners, and details about the procedure are elaborated by Shabani, Ademi, et al. (2022). In order to investigate the effect of boundary conditions on the dynamic characteristics, as was highlighted by Salehi & Erduran (2022), two models were developed, which are the fixed base model (FB) and the model, by considering the effect of soil-structure interaction (SSI) as depicted in Fig. 5 (c) and (d), respectively. In the SSI model, the direct method has been utilized by modeling the foundation and the soil box, as elaborated by Shabani, Feyzabadi, et al. (2022). The first and the second modes of both models are transversal in X and Y directions, the third mode is the torsional mode, and the fourth and fifth modes are transversal in X and Y directions, respectively.

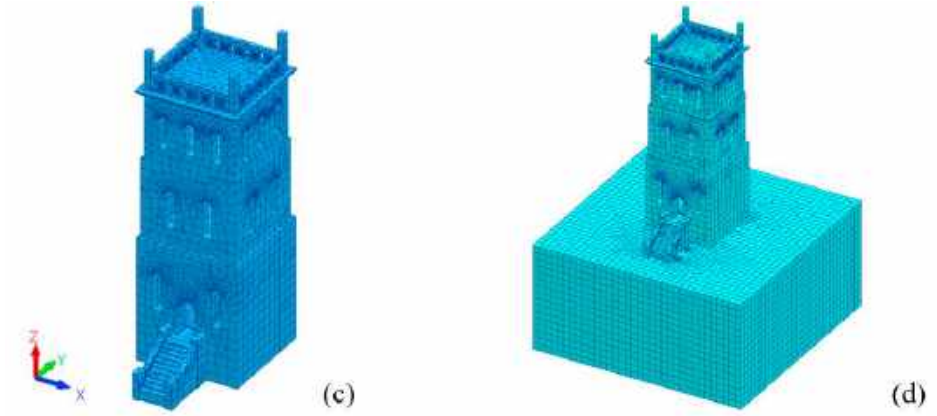

Fig. 5. (a) Slottsfjell Tower in Tønsberg (b) old Tunsberghus fortress based on Norli (2021), 3D FEM of (c) fixed-base model and (d) the model with considering SSI.

The edges of the inner sides of each floor, including the roof, were selected as the optimized candidates for installing seven sensors to perform the OSP analysis. Fig. 6 shows the optimum sensor configurations and the MAC matrix for each OSP method applied to the FB model. Results depict that the sensor elimination methods except for the EIM are robust enough to detect the best locations by considering the MAC as a criterion. The roof has allocated the largest number of sensor locations, and all methods prescribe installing sensors neither on the first floor nor in the Z direction. Based on the IGR and SEAMAC results, the second floor is as important as the third floor for sensor installation and AVT.

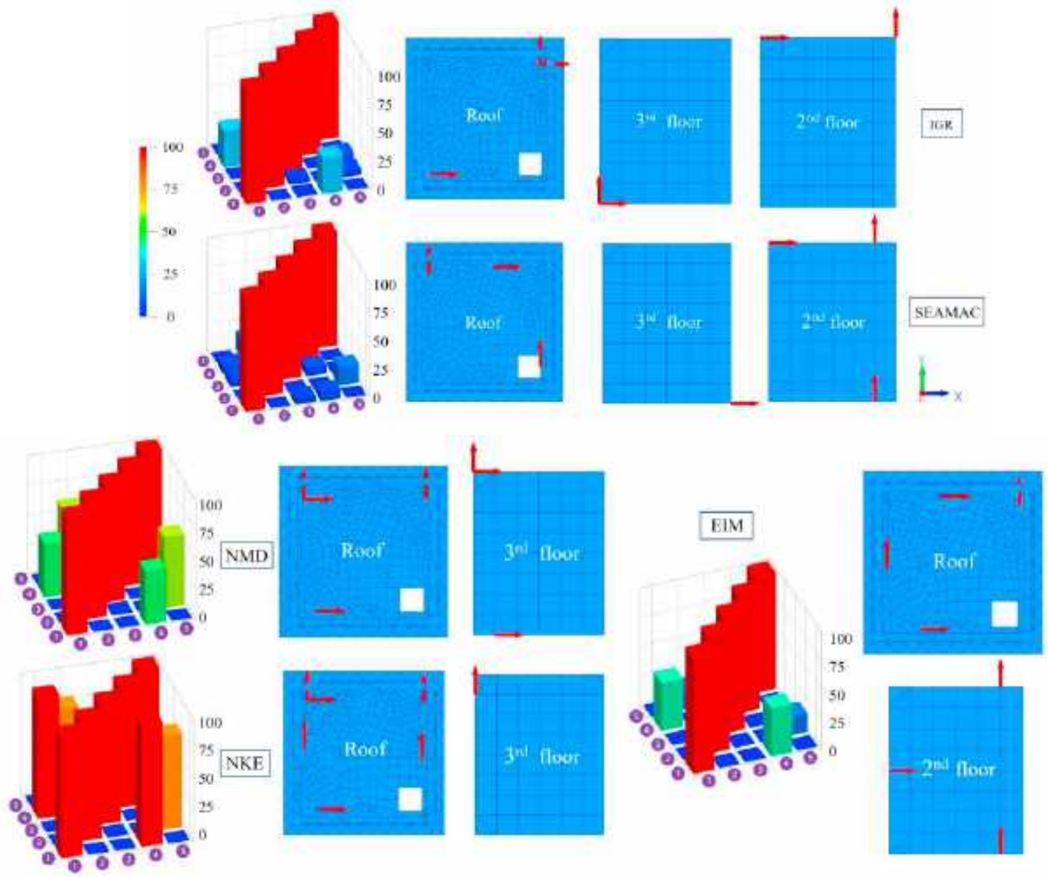

Fig. 6. The results of the OSP of the fixed-base model of the Slottsfjell tower, including the MAC matrices and the prescribed locations.

OSP of the model considering SSI was performed on the Slottsfjell tower, and the results are presented in Fig. 7 for all five methods. The MAC matrices were not changed significantly, but the leading locations were shifted from the third floor to the second floor. This could be due to the flexibility of the boundary conditions of the tower because of considering the effect of SSI. Therefore, except for the roof, the optimum locations should not necessarily be on the upper floors, and the second and third floors are the essential floors for installing the sensors.

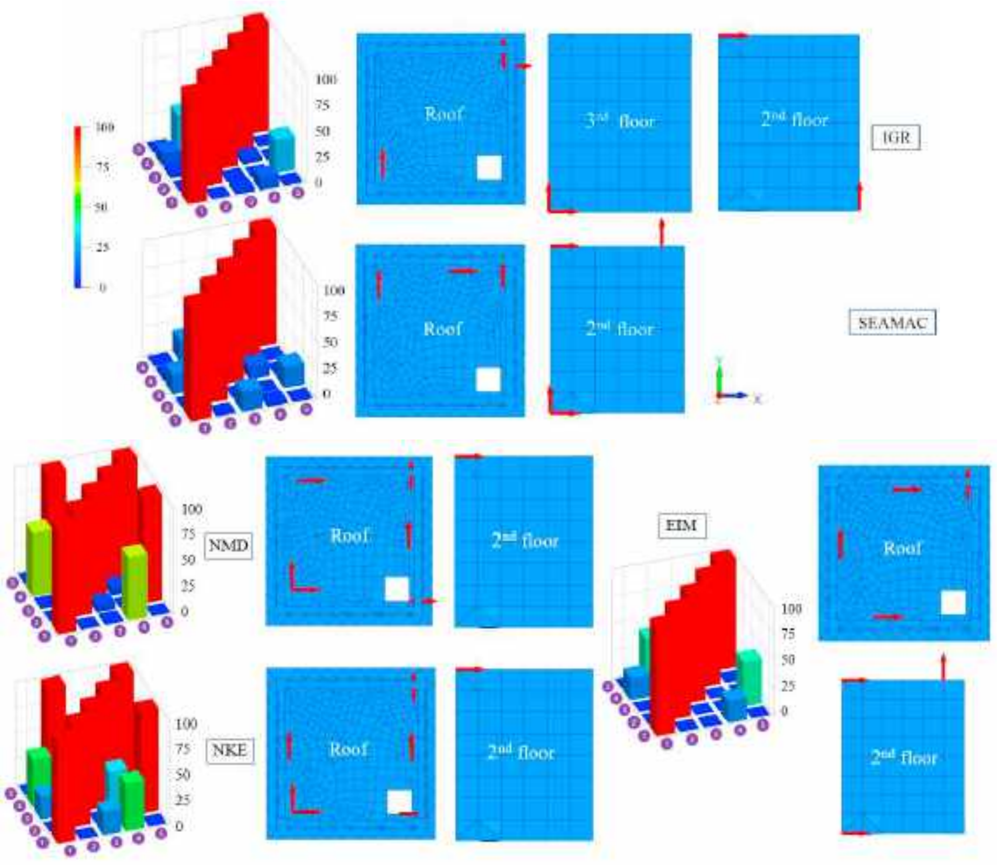

Fig. 7. The results of the OSP of the Slottsfjell tower model considering SSI, including the MAC matrices and the prescribed locations.

4. Conclusion

Identifying the optimized locations of the limited numbers of accelerometers to derive the mode shapes of structures can be done by applying the OSP methods on the FEMs with initial material properties. Since destructive tests are not permitted to define the material properties of historical structures, OSP methods are recommended before performing AVT. The application of different OSP methods on the FEMs of a stone masonry arch bridge and a stone masonry tower was investigated. The results revealed that sensor elimination methods are more robust than the sensor metrices methods by considering the MAC as a criterion. For the masonry arch bridge, the sensors should cover the locations in the middle of the spandrel walls, on top of the arches, and locations between the top of the arches and two sides of the bridge. The roof is the most important place for installing the sensors, and installing sensors on the first floor was not recommended. Furthermore, by modeling the soil box and foundation based on the direct method for considering the SSI, the MAC matrices were not changed significantly, but the candidate sensor locations were shifted from the third floor to the second floor. Thus, the sensors should cover the roof, second, and third floors, respectively. Unlike for the Slottsfjell tower, the vertical (Z) direction is crucial to be recorded for the Roman bridge. The SEAMAC is considered an efficient OSP method due to its formulation based on the numerical analysis in this study. However, in order to confirm these findings, the results of the numerical analysis should be compared to the results of the OMA, which are based on the AVT.

Acknowledgements

This work is a part of the HYPERION project. HYPERION has received funding from the European Union's Framework Programme for Research and Innovation (Horizon 2020) under grant agreement No 821054. The contents of this publication are the sole responsibility of Oslo Metropolitan University (Work Package 5, Task 2) and do not necessarily reflect the opinion of the European Union.

References

Angjeliu, G., Coronelli, D., & Cardani, G., 2020. Development of the simulation model for Digital Twin applications in historical masonry buildings: The integration between numerical and experimental reality. Computers & Structures, 238, 106282. doi:https://doi.org/10.1016/j.compstruc.2020.106282

Danciu, L., Nandan, S., Reyes, C., Basili, R., Weatherill, G., Beauval, C., Rovida, A., Vilanova, S., Sesetyan, K., Bard, P.-Y., Cotton, F., Wiemer, S., & Giardini, D. (2021). *The 2020 update of the European Seismic Hazard Model: Model Overview, EFEHR Technical Report 001, v1.0.0,* . Retrieved from

Demirlioglu, K., Gonen, S., & Erduran, E. (2023). On the Selection of Mode Shapes Used in Optimal Sensor Placement. In *Sensors and Instrumentation, Aircraft/Aerospace and Dynamic Environments Testing, Volume 7* (pp. 85-92): Springer.

FEMtools. (2021). *Dynamic Design Solutions, FEMtools 4.1, Pretest and correlation analysis user guide*. Retrieved from Leuven, Belgium:

Forgács, T., Rendes, S., Ádány, S., & Sarhosis, V. (2020). *Mechanical Role of Spandrel Walls on the Capacity of Masonry Arch Bridges.* Paper presented at the Proceedings of ARCH 2019, Cham.

Ghiassi, B., Vermelfoort, A. T., & Lourenço, P. B. (2019). Chapter 7 - Masonry mechanical properties. In B. Ghiassi & G. Milani (Eds.), *Numerical Modeling of Masonry and Historical Structures* (pp. 239-261): Woodhead Publishing.

Günther, A., Hervás, J., Van Den Eeckhaut, M., Malet, J.-P., & Reichenbach, P. (2014, 2014//). *Synoptic Pan-European Landslide Susceptibility Assessment: The ELSUS 1000 v1 Map.* Paper presented at the Landslide Science for a Safer Geoenvironment, Cham.

Günther, A., Van Den Eeckhaut, M., Malet, J.-P., Reichenbach, P., & Hervás, J., 2014. Climate-physiographically differentiated Pan-European landslide susceptibility assessment using spatial multi-criteria evaluation and transnational landslide information. Geomorphology, 224, 69-85. doi:https://doi.org/10.1016/j.geomorph.2014.07.011

Miccoli, S., Gil-Martín, L. M., & Hernández-Montes, E., 2021. New historical records about the construction of the Arch of Ctesiphon and their impact on the history of structural engineering. Notes and Records: the Royal Society Journal of the History of Science, 0(0). doi:https://doi.org/10.1098/rsnr.2021.0025

Norli, A. B. (2021). *Norsk Borgesenster 2021, Vestfoldmuseene*. Retrieved from Tønsberg, Norway, (in Norwegian): https://dms-cf-03.dimu.org/file/013AmNa3rfhc

Ostachowicz, W., Soman, R., & Malinowski, P., 2019. Optimization of sensor placement for structural health monitoring: a review. Structural Health Monitoring, 18(3), 963-988. doi:doi:10.1177/1475921719825601

Pallarés, F. J., Betti, M., Bartoli, G., & Pallarés, L., 2021. Structural health monitoring (SHM) and Nondestructive testing (NDT) of slender masonry structures: A practical review. Construction and Building Materials, 297, 123768. doi:https://doi.org/10.1016/j.conbuildmat.2021.123768

Psycharis, I. N., Avgenakis, E., Taflampas, I. M., Kroustallaki, M., Farmakidou, E., Pikoula, M., Michailidou, M., & Moropoulou, A. (2019). *Seismic Response of the Temple of Pythian Apollo in Rhodes Island and Recommendations for Its Restoration.* Paper presented at the First International Conference on Transdisciplinary Multispectral Modelling and Cooperation for the Preservation of Cultural Heritage, Cham.

Salehi, M., & Erduran, E., 2022. Identification of boundary conditions of railway bridges using artificial neural networks. Journal of Civil Structural Health Monitoring, 1-24.

Shabani, A., Ademi, A., & Kioumarsi, M. (2022). Structural Model Updating of a Historical Stone Masonry Tower in Tønsberg, Norway. In (pp. 576-585). Cham: Springer International Publishing.

Shabani, A., Alinejad, A., Teymouri, M., Costa, A. N., Shabani, M., & Kioumarsi, M., 2021. Seismic Vulnerability Assessment and Strengthening of Heritage Timber Buildings: A Review. Buildings, 11(12), 661. Retrieved from https://www.mdpi.com/2075-5309/11/12/661

Shabani, A., Feyzabadi, M., & Kioumarsi, M., 2022. Model updating of a masonry tower based on operational modal analysis: The role of soil-structure interaction. Case Studies in Construction Materials, 16, e00957. doi:https://doi.org/10.1016/j.cscm.2022.e00957

Shabani, A., Kioumarsi, M., Plevris, V., & Stamatopoulos, H., 2020. Structural Vulnerability Assessment of Heritage Timber Buildings: A Methodological Proposal. Forests, 11(8), 881. doi:https://doi.org/10.3390/f11080881

Shabani, A., Kioumarsi, M., & Zucconi, M., 2021. State of the art of simplified analytical methods for seismic vulnerability assessment of unreinforced masonry buildings. Engineering Structures, 239, 112280. doi:https://doi.org/10.1016/j.engstruct.2021.112280

Shabani, A., Skamantzari, M., Tapinaki, S., Georgopoulos, A., Plevris, V., & Kioumarsi, M., 2022. 3D simulation models for developing digital twins of heritage structures: challenges and strategies. Procedia Structural Integrity, 37, 314-320. doi:https://doi.org/10.1016/j.prostr.2022.01.090

Tan, Y., & Zhang, L., 2020. Computational methodologies for optimal sensor placement in structural health monitoring: A review. Structural Health Monitoring, 19(4), 1287-1308. doi:10.1177/1475921719877579

Valagussa, A., Frattini, P., Crosta, G., Spizzichino, D., Leoni, G., & Margottini, C., 2021. Multi-risk analysis on European cultural and natural UNESCO heritage sites. Natural Hazards, 105(3), 2659-2676. doi:https://doi.org/10.1007/s11069-020-04417-7

Paper X

Shabani, A., Kioumarsi, M.

Seismic assessment and strengthening of a historical masonry bridge considering soil-structure interaction

(2023) Engineering Structures, https://doi.org/10.1016/j.engstruct.2023.116589.

Engineering Structures 293 (2023) 116589

Contents lists available at ScienceDirect

Engineering Structures

journal homepage: www.elsevier.com/locate/engstruct

Seismic assessment and strengthening of a historical masonry bridge considering soil-structure interaction

Amirhosein Shabani *, Mahdi Kioumarsi

Department of Built Environment, Oslo Metropolitan University, Pilestredet 35, 0166 Oslo, Norway

ARTICLE INFO

Keywords:
Digital twin
Seismic fragility
Masonry arch bridge
Soil-structure interaction
Operational modal analysis
Seismic strengthening
FRCM systems

ABSTRACT

A holistic methodology for developing the digital twins and conducting seismic vulnerability assessments of masonry arch bridges is proposed and applied to a historical stone masonry bridge. In this light, digital cameras, drones, and 3D laser scanners were utilized for 3D geometric documentation of the bridge. 3D finite element (FE) models were constructed and calibrated based on the operational modal analysis results derived from the accelerometer sensors. The fragility curves for different limit states were derived by performing a multi-stripe analysis (MSA). The effect of soil-structure interaction (SSI) on the calibration results and seismic response of the bridge was evaluated. The results of the visual inspection, model calibration, and seismic analysis revealed that the central pier and the arches are the most susceptible parts of the bridge. Therefore, three strengthening techniques were proposed, and corresponding numerical models were developed. The first model was developed by enhancing the mechanical properties of the vulnerable parts of the bridge, and the two other models were built by covering the central pier's outer surface with polyparaphenylene benzobisoxazole (PBO) and carbon fiber-reinforced concrete mortar (FRCM) layers. Results revealed that the strengthening techniques improved the seismic response of the bridge when subjected to transverse seismic excitations. Negligible differences in the displacement response and crack width of the strengthened models were observed from the nonlinear dynamic analysis.

1. Introduction

Masonry arch bridge conservation is crucial for authorities because of their importance as infrastructure for the road and railway networks and their merit as cultural heritage assets [1]. However, masonry arch bridges are susceptible to earthquake loads because masonry is a brittle construction material, and the bridges are not designed based on current design codes. Moreover, their structural condition has changed due to material decay, fatigue, boundary condition changes, and applied load changes, including higher axle loads and vehicle speeds, since the time that they were built [2]. Masonry bridges comprise around 25% of road bridges and around 45% of railway bridges in Europe [3]. Therefore, a reliable modeling and analysis strategy is required to increase their resiliency.

Efficient numerical modeling and simulation of masonry arch bridges have been an interesting and challenging problem for researchers and structural engineers [4–6]. Masonry arch bridges are heterogeneous structures composed of stone or brick, mortar, and backfill soil that have a distinct architecture due to the presence of arches. Furthermore, finding a solution for considering the effects of masonry and backfill soil interaction and applying appropriate boundary conditions are two pivotal issues that should be taken into account [2,7]. Discrete element modeling is considered the most accurate modeling approach for the nonlinear analysis of masonry arch bridges, with the highest level of computational effort among other methodologies [8,9]. However, by employing acceptable simplifications in the modeling procedure and diminishing the level of computational efforts, the homogenous finite element (FE) method can be an accurate enough solution for seismic analysis of masonry bridges [10–12]. Soil-structure interaction (SSI) effects were usually neglected for nonlinear analysis of various masonry bridges, and fixed base boundary conditions were applied [9,13,14]. Nevertheless, the structure and foundation interaction with the surrounding soil could be influential on the structural response [15]. The inertial interaction effect that causes additional deformations in the soil and changes the base motion is more pronounced for heavy structures such as nuclear power plants and masonry arch bridges [15–19].

Defining a structure's precise material properties is an essential part

---

* Corresponding author.
E-mail addresses: amirhose@oslomet.no (A. Shabani), mahdi.kioumarsi@oslomet.no (M. Kioumarsi).

https://doi.org/10.1016/j.engstruct.2023.116589
Received 16 January 2023; Received in revised form 16 June 2023; Accepted 9 July 2023

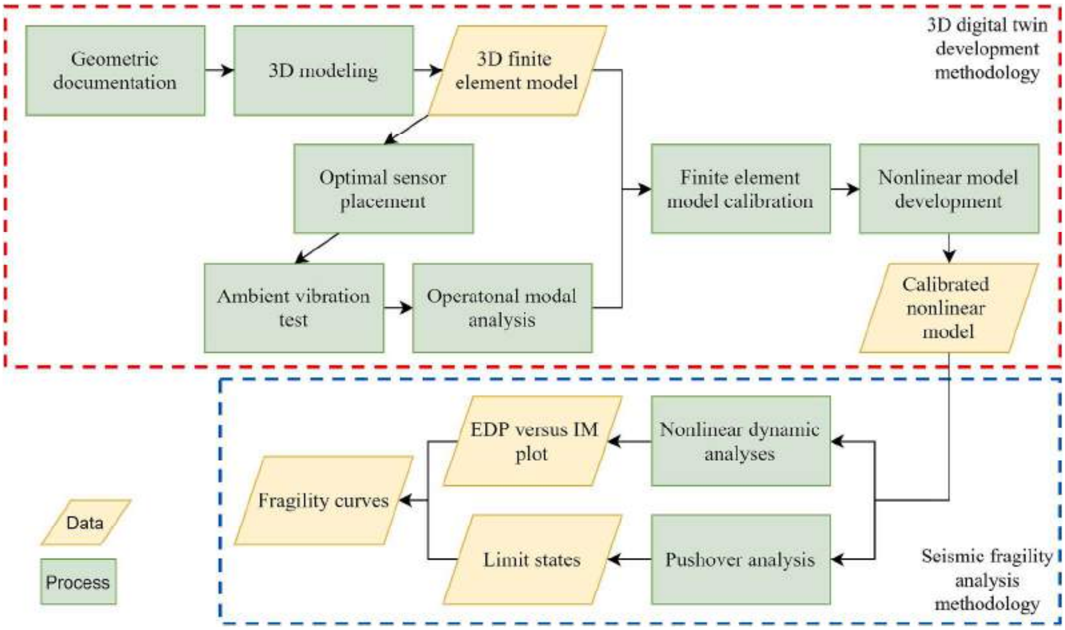

Fig. 1. Methodology of developing 3D digital twins and seismic fragility of historic structures.

of developing its digital twin [20]. However, destructive tests to determine the material properties of masonry arch bridges are usually forbidden because they are considered cultural heritage assets. Furthermore, historical structures suffer from various types of risks that can influence their material properties. For this purpose, calibration of the historical masonry arch bridges model based on the operational modal analysis (OMA) results has recently gained considerable attention [21–24]. The effect of model calibration on the seismic behavior of the masonry structures highlights the importance of this step for developing a robust and accurate numerical model [23,25].

After seismic analyses of the updated numerical models, proposing an efficient and applicable strengthening technique is the final part of an assessment and retrofitting methodology. When retrofitting cultural heritage structures, it is important to follow five key principles: respect for authenticity, minimal structural intervention, compatibility, reversibility (the ability to remove changes), and durability. These guidelines aim to ensure that any changes made to the structure preserve its historical and cultural significance while allowing for its long-term preservation and maintenance [26,27]. However, it is difficult to find a strengthening strategy that satisfies all these rules [26]. A few studies investigated the seismic response of masonry arch bridges strengthened by using fiber-reinforced cementitious matrices (FRCM) [28,29], fiber-reinforced polymer (FRP) composites [30,31], steel anchorage [32], or enhancing the existing masonry mechanical properties [33].

Despite the aforementioned investigations, some gaps can be found, including limitations regarding the SSI effects, numerical modeling aspects, and strengthening strategies. The FE model calibration of a masonry tower, considering SSI effects and comparing the results with the calibrated fixed base model, was investigated by performing a linear time history analysis [34]. Nevertheless, a research study is required to investigate the SSI effects on the seismic behavior of masonry arch bridges, considering the material properties' nonlinearity. Furthermore, because of the high computational efforts involved in the nonlinear analysis of full-scale masonry bridges, the seismic analysis of these structures was typically limited to applying a number of seismic records instead of performing a seismic fragility analysis based on the nonlinear analysis of a group of records with different intensities and properties. The strengthening proposals have also been limited to the retrofitting of spandrel walls or arches of the bridges, and a numerical investigation focusing on the strengthening of the eroded piers of the bridges should be carried out. In this paper, a methodology for deriving the seismic fragility curves of masonry arch bridges for different limit states is proposed and applied to a case study. Accurate geometric documentation of the bridge was done, and two 3D FE models were created for further analysis; in one of them, the SSI is considered, but in another model, the effect was neglected by considering rigid boundary conditions. On the other hand, ambient vibration tests (AVT) were carried out to determine the dynamic characteristics of the case study. FE model calibration was performed for both models, and the material properties were updated. Nonlinear analyses were performed on a model with SSI to obtain the fragility curves. A comparative study was performed to investigate the effect of considering the SSI effects during the whole process. Vulnerable structural parts were detected after seismic damage assessment and three different strengthening techniques were proposed. 3D models of the strengthened bridges were developed, and nonlinear analyses were performed to investigate the efficiency of the strategies.

2. Methodology and overview of the case study

2.1. Methodology

Geometric documentation of a structure is essential for developing digital twins, and various methods have evolved to automate this step in the fastest and most accurate way using different types of digital sensors and instruments. After deriving the geometries, the 3D FE model is constructed, and initial material properties are assigned to different parts based on the empirical equations or limited experimental tests on the construction material.

The material properties of the FE model are calibrated to match the modal properties of the FE model with those recorded experimentally. AVT is used to determine the structure's modal properties. Next, the natural frequencies and their corresponding mode shapes are defined by performing the OMA [35]. Before performing the AVT, it is recommended to conduct an optimal sensor placement (OSP) analysis to determine the best locations for the accelerometers [36]. The numerical model can be calibrated using one of the various numerical approaches presented to minimize the modal properties of the real structure and the numerical model [37,38]. The whole methodology for developing the 3D digital twin is presented in the red-dotted rectangle of Fig. 1.

To evaluate the seismic performance of the structure, the damage

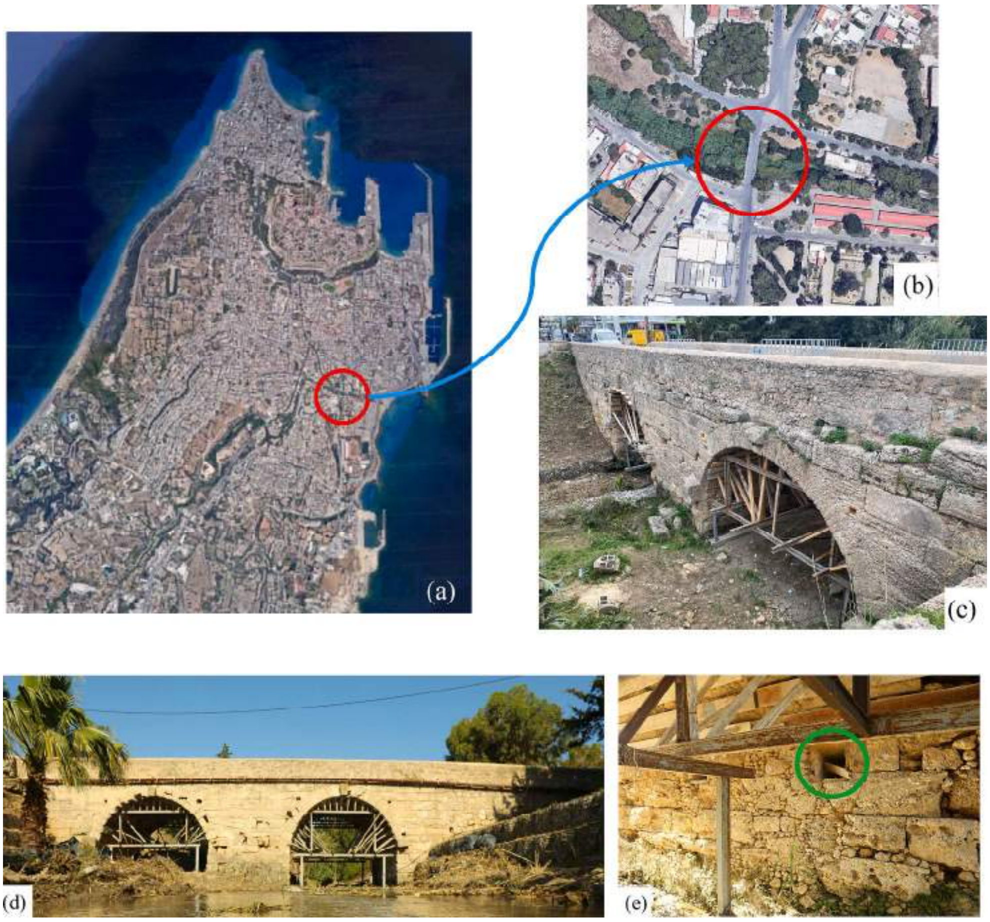

Fig. 2. (a) Rhodes Island in Greece and location of the Roman bridge, (b) top view of the Roman bridge, (c) and (d) Roman bridge from different views, and (e) holes in the central pier with erosion.

limit states are defined by performing a nonlinear pushover analysis. Nonlinear time history analysis is considered the most accurate seismic analysis method, but it requires a high computational effort [39]. A suitable nonlinear material model should be defined for the structure, and nonlinear time history analyses should be carried out by applying seismic records to the structure. The seismic excitations with various intensity measures (IM) are applied to the structure to perform the multi-stripe analysis (MSA) [40]. Seismic fragility curves can also be derived using the efficient methodology by maximizing the likelihood function suggested in [41]. The steps for seismic fragility analysis of the calibrated nonlinear model are illustrated in the blue-dotted rectangle of Fig. 1.

Various strengthening techniques are proposed after defining the most susceptible structural components through the seismic analysis of the calibrated model. Then, corresponding strengthened FE models are developed, and seismic analysis can be performed by applying a set of seismic records that impose a specific damage state on the structure. Finally, a comparative study of the structural demands of the strengthened models reveals the optimal strengthening proposal.

2.2. *Overview of the case study*

The Roman bridge is on the east coast of Rhodes Island, Greece (see Fig. 2 (a)) and was built across the stream of Rhodini before its outfall to the Mediterranean Sea, as illustrated in Fig. 2 (b). The bridge is 8.4 m wide with two spans of 6.4 m. The thickness of the masonry arch and spandrels is 0.6 m. The bridge was built during the Graeco-Roman era, around the first century BC. Based on the riverbed, the stream only passes through the southern arch, and erosion of the central pier was reported in different old books and diaries [42]. Fig. 2 (c) and (d) show different perspectives of the Roman bridge.

There are two holes on the south side and three on the north side of the bridge's central pier. Fig. 2 (e) highlights one of the holes in a green circle. These holes, with a length and width of 0.4 m and a depth of 0.8 m, may be used as support for the wooden logs. However, these openings can reduce the weight of the structure and diminish the possibility of water flow damage to the structure. However, based on the iron hinges attached to the sides of the holes and the Christian crosses engraved on blocks above one of the holes, it can be concluded that they were later used as storage closets [42].

The Roman bridge is one of the few remaining historical bridges in Greece. The bridge is used by both cars and heavy trucks and is considered one of the main roads in the eastern part of the island. Therefore, the conservation of the bridge is critical not just because of its historical significance but also because of its infrastructural importance as part of the island.

Cracks and spalling of the stone units beneath the arches and vegetation of the central pier and erosion of this part (see Fig. 2 (e)) are the existing damages that were investigated during the visual inspection of the bridge. Temporary scaffolds were built to avoid future damage beneath the arches and spalling stones. A robust and permanent strengthening strategy should be proposed for the preservation of this monumental infrastructure. Rhodes Island is situated in a highly seismic zone with a peak ground acceleration (PGA) of 0.35–0.55 g at a 10% probability of exceedance in 50 years [43], and documentation shows that some of the earthquakes were associated with tsunamis [44]. For this purpose, the presented methodology was applied to this case study to improve its resiliency to earthquake risks.

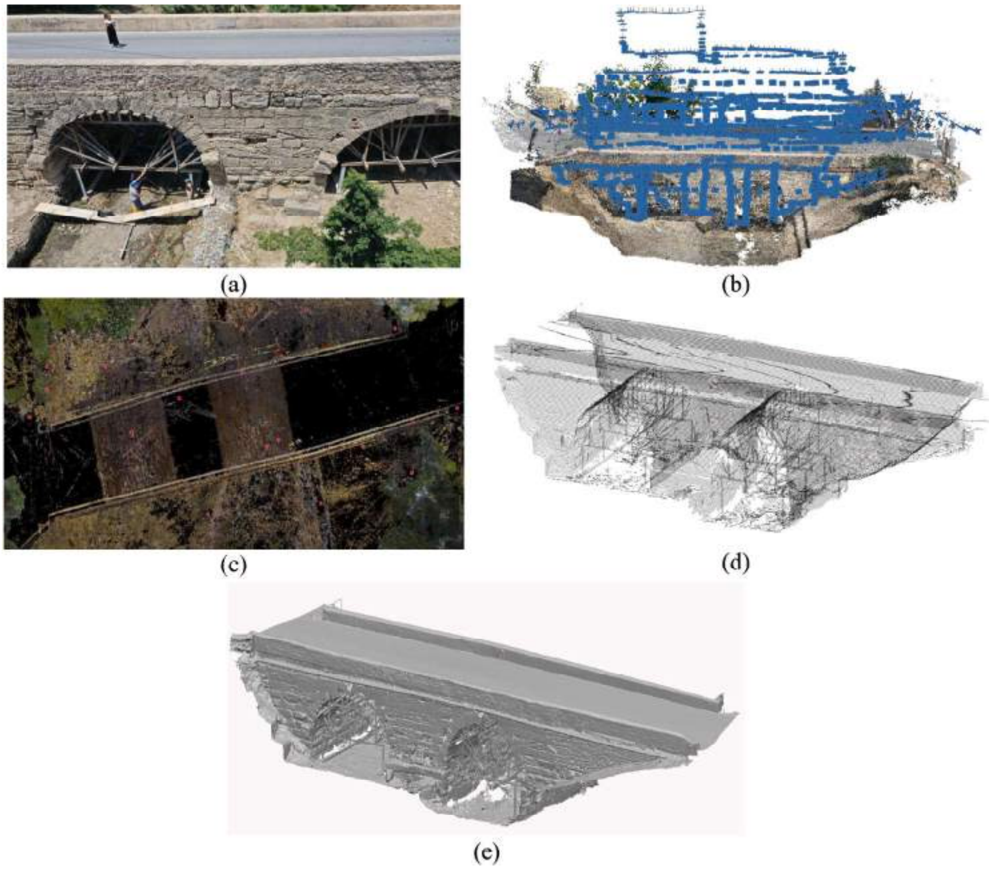

Fig. 3. (a) Geometric documentation campaign, (b) the position of the oriented cameras, (c) dense point cloud, (d) cross-section model, and (c) 3D light model of the Roman bridge.

3. 3D digital twin development of the bridge

3.1. 3D modeling of the bridge

A holistic methodology for deriving the 3D geometric documentation of structures was presented in [45,46]. Aerial images using drones and ground images using cameras are provided for the Roman Bridge, as depicted in Fig. 3 (a). A total of 271 ground digital images were taken, and 2576 aerial images using drones were taken with lower resolution than the ground images because of difficulties in accessing some parts of the structure. Next, the digital images were processed in image-based modeling software through filtering and noise reduction to develop the dense point cloud of the structure. The acquired images were reoriented with high accuracy via the automated structure of the motion process, as depicted in Fig. 3 (b). On the other side, 3D laser scanners are utilized to fill the gaps in the point clouds from the digital images and provide the final dense point cloud. Twenty-four scans were carried out using 3D laser scanners. A local coordinate system was made using two total stations to define target points for the point clouds from laser scanners and ground control points for the orientation of images. Georeferencing avoids possible errors when combining and processing the datasets from different instruments. The final 3D model can be developed by processing the triangulated irregular network representation model in such a way that each point is converted to a polygon object [46]. The 3D dense point clouds, a 3D light model, and the cross sections obtained following this process are illustrated in Fig. 3 (c), (d), and (e), respectively.

For creating the 3D FE model of the bridge, the dimensions were derived from the obtained 3D model from the previous step using DIANA FEA software [47]. Five main parts were considered for modeling the bridge, including arches, spandrel walls, backfill, piers, and parapets, as illustrated in Fig. 4 (a). The foundation and surrounding soils were modeled for modeling the SSI effects, as illustrated in Fig. 4 (b). The holes on two sides of the central pier were also modeled.

Two models were constructed. The first model (fixed-base model) has rigid boundary conditions without modeling foundations and soil media, neglecting the soil-foundation-bridge interaction effects, as illustrated in Fig. 4 (a). The second model (SSI model) was developed using the direct method to consider the SSI effects by modeling the soil and foundation parts, as depicted in Fig. 4 (b) [15]. The soil box was modeled with an equal length and width of 180 m. The depth of the soil was considered 30 m above the bedrock based on [17,48]. Pinned supports were applied to the four sides around the soil and one side at the bottom of the soil box [49–51]. Foundations are also modeled in three positions, embedded in the soil at a depth of 1.5 m beneath the piers.

Contact interface elements with a high initial stiffness value in normal compression and tangential friction with a tension cutoff were modeled to simulate the interaction between backfill and masonry media [1,13]. Therefore, the interface can transform the shear and compression normal stresses, but separation appears in tension between the foundation and the soil media. Although the interface element increases the computational effort by increasing the number of elements, it can simulate the actual interaction and avoid early convergence problems due to the high differences between the stiffness of the two media [52]. The contact interface element between the masonry and backfill soil domains follows the Coulomb friction model in shear with zero cohesion and a friction coefficient of 0.4 rad [53]. The effect of soil-foundation interaction was simulated using a nonlinear interface element [54]. The interface element has high normal and shear stiffness with a tension cutoff.

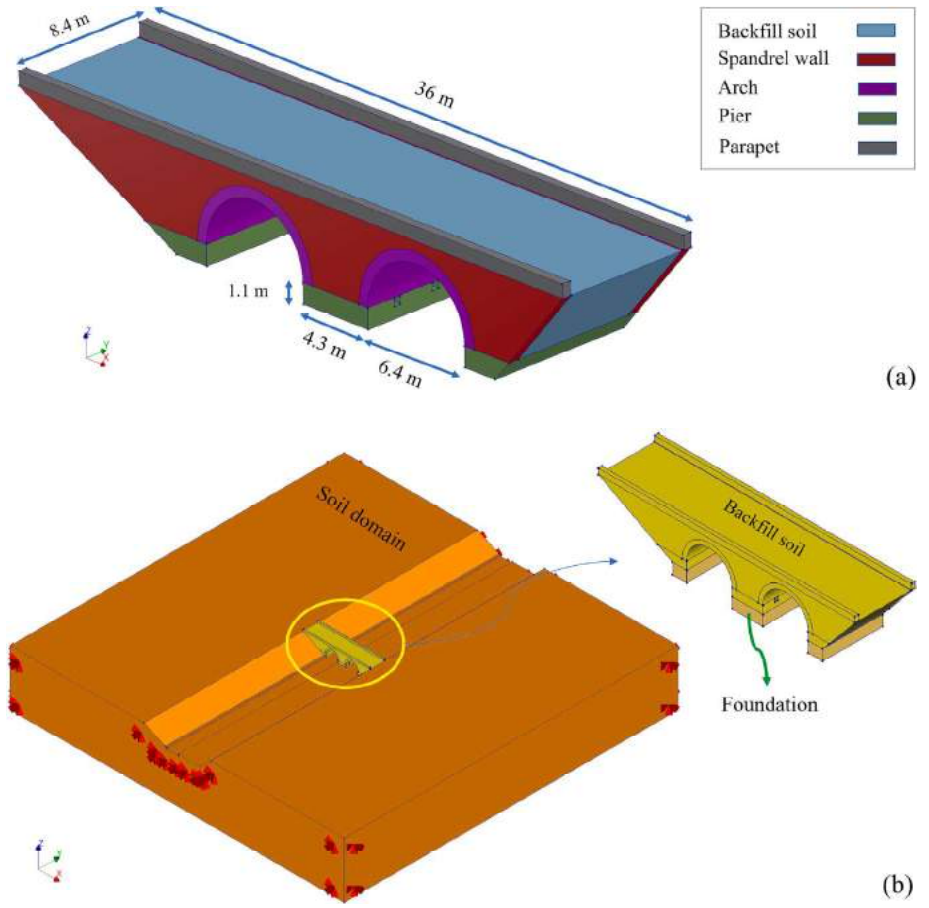

Fig. 4. (a) Fixed-base 3D model with components of the bridge in different colors, and (b) SSI model of Roman bridge.

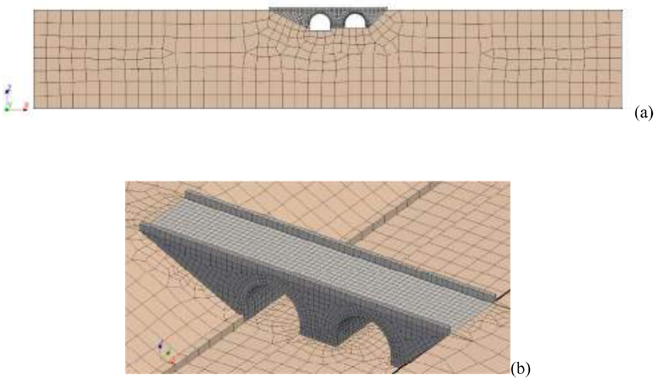

Fig. 5. (a) 3D mesh of the SSI model (b) mesh details of the bridge.

3.2. Initial material properties

The bridge is made of Sfouggaria stone, which is an ancient local stone that was used for the construction of monuments and has a compressive strength (f_b) of 9 MPa [55]. The compressive strength of the homogenized masonry was considered to be 2.503 MPa, calculated based on Equation (1) [56,57], considering soft mortar with compressive strength (f_m) of 1 MPa.

$$f_c = 0.6 f_b^{0.65} f_m^{0.35} \tag{1}$$

The elastic modulus of the masonry was assumed 1001.2 MPa, calculated as 400 times of the f_c [56]. Furthermore, the initial elastic modulus of the backfill soil was assumed to be 0.3 MPa [58]. Hard soil with an elastic modulus of 6 MPa was considered for the soil domain [34]. Note that the density and Poisson ratio of all materials, including the masonry and backfill soil, were considered to be 2200 $\frac{kg}{m^3}$, and 0.3, respectively. Nevertheless, the density of the soil was assumed to be 2000 $\frac{kg}{m^3}$ as suggested in [34].

3.3. Mesh size

Adaptive meshing with a size of 0.6 m was considered for the parapets and backfill soil. After conducting a mesh sensitivity analysis, a mesh size of 0.5 m was used to mesh the spandrel walls and foundations, while a mesh size of 0.4 m was used for the central pier and arches, as shown in Fig. 5. The maximum mesh size of the soil medium was defined based on the following equation [59]:

$$l_{max} \leq \frac{\lambda_{min}}{10} \leq \frac{V_{s,min}}{10 f_{max}} \tag{2}$$

where λ is the wavelength of the passing wave, V_s is the minimum shear wave velocity, and f_{max} is the maximum frequency of interest, typically around 10–15 Hz, as suggested in [59]. A shear wave velocity of 600 $\frac{m}{s}$ for the soil was reported by the responsible partner of the project, and the soil was categorized as hard soil. In order to minimize the maximum size of the mesh elements, 15 Hz was considered for the f_{max}. The maximum mesh size of the soil was set to 4 m, and a finer mesh was considered around the bridge by limiting the mesh size of the edges of the soil part to 2 m, as illustrated in Fig. 5.

The bridge model comprises 13,277 3D mesh elements and 1962 contact interface elements between the backfill and the masonry media. The soil box and the foundations are composed of 49,870 3D mesh

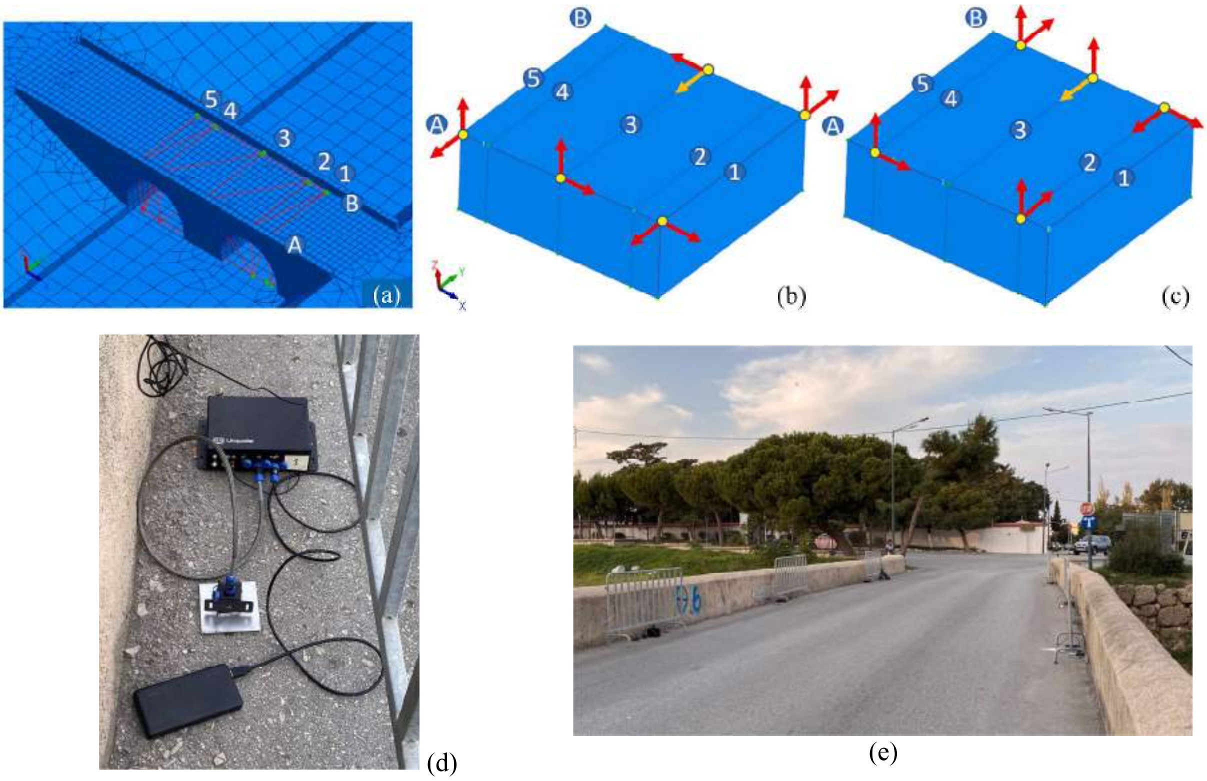

Fig. 6. (a) Optimal sensor locations and sensors' configuration of the (b) first and (c) second test setups. (d) From top to bottom: datalogger, accelerometer sensor, and power bank, and (e) AVT campaign of the Roman Bridge.

elements with 916 contact interface elements to simulate the soil-foundation-structure interaction.

3.4. Ambient vibration testing

After developing the 3D FE model of the bridge with the corresponding material properties for each part, ambient vibration testing was done for modal identification and numerical model calibration.

The accelerometer locations were chosen based on the OSP analyses on the preliminary FE model with the same elastic material properties. The modal assurance criterion (MAC) matrix was considered the acceptance criteria, and five OSP methods were applied to investigate the best sensor locations. The effective independence methods and sensor elimination using MAC are two OSP methods based on the sensor

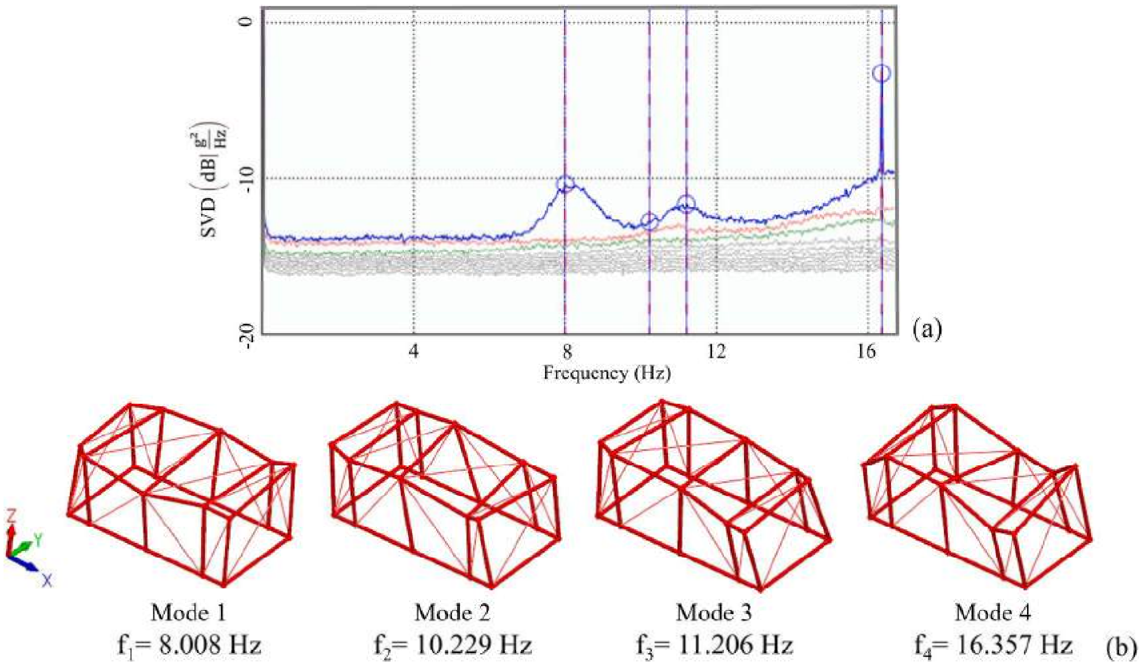

Fig. 7. (a) SVD graph of the FDD method, (b) mode shapes and corresponding frequency values of the first four natural modes of the bridge.

elimination strategies [60]. The MAC matrices of these methods are predominantly diagonal; therefore, these methods reveal the best configuration of the sensors. Therefore, based on the OSP results, the top of the central pier and the locations between the top of the arches and the two endings of the bridge with an approximate distance of 2 m were chosen for installing the sensors. More detail about the procedure can be found in [60].

Fig. 6 (a) shows the optimized locations of the sensors in five rows and on two sides (A and B). Fig. 6 (b) and (c) illustrate the measured direction of the sensors in the first and second test setups. The locations of the outer parts (rows 1 and 5) in the first setup and the inner rows (rows 2 and 3) in the second setup were chosen to install the sensor. However, row 3 was determined to be one of the most important locations prescribed almost by all the OSP analysis results [60]. Row 3, side B in the Y direction, highlighted in Fig. 6 (b) and (c), was selected as the reference measurement direction to combine all the sensors' data from the two test setups.

After determining the best sensor locations, five 3-axis MEMS digital Unquake accelerometers (see Fig. 6 (d) with a sampling rate of 250 Hz were installed on the two sides of the bridge in two test setups. Note that the accelerometers were connected to power banks, as illustrated in Fig. 6 (d), instead of urban electricity to reduce the measurement noise. Because the Z direction of the accelerometer was not sensitive enough to record the ambient vibrations, this direction was neglected from the measurements, and the sensors' data were collected from the two other axes. The data from the sensor in each test setup was synchronized based on the global positioning system (GPS) antenna [34]. Fig. 6 (e) shows the accelerometer sensors installed on two sides of the road.

3.5. Operational modal analysis

Firstly, the fast Fourier transform analysis was performed for each sensor measurement in each direction, and the natural frequency values were detected. To define the mode shapes, all synchronized sensor data from the setups were imported to the ARTeMIS modal software package to perform OMA on a sensor network [61]. Frequency Domain Decomposition (FDD), Enhanced Frequency Domain Decomposition, and Curve-Fitted Enhanced Frequency Domain Decomposition methods are three frequency-domain OMA methods that were employed for the dynamic identification of the bridge [62]. Results reveal a negligible difference between the natural frequency values derived from the three methods mentioned. Fig. 7 (a) depicts the singular value decomposition (SVD) graph of the FDD method and the first four peaks that show the first four natural modes of the bridge. The frequency values and the corresponding mode shapes are illustrated in Fig. 7 (b). The first, third, and fourth modes are predominantly in the Y direction, and the second mode is in the X direction of the bridge.

3.6. Calibration of the model

The objective of the FE model update is to minimize the differences between the natural frequencies of the numerical model and the real structure and to increase the MAC values of the correlated modes by changing the material properties. For this purpose, a sensitivity-based parameter estimation method was utilized using the FEMTools software package [63]. The functional relationship between the parameters and structural modal properties can be expressed in terms of the linear term of a Taylor series expansion as follows:

$$\{\Delta R\} = [S]\{\Delta P\} \tag{3}$$

where ΔR is the difference between a vector containing the reference and predicted system responses, ΔP is the difference between a vector containing the given state and predicted system parameters, and S is the sensitivity matrix. In this paper, a model updating was carried out by minimizing a weighted error (E) according to Equation (4) using the Bayesian parameter estimation expression.

Table 1
The ADF and MAC values of SSI and fixed-base models after calibration.

Model type	FEA Mode	Frequency (Hz)	OMA Mode	Frequency (Hz)	ADF (%)	MAC (%)
SSI model	1	8.343	1	8.007	4.19	71.7
	2	10.462	2	10.22	2.28	66.4
	4	11.222	3	11.206	0.14	70.5
	16	14.926	4	16.357	8.75	60.1
Fixed-base model	1	8.458	1	8.007	5.62	70.4
	2	10.897	2	10.229	6.53	67.2
	3	11.586	3	11.206	3.39	70

$$E = \{\Delta R\}'[C_R]\{\Delta R\} + \{\Delta P\}'[C_P]\{\Delta P\} \tag{4}$$

where C_R and C_P represent weighting matrices expressing confidence in the model responses and parameters, respectively [63]. For the model updating of the bridge, no range was considered for the change of the elastic modulus value [1,23]. To account for the variability of the density and Poisson ratio across different components of the model, a range of 25% was set as the upper and lower bounds for these parameters. But these bounds were not considered for the elastic modulus values.

The absolute difference in natural frequency (ADF) and MAC values of both models is presented in Table 1. The MAC matrices and the correlated mode shapes are presented in Fig. 8 for both models. The bridge was calibrated with a minimum MAC of 60.1% for all four modes of the SSI model. But the fixed-base model could not be correlated to the test results for the fourth mode. Considering the SSI effects that increase the number of parameters, the SSI model has a better correlation with OMA results compared to the fixed-base model. The MAC matrix of the SSI model shows some predominantly soil-contributed modes that can be defined by investigating the mass participation vectors. Therefore, the four first dominant structure modes were paired with the OMA modes in order.

The updated E of each bridge portion is illustrated in Fig. 9 (a). The erosion of the central pier detected through the visual inspection is reported in Fig. 9 (a) by checking the E values of this part, which are relatively low compared to the other masonry parts. Note that the indices R, L, and C represent the location of the section, considering that the left side is the side closest to the stream bed. The terms B and F denote the back and front sides, as illustrated in Fig. 9 (b). The calibrated E values of the central, left, and right foundations are 852.189, 958.79, and 1012.6 MPa, respectively, and the soil elastic modulus is 5470 MPa. The E values of the backfill soil are increased by 55% and 78% for SSI and fixed-base models, respectively, showing that the initial assumption underestimates the stiffness of this part. The updated material properties of each component of both bridge models are presented in Tables A1 and A2 in the appendix.

3.7. Nonlinear model development

The first step towards performing a robust enough seismic evaluation methodology is to define proper nonlinear material behavior. In this light, the total strain-based crack model was utilized to represent the nonlinear behavior of the stone masonry part [47]. Note that the maximum compressive strength of each part was computed as 0.2% of the E value, and the maximum tensile strength was calculated as 15% of the compressive strength based on the empirical rules presented in [56,57]. The fracture energy in compression and tension would be calculated as 1.6 and 0.029 times the maximum compressive strength [56,57]. Fig. 10 depicts the stress–strain curves of the total strain-based crack model. Note that the area under the exponential softening curve is calculated based on the tension fracture energy divided by the definition of the crack bandwidth (h) of an element [47]. For the compression part, the area under the parabolic curve is calculated based on the

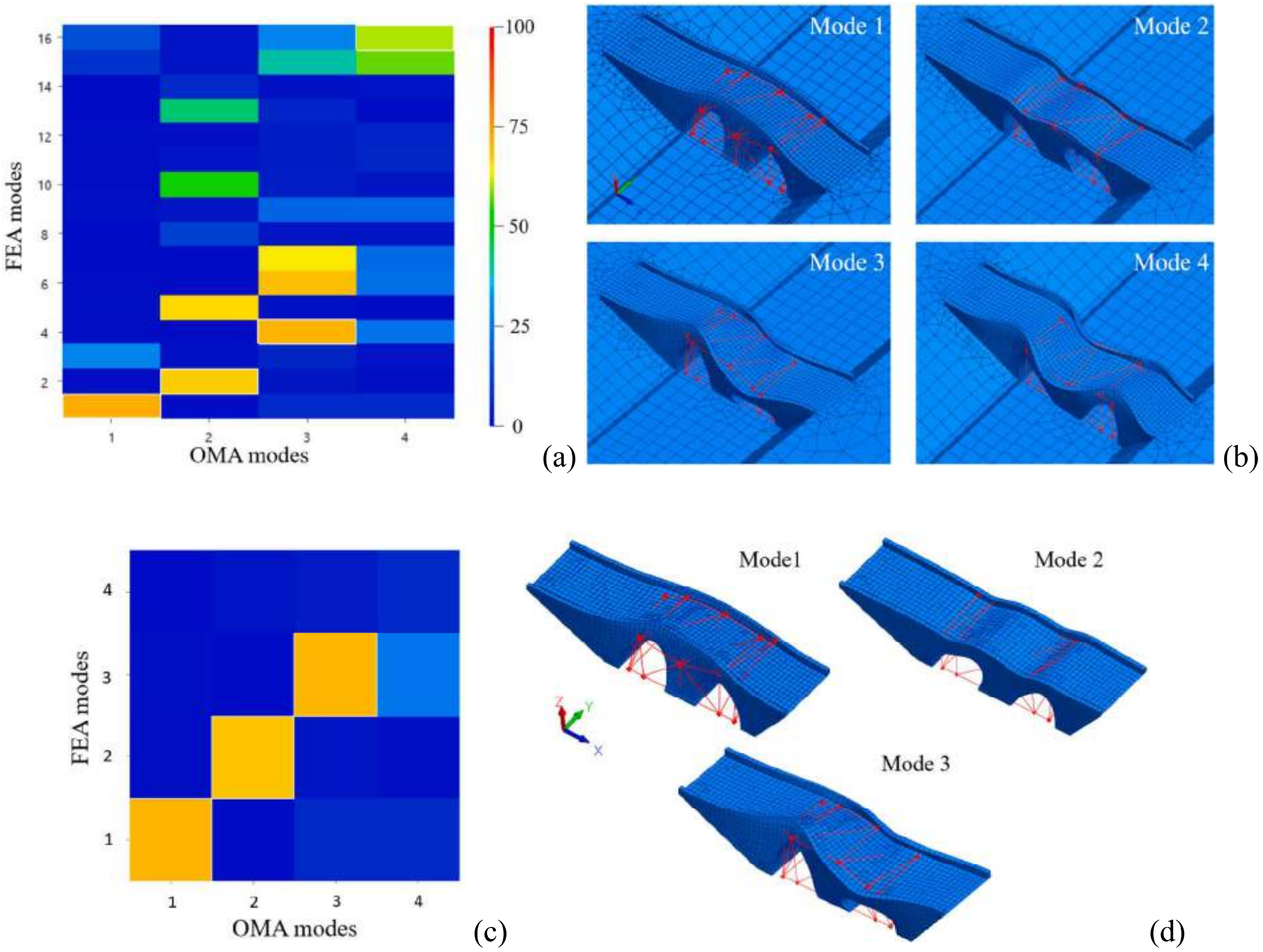

Fig. 8. (a) MAC matrix and (b) mode shape correlations of the SSI model, (c) MAC matrix, and (d) mode shape correlations of the fixed-base model.

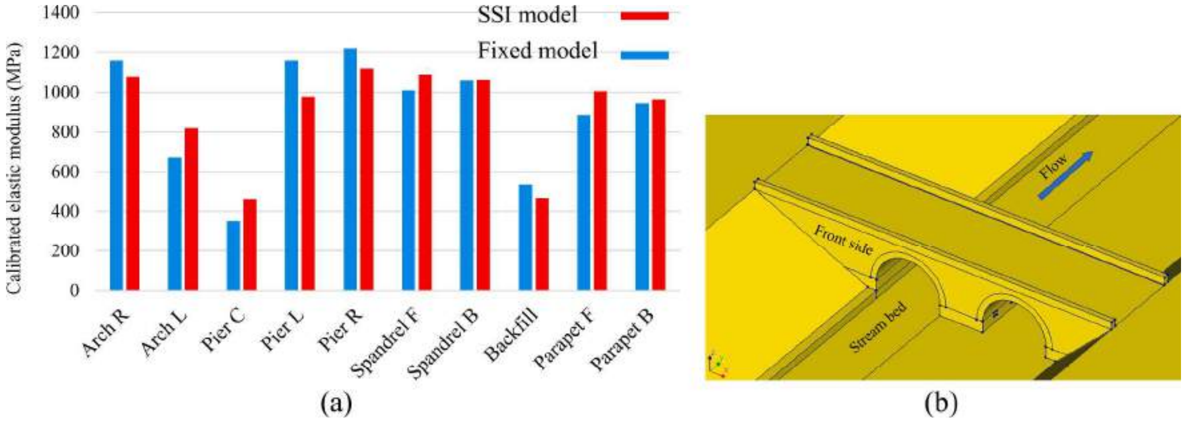

Fig. 9. (a) Updated E values of different parts of the SSI and fixed-base models and (b) stream bed location and the front side of the bridge model.

compression fracture energy divided by h to define the stress–strain curve of the masonry. The shear capacity of the masonry part decreases to zero until the part is sufficiently damaged. The mechanical properties of each bridge component were calculated and presented in the appended Tables A1 and A2. The Mohr-Coulomb material model, which is a simpler material model than the total strain crack model, was chosen to simulate the backfill soil behavior with a cohesion of 0.05 MPa, a friction angle of 0.35 rad, and maximum tensile strength of 0.05 MPa [64].

The soil is simulated based on the Hardin-Drnevich material model, an elastic model with a nonlinear shear stress-shear strain relationship [65]. In the Hardin-Drnevich model, the relationship between shear stress and shear strain is defined by:

$$\tau = \frac{G_{max}\gamma}{1 + \frac{\gamma}{\gamma_r}} \tag{5}$$

where γ and γ_r are shear strain and characteristic shear strain of the soil, and G_{max} is the maximum shear modulus calculated based on:

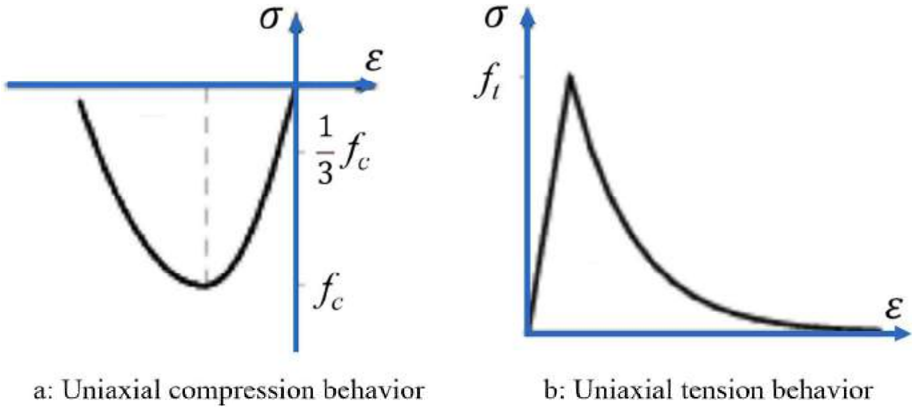

Fig. 10. Stress–strain diagrams of the homogenized stone masonry based on the total strain-based crack for (a) tension and (b) compression.

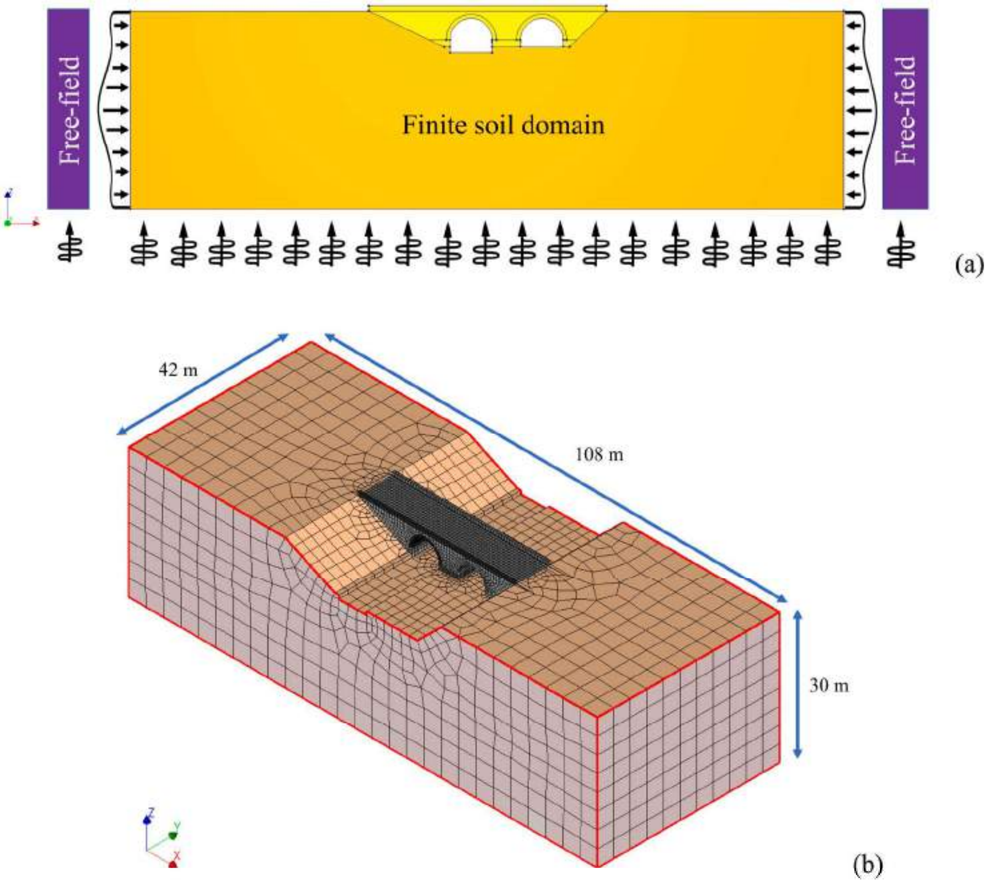

Fig. 11. (a) Schematic representation of the free-field elements and (b) dimension of the SSI model with free-field boundary elements.

$$G_{max} = \frac{E}{2(1+\vartheta)} \quad (6)$$

where ϑ is the Poisson ratio of soil. γ_r was considered 0.0015 for the surrounding soil based on [65].

In geotechnical dynamic problems, considering either rigid or free boundary conditions for the soil leads to unrealistic results. Furthermore, the very large soil domain considered for the SSI model in this study is another strategy that leads to high computational effort for performing nonlinear dynamic analysis. To tackle these limitations, free-field boundary conditions can be utilized by decreasing the size of the soil part. The free-field motions around the soil part are converted into boundary tractions applied to the finite soil part. The free field affects the behavior of the main model, not vice versa. Furthermore, the free-field elements have dashpots to absorb the outgoing waves, which causes unrealistic effects on the main model using rigid boundary conditions [66,67]. Fig. 11 (a) illustrates the schematic representation of the free-field boundary element where compressive loads are applied to the finite soil domain as an example. A new model with dimensions more than three times those of the bridge in the corresponding direction was developed, and free-field elements were assigned to the four sides of the finite soil domain [18]. Note that rigid boundary conditions were applied to the bottom face. The SSI model with free-field elements with dimensions is depicted in Fig. 11 (b). The SSI model with free-field elements was only utilized for performing nonlinear dynamic analysis.

Table 2
Quantitative and qualitative description of three performance levels of masonry arch bridges.

Performance level	Functionality (F)	Life safety (LS)	Near collapse (NC)
Quantitative description	Displacement corresponds to 75% of the maximum base shear (or acceleration)	Displacement corresponds to the first point on the pushover curve with a tangential stiffness equals to 7% of the initial (elastic) stiffness	Displacement corresponds to 90% of the maximum displacement attained on the pushover curve
Qualitative description	Structure is mostly elastic with little or no damage. Traffic is not interrupted, and damage can be repaired in a couple of days	Plasticity starts increasing before and after this performance level. The bridge is expected to suffer medium to significant damage. Still, it should be feasible to repair but cannot be used for a short duration	The damage is heavy and distributed to the extent that the bridge is near to collapse state. The bridge may even be out-of-service or replaced completely

4. Seismic analysis

4.1. Pushover analysis and defining limit states

A predefined performance limit state definition for seismic assessment of masonry bridges in the transverse direction is not available. Thus, a structure-specific methodology based on the nonlinear pushover curve is followed to define the Roman bridge's limit states [68]. In this light, the three performance levels are defined and qualitatively presented in Table 2, and the method for defining the limit state values based on the displacement values of the crown points is elaborated in Table 2. The relationship between performance levels and damage states is shown in Fig. 12 (a). A modal pushover analysis was performed with a load pattern based on the first mode shape, and the pushover curve in terms of displacement of the node between two arches in the parapet element (crown point) versus base shear is plotted in Fig. 12 (b). The limit states are calculated and illustrated in Fig. 12 (b), which are 3.784 mm, 4.983 mm, and 8.387 mm for functionality (F), life safety (LS), and near collapse (NC) limit states, respectively.

4.2. Seismic record selection

Probabilistic seismic hazard analysis (PSHA) is performed based on the SHARE area source model [69] for the bridge site located at

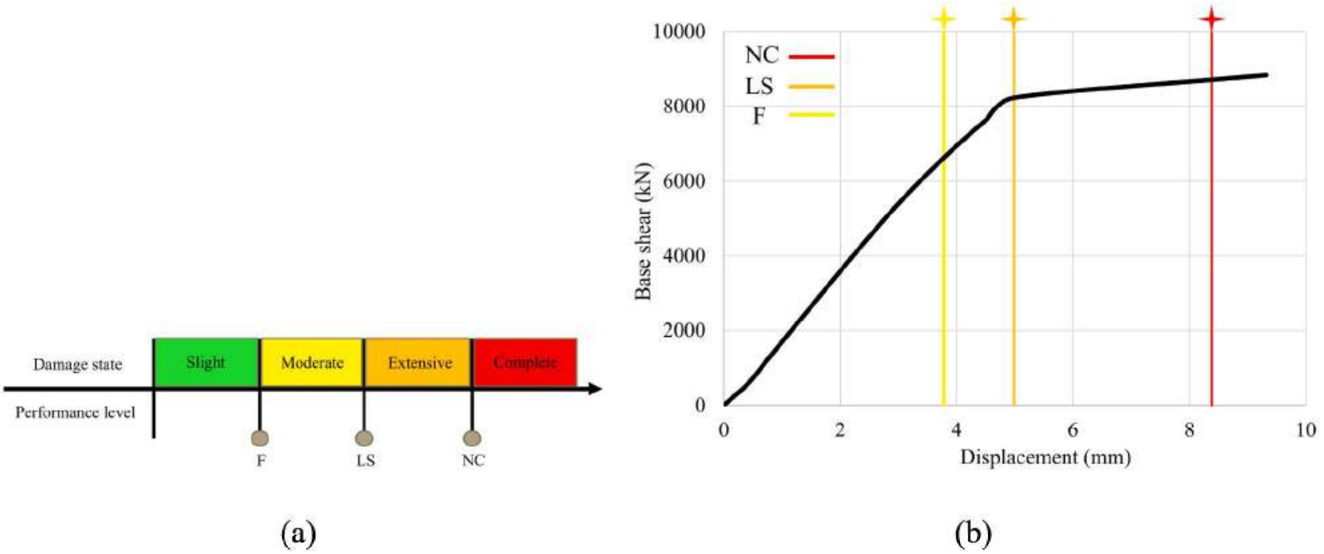

Fig. 12. (a) Relationships between performance levels and damage states, and (b) pushover curve and performance limits of the Roman bridge.

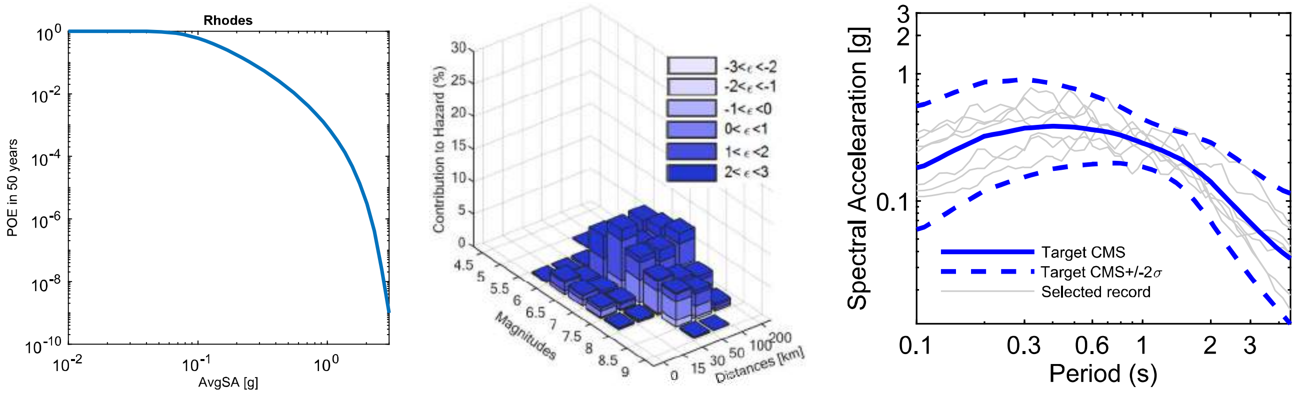

Fig. 13. (a) Hazard curve for AvgSA, (b) Disaggregation of the hazard, and (c) selected records based on the CS record selection approach for the 10% probability of exceedance in 50 years.

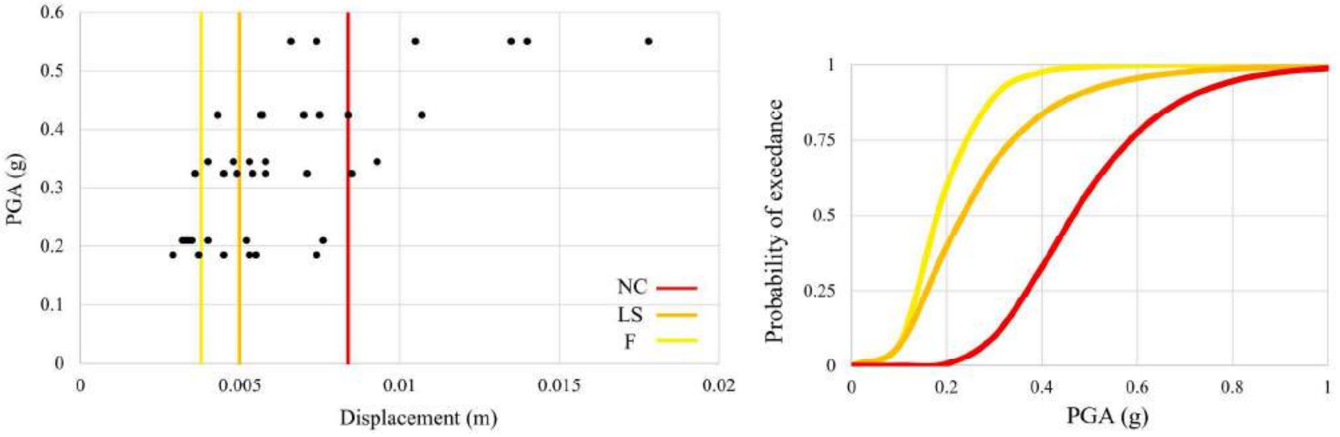

(a) (b)

Fig. 14. (a) MSA results with performance limit values and (b) seismic fragility curves of the case study.

coordinates 28.219°E, 36.439°N. It is assumed that the bridge is located on hard soil with a 600 m/s average shear wave velocity for the top 30 m of the soil (V_{s30}) consistent with the hard soil, which was assumed in the model updating process. The ground motion prediction equation (GMPE) proposed by Boore and Atkinson is used for all purposes of this study, considering all the seismic sources within 200 km of the site [70]. Fig. 13 (a) illustrates the hazard curve at the selected site based on the average spectral acceleration (AvgSA) in the period range of [0.2, 2.0] s with a 0.1 s increment. OpenQuake [71], an open-source software for seismic hazard and risk assessment developed by the Global Earthquake Model Foundation, is used to perform the seismic hazard and disaggregation computations of this study. Fig. 13 (b) shows the disaggregation of the hazard for a 10% probability of exceedance in 50 years.

Five suites of records for five IM levels corresponding to 10.0%, 2.0%, 1.0%, 0.6%, and 0.2% probability of exceedance in 50 years were selected and scaled based on the conditional spectrum (CS)-based method [72]. At each IM level, seven pairs of records from the NGA-West database [73] were selected to match the target spectrum. The selection is based on the approximate method of CS using the mean scenarios from the hazard [74]. Fig. 13 (c) depicts the conditional mean spectrum (CMS) of the seven records selected for the IM level with a 10% probability of exceedance in 50 years as a sample.

In this study, each record was scaled to the median PGA value of its IM records due to the simplicity of using the term PGA instead of AvgSA. This assumption is consistent with the project goal, which is the large-scale seismic assessment of the Rhodes and maintains the hazard consistency of the site.

4.3. MSA and seismic fragility curves

The MSA method is based on the assumption that the response of a structure can be approximated as a series of intervals, or "stripes," each

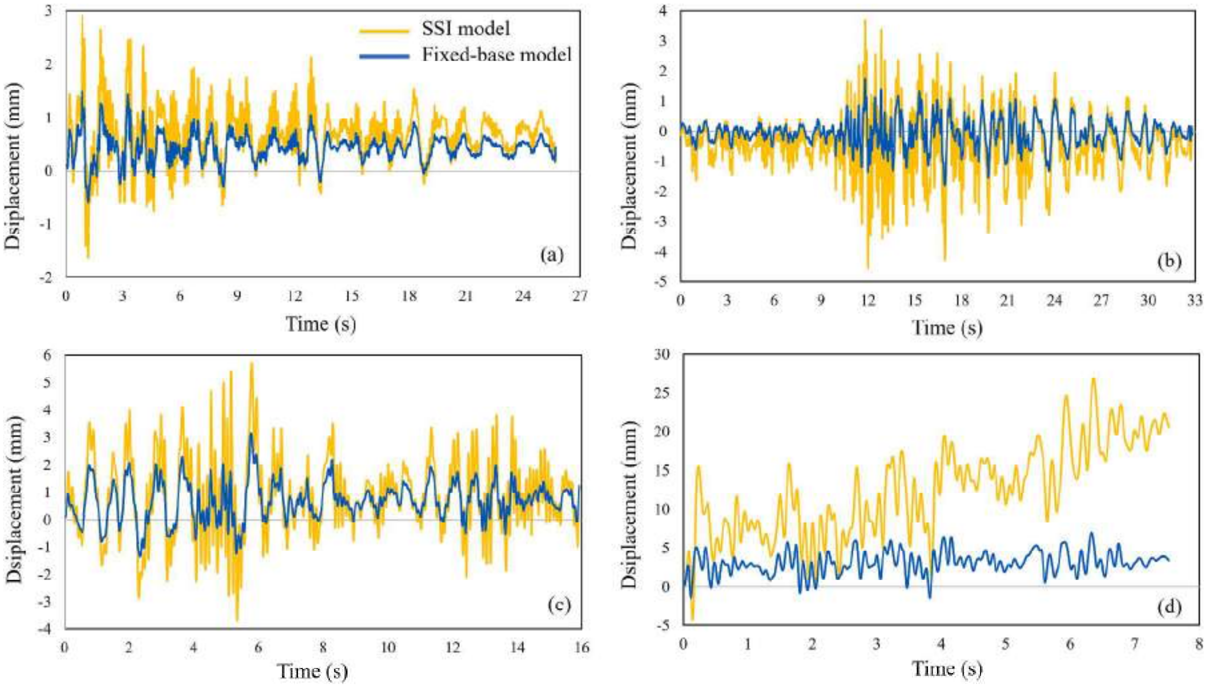

Fig. 15. Displacement response time history of the crown nodes of the models subjected to the seismic records that impose (a) slight, (b) moderate, (c) extensive damages, and (d) complete collapse to the SSI model.

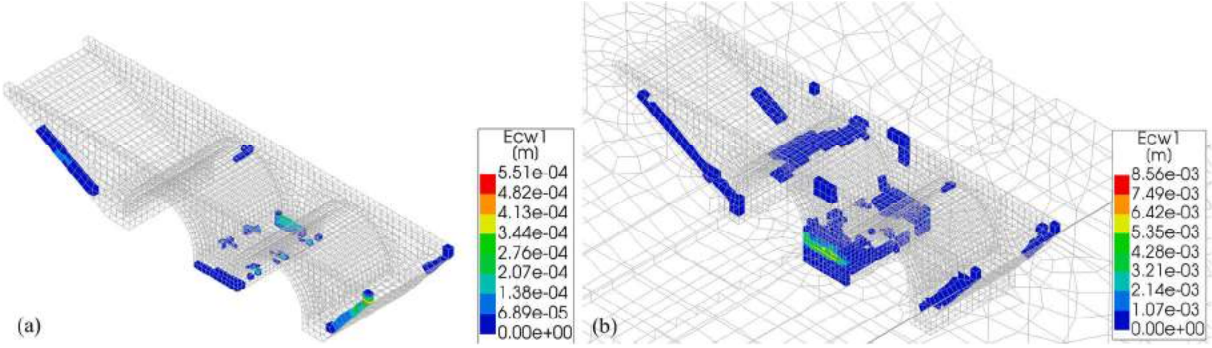

Fig. 16. Crack pattern and width of (a) fixed-base and (b) SSI models subjected to the seismic record that imposed extensive damages to the SSI model.

of which is characterized by a different ground motion intensity level [40]. By means of MSA, the performance of a structure is evaluated under a range of ground motion intensities, from relatively weak events to very strong events, which allows engineers to identify vulnerabilities and develop effective strategies for reducing earthquake risk.

The PGA values of the five seismic record sets were scaled to the PGA values of the selected seismic records based on the CS approach. However, to apply stronger ground motions to evaluate the structure in the complete collapse damage state, the last two record sets with IM levels of 4 and 5 were scaled to PGA, 0.55 g, and 0.67 g, respectively. Therefore, seven groups of records with seven PGA values were applied to the SSI model with free-field boundary conditions, and MSA was carried out [40] considering 5% of the Rayleigh damping ratio for the first and third natural modes in the transverse direction [75]. Note that for the sake of decreasing the level of computational effort, each seismic record was applied to the bridge during the excitation's significant duration.

Fig. 14 (a) illustrates the maximum crown displacement values versus PGA values of each stripe and the three calculated limit states. The crack pattern and width of the models reveal that the central pier is the most critical structural component, and the arches are the second most susceptible members.

The fragility curves' parameters were estimated by maximizing a likelihood function. In other words, the distribution derived from the parameters has the highest likelihood of having produced the observed data from the MSA [41]. The fragility curves were produced for the three limit states and are illustrated in Fig. 14 (b). The probability of complete collapse of the bridge subjected to seismic records with PGA greater than 0.46 g is more than 50%. The results from the fragility curves can be utilized for post-earthquake management strategies at a building or large scale.

4.4. The effect of SSI on the seismic behavior

The effect of SSI on the seismic behavior of the bridge is investigated by comparing the results of the nonlinear time history analysis of the two calibrated models. In this light, four seismic excitations were chosen that impose slight, moderate, and extensive damages and complete collapse with PGA values of 0.18 g, 0.32 g, 0.42 g, and 0.55 g, respectively, based on the MSA. The seismic records were applied to the models to highlight the displacement differences, as illustrated in Fig. 15. The differences are not inevitable, which is drastically high for the ground motion with the highest PGA.

The numerical models at the end of the nonlinear time history analysis that impose extensive damage to the bridge with crack patterns are shown in Fig. 16 as an example. The maximum crack width of the SSI model is 15.5 times bigger than that of the fixed base model. Furthermore, the cracks are limited to the bridge's central pier in the fixed-base model, but in the SSI model, more cracks can be detected in the central pier and the left arch. Therefore, the fixed-base models dangerously underestimate the seismic behavior of masonry bridges in the transverse direction.

Table 3
Material properties of the enhanced stone masonry.

Parameter	Value for the enhanced masonry
Compressive strength (MPa)	3.539
Tensile strength (MPa)	0.531
Elastic modulus (MPa)	1769.5
Fracture energy in compression (for the f_c lower than 12 MPa) (N/mm)	5.662
Fracture energy in tension (N/mm)	0.015

5. Seismic strengthening proposals

The model calibration, the seismic analyses, and the visual inspection show that the central pier and the aches are the most susceptible structural elements of the Roman bridge. Hence, three strengthening strategies are proposed to ensure the bridge's safety during seismic events.

The first strengthening strategy involves removing the backfill and enhancing the arches by replacing the existing stone masonry with Sfouggaria stones with a compressive strength of 9 MPa. The stones would be mounted and connected via lime mortar with a punch test of less than 20 mm and a compressive strength of 4 MPa. The same stone would be chosen to maintain the consistency of the structure. To strengthen the central pier, the vegetation around it would be removed, and the stones around the pier would be replaced and connected via lime mortar with a depth of 0.5 m. Finally, the backfill would be refilled. A FE model labeled "newmat" was developed by modifying the material properties of the arches and the central pier. The compressive strength of the enhanced masonry was calculated as 3.539 MPa based on the mechanical properties of the stone and mortar using Equation (1) [56,57]. The tensile strength was considered 15% of the compressive strength [1], and the elastic modulus, fracture energy in compression, and tension were considered 500, 1.6, and 0.029 times the compressive strength, as suggested in [56,57]. Table 3 shows the material properties of the enhanced stone masonry.

Replacing the stone masonry of the arch and central pier keeps the consistency and respects the authenticity of this historic infrastructure by using the same material. Strengthening the arches with the improved masonry material, like the first strategy, and strengthening the central pier using fiber-reinforced concrete mortar (FRCM) is another strengthening strategy. Strengthening the pier with FRCM systems can be less challenging and more cost-effective than replacing the existing material with improved stone masonry material. Furthermore, low maintenance and high durability are advantages of using FRCM systems for strengthening purposes [76]. However, the texture of the central pier would be changed, and FRCM systems are not in harmony with stone masonry in terms of mechanical properties.

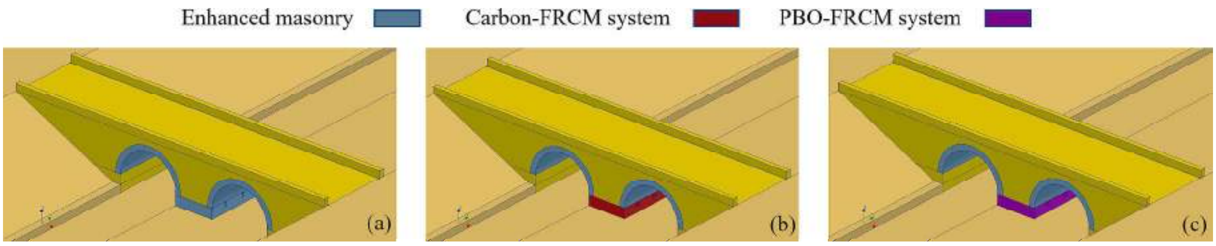

Fig. 17. (a) Newmat and (b) Carbon-FRCM and (c) PBO-FRCM numerical models.

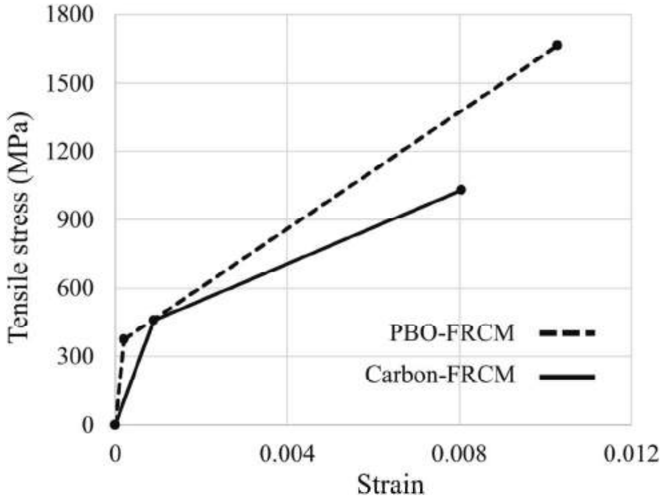

Fig. 18. The stress–strain curve of FRCM systems in tension.

The third strategy involves strengthening the arches with improved masonry material and using a FRCM system to strengthen the central pier. Polyparaphenylene benzobisoxazole (PBO) and carbon FRCM systems [77,78] could be the potential FRCM systems for strengthening the pier element. For this aim, two FE models were made by modeling the Carbon-FRCM and PBO-FRCM layers covering the central pier with a thickness of 0.05 m, as depicted in Fig. 17 (b) and (c).

The phenomenological laws of the FRCM systems associated with the tensile stress–strain curves are presented in Fig. 18 based on [79]. The idealized tensile stress–strain curve is initially linear until the cracking of the cementitious matrix. Then the curve continues until the ultimate capacity. Fig. 18 shows that the elastic modulus maximum tensile strength of PBO-FRCM is larger than that of the carbon-FRCM system. However, the cracking of the cementitious matrix happens sooner in PBO-FRCM systems than in carbon-FRCM systems.

Debonding between FRCM layers and masonry is less probable [80,81]. Therefore, as a simplified assumption, a perfect bond between the FRCM layers and the masonry was assumed in the numerical models [32,78,82]. Modal analysis was performed. The fundamental frequencies of the newmat, PBO-FRCM, and carbon-FRCM models are 10.014 Hz, 10.598 Hz, and 10.554 Hz, respectively. Therefore, the elastic stiffness of the strengthened models is increased by 25%, 32.3%, and 31.8%, respectively.

5.1. Seismic response of the strengthened models

The seismic response of the strengthened models was evaluated by updating the Rayleigh damping factors of the three models to account for changes in their modal properties. The excitations that impose the median displacement demand of the last three stripes were chosen as records (a), (b), and (c) with PGA values of 0.42 g, 0.55 g, and 0.66 g. Record (a) imposes extensive damage to the existing structure excitations, while the other two records force complete collapse.

The excitations were applied to the three strengthened models. The crown displacement time history responses of the three strengthened models and the existing structure model subjected to the three selected seismic excitations are presented in Fig. 19. The displacement time history of the strengthened models showed negligible differences, indicating that the strengthening strategies had effectively improved the seismic behavior of the bridge. Fig. 19 (d) shows the models' maximum displacements, highlighting the improvement in seismic performance.

The results revealed that the efficiency of the strengthening models increased with more intensive seismic excitations. The PBO-FRCM system was found to be the best model with the least maximum displacement among the strengthening models. The differences between the maximum displacements of the PBO- and carbon-FRCM models were negligible. These findings demonstrate the proposed strengthening methods' efficacy in enhancing the bridge's seismic resistance, particularly when subjected to high-intensity seismic events.

The crack patterns and widths of the models were analyzed to assess the effectiveness of the strengthening strategies. The crack patterns and the crack widths of the models are plotted in Fig. 20. The results reveal that cracks would disappear in arches by enhancing the mechanical properties of the masonry part of the arches. The maximum crack width is decreased for all strengthened models, which is significant for the higher intensities, which are records (b) and (c).

The crack patterns in both FRCM-strengthened models were limited to the region between the masonry pier covered with FRCM and the upper part. Cracks with a width of less than 2 mm were observed in this region due to the high stiffness difference between the upper masonry part and the strengthened pier. On the other hand, the cracks in the existing structure model and the newmat model were concentrated in the middle of the central pier.

The crack width of the newmat model was lower than the FRCM-strengthened models subjected to the record (a), with the lowest intensity due to the material consistency. However, with increasing excitation intensities, the crack width of the FRCM models was lower than the newmat model. Among the FRCM-strengthened models, the PBO-FRCM model exhibited the lowest crack width, and differences between the crack widths of the FRCM-strengthened models were not negligible.

Considering the Roman bridge's significance as a cultural heritage asset, enhancing the mechanical properties of the masonry material of the central pier and the arches would be the most appropriate strengthening strategy. This strategy would harmonize with the existing structure, and discontinuities in mechanical properties would not appear. However, employing FRCM systems for strengthening the central pier would change the bridge's texture and appearance. Despite this, the results of the crack width analysis for models subjected to more substantial ground motions demonstrate the effectiveness of these systems in enhancing the bridge's seismic performance.

The results of this part of the study have significant implications for the maintenance and preservation of historic masonry structures such as the Roman bridge. By evaluating and comparing the performance of different strengthening strategies under seismic loads, the study provides valuable insights for engineers and conservationists seeking to ensure the long-term structural stability and safety of such heritage

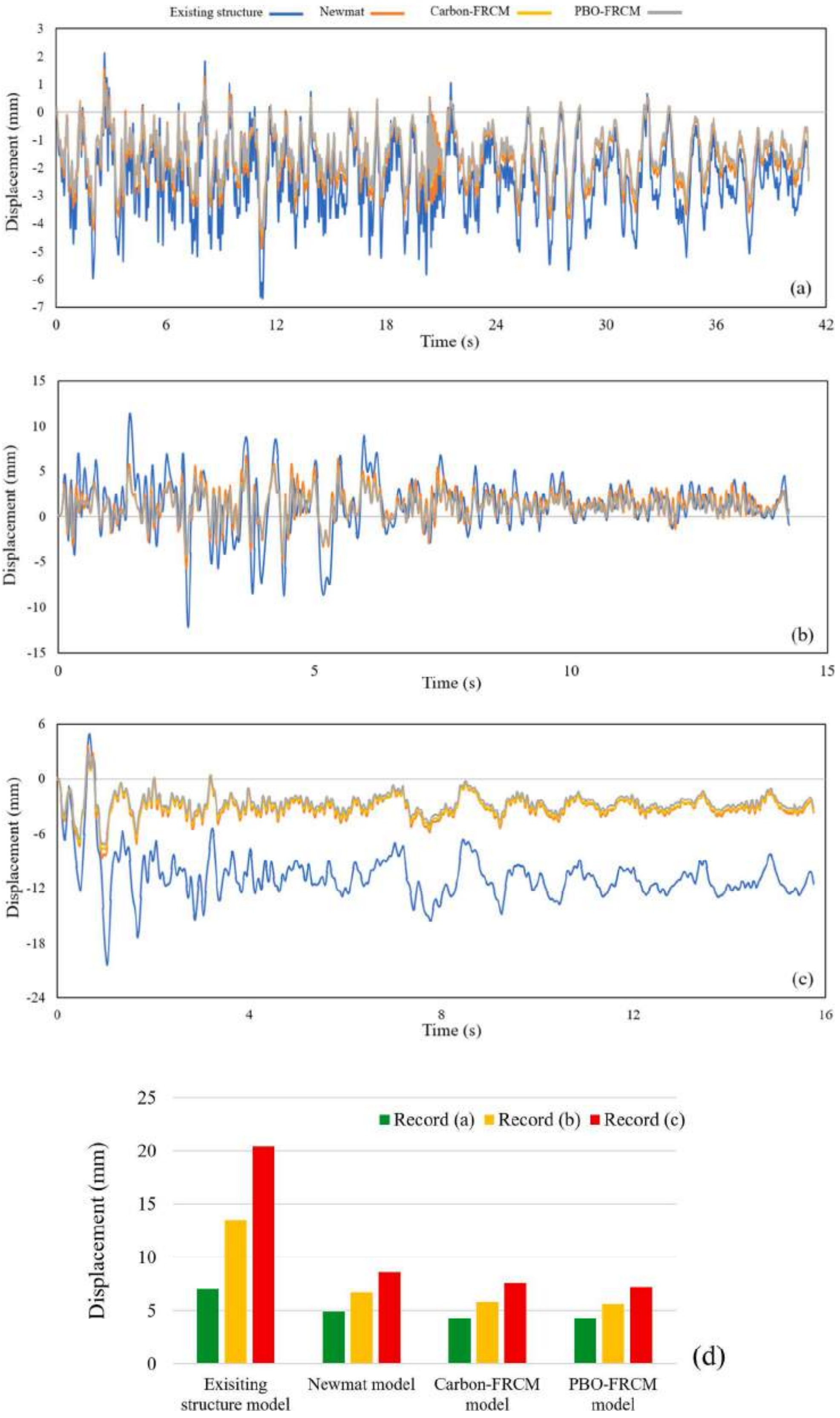

Fig. 19. Displacement time history response of the crown nodes of the SSI and strengthened models subjected to record (a), (b), (c), and (d) maximum displacement values.

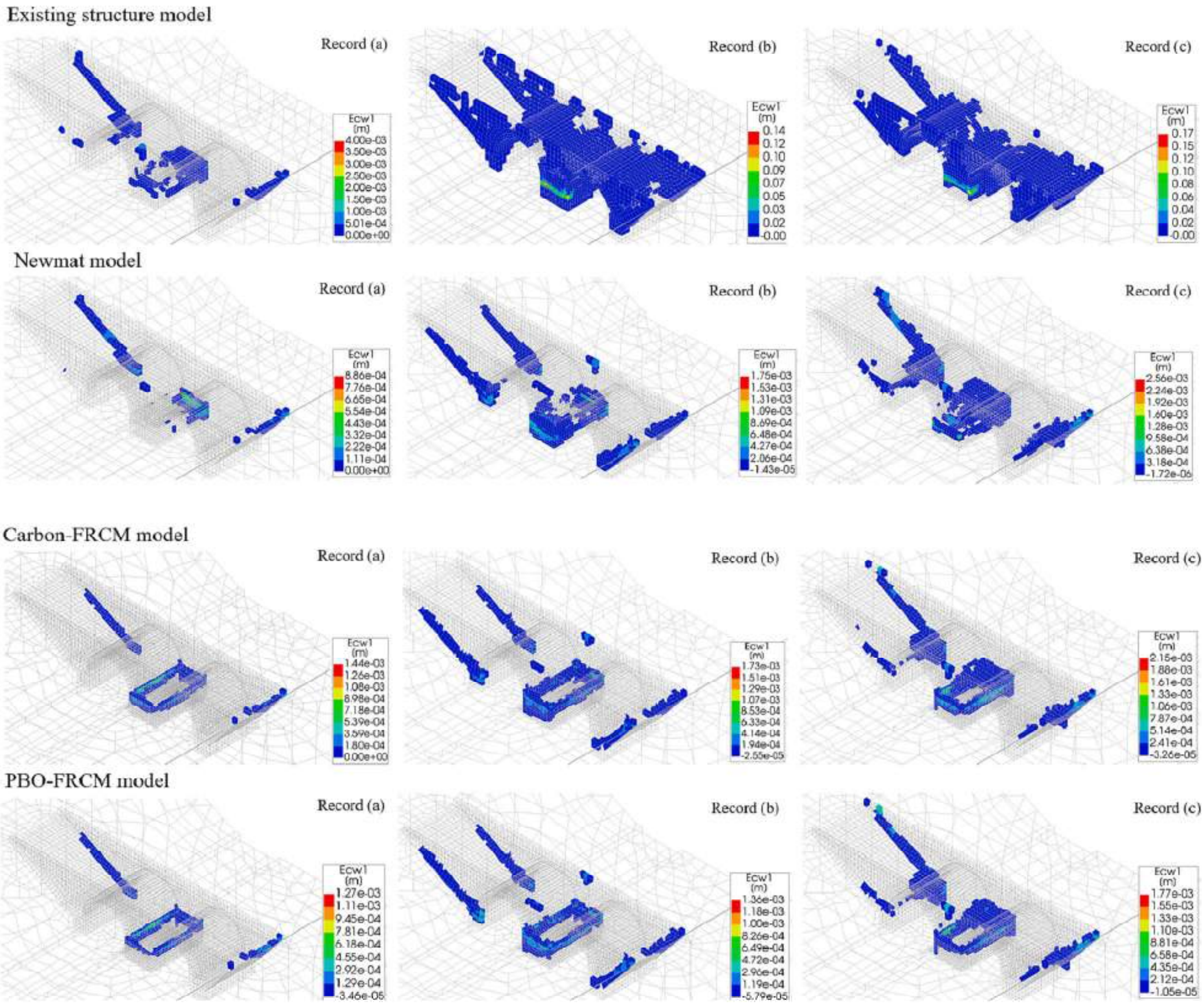

Fig. 20. Crack patterns and width values of the existing structure model and strengthened models subjected to the three chosen seismic excitations.

assets. The findings suggest that using FRCM systems can effectively enhance the seismic resistance of masonry arch bridges without compromising their aesthetic and historical value. However, selecting the most suitable strengthening strategy should be based on a comprehensive assessment of the bridge's existing condition, structural characteristics, and historical significance. In conclusion, this study highlights the importance of a multidisciplinary and collaborative approach to the conservation of cultural heritage structures, considering both technical and cultural aspects.

6. Conclusions

This paper presented a methodology composed of two main steps: geometric documentation and model calibration, resulting in the 3D nonlinear model of a historical stone masonry bridge. Afterward, MSA is performed to define the fragility curves of the case study for three performance levels. Note that two models, SSI and fixed-base models with and without SSI, were developed. Both models were calibrated based on the OMA results. After determining the susceptible parts of the bridge through visual inspection, model calibration, and seismic analysis, three strengthening strategies were proposed, and three models were developed. In the newmat model, the mechanical properties of the masonry of the central pier and arches are improved using Sfouggaria stone and a firmer lime mortar. In the PBO and Carbon–FRCM models, the arches are strengthened using improved masonry, but the central pier is covered with the mentioned FRCM systems.

- The calibration of the models confirms the structural damages to the central pier and arches of the bridge detected based on the visual inspection. The MSA of the SSI model with free-field boundary elements reveals that the damages to the susceptible part are worsened by increasing the seismic intensities.
- Seismic fragility curves are helpful for management strategies and post-earthquake loss estimation at a single structure or on a large scale. The fragility curves of the SSI model show that the probability of complete collapse of the bridge subjected to seismic records with PGA greater than 0.46 g is more than 50%.
- The seismic behavior of SSI and fixed-base models in terms of displacement, crack pattern, and crack width shows that neglecting the SSI effects underestimates the seismic behavior of masonry bridges in the transverse direction.
- A comparative study of the seismic response of the strengthened bridge models subjected to three seismic records reveals that the newmat model would be the best strengthening strategy that improves the seismic behavior of the bridge and satisfies the criteria concerning the strengthening of historic structures. Compared to using FRCM systems to cover and strengthen the central pier, the strengthening strategy with improved masonry keeps the consistency

Table A1
Updated material properties of the SSI model.

Component name	E (MPa)	ρ (kg/m^3)	ϑ	f_c(MPa)	f_t(MPa)	g_{f_c} (N/mm)	g_{f_t} (N/mm)
Arch R	1078.39	1936.39	0.297	2.158	0.323	3.451	0.009
Arch L	818.393	2750	0.291	1.637	0.245	2.619	0.007
Soil	5470.21	1809.92	0.306				
Pier C	462.414	2243.91	0.285	0.925	0.139	1.479	0.004
Pier L	977.554	2195.7	0.302	1.955	0.293	3.128	0.008
Pier R	1118.09	2051.42	0.296	2.236	0.335	3.578	0.009
Spandrel F	1088.86	2192.93	0.306	2.178	0.327	3.484	0.009
Spandrel B	1064.6	2103.73	0.307	2.129	0.319	3.407	0.009
Backfill	466.463	2408.02	0.250				
Foundation C	852.189	2208.05	0.276	1.704	0.256	2.728	0.007
Foundation L	985.79	2200.87	0.3	1.971	0.296	3.154	0.008
Foundation R	1012.6	2200.11	0.301	2.025	0.304	3.24	0.009
Parapet F	1005.45	2093.24	0.3	2.011	0.302	3.217	0.009
Parapet B	963.146	2037.97	0.3	1.926	0.289	3.082	0.008

Table A2
Updated material properties of the fixed-base model.

Component name	E (MPa)	ρ (kg/m^3)	ϑ	f_c(MPa)	f_t(MPa)	g_{f_c} (N/mm)	g_{f_t} (N/mm)
Arch R	1158.35	1650	0.258	2.317	0.348	3.707	0.01
Arch L	670.37	2750	0.263	1.341	0.201	2.145	0.006
Pier C	350.35	2243.93	0.286	0.701	0.105	1.121	0.003
Pier L	1158.27	2193.84	0.299	2.317	0.347	3.706	0.01
Pier R	1222.97	2194.24	0.304	2.446	0.367	3.914	0.011
Spandrel F	1008.29	1980.5	0.306	2.017	0.302	3.227	0.009
Spandrel B	1057.31	1838.88	0.300	2.115	0.317	3.383	0.009
Backfill	534.967	2750	0.225	1.070	0.160	1.712	0.005
Parapet F	884.337	1913.03	0.301	1.769	0.265	2.830	0.008
Parapet B	944.662	1895.6	0.300	1.889	0.283	3.023	0.008

of the structure in harmony with other parts of the bridge without increasing the stiffness significantly and respecting the originality of the historic structure.

- However, FRCM systems can be more cost-effective, durable, and resilient when the structure is subjected to strong ground motions than the improved masonry strategy. The PBO-FRCM system is more effective than the carbon-FRCM system in terms of crack width for strengthening the central pier, although the differences in maximum displacement responses of the crown nodes are negligible.

It is emphasized that, in this paper, a linear material model was considered for the soil part with nonlinear shear stress–strain behavior. Therefore, seismic analysis of the bridge with free-field elements and a nonlinear material model for the soil part would be a future study. An on-site test for investigating the mechanical properties of the soil will improve the authenticity of the work and decrease the uncertainty level of the study. Furthermore, predefined limit state definitions should be defined and presented in seismic assessment codes by performing nonlinear pushover analysis of masonry arch bridges in the transverse direction with different geometries and material properties.

CRediT authorship contribution statement

Amirhosein Shabani: Conceptualization, Methodology, Software, Validation, Formal analysis, Investigation, Resources, Data curation, Writing – original draft, Writing – review & editing, Visualization. **Mahdi Kioumarsi:** Methodology, Investigation, Resources, Writing – review & editing, Visualization, Supervision, Project administration, Funding acquisition.

Declaration of Competing Interest

The authors declare that they have no known competing financial interests or personal relationships that could have appeared to influence the work reported in this paper.

Data availability

The authors do not have permission to share data.

Acknowledgments

This work is a part of the HYPERION project. HYPERION has received funding from the European Union's Framework Programme for Research and Innovation (Horizon 2020) under grant agreement no. 821054. The contents of this publication are the sole responsibility of Oslo Metropolitan University (Work Package 5, Task 2) and do not necessarily reflect the opinion of the European Union. The authors appreciate the comment and supervision of Dr. Dimitrios Vamvatsikos and Dr. Mohsen Kohrangi concerning the seismic record selection and analysis sections. We thank the Ephorate of Antiquities of the Dodecanese for their assistance during the tests.

Appendix A. Calibrated material properties

In this appendix, the calibrated material properties of different components of the bridge are presented for SSI and fixed-base models. Note that E, ρ, g_{f_c}, g_{f_t} refer to the elastic modulus, density, fracture energy in compression, and fracture energy in tension, respectively.

Tables A1 and A2

References

[1] Gönen S, Soyöz S. Seismic analysis of a masonry arch bridge using multiple methodologies. Eng Struct 2021;226:111354. https://doi.org/10.1016/j.engstruct.2020.111354.

[2] Sarhosis V, De Santis S, de Felice G. A review of experimental investigations and assessment methods for masonry arch bridges. Struct Infrastruct Eng 2016;12:1439–64. https://doi.org/10.1080/15732479.2015.1136655.

[3] Helmerich R, Niederleithinger E, Trela C, Bień J, Kamiński T, Bernardini G. Multi-tool inspection and numerical analysis of an old masonry arch bridge. Struct Infrastruct Eng 2012;8:27–39. https://doi.org/10.1080/15732471003645666.

[4] de Felice G. Assessment of the load-carrying capacity of multi-span masonry arch bridges using fibre beam elements. Eng Struct 2009;31:1634–47.

[5] Audenaert A, Fanning P, Sobczak L, Peremans H. 2-D analysis of arch bridges using an elasto-plastic material model. Eng Struct 2008;30:845–55.

[6] Pantò B, Grosman S, Macorini L, Izzuddin BA. A macro-modelling continuum approach with embedded discontinuities for the assessment of masonry arch bridges under earthquake loading. Eng Struct 2022;269:114722. https://doi.org/10.1016/j.engstruct.2022.114722.

[7] Papa T, Grillanda N, Milani G. Three-dimensional adaptive limit analysis of masonry arch bridges interacting with the backfill. Eng Struct 2021;248:113189. https://doi.org/10.1016/j.engstruct.2021.113189.

[8] Lemos JV. Discrete Element Modeling of Masonry Structures. International Journal of Architectural Heritage 2007;1:190–213. https://doi.org/10.1080/15583050601176868.

[9] Saygılı Ö, Lemos JV. Seismic vulnerability assessment of masonry arch bridges. Structures 2021;33:3311–23. https://doi.org/10.1016/j.istruc.2021.06.057.

[10] Milani G, Lourenço PB. 3D non-linear behavior of masonry arch bridges. Comput Struct 2012;110:133–50.

[11] D'Altri AM, Sarhosis V, Milani G, Rots J, Cattari S, Lagomarsino S, et al. Modeling Strategies for the Computational Analysis of Unreinforced Masonry Structures: Review and Classification. Arch Comput Meth Eng 2020;27:1153–85. https://doi.org/10.1007/s11831-019-09351-x.

[12] Reccia E, Milani G, Cecchi A, Tralli A. Full 3D homogenization approach to investigate the behavior of masonry arch bridges: The Venice trans-lagoon railway bridge. Constr Build Mater 2014;66:567–86. https://doi.org/10.1016/j.conbuildmat.2014.05.096.

[13] Zampieri P, Tetougueni CD, Pellegrino C. Nonlinear seismic analysis of masonry bridges under multiple geometric and material considerations: Application to an existing seven-span arch bridge. Structures 2021;34:78–94. https://doi.org/10.1016/j.istruc.2021.07.009.

[14] Simos N, Manos GC, Kozikopoulos E. Near- and far-field earthquake damage study of the Konitsa stone arch bridge. Eng Struct 2018;177:256–67. https://doi.org/10.1016/j.engstruct.2018.09.072.

[15] Anand V, Satish Kumar SR. Seismic Soil-structure Interaction: A State-of-the-Art Review. Structures 2018;16:317–26. https://doi.org/10.1016/j.istruc.2018.10.009.

[16] Zani G, Martinelli P, Galli A, di Prisco M. Three-dimensional modelling of a multi-span masonry arch bridge: Influence of soil compressibility on the structural response under vertical static loads. Eng Struct 2020;221:110998. https://doi.org/10.1016/j.engstruct.2020.110998.

[17] Güllü H, Özel F. Microtremor measurements and 3D dynamic soil–structure interaction analysis for a historical masonry arch bridge under the effects of near- and far-fault earthquakes. Environ Earth Sci 2020;79:338. https://doi.org/10.1007/s12665-020-09086-0.

[18] Bayraktar A, Hökelekli E. Nonlinear soil deformability effects on the seismic damage mechanisms of brick and stone masonry arch bridges. Int J Damage Mech 2021;30:431–52. https://doi.org/10.1177/1056789520974423.

[19] Zani G, Martinelli P, Galli A, Gentile C, Prisco Md. Seismic Assessment of a 14th-Century Stone Arch Bridge: Role of Soil–Structure Interaction. Journal of Bridge Engineering, 2019.24:05019008, doi:10.1061/(ASCE)BE.1943-5592.0001441.

[20] Angjeliu G, Coronelli D, Cardani G. Development of the simulation model for Digital Twin applications in historical masonry buildings: The integration between numerical and experimental reality. Comput Struct 2020;238:106282. https://doi.org/10.1016/j.compstruc.2020.106282.

[21] Tajali M, Ataei S, Miri A, Ahmadi E, Kashani MM. Seismic assessment of a railway masonry arch bridge using sensor-based model updating. Proceedings of the Institution of Civil Engineers - Bridge Engineering.0:1-12, 10.1680/jbren.22.00019.

[22] Bayraktar A, Altunişik AC, Birinci F, Sevim B, Türker T. Finite-element analysis and vibration testing of a two-span masonry arch bridge. J Perform Constr Facil 2010;24:46–52.

[23] Aytulun E, Soyoz S, Karcioglu E. System Identification and Seismic Performance Assessment of a Stone Arch Bridge. J Earthq Eng 2022;26:723–43. https://doi.org/10.1080/13632469.2019.1692740.

[24] Bautista-De Castro Á, Sánchez-Aparicio LJ, Carrasco-García P, Ramos LF, González-Aguilera D. A multidisciplinary approach to calibrating advanced numerical simulations of masonry arch bridges. Mech Syst Sig Process 2019;129:337–65. https://doi.org/10.1016/j.ymssp.2019.04.043.

[25] Altunişik AC, Okur FY, Genç AF, Günaydin M, Karahasan O. Automated Model Updating Effect on the Linear and Nonlinear Dynamic Responses of Historical Masonry Structures. Exp Tech 2018;42:605–21. https://doi.org/10.1007/s40799-018-0271-0.

[26] Yavartanoo F, Kang THK. Retrofitting of unreinforced masonry structures and considerations for heritage-sensitive constructions. Journal of Building Engineering 2022;49:103993. https://doi.org/10.1016/j.jobe.2022.103993.

[27] Valluzzi MR, Modena C, de Felice G. Current practice and open issues in strengthening historical buildings with composites. Mater Struct 2014;47:1971–85. https://doi.org/10.1617/s11527-014-0359-7.

[28] D'Ambrisi A, Focacci F, Luciano R, Alecci V, De Stefano M. Carbon-FRCM materials for structural upgrade of masonry arch road bridges. Compos B Eng 2015;75:355–66.

[29] Zampieri P, Simoncello N, Gonzalez-Libreros J, Pellegrino C. Evaluation of the vertical load capacity of masonry arch bridges strengthened with FRCM or SFRM by limit analysis. Eng Struct 2020;225:111135.

[30] Simoncello N, Zampieri P, Gonzalez-Libreros J, Perboni S, Pellegrino C. Numerical analysis of an FRP-strengthened masonry arch bridge. Frontiers in Built Environment 2020;6:7.

[31] Tao Y, Stratford T, Chen J-F. Behaviour of a masonry arch bridge repaired using fibre-reinforced polymer composites. Eng Struct 2011;33:1594–606.

[32] Bayraktar A, Hökelekli E. Seismic performances of different spandrel wall strengthening techniques in masonry arch bridges. International Journal of Architectural Heritage 2021;15:1722–40.

[33] Behnamfar F, Afshari M. Collapse Analysis and Strengthening of Stone Arch Bridges Against Earthquake. International Journal of Architectural Heritage 2013;7:1–25. https://doi.org/10.1080/15583058.2011.606594.

[34] Shabani A, Feyzabadi M, Kioumarsi M. Model updating of a masonry tower based on operational modal analysis: The role of soil-structure interaction. Case Stud Constr Mater 2022;16:e00957.

[35] Reynders E. System identification methods for (operational) modal analysis: review and comparison. Arch Comput Meth Eng 2012;19:51–124.

[36] Tan Y, Zhang L. Computational methodologies for optimal sensor placement in structural health monitoring: A review. Struct Health Monit 2020;19:1287–308.

[37] Arora V. Comparative study of finite element model updating methods. J Vib Control 2011;17:2023–39.

[38] Mottershead JE, Link M, Friswell MI. The sensitivity method in finite element model updating: A tutorial. Mech Syst Sig Process 2011;25:2275–96.

[39] Shabani A, Kioumarsi M, Zucconi M. State of the art of simplified analytical methods for seismic vulnerability assessment of unreinforced masonry buildings. Eng Struct 2021;239:112280. https://doi.org/10.1016/j.engstruct.2021.112280.

[40] Jalayer F, Cornell C. Alternative non-linear demand estimation methods for probability-based seismic assessments. Earthq Eng Struct Dyn 2009;38:951–72.

[41] Baker JW. Efficient Analytical Fragility Function Fitting Using Dynamic Structural Analysis. Earthq Spectra 2015;31:579–99. https://doi.org/10.1193/021113eqs025m.

[42] Bougia P. Ancient bridges in Greece and Coastal Asia Minor. USA: University of Pennsylvania; 1996.

[43] Pagani M, Garcia-Pelaez J, Gee R, Johnson K, Poggi V, Silva V, et al. The 2018 version of the Global Earthquake Model: hazard component. Earthq Spectra 2020;36:226–51.

[44] Stiros S, Papageorgiou S, Kontogianni V, Psimoulis P. Church repair swarms and earthquakes in Rhodes Island. Greece Journal of Seismology 2006;10:527–37. https://doi.org/10.1007/s10950-006-9035-x.

[45] Shabani A, Skamantzari M, Tapinaki S, Georgopoulos A, Plevris V, Kioumarsi M. 3D simulation models for developing digital twins of heritage structures: challenges and strategies. Procedia Struct Integrity 2022;37:314–20. https://doi.org/10.1016/j.prostr.2022.01.090.

[46] Tapinaki S, Skamantzari M, Anastasiou A, Koutros S, Syrokou E, Georgopoulos A. 3D Holistic documentation of heritage monuments in Rhodes. The International Archives of Photogrammetry, Remote Sensing and Spatial Information Sciences 2021;46:739–44.

[47] DIANA. DIANA FEA, Diana User's Manual, Release 10.4. In DIANA FEA BV, Delft University of Technology, Netherland. 2020.

[48] Anderson JG, Lee Y, Zeng Y, Day S. Control of strong motion by the upper 30 meters. Bull Seismol Soc Am 1996;86:1749–59.

[49] Tabatabaiefar HR, Massumi A. A simplified method to determine seismic responses of reinforced concrete moment resisting building frames under influence of soil–structure interaction. Soil Dyn Earthq Eng 2010;30:1259–67. https://doi.org/10.1016/j.soildyn.2010.05.008.

[50] Güllü H, Karabekmez M. Effect of near-fault and far-fault earthquakes on a historical masonry mosque through 3D dynamic soil-structure interaction. Eng Struct 2017;152:465–92. https://doi.org/10.1016/j.engstruct.2017.09.031.

[51] Torabi H, Rayhani MT. Three dimensional Finite Element modeling of seismic soil–structure interaction in soft soil. Comput Geotech 2014;60:9–19. https://doi.org/10.1016/j.compgeo.2014.03.014.

[52] Kioumarsi M, Plevris V, Shabani A. Vulnerability assessment of cultural heritage structures. In ECCOMAS Congress 2022 - 8th European Congress on Computational Methods in Applied Sciences and Engineering. Oslo, Norway. 2022.

[53] Fanning PJ, Boothby TE. Three-dimensional modelling and full-scale testing of stone arch bridges. Comput Struct 2001;79:2645–62. https://doi.org/10.1016/S0045-7949(01)00109-2.

[54] Homaei F, Yazdani M. The probabilistic seismic assessment of aged concrete arch bridges: The role of soil-structure interaction. Structures 2020;28:894–904. https://doi.org/10.1016/j.istruc.2020.09.038.

[55] Psycharis IN, Avgenakis E, Taflampas IM, Kroustallaki M, Farmakidou E, Pikoula M, et al. Seismic Response of the Temple of Pythian Apollo in Rhodes Island and Recommendations for Its Restoration. In: In. Cham: Springer International Publishing; 2019. p. 160–77.

[56] Ghiassi B, Vermelfoort AT, Lourenço PB. Chapter 7 - Masonry mechanical properties. In: Ghiassi B, Milani G, editors. Numerical Modeling of Masonry and Historical Structures. Woodhead Publishing; 2019. p. 239–61.
[57] CEB-FIP. CEB-FIP Model Code 90, CEB Bulletin D'Information No. 213/214. In. London (UK): May. 1993.
[58] Shabani A, Kioumarsi M, Plevris V. Performance-based Seismic Assessment of a Historical Masonry Bridge: Effect of Pulse-like Excitations. Frontiers of Structural and Civil. Engineering 2023. https://doi.org/10.1007/s11709-023-0972-z.
[59] Kuhlemeyer RL, Lysmer J. Finite element method accuracy for wave propagation problems. Journal of the Soil Mechanics and Foundations Division 1973;99:421–7.
[60] Shabani A, Kioumarsi M. Optimal sensor placement techniques for modal identification of historical masonry structures. Procedia Struct Integrity 2022;42: 147–54. https://doi.org/10.1016/j.prostr.2022.12.018.
[61] SVIBS. ARTeMIS Modal, Structural Vibration Solution. In. Aalborg, Denmark 2022.
[62] Zahid FB, Ong ZC, Khoo SY. A review of operational modal analysis techniques for in-service modal identification. J Braz Soc Mech Sci Eng 2020;42:398. https://doi.org/10.1007/s40430-020-02470-8.
[63] FEMtools. Dynamic Design Solutions, FEMtools 4 user guide. In. Leuven, Belgium. 2021.
[64] Hokelekli E, Yilmaz BN. Effect of Cohesive Contact of Backfill with Arch and Spandrel Walls of a Historical Masonry Arch Bridge on Seismic.
[65] Hardin BO, Drnevich VP. Shear Modulus and Damping in Soils: Design Equations and Curves. Journal of the Soil Mechanics and Foundations Division 1972;98: 667–92. https://doi.org/10.1061/JSFEAQ.0001760.
[66] Nielsen AH. Absorbing boundary conditions for seismic analysis in ABAQUS. In ABAQUS users' conference. 2006. p. 359-76.
[67] Longo M, Sousamli M, Korswagen PA, van Staalduinen P, Rots JG. Sub-structure-based 'three-tiered' finite element approach to soil-masonry-wall interaction for light seismic motion. Eng Struct 2021;245:112847. https://doi.org/10.1016/j.engstruct.2021.112847.
[68] Gönen S, Soyöz S. Reliability-based seismic performance of masonry arch bridges. Struct Infrastruct Eng 2021:1–16. https://doi.org/10.1080/15732479.2021.1918726.
[69] Woessner J, Laurentiu D, Giardini D, Crowley H, Cotton F, Grünthal G, et al. The 2013 European seismic hazard model: key components and results. Bull Earthq Eng 2015;13:3553–96.
[70] Boore DM, Atkinson GM. Ground-motion prediction equations for the average horizontal component of PGA, PGV, and 5%-damped PSA at spectral periods between 0.01 s and 10.0 s. Earthq Spectra 2008;24:99–138.
[71] Pagani M, Monelli D, Weatherill G, Danciu L, Crowley H, Silva V, et al. OpenQuake engine: An open hazard (and risk) software for the global earthquake model. Seismol Res Lett 2014;85:692–702.
[72] Kohrangi M, Bazzurro P, Vamvatsikos D, Spillatura A. Conditional spectrum-based ground motion record selection using average spectral acceleration. Earthq Eng Struct Dyn 2017;46:1667–85.
[73] Chiou B, Darragh R, Gregor N, Silva W. NGA project strong-motion database. Earthq Spectra 2008;24:23–44.
[74] Lin T, Harmsen SC, Baker JW, Luco N. Conditional spectrum computation incorporating multiple causal earthquakes and ground-motion prediction models. Bull Seismol Soc Am 2013;103:1103–16.
[75] Bertolesi E, Milani G, Lopane FD, Acito M. Augustus Bridge in Narni (Italy): Seismic Vulnerability Assessment of the Still Standing Part, Possible Causes of Collapse, and Importance of the Roman Concrete Infill in the Seismic-Resistant Behavior. International Journal of Architectural Heritage 2017;11:717–46. https://doi.org/10.1080/15583058.2017.1300712.
[76] Estevan L, Baeza FJ, Bru D, Ivorra S. Stone masonry confinement with FRP and FRCM composites. Constr Build Mater 2020;237:117612. https://doi.org/10.1016/j.conbuildmat.2019.117612.
[77] Babaeidarabad S, Caso FD, Nanni A. URM Walls Strengthened with Fabric-Reinforced Cementitious Matrix Composite Subjected to Diagonal Compression. J Compos Constr 2014;18:04013045. https://doi.org/10.1061/(ASCE)CC.1943-5614.0000441.
[78] Wang X, Ghiassi B, Oliveira DV, Lam CC. Modelling the nonlinear behaviour of masonry walls strengthened with textile reinforced mortars. Eng Struct 2017;134: 11–24. https://doi.org/10.1016/j.engstruct.2016.12.029.
[79] Arboleda D, Carozzi FG, Nanni A, Poggi C. Testing Procedures for the Uniaxial Tensile Characterization of Fabric-Reinforced Cementitious Matrix Composites. J Compos Constr 2016;20:04015063. https://doi.org/10.1061/(ASCE)CC.1943-5614.0000626.
[80] Bertolesi E, Carozzi FG, Milani G, Poggi C. Numerical modeling of Fabric Reinforce Cementitious Matrix composites (FRCM) in tension. Constr Build Mater 2014;70: 531–48.
[81] Scacco J, Ghiassi B, Milani G, Lourenço PB. A fast modeling approach for numerical analysis of unreinforced and FRCM reinforced masonry walls under out-of-plane loading. Compos B Eng 2020;180:107553.
[82] Tedesco A, Forestieri G. FRCM reinforcement systems in historical masonries of savuto castle, italy. J Archit Eng 2019;25:05019003.